JAERI-M
90-025

NEANDC(J)-149/U
INDC(JPN)-136/L

PROCEEDINGS OF THE 1989 SEMINAR ON NUCLEAR DATA

February 1990

(Eds.) Yutaka NAKAJIMA and Masayuki IGASHIRA*

日本原子力研究所
Japan Atomic Energy Research Institute

JAERI-Mレポートは、日本原子力研究所が不定期に公刊している研究報告書です。
入手の問合わせは、日本原子力研究所技術情報部情報資料課（〒319-11茨城県那珂郡東海村）あて、お申しこしください。なお、このほかに財団法人原子力弘済会資料センター（〒319-11茨城県那珂郡東海村日本原子力研究所内）で複写による実費頒布をおこなっております。

JAERI-M reports are issued irregularly.
Inquiries about availability of the reports should be addressed to Information Division Department of Technical Information, Japan Atomic Energy Research Institute, Tokai-mura, Naka-gun, Ibaraki-ken 319-11, Japan.

編集兼発行　日本原子力研究所
印　　刷　いばらき印刷㈱

JAERI-M 90-025

Proceedings of the 1989 Seminar on Nuclear Data

(Eds.) Yutaka NAKAJIMA and Masayuki IGASHIRA*

Japanese Nuclear Data Comittee
Tokai Research Establishment
Japan Atomic Energy Research Institute
Tokai-mura, Naka-gun, Ibaraki-ken

(Received January 31, 1990)

The 1989 Seminar no Nuclear Data was held at Tokai Research Establishment of Japan Atomic Energy Research Institute, on November 16 and 17, 1989. This Seminar was organized by Japanese Nuclear Data Comittee (JNDC) and Nuclear Data Center, JAERI. In an oral session, review and benchmark tests of JENDL-3 were presented, which were followed by lively discussion. Data need of other nuclear data than neutron induced reaction data were also presented. In addition, several topical talks were given. In a poster session, twenty papers on evaluation and measurement was presented and fruitful discussions were made. In this proceedings, thirty-four papers given in the seminar are compiled.

Keywords: Nuclear Data, Benchmark Test, JENDL, Evaluation, Measurement, Proceedings

* Tokyo Institute of Technology

Program Comittee

Masayuki IGASHIRA (Chairman)	(Tokyo Institute of Technology)
Kazuki HIDA	(Toshiba Corporation)
Yujiro IKEDA	(Japan Atomic Energy Research Institute)
Tomohiko IWASAKI	(Tohoku University)
Norio KISHIDA	(Century Research Center Corporation)
Tsuneo NAKAGAWA	(Japan Atomic Energy Research Institute)
Yutaka NAKAJIMA	(Japan Atomic Energy Research Institute)
Koji OISHI	(Shimizu Corporation)
Keiichi SHIBATA	(Japan Atomic Energy Research Institute)
Masayoshi SUGIMOTO	(Japan Atomic Energy Research Institute)
Junji YAMAMOTO	(Osaka University)

JAERI－M 90－025

1989年核データ研究会報文集

日本原子力研究所東海研究所
シグマ研究委員会
(編)中島　豊・井頭　政之*

（1990年1月31日受理）

1989年核データ研究会は，1989年11月16日と17日の両日，日本原子力研究所東海研究所において開催された。この研究会は，シグマ研究委員会と原研核データセンターによって開かれたものである。JENDL－3の総合的レビューとベンチマークテストの結果が紹介され，活発な討論が行われた。中性子入射以外の核データの要求についても紹介された。さらに，トピックス的な講演もなされた。ポスター発表では，評価や測定に関する20件の報告があり，有意義な議論がなされた。本報文集は，研究会で報告された34件の論文をまとめたものである。

プログラム委員会

井頭　政之（委員長）	（東京工業大学）
肥田　和毅	（（株）東芝）
池田裕二郎	（日本原子力研究所）
岩崎　智彦	（東北大学）
岸田　則生	（センチュリリサーチセンタ（株））
中川　庸雄	（日本原子力研究所）
中島　　豊	（日本原子力研究所）
大石　晃嗣	（清水建設（株））
柴田　恵一	（日本原子力研究所）
杉本　昌義	（日本原子力研究所）
山本　淳治	（大阪大学）

東海研究所：〒319－11　茨城県那珂郡東海村白方字白根2－4
* 東京工業大学

Contents

目　　次

1. Program of the 1989 Seminar on Nuclear Data

November 16(Thuirsday)

		Speaker
	1. Opening Address	
11:00 - 11:05		N.Shikazono(JAERI)
	2. Review of JENDL-3 (I-1)	
	Chairman:A. Zukeran(Hitachi)	
11:05 - 11:15	On Accomplishment of JENDL-3	S.Igarasi(NEDAC)
11:15 - 12:00	Thermal Reactor Benchmark Test of JENDL-3	S.Iijima(Toshiba)
12:00 - 13:10	Lunch	
	3. Review of JENDL-3(I-2)	
	Chairman:A. Zukeran(Hitachi)	
13:10 - 13:55	Review of JENDL-3 Data from Viewpoint of FBR Benchmark Test	Y.Kikuchi(JAERI)
13:55 - 14:25	JENDL-3 FP File	T.Watanabe(KHI)
14:25 - 14:40	Coffee Break	
	4. Review of JENDL-3(II)	
	Chairman:Y. Kanda(Kyushu Univ.)	
14:40 - 15:25	Benchmark Test for Fusion Reactor	H.Maekawa(JAERI)
15:25 - 16:10	Shielding Benchmark Test of JENDL-3	M.Kawai(Toshiba)
16:10 - 16:40	Benchmark Test of JENDL-3 Dosimetry File	M.Nakazawa(Univ. of Tokyo)
	5. Topics(I) Chairman:H.Kitazawa(Tokyo Inst. of Technol.)	
16:40 - 17:25	The Optical Potential for Neutrons and Charged Particles	T.Osawa(Kinki Univ.)
18:00 - 20:00	Reception(at Akogigaura club)	

November 17(Friday)

Speaker

6. Poster Session

9:00 - 10:30 (20 papers were presented)

7. Topics(II) Chairman:I.Kimura(Kycto Univ.)

10:30 - 11:15 Current Topics in Nuclear Fission Research A.Iwamoto(JAERI)

11:15 - 12:00 Topics at the NEANDC Specialists' Meeting on Neutron Activation Cross Sections for Fission and Fusion Energy Applications Y.Ikeda(JAERI)

12:00 - 13:10 Lunch

8. Other Nuclear Data than Neutron Induced Reaction Data
Chairman:N.Yamamuro(Data Eng. Inc.)

13:10 - 13:55 Review of Nuclear Data Required for Nuclear Transmutation Systems of Long-Lived Radioactive Waste Utilizing Particle Accelerators
N.Kishida(CRC)

13:55 - 14:40 Status of the Demand for Charged Particle Nuclear Data
H.Matsunobu(SAEI)

14:40 - 15:20 Compilation of Charged Particle Nuclear Reaction Database and Database Conversion for International Coordination
M.Chiba(Hokkaido Univ.)

15:20 - 15:35 Coffee Break

9. Topics(III) Chairman:M.Baba(Tohoku Univ.)

15:35 - 16:20 Development Plan in JAERI for High Intensity Proton Linear Accelerator
M.Mizumoto(JAERI)

10. Closing Address

16:20 - 16:25 T.Katoh(Nagoya Univ.)

2. Papers Presented in Oral Session

2.1 Review of JENDL-3

2.1.1 On Accomplishment of JENDL-3

Sin-iti IGARASI
Nuclear Energy Data Center
Tokai-mura, Naka-gun, Ibaraki-ken

The third version of Japanese Evaluated Nuclear Data Library, JENDL-3, was accomplished at the end of September, 1989, by the compilation group of JENDL-3 in JAERI/Nuclear Data Center and the members of Japanese Nuclear Data Committee (JNDC). Working groups of JNDC have been still doing some detailed benchmark tests of JENDL-3, in order to comprehend its characteristics. This seminar is going to focus its main subject on this matter, and a part of their results or interim reports will be presented. Prior to proceeding to the main session, a short review of JENDL-3 will be done.

An ad hoc planning committee for JENDL-3 was set up in 1980 to discuss purpose, strategy and contents of JENDL-3. Its final report mentioned, (i) addition of nuclides to those of JENDL-2 should be limited to some important ones for nuclear engineering, (ii) photon production data should be evaluated for several important nuclides, and (iii) nuclear data for fast neutron, in particular, double differential cross section (DDX) should be contained. Following this guideline, evaluation work for JENDL-3 started in 1982.

A preliminary data set, JENDL-3PR1, was made in 1984, replying to requests of the fusion neutronics study group in Japan. Some reports related to JENDL-3PR1 were presented in Santa Fe Conference in 1985, and won good reputation. In 1986, the compilation group of JENDL-3 made a test version of JENDL-3, JENDL-3T, for a preliminary study of benchmark tests for FBR. Interim results of this study were reported in Mito Conference and Jacksonhole Conference in 1988. Merits and defects of the test-version were found out through these studies.

Reflecting on the results of the preliminary studies, JNDC decided to make reevaluation of the data to correct the defects, in

spite of approaching deadline of compilation work for JENDL-3. Finally, compilation of JENDL-3 was attained, including the data of 324 nuclides, 172 of which are fission products.

Through the work of JENDL-3, the compilation group felt that the two preliminary test-version gave confusion to users, because of their unlimited dissemination. Although test-version may be needed, dissemination of the files as well as the results obtained by the preliminary studies should be restricted. The test versions and the preliminary results sometimes pretended to be the characteristics of JENDL-3, and their own defects gave users some wrong impression that JENDL-3 would be worse than JENDL-2. Since it is not easy to relieve such wrong information, preliminary version should be used more carefully.

JNDC should have a review group for evaluated data. The compilation group found in the data compilation work that in a few evaluation some important data might be missed out to be investigated. Such innocent incidents should be detected by the review group before the data compilation work started. The compilation group performed also the part of the data-review for JENDL-3, but a special group should play it in future.

JENDL-3 will be released openly soon. JAERI/Nuclear Data Center and JNDC will make efforts to increase its use, to collect information from users about their use of JENDL-3, and to make future plans of nuclear data evaluation in JNDC.

Recently, international cooperation of nuclear data activities including nuclear data evaluation has been going on, in particular, between JENDL, JEF and ENDF. Since JNDC has its own future plans for nuclear data activities, achievement of the plans should be the first priority in the work of JNDC. However, JNDC must coordinate the plans by considering the international cooperation which will be more and more important to attain the activities of JENDL. The author wishes the international cooperation to bring JENDL to be a data file of wider and higher quality, and JENDL to come to be able to provide the other data files with its sophisticated evaluation.

2.1.2 Thermal Reactor Benchmark Test of JENDL-3

Shungo Iijima
Nuclear Engineering Laboratory, Toshiba Corporation
4-1 Ukishima-cho, Kawasaki-ku, Kawasaki, 210

Thermal reactor benchmark tests of JENDL were performed at JAERI for past several years using two different analysis methods, i.e., SRAC code system and MGCL+KENO-IV system. Tests were made with criticals of highly compact assemblies, low-enriched lattices and aqueous solutions of various concentrations fueled with ^{235}U, ^{239}Pu and ^{233}U. Results of tests are summarized. Main results of tests are :

(1) For aqueous solutions of ^{235}U, ^{239}Pu and ^{233}U, JENDL-3 gives a better trend of K_{eff} versus fuel concentrations than JENDL-2, due to a harder fission spectrum adopted in JENDL-3. This is a strong support to JENDL-3.

(2) However, SRAC results for 235U systems are systematically low by about 1.5 % Δk while the results with MGCL+KENO-IV are in excellent agreement with experimental data. The method dependence must be clarified. For Pu systems of TCA lattices and nitrate aqueous solutions, both methods give consistent results and in good agreement with experimental data.

(3) Lattice parameters of ^{235}U criticals are predicted well with JENDL-3 except that ρ_{28} is overestimated by 5 %. For PROTEUS compact Pu lattices, the lattice parameters are predicted within 5 % except for the F8/F9 of 50 % void case. For very compact $^{235}U/Th$, $^{233}U/Th/D_2O$ moderated ETA cores the lattice parameters are not calculated well.

1. Introduction

For past several years thermal reactor benchmark tests of JENDL-2 and JENDL-3 have been performed by T. Takano and Y. Komuro[1-3] at JAERI with ^{235}U, ^{239}Pu and ^{233}U systems. In some cases ENDF/B-IV and ENDF/B-V were also used to compare with JENDL. In the present paper their results are summarized and discussed. Comparison was also made with the results of tests of ENDF/B files performed in U.S.[4] to draw as general conclusion as possible.

Reactor systems used for testing are the highly enriched bare metal, the compact and loose low-enriched lattices, and aqueous solutions of varying H/Fuel ratios fueled with ^{235}U, ^{239}Pu and ^{233}U. Some of them are of hard neutron spectra with fissions occurring dominantly in epi-thermal or fast energies. We shall discuss here mainly the testing results of well-thermalized systems to draw observations concerning the thermal and epi-thermal nuclear data of JENDL-3.

Takano made calculations with a lattice calculation code, SRAC code,[5] with ANISN in P_1-S_8 approximation or 2-dimensional diffusion theory code. Komuro used 137-group MGCL library[6] and a Monte Carlo criticality code KENO-IV in JACS system[7]. For infinite cell model, SRAC calculation was confirmed to be in good agreement with the calculation by VIM Monte Carlo code using JENDL-2. (Takano, Tsuchihashi, priv. comm.)

It is to be mentioned that most of the benchmark test results quoted here are not yet published. In fact, some results are mutually inconsistent and some seem to be not reasonable when compared with U.S benchmark results using ENDF/B-IV and ENDF/B-V. Therefore, numerical results presented here may not the final ones, pending reconfirmation.

In Sec. 2 thermal cross sections of main fissile and fertile nuclides and fission spectrum data are summarized. In Sec. 3, thermal reactor data used for benchmark test are described. Criticality calculations are presented in Sections 4. Calculated lattice parameters are compared with experimental data in Sec. 5. Comparison was made with the available test results in U.S. Concluding remarks are stated in Sec. 6.

2. Nuclear Data

Table 1 gives the JENDL-2 values and JENDL-3/JENDL-2 ratios of 2200m/s cross sections and infinite dilution resonance integrals for main fissile and fertile nuclides. Yeta values of JENDL-3 are larger than that of JENDL-2 by 0.3 % for U-235 and Pu-239. The Pu-239 resonance integral of JENDL-3 is about 5 % smaller than that of JENDL-2. Hence, the difference between JENDL-2 and JENDL- 3 concerning cross sections for well-moderated thermal reactor is not very significant.

Important difference between JENDL-2 and JENDL-3 for thermal reactors is that of the fission spectrum. U-235 fission spectrum of JENDL-2 and the JENDL-3/ JENDL-2 ratio are shown in Fig. 1. For energies below 100 keV, JENDL-3 gives about 15 % lower spectrum than JENDL-2, while for energies between 2 and 6 MeV JENDL-3 gives about 5 % higher spectrum. This trend is the same for Pu-239 and U-233 fission spectra. It is expected that JENDL-3 will give a lower K_{eff} than JENDL-2 for high leakage system because of a harder fission spectrum. Both libraries will give about the same results for low leakage systems.

3. Thermal reactor benchmark data

References to thermal reactor data used as benchmark are listed in Table 2 classified according to the authors. Tables 3, 4 and 5 give more details of reactor data categorized according to ^{235}U, ^{239}Pu and U/Th/D_2O systems, respectively.

4. Criticalities

Tables 6, 7 and 8 give the summary of calculated eigenvalues for ^{235}U, ^{239}Pu and ^{233}U systems, respectively. Figures 3, 4 and 5 show the eigenvalues of aqueous solutions versus H/^{235}U, H/^{239}Pu and H/^{233}U concentrations, respectively. Present calculation was compared with the results of benchmark test performed in U.S using ENDF/B-IV and B-V when available.

Before discussing the results of testing, the following points are commented.

(a) There are no cases where SRAC system and MGCL+KENO-IV are compared simultaneously. This makes the comparison of the results of both methods somewhat indirect.

(b) The compact lattices and metal spheres are not appropriate for test of thermal nuclear data. We shall not put stress on the results for these assemblies.

(c) For ^{235}U aqueous solutions, anomalous jumps are seen in the plot of K_{eff}'s versus H/^{235}U concentrations, the jumps occurring at the UO_2F_2 solutions given in the report of McNeany & Jenkins (surrounded by parethesis). Takano noted that the convergence of eigenvalue calculation of these cases was extremely slow, the reason being unknown. Hence, these cases were excluded from comparison.

(d) For Pu aqueous solutions, Hardy[4] remarked that there are uncertainties in the specification of Pu concentration. Care may be necessary on the results of the Pu aqueous solutions.

(e) Figure 2 shows the coarse comparison of the experimental data and the simple point model one-group calculation of critical masses and critical radii of bare spheres of U-235 aqueous solutions. In the point model, M^2 was taken as 33 cm^2 from neutron age data for U-water lattice, and the calculated reflector savings of 3.0 cm for bare sphere and 6.5 cm for water reflected sphere independent of H/U concentrations. Though simple in theory, calculation reproduces the feature of experimental data very nicely. This indicates that the systems shown here are well-thermalized ones. It is also understood from the critical radius data that the system of H/U < 1000 has small radius and hence is of high leakage core.

Keeping above points in mind we observe the following points from the results of eigenvalue calculations.

4.1 Criticalities of U-235 assemblies

(1) SRAC (+ANISN or 2D diffusion theory) underestimates the K_{eff} of all ^{235}U systems systematically by about 1 - 1.5 % using JENDL-3 compared with experiments and also with U.S calculation using ENDF/B-V. Results for the early U and UO_2 lattices are discussed in Appendix.

MGCL+KENO-IV gives K_{eff}'s of TCA lattices and water-reflected cylinders of 4.9 w/o enriched UO_2F_2 aqueous solutions in excellent agreement with experimental data. The MGCL results using ENDF/B-V are consistent with U.S. benchmark calculation of TRX lattices. For bare cylinders of UO_2F_2 aqueous solutions, MGCL+KENO-IV underestimates the eigenvalues by nearly 2 % Δk with JENDL-3 and ENDF/B-V. This may be because of an unpredictable effect of the room scattering.

Systematic underprediction with SRAC is difficult to understand. A simultaneous comparison of SRAC and MGCL to clear the

method dependence is the top priority of the next work.

(2) For ^{235}U aqueous solutions, JENDL-3 gives lower K_{eff}'s than JENDL-2 because of a harder fission spectrum of JENDL-3. As leakage becomes small, both files tend to give the same K_{eff}'s.

4.2 Criticalities of Pu-239 assemblies

(1) For Pu systems, both SRAC calculation for aqueous solutions and MGCL+KENO-IV calculation for TCA lattices agree well with experimental data. This is in contrast to the observations for ^{235}U system.

(2) In case of Pu aqueous solutions, all calculations show the trend to give higher K's for lower H/Pu concentration and lower K's for higher H/Pu concentration. Except for the case of H/Pu = 1200, JENDL-3 gives the best trend and values because of a harder fission neutron spectrum.

However, the difference between the eigenvalues calculated with JENDL-2 and JENDL-3 for dilute systems is not understandable. As long as the thermal cross sections are concerned, both libraries are expected to give about the same eigenvalues for well-thermalized systems. The reason should be clarified. Comparison with MGCL+KENO-IV calculation is also recommended.

4.3 Criticalities of U-233 assemblies

For U-233 aqueous solutions, JENDL-3 gives better results and trend than JENDL-2 and ENDF/B-IV, but the average value is about K = 0.985. The K_{eff} of bare metal is overestimated by 3 % Δk.

5. Lattice parameters

5.1 Lattice parameters of U-235 assemblies (TRX-1, TRX-2)

Table 9 shows the comparison of calculation and experiments of lattice parameters of TRX-1 and TRX-2 assemblies. Calculation was made by Takano with SRAC code. Hardy[4] gives the corrected experimental data of δ_{28} as listed in Table 9 instead of the values given by 1974 CSEWG specification. With these corrected values the C/E ratios were improved by about 4 % for both TRX-1 and TRX-2.

5.2 Lattice parameters of Pu assemblies (PTOTEUS cores)

Table 10 and Fig. 6 give the measured and calculation-to experiment ratios of K_∞ and lattice parameters of PROTEUS cores. The variation of K_∞ to voidage represents the void reactivity. This is predicted well with both JENDL-2 and JENDL-3.

Lattice parameters of 6 w/o Pu cores are also predicted well within 5 % except for F8/F9 for 42.5 % void case. The results for 8 w/o cores exhibit different C/E behaviors compared to that for 6 w/o cores, making the judgement difficult. Since PROTEUS cores are not well thermalized, epi-thermal and fast cross sections are playing important roles. Takano made the cell parameter calculation with VIM Monte Carlo code using JENDL-2. The results were in agreement with SRAC within 1 % !. Our general feeling is that both JENDL-2 and JENDL-3 give reasonable results.

5.3 Lattice parameters of U/Th/D_2O assemblies (ETA-1,-2)

Table 11 gives the measured and C/E ratios of lattice parameters of ETA-1 and ETA-2 cores. These cores are of very hard neutron spectra, more than 60 % of fissions occurring epithermally and about 10 % of these above 1 MeV (74Ha).

The agreement between experiment and calculation is not very good, especially for f2/f5 and C2/F5 in ETA-1 and f2/f3 and C2/F3 in ETA-2. In ETA-1, f2/f5 was measured at the center rod of 9-rod cell. Other parameters are the cell-averaged values. Hardy noted that the cell-averaged value of f2/f5 is 6.3 % less than f2/f5 of central rod. This may be a part of the reason of the disagreement between calculation and experiment.

Underestimation of conversion ratios is also seen for the dosimetry data in CFRMF field of Th fission and capture cross sections. The CFRMF experimental data and the C/E ratios are

	Exp.	JENDL-3T	IRDF
232Th(n,f)	19.6 mb(5%)	0.995	0.949
232Th(n,γ)	290 mb(3.7%)	0.863	0.907

6. Concluding remarks

The effort of integral testing of JENDL has been directed hitherto mainly to fast reactors and fusion reactors, not to thermal reactor systems. However, it must be stressed that the the verification of the applicability of JENDL to thermal reactors is very important in gaining its reliability and reputation. This will be more true as the fuel cycle evaluation becomes more important immediate problems.

Concerning criticality calculation, JENDL-3 is in a better shape than JENDL-2, especially for MOX reactors and criticality safety problems. For U-235 systems the most worrying problem is that the criticality calculation depends significantly on the analysis method.

Lattice parameters of TRX-1 and TRX-2 are predicted well except that ρ_{28} is overestimated by 3 - 5 %. Since the conversion ratios are calculated very well (C/E=1.00-1.01), the

overestimation of ρ_{28} is probably not important problem. PROTEUS, ETA-1 and ETA-2 have hard neutron spectrum cores. They pose interesting tests of epi-thermal cross sections. But, at the same time, the benchmark testing with well-thermalized Pu lattices is desirable.

Acknowldegement :

Author is thankful to H. Takano and Y. Komuro at JAERI for communicating unpublished reports of benchmark analysis results. He is indebted to K.Tsuchihasi of JAERI for valuable comments on calculational method. He appreciates M. Yamamoto, M. Ueda and K. Sakurada of Toshiba for discussions of experimental techniques and thermal reactor analysis.

References :

(1) Takano, H., Kaneko, K. : Thermal and Fast Reactor Benchmark Tests of JENDL-3T, Proc. Nuclear Data for Science and Technology, 1988, Mito, p. 521

(2) Takano, H., Komuro, Y. : Benchmark Tests , Thermal and Fast Reactors. Japanese Evaluated Nuclear Data Library Version 3, JENDL-3 , JAES, 31,1190 (1989) (in Japanese)

(3) Komuro, Y. : Nuclear Data News No. 29, 1987
Takano, H. : Nuclear Data News No. 32, 1989

(4) Hardy. J. :ENDF/B data Testing Results for Thermal Reactor Benchmarks, Proc. Thermal Reactor Benchmark Calculations, Techniques, Results and Applications, 1983, BNL, NP-2855, Sec. 16.

(5) Tsuchihashi, K. et al. : JAERI-1285(1983), JAERI-1302(1986)

(6) Naito, Y., Tsuruta, S., Matsumura, T., Ohuchi. T. : MGCL-Processor, A Computer Code System for Processing Multigroup Constants Library MGCL, JAERI-M 9396(1981)

(7) Katakura, J., Naito, Y., Komuro, Y. : Development of the Computer Code System JACS for Criticality Safety, Trans. Am. Nucl. Soc.,41, 329 (1982)

Appendix : On Criticality Calculation of Early U and UO_2 lattices

Early U and UO_2 lattices specified by Strawbridge and Barry have been the great sources of reactor physics data. The calculated cell eigenvalues by SRAC code using JENDL-3 are on the average 0.982(±1%) and 0.990(± 0.8%) for UO_2 and U lattices, respectively, the standard deviation being the average of deviations from the average eigenvalue as shown in Fig. A1.

The averaged eigenvalue is much worse than that calculated by Strawbridge and Barry in 1964. This is insulting.

The dispersion of eigenvalues is quite large particularly in case of UO_2 lattices, reaching to about 5 % Δk at maximum. This indicates that the specifications of these assemblies may not have been proper. Strawbridge and Barry noted that the experimental buckling data of BAW were doubtful in the sense that asymptotic region was not attained. They made PDQ calculation for BAW lattices and obtained K = 0.992 instead of the lattice eigenvalues K = 0.986 for BAW lattices, resulting in a better overall agreement. Hence, a proper selection of experimental data is necessary.

Concerning the underestimation of eigenvalues by 1 - 2 % with JENDL-3, Saji at MAPI noted that the effect of choice of spatial meshes on eigenvalue in SRAC cell calculation is significant. However, according to Tsuchihashi the example cell calculation with Monte Carlo VIM code was in good agreement with SRAC calculation.

Should we give up to consider more about the early criticals as benchmark data because the reactor specifications may be inaccurate for a number of cases, or should we continue the analysis with more effort until we shall get reasonable results ? We may expect the results of re-analysis being made by Saji.

Table 1 Thermal Cross Sections and Resonance Integrals of JENDL-2 and JENDL-3

		ν	σ_f^0(b)	σ_γ^0(b)	I_f(b)	I_γ(b)	η
U-233	J2	2.493	529.8	45.3	771.4	138.6	2.297
	J3/J2	1.000	1.000	1.000	1.001	0.999	1.000
U-235	J2	2.429	583.9	96.0	278.7	153.3	2.086
	J3/J2	1.0029	1.000	1.000	0.987	0.994	1.003
Pu-239	J2	2.881	741.7	270.2	301.5	195.2	2.112
	J3/J2	1.001	1.007	1.000	0.992	0.949	1.003
U-238	J2	-	-	2.70	2.05	279.0	-
	J3/J2	-	-	0.993	1.000	1.000	-

Table 2 References to Thermal Reactor Benchmark Data

Abbrev.	Authors	References and Contents
(65St)	L.E.Strawbridge & R.F.Barry	Nucl.Sci.Eng. 23,58(1965). compilation. early U,UO_2 lattices.
(78Ts)	H. Tsuruta et al.	JAERI-1254(1978) UO_2, MOX lattice
(74Cs)	CSEWG Benchmarks	ENDF-202, 1974 TRX-1,-2, BAPL-UO2 lattice (*) U-235 aqueous solutions Pu aqueous solutions PNL MOX lattice(*)
(65Jo)	Johnson & Kronin	ORNL-3714, Vol. 1(1964) 4.9 w/o enr. U aqueous solutions
(84Ch)	R.Chawla et al.	Nucl.Tech 67,360(1984), 73,296(1984) PROTEUS 6, 8 w/o Pu compact lattice
(74Ha)	J.Hardy, Jr. et al.	Nucl.Sci.Eng. 55,401 (1974) ETA-1,-2
(78Mc)	S.R. McNeany & J.D.Jenkins	Nucl.Sci.Eng. 65,441 (1978). compilation. U-233 aqueous solution U-235 metal sphere

(*) Not used in the present benchmark test.

Table 3 U-235 Benchmark Systems

(1) U and UO_2 lattices

a. 116 U & UO_2 lattices specified by Strawbridge & Barry

Early 61 metallic U and 55 UO_2 lattices.
Lattice specifications and experimental bucklings are given.
U-metal lattices : 1.0-3.0 w/o enr. U metal rod of 0.5-2.3 cm dia., Al clad., , H_2O/U = 1 - 10.
UO_2 lattices : 1.3-4.0 w/o enr. U rod of 0.75-1.5 cm dia., clad with Al,SS-304. H_2O/U = 2.5-10. Some lattices are of H_2O/D_2O mixture, and/or contain 800-4000 ppm B=10.

b. Bettis TRX-1 and TRX-2 lattices specified by CSEWG(74Cs).

Eigenvalues and lattice parameters are given.
1.3w/o enr. U metal rod of 0.387" diameter clad with Al.
V_W/V_F= 2.35 (TRX-1), = 4.02(TRX-2).

c. JAERI TCA UO_2-water lattices by Tsurura(78Ts).

2.6 w/o enr. UO_2/ rod of 1.25 cm dia. clad with Al.
V_W/V_F = 1.5 - 3.0.
Critical water heights for various configurations.

(2) Criticality safety problems

a. U-235 metal bare sphere cited by McNeany and Jenkins(78Nc)

99.99 w/o enr. U-235 metal of 16.4068 cm diameter.
Experiment by Paxton, H.C. : LA-3067-MS, Rev.p.50 (1975)

b. UO_2F_2 aqueous solutions by Johnson & Kronin(64Jo).

4.9 w/o enr. U-235. Bare and reflected cylinders.
H/U = 450-870.

c. UO_2F_2 aqueous solutions by McNeany & Jenkins(78Mc).

High enr. U-235. Bare sphere and cylinder. H/U = 50,1400.
Experiments by Fox, ORNL-2389(1958), ORNL-2609(1958).

d. Highly enriched U nitrate solutions. Bare sphere.(74Cs).
H/U = 27 - 2052.

Table 4 Pu Benchmark Systems

(1) MOX lattice

a. JAERI TCA MOX-water lattices by Tsuruta et al.(78Ts)

3.0 w/o enriched PuO_2-nat UO_2/water lattices.
Pu239/Pu240/Pu241 = 68.2/22.6/7.3
V_W/V_F = 2.4 - 5.55.
Critical water heights for various configurations including water gaps and liquid poison..

b. PROTEUS ($K_\infty \simeq 1$) zoned lattices by Chawla et al.(84Ch).

Average 6 w/o and 8 w/o PuO_2/(PuO_2+depl.UO_2) cores.
Pu239/Pu240/Pu241=80/18/2.
V_F/V_M = 2, highly compact lattice.
Moderated by water or dowtherm(50% void) or 100% void.
K and lattice parameters are given.

(2) Criticality Safety

Pu239 nitrate solutions specified by CSEWG(74CS).

High enr. Pu-239. Bare spheres.
H/Pu-239 = 131 - 1204. Specified by CSEWG(74CSEWG).

Table 5 U/Th/D_2O and U-233 Benchmark Systems

(1) $UO_2/ThO_2/D_2O$ lattice zone in TRX driver by Hardy(74Ha).

Zone diameter = 66 cm, V_M/V_F = 2.
a. ETA-1 : 9-rod cell, 6.7 w/o $235UO_2$-ThO_2, 232Th/235U=15
b. ETA-2 : 4-rod cell, 3.0 w/o $233UO_2$-ThO_2, 232Th/233U=33
Lattice parameters are given.

(2) Criticality Safety

U-233 nitrate aqueous solutions by McNeany & Jenkins(78Mc).
High enr. U-233. Bare spheres.
H/U233 = 0 - 1986. By McNeany and Jenkins(78Mc).

Table 6 ^{235}U Thermal Reactors. Summary of Calculated K_{eff}'s

	ENDF/B-IV	ENDF/B-V	JENDL-2	JENDL-3
U-lattice			0.989*	0.990*
TRX-1	0.988#	0.996#	0.982*	0.983*
TRX-2	0.994#	0.998#	0.986*	0.987*
TCA lattice	0.995$	1.001$		0.998$
^{235}U metal sphere			1.013*	1.013*
UO_2F_2 aqueous solutions(4.9 w/o enr.U-235)				
reflected cyl.	0.988$	0.997$		0.996$
bare cyl.	0.973$	0.984$		0.983$
^{235}U nitrate aqueous solutions				
bare sphere	0.993-1.01#	0.997-1.005#		0.98-0.985*

*) Takano : SRAC+ANISN or 2D diffusion.
$) Komuro : MGCL+KENO-IV
#) Hardy, J. : BNL conf. 1983

Table 7 ^{239}Pu Thermal Reactors. Summary of Calculated K_{eff}'s

	ENDF/B-IV	ENDF/B-V	JENDL-2	JENDL-3
TCA MOX	0.993$	0.996$		0.998$
Nitrate solutions, Bare sphere.				
$H/^{239}Pu$ = 131	1.019#		1.0185*	0.9975*
= 578	1.015#	1.011#	1.014*	0.9955*
= 700	1.022#	1.021#	1.021*	1.002*
= 911	1.009#	1.007#	1.0075*	0.993*
=1204	1.000#	1.000#	0.999*	0.985*

*) Takano : SRAC+ANISN or 2D diffusion.
$) Komuro : MGCL+KENO-IV
#) Hardy, J. : BNL conf. 1983

Table 8 ^{233}U, Th-related Thermal Reactors. Calculated K_{eff}'s

			ENDF/B-IV	JENDL-2	JENDL-3
ETA-1 : $^{235}U/Th/D_2O$+TRX driver				0.996*	0.991*
ETA-2 : $^{233}U/Th/D_2O$+TRX driver				0.999*	0.992*
Aqueous solutions, Bare sphere.					
$H/^{233}U$	= 0	metal	0.967#	1.006*	1.030*
	= 195	nitrate	1.028#	1.037*	0.987*
	= 381	UO_2F_2	1.013#	1.019*	0.9745*
	=1535	nitrate	0.996#	1.008#	0.9915*
	=1986	nitrate	0.991#	0.986#	0.980*

*) Takano : SRAC+ANISN or 2D diffusion.
#) McNeany & Jenkins, (78Mc)

Table 9 Lattice Parameters of TRX-1 and TRX-2.
Experimental Data and Calculation-to-Experiment Ratios.

	Exp.	ENDF/B-IV	EBDF/B-V	JENDL-2	JENDL-3
TRX-1 :					
K	1.000	0.988	0.996	0.982	0.983
ρ_{28}	1.320 +0.021	1.05	1.03	1.04	1.05
δ_{25}	0.0987+0.0010	1.01	1.02	1.01	1.00
F28/F25	0.0946+0.0041	1.01	1.05	1.02	1.06
C28/F25	0.797+0.008	1.01	1.00	1.01	1.01
TRX-2 :					
K	1.00	0.994	0.998	0.986	0.987
ρ_{28}	0.387+0.016	1.03	1.01	1.02	1.03
δ_{25}	0.0614+0.0008	0.99	1.00	0.99	0.99
F28/F25	0.0693+0.0035	0.98	1.01	0.99	1.03
C28/F25	0.647+0.006	1.00	0.99	1.00	1.00

Note :
(1) #)Hardy, J. : Ref.4, *)Takano, H. : SRAC+2D diffusion calculation.
(2) ρ_{28} = C28(epi-Cd)/C28(sub-Cd)
δ_{25} = F25(epi-Cd)/F25(sub-Cd),
F25,F28 and C28 are the macroscopic fission and capture rates.

Table 10 Lattice Parameters of PROTEUS Cores
Experimental Data and Calculation-to-Experiment Ratios

		6-w/o Pu Core			8-w/o Pu core		
Void,%		0 %	42.5 %	100 %	0 %	42.5 %	100 %
K_∞	Exp	1.045(1.1)	0.991(1.5)	0.905(0.8)	-	-	-
	J-2	0.999	0.990	0.989			
	J-3	1.002	0.995	1.009			
C28/F49	Exp	0.0691(2.2)	0.0874(2.0)	0.148(1.5)	0.0748(3)	0.0939(2.8)	0.144(2)
	J-2	0.976	1.002	1.036	1.055	1.044	1.031
	J-3	0.980	1.008	1.023	1.060	1.050	1.017
f28/f49	Exp	0.00987(2.5)	0.0111(2.3)	0.0193(2.0)	0.0119(2.8)	0.0141(2.6)	0.0222(2.4)
	J-2	1.006	1.072	1.027	1.064	1.055	1.008
	J-3	1.043	1.109	1.074	1.104	1.094	1.058
f25/f49	Exp	0.988(2.0)	1.032(1.8)	1.091(1.5)	0.946(2.1)	1.050(1.8)	1.056(1.7)
	J-2	0.996	1.055	1.043	1.055	1.063	1.066
	J-3	0.993	1.051	1.011	1.051	1.059	1.037
f41/f49	Exp	1.78(4.5)	1.75(3.5)	1.46(2.5)	1.887(3.1)	1.959(2.7)	1.624(2.4)
(f_{23}/f_{49})	J-2	0.949	1.040	1.008	1.035	1.064	0.974
	J-3	0.957	1.054	1.011	1.044	1.070	0.986

Note (1) Infinite cell model caluclation by SRAC.(Takano, H.)
(2) Number in parenthesis is the experimental error in %.
(3) f (small character) is the microscopic reaction rate (/atom).
F and C (capital letter) are the macroscopic reaction rate.
(4) For 8 w/o Pu core, f41/f49 means f23/f49 ratio.

Table 11 Lattice Parameters of ETA-1 and ETA-2 Cores
Experimental Data and the Calculation-to-Experiment Ratios

	Expe riment	JENDL-2	JENDL-3
ETA-1 : (6.7w/o ^{235}U.)			
ρ_{02}	10.54+0.15	0.96	0.98
δ_{25}	1.74+0.02	1.05	1.04
δ_{02}	0.0166+0.0009	0.81	0.84
C02/F25	0.867+0.009	0.92	0.96
ETA-2 : (3.0w/o ^{233}U)			
ρ_{0}	8.89+0.15	0.94	0.95
δ_{23}	2.96+0.08	1.04	1.03
δ_{02}	0.0181+0.0014	0.94	1.05
C02/F23	1.047+0.002	0.89	0.93

Note
(1) Calculation by SRAC+2D diffusion theory with TRX-driver.
(2) ρ_{02} : Th-238 epi-Cd/sub-Cd capture rate ratio.
δ_{25} : U-235 epi-Cd/sub-Cd fission rate ratio.
δ_{02} : microscopic fission rate ratio of Th-232 to U-235.
δ_{02} : microscopic fission rate ratio of Th-232 to U-233.
C02/F25 : macroscopic ratio of Th-232 capture to U-235 fission.
C02/F23 : macroscopic ratio of Th-232 capture to U-233 fission.

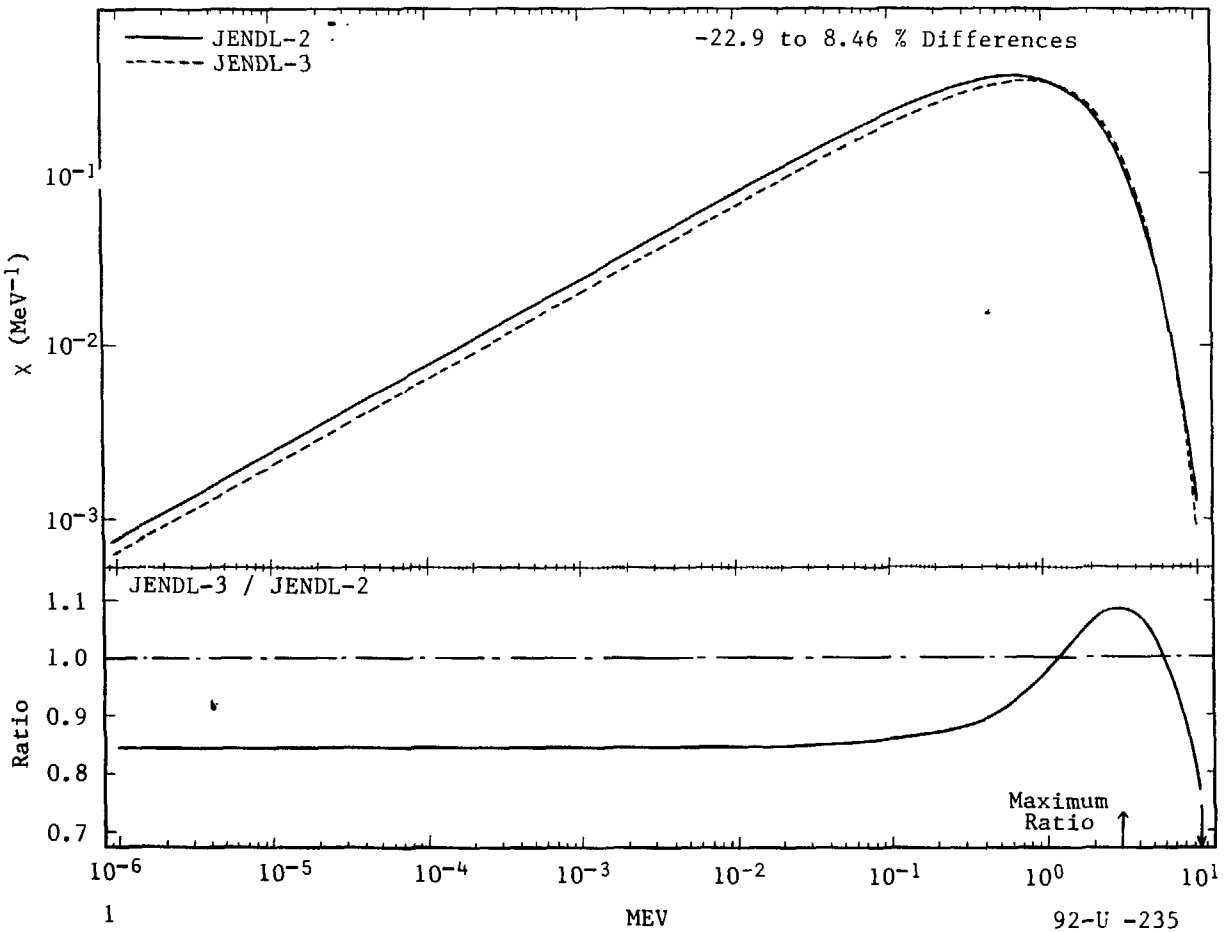

Fig. 1 U-235 fission spectrum of JENDL-2 and the JENDL-3/JENDL-2 ratio

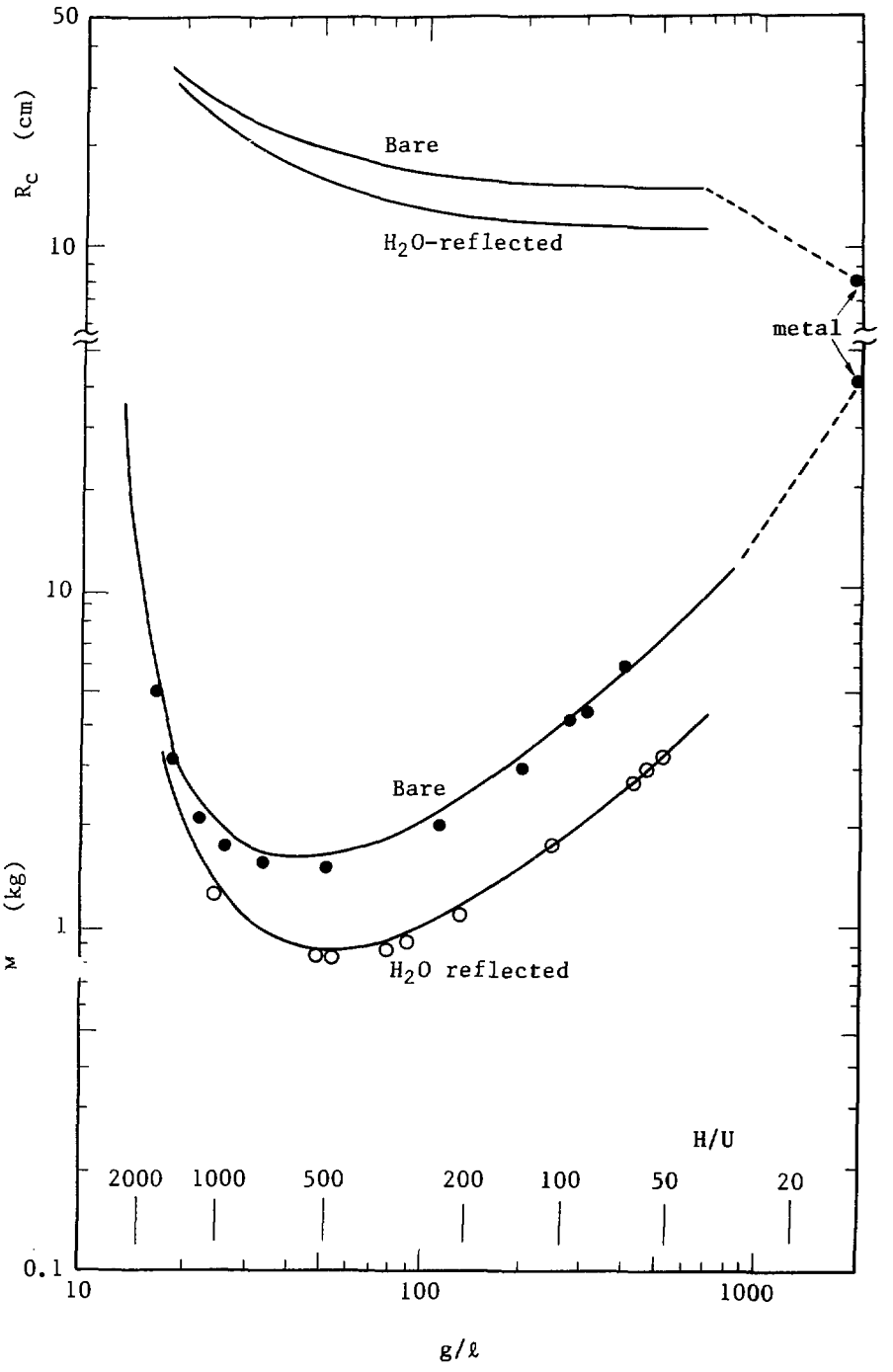

Fig. 2 Critical masses and critical radii of bare and water-reflected U-235 aqueous solutions. Solid line is the simple point model one-group calculation.
Solid and white circles are experimental data.

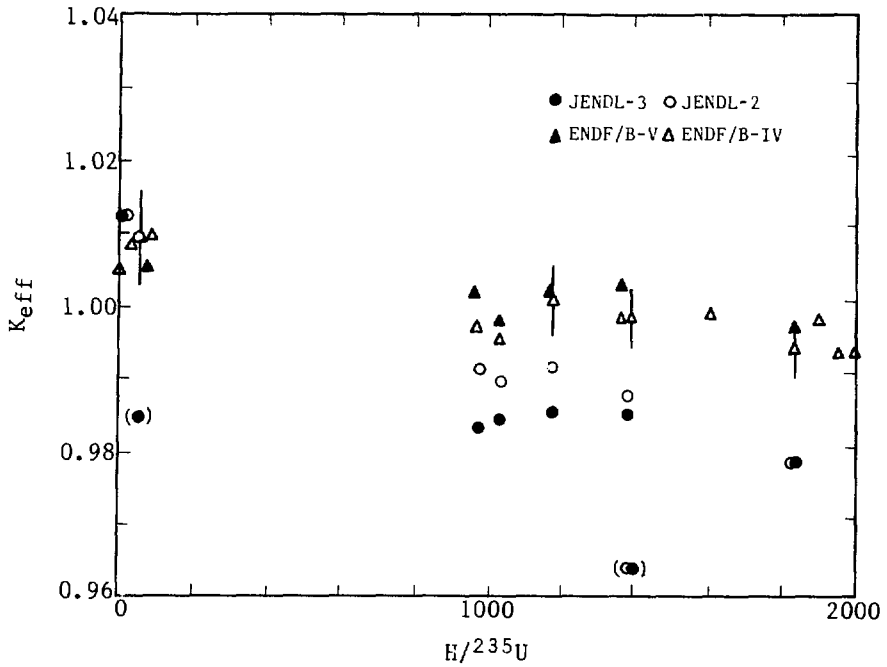

Fig. 3 Effective multiplication factors of bare spheres of ^{235}U nitrate aqueous solutions.
SRAC+ANISN calculations (Takano, H.) are shown by circles, and U.S benchmark results by triangles. The circles in parentheses are for the UO_2F_2 solutions specified by McNeany and Jenkins.

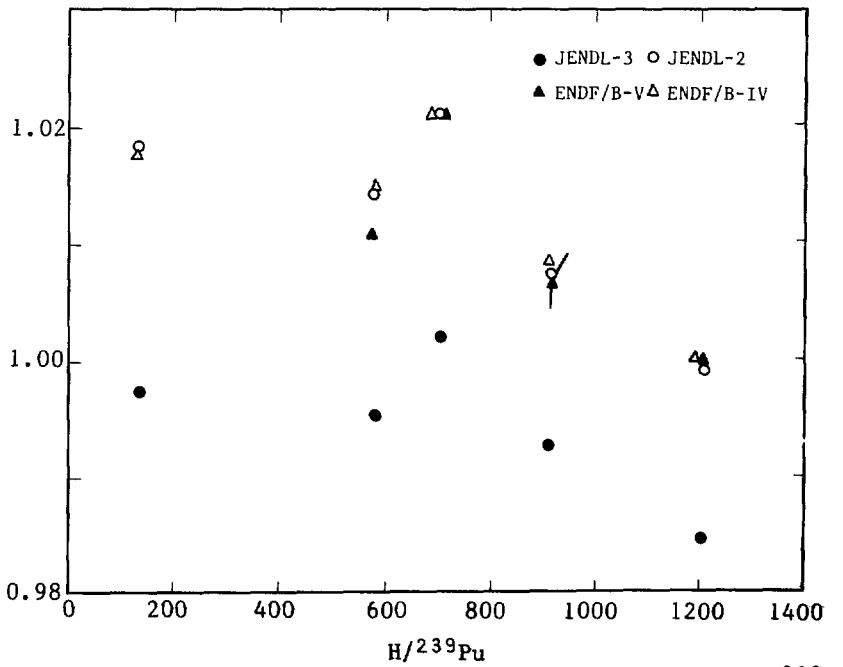

Fig. 4 Effective multiplication factors of bare spheres of ^{239}Pu nitrate aqueous solutions.
SRAC+ANISN calculations (Takano, H.) are shown by circles, and U.S. benchmark results by triangles.

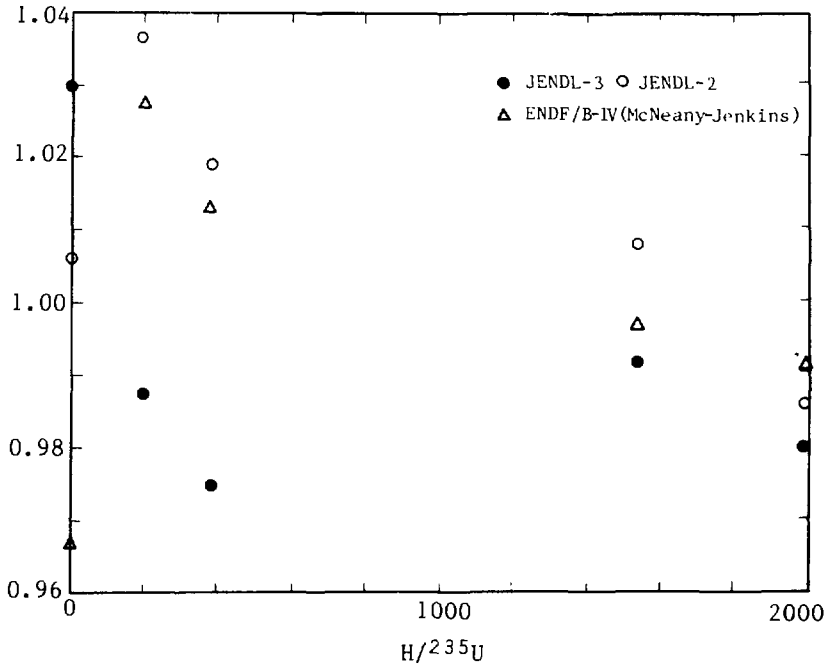

Fig. 5 Effective multiplication factors of bare spheres of ^{233}U nitrate aqueous solutions. Calculation with SRAC+ANISN (Takano, H.) are shown by circles. Calculation by McNeany and Jenkins using ENDF/B-IV is given by triangle points.

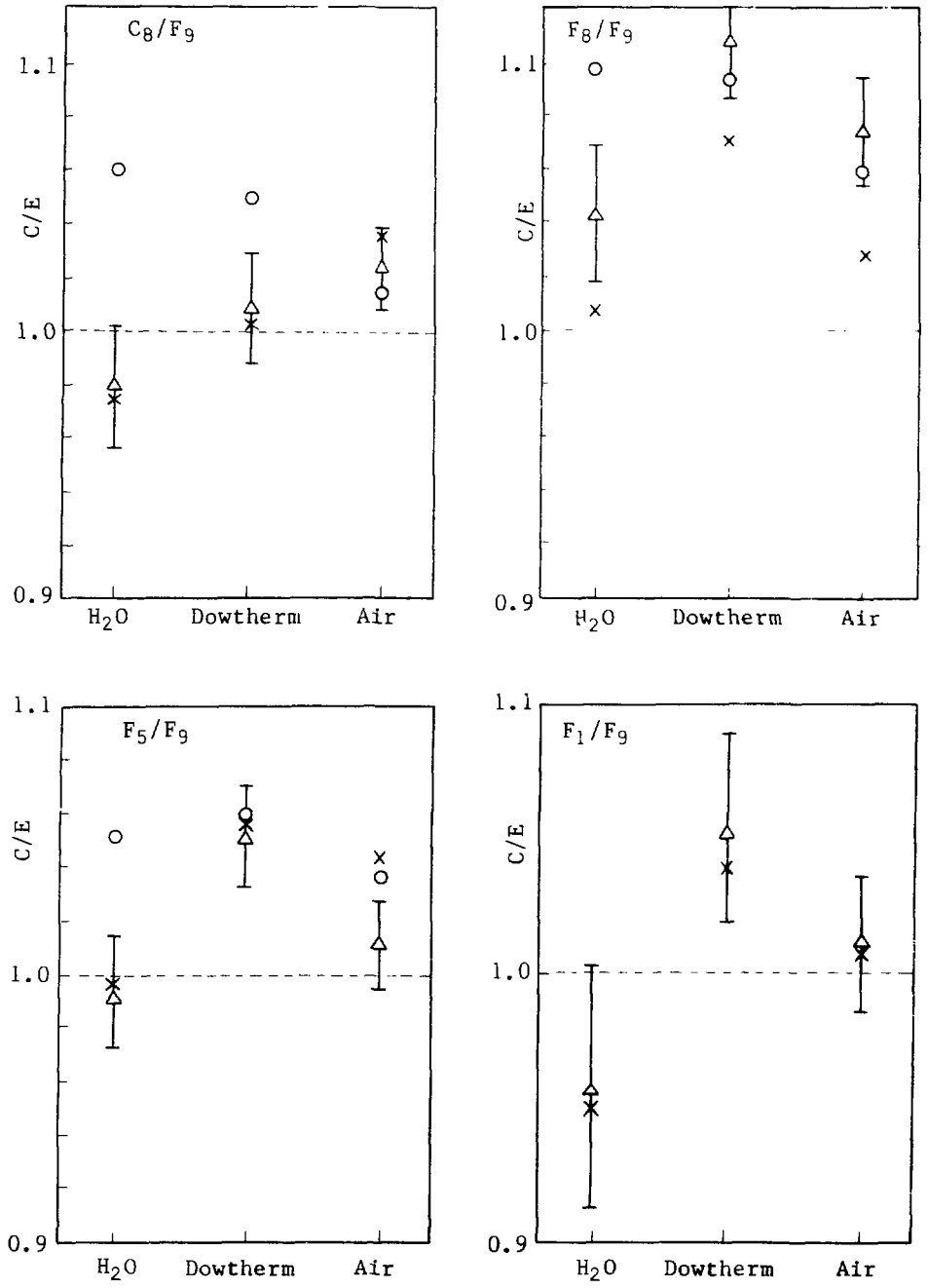

Fig. 6 The calculation-to-experiment ratios of lattice parameters of PROTEUS core.
Calculation with SRAC code by Takano, H.
6w/o Pu core: Δ (JENDL-3), × (JENDL-2).
8w/o Pu core: o (JENDL-3)

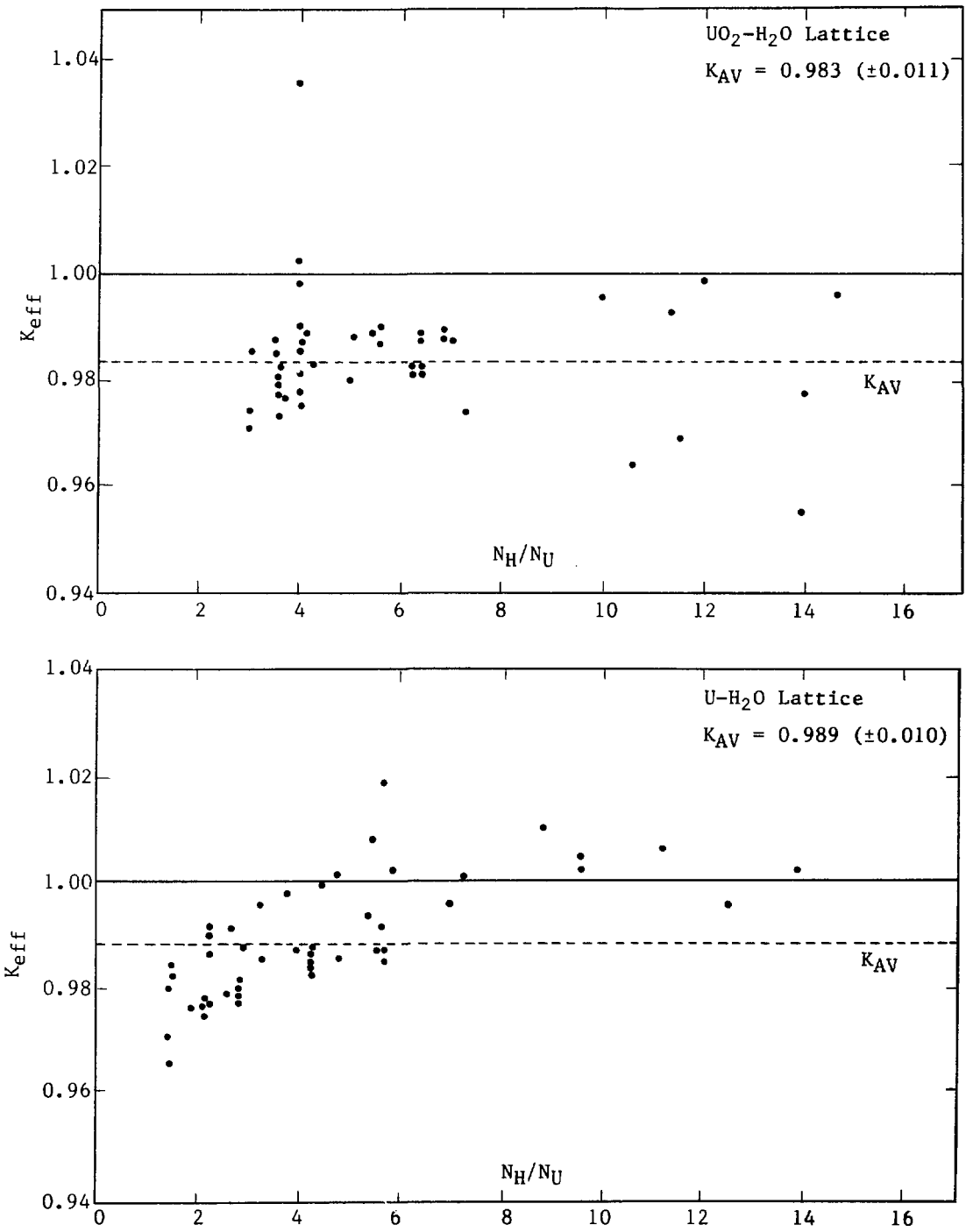

Fig. A1 Dispersion of calculated cell eigenvalues of early UO_2 and U lattices. Calculation with SRAC code using JENDL-2 by Takano, H.

2.1.3 Review of JENDL-3 Data from Viewpoint for FBR Benchmark Tests

Yasuyuki KIKUCHI
Nuclear Data Center
Department of Physics
Japan Atomic Energy Research Institute

Abstract

Results of FBR benchmark tests are reviewed. JENDL-3 predicts various FBR characteristics much better than JENDL-2. Particularly C/E values of sodium void coefficients and Doppler coefficients are much improved and space dependences observed with JENDL-2 for reaction rates, sodium void coefficients and control rod worth nearly disappear. On the other hand, it was pointed out that there exist a slight core dependence for effective multiplication factors and overestimation of threshod reaction rates.

Concerning these points, the JENDL-3 data were reviewed by comparing the JENDL-2 data. Simultaneous evaluation was adopted for principal actinide nuclides. As a results, fission cross sections of ^{235}U and ^{239}Pu are lower than those of JENDL-2 below a few hundred keV. Lower capture cross section and higher inelastic scattering cross section were adopted for ^{238}U. A harder fission spectrum of Madland-Nix type was assumed.

Considering the results of the benchmark tests and the characteristics of the JENDL-3 data. The following can be concluded. The balance of JENDL-3 is much better than that of JENDL-2. The low fission cross sections of ^{235}U and ^{239}Pu and the low capture cross section of ^{238}U seem to be reasonable. On the other hand, further study will be required for the inelastic scattering cross section of ^{238}U and the fission spectrum.

1. Introduction

The compilation of JENDL-3 was completed in October 1989. JENDL-3 is now open for use in all the world. Before the release of JENDL-3, various benchmark tests have been performed. Some modification of the evaluated data has been made by considering the results of the benchmark tests. A global review of JENDL-3 was already published[1].

Benchmark tests on FBR characteristics was made by JNDC Working Group on FBR Benchmark Tests. The detailed results will be soon published[2]. Sensitivity analysis were also applied to understand the results of benchmark testing[3].

In this brief report, I review the results of benchmark testing and the characteristics of JENDL-3 evaluation, and discuss reliability of JENDL-3 data from viewpoint of the FBR benchmark tests.

2. Review of FBR Benchmark Tests

The FBR benchmark tests were performed for 21 international benchmark cores, FCA-IX series cores and ZPPR-9. The results are briefly summarized in the following.

1) Effective multiplication factor: Table 1, Figs. 2 and 3

The C/E values are satisfactory. However there exist a tendency to overestimate it in large Pu cores. For U cores JENDL-3 underestimates it in cores with hard spectra.

2) Central reaction rate ratios: Table 2

A ratio of ^{239}Pu fission to ^{235}U fission is improved compared with JENDL-2. However threshold reactions such as ^{238}U fission and ^{240}Pu fission seem to be a little overestimated in the 21 benchmark cores, but are satisfactory in ZPPR-9. It should be noted that the experimental data of ^{238}U fission to ^{239}Pu fission ratio are considerably discrepant between foil and micro fission counter measurements in ZPPR-9. As to a ^{238}U capture to ^{239}Pu fission, JENDL-3 gives satisfactory results in the 21 benchmark cores, but overestimates it about 4% in ZPPR-9.

3) Reaction rate distributions: Fig. 3

With JENDL-3, little space dependence is observed as shown in Fig. 3 and the C/E values are predicted within 3% even at the outer

core. On the other hand, considerable overestimation is observed with JENDL-2 when leaving from the core center.

4) Sodium void coefficients: Fig. 4

With JENDL-3, the C/E values are independent on the void volume and stay near unity within 7%. On the other hand, the coefficients calculated with JENDL-2 are more than 20% overestimated and the overestimation reaches 40% when the void volume becomes large.

5) Control rod worth

In ZPPR-9, the C/E values of control rod worth change more than 30% between core center and outer ring. This space dependence is little seen with JENDL-3.

6) Doppler coefficients: Table 3

Underestimations of about 10% observed with JENDL-2 are much improved to about 5% with JENDL-3.

3. Review of JENDL-3 evaluation

Characteristics of JENDL-3 data are summarized in the following by comparing with data of JENDL-2.

1) Simultaneous evaluation method was applied[4] to principal actinide isotopes, i.e., ^{235}U, ^{238}U, ^{239}Pu, ^{240}Pu and ^{241}Pu. As a result fission cross sections of ^{235}U and ^{239}Pu become considerably lower than those of JENDL-2 below a few hunched keV as shown in Figs. 5 and 6. The values of JENDL-2 were artificially increased so as to keep the k-eff values high enough.

2) The lower values were adopted for ^{238}U capture cross section below 200 keV on the basis of new experimental data of Kazakov et al.[5] as seen in Fig. 7.

3) Direct inelastic scattering effect was considered for ^{238}U. Consequently the total inelastic scattering cross section becomes large than that of JENDL-2. Recently, however, Baba et al.[6] measured the inelastic scattering cross sections of ^{238}U. Their data lies between JENDL-2 and JENDL-3 as seen in Fig. 8.

4) The fission spectrum formula by Madland and Nix[7] was adopted for principle fission nuclides. Consequently the spectrum is harder than that of JENDL-2 which is based on Watt formula as seen in Fig. 9.

5) New evaluation of structural material results in lower capture

cross section for Cr and Ni as seen in Figs. 10 and 11.

6) Number of prompt fission neutrons (ν) of ^{235}U has some structure and becomes lower below 100 keV than JENDL-2 as seen in Fig. 12. There are little difference between JENDL-2 and JENDL-3 for ν-value of ^{239}Pu.

7) Direct and preequilibrium effects were considered for many light and structural materials, resulting in better reproduction of emitted neutron spectra at high energy region. However this affects little the FBR characteristics.

8) Gamma-ray production data were contained for important nuclides.

4. Discussion

Considering the results of the FBR benchmark tests and the characteristics of JENDL-3 data, the following can be said.

1) Space dependence problems

The space dependences of reaction rates, sodium void coefficients and control rod worths have bothered users of JENDL-2. The space dependences nearly disappear with JENDL-3. This suggests that the JENDL-3 data are well balanced particularly among neutron production, absorption and leakage. This balance is partly a result of the simultaneous evaluation for the main actinides.

The original fission cross sections of ^{235}U and ^{235}Pu in JENDL-2 evaluation were lower and not so different from those of JENDL-3. After benchmark tests, however, they were artificially increased, because original JENDL-2 data underestimated the effective multiplication factors by about 2%. This artificial increase of the fission cross sections might have disturbed the balance of JENDL-2 data.

2) Effective multiplication factor

From the discussion above mentioned, there occurs a question how the low fission cross sections of JENDL-3 can be compensated in the effective multiplication factors. Comparing the data between JENDL-2 and JENDL-3, the lower fission cross sections might be compensated with

(1) lower capture cross section of ^{238}U,

(2) lower capture cross section of Cr and Ni,

and (3) harder fission spectrum.

If this is the case for Pu-cores, then we can understand that the lower ν-value of ^{235}U causes the underestimation of the effective multiplication factor in U-cores.

The higher inelastic scattering cross section of ^{238}U seems to decrease the effective multiplication factor. But this effect is also related with the slowing down matrix. This will be discussed next.

3) Inelastic scattering and slowing down matrix

Comparing the inelastic scattering cross section of ^{238}U between JENDL-2 and JENDL-3, most of the difference consists of direct inelastic scattering to low-lying levels. On the other band, the increase of the inelastic scattering cross section in JENDL-3 causes decrease of the elastic scattering cross section, since there exist little difference in the total cross section.

In neutron transport calculation with multi-group constants whose group number is less than 100, the slowing down effects above a few hundred keV region are analogous between the elastic scattering and inelastic scattering to low-lying levels. Hence there may appear little difference in the FBR characteristics between JENDL-2 and JENDL-3.

In order to verify this argument, Takano made a trial calculation[8] for ZPPR-9 on the basis of JENDL-2 by replacing the inelastic scattering cross section and the slowing down matrix of ^{238}U as follows.

Case 0: σ_{in} = JENDL-2, Matrix = JENDL-2
Case 1: σ_{in} = JENDL-3, Matrix = JENDL-3
Case 2: σ_{in} = JENDL-2, Matrix = JENDL-3
Case 3: σ_{in} = JENDL-3, Matrix = JENDL-2

The results are given in Table 4. Little change is observed, when both the inelastic scattering cross section and the slowing down matrix are replaced (Case 0 vs. Case 1). On the other hand, in Case 2 where only the slowing down matrix was replaced to that of JENDL-3, the effective multiplication factor and ^{238}U fission to ^{235}U fission ratio are much overestimated because of insufficient slowing down effects and vice versa in Case 3.

This problem was also pointed by Takeda[9] from his experience on sensitivity analysis. The effects of changing the fission and capture cross sections are well predicted with the sensitivity coefficients. However, the scattering components are not well predicted with the

sensitivity coefficients of the scattering cross section.

4) Threshold reaction rate and fission spectrum

The threshold reaction rates seems to be overestimated in the 21 benchmark cores as given in Table 2, though the ^{238}U fission to ^{235}U fission ratio is well-predicted in ZPPR-9. This suggests that the spectrum is too hard in MeV region with JENDL-3. This may be partly caused by the fission spectrum of Madland-Nix type. Recent evaluation of ^{252}Cf fission spectrum by Mannhart[10] recommends softer spectrum than that of Madland-Nix. Further study will be required for the fission spectrum as well as the inelastic slowing down.

5) Sodium void coefficients

Sodium void coefficients were overestimated by more than 20% with JENDL-2. This overestimation mainly comes from slowing down term, because the increase of adjoint spectrum is too rapid from 10 keV to 1 MeV as shown in Fig. 13.

Sensitivity analyses showed that fission and capture cross sections of ^{239}Pu had large sensitivity coefficients below 1 keV. Here it is checked whether the improvement with JENDL-3 can be explained with the change of ^{239}Pu cross sections.

Figure 14 shows the sensitivity coefficients of ^{239}Pu cross sections, change of ^{239}Pu cross sections from JENDL-2 to JENDL-3 and the ^{239}Pu contribution to improve the sodium void coefficients. It is understood from figures that the change due to ^{239}Pu fission cross section is to the opposite direction and the change due to ^{239}Pu capture cross section to the right direction, and that ^{239}Pu cross sections contribute to decrease the sodium void coefficients only by 0.8%. Hence it is concluded that the significant improvement of sodium void coefficients with JENDL-3 is not caused by a single nuclide such as ^{239}Pu but by the balance of all the nuclides.

5. Conclusion

The following can be concluded on the JENDL-3 data from the above discussion.

1) The balance of the JENDL-3 data is much better than that of the JENDL-2 data, resulting in disappearance of the space depences of reaction rates, sodium void coefficients and control rod worths, and

also resulting in significant improvement of the C/E values of sodium void coefficients and Doppler coefficients.

2) The results of simultaneous evaluation for JENDL-3 are reliable including the low fission cross sections of ^{235}U and ^{239}Pu.

3) The low capture cross section fo ^{238}U seems reasonable.

4) The harder fission spectrum than JENDL-2 seems reasonable. However, there remains some questions whether the JENDL-3 spectrum is too hard.

5) The inelastic scattering cross section of ^{238}U should be further studied. This should be done by considering the partial inelastic scattering and the fission spectrum above mentioned. This study will be made as a task item of NEACRP/NEANDC international cooperation for evaluation.

6) The ν-value of ^{235}U seems too small, resulting in the underestimation of the effective multiplication factors in U cores.

It is also to be noted that the scattering problems cannot be easily treated with sensitivity analysis. This should be carefully considered, when the group cross sections are adjusted with the integral data.

Acknowledgment

The author with to thank H. Takano and T. Takeda for informing him of the results of various benchmark tests and sensitivity analyses. He also acknowledge members of Working Group on FBR Benchmark Test of JNDC and members of JENDL-3 compilation group for their helpful discussion.

References

1) Asami T. et al.: J. At. Energy Soc. Japan, 31, 1190 (1989) [in Japanese]
2) Takano H. and Kaneko K.: Paper to be presented at PHYSOR'90, Marseille, April 1990.
3) Aoyama T. et al.: JAERI-M 86-004 (1986).
4) Kanda Y. et al.: Proc. Int. Conf. Nuclear Data for Basic and Applied Science, Santa Fe, 1985, p.1567 (1986), Gordon and Breach.
5) Kazakov L.E. et al.: Yad. Konst., 3, (1986).
6) Baba M. et al.: JAERI-M 98-143 (1989).
7) Madland D.G. and Nix J.R.: Nucl. Sci. Eng., 81, 213 (1982).
8) Takano H.: Private Communication, 1989.
9) Takeda T.: Private Communication, 1989.
10) Mannhart W.: IAEA-TECDOC-335 (1984).

Table 1 C/E values of effective multiplication factor

	JENDL-2	JENDL-3
21 Benchmark Cores		
All Cores	1.004	1.002
U Cores	1.005	0.997
Pu Cores	1.004	1.004
ZPPR-9	0.999	1.006

Table 2 C/E values of central reaction sate ratios

		JENDL-2	JENDL-3
28F/25F	Pu cores	1.05	1.12
	U cores	0.98	1.04
	All cores	1.03	1.10
	ZPPR-9	0.94	1.00
49F/25F	Pu cores	0.97	0.99
	U cores	0.99	0.99
	All cores	0.97	0.99
	ZPPR-9	0.98	1.00
40F/25F	Pu cores	1.07	1.12
	U cores	1.04	1.09
	All cores	1.06	1.11
	ZPPR-9	-	-
28F/49F	Pu cores	1.02	1.00
	U cores	0.96	0.94
	All cores	0.99	0.98
	ZPPR-9	1.05	1.04

Table 3 C/E values of Doppler coefficients in ZPPR-9

Temperature (K)	JENDL-2	JENDL-3
298 - 487.5	0.91	0.94
298 - 644.4	0.92	0.96
298 - 794.0	0.88	0.92
298 - 935.4	0.93	0.97
298 - 1087	0.92	0.96

Table 4 Effect of the inelastic scattering cross section and slowing down matrix of ^{238}U on k_{eff} and reaction ratio for ZPPR-9

Case 0: σ_{in} = JENDL-2, slowing down matrix = JENDL-2
Case 1: σ_{in} = JENDL-3, slowing down matrix = JENDL-3
Case 2: σ_{in} = JENDL-2, slowing down matrix = JENDL-3
Case 3: σ_{in} = JENDL-3, slowing down matrix = JENDL-2

	Case 0	Case 1	Case 2	Case 3
k_{eff}	0.9991	0.9995	1.0158	0.9807
F8/F5	1.07	1.06	1.19	0.93
F9/F5	0.97	0.97	0.98	0.96
C8/F9	0.99	0.99	0.97	1.00

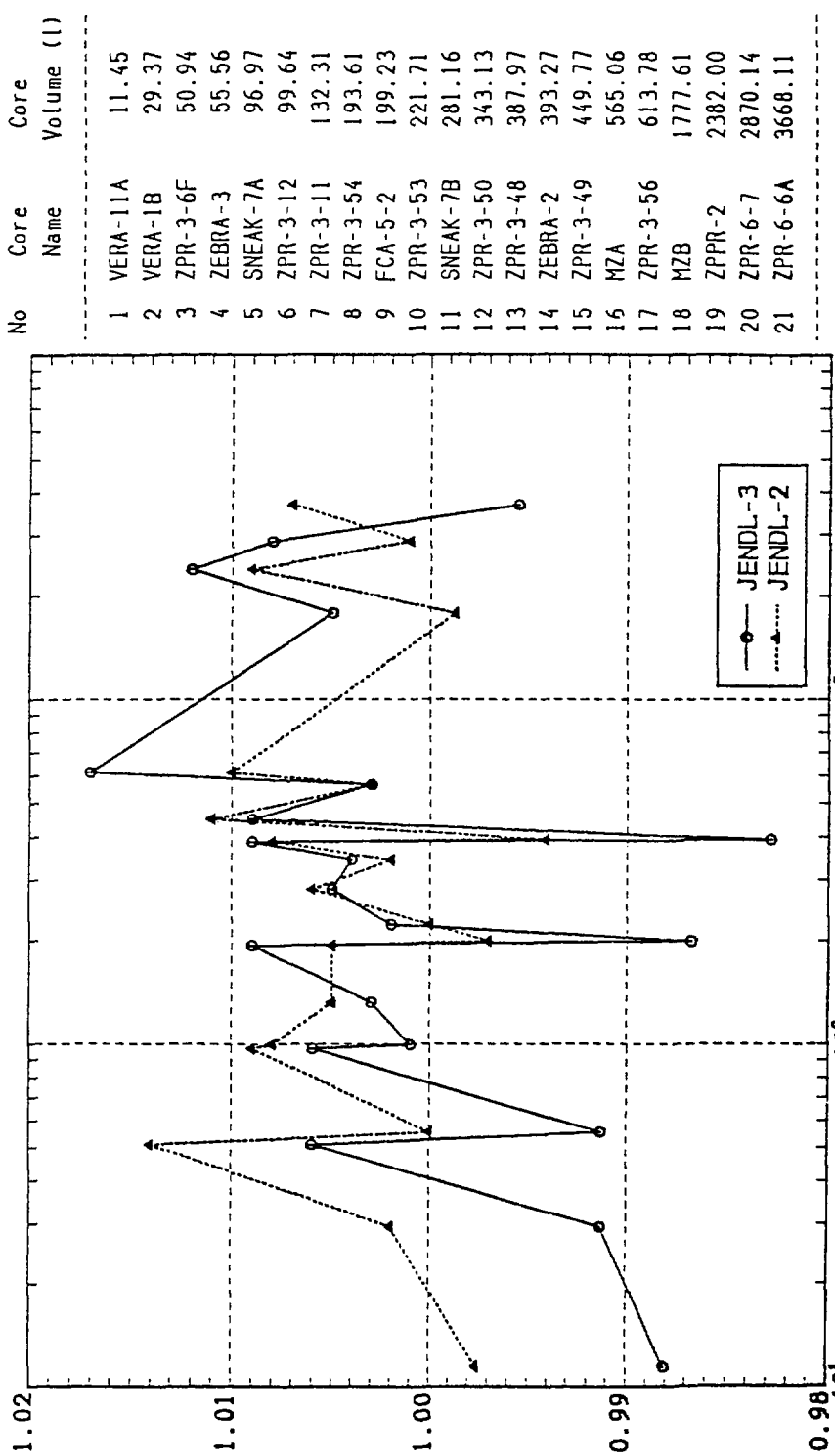

Fig. 1 C/E values of effective multiplication factor for the 21 benchmark cores

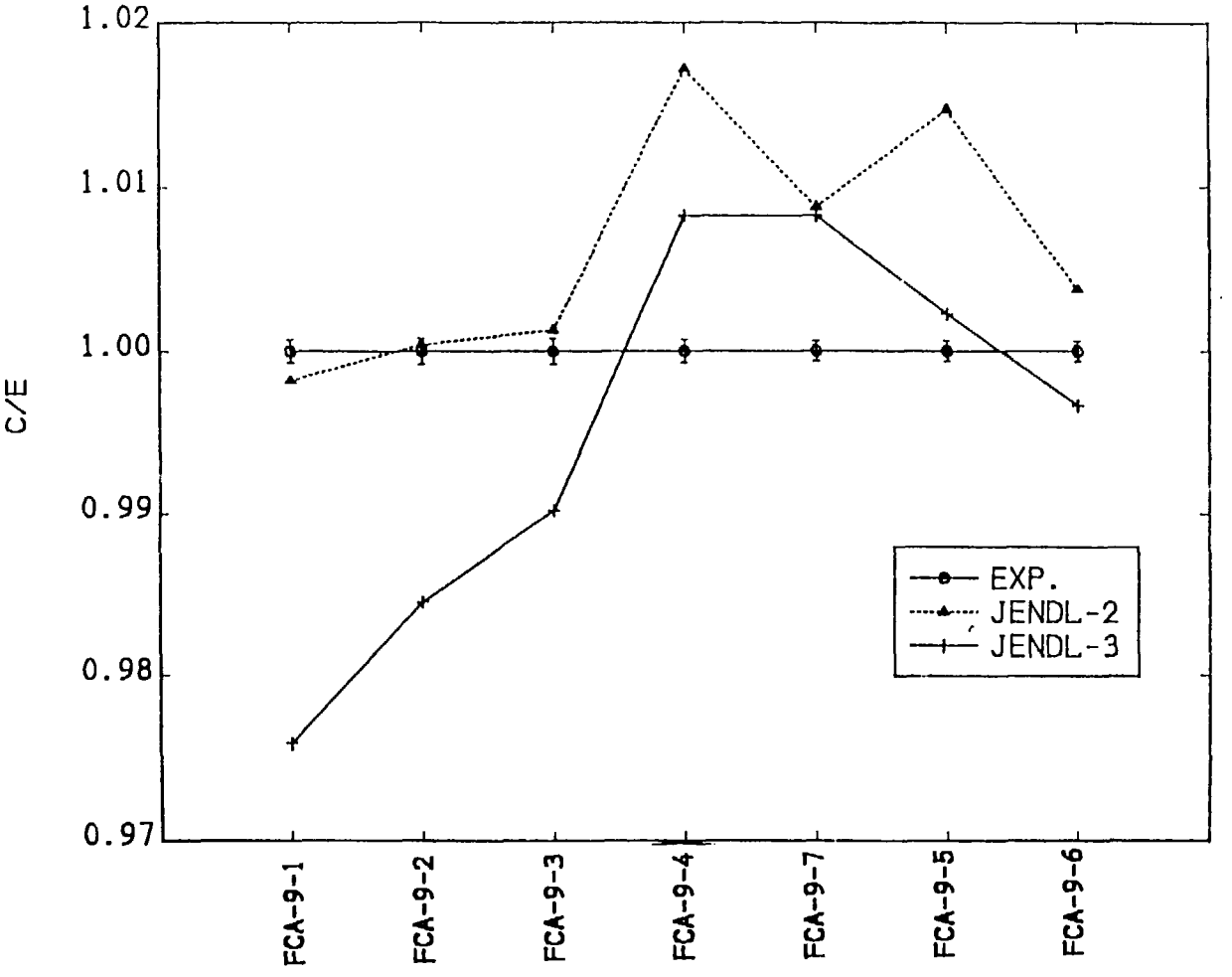

Fig. 2 C/E values of effective multiplication factor for the FCA-IX series cores. Along the horizontal live from left to right, the neutron spectrum becomes soft.

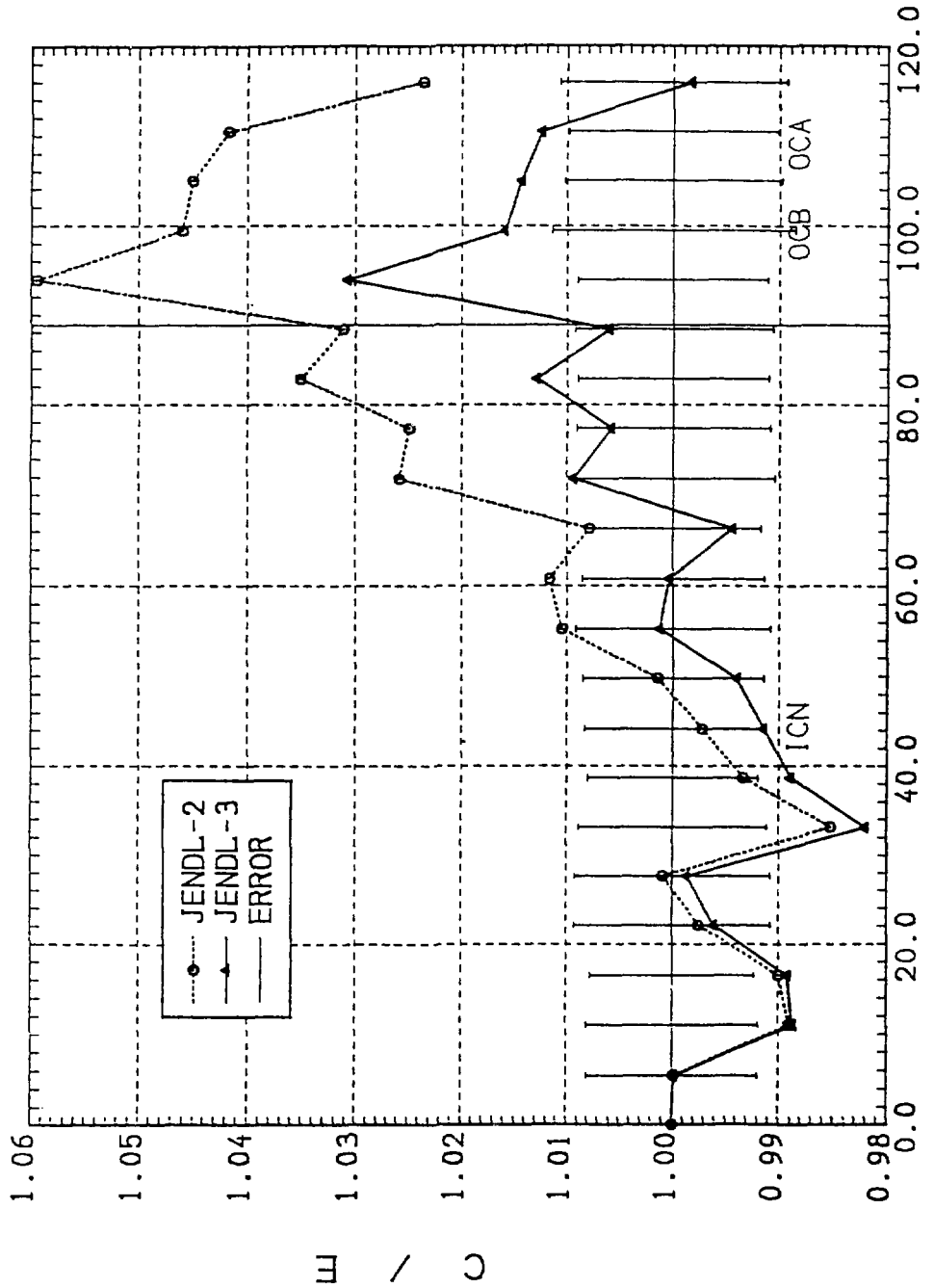

Fig. 3 Space dependence of ^{239}Pu fission rate in ZPPR-9

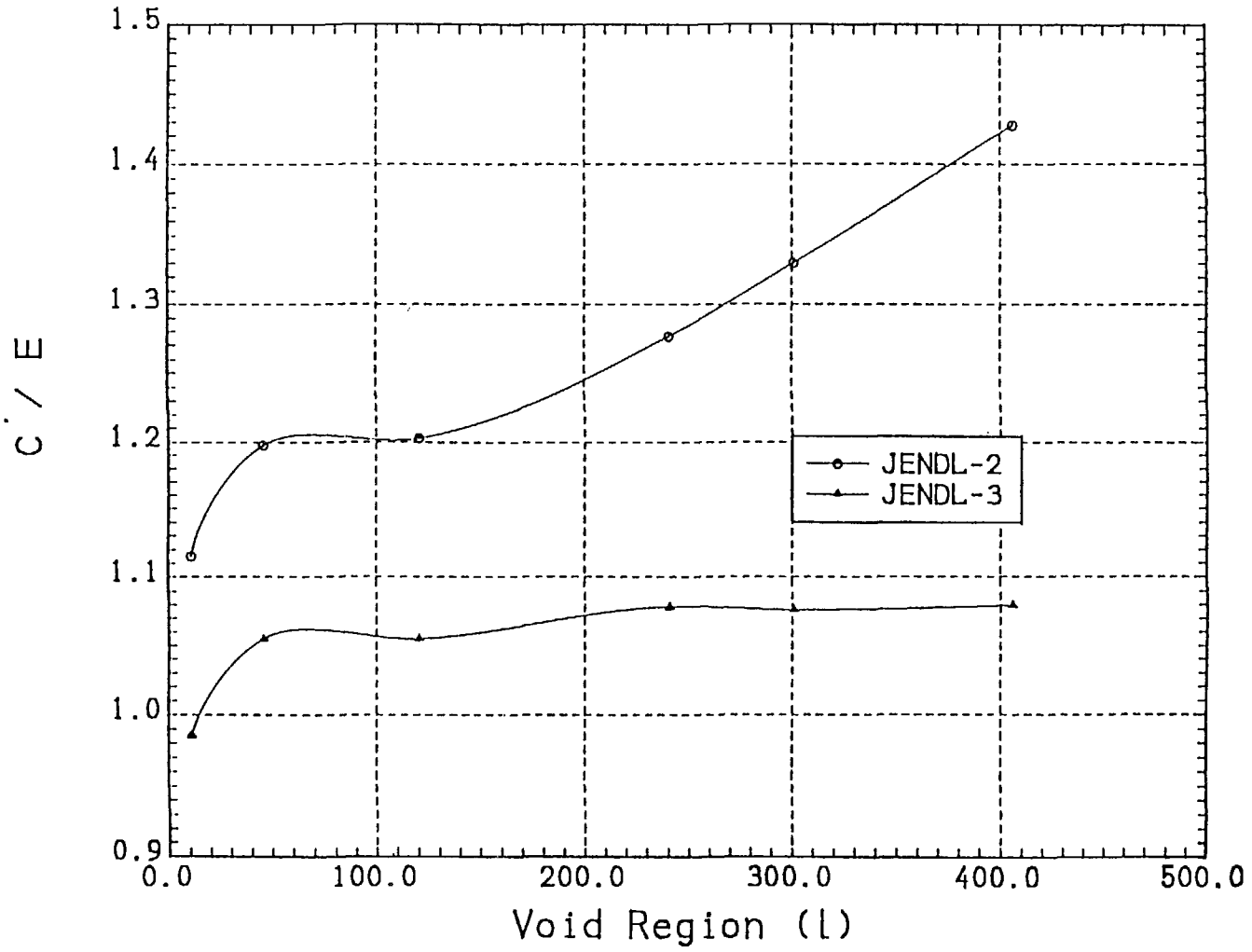

Fig. 4 Void volume dependence of sodium void coefficients (C/E value) in ZPPR-9

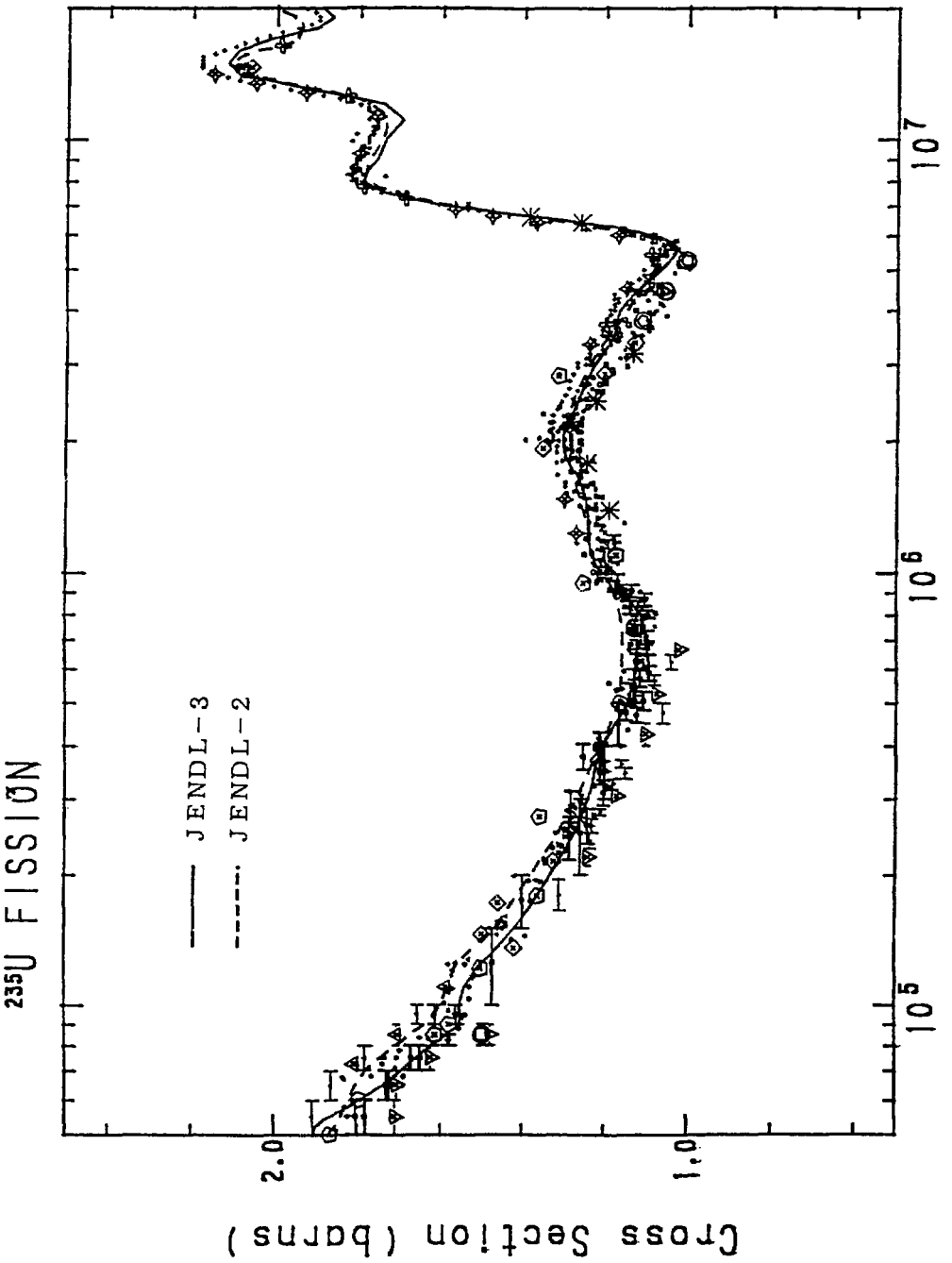

Fig. 5 Fission cross section of ^{235}U

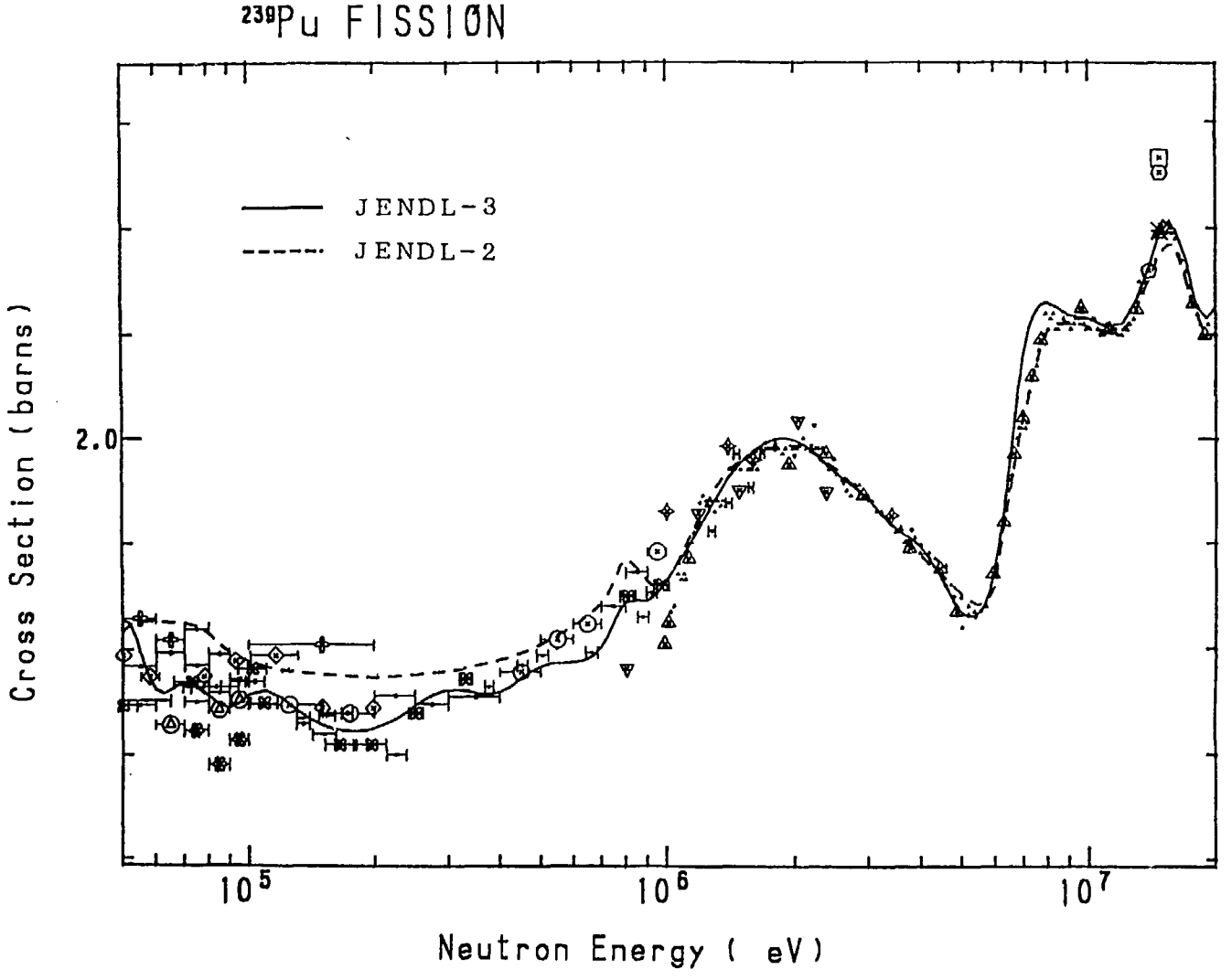

Fig. 6 Fission cross section of ^{239}Pu

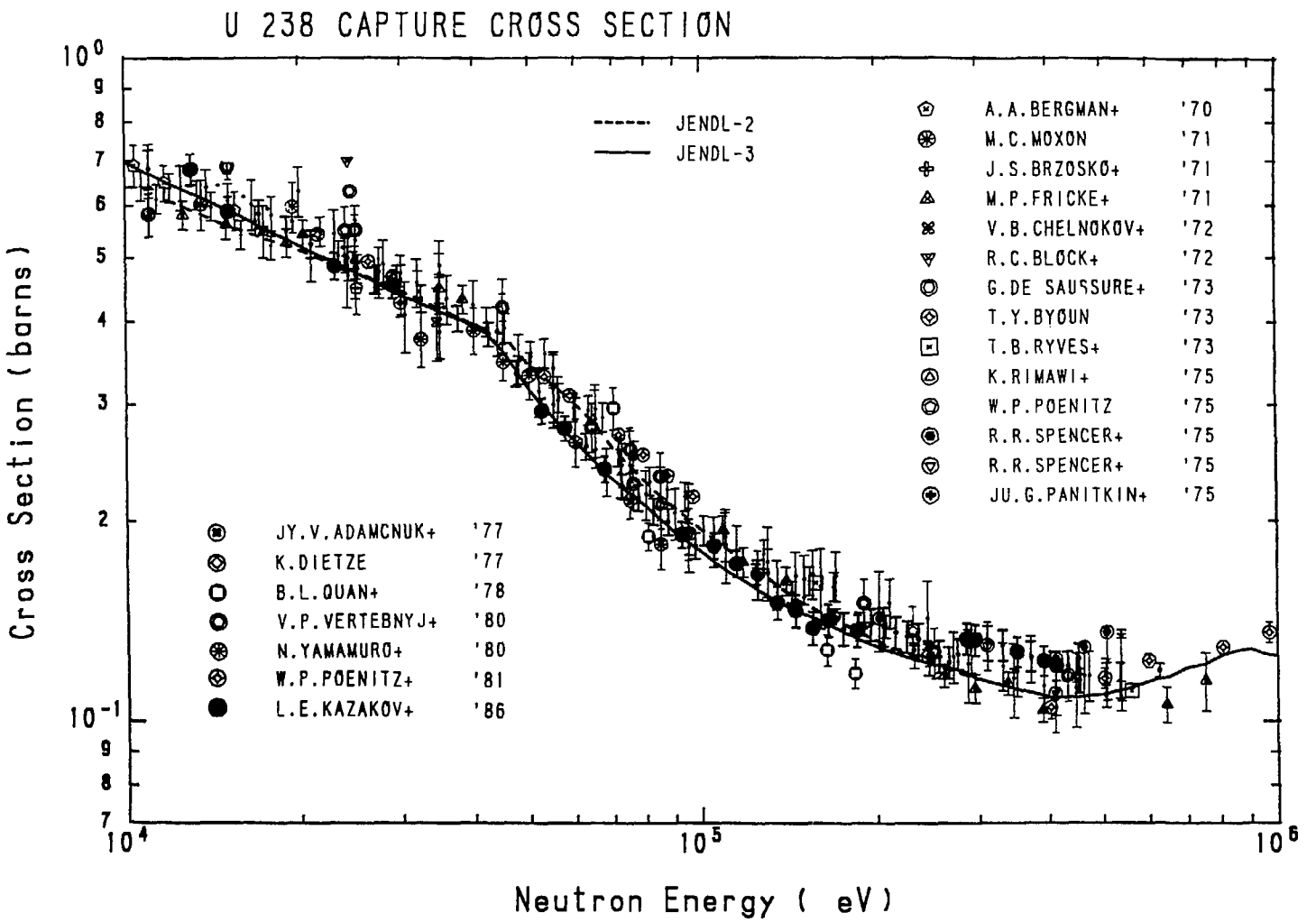

Fig. 7 Capture cross section of ^{238}U

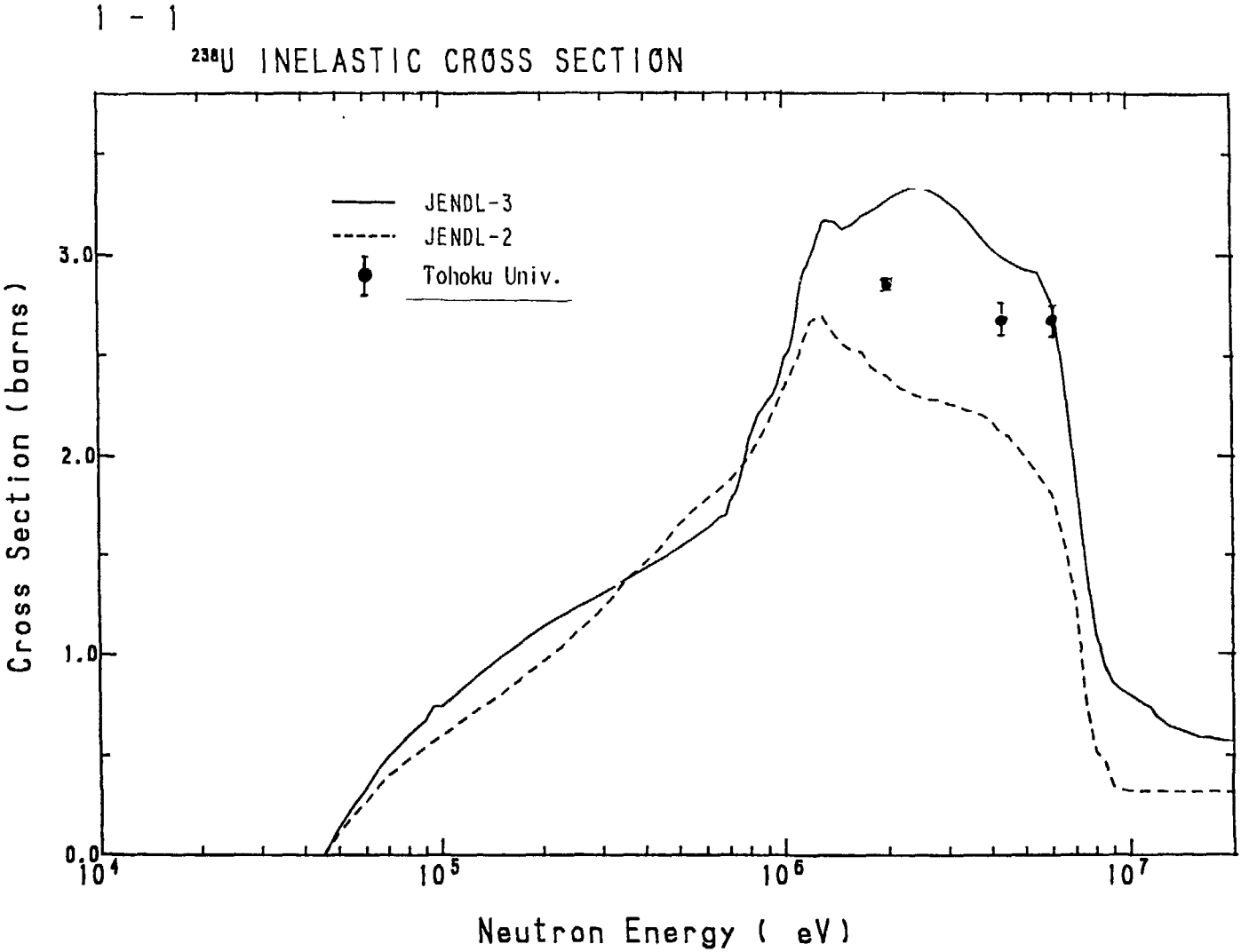

Fig. 8 Total inelastic scattering cross section of ^{238}U

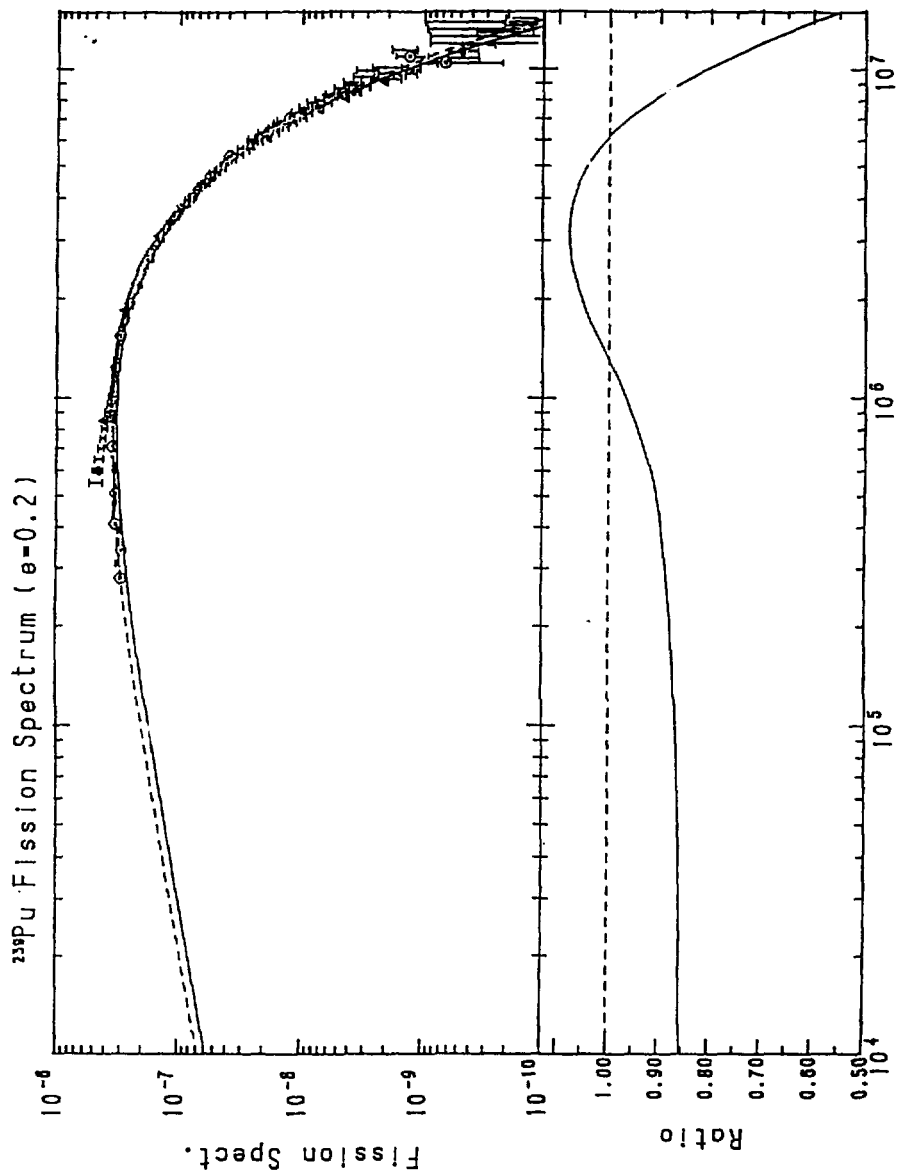

Fig. 9 Fission spectrum of ^{239}Pu

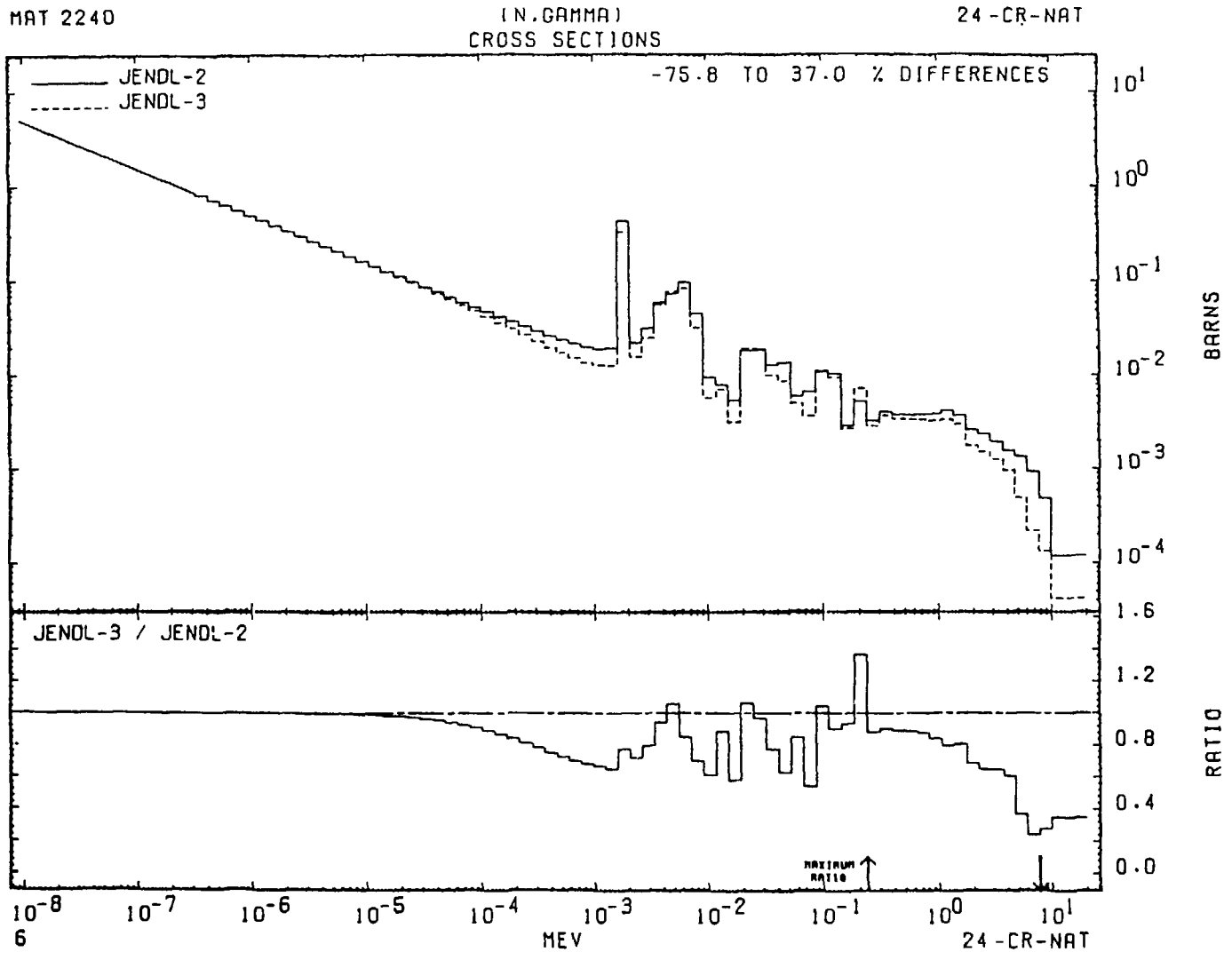

Fig. 10 Capture cross section of ^{nat}Cr

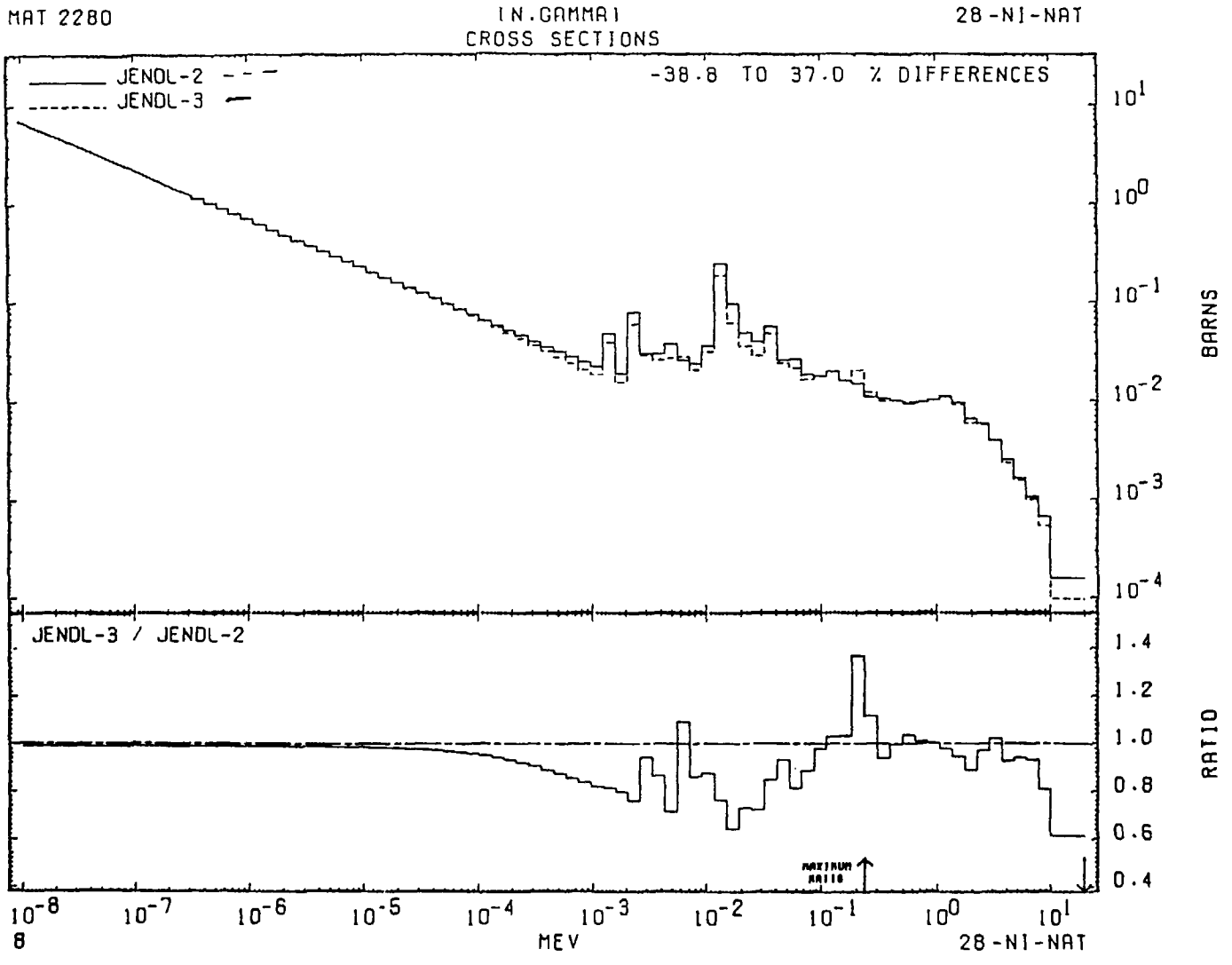

Fig. 11 Capture cross section of ^{nat}Ni

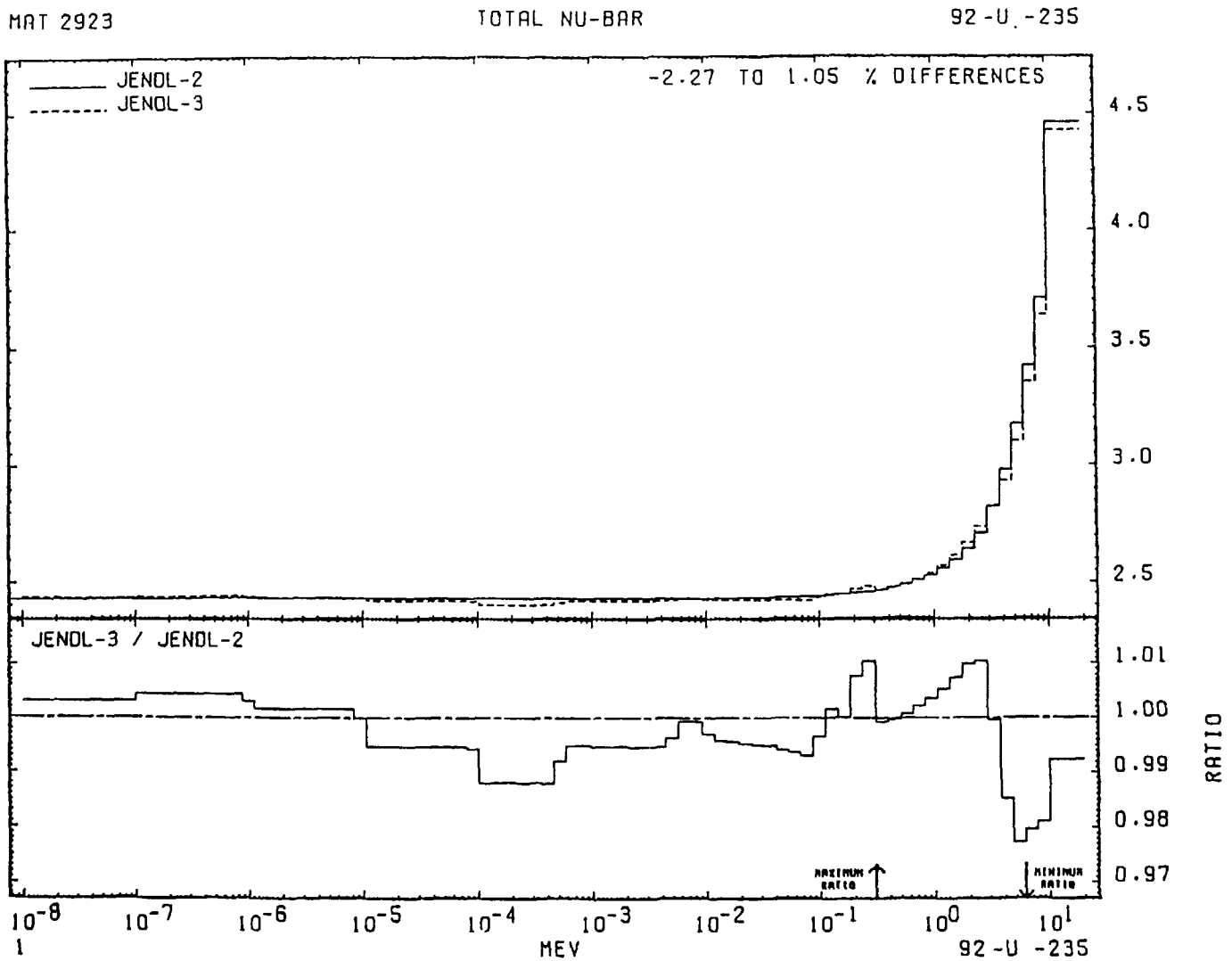

Fig. 12 Number of neutron emission per fission of ^{235}U

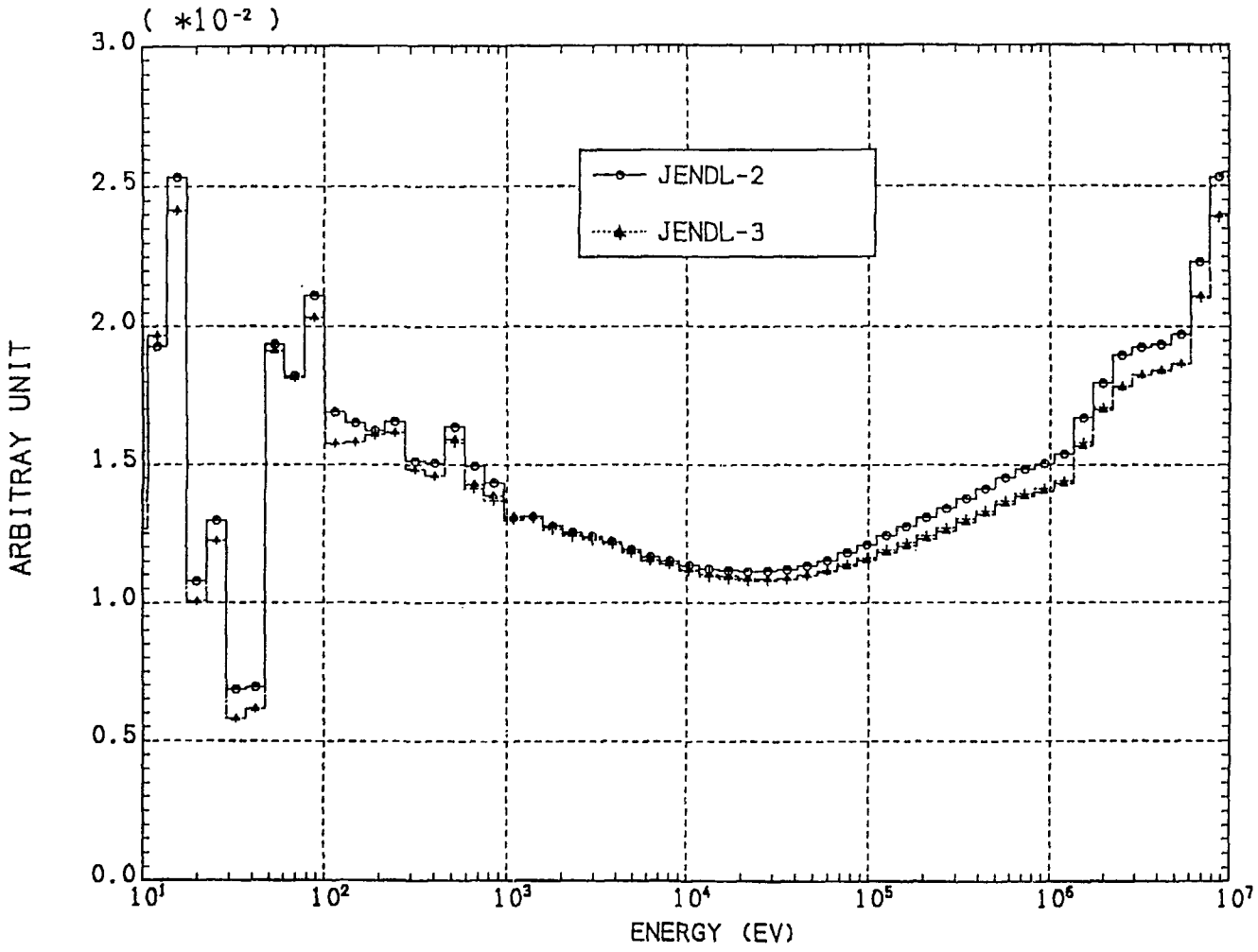

Fig. 13 Comparison of adjoint neutron spectrum at core center of ZPPR-9

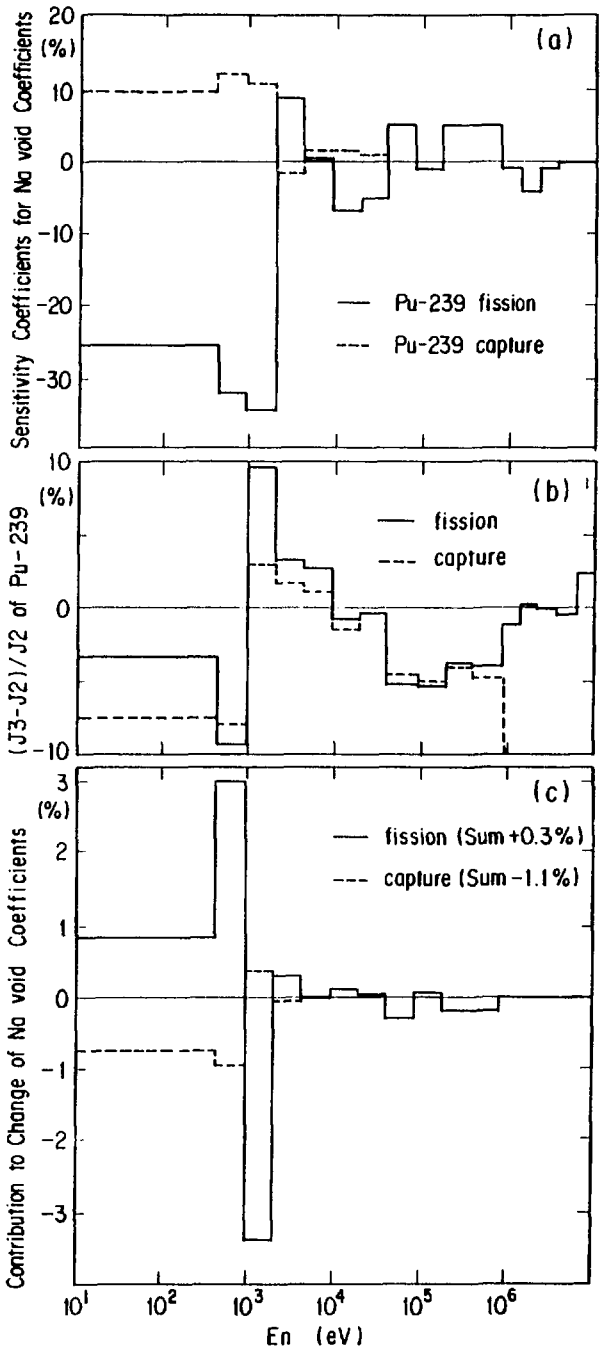

Fig. 14 Sensitivity analysis of Na void coefficients

a) Sensitivity coefficients of ^{239}Pu cross sections

b) Relative change of ^{239}Pu cross sections between JENDL-3 and JENDL-2: (JENDL-3 - JENDL-2)/JENDL-2

c) Contribution of ^{239}Pu cross sections to change of Na void coefficients

2.1.4 JENDL-3 FP Data File

JNDC FPND Sub-Working Group
T. Watanabe (KHI), M. Kawai, S. Iijima (TOSHIBA),
H. Matsunobu (SAEI), T. Nakagawa, Y. Nakajima, T. Sugi (JAERI),
M. Sasaki (MAPI), A. Zukeran (HITACHI)

Abstract

Evaluation work for JENDL-3 FP data file has been continued since 1985, and now evaluation work is on its final stage.

In this presentation, current status, contents of the file, evaluation methods, and discussion on evaluated data are briefly given.

1. Introduction

JENDL-2 FP data file[1] contains the evaluated data for 100 FP nuclides, important mainly for FBR calculation.

However, the number of FP nuclides is not enough to general application, such as burnup calculation of various type of reactors[2,3], neutron dosimetry, diagonostics, and nuclear transmutation calculation in fission and fusion reactors. Reaction types considered in the JENDL-2 FP data file are insufficient for these applications, radiation damage and activation analysis. So the number of nuclides and reaction types has been extended for JENDL-3 as shown in Table 1 and Fig. 1.

It was the main target of JENDL-2 FP data evaluation to evaluate accurately capture cross section. However, accuracy of the capture cross sections was not always enough to satisfy the required accuracy of 10 - 30[1]%. It seems that the uncertainty might come from the discrepancies in resolved resonance parameters[4]. In the integral test comparing with reactivity measurements in STEK reactor[5], many nuclides with small

absorption cross section showed large discrepancies between the calculations and the measurements. From Fig. 2, it is seen that these discrepancies depend on scattering component of the reactivity, and particularly come from inelastic scattering cross sections.

In order to overcome these discrepancies, evaluation of resolved resonance parameters and cross sections based on recent experimental data and more refined nuclear models is necessary.

The integral test of JENDL-2 also suggested the necessity of reevaluation of data for several isotopes such as ^{152}Eu and ^{154}Eu which have no experimental data[6].

2. Computer programs for evaluation

Programs shown in Fig. 3 were used to evaluate the data and to compile JENDL-3 FP data file.

The multilevel Breit-Wigner formula was employed in the resolved resonance region. Resonance parameters from EXFOR or other literature were stored and handled with REPSTOR code. Parameters of each level was determined by taking account of recent experimental data and Mughabghab's evaluation as well as JENDL-2. If values of orbital angular momentam ℓ or spin J were not given, PASSIGN and JCONV codes were used to determine them.

In PASSIGN code, the method of Bollinger and Thomas[7] is applied to assign ℓ value.

Using Bayesian theorem, the probability Pp(gΓn) that the level of resonance is excited by p wave neutron is expressed as follows.

$$P_p(g\Gamma n) = \left[1 + a_1 \sqrt{\frac{\langle g_1 \Gamma n_1 \rangle}{\langle g\Gamma n_0 \rangle}} \exp\left[\frac{g\Gamma n}{2}\left(\frac{1}{\langle g\Gamma n_1 \rangle} - \frac{1}{\langle g\Gamma n_0 \rangle}\right)\right]\right]^{-1}$$

$$\langle g\Gamma n_0 \rangle = \sqrt{E}\, D_{obs}\, S_0$$

$$\langle g\Gamma n_1 \rangle = 7.3\times10^{-8} A^{2/3} E^{3/2} D_{obs}\, S_1$$

S_0, S_1, Dobs are s and p wave strength functions and the observed level spacing respectively. A is atomic mass and a_I is a ratio of apriori probability of s and p wave resonance. If E < 0 or P_p < 0.5, then ℓ was assigned to be 0, and if P_p > 0.5, ℓ was assumed to be 1.

Spin J value is assigned with JCONV code to satisfy the following probability distribution.

$$P(J)=(2J+1)\exp[-\frac{J(J+1)}{2\sigma^2}]/\sum_J(2J+1)\exp[-\frac{J(J+1)}{2\sigma^2}]$$

where σ^2 is a spin cutoff factor.

Below 100 kev, unresolved resonance parameters were determined with ASREP code[8]. Nuclear radius R' is determined to reproduce the total cross section at 100 kev, and level spacing D to express the capture cross section under the assumption of the fixed $\Gamma\gamma$ value.

Above 100 kev, the spherical optical model and the statistical theory were employed to estimate the capture, elastic, compound inelastic scattering and total cross sections with CASTHY code[9].

Direct inelastic cross section was calculated with DWBA code DWUCKY[10] for even mass FP nuclei around fission yield peak.

Multistep evaporation and preequilibrium model code PEGASUS[11] calculation was applied to calculate threshold cross sections for all nuclides. And these threshold cross sections and direct inelastic cross sections were taken into account as competing cross sections in statistical model calculation with CASTHY code.

In Mev region direct/semidirect capture cross section is also taken into account with following formula[12].

$$\sigma_{ny}^{DSD}(En) = K\left[6\left(\frac{Z}{A}\right)^{2} \cdot \frac{R^4\, En^{1/2}\, Ey\, 10^{-10}}{(2+0.5En+16.8En^{1/2}/R)}\right]$$

$$\cdot\left[1 + \frac{0.75E_R\, Ey - 0.61E_R}{(Ey-E_R)^2 + (\Gamma R/2)^2}\right]$$

R	Nuclear Radius
E_R	$80A^{1/3}$
ΓR	5.0Mev
β	Nuclear Deformation
Ey	En + Sn/2
Sn	Neutron Separation Energy of Daughter
K	Normalization Constant

Level density parameters at low excited energies were evaluated on the basis of recommended level schemes in the Evaluated Nuclear Structural Data File (ENSDF)[13]. The program ENSDFRET retrieves the level scheme data from ENSDF. LVLPLOT makes a staircase plot of number of excited levels. LEVDENS determines the parameters of Gilbert Cameron's level density formulas so as to fit to the staircase plot of levels, and observed level spacings. The optical model parameters were evaluated with the NDES[14] so as to fit the experimental data of total cross sections, neutron strength functions and nuclear radius. The determined parameters were stored into a data base.

These parameters were used for calculations with CASTHY and PEGASUS. The input and the job control data of CASTHY for many nuclides were made one by one with the JOBSETTER code using PARAMFL as a data base.

3. Important parameters for calculation

Resolved resonance parameters were adopted mostly from JENDL-2 and Mughabghab et al[15]. Status of the resonance parameters is shown in Table 2.

For most nuclides, the spherical optical potentials used in JENDL-2 were also adopted basically[16] in the CASTHY calculation. However, some revision were made as shown in Table 3. These potentials are also adopted to evaluate direct inelastic scattering cross sections with DWUCKY and threshold reaction cross sections with PEGASUS. To calculate the inverse reaction cross sections due to charged particles, grobal fit optical model parameters[17~20] were adopted.

Nuclides of which direct inelastic scattering cross section was evaluated are shown in Table 4. Nuclear deformation parameters to these nuclides were adopted from literatures[21,22].

Level density parameters of the Gilbert - Cameron's formula were newly determined[23,24] from low-lying levels and the observed resonance spacings. When these data were not available, the systematics for 'a' shown in Table 5 and the following T were used.

$$T = 65/A \qquad A < 100$$
$$= 0.65 - 0.00242\ (A - 100) \qquad A > 100$$

where A is a nuclear mass number.

The gamma-ray strength functions were adjusted to fit the capture cross sections. Its systematics was investigated by using the ratio of radiation width to observed level spacing[25]. From the local systematics, gamma-ray strength functions were estimated for the nuclides which had no experimental capture cross sections.

Systematics of ratio of capture cross section at 2200 m/s (σ_c^{2200}) to σ_c calculated with CASTHY and observed level spacing were investigated and used to estimate σ_c^{2200} in the case where no measured data were available as shown in Fig. 4.

The Kalbach's constant K, which represents the strength of the pre-equilibrium transition rate, was estimated as $K = 0.1/(g/A)^3$ (±50%), where g is the single particle level density of the composite nucleus. The estimation is based on the expression of two-body interaction in nuclear matter by Kikuchi and Kawai[26]. The value of K and level density parameters of some nuclides were adjusted to the measured (n,2n) cross sections.

4. Results

In Table 6, comparison of σc^{2200} and resonance integrals are shown for nuclides which have large discrepancies from ENDF/B-V and for dominant nuclides for thermal reactors. Large discrepancies are found for the nuclides which have no measured thermal corss sections and resonance integrals. Summations weighted by ^{235}U thermal fission yields differ from ENDF/B-V by 25.6% to σc^{2200} and by 1.4% to resonance integrals, respectively.

As for kev region, capture cross section comparison between JENDL-3 and 2 is shown in Table 7 for strong absorbers important for FBR burnup calculation. For most nuclides in this Table, capture cross sections of JENDL-3 are almost the same as that of JENDL-2, however, for ^{107}Pd, ^{149}Sm, ^{151}Eu, modification of capture cross sections from JENDL-2 are in the direction to get better c/E of integral test. As in the resonance region, the cross sections were improved largely, and σc, σin, σel are evaluated with more refined method as shown Fig. 3, we expect to have better C/E to the integral test than that of JENDL-2.

About 95% evaluation work finished and check of evaluated results, graph check and production of comment file are now in progress. It will be completed in early time of 1990.

References

1) T. Aoki et al.: Proc. Int. Conf. on Nuclear Data for Basic and Applied Science, May 1985 Santa Fe vol. 2, p.1627 Gordon and Breach Sci. Pub. (1985)
2) S. Iijima et al.: J. Nucl. Sci. Technol., 19, 96 (1982)
3) S. Iijima et al.: JAERI-M 87-025, p.230 (1987)
4) M. Kawai et al.: JAERI-M 88-065, p.57 (1988)
5) T. Watanabe et al.: JAERI-M 86-080, p.30 (1986)
6) T. Watanabe et al.: JAERI-M 88-065, p.148 (1988)
7) L.M. Bollinger and G.E. Thomas: Phys. Rev. 177, 1293 (1968)
8) Y. Kikuchi: private communication
9) S. Igarasi: J. Nucl. Sci. Technol. 12, 67 (1975) and private communication
10) S. Yamamuro: JAERI-M 88-140 (1988)
11) S. Iijima et al.: JAERI-M 87-025, p.337 (1987)
12) V. Benzi and G. Reffo: CCDN-NW/10, p.6 (1969)
13) J. K. Tuli: BNL-NCS-51655
T. Tamura: JAERI-M 85-035, p.330 (1986)
14) T. Nakagawa: J. At. Energy Soc. Japan 22, 559 (1980)
15) S.F. Mughabghab et al.: Neutron Cross Sections vol.1 part A & B Academic Press (1981, 1984)
16) S. Iijima and M. Kawai: J. Nucl. Sci. Technol. 20, 77 (1983)
17) F.G. Perey: Pnys Rev. 131, 745 (1963)
18) J.R. Huizenga and G. Igo: Nucl. Phys. 29, 462 (1962)
19) J.M. Lohr and W. Haeberli: Nucl. Phys. A232, 381 (1974).
20) F.D. Becchetti Jr. and G.W. Greenless: Polarization Phenomena in ar Reactions (H.H. Barshall and W. Haeberli, eds), p. 682 The university of Wisconsin Press. (1971)
21) S. Raman et al.: At. Data and Nucl. Data Table 42, 1 (1989)
22) R.H. Spear: At. Data and Nucl. Data Table 42, 55 (1989)
23) S. Iijima et al.: J. Nucl. Sci. Technol. 21, 10 (1984)
24) S. Iijima et al.: to be published

25) M. Kawai et al.: Proc. Int. Conf. on Nucl. Data for Sci. and Technol. May 1988 Mito p.569 (1988)

26) K. Kikuchi and M. Kawai : Nuclear Matter and Nuclear Reactions (1968)

Table 1 Contents of JENDL-3 FP Data File

Nuclide	172		
	Z= 33	—	65
	As	—	Tb
Energy	10^{-5}	—	2×10^{7} ev
Reaction	σ_{total}		
	σ_{el}		
	$\sigma_{capture}$ (Compound+Direct/Semi Direct)		
	σ_{in} (Compound+Direct)		
	$\sigma_{n,\,2n}$		
	$\sigma_{n,\,3n}$		
	σ_{p}, σ_{α}, σ_{np}, $\sigma_{n\alpha}$, σ_{2n}, σ_{3n}, σ_{d}, σ_{t}		

Table 2 Status of Resolved Resonance Parameters

1. Nuclides with Newly Evaluated Resolved Resonance Parameters (71 Nuclides)

As-75, Se-74, 76, 77, 78, 80, 82, Br-79, 81,
Kr-78, 80, 82, 86, Rb-85, 87, Zr-91, 93, 96, Nb-94,
Ru-99, 101, 102, Pd-102, 107, Ag-110m, Cd-106, 108, 111,
In-113, Sn-112, 114, 115, 116, 117, 118, 119, 120, 122,
124, Sb-121, 123, Te-122, 123, 124, 125, 126, 130, I-127,
Xe-124, 126, 128, 129, 130, 136, Ca-133, 134,
Ba-130, 135, 137, 138, La-138, 139, Ce-140, 141, 142,
Nd-147, Pa-148m, Sm-148, Eu-154, Gd-152, 154

2. Adopted from JENDL-2 (69 Nuclides)

3. Nuclides without Resolved Resonance Parameters (32 Nuclides)

—; JENDL-2 FP

Table 3 Optical Model Parameters

Application range	V_0	R_0	a_0	W_S	R_S	a_s	V_{so}	R_{so}	a_{so}	Change from JENDL-2
As – Rb	46–0.25E	5.7	0.62	7.0	6.2	0.35	7.0	5.7	0.62	Sr's OMP with R changed
Sr – Mo	46–0.25E	5.893	0.62	7.0	6.393	0.35	7.0	5.893	0.62	
Tc – Rh	47.5	5.9723	0.62	9.74	6.5942	0.35	7.0	5.97	0.62	Rso
Rd – Cd	50.1–0.5528E	5.972	0.56	8.165	6.594	0.44	5.261	5.97	0.267	New OMP
In – Sb	47.64–0.473E	6.2556	0.62	9.744	6.4687	0.35	7.0	6.241	0.62	Rso
Te – Xe	45.97–0.199E	6.481	0.62	6.502	6.9257	0.35	7.0	6.49	0.62	Ro, Rso
^{133}Cs	46.0–0.25E	$1.16A^{1/3}$ +0.6	0.62	7.0	$1.16A^{1/3}$ +1.1	0.35	7.0	$1.16A^{1/3}$ +0.6	0.62	Igarasi's OMP
^{134}Cs – ^{137}Cs	46.0–0.125E +0.0004E^2	$1.16A^{1/3}$ +0.6	0.62	7.0	$1.16A^{1/3}$ +1.1	0.35	7.0	$1.16A^{1/3}$ +0.6	0.62	
Ba	41.8	6.8886	0.62	2.931	7.0986	0.35	7.0	6.89	0.62	Rso
La – Ce	41.8	$1.327A^{1/3}$	0.62	2.95+0.789E	$1.367A^{1/3}$	0.35	7.0	$1.327A^{1/3}$	0.62	
Pr	46	$1.16A^{1/3}$ +0.6	0.62	7	$1.16A^{1/3}$ +0.6	1.0	7.0	$1.16A^{1/3}$ +0.6	0.62	Moldouer
^{142}Nd – ^{143}Nd	45.76	$1.29A^{1/3}$	0.6	6.97	$1.23A^{1/3}$	0.45	7.0	$1.28A^{1/3}$	0.6	
^{144}Nd – ^{148}Nd	47.94	6.718	0.6	9.13	7.564	0.45	7.0	6.771	0.6	
^{150}Nd	47.94	$1.27A^{1/3}$	0.6	9.13	$1.43A^{1/3}$	0.45	7.0	$1.28A^{1/3}$	0.6	
Pm	46	$1.16A^{1/3}$ +0.6	0.62	7.0	$1.16A^{1/3}$ +0.6	1.0	7.0	$1.16A^{1/3}$ +0.6	0.62	Moldouer
^{144}Sm, ^{148}Sm, ^{150}Sm, ^{154}Sm	46.96–0.0172E	$1.19A^{1/3}$	0.655	8.455	$1.44A^{1/3}$	0.448	7.0	$1.28A^{1/3}$	0.6	New OMP
^{147}Sm, ^{149}Sm	43.42–0.1879E	$1.355A^{1/3}$	0.6	9.875–0.0019E	$1334A^{1/3}$	0.45	7.0	$1.355A^{1/3}$	0.6	New OMP
Eu	44.77–0.0164E	$1.272A^{1/3}$	0.475	6.878–0.1408E	$1.44A^{1/3}$	0.45	7.0	$1.272A^{1/3}$	0.48	New OMP
Gd	38.0	7.439	0.47	8.0	7.439	0.52	7.0	7.439	0.47	
Tb	40.7–0.016E	$1.324A^{1/3}$	0.47	11.3	$1.338A^{1/3}$	0.47	7.0	$1.324A^{1/3}$	0.47	New OMP

Table 4 Nuclides List of DWBA Calculation

$^{96}Ru^{*}$	$^{98}Ru^{*}$	^{100}Ru	^{102}Ru	$^{104}Ru^{*}$	
$^{104}Pd^{*}$	^{106}Pd	^{108}Pd	^{110}Pd		
^{106}Cd	^{108}Cd	^{110}Cd	^{112}Cd	$^{114}Cd^{*}$	$^{116}Cd^{*}$
$^{130}Ba^{(R)}$	^{132}Ba	^{134}Ba	$^{136}Ba^{*}$	^{138}Ba	
^{140}Ce	^{142}Ce				
^{142}Nd	^{144}Nd	^{146}Nd	^{148}Nd	^{150}Nd	
^{144}Sm					

* ; β_2 only
(R) ; Rotational

Table 5 Systematics of Level Density Parameter a

$$a = A\frac{C_1 (N-N_1) + C_2 (N_2-N)}{N_2-N_1} + C_3 \ (MeV^{-1})$$

A : Atomic Mass Number
N : Neutron Number

N	N_1	N_2	C_1	C_2	C_3
$N \leqq 17$	1	17	0.0	0.0	4.0
$18 \leqq N \leqq 27$	18	27	0.15	0.15	0.0
$28 \leqq N \leqq 41$	28	41	0.193	0.122	0.0
$42 \leqq N \leqq 49$	42	49	0.155	0.187	0.0
$50 \leqq N \leqq 59$	50	59	0.185	0.104	0.0
$60 \leqq N \leqq 81$	60	81	0.114	0.182	0.0
$82 \leqq N \leqq 88$	82	88	0.166	0.100	0.0
$89 \leqq N \leqq 98$	89	98	0.124	0.171	0.0
$99 \leqq N \leqq 116$	99	116	0.123	0.123	0.0
$117 \leqq N \leqq 126$	117	126	0.041	0.116	0.0
$127 \leqq N \leqq 139$	127	139	0.154	0.058	0.0
$140 \leqq N \leqq 146$	140	146	0.124	0.141	0.0
$N \leqq 147$	147	200	0.120	0.120	0.0

Table 6 Comparison of Thermal Capture Cross Sections and Resonance Integrals between ENDF/B-V

Values of $\left| \frac{\text{ENDF/B-V}}{\text{JENDL-3}} - 1 \right|$ are given

NULIDE	σc (2200m/s)	RI	Remarks
Rh—105	0.0	1.89	NO RRP
Xe—135	0.0	0.003	
Nd—143	0.015	0.012	
Pm—147	0.085	0.032	
Pm—149	0.0	0.489	NO RRP
Sm—149	0.041	0.071	
Eu—151	0.0	0.081	
Sn—114	7.835	0.353	
Sb—124	0.626	0.927	NO RRP
I—131	0.991	0.898	NO RRP
Xe—131	0.059	0.129	
Xe—133	0.0	2.956	
Ba—135	0.004	0.233	
Ce—141	0.004	0.952	
Nd—147	0.886	0.027	
Pm—148	0.0	14.926	
Sm—147	0.123	3.440	
Sm—153	0.214	2.994	NO RRP
Eu—156	119.5	4.738	NO RRP
Weighted SUM	0.256	0.014	

Table 7 Comparison of σ_c with JENDL-2

NUCLIDE	σc (JENDL-3) / σc (JENDL-2)	C/E of JENDL-2 INTEGRAL TEST	
		STEK	EBR or CFRMF
^{105}Pd	~1 (<200KeV)	0.98	
^{103}Rh	~1	1.06	
^{101}Ru	~1	1.01	
^{99}Tc	~1 (<500KeV)	0.9	1.23
^{133}Cs	~1	0.8	0.91
^{107}Pd	~0.95(<100KeV)	0.97	
^{149}Sm	~1.05	1.0	0.88~0.97
^{97}Mo	~1 (<200KeV)	1.04	
^{95}Mo	~1 (<1MeV)	1.03	
^{147}Pm	~1 (<1MeV)	0.91	1.1
^{145}Nd	~1	0.88	0.81
^{151}Sm	~0.8	0.99	
^{135}Cs	~1	0.88	
^{131}Xe	~1	1.05	
^{109}Ag	~1 (<400KeV)	0.83	0.67
^{143}Nd	~1	0.91	0.85
^{102}Ru	~1 (<3MeV)	2.09	1.02
^{153}Eu	~1	0.94	0.88
^{104}Ru	~1 (<1MeV)	1.25	0.95
^{151}Eu	~1.1 (<70KeV)	0.86	0.68

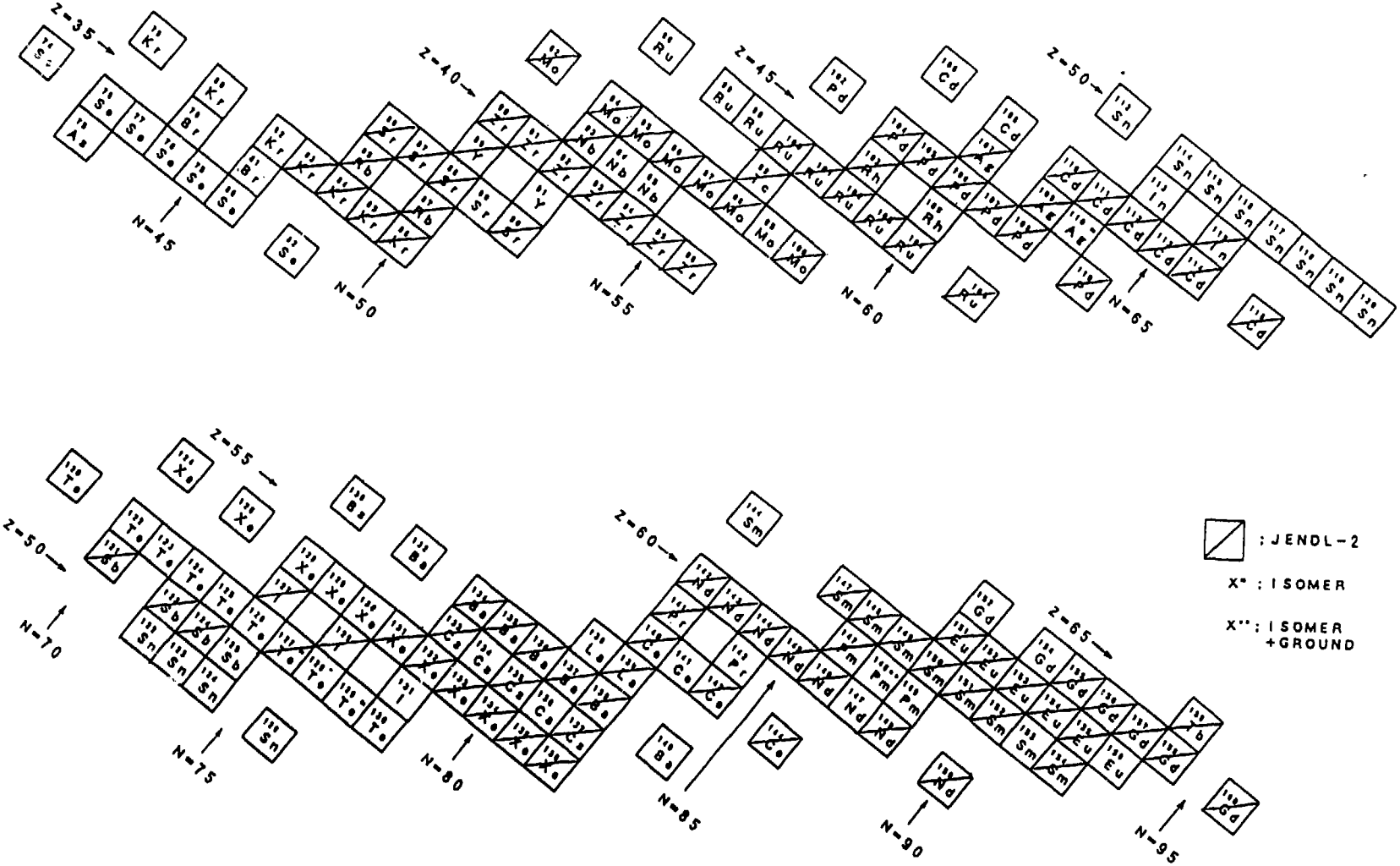

Fig. 1 Nuclides in JENDL-3 FP data file

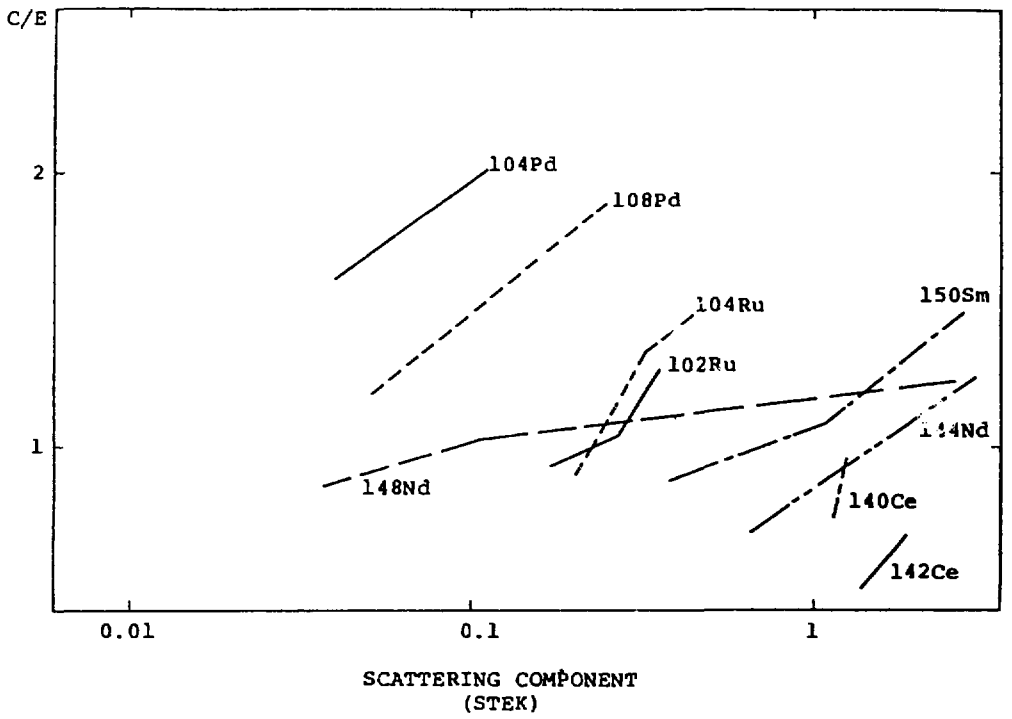

Fig. 2 C/E of STEK integral test for weak absorbers

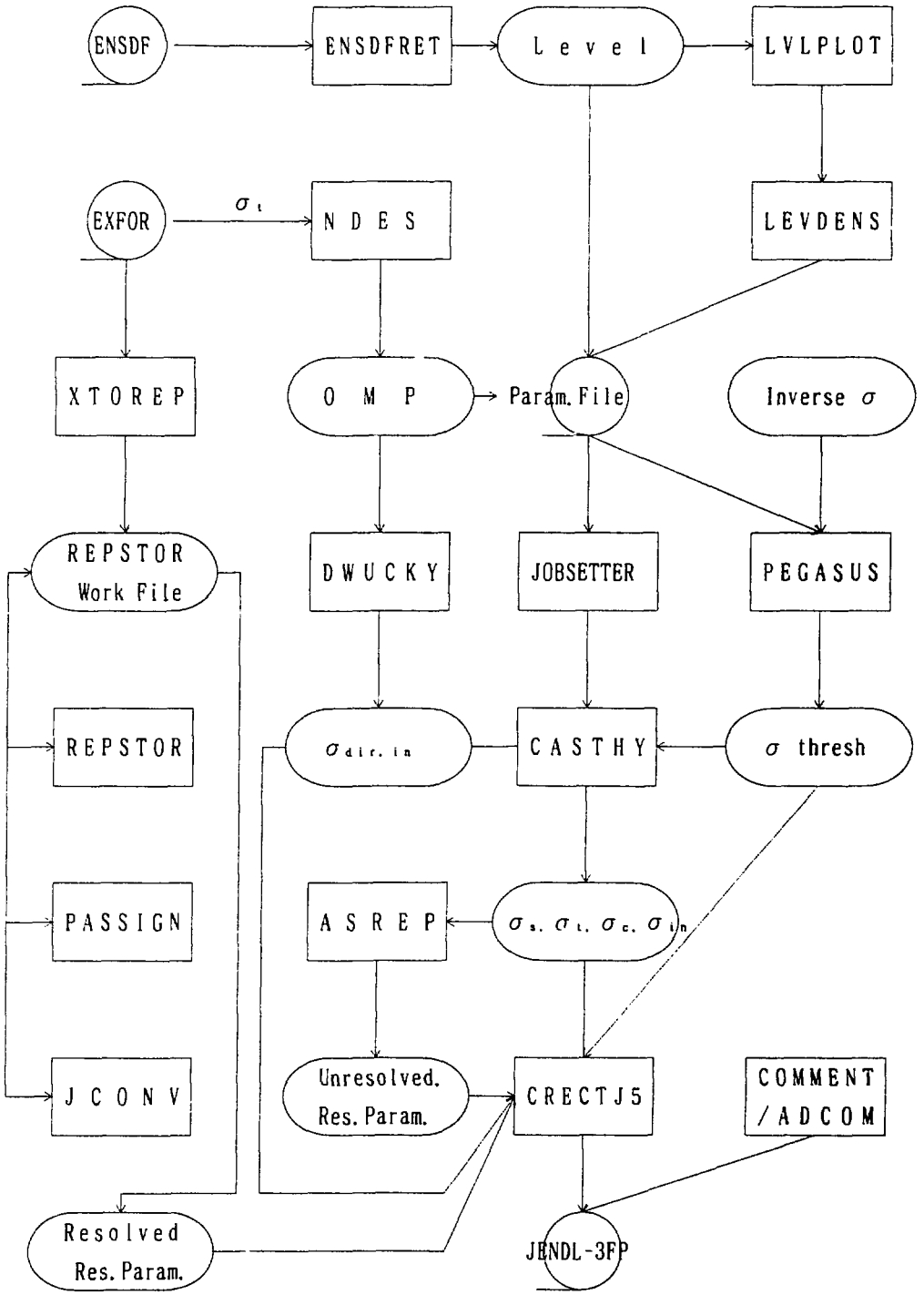

Fig. 3 Evaluation system

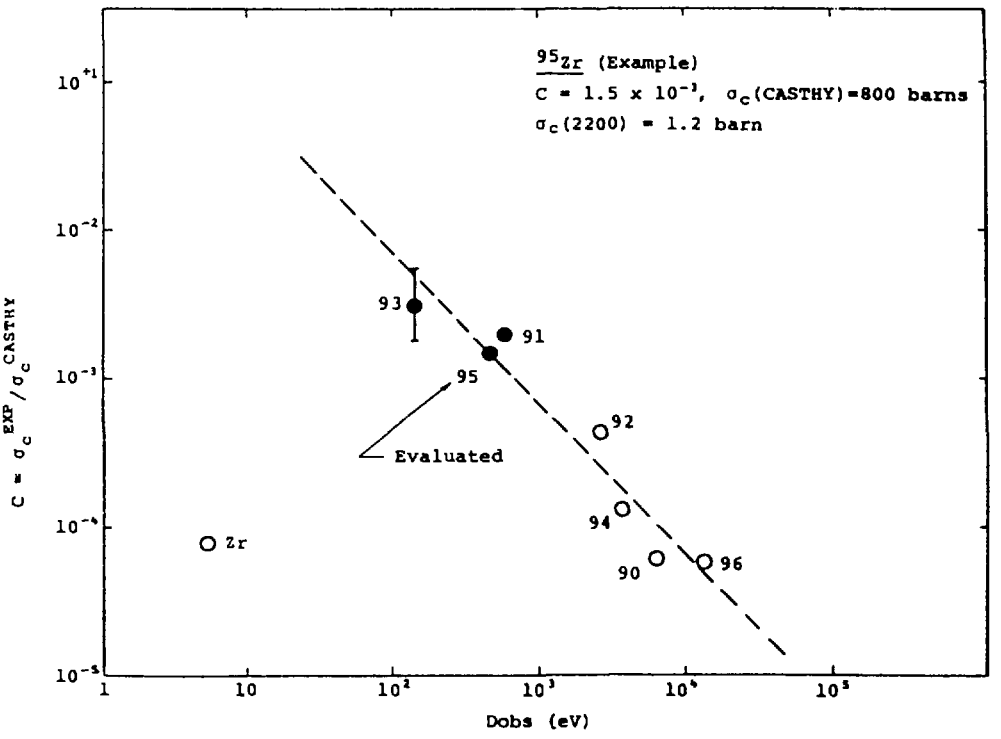

Fig. 4 σ_c^{2200} evaluation using systematics

2.1.5 Benchmark Test for Fusion Reactor

Hiroshi MAEKAWA
Japan Atomic Energy Research Institute
Tokai-mura, Naka-gun, Ibaraki-ken, 319-11 Japan

Fusion Neutronics Integral Test Subworking Group*
in Japanese Nuclear Data Committee

ABSTRACT

The cross section set, as a standard set for fusion neutronics, was prepared for the benchmark test of JENDL-3. The set named FUSION-J3 consists of 40-group gamma and kerma as well as 125-group neutron. This report is based on the benchmark tests performed by four groups. The status of nuclear data is discussed for 14 nuclei in JENDL-3. The Be and Pb data, whose problems were pointed out for JENDL-3T, have improved remarkably. The benchmark test for gamma-ray has been done for only Si, Ti and W. The benchmark tests for the other gamma-ray data and nuclear heating will be carried out soon.

---

* Members of Subworking Group : H. Maekawa (Leader), H. Handa, A. Hasegawa, C. Ichihara, T. Iguchi, S. Iwasaki, K. Kobayashi, K. Kosako, M. Kawai, K. Maki, S. Mori, M. Nakagawa, Y. Oyama, Y. Seki, H. Sekimoto, K. Sin, A. Takahashi, K. Ueki, J. Yamamoto
(Members with underline are contributors of this report.)

1. INTRODUCTION

The first activity of Fusion Neutronics Integral Test Subworking Group was to perform the benchmark test of JENDL-3T. For this purpose, the 125-group cross section set for ANISN and DOT3.5, named FSX125/J3T[1], was distributed to universities and institutes. The cross section library for the Monte Carlo code MCNP was also distributed by the MCNP Library Compilation Subworking Group in Research Committee on Reactor Physics. Results of these benchmark tests were reported at the 24th and 25th meetings of Subcommittee on Fusion Reactor in Research Committee on Reactor Physics and at the 1987 Seminar on Nuclear Data[2]. Discussions at the latter meeting concentrated mainly upon the problem in the data of Be and Pb.

The following conclusion was drawn from the benchmark test: Tritium production rates in a fusion blanket contained mainly Li_2O or Li can be estimated by the use of JENDL-3T nuclear data within 5%. But the accuracy of tritium production rate estimated is unsatisfactory for a blanket with Be or Pb neutron multiplier. Re-evaluation was strongly recommended for the nuclear data of Be and Pb.

The cross section set for ANISN and DOT3.5, as a standard cross section set for fusion neutronics, was prepared for the benchmark test of JENDL-3. The specifications of set are the same as those of the FSX125/J3T except for the gamma data. The set named FUSION-J3 consists of 40-group gamma and kerma as well as 125-group neutron. The feature of FUSION-J3 is described separately in this proceedings.[3]

Benchmark test plan of JENDL-3 for fusion neutronics is summarized in Table 1. Most of experimental data used in the benchmark test were produced in Japan. At the second meeting of Fusion Neutronics Integral Test Subworking Group held on Nov. 9, 1989, some results of JENDL-3 benchmark test were reported by FNS and OKTAVIAN/KUR groups. A calculational result for the shielding benchmark problem[3], which was one of ITER activities, was also reported at the meeting. This report is based mainly on the contents reported and discussed at the meeting, and on the benchmark test done by Nakagawa using the MORSE-DD code[4].

2. STATUS OF NUCLEAR DATA IN JENDL-3 RELEVANT TO FUSION NEUTRONICS

The following comments on JENDL-3 are pertinent from the present benchmark tests.

^{7}Li

As the data of ^{7}Li were a little modified from JENDL-3T based on the previous benchmark test[2], the status of ^{7}Li data seams to be good enough for fusion reactor design. A sample of benchmark test[d] is shown in Fig. 1.

^{9}Be

Measured and calculated angular neutron flux spectra on Be slab[c] is shown in Fig. 2. The calculated result based on JENDL-3 is improved largely in the range of 4 ~ 10 MeV. While there still exists an overestimation in 1 ~ 2 MeV. The same result was observed in the analysis of leakage spectrum from a Be sphere[d] shown in Fig. 3. From these analyses of time-of-flight experiments and of integral experiments on Be assembly and Be-sandwich Li_2O assembly, the status of Be data is fairly well.

^{12}C

Agreement is excellent on the whole for the angular flux spectra on graphite slabs[c] shown Fig. 4. As the data for the second inelastic level in JENDL-3 was modified from those in JENDL-3PR2, the agreement improved remarkably at the peak near 7 MeV. A sample of C/E distribution[a] is shown in Fig. 5 for $^{27}Al(n,\alpha)^{24}Na$ in a graphite assembly. The status of ^{12}C data is very good.

^{14}N

The data of (n,d), (n,t) etc. in JENDL-3 were modified from those in JENDL-3T. Angular neutron flux spectrum on liquid nitrogen[b] is shown in Fig. 6. There is a large difference between calculated and measured spectra. It is not clear right now the reason why such large deviation exists. In order to check the nuclear data processing code, an analysis using the Monte Carlo code MCNP is being carried out.

^{16}O

Angular neutron flux spectrum on liquid oxygen[b] is shown in Fig. 7. As the difference between JENDL-3 and JENDL-3T data is a little, almost the same results are observed between them. From this analysis and the results of benchmark test using the integral experiment on the Li_2O assembly, the data of ^{16}O are reasonable.

Al

Neutron leakage spectrum from Al sphere[e] is shown in Fig. 8. A fairly well agreement is observed between calculated and measured spectra.

Si

Neutron and gamma-ray spectra from Si sphere[f] are shown in Fig. 9. From this benchmark test, the status of both neutron and gamma-ray data for Si seam to be good enough for fusion neutronics analysis.

Ti

Neutron and gamma-ray spectra from Ti sphere[f] are shown in Fig. 10. There are some problems in both neutron and gamma-ray data.

Mn

From the analysis of TOF experiment on Mn sphere[e], the status of Mn data is good.

Cr

From the analysis of TOF experiment on Cr sphere[e], the status of Cr data is fairly well. But there is some deviation between the calculated and measured spectra below 1 MeV shown in Fig. 11.

Cu

From the analysis of TOF experiment on Cu sphere[e], the status of Cu data is fairly well.

Mo

From the analysis of TOF experiment on Mo sphere[e], there are some problems in the Mo data.

W

Neutron and gamma-ray spectra from W sphere[4] are shown in Fig. 12. From this analysis, there are some problems in both neutron and gamma-ray data.

Pb

A sample of angular neutron flux spectra on Pb slabs[b] is shown in Fig. 13. Excellent agreement is observed between calculated and measured spectra except the region between 5 and 11 Mev. If the number of inelastic level increases more than present limit in JENDL-3 or bunched levels are used, a good agreement should be obtained.[5]

3. CONCLUDING REMARKS

Using the nuclear data of JENDL-3, it is expected to estimate the tritium production rate in a typical fusion blanket within about 5~10%. Most types of reaction rates in it can be estimated within about 10%. The Be and Pb data, of which problems were pointed out for JENDL-3T, have improved remarkably.

The benchmark test relevant to the gamma-ray data has been done for only Si, Ti and W. The benchmark tests for the other gamma-ray data and nuclear heating will be carried out soon. It is expected that these tests give useful informations for the evaluation of JENDL-3.

REFERENCES

1) Kosako K., et al.: "Neutron Cross Section Libraries for Analysis of Fusion Neutronics Experiments," JAERI-M 88-076 (1988) (In Japanese)
2) Maekawa H.: "Fusion Neutronics Integral Test for JENDL-3T," Proc. 1987 Seminar on Nuclear Data, JAERI-M 88-065, pp198-211 (1988).
3) Maki K., et al.: "Comparison of Calculated Shielding Properties by JENDL-3 with Those by ENDF/B-IV," In this proceedings.
4) Mori T., et al.:"One-, Two- and Three-Dimensional Transport Codes Using Multi-Group Double-Differential Form Cross Sections," JAERI 1314 (1988)
5) Mizumoto M.: Private communication.

Table 1 Benchmark test plan of JENDL-3 for fusion neutronics

Organiztion	Benchmark Problem	Personnel	Standard analysis	Additional analysis
JAERI	·Integral experiments on Li_2O, C, Li_2O-C, Be, Fe, & Be-sansich Li_2O asemblies	H. Maekawa K. Kosako S. Yamaguchi K. Oishi	DOT3.5[a]	MCNP
	·TOF experiments on Li_2O, C, Li, Be, Fe, Pb, LN_2 & LO_2 slabs	Y. Oyama H. Maekawa	DOT3.5[b]	MCNP[c] MORSE-DD
	·Pulsed Sphere Program (LLNL), ^6Li, ^7Li, C, O, Fe, Pb, P.E., H_2O, Be	M. Nakagawa T. Mori		MORSE-DD[d]
	·Experiment on SS316 assembly at ORNL	K. Sakurai		MORSE MCNP
University	·Integral experiments on Li & Pb-Li spheres	T. Iguchi K. Sugiyama	ANISN	MCNP
Osaka Univ.	·TOF experiments on Li, Pb, SS316 & concrete assemblies	A. Takahashi J. Yamamoto	ANISN	MCNP
KURRI Osaka Univ.	·n & γ spectra measurements on Nb, Li, CF_2, Al, Si, Ti, Cr, Co, W, Pb, As, Se, LiF, Mn, Cu, Zr & Mo spheres	C. Ichihara J. Yamamoto	ANISN[e]	MCNP[f]
Kyoto Univ.	·Backscattering experiments on concrete & SS304 assemblies	K. Shin	ANISN	MCNP
TIT	·Spectra in LiF, C, H_2O & LiF-C assembies	H. Sekimpto	MORSE	
Tohoku Univ.	·TOF experiments on P.E. & Pb assemblies	S. Iwasaki		MCNP
Toshiba	·Pulsed Sphere Program (LLNL)	M. Kawai M. Uematsu	ANISN MORSE	MCNP
KHI	·Pulsed Sphere Program (LLNL), H_2O, Fe ·Fe sphere (Illinois Univ.)	S. Mori	ANISN DOT3.5	MCNP

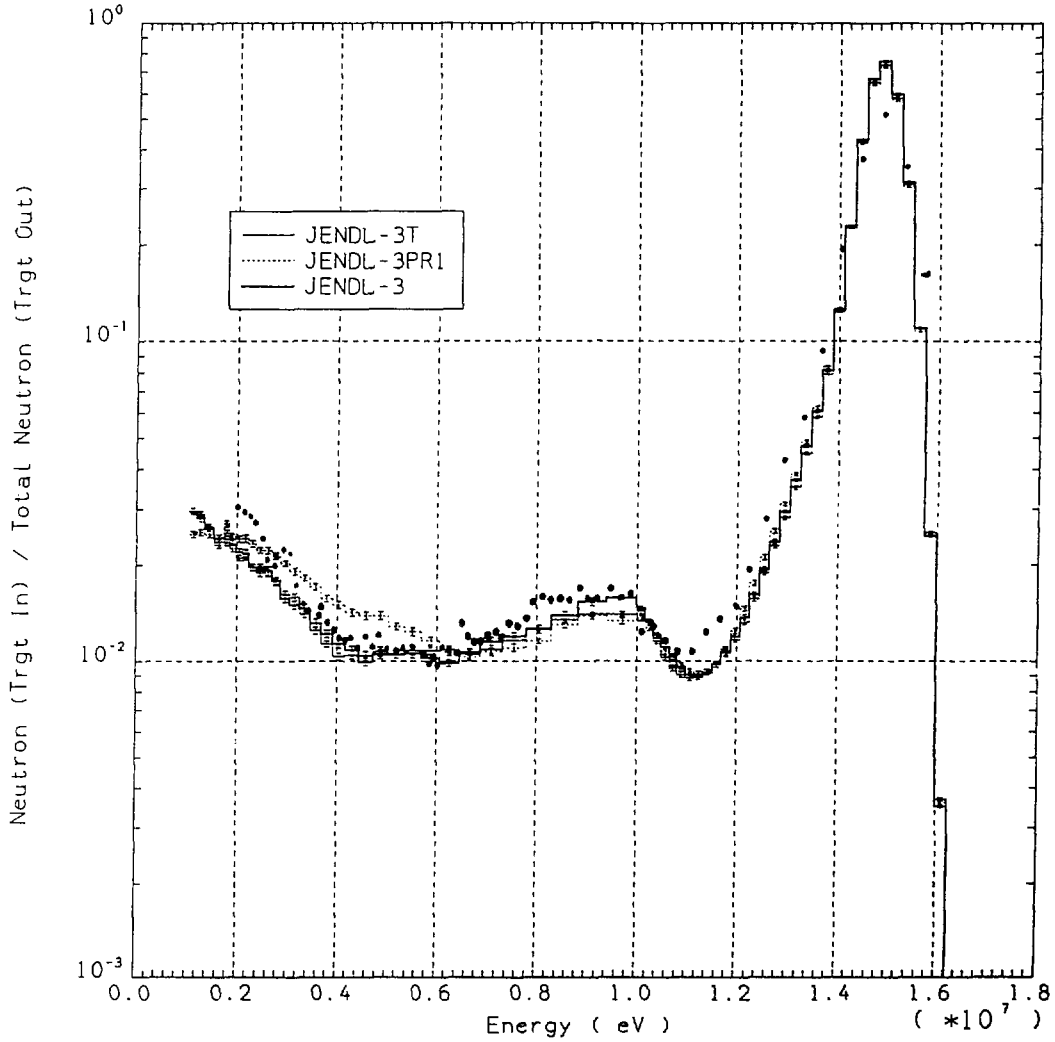

Fig. 1 Neutron leakage spectrum from Li-7 sphere (0.5 mfp), 30°

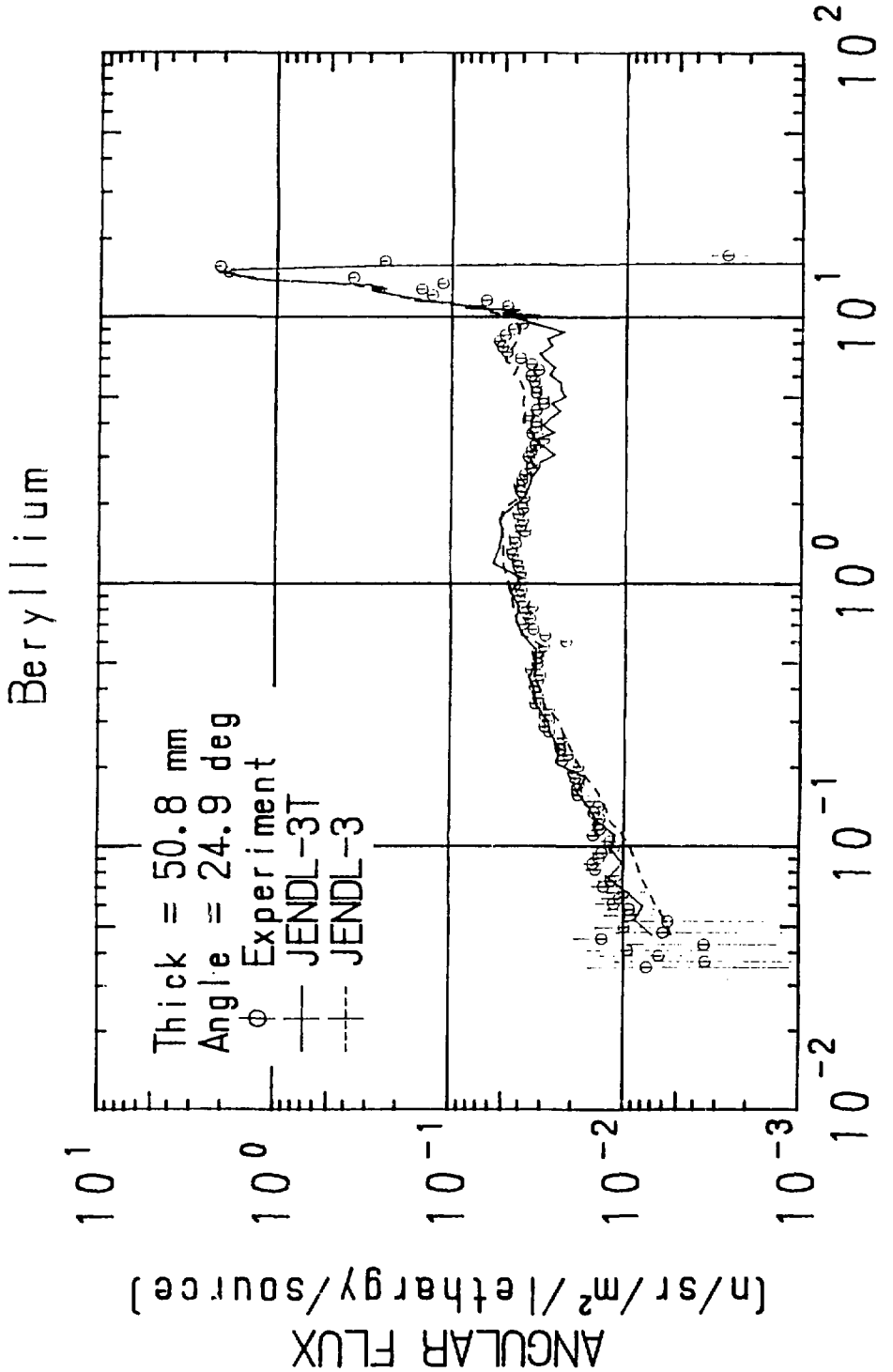

Fig. 2 Angular neutron flux spectrum on Be slab

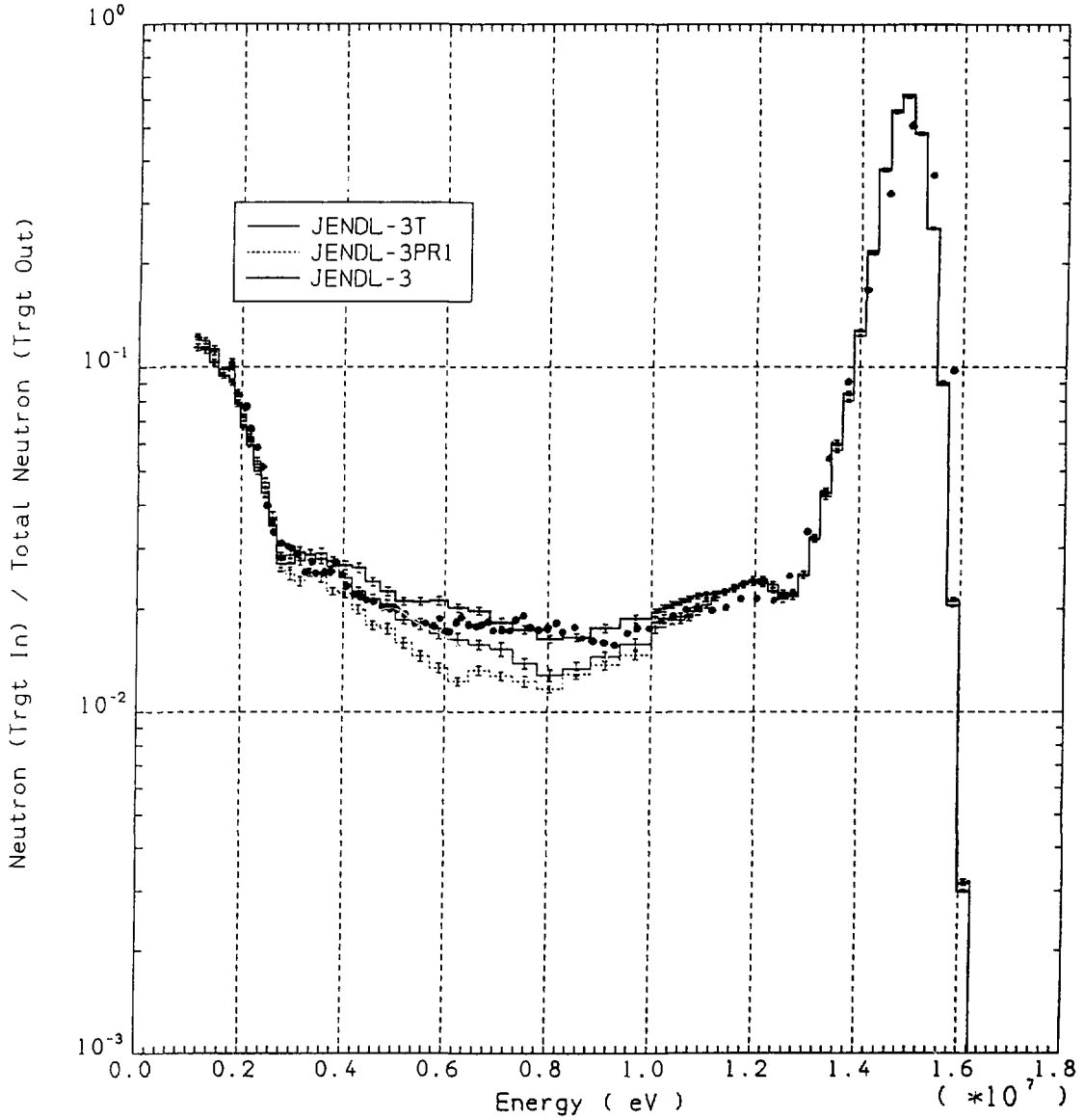

Fig. 3 Neutron leakage spectrum from Be sphere (0.8 mfp).

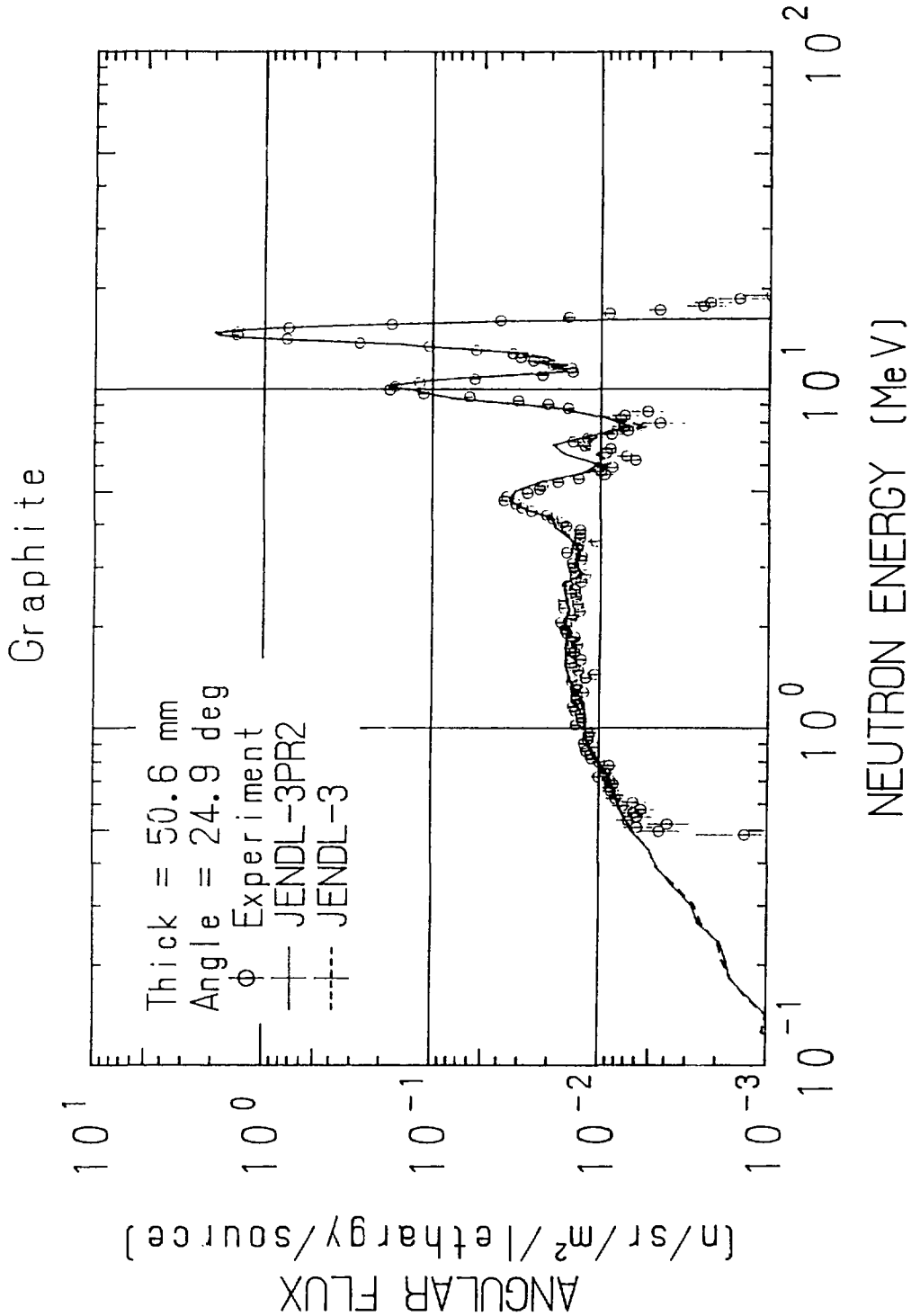

Fig. 4 Angular neutron flux spectrum on graphite slab

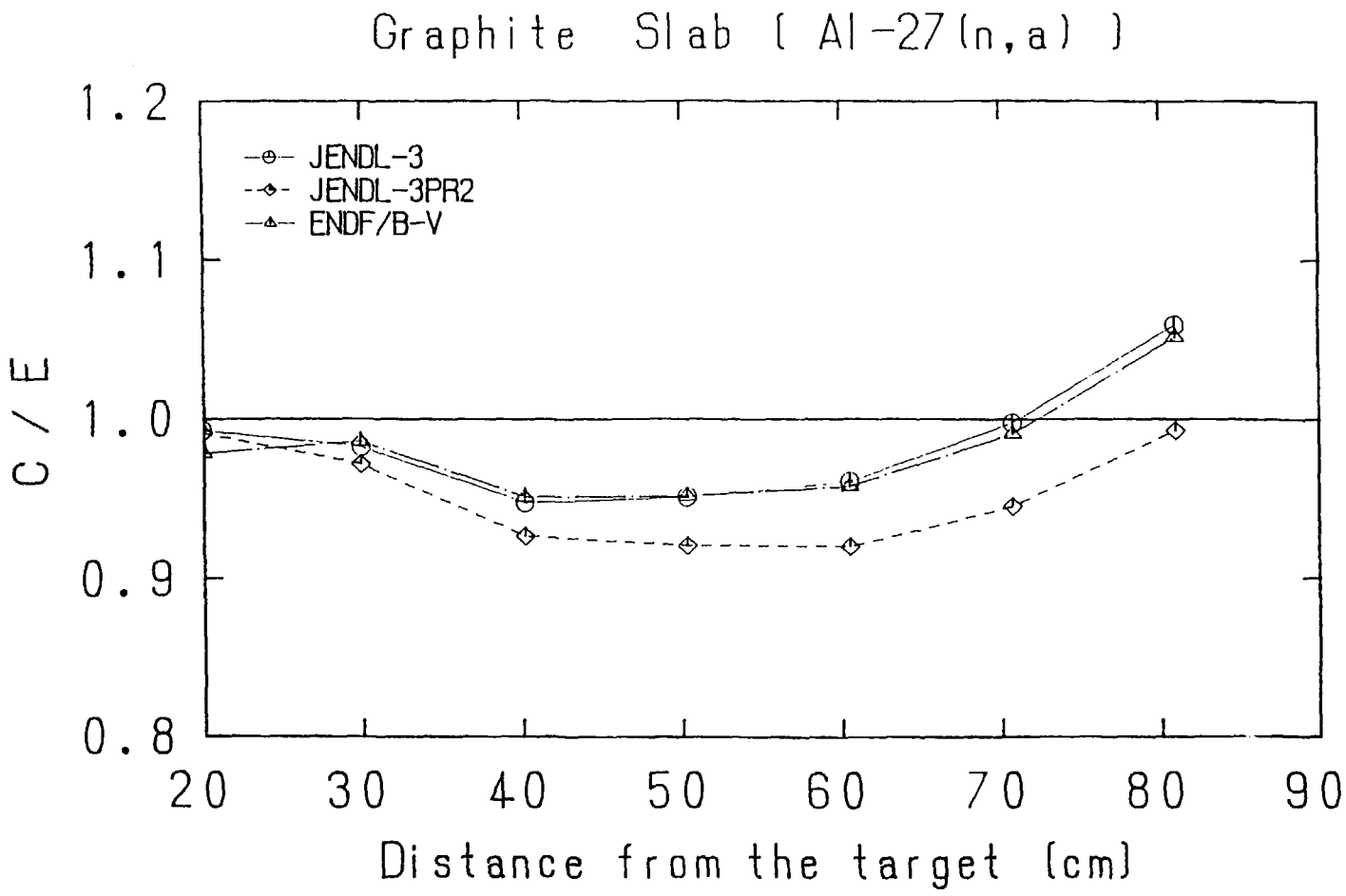

Fig. 5 C/E distribution of $^{27}Al(n,\alpha)^{24}Na$ in graphite cylindrical assembly

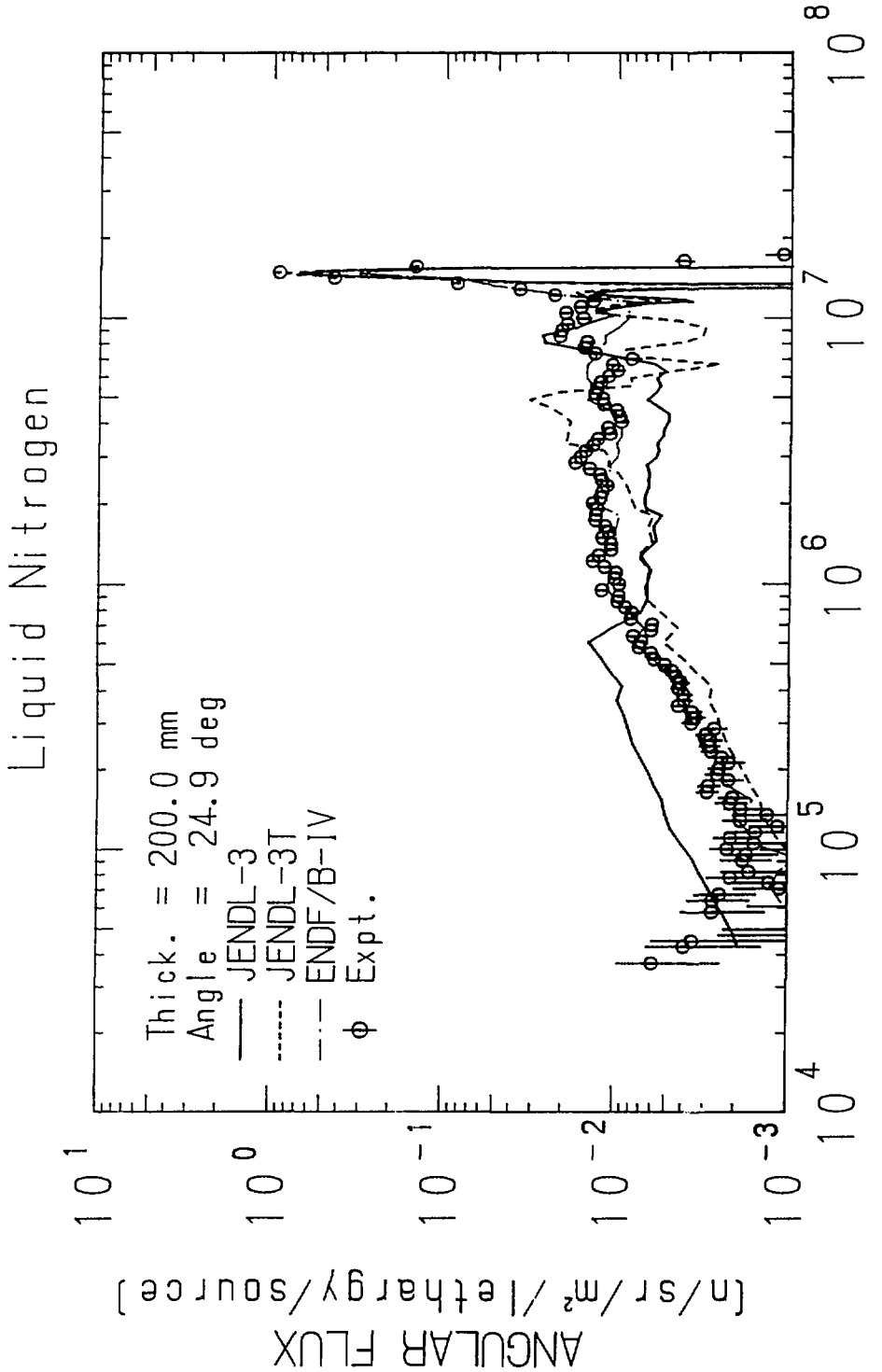

Fig. 6 Angular neutron flux spectrum on liquid nitrogen slab

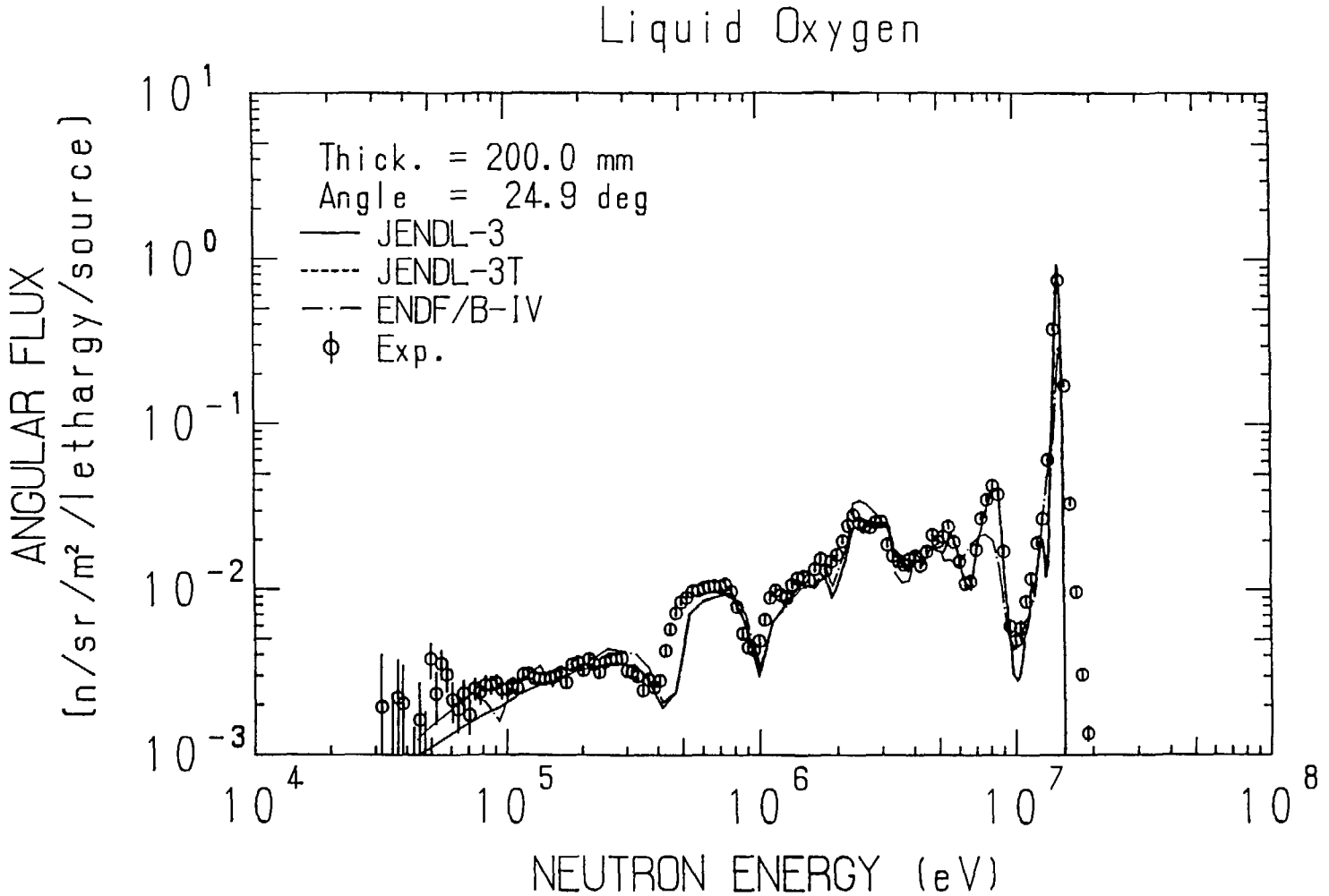

Fig. 7 Angular neutron flux spectrum on liquid oxygen slab

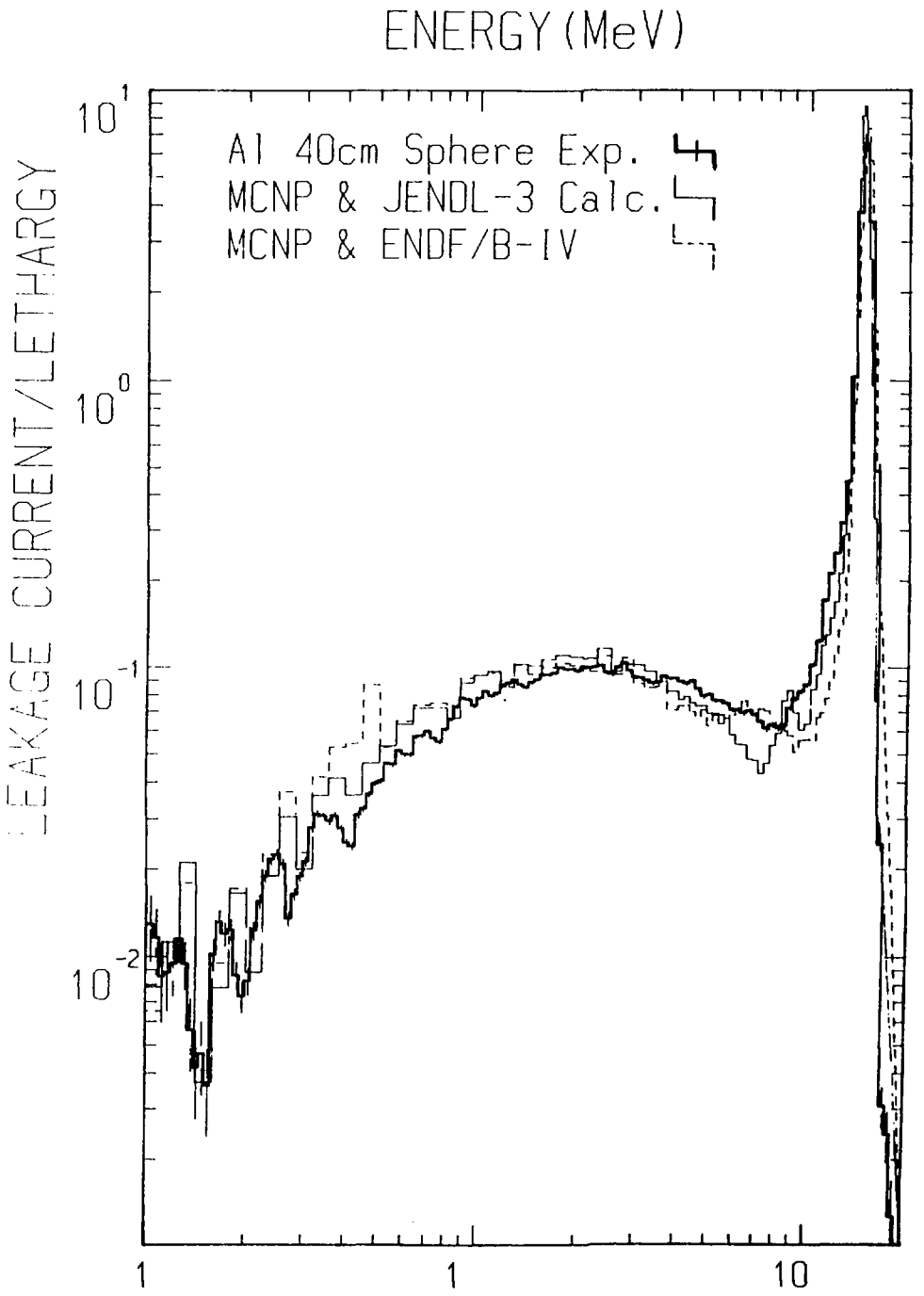

Fig. 8 Neutron leakage spectrum from Al sphere

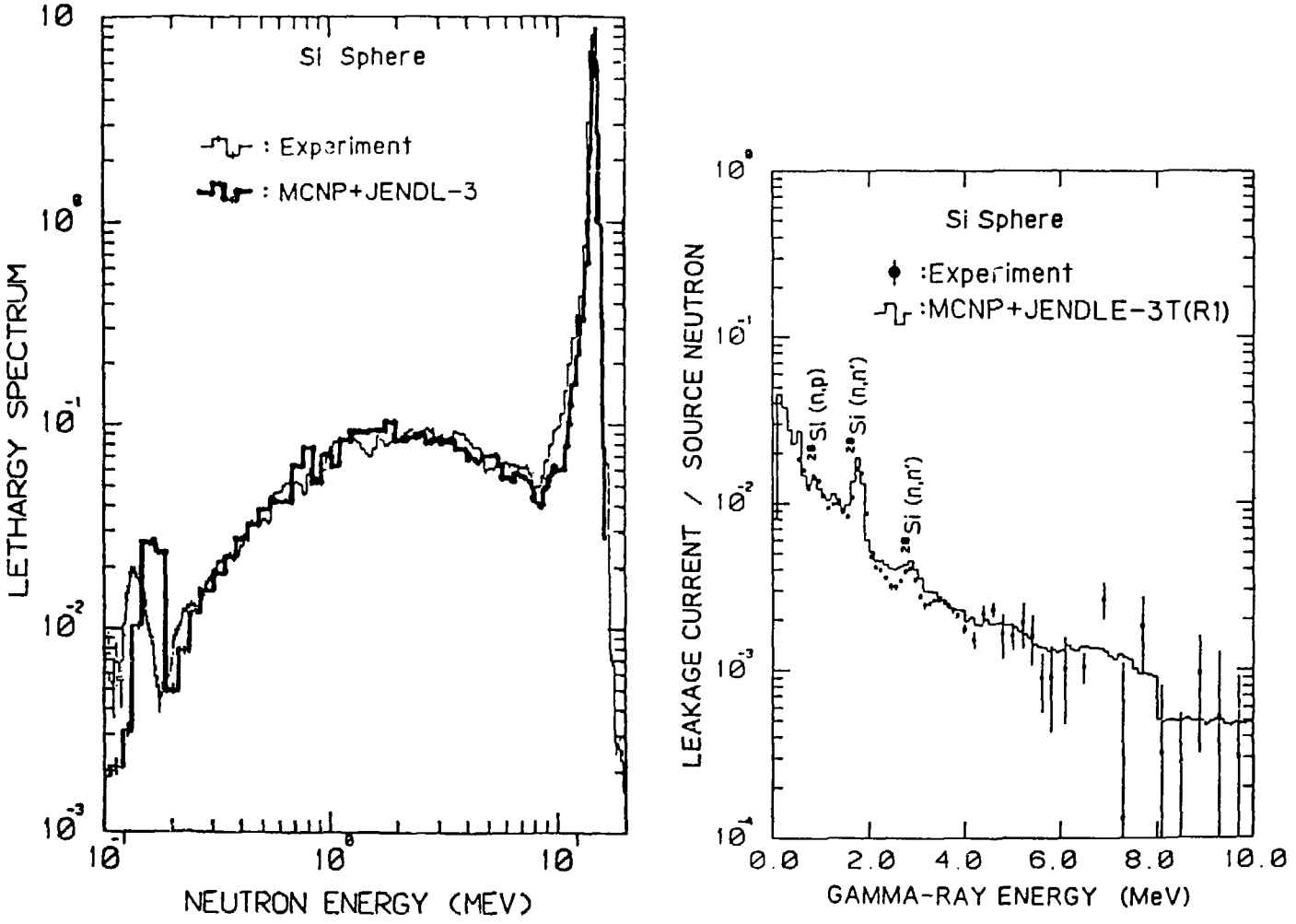

Fig. 9 Neutron and gamma-ray leakage spectra from Si sphere

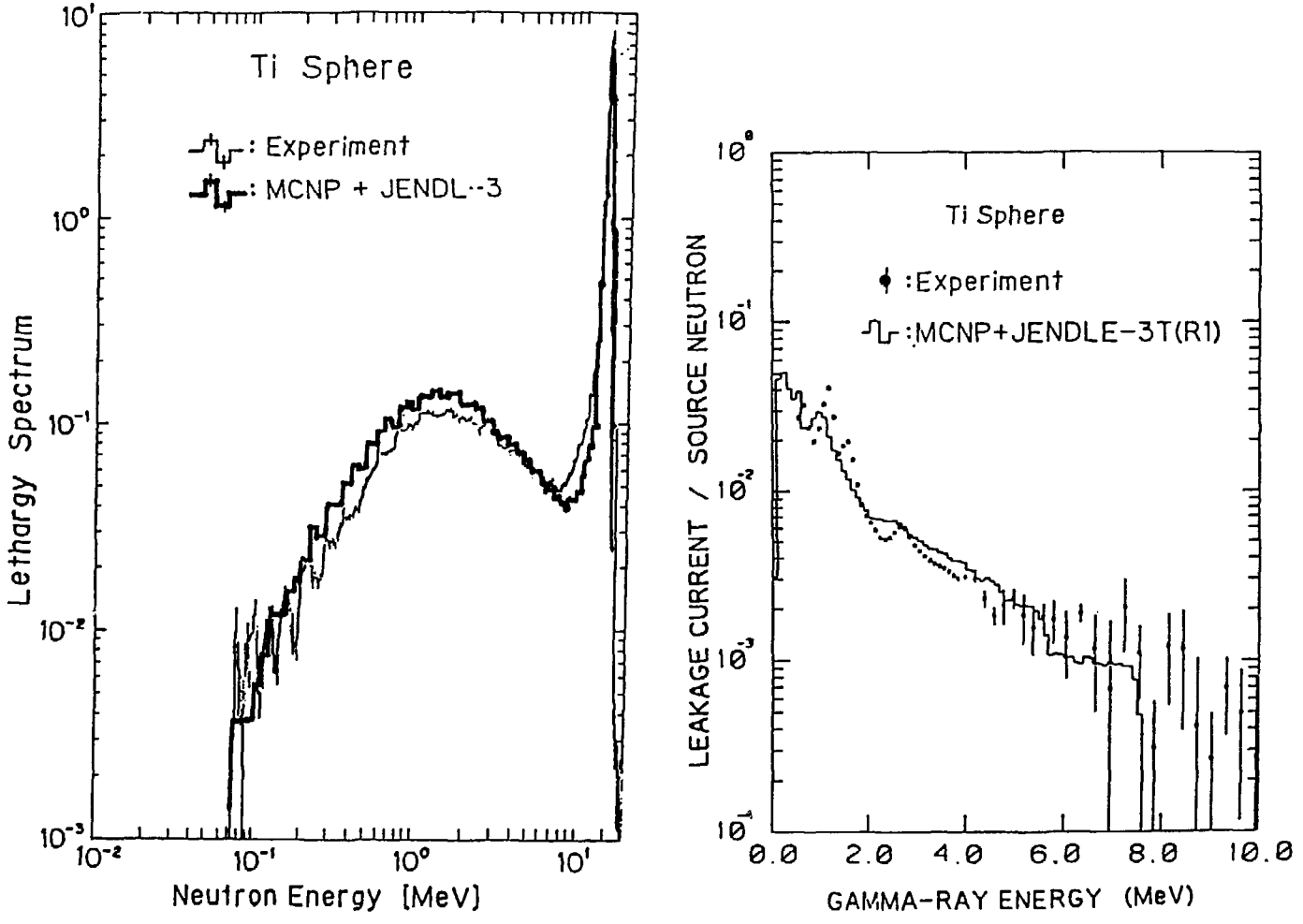

Fig. 10 Neutron and gamma-ray leakage spectra from Ti sphere

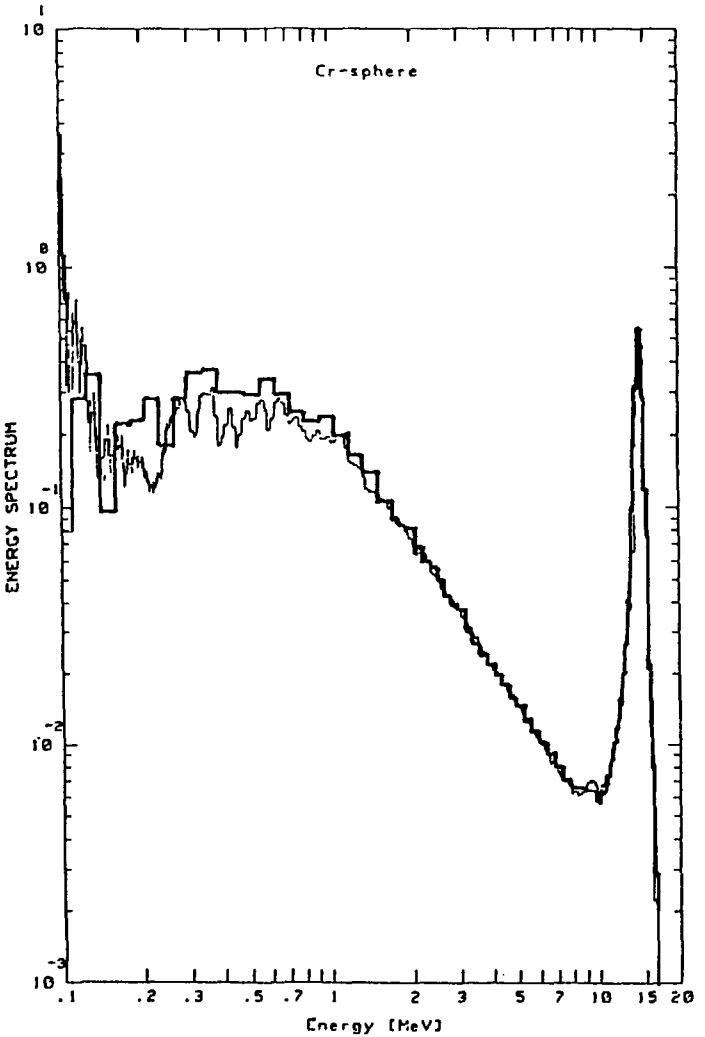

Fig. 11 Neutron leakage spectrum from Cr sphere

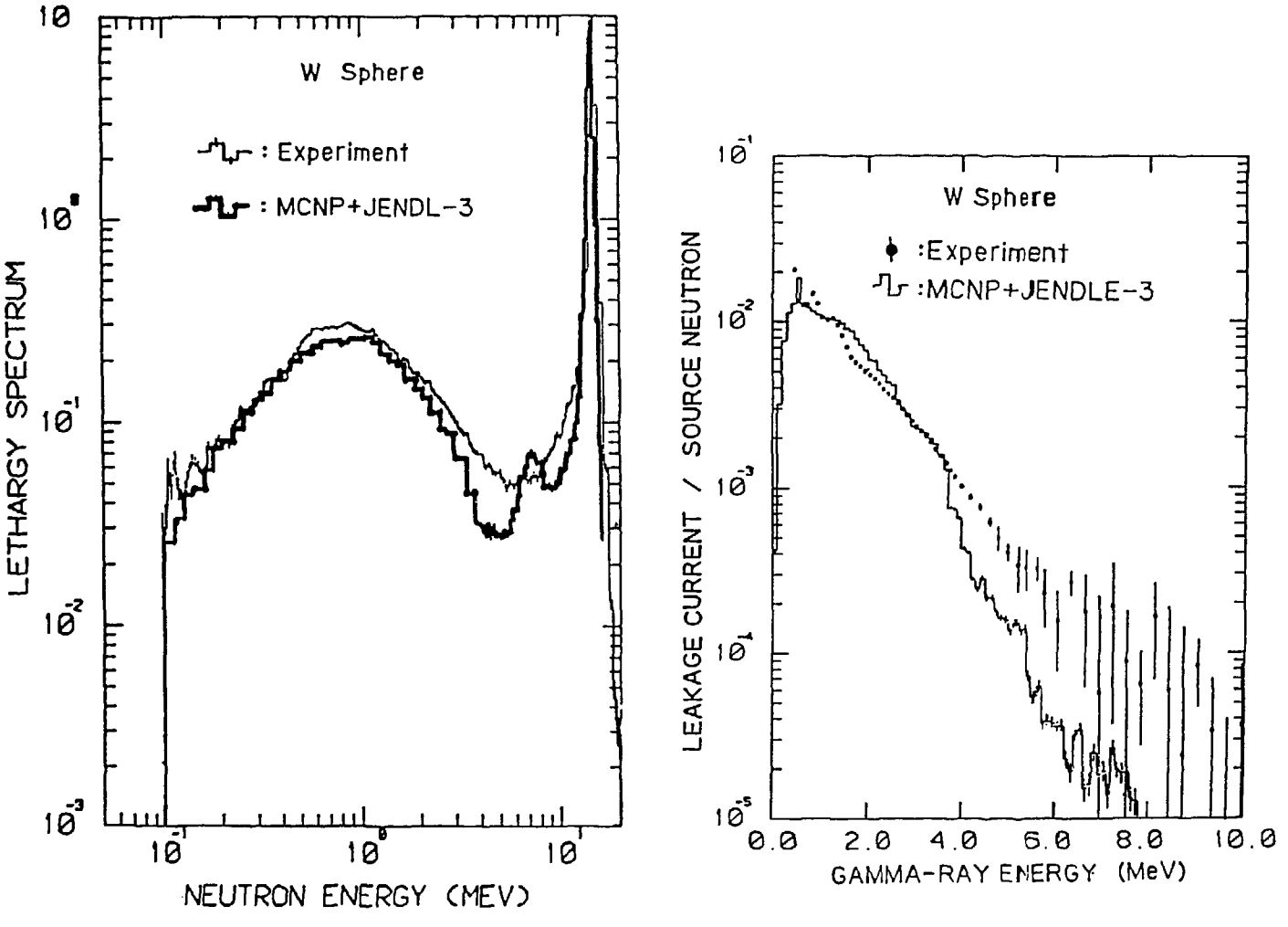

Fig. 12 Neutron and gamma-ray leakage spectra from W sphere

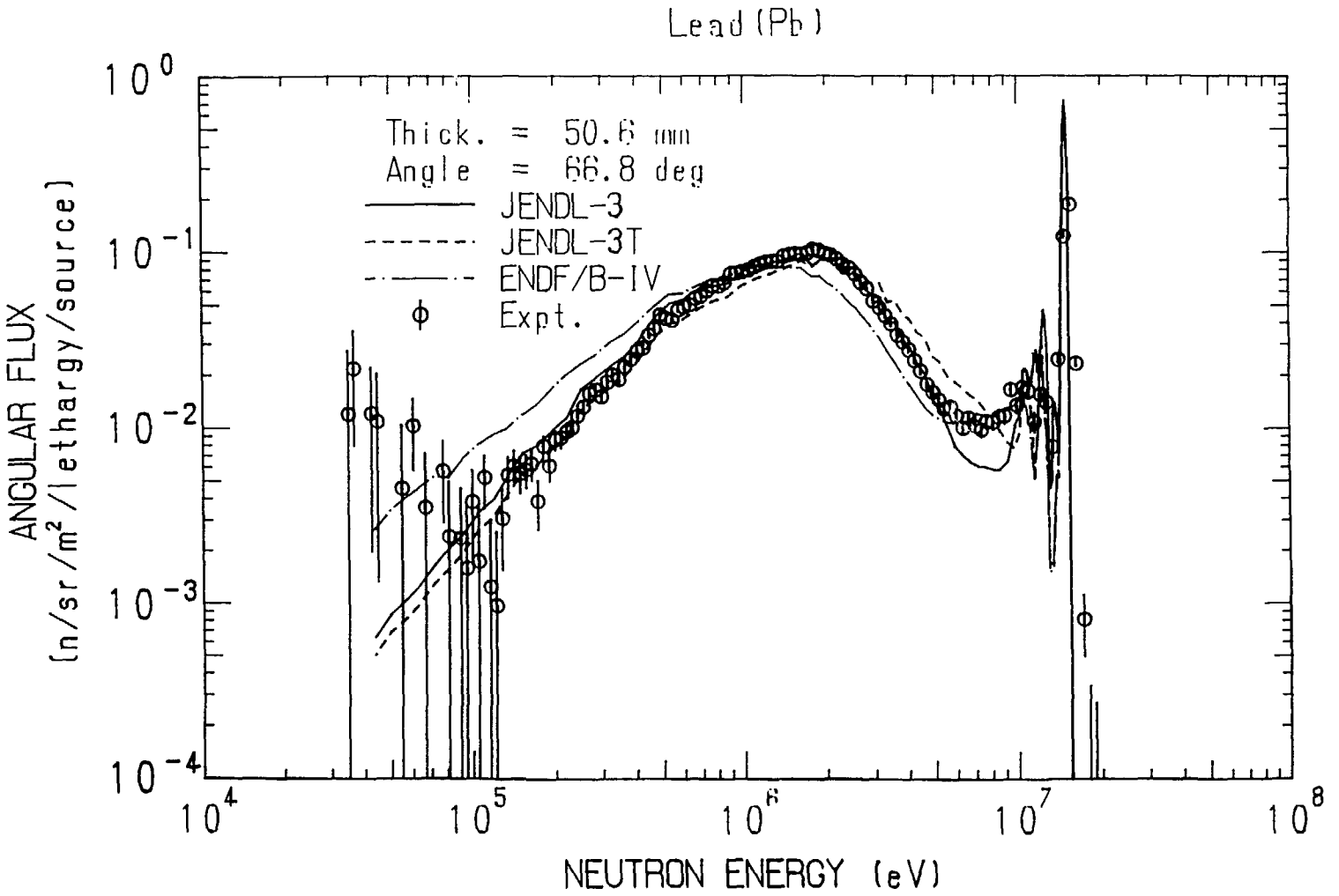

Fig. 13 Angular neutron flux spectrum on Pb slab

2.1.6 Shielding Benchmark Test of JENDL-3

M. Kawai[1], A. Hasegawa[2], K. Ueki[3], N. Yamano[4], K. Sasaki[5], Y. Matsumoto[6], M. Takemura[7], N. Ohtani[8], H. Tsunoda[9], K. Sakurai[2], Y. Itoh[2], M. Uematsu[1] and Y. Oka[10].

1) Toshiba, 2) JAERI, 3) SRI, 4) SAEI 5) MAPI, 6) MES, 7) KHI, 8) PNC, 9) MRI and 10) U. Tokyo

Abstract

The integral test of JENDL-3 for shielding application was made on a cross sections of carbon, sodium and iron by analyzing the various shielding benchmark experiments: Broomstick experiments at ORNL for iron and sodium, neutron transmission experiments for sodium at ORNL, iron and carbon, ASPIS deep penetration experiments for iron, measurements of leakage spectrum from iron spheres at KfK, angular neutron spectrum measurements in graphite block at RPI. Analyses were made with radiation transport codes ANISN (1D, Sn), DIAC (1D, Sn), DOT-3.5 (2D, Sn) and MCNP (3D, point Monte Carlo). It was observed that revising JENDL-3T iron data resulted in an improvement in reproducing the experimental data, particularly in the MeV neutron energy region. For sodium, JENDL-3 gave better results than JENDL-2 and ENDF/B-IV. For carbon, JENDL-3 gave better agreement, compared to ENDF/B-IV. The conclusion is that JENDL-3 is highly applicable to the reactor shielding analyses.

1. INTRODUCTION

The JENDL-3 shielding benchmark test was made as an activity of JNDC Shielding benchmark testing Sub-working group for clarifying the JENDL-3 applicabilty to shielding analyses. The test scope was to analyze the shielding benchmark experiments for Li-6, Li-7, Be-9, carbon, oxygen, sodium, iron, chromium, nickel and niobium, mainly with the sources of nuclear reactors or the photo neutron. This paper is an interim report about the results for important elements of iron, sodium and carbon. The test has been made by analyzing the following shielding experiments:

1) Broomstick experiments[1] made at ORNL to test total cross

sections,

2) ORNL neutron transmission experiments of iron block[2] (10 to 90 cm thick) and sodium cylinder[3] (3.0 meters and 4.6 meters long), using the collimated neutron beam from the TSF reactor,
3) ASPIS deep penetration experiments[4] (140 cm thick iron) using fission neutron source,
4) KfK leakage spectrum measurements[5] from iron spheres (15 to 40 cm diameter) using the Cf-252 neutron source,
5) RPI angular neutron spectrum measurement[6] (so called Profio's experiment) in a 132x152x152 cm graphite block using a photo-neutron source with the time of flight method,
6) ORNL experiments of neutron transmission through the graphite block[7] (10 to 60 cm thick) using the broad neutron beam source from the TSF reactor.

Analyses were made with radiation tranport codes ANISN (1D Sn), DIAC (1D, Sn), DOT-3.5 (2D, Sn) and MCNP (3D point Monte Carlo). Group constants with P5 anisotropy for Sn calculations were generated from JENDL-3 as well as JENDL-3T and ENDF/B-IV by cross section processing system PROF-GROUCH-G2/B or RADHEAT-V4, which were developed at JAERI. The pointwise cross section library for MCNP was prepared by NJOY code system. In the previous integral tests on JENDL-3T, the overall applicability of the iron, sodium and carbon data in JENDL-3T to the shielding problems was confirmed, except for the total and inelastic scattering cross sections of iron for which reevaluation was required in the energy range above 0.8 MeV.[8] Then, the iron cross sections in the high energy region were modified for JENDL-3. Accordingly, reanalyses were made only for iron, and the reults for sodium and carbon presented here are the same as those for JENDL-3T.

2. RESULTS

Major results of the present work are compared with those for JENDL-3T in Table 1. The following are descriptions about the results for each material.

2.1 Iron

For the Broomstick experiment, the uncollided neutron spectrum, calculated from JENDL-3, agrees with the experiment above 5 MeV; as shown in Fig. 1. However, the discrepancy between the calculations and the measurements remains below 5 MeV, as was observed in the JENDL-3T

results.

The ORNL transmission experiments were reanalyzed with the DOT-3.5 and MCNP codes, since DOT-3.5 underestimated the flux along the center axis, because of the ray-effect in Sn approximation and group collapsing effect. Table 2 shows that the MCNP results for the on-axis data agree, within 18% errors. The values in parenthesis are uncollided flux contribution to the detector response. Table 3 shows the results for the off-center axis data. The calculated values, with both MCNP and DOT-3.5, agree with each other within the Monte Carlo statistical errors for the 12 inch thick sample. Therefore, the DOT-3.5 results for the off-center data are considered to be reliable for the integral test. As a whole, the JENDL-3 results are similar to those for JENDL-3T, and agree with the experimental data for neutron flux and the Bonner ball responses within 30% error.

For the ASPIS experiment, the neutron spectrum, calculated with JENDL-3 is improved in the energy range above 1 MeV, as shown in Fig. 2. Agreement with the experiment results is remarkably good, near the 24-keV window, while the ENDF/B-IV shows an overprediction. Figures 3 and 4 show that MCNP gave a better neutron spectrum, at around 1 MeV, than DOT-3.5. The spatial distribution for $^{32}S(n,p)$ reaction became nearly constant (i.e. ~1.4) as observed in Fig. 5.

For the KfK experiment, slightly better agreement with the experimental data is observed in the JENDL-3 results, than JENDL-3T, as shown in Fig. 6. It is interesting to note that there is a large difference between neutron spectra from JENDL-3 and ENDF/B-IV in a neutron spectrum below 20 keV, where no experimental data is available.

2.2 Sodium

The spectrum of neutrons transmitted through the 10-ft thick sodium sample was calculated with DOT-3.5. The results agreed with the measured spectrum at ORNL with the C/E values 1.0 - 1.3, although there is a hydrogen impurity ambiguity in the sample. The results are shown in Fig. 7. The calculated and measured Bonner ball responses are compared in Fig. 8 in case of the 10-foot long sample. The C/E values for the Bonner ball response ranged from 0.75 to 0.97 for the 10 ft long sample, and from 0.74 to 1.05 for the 15-ft long sample.. These results are better than those of JENDL-2 and ENDF/B-IV, while the Broomstick experiment showed that the sodium total cross section above 1 MeV may have been underevaluated by several percent at maximum.

2.3 Carbon

Profio's experiment was available. There are some differences between the measured neutron spectra in the high energy measurement

above 800 keV and those in the lower energy measurement. The latter were obviously discrepant from the calulations from various nuclear data libraries[9]. Therefore, the present integral test was made in the energy range above 800 keV. The result is fairly good, as shown in Fig. 9 (C/E = 0.8 - 1.3).

The ORNL neutron transmission experiments, with a fast neutron spectrum simulating a blanket leakage spectrum, were analyzed with the 21-group S8 calculation. The C/E values, for the results obtained with JENDL-3, JENDL-2 and ENDF/B-IV, are give in Table 4. The values of JENDL-3 are moderate and nearest to unity among the three libraries. Although some ambiguities remain in the few-group calculations, it can be said that the carbon cross section of JENDL-3 is satisfactory for shielding application.

3. Discussion and Concluding Remarks

Table 1 shows that the cross sections of carbon, sodium and iron in JENDL-3 reproduce the shielding experimental data obtained in the fast neutron field within an error of 30%. Besides, the discrepancy between the calculations and the experiments does not come only from the poorness of the nuclear data libraries. In Table 3, MCNP gives slightly larger values than DOT-3.5. This tendency is more obvious in the neutron spectrum in the energy region between 0.8 MeV and 2 MeV of the ASPIS iron benchmark experiments, given in Figs. 2 and 4. This tendency comes from the difference in cross section treatment in the codes: groupwise cross section in DOT-3.5 and pointwise cross section in MCNP. Accordingly, the difference in the calculated results becomes larger in the deeper transmission in iron. On the other hand, some experimental data have inconsistencies, as found in the results of the Profio's experiments. Reliability of the spectra, measured with a proton recoil counter, may decrease above 1 MeV. The inconsistency in reproductiveness for the MeV neutron spectrum, in the overprediction in the KfK experiments and the underprediction in the ASPIS experiments, is possibly due to the poor reliabilty of measured data.

However, it must be pointed out that JENDL-3 seems to underpredict the neutron spectrum in the energy range between 1 MeV and 3 MeV, as shown in the analyses on the Broomstick experiments. If the iron total cross sections of JENDL-3 and ENDF/B-IV are compared, deeper dips and sharper peaks can be observed in the ENDF/B-IV. Such a fine structure is not observed in the available experimental data. The structure is, however, guessed to be obtained with some kinds of unfolding techniques in ENDF/B-IV and it brings better agreement between the calculated and the measured neutron spectra. The large

discrepancy between JENDL-3 and ENDF/B-IV is also observed in the calculated neutron spectra below 20 keV, particularly in the KfK experiments. For 27 keV resonance cross sections of iron, JENDL-3 shows a better agreement with the recent experimental data, which give a shallower valley in the 24 keV minimum than ENDF/B-IV evaluated on the basis of the older data. Accordingly, JENDL-3 gave better results in the resonance energy region above 10 keV in the ASPIS experiment. However, it cannot entirely explain the difference in the KfK experiment. It is generally said that the leakage spectrum is more influenced by the scattering cross sections than the spectrum in the medium. New integral experiments, similar to the KfK experiments, will probably lead obtaining better iron cross sections.

For carbon and sodium, JENDL-3 gave the best results. However, the number of the experiments analyzed is less than for the iron case. Further test are desirable to confirm the JENDL-3 validity. The integral tests for the other elements are now in progress. Results will be reported in the near future. In conclusion, it can be said that JENDL-3 is highly applicable to the reactor shielding analyses.

References

1) R.E. Maerker, ORNL-TM-3867 (revised) and ORNL-TM-3870 (revised) (1972).
2) R.E. Maerker and F.J. Muckenthaler, ORNL-4892 (1974).
3) R.E. Maerker, et al., ORNL-4880 (1974).
4) M.D. Carter and A. Packwood, Proc. Spec. Mtg. on Sensitivity Studies and Shielding Benchmarks, October 1975, Paris, p. 111, OECD (1975).
5) H. Werle, et al., NEACRP-U-73, p. 8 (1976).
6) A.E. Profio, ORNL-RSIC-25 (1969).
7) D.T. Ingersol and N. Ohtani, Proc. of ANS Topcal Conf. on Theory and Practices in Radiation Protection and Shield, April 1988, Knoxville, Vol. 2, p.346 (1988)
8) M. Kawai, et al., Proc. Int. Conf. on NUclear Data for Science and Technology, May 1988, Mito, p. 509, (1988).
9) H. Kotegawa, et al., JAERI-M 87-010 (1987).

Table 1 Summary of results mainly for detector responses

Material	Experiment	Analysis	JENDL-3T	JENDL-3
Iron	Broomstick	Analytic	0.5 - 1.8	0.5 - 1.2
	ORNL: Bonner	DOT-3.5	0.96 - 1.34	0.90 - 1.12
	ditt.	MCNP	0.86 - 1.09	0.82 - 1.07
	ASPIS: S,In, Rh	DOT-3.5	0.5 - 1.3	0.4 - 1.4
	Rh	MCNP	0.68 - 1.05	0.77 - 1.09
	KFK: Flux(>63keV)	DIAC	1.08 - 1.1	0.95 - 1.12
Sodium	Broomstick	Analytic	1.24 + 0.19	Same as left
	ORNL: Bonner	DOT-3.5	0.75 - 1.05	Same as left
Carbon	RPI: Flux(>1 MeV)	ANISN	0.8 - 1.3	Same as left
	ORNL: Bonner	DOT-3.5	0.8 - 1.1	Same as left

Table 2 C/E values for Bonner ball responses calculated with MCNP for ORNL iron benchmark experiment

Sample Thick.	Detector Size	Exp.	Calc.	C/E Values		
				JENDL-3	JENDL-3T	ENDF/B-IV
12"	3"	2.32	1.90	0.82(67%)	0.87(67%)	0.88(69%)
	6"	18.5	17.6	0.95(73%)	0.99(72%)	1.03(74%)
	10"	9.89	8.32	0.84(77%)	0.86(67%)	0.95(78%)
36"	3"	0.243	0.234	0.96(17%)	0.95(20%)	0.98(17%)
	6"	1.08	1.16	1.07(27%)	1.09(29%)	1.07(25%)
	10"	0.368	0.343	0.93(33%)	0.95(35%)	1.00(29%)

Table 3 C/E values of Bonner ball responses for ORNL iron benchmark experiments

Sample Thick.	Detector position	Detector Type	Exp.	C/E Values		
				DOT JENDL-3	DOT JENDL-3T	MCNP JENDL-3
4"	164" 15	NE213	1.74	1.24	1.21	-
	45	NE213	0.85	1.32	1.29	-
12"	141" 15	3" BB	0.577	1.00	0.98	1.08
	15	6" BB	3.54	1.26	1.32	1.34
	15	10" BB	1.58	1.15	1.23	1.21
	141" 45	3" BB	0.411	0.94	1.07	1.12
	45	6" BB	2.39	1.23	1.30	1.41
	45	10" BB	1.04	1.07	1.13	1.25
12"	156" 15	NE213	0.265	0.91	0.88	-
	45	NE213	0.157	0.85	0.83	-
	15" 50	NE213	74.5	1.34	1.44	-
24"	128" 15	3" BB	0.367	0.90	0.96	-
	15	6" BB	1.70	1.05	1.25	-
	15	10" BB	0.600	0.90	1.11	-
	128" 45	3" BB	0.245	0.97	1.05	-
	45	6" BB	1.13	1.12	1.34	-
	45	10" BB	0.405	0.93	1.16	-
36"	115" 15	3" BB	0.181	0.73	0.94	-
	15	6" BB	0.700	0.82	1.17	-
	15	10" BB	0.227	0.67	0.98	-
	115" 45	3" BB	0.128	0.87	1.11	-
	45	6" BB	0.475	1.00	1.43	-
	45	10" BB	0.151	0.82	1.22	-

Table 4 C/E values of Bonner ball responses calculated with DOT-3.5 for ORNL graphite benchmark experiment

Graphite Thickness	Library	C/E Values for Detector of					
		Bare	BF3/Cd	3"BB	6"BB	8"BB	10"BB
10.16 cm	JENDL-3	0.95	0.85	1.06	1.01	0.98	1.03
	JENDL-2	0.95	0.90	1.04	0.96	0.92	0.95
	ENDF/B-IV	1.23	1.13	1.28	1.16	1.12	1.15
30.48 cm	JENDL-3	0.89	0.86	1.00	0.98	0.95	0.97
	JENDL-2	0.84	0.81	0.94	0.91	0.88	0.88
	ENDF/B-IV	-	-	-	-	-	-
60.96 cm	JENDL-3	0.78	0.80	0.94	0.95	0.95	0.97
	JENDL-2	0.73	0.76	0.90	0.90	0.89	0.88
	ENDF/B-IV	0.75	0.89	1.06	1.04	1.03	1.01

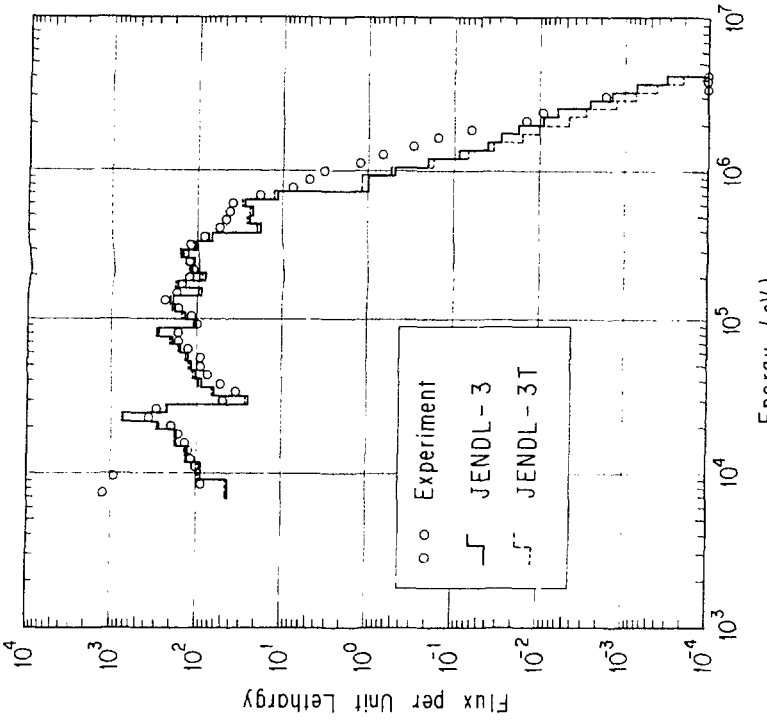

Fig. 2 Comparison of neutron spectrum at 85.41 cm depth calculated by DOT-3.5 with the measured data in ASPIS experiments

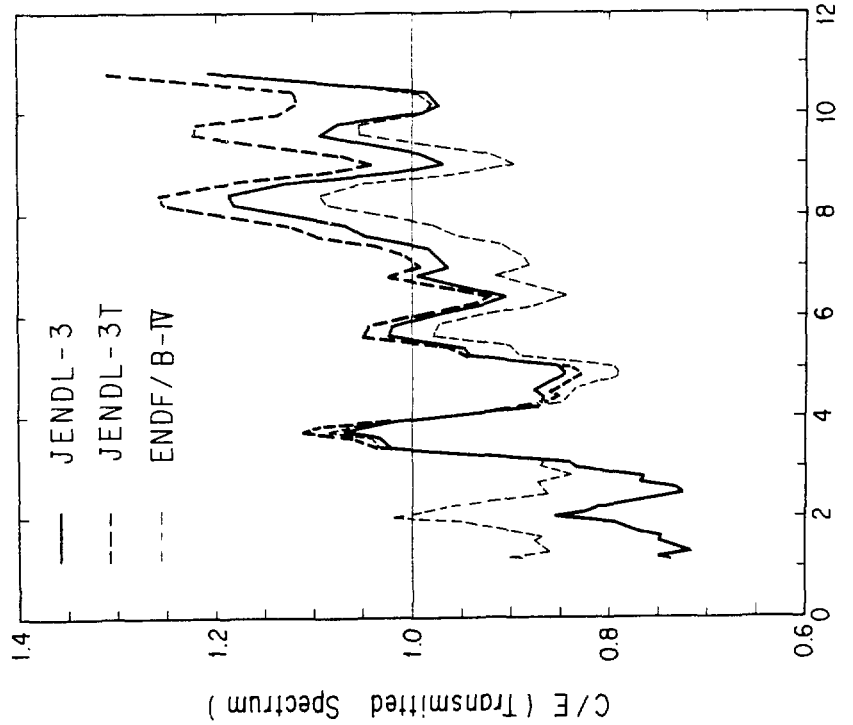

Fig. 1 C/E values for uncollided spectrum in ORNL broomstick experiments

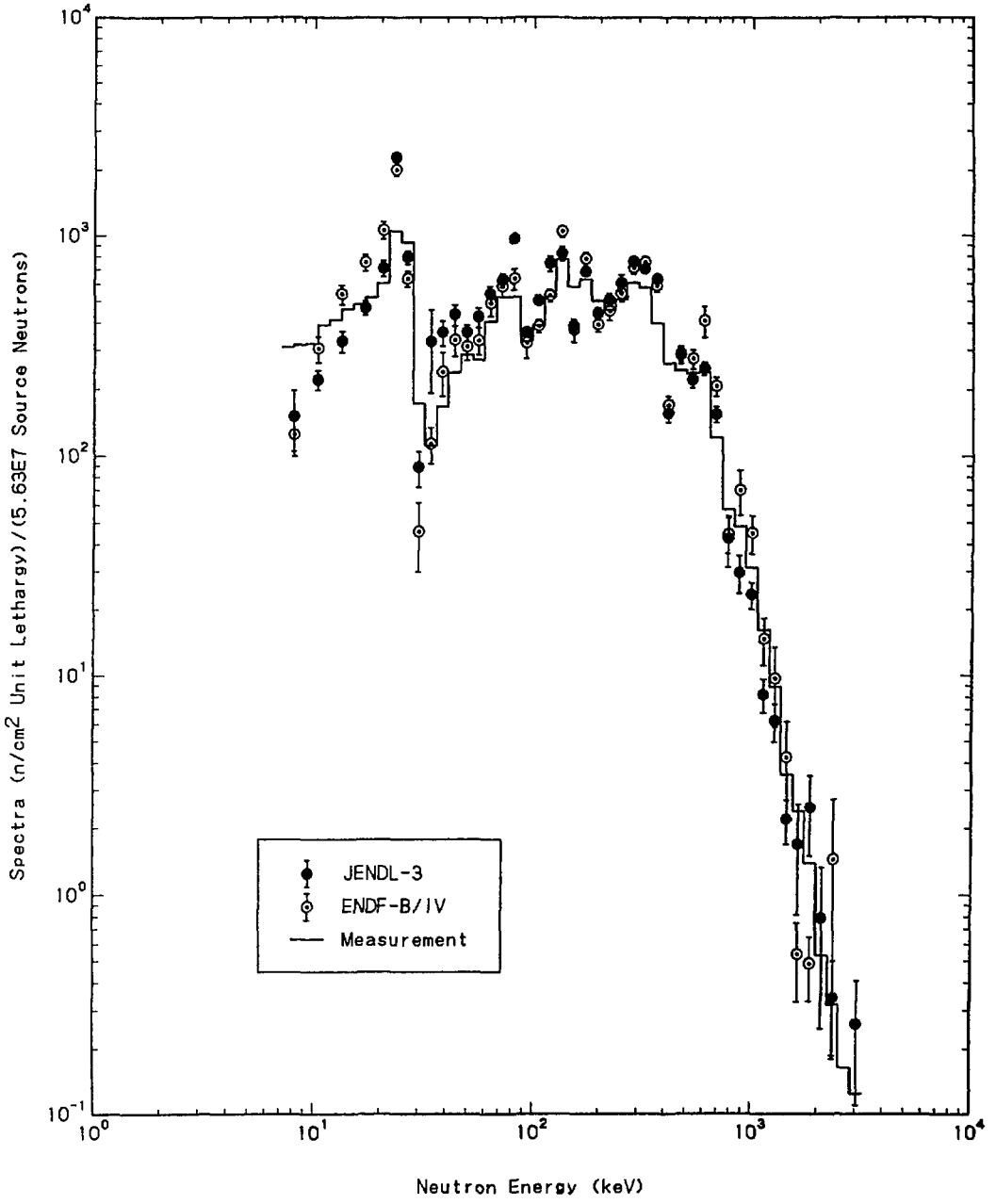

Fig. 3 Comparison of neutron spectrum at 56.83 cm depth calculated by MCNP with the measured data in ASPIS experiments

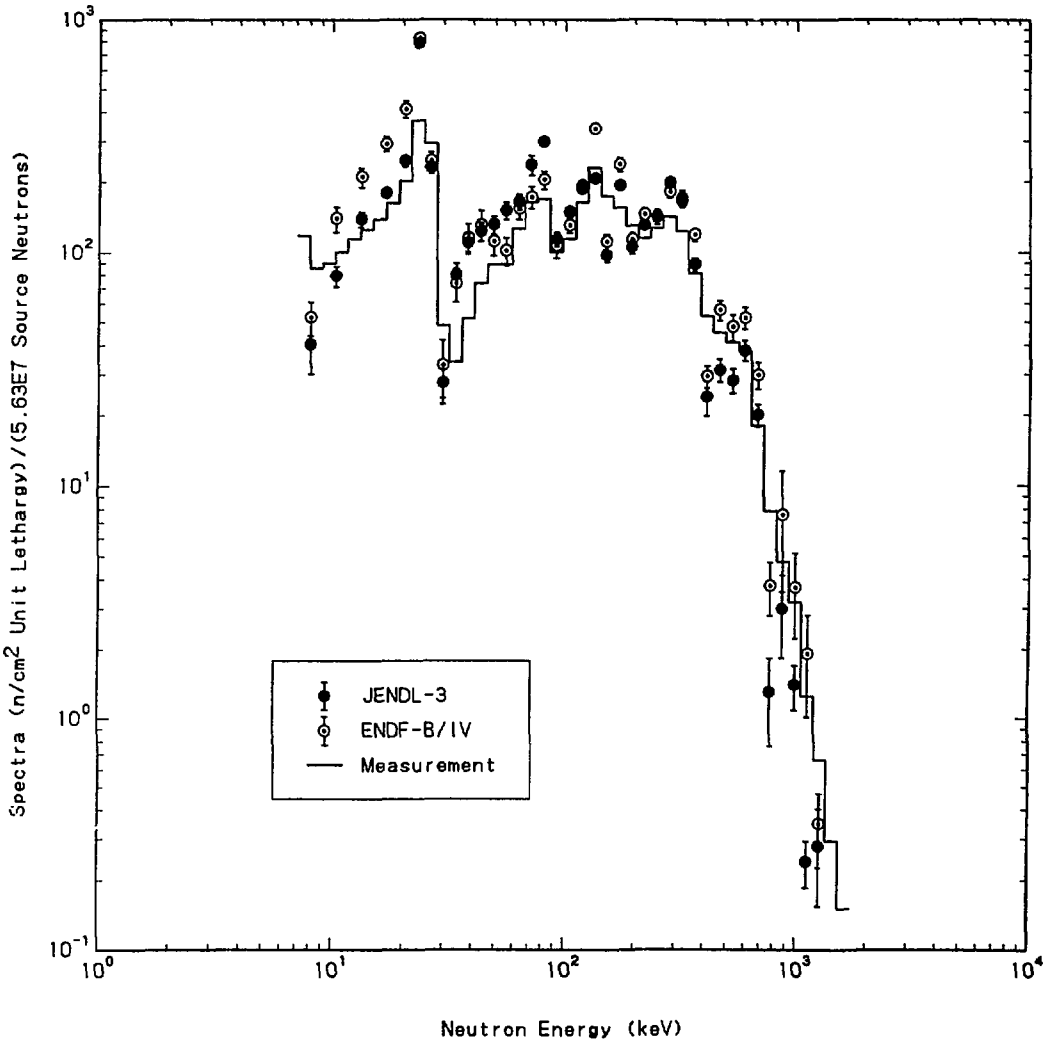

Fig. 4 Comparison of neutron spectrum at 85.41 cm depth calculated by MCNP with the measured data in ASPIS experiments

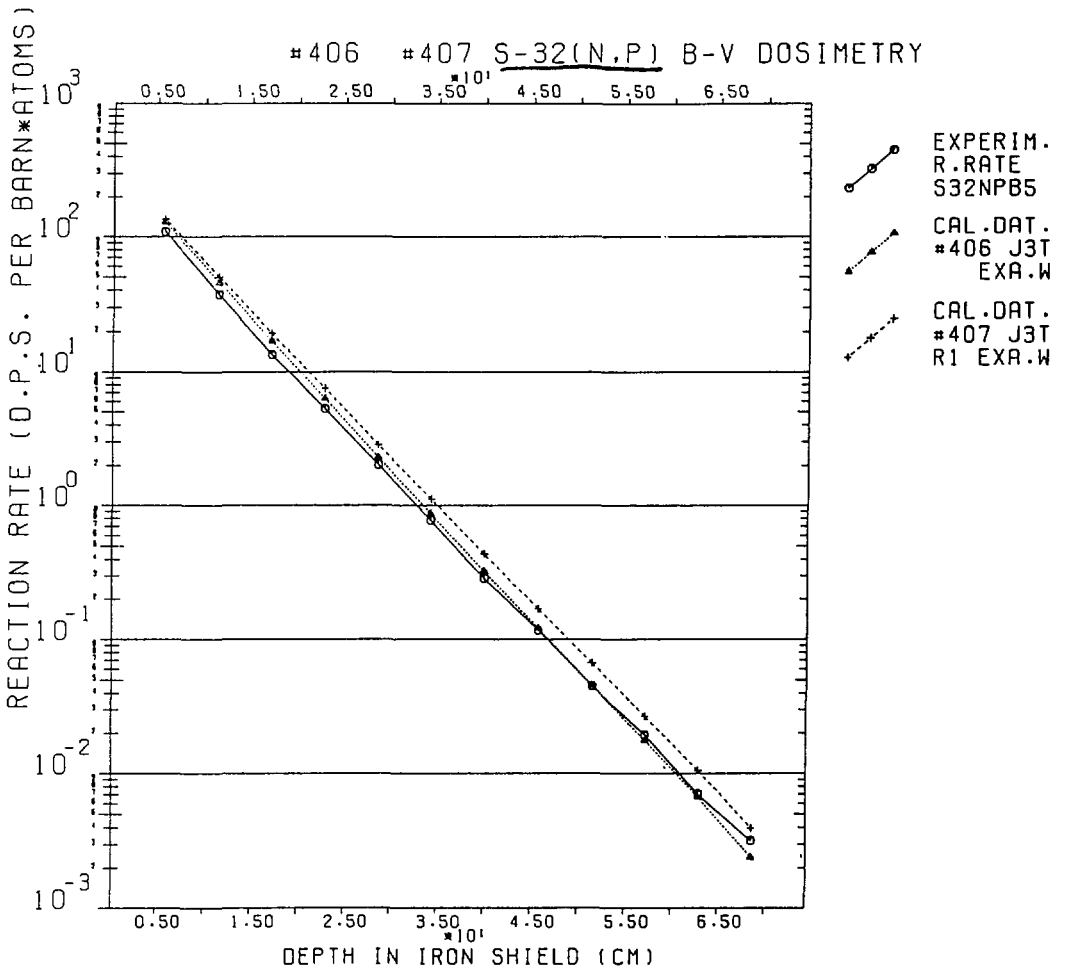

Fig. 5 Comparison of DOT-3.5 calculated and measured $^{32}S(n,p)$ reaction rates in ASPIS experiments

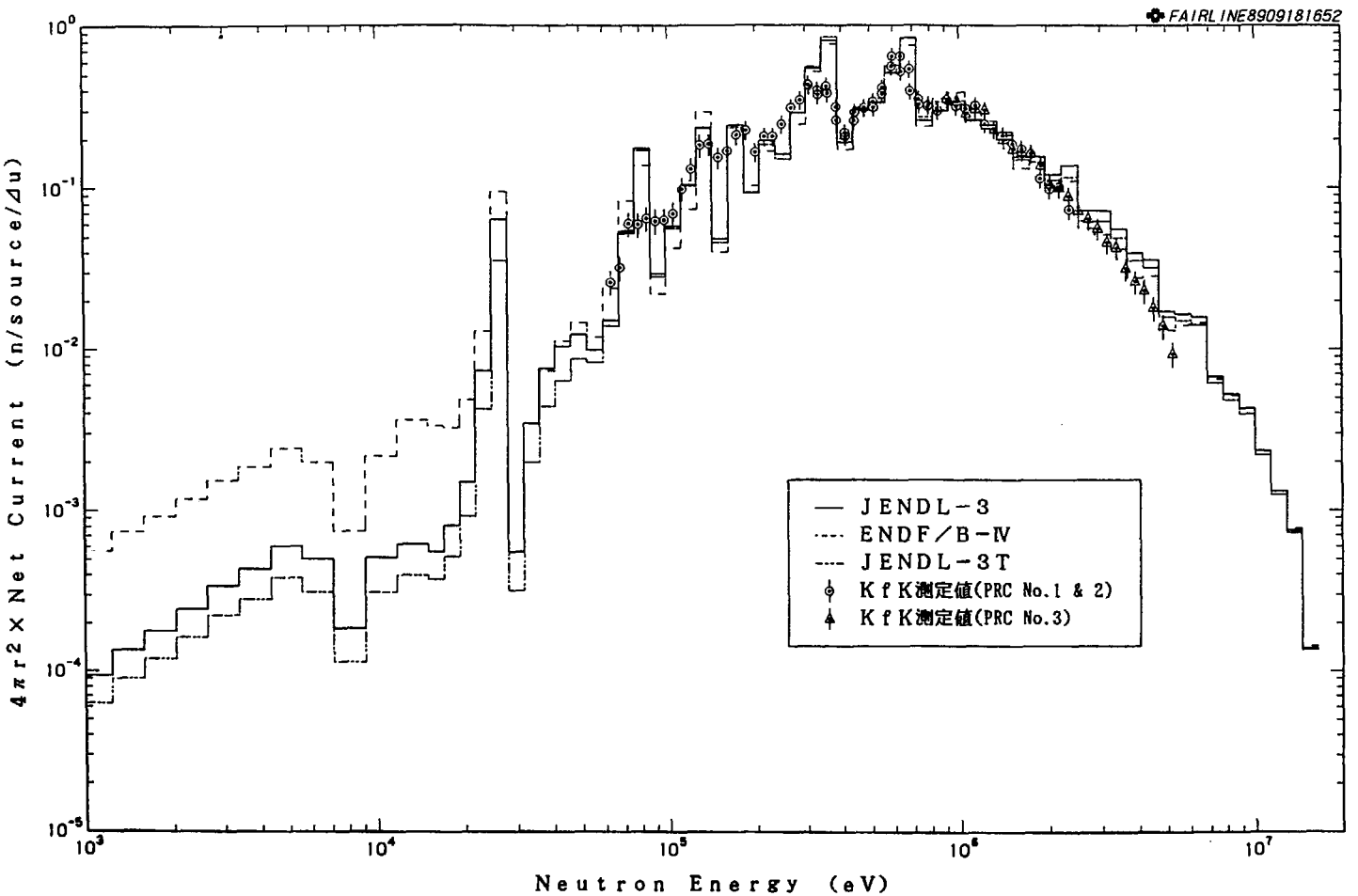

Fig. 6 Comparison of leakage neutron spectra calculated by DIAC with the measured data in KFK experiments

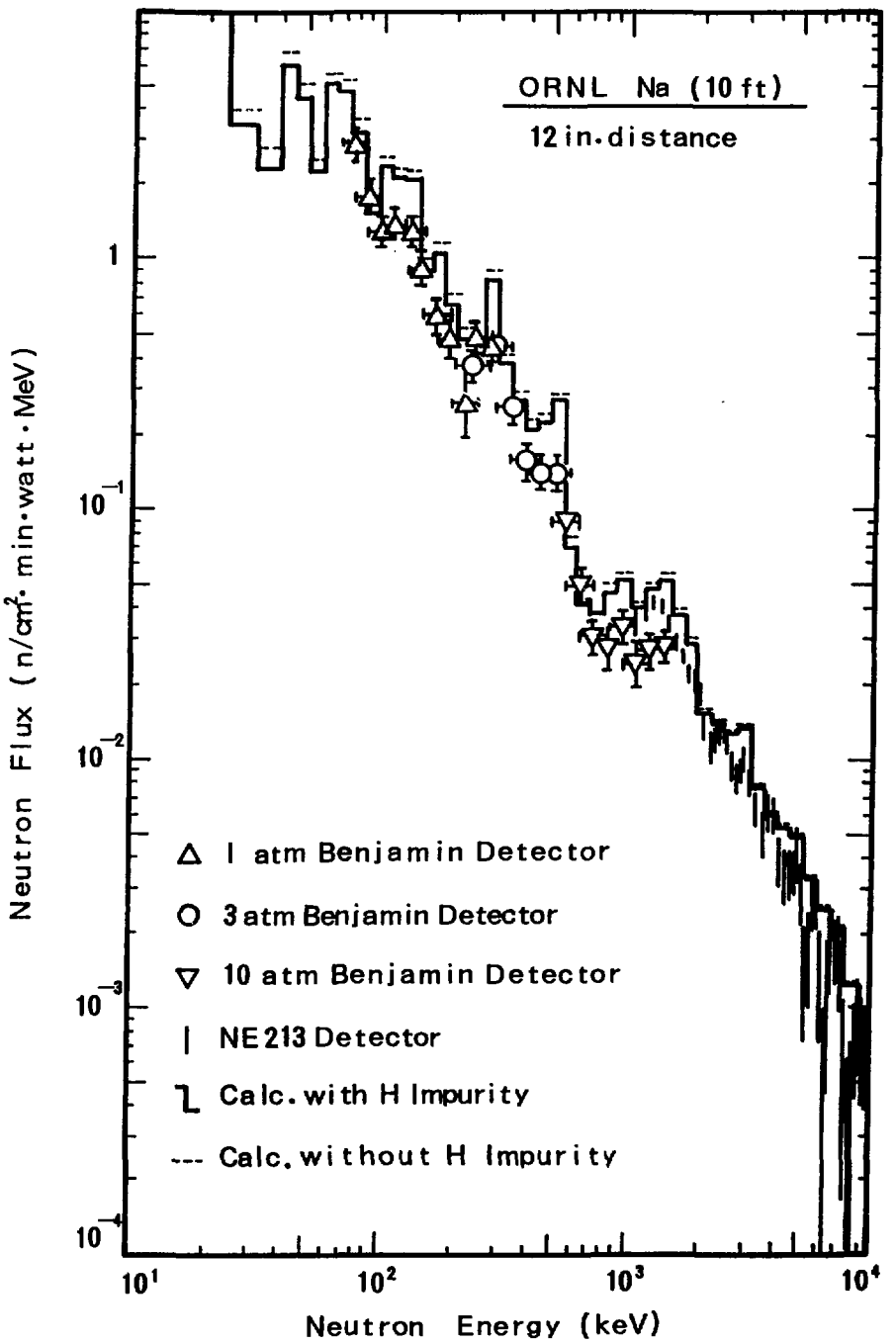

Fig. 7 Comparison of neutron spectrum transmitted through 10 Ft sodium sample depth calculated by DOT-3.5 with measured data in ASPIS experiments

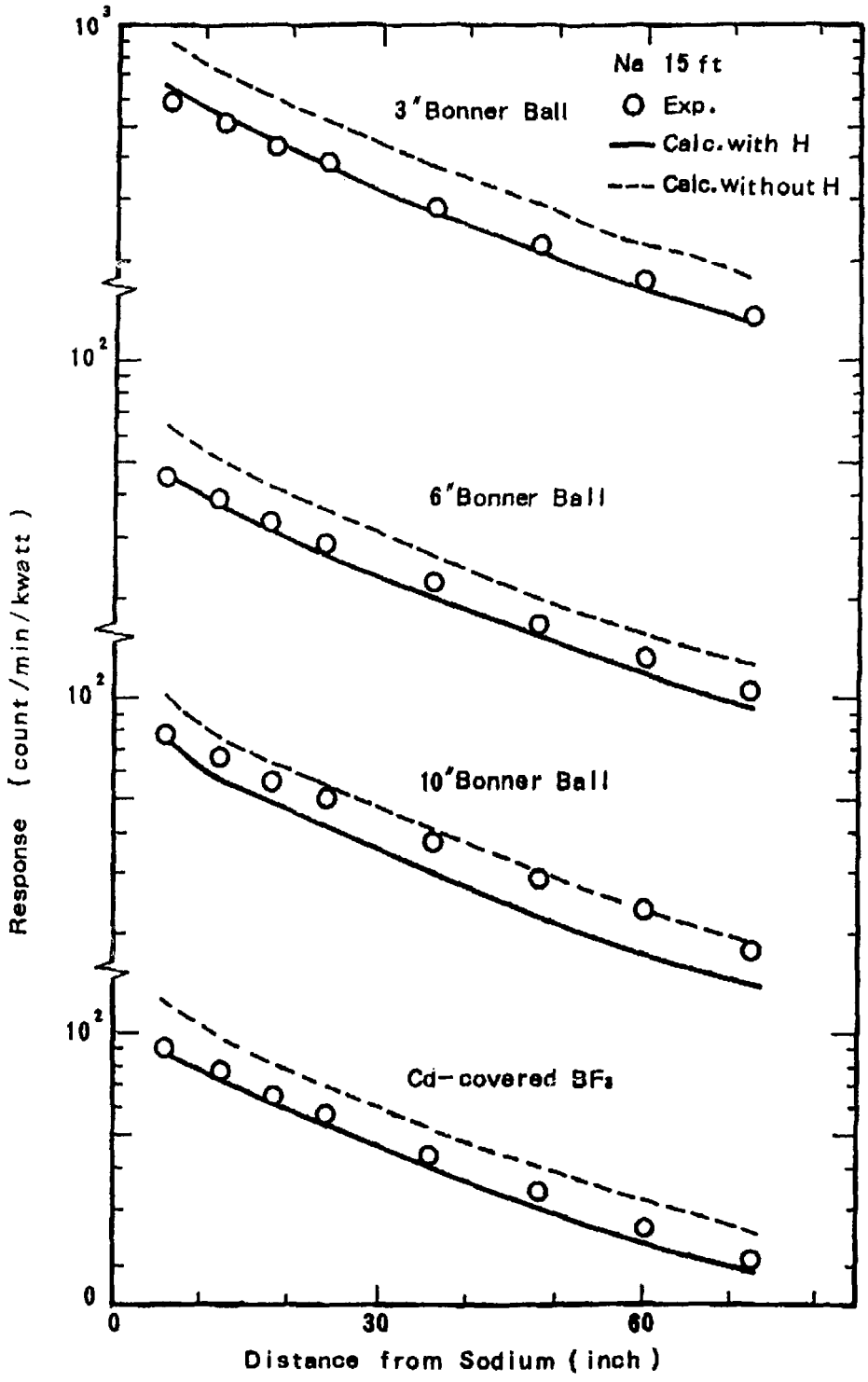

Fig. 8 Comparison of Bonner ball responses behind the 10 Ft sodium sample between DOT-3.5 calculations and the experiments

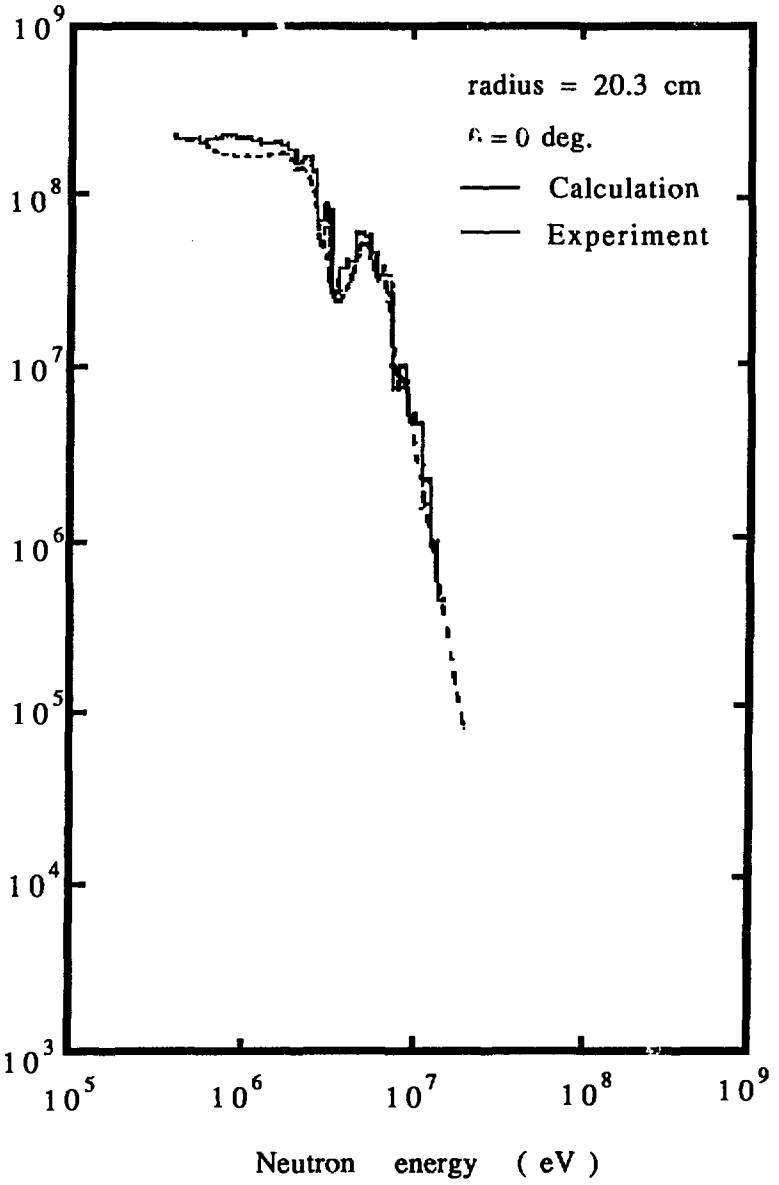

Fig. 9 Comparison of ANISN calculated and measured angle-dependent neutron spectra in the graphite block for Profio's experiment

2.1.7 Benchmark Test of JENDL-3 Dosimetry File

M. Nakazawa and Dosimetry Sub-WG,
University of Tokyo
7-3-1, Hongo, Bunkyo-ku, Tokyo

Present status of JENDL-3 Dosimetry-file has been reviewed, and generally better agreements have been obtained for the dosimetry reaction rates between calculation and experiment in several benchmark neutron fields such as Cf-252 fission spectrum. In this comparison, special attention has been paid to the uncertainty estimations of each reaction rate values. The covariance of reaction cross-section of IRDF has been tentatively applied here and the covariance of benchmark neutron spectrum has been assumed practically.

1. Introduction

JENDL-3 dosimetry file has been edited as a special purpose file of the JENDL-3 general purpose file. In order to check the accuracy of this JENDL-3 dosimetry file, a series of benchmark test has been carried out by the Dosimetry sub working group members.

The benchmark neutron fields in this dosimetry test program are mainly selected from the date file of IRDF-82, which are Cf-252 spontaneous fission spectrum, U-235 thermal fission spectrum, CFRMF and YAYOI. In order to test the applicability to fusion reactor neutronics, another benchmark fields of 14MeV neutron are added, which are JAERI-FNS 14MeV neutron source, and Li(d,n) neutron field in the Tohoku

University.

This kind of dosimetry benchmark test has been already carried out for the tentative version of JENDL-3 called as JENDL-3T dosimetry file, the results of which have been already reported in this previous seminar of 1988, (1).

2. JENDL-3 Dosimetry File

Table 1 shows the list of dosimetry reactions which are expected to be included in the JENDL-3 Dosimetry file, and presently 49 reaction cross-sections have been collected in the first version of JENDL-3 dosimetry file.

In the production of JENDL-3 Dosimetry file, at first, point-wise data are obtained using RESENDD code for resonance parameter processing, then 620 group-wise cross section data, which is the same as the SAND-II code group structure, are calculated using the CRECTJ5 code to average the point-wise data with the weighting function of F(E)=1.0.

Unfortunately, there is no uncertainty data in the present JENDL-3 library, so the covariance file of the IRDF-82 has been adopted tentatively in the present testing of JENDL-3 dosimetry file.

3. Results and Discussion

Table 2 and Fig.1 show the typical results in the two fission spectra, where it should be commented that neutron spectra of cf-252 and U-235 have been adopted from Dr. Manhart evaluated result and JENDL-3 data respectively. In this calculation, the systematic uncertainty of neutron spectra has been neglected because it dose not affect to the average

cross section. On the other hand, the random uncertainty of neutron spectra has been assumed like

$$\text{relative error } (\varepsilon\%) = \begin{cases} 20\% & \cdots \text{ U-235} \\ 5\% & \cdots \text{ Cf-252} \end{cases}$$

when the lethargy width(Δu) of spectrum is 0.1465 as the group structure of SAND-II library. One important comment on this random error, the relative error is modified as to keep the equation of $\varepsilon^2 \cdot \Delta u = \text{const}$, when the lethargy width u is changed in the calculational procedure.

From these comparisons, some clear discrepancies can be pointed out for several reactions, such as Ni-60(n,p) in Cf-252 spectrum, Ni-58(n,p), Cu-63(n,2n), I-127(n,2n) in U-235 spectrum. For these reactions, the uncertainty of experimental data should be reviewed again.

Fig.2 shows the benchmark test results in the typical fast reactor neutron fields, at present no any critical comment can not be found except the reaction of Fe-58(n, r).

Fig.3 shows the comparison of cross section curves in the 14MeV energy region the neutron spectrum of which is typical one in the surface region of fusion reactor blanket, as is given in Fig.4. Through the data evaluations of JENDL-3 in this energy region, this JAERI-FNS benchmark data have been already referenced, so this good agreements between the JAERI-FNS data and the JENDL-3 are as expected. And when compared with ENDF/B-∇ results, JENDL-3 gives a little better agreements.

Fig.5 shows the benchmark test results in the Li(d,n) neutron field, the spectrum of which is given in Fig.6. A little discrepancy can be found for the reaction of Co-

59(n,2n), then its experimental error are going to be rechecked.

The Largest discrepancy through these comparisons has been found in the reaction of Fe-58(n,r), which has been compared with the IRDF-82 data in Fig.7. Main difference has been observed in the resonance energy region, especially in the base cross section values between the resonances.

4. Conclusion

Present status on the JENDL-3 dosimetry benchmark test and its important results have been reviewed, and several reactions for which re-check is requested, can be pointed out. In order to improve this JENDL-3 dosimetry -file, additional evaluation are necessary especially for (n,n') reactions of Nb-93, Rh-103, In-115 and Hg-199 nucleides which can not be obtained from the present JENDL-3 library. And covariance data are requested for more quantitative comparison with experimental data, and for the neutron spectrum unfolding and/or adjustment application.

Member of Dosimetry sub-working group;

A.Hasegawa, Y.Ikeda, K.Sakurai, T.Nakagawa (JAERI),
S.Iigima (Toshiba), K.Kobayashi (KURRI),
S.Iwasaki (Tohoku Univ.),
T.Iguchi, M.Nakazawa (Univ.of Tokyo)

Table 1 Nuclear reaction list of JENDL-3 dosimetry file
(Underlined reactions are not in the present file.)

1.	Li- 6(n,t)α	J3	18.	Fe-58(n,γ)	J3	32.	U-235(n,f)	J3
2.	B-10(n,α)	J3	19.	Co-59(n,2n)	J3	33.	U-238(n,f)	J3
3.	F-19(n,2n)	J3		Co-59(n,γ)	J3		U-238(n,γ)	J3
4.	Na-23(n,2n)	J3		Co-59(n,α)	J3	34.	Np-237(n,f)	J3
	Na-23(n,γ)	J3	20.	Ni-58(n,2n)	J3	35.	Pu-239(n,f)	J3
5.	Mg-24(n,p)	J3		Ni-58(n,p)	J3	36.	Am-241(n,f)	J3
6.	Al-27(n,p)	J3	21.	Ni-60(n,p)	J3			
	Al-27(n,α)	J3	22.	Cu-63(n,2n)	J3	37.	Mn-55(n,γ)	J3
7.	P-31(n,p)	J3		Cu-63(n,γ)	J3	38.	Nb-93(n,2n)	J3
8.	S-32(n,p)	J3		Cu-63(n,α)	J3	39.	Rh-103(n,2n)	J3
9.	Sc-45(n,γ)	J3	23.	Cu-65(n,2n)	J3	40.	Eu-151(n,γ)	J3
10.	Ti-46(n,p)	J3	24.	Zn-64(n,p)	—	41.	W-186(n,γ)	J3
11.	Ti-47(n,p)	J3	25.	Zr-90(n,2n)	J3	42.	Ag-109(n,γ)	J3
	Ti-47(n,n'p)	J3	26.	Nb-93(n,n')-m	—	43.	Ta-181(n,γ)	J3
12.	Ti-48(n,p)	J3	27.	Rh-103(n,n')-m	—	44.	Hg-199(n,n')	—
	Ti-48(n,n'p)	J3	28.	In-115(n,n')-m	—	45.	Li- 7(n,n'α)	J3
13.	Mn-55(n,2n)	J3		In-115(n,γ)	J3	46.	Al-27(n,t)	—
14.	Fe-DPA(ASTM)	—	29.	I-127(n,2n)	J3	47.	Ti-49(n,n'p)	J3
15.	Fe-DPA(EUR)	—	30.	Au-197(n,γ)	—	48.	Fe-57(n,n'p)	J3
16.	Fe-54(n,p)	J3	31.	Th-232(n,f)	J3	49.	Au (n,2n)	—
17.	Fe-56(n,p)	J3		Th-232(n,γ)	J3			

Note: Reactions from No.1 through No.36 are those included in IRDF. Reactions No.37 through No.49 are the new entries.

Table 2 Relative deviations of calculated reaction-rates from experimental data in fission spectrum field

核 反 応	Cf-252 field J-3/exp±std error% $\left(\frac{4C}{C}, \frac{4E}{E}\right)$*	U-235 fission spectrum J-3/exp±std error% $\left(\frac{4C}{C}, \frac{4E}{E}\right)$
Na-23 (n,2n)	—	1.007±15.4%(12.4,9.1) (A)
Mg-24 (n,p)	1.132± 4.8%(4.2, 2.4) (M)**	1.035± 6.5 (4.9, 4.2) (M)
Al-27 (n,p)	1.037± 4.3 (3.8, 2.2) (M)	1.058± 8.4 (4.7, 6.0) (M)
(n,α)	0.971± 5.5 (5.3, 1.4) (M)	0.918± 6.7 (6.0, 4.0) (M)
P-31 (n,p)	—	1.109± 7.5 (4.4, 6) (C)
S-32 (n,p)	1.030± 4.3 (2.5, 3.5) (M)	1.077± 6.9 (3.5, 6) (C)
Ti-46 (n,p)	0.935± 2.5 (1.8, 1.7) (M)	0.945± 5.8 (3.0, 4.9) (M)
Ti-47 (n,n'p)	—	—
(n,p)	1.065± 2.2 (1.6, 1.6) (M)	1.090± 5.7 (2.8, 5.0) (M)
Ti-48 (n,n'p)	—	—
(n,p)	0.921± 2.4 (1.5, 1.9) (M)	0.873± 5.5 (2.6, 4.9) (M)
Ti-49 (n,p)	—	—
Mn-55 (n,2n)	1.160± 4.3 (3.7, 2.3) (M)	0.957± 6.9 (4.8, 5) (C)
Fe-54 (n,p)	1.009± 3.8 (3.6, 1.3) (M)	1.000± 6.5 (4.2, 5) (M)
Fe-56 (n,p)	0.957± 4.8 (4.5, 1.7) (M)	0.920± 7.3 (5.1, 5.2) (M)
Fe-57 (n,n'p)	—	—
Co-59 (n,2n)	1.017± 3.9 (3.2, 2.5) (M)	0.813± 6.6 (4.4, 4.9) (M)
(n,α)	1.036± 2.1 (1.1, 1.8) (M)	0.972± 6.0 (2.5, 5.5) (M)
Ni-58 (n,2n)	0.921± 3.9 (2.0, 3.3) (M)	0.622± 6.1 (3.3, 5.1) (M)
(n,p)	0.982± 1.8 (1.3, 1.3) (M)	0.982± 5.6 (2.7, 4.9) (M)
Ni-60 (n,p)	1.4 ± 5.2 (1.5, 5) (C)	1.092±17.6 (2.7, 17) (A)
Cu-63 (n,2n)	1.144± 4.3 (1.9, 3.8) (M)	1.583± 9.5 (3.2, 8.9) (A)
(n,α)	1.023± 5.8 (5.5, 1.9) (M)	1.069±13 (6.0, 12) (C)
Cu-65 (n,2n)	—	—
Nb-93 (n,2n)	—	—
I-127 (n,2n)	—	1.305± 7.3 (3.9, 6.2) (C)
Th-232 (n,f)	0.969±17 (1.2, 17) (C)	0.978± 7.5 (2.8, 7) (C)
U-238 (n,f)	0.987± 1.9 (0.9, 1.7) (M)	1.023± 4.1 (2.8, 3) (C)
Np-237 (n,f)	0.993± 2.3 (1.6, 1.7) (M)	1.024± 5 (3.0,4) (C)

* $\frac{4C}{C}$=error in calculation (%)

$\frac{4E}{E}$=Experimented error (%)

**, Exp. data
(M) : Manhart or best fit value
(C) : D.E. Cullen (1983), NSE83, 497
(A) : A. Calamand (1974)

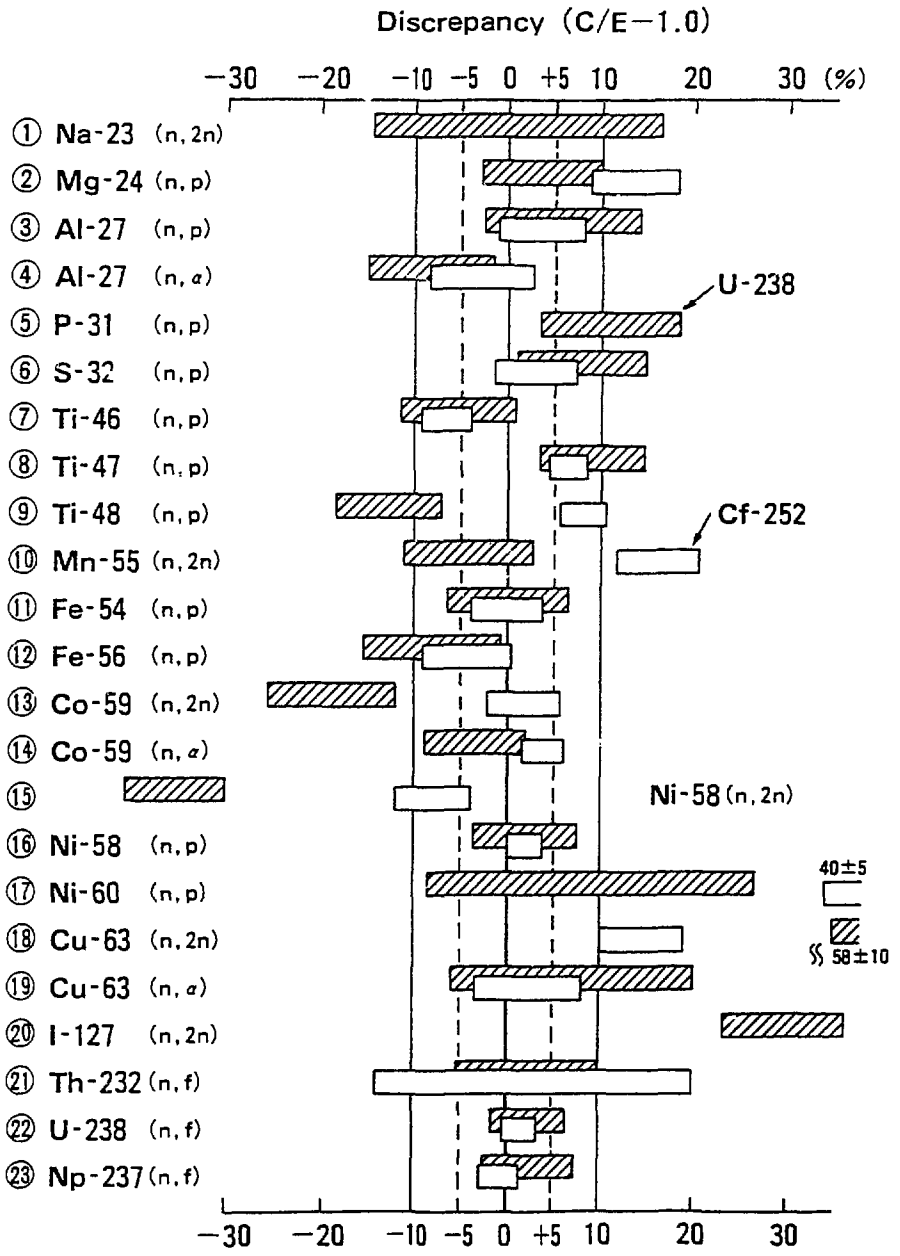

Fig. 1 Benchmark test results in Cf-252 and U-235 fission spectra

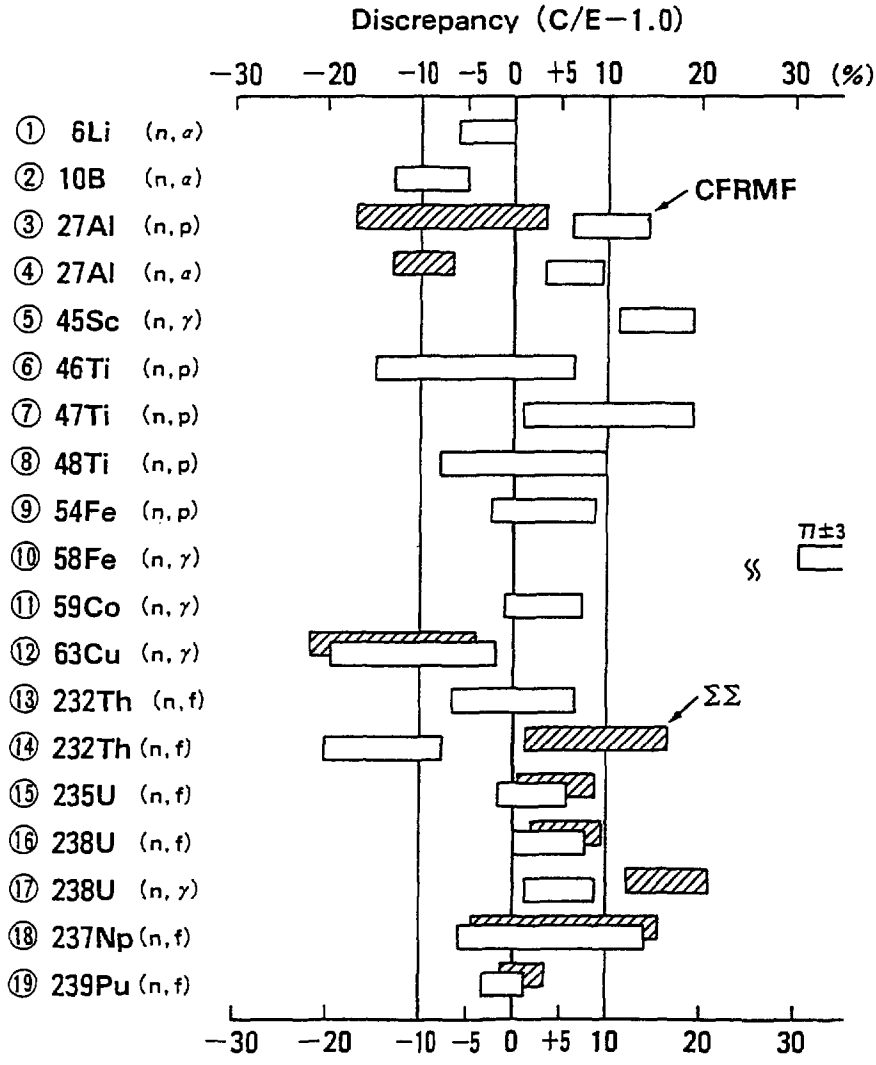

Fig. 2 Benchmark test results in fast reactor spectra of CFRMF and sigma-sigma

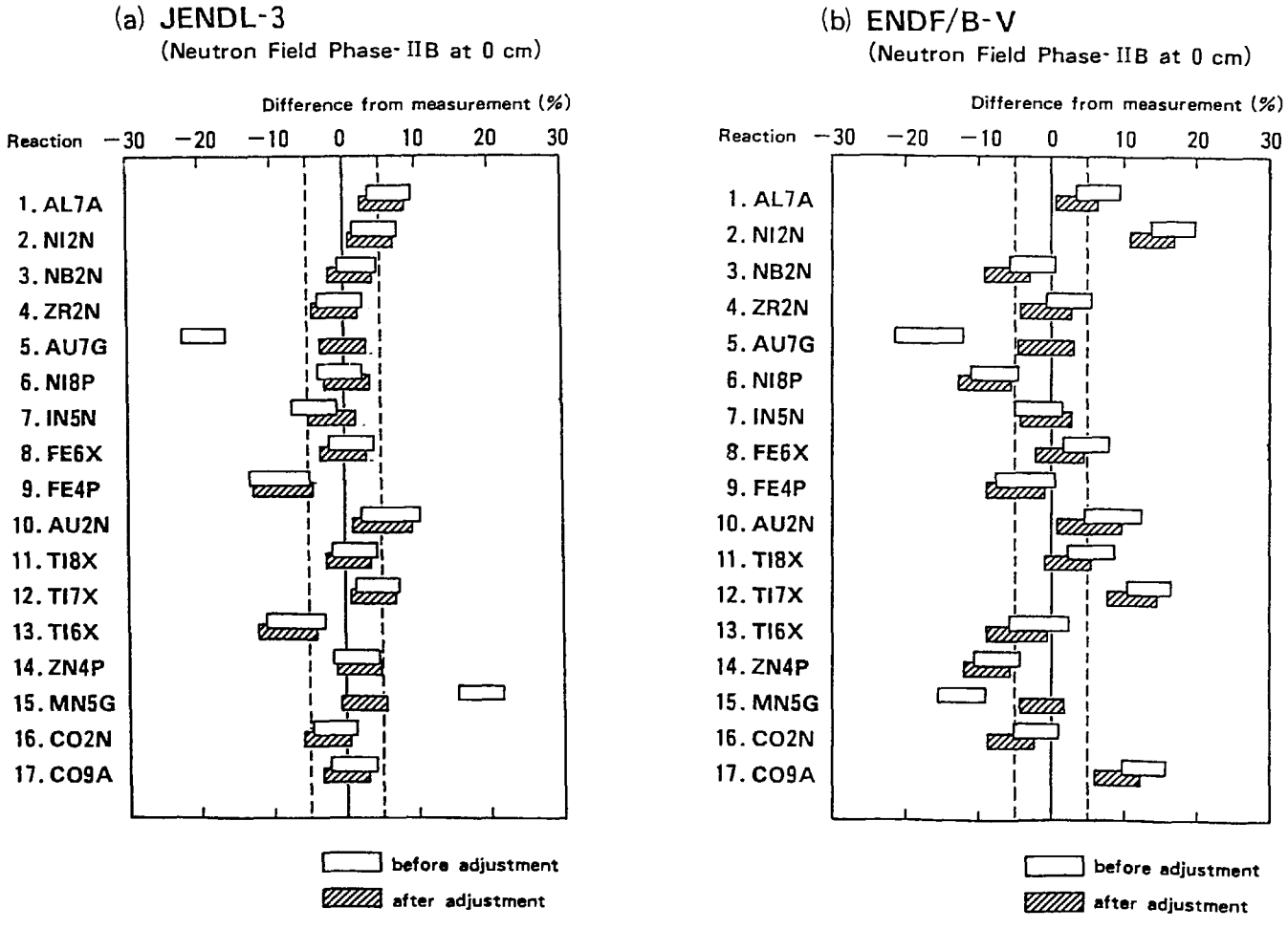

Fig. 3 Benchmark test results in 14 MeV spectrum
(a) JENDL-3, (b) ENDF/B-V
(Neutron spectrum is given in Fig. 4.)

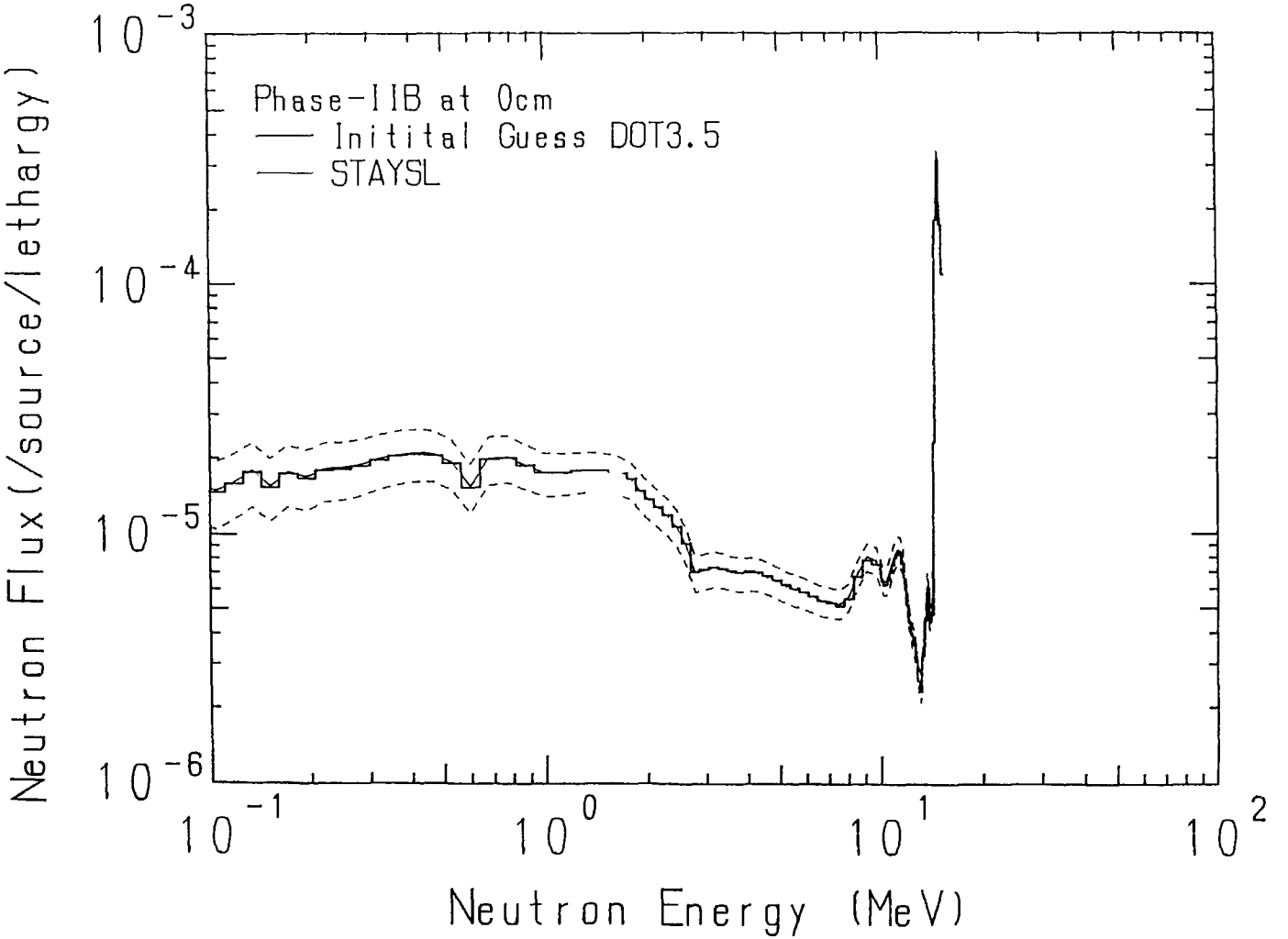

Fig. 4 Benchmark neutron spectrum in JAERI-FNS 14 MeV field

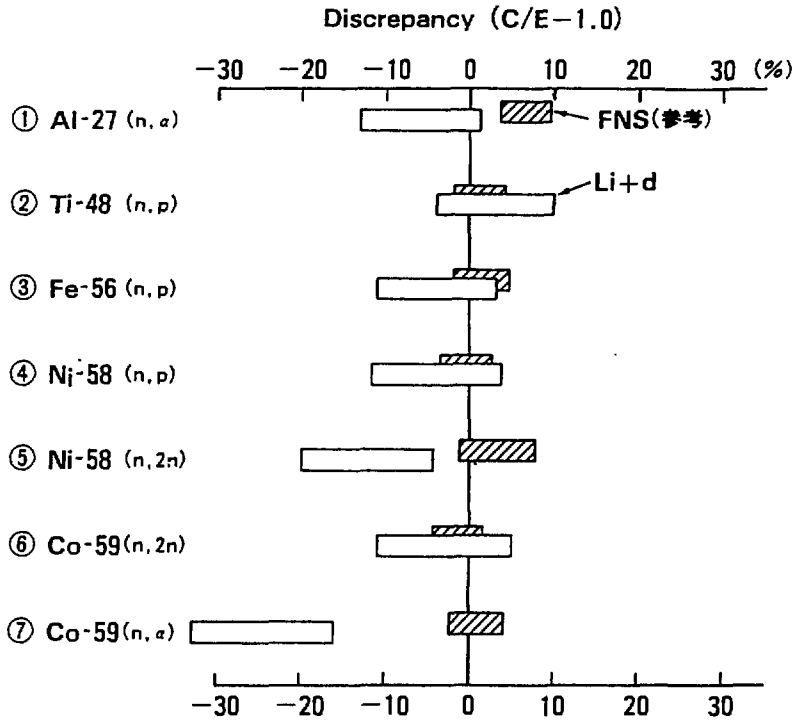

Fig. 5 Benchmark test results in Li(d,n) spectrum field

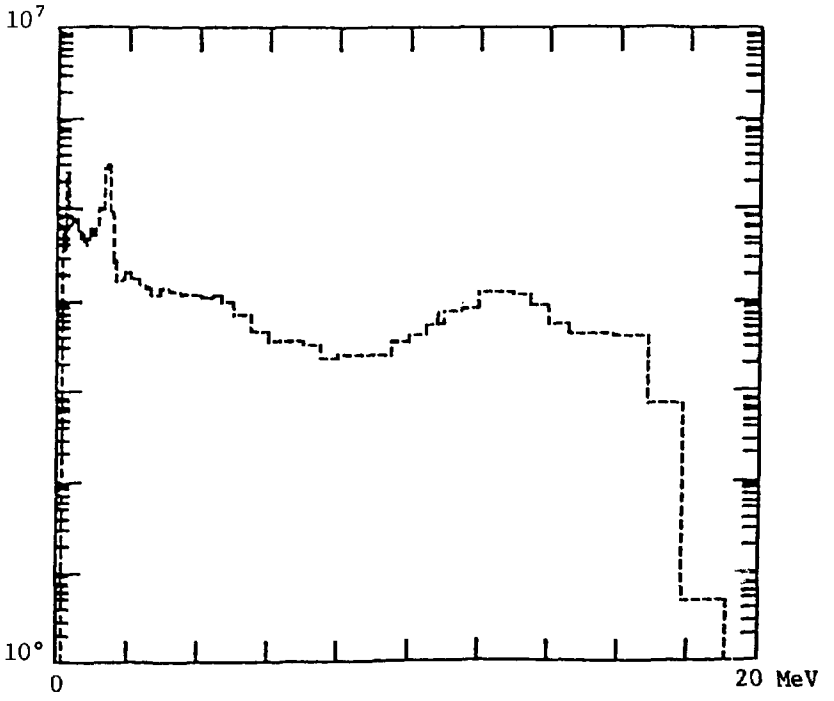

Fig. 6 Benchmark neutron spectrum of Li(d,n) field of Tohoku University

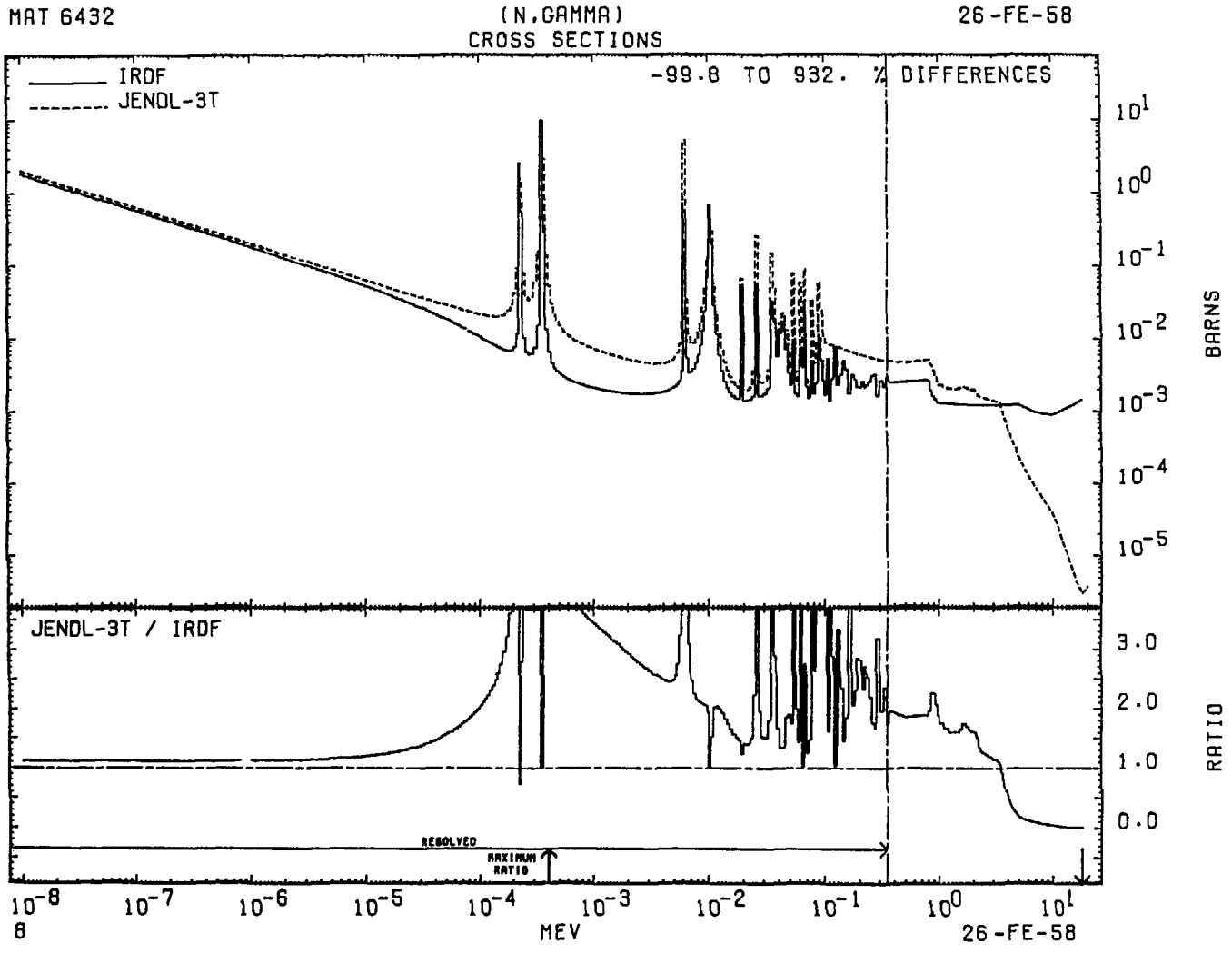

Fig. 7 Comparison of Fe(n,γ) reaction between JENDL-3 and IRDF

2.2 Topics (I)

2.2.1 The Optical Potential for Neutrons and Charged Particles

Takaaki Ohsawa

Atomic Energy Research Institute, Kinki University
3-4-1 Kowakae, Higashi-osaka, Osaka 577

Abstract: Problems and recent topics in the study on the nuclear optical model are described with particular reference to the application to nuclear data evaluation. This includes the following items: *(a)* Global optical potentials and their validity; *(b)* Regional optical potentials; *(c)* Nonlocal and equivalent local potentials; (d) Ambiguities in the optical potential parameters; *(e)* Application of dispersion relations; *(f)* Optical potentials for the calculation of the inelastic scattering cross section.

1. Introduction: A Historical Overview

The study of the optical-model potential (OMP) has quite a long history. For convenience of explanation, we divide the historical development into four stages (Fig.1). The first-generation OMP began with the well-known work of Feshbach, Porter and Weisskopf[1]. They showed that the overall features of the total and reaction cross sections, including the size resonances, can be represented for nuclei over a wide range of masses and energies even with a simple square-well potential,

$$V(r) = U + iW \quad \text{for } r < R \qquad (1)$$
$$= 0 \quad \text{for } r > R$$

with U = 42 MeV, W = 1.26 MeV and $R = 1.45A^{1/3}$. This fact suggests that the overall features of the interaction of neutrons with the nucleus are determined by average nuclear properties. This idea was congenial with that of the shell model which had just been developed at that time. It is worth noting that another theoretical investigation by Brueckner *et al.*[2] of nuclear matter provided a ground for future development of the microscopic approach to the OMP determination.

The attempts to make a more realistic potential led to the second-generation OMP. This included ameliorations in many respects: the potential shape was assumed to have the Woods-Saxon form with the imaginary part

changing from surface absorption to volume absorption as the incident energy increases; the spin-orbit coupling term was introduced in order to analyze the polarization data; energy-dependence was introduced so as to take into account effectively the nonlocal nature of the nuclear field. Application of this OMP extended into two disrections, one aiming at obtaining the best fit parameter set to a specific measurement, another looking for a set generally applicable to a large range of masses and energies. In the process of parameter search it was found that there existed two different kinds of ambiguities, *i.e.*, continuous and discrete ambiguities.

Extensive analyses of data by means of this second-generation OM have revealed that the spherical OM has deficiencies in several respects, mainly because only one (entrance) channel is explicitly considered in this model. The OM was thus generalized so as to take into consideration a few strongly or moderately coupled channels with a great success. Computer codes based on the coupled-channel theory have now become easily accecible owing to the progress of high-speed computers. On the other hand, microscopic approach of constructing the potential starting from the nucleon-nucleon interactions has recently come into the phase of quantitative comparison with empirical data. Another recent topic is the finding that the dispersion relation plays an important role in analyzing the interdependence of the real and imaginary parts of the OMP. These findings together with employment of sophisticated formalisms constitute a new stage of the development of the OM, *i.e.* the third-generation OM.

Possible future development into the fourth-generation OM will hopefully lead to happy marriage of empirical and microscopic approaches.

2. Limitations of the Spherical Optical Model

In spite of widespread use of the spherical optical model potential (SOMP) in the analyses of experimental data and for evaluation purposes, there are some problems encountered in its applications. These problems are classified into two groups, *i.e.* those that can be solved or improved within the framework of the SOMP, and those requiring advanced treatments.

A. Problems solvable within SOMP

Examples of this class include *(a)* the continuous ambiguities and *(b)* disagreement between SOMP-calculation and measurement of the s-wave strength function and reaction cross section near the magic region around $A \simeq 100$ (Fig.2). The first of these can be solved by increasing the accuracy

and extending the energy region of the experimental data. The second problem is a reflection of the fact that there does not exist a suitable shell-model orbit for a *s*-wave neutron to transfer satisfying the parity conservation rule.

A prescription to solve this discrepancy was proposed by Moldauer[3]. He showed that the agreement was able to be improved by adopting larger nuclear radius for imaginary part than for the real part (see section 3 below).

Another possibility will be to look for a *regional* OMP, mentioned later, that appropreately describes the behavior of the cross sections for nuclei in each shell region.

B. Problems requiring advanced treatments

In Fig.2 we also observe that the SOM calculation overestimates the strength function in the region around $A \simeq 160$. This discrepancy cannot be solved within the SOM formalism, while the coupled-channel(CC) formalism predicts a splitting of the peak, in better agreement with the measurements. This is a manifestation of the effects of nuclear deformation.

The differential cross sections of even Sm-isotopes present another good example of the effects of nuclear deformation[4]. As can be seen in Fig.3, we can observe apparent trends in the elastic scattering cross sections of 50 MeV-alpha particles, the diffraction pattern becoming less pronounced and the slope of the envelope becoming steeper as mass number increases. Different set of parameters for each isotope should be used to obtain good representation of the data in the framework of the SOM, while CC calculations using the *same* optical potential but different deformation parameters for each isotope can reproduce the cross section very well.

The analysis of neutron inelastic scattering on actinides also requires CC calculations. The inclusion of the direct process is one of the reasons for the drastic change of the evaluations of inelastic scattering cross sectios for actinides in JENDL-3. This problem will be discussed later in a separate section.

3. Genealogy of the Global Optical Potentials

Efforts have been made to find out the best set of OMP parameters based on a comprehensive experimental data. Historical development of the global OMP (with emphasis on neutron OMP) is briefly reviewed below.

(a)Perey-Buck (1962)

The earliest global analysis of neutron scattering was made by Perey and Buck[5] using a nonlocal potential with a Gaussian nonlocal function:

$$V(r,r') = V(p)H(|r-r'|) \tag{2}$$

$$H(|r-r'|) = \frac{1}{\pi^{3/2}\beta^3} \exp[-(r-r')^2/\beta^2] \tag{3}$$

where $p=(r+r')/2$ and β is the range of nonlocality. From analyses of neutron scattering data in the range of 1-25 MeV, they obtained a set V = 71 MeV, W = 15 MeV, r_0 = 1.22 fm, a = 0.65 fm, β = 0.85 fm, V_{so} = 7.2 MeV and a_s = 0.47 fm.

(b)Wilmore-Hodgson (1964)

Wilmore and Hodgson[6] tried to obtain a local potential equivalent to that of Perey and Buck[5] as it is more convenient to use the local potential for practical calculations. They gave the following set (energies in MeV, lengths in fm):

$$\begin{aligned} V_R &= 47.01-0.267E-0.0018E^2 \\ W_D &= 9.52-0.053E \\ V_{so} &= 0 \\ r_R &= 1.322-0.00076A+(4\times10^{-6})A^2-(8\times10^{-9})A^3 \\ r_D &= 1.266-0.00037A+(2\times10^{-6})A^2-(4\times10^{-9})A^3 \\ a_R &= 0.66 \\ a_D &= 0.48. \end{aligned} \tag{4}$$

This potential is able to fit a wide range of neutron data. The negative sign of the enegy-dependent term of the imaginary part is unphysical, the reason for which is not clear.

(c)Moldauer (1962-1964)

The Perey-Buck potential was was successful in reproducing overall behavior of the s-wave strength function but failed to explain the lower values around $A \simeq 100$. Moldauer[3] found that the problem can be solved by making the imaginary part peak a bit outside the nuclear radius:

$$\begin{aligned} V_R &= 46 \\ W_G &= 14 \qquad \text{(surface-peaked Gaussian form)} \\ V_{so} &= 5 \\ R_R &= 0.6+1.16A^{1/3}, \qquad a_R = 0.62 \\ R_G &= 1.1+1.16A^{1/3}, \qquad b = 0.5 \end{aligned} \tag{5}$$

$R_{so}=0.6+1.16A^{1/3}$, $a_{so}=0.62$.

It should however be noted that this set was devised so as to be used for E_n < 1 MeV.

(d)Becchetti-Greenlees (1969)

One of the most extensively used global OMPs is that proposed by Becchetti and Greenlees[7]. This potential was first derived for protons based on fits to extensive differential cross section and polarization data for E_p = 10-40 MeV and A = 58-208. This potential was then converted into a neutron potential using the following assumptions:

- Energy-dependence of V_R, W_V and W_D is the same as for proton potential (V_R: $-0.32E$, W_V: $+0.22E$, W_D: $-0.25E$).
- The sign of the isospin-dependent term is inverted according to the Lane model[8] ($24.0(N-Z)/A \rightarrow -24.0(N-Z)/A$).
- The geometry parameters for the real part (r_R, a_R) and the depth and geometry parameters for the spin-orbit term (V_{so}, r_{so}, a_{so}) are the same for neutron- and proton-OMPs.

The depth and geometry parameters of the volume imaginary part was changed so as to fit the neutron data, resulting in a larger depth and a smaller radius.

$$
\begin{aligned}
V_R &= 56.3-0.32E-24.0\eta \\
W_D &= 13.0-0.25E-12.0\eta \\
W_V &= 0.22E-1.56 \\
V_{so} &= 6.2 \\
r_R &= 1.17\ (\mathrm{fm}), \quad a_R = 0.75 \\
r_D &= 1.26\ (\mathrm{fm}), \quad a_D = 0.58 \\
r_V &= 1.26\ (\mathrm{fm}), \quad a_V = 0.75 \\
r_{so} &= 1.01\ (\mathrm{fm}), \quad a_{so} = 0.75
\end{aligned}
\qquad (6)
$$

where $\eta = (N-Z)/A$. This OMP is applicable for E_n < 50 MeV and A > 40.

(e)Rapaport(1979)

Raparort[9] proposed an OMP that fitted neutron angular distributions between 7-26 MeV fo. singly or doubly closed-shell nuclei in the range A = 40-208:

$$
\begin{aligned}
V_R &= 54.19-0.33E-(22.7-0.19E)\eta \\
W_D &= 4.28+0.4E-12.8\eta \qquad (E \le 15\ \mathrm{MeV}) \\
&= 14.0-0.39E-10.4\eta \qquad (E \ge 15\ \mathrm{MeV}) \\
W_V &= 0 \qquad (E \le 15\ \mathrm{MeV}) \\
&= -4.3+0.38E \qquad (E \ge 15\ \mathrm{MeV})
\end{aligned}
$$

$$V_{SO} = 6.2 \qquad (7)$$

$r_R = 1.198, \quad a_R = 0.663$

$r_D = 1.295, \quad a_D = 0.59$

$r_I = 1.295, \quad a_I = 0.59$

$r_{SO} = 1.01, \quad a_{SO} = 0.75$

This set is claimed to be applicable for $7 < E_n < 30$ MeV and for $A > 16$.

(f)Walter-Guss (1985)

One of the newest global OMPs is the one proposed by Walter and Guss[10]. On the basis of the scattering data collected at TUNL and other institutes, they primarily concentrated on the data in the energy range $10 < E_n < 24$ MeV, where the energy- and radial dependence of the absorptive well was poorly defined. By leaning on the analyzing power data, new constraints on the spin-orbit term was defined. A peculiar point of the OMP is that it employed a logarithmic energy dependence:

$$V_R = 52.56-0.31E-(16.5-0.081E)\eta \qquad (E < 40 \text{ MeV})$$

$$= 52.56-12.4[1+\ln(E/40)]+(16.5-3.24[1+\ln(E/40)])\eta \qquad (E > 40 \text{ MeV})$$

$$W_D = 10.85-0.157E-14.94\eta \qquad (E > 9.9 \text{ MeV})$$

$$W_I = -0.963+0.153E \qquad (E < 39.4 \text{ MeV})$$

$$= -0.963+0.153E[1-0.33\ln(E/39.4)] \qquad (E > 39.4 \text{ MeV})$$

$$V_{SO} = 5.767-0.015E+2.0\eta \qquad (8)$$

$$W_{SO} = 0.791-0.018E$$

$r_R = 1.219, \quad a_R = 0.688$

$r_D = 1.2\cdot, \quad a_D = 0.512$

$r_I = 1.38\cdot /A, \quad a_I = 0.557-0.462/\sqrt{A}$

$r_{ISO} = 1.103, \quad a_{ISO} = 0.560$

$r_{WSO} = 1.364, \quad a_{WSO} = 0.632$

The range of applicability is $10 < E_n < 80$ MeV and $A > 53$.

4. Regional Optical Potential —— "Shell-by-shell" approach

There is a difference between fundamental requirements of the *global* and particular OMPs. The global OMP aims at maximum generality, while the particular OMP aims at maximum accuracy in reproducing the experimental data. Actually, however, "off-the-shelf" global OMP are often not adequate for detailed analysis, while increased accuracy of fitting by particular OMP is paid for by reduced generality. It is not easy to reconcile the two requirements. A possibilty is to find out an OMP that has been optimized over a limited mass and energy range. Attempts toward this direction has

recently been started.

A. 1p-shell region

Based on the neutron scattering data on ^{6}Li, ^{7}Li, ^{9}Be, ^{10}Be, ^{12}C, ^{13}C, ^{14}N, ^{16}O over the energy range 7 to 15 MeV, Dave and Gould (1983)[11] derived a OMP parameter set for *1p*-shell nuclei. Although the low level density of the conpound nucleus makes it queationable to apply the OM to scattering from light nuclei, it is empirically clear that OM analysis can reproduce the data for *1p*-shell nuclei quite accurarely. Many of the *1p*-shell nuclei are nonspherical, but it is known that deformation effects can be masked by suitable choices of SOM parameters. They obtained the following set:

$$
\begin{aligned}
&V_R = 45.14 - 0.020E - 23.48\eta \\
&W_D = 11.32 + 0.237E - 16.08\eta \\
&V_{so} = 5.5 \\
&r_R = 1.508 - 0.0133A, \qquad a_R = 0.5 \\
&r_D = 1.353, \qquad a_D = 0.200 \\
&r_{so} = 1.15, \qquad a_{so} = 0.5
\end{aligned}
\tag{9}
$$

B. 2p-1d shell region

In an effort to analyze the neutron scattering data for ^{27}Al, ^{28}Si, ^{32}S over the energy range 14-40 MeV, Martin[12] obtained the OMP parameters for the *2p-1d* shell nuclei.

$$
\begin{aligned}
&V_R = (52.6\pm2.6) - (0.26\pm0.03)E - (17.6\pm3.5)\eta \\
&W_D = (10.1\pm0.5) - (0.15\pm0.02)E - (15.7\pm2.7)\eta \\
&W_I = (-2.9\pm0.3) + (0.2\pm0.02)E \\
&V_{so} = 5.7\pm0.7 \\
&r_R = 1.18\pm0.08, \qquad a_R = 0.66\pm0.07 \\
&r_D = r_I = 1.28\pm0.19, \qquad a_D = a_I = 0.55\pm0.07 \\
&r_{so} = 1.00\pm0.01, \qquad a_{so} = 0.41\pm0.08
\end{aligned}
\tag{10}
$$

C. N=82 shell region

Phillip *et al.*[13] measured transmission data for ^{140}Ce and transmission ratios for ^{142}Ce, ^{141}Pr, and ^{139}La over the extended enegy range 5-50 MeV. These nuclei (except ^{142}Ce) have a closed shell (N=82). They obtained an OMP parameter set in the primary fit to the ^{140}Ce total cross section:

$$
\begin{aligned}
V_R &= 49.4 - 0.32E - (17.0 - 0.111E)\eta \qquad (E < 25\ \text{MeV}) \\
&= 45.88 - 0.159E - (15.58 - 0.054E)\eta \qquad (E > 25\ \text{MeV})
\end{aligned}
$$

$$W_G = 7.456+1.4E-26\eta \qquad (E < 5\ \text{MeV})$$
$$= 16.32[1-\exp(-E/2.3)]-26\eta \qquad (E > 5\ \text{MeV}) \qquad (11)$$
$$V_{SO} = (\text{not given in the paper})$$
$$r_R = r_G = r_{SO} = 1.26, \qquad a_R = a_{SO} = 0.7$$
$$b = 1.0$$

It should be noted that this OMP employed the Gaussian shape for the surface imaginary term.

D. Actinide region

Madland and Young[14] tried to derive a regional OMP on a shell-by-shell basis for a narrow range of mass number in the actinide region for the neutron energy range of 10 keV-10 MeV. Starting from the SOM, after re-optimizations in three steps, they arrived at an approximate SOMP. A method was proposed for determining a deformed OMP from the approximate SOMP. This method utilized scaling transformations between the CC- and SOM-values for the real depth V_R and the product $W_D a_D$

$$V_R(\text{CC})/V_R(\text{SOM}) \simeq 1.025 \qquad (12a)$$
$$W_D a_D(\text{CC})/W_D a_D(\text{SOM}) \simeq 0.705 \qquad (12b)$$

obtained empirically from the iteration calculations for ^{238}U. Eq.(12b) can be interpreted as follows. In the SOM-calculations for deformed nuclei, the effects of coupling to the low-lying collective states are effectively included in the imaginary part, while in the CC-calculations the effects are separated out, since the the couplings are explicitly treated, resulting in smaller imaginary depth.

5. Nonlocality and Equivalent Local Potential

Since the nuclear force is essentially nonlocal, so is the OMP too. However, because of the complexity of calculations based on the nonlocal potential, efforts have been devoted to finding an local potential equivalent to nonlocal potential. It is now well recognized that the nonlocal potential is equivalent to a momentum-dependent potential, which appears as energy dependence in the depth parameters. The parameters of the equivalent OMP are determined so that it should provide an equivalent elastic scattering cross section, *i.e.* equivalent wave function outside the nuclear radius.

A. Trivially Equivalent Local Potential (TELP)

The Schroedinger equation describing the wave function in the nonlocal potential is written as

$$\frac{h^2}{2\mu}\left\{\frac{d^2}{dr^2} + k^2 - \frac{\ell(\ell+1)}{r^2}\right\}\chi_\ell(r) = \int V_\ell(r,r')\chi_\ell(r')dr'. \qquad (13)$$

If we take a potential for the ℓ-th partial wave

$$U_\ell^{TELP}(r) = \int V_\ell(r,r')\chi_\ell(r')dr' \Big/ \chi_\ell(r'), \qquad (14)$$

it is evident that this trivially equivalent local potential(TELP) will provide exactly the same solution for all r as the nonlocal one. However TELP is not useful since it has very complex and peculiar properties such as,

i) The TELP does not have a smooth behavior; $U_\ell^{TELP}(r)$ diverges when $\chi_\ell(r)$ in the denominator approaches zero. U_ℓ^{TELP} becomes infinite at $r = 0$ because the χ_ℓ equals zero at the origin.

ii) The TELP is different for every partial wave.

iii) The TELP has a complicated enegy-dependence which is different for different partial wave.

This odd potential is not the kind of local potential we want.

B. Approximately Equivalent Local Potential (AELP)

The equivalent local potential we want is something that has a simple behavior yet generates approximately the same wave function. The wave function $\chi^{(L)}$ in this local potential is related to the wave function $\chi^{(NL)}$ in the nonlocal potential by

$$\chi^{(NL)}(r) = F(r)\chi^{(L)}(r). \qquad (15)$$

The wave-function correction factor $F(r)$ should approach unity when $r \longrightarrow \infty$ for scattering waves. Perey and Buck[5] have shown that, by factorizing the nonlocal potential $V(r,r')$ into two parts as shown in eqs.(2) and (3), local potentials should be found, which were almost equivalent to the nonlocal one at a particular energy, in the sense that they reproduced the nonlocal angualr distribution. The following relation was found to hold:

$$U^{(N)}(r) = U^{(NL)}(r)\exp\left[\frac{\mu\beta^2}{2h^2}\left[E - U^{(NL)}(r)\right]\right]. \qquad (16)$$

Here it should be reminded that, by definition of the *equivalence*, the wave functions generated with the AELP are not always identical to the nonlocal ones inside the nucleus; the correction factor $F(r)$ is given, in the local-energy approximation, as

$$F(r) = \left[1 + \frac{\partial U^{(L)}}{\partial E}\right]^{-1/2} . \tag{17}$$

Actually, it is known that $\mathrm{Re}F(r) \simeq 0.85$ for $r < R$. Thus the use of the AELP in DWBA calculation leads to overestimation of the cross section, when there is a considerable contribution from internal wave function. This is in fact the case for nucleons and light particles. Fig.4[15] is an example of manifestation of this effect. This may also be one of the reasons for disagreement between experiment and DWBA calculation of direct inelastic scattering cross sections normalized by transition probability data.

In conclusion, it should be kept in mind that *a part of information contained in the nonlocal potentials is lost in transforming to equivalent local potentials.*

6. Dispersion Relation — A Farewell to the Woods-Saxon Form

One of the recent topics of the study of the OM is the application of the dispersion relation in determining and tuning the OMP. It has long been customary to determine the real and imaginary parts assuming implicitly that the two parts are independent each other. However, strikingly, the dispersion relation predicted that the nonlocal real part $V(r,r';E)$ and imaginary part $W(r,r';E)$ at energy E were interrelated accoding to the following formula:

$$V(r,r';E) = \frac{1}{2\pi}\int_{-\infty}^{+\infty} \frac{W(r,r';E')}{E' - E} dE' , \tag{18a}$$

$$W(r,r';E) = -\frac{1}{2\pi}\int_{-\infty}^{+\infty} \frac{V(r,r';E')}{E' - E} dE' . \tag{18b}$$

These relations readily follow from the Cauchy's integral formula. Defining equivalent local potentials as

$$V(r;E) = \int V(r,r';E) d^3r , \tag{19a}$$

$$W(r;E) = \int W(r,r';E) d^3r , \tag{19b}$$

we have

$$V(r;E) = \frac{1}{2\pi}\int_{-\infty}^{+\infty}\frac{W(r;E')}{E' - E}dE' , \tag{20a}$$

$$W(r;E) = -\frac{1}{2\pi}\int_{-\infty}^{+\infty}\frac{V(r;E')}{E' - E}dE'. \tag{20b}$$

From eq.(20a) we learn that, if the imaginary part is surface-peaked, as is usually the case for low-energy reactions, we have a surface-peaked real component. This results in a "wine-bottle shape" when there is an additional constructive component at the surface.

Some examples of application of the dispersion relations follow below.

(a)Ahmad and Haider (1976)

Armad and Haider[16] used the dispersion relation to calculate the surface-peaked component of the real potential from the surface-peaked component of the imaginary potential. They used the OMP obtained by Van Oers[17] for elastic scattering of 10-60 MeV protons on ^{40}Ca. The depth $W_s^{\,0}(E)$ of the surface-peaked imaginary potential of the derivative Woods-Saxon form is shown in the inset of Fig.5 and described as

$$W_s^{\,0}(E) = 0.38\exp(-[(E-13.84)/25.58]^2). \tag{21}$$

The real surface term can now be computed using eqs.(20a) and (21). The calculated $V_s(E,R)$ [$R = r_v A^{1/3}$], which is a measure of $V_s(E,r)$, is shown in Fig.5 for two different values of the diffuseness a_v of the imaginary part. It is seen that the contribution of the term $W_s^{\,0}(E)$ to the real potential is significant in some energy regions, particularly around 10 MeV.

(b)Su Zong Di and Hodgson (1989)

The addition of the real surface component has also the effect of increasing the effective radius and surface diffuseness of the real potential. Su Zong Di and Hodgson[18] investigated the effect on the total cross section of increasing the radius of the real potential. They found that the total cross section increased with increasing radius for energies above 3 MeV, as expected, whereas at lower energies the cross section decreased as the radius increased (Fig.6). The total cross section was calculated for ^{40}Ca including the dispersion term. It was found that the cross section became less than that given by the global OMP of Wilmore and

Hodgson[6] in the low energy region, and in general accord with the experimental data (Fig.7). The authors concluded that the total cross section at low energies was governed by Ramsauer-like interference effects that made it rather sensitive to quite small changes in the real potential, such as those introduced by including the dispersion term.

(c)Kitazawa, Harima and Mukai (1989)

In an effort to evaluate the $^{27}Al(n,\alpha)$ reaction cross section, Kitazawa, Harima and Mukai[19] determined an alpha-particle OMP that was consistent with the dispersion formula and physical invariants of the OMP. The OMP also conformed to the information obtained from the nuclear rainbaw scattering at intermediate enegies. Using this OMP, they were able to reproduce successfully the observed $^{27}Al(n,\alpha)^{24}Na$ reaction cross sections for incident neutron energies below 20 MeV (Fig.8).

As we have seen above, the dispersion relation throws light on the problems that have been difficult to solve hitherto. It introduces a new degree of freedom to the OMP by relaxing the constraint of the traditional Woods-Saxon form on one hand, introducing at the same time a new constraint on the relation between the real and imaginary parts of the OMP on the other hand. What the dispersion relation tells us is that the OMP should satisfy the two equations (19a,b) concurrently in order to be consistent. In the above examples, the dispersion relation (19a) was used to derive the real surface component from the imaginary surface potential. Does the resultant potential satisfies another equation (20b)? --- Here is the next question to be answered.

7. Optical Potentials for the Calculation of Inelastic Scattering

There are two processes in inelastic scattering of particles on a nucleus, *i.e.*, direct interaction (DI) and compound-nuclear (CN) processes. Inclusion of DI process is essential in the analysis of inelastic scattering on deformed nuclei, such as actinides.

The present author[28] proposed a unified method of calculating the inelastic scattering cross section, taking into consideration both the DI and CN processes. As is shown schematically in Fig.9, the inelastic channels are divided into three classes according to the strength of coupling to the ground state (g.s.). The strongly coupled channnels (g.s.-rotational-band states, for instance) are treated by means of the CC theory combined with the Hauser-Feshbach (HF) formalism through Satchler's general-

ized transmission coefficients[21] (we call this *CC/HF method* as contrasted to the conventional *SOM/HF method*). Inelastic scattering to the moderately coupled channels (*e.g.*, vibrational states) are calculated by applying the DWBA formalism. The effects of the weakly coupled channels are included in the imaginary part of the OMP.

Two comments are made below in regard to the OMP to be used in these calculations.

A. Entrance- and Exit-Channel Optical Potentials for the CC/HF Method

The CC/HF calculation requires two OMPs; one for the entrance-channel calculation by a CC code, such as JUPITOR-1[22], another for the exit-channel calculation with a HF code, such as ELIESE-3[23]. The first should be the CC-OMP with appropriate deformation parameters β_2 and β_4 that have been determined so as to reproduce the experimental data. As the latter was chosen the spherical OMP without deformation parameters.

It should be emphasized that the differences between the CC/HF method and the customary SOM/HF method lie not only in the fact that the DI process is accounted for, but also the CN process suffers a considerable change owing to a change in the generalized transmission coefficients, as is shown in Fig.10 for the case of ^{232}Th + n. Thus for example,

i) The *p*-wave contribution is increased in the several-hundred-keV region, resulting in better agreement of the total cross section over the region.

ii) The inelastic scattering to the continuum is higher than that from SOM/HF method by up to 15%, resulting in a greater energy loss of incident neutrons.

iii) The CN formation cross section is increased up to 25% over the entire energy range up to 20 MeV, resulting in enhanced cross sections for the reactions proceeding by way of the CN.

In this repect, one can say that simple combination of HF and DWBA methods for this purpose risks neglecting these effects.

The point ii) is important from reactor physics' point of view, since this results in enhanced moderation of MeV-neutrons in fast reactors.

B. Asymmeric Distorted Wave Approximation

Inelastic scattering to moderately coupled states can be calculated using the DWBA code, such as DWUCK[24]. Since the coupling is not supposed to be so strong, the effect of loss of probability flux by way of DI is not reflected in the transmission coefficients; instead, generalized trans-

mission coefficients fron CC/HF method was used to calculate the CN component of the inelastic scattering cross section.

An asymmetric form of the distorted-wave approximation for inelastic scattering has been proposed by Satchler[25] and Asquitto, Petersen and Seglie[26] and studied further by Kubo and Hodgson[27]. It has been found that the transition amplitudes calculated with the exit-channel wave function generated by a 'bare' OMP reproduce the exact results a little more accurately than the conventional DWBA ('DW method', according to the terminology of Satchler[25]). That is to say, in this method, a SOMP that reproduce the elastic scattering is used for the entrance channel, while a bare OMP (*i.e.*, CC-OMP) is employed as the exit-channel distorting potential in the calculation of the transition amplitude:

$$T_{a\,b} = \langle \psi_b | H' | \psi_a \rangle \tag{22}$$

where ψ_a is the wave function generated with the SOMP that reproduce the elastic scattering, ψ_b the wave function generated with the bare OMP. This method is reasonable because the effects of channel coupling is explicitly taken into consideration by the transition amplitude itself.

8. Concluding Remarks

Some remarks regarding the use of OM are summarized below:

(a) In reference to the use of the OM, most of the JENDL-2 evaluations were based on the spherical OMP, whereas in the JENDL-3 evaluations the CC and DWBA codes have been extensively used to consider the direct processes; this means that we have advanced from the second-generation to the third-generation OMP. The next step will be to proceed to a detailed study of the OMP, such as deviations from the Woods-Saxon form, relativistic OMP at higher energies, *etc.*

(b) Systematic approach to the regional OMPs on the "shell-by-shell" basis will possibly provide OMPs with adequate range of applicability as well as reasonable accuracy.

(c) The *equivalent local OMP* is equivalent to the nonlocal OMP only in the sense that it generates approximately the same wave function to the original one outside the nucleus, and does not garantee full equivalence of the wave function inside the nucleus.

(d) Application of the dispersion relation has revealed that there is a deviation from the Woods-Saxon form in the real part of the OMP. It also leads effectively to introduction of energy-dependence to the nuclear

radius.

(e) In the use of the CC/HF method, one should be aware of the fact that not only the direct component is considereed but also the CN component is changed from the SOM/HF method. The ADWA is known to give slightly better results than the conventional DWBA for moderately coupled channnels.

Acknowledgments

The author is very indebted to Dr. P.E.Hodgson of the Oxford University and to Drs. H.Kitazawa and Y.Harima of Tokyo Institute of Technology for providing manuscripts of their works to the author prior to publication.

References

1) H. Feshbach, C. E. Porter and V. F. Weisskopf, Phys. Rev. 94, 448(1954)
2) K. A. Brueckner and J. L. Gammel, Phys. Rev. 109,1023 (1958)
3) P. A. Moldauer, Nucl. Phys. 47, 65 (1963)
4) N. K. Glendenning, D. L. Hendrie and O. N. Jarvis, Phys. Lett. 26B, 131 (1968)
5) F. G. Perey and B. Buck, Nucl. Phys. 32, 353 (1962)
6) D. Wilmore and P. E. Hodgson, Nucl. Phys. 55, 673 (1964)
7) F. D. Becchetti,Jr., and G. W. Greenlees, Phys. Rev. 182, 1190 (1969)
8) A. M. Lane, Phys. Rev. Lett. 8,171 (1962); Nucl. Phys. 35,676 (1962)
9) J. Rapaport, V. Kulkarni and R. W. Finlay, Nucl. Phys. A330, 15(1979); J. Rapaport, Phys. Rep., 87, 25 (1982)
10) R. L. Walter and P. P. Guss, *Proc. Int. Conf. on Nuclear Data for Basic and Applied Science*, Santa Fe, 1985, p.1079
11) J. H. Dave and C. R. Gould, Phys. Rev. C28, 2212 (1983)
12) Ph. Martin, Nucl. Phys. A466, 119 (1987)
13) T. W. Philip, H. S. Camarda and R. M. White, *Proc. Symp. on Neutron Cross Sections from 10 to 50 MeV*, (1980) p.769
14) D. G. Madland and P. G. Young, *Proc. Int. Conf. on Neutron Physics and Nuclear Data*, Harwell, 1979 p.349
15) K. K. Seth, J. Picard and G. R. Satchler, Nucl. Phys. A140, 577 (1970)
16) I. Ahmad and W. Haider, J. Phys. G 2, L157 (1976)
17) W. T. H. Van Oers, Phys. Rev. C3, 1550 (1971)
18) Su Zong Di and P. E. Hodgson, to be published. (1989)
19) H. Kitazawa, Y. Harima and N. Mukai, unpublished.
20) T. Ohsawa *et al.*, *Proc. Int. Conf. on Nuclear Data for Basic and*

Applied Science, Santa Fe, 1985 p.1193;
T. Ohsawa, *Proc. 1986 Seminar on Nuclear Data*, p.320 (1987)
T. Ohsawa *et al.*, *Research on Thorium Fuel*, SPEY 21, Reports of Special Project Research on Energy under Grand-in-Aid of Scientific Research of the Ministry of Education, Science and Culture, Japan, p.35 (1987)

21) G. R. Satchler, Phys. Lett. 7, 55 (1963)
22) T. Tamura, Rev. Mod. Phys. 37, 679 (1965)
23) S. Igarasi, JAERI-1224 (1972)
24) P. D. Kunz, COO-535-606 and -613 (1969)
25) G. R. Satchler, *Lectures in Theoretical Physics*, Vol.VIII, p.73 (1965)
G. R. Satchler, *Direct Nuclear Reactions*, Oxford (1982)
26) R. J. Asquitto, J. F. Petersen and E. A. Seglie, Phys. Rev. Lett. 41, 1159 (1978)
27) K. I. Kubo and P. E. Hodgson, Phys. Lett. 100B, 453 (1981)

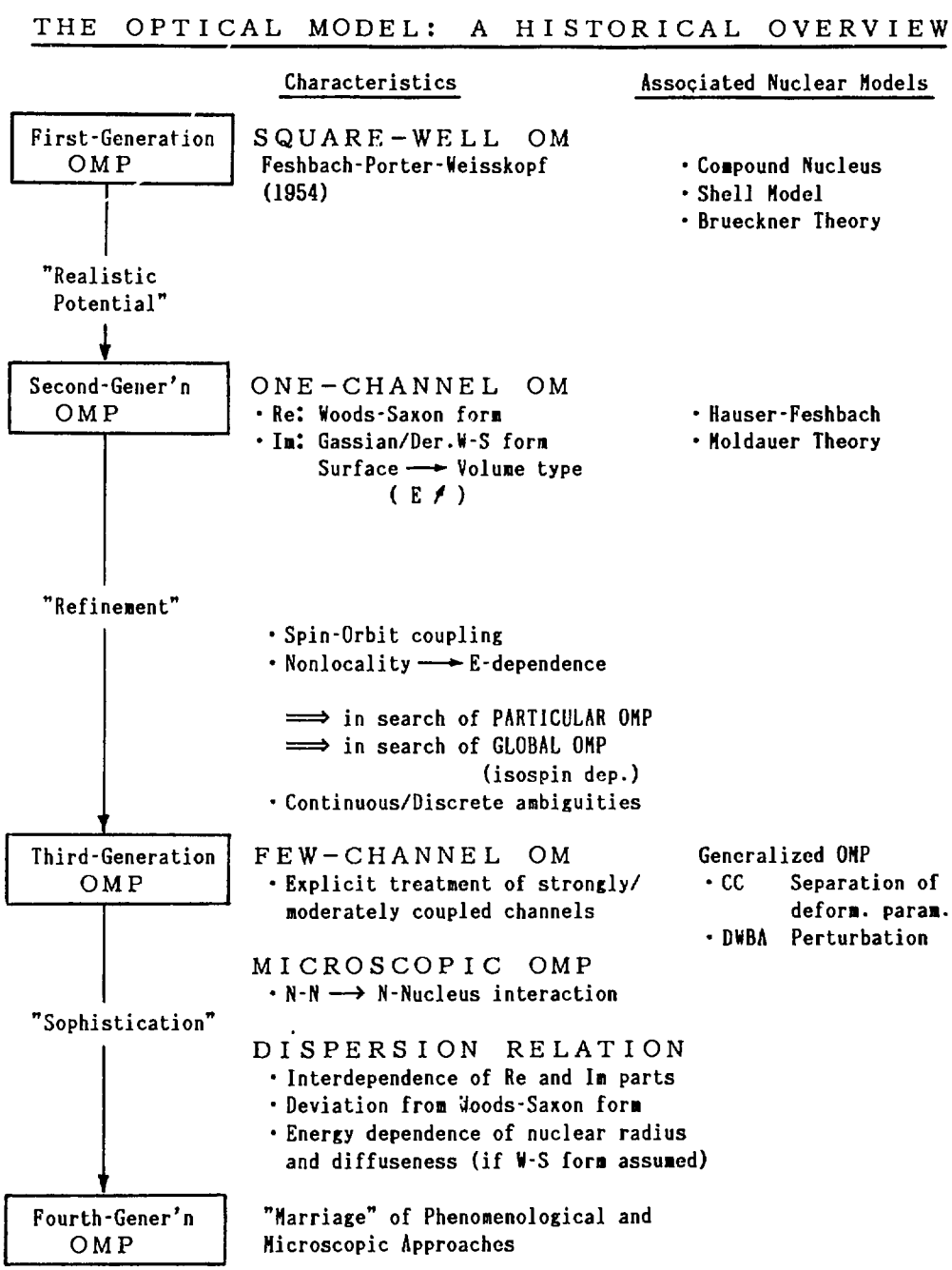

Fig. 1 Historical development of the optical model

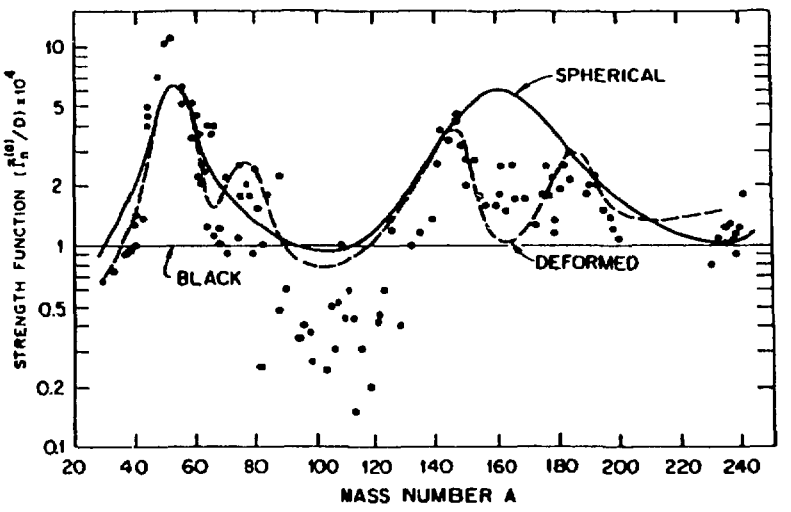

Fig. 2 Neutron s-wave strength function vs. mass number A.[25]

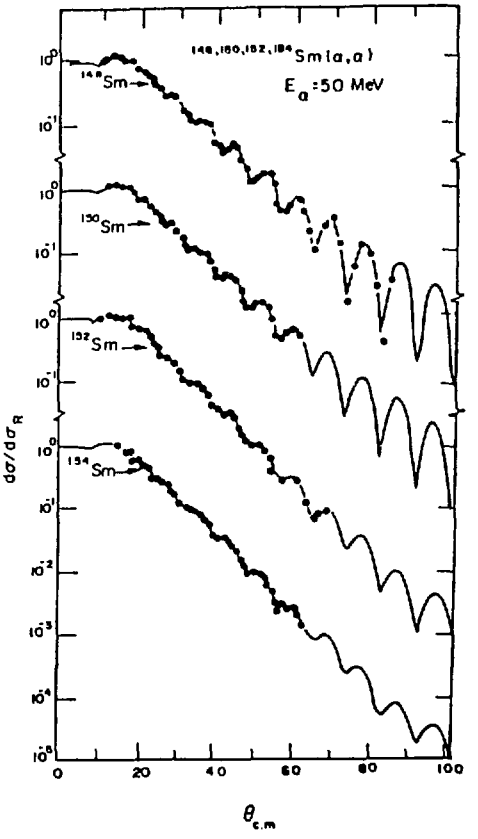

Fig. 3 Differential cross sections for the elastic scattering of 50 MeV alpha particles by the even samarium isotopes compared with CC calculations using the same OMP but different deformation parameters for each isotope.[4]

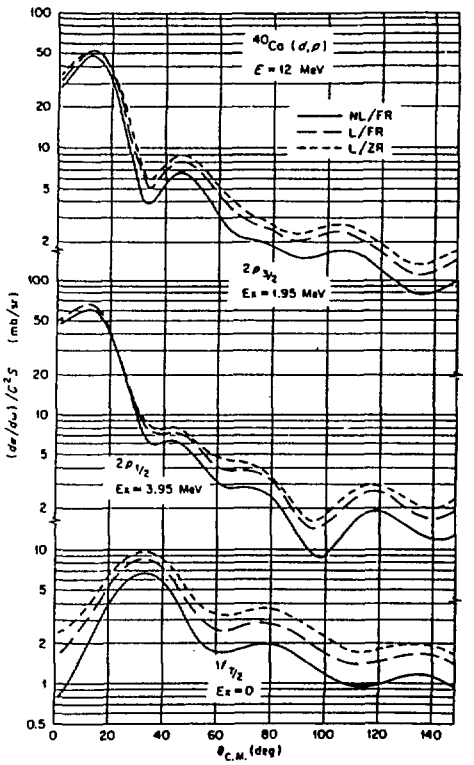

Fig. 4
Comparison of ^{40}Ca(d,p) cross sections calculated with and without corrections for nonlocality of the distoring potential (labeled as NL and L, respectively). Also shown are the results of making the zero-range approximation (ZR) instead of treating the finite-range (FR) correctly.[15]

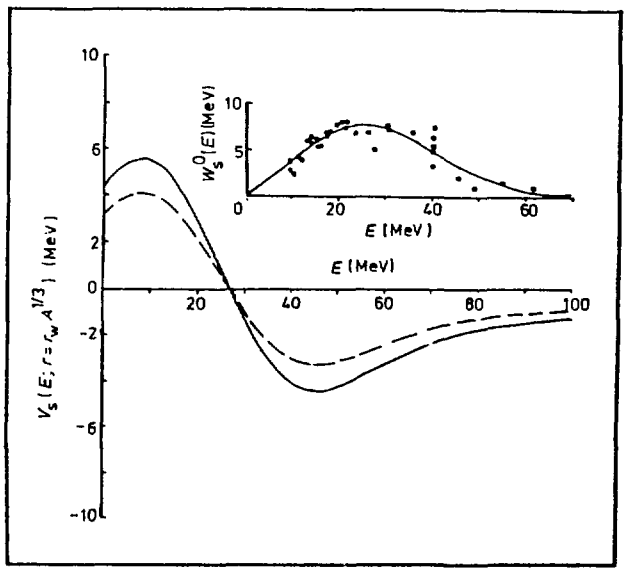

Fig. 5 The real surface part of the optical potential is shown as a function of energy for aw = 0.549 (full curve) and aw = 0.732 (broken curve). The inset shows the imaginary surface depth as a function of energy.[16]

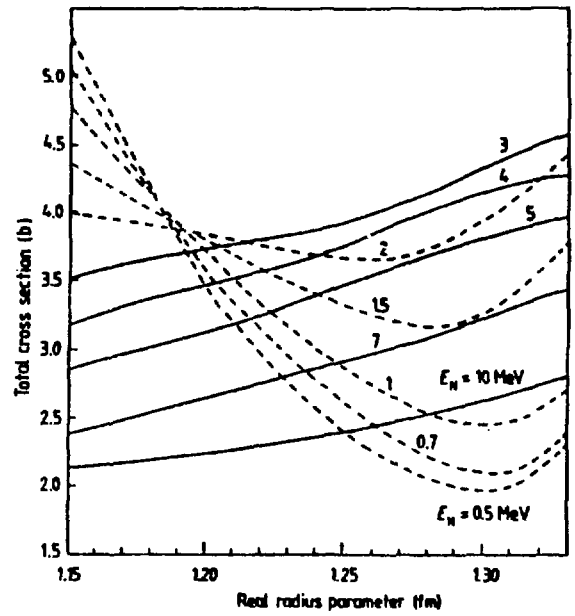

Fig. 6 Total cross section for $^{40}Ca+n$ as a function of radius of the real potential for several energies.[18)]

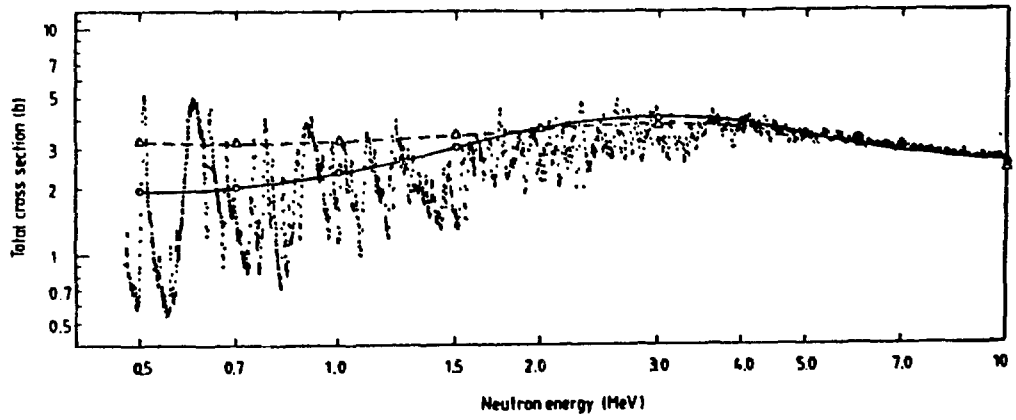

Fig. 7 Total cross section for $^{40}Ca+n$ compared with OM calculations using the Wilmore-Hodgson OMP (dashed curve) and an OMP including the dispersion term (full curve).[18)]

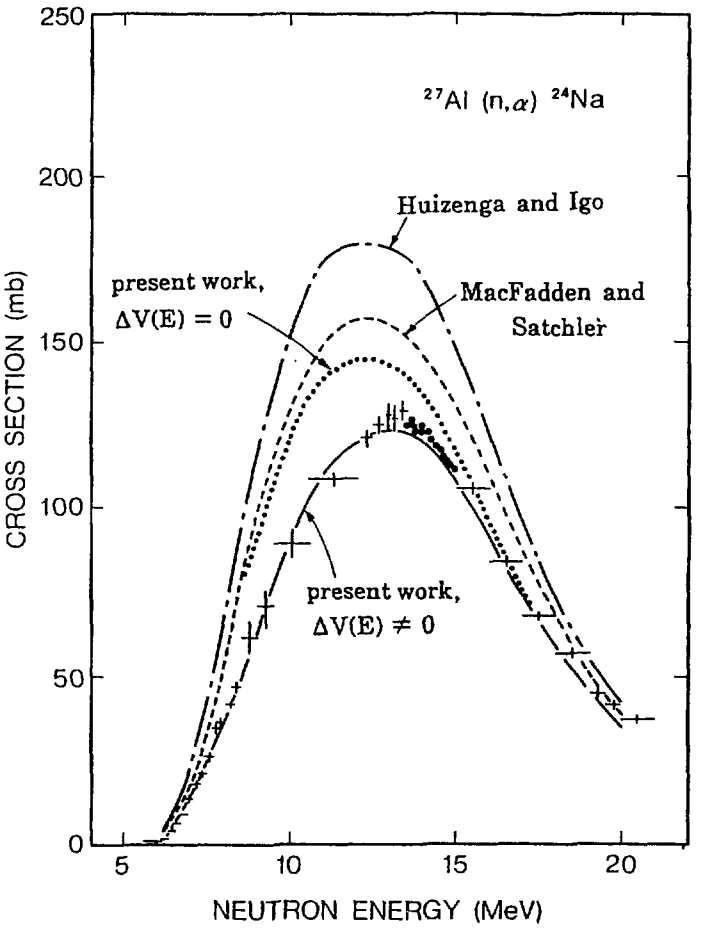

Fig. 8 Calculated and experimental $^{27}Al(n,\alpha)^{24}Na$ reaction cross sections. Calculated values with different OMP sets are shown.[19]

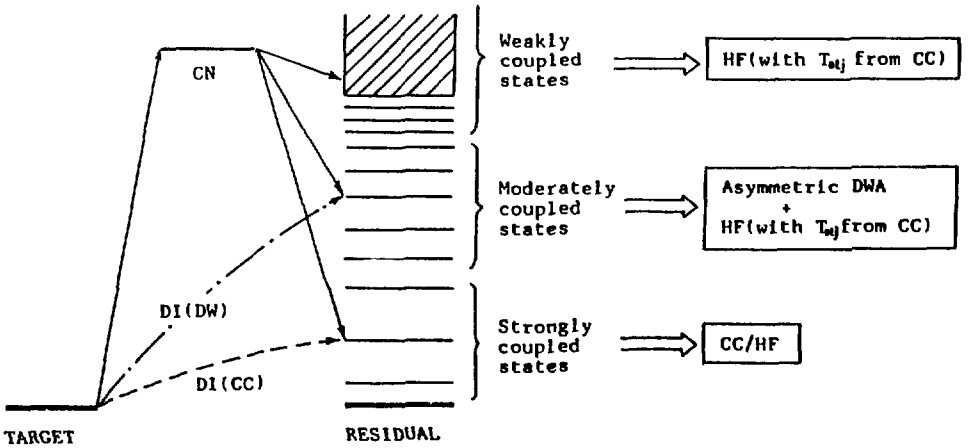

Fig. 9 Schematic representation of three classes of processes of neutron inelastic scattering.[20]

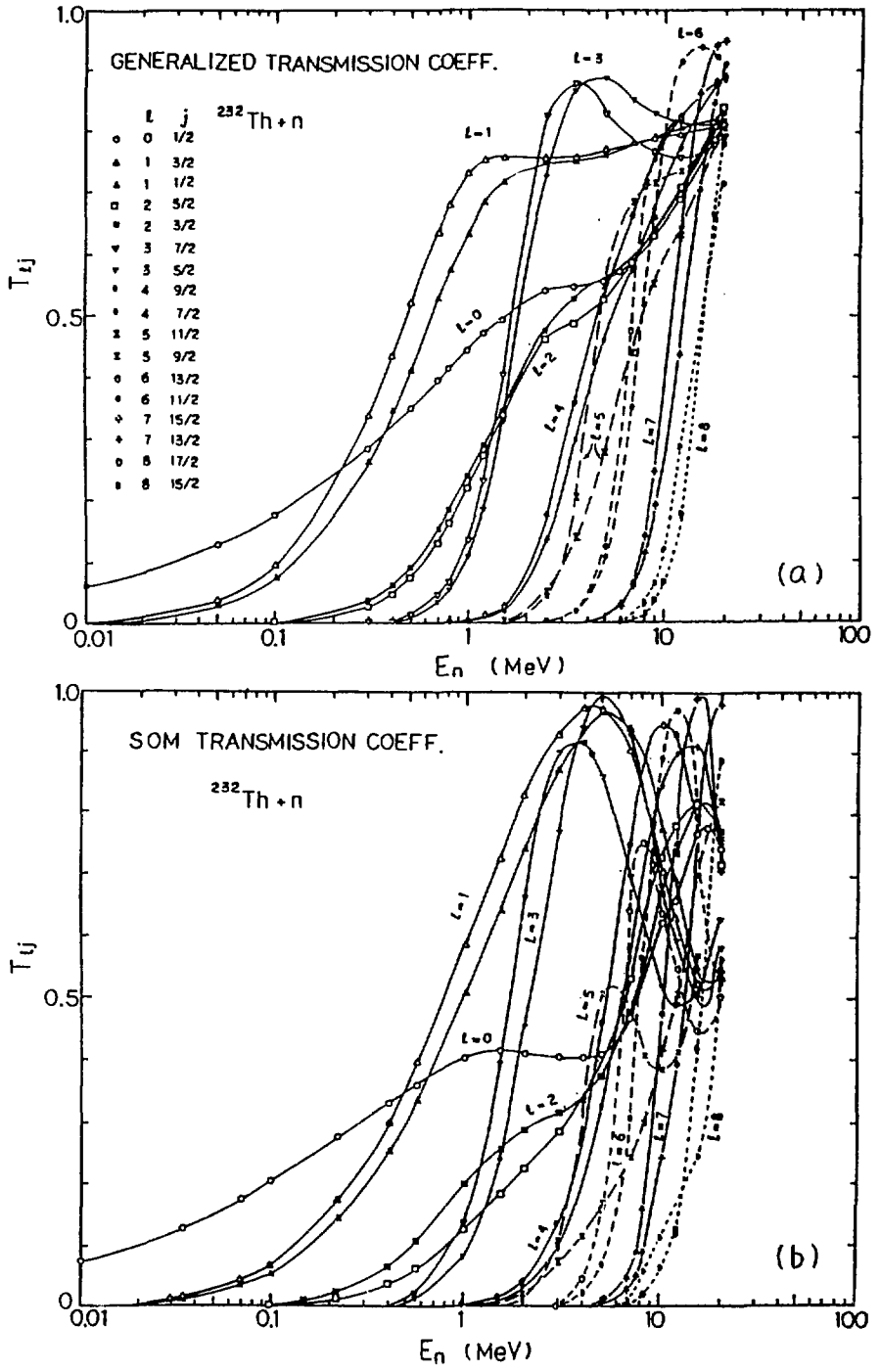

Fig. 10 Comparison of the neutron transmission coefficients calculated with CC and SOM.[20)]

2.2.2 Current Topics in Nuclear Fission Research

Akira Iwamoto

Japan Atomic Energy Research Institute
Tokai–mura, Ibaraki–ken, JAPAN

This year is the 50th anniversary of the discovery of nuclear fission by Otto Hahn and Fritz Strassmann [1]. From the point of view of the fundamental physics research, nuclear fission was one of the oldest motivation of the nuclear physics. In this 50 years, many aspects of nuclear fission phenomena have been investigated. Owing to the nature that the nuclear fission involves a dynamical treatment of finite–many–body systems, there have been always some challenging new topics in nuclear fission research in these 50 years. By solving these problems one by one, we have come closer to the understanding of the nuclear fission dynamics. As examples of current topics in nuclear fission research, I will choose and discuss the following three: 1) Cold fission phenomena. 2) Heavy–particle radioactivity phenomena. 3) Transient effect phenomena.

1. Cold fission

The asymmetric mass distribution for the spontaneous fission of the actinide nuclei is one of the most well known feature of the nuclear fission. For the very heavy members of the actinide nuclei a remarkable deviation were found rather recently from this feature. This phenomena is called as cold fission, because the intrinsic excitations of two fragments are quite low compared with those of the neighboring systems. Although there were some precursor phenomena which were observed earlier, the typical cold fission was discovered at the end of 1970's for ^{258}Fm and ^{259}Fm in Berkeley [2]. After this first discovery, the same phenomena were observed for ^{259}Md, ^{260}Md, ^{258}No and ^{262}No [3]. In Fig.1 the mass distributions for the heavy actinide nuclei are shown schematically. The Fm isotopes are most typical examples where as the neutron number increases from 156 to 157, the symmetric component increases and partially fills the dip for the symmetric mass distribution. This is a precursor phenomena which proceeds the drastic change which happens when the neutron number increases from 157 to 158. The mass distribution changes suddenly to

symmetric one and at the same time, the width of the mass distribution becomes quite narrower. It's a surprise that only one difference of neutron number causes such a big change!

Another characteristic of the cold fission phenomena is seen in the mean value of the relative kinetic energy between two fragments which is shown in Fig.2. It is seen that the typical cold fission phenomena is occurring in ^{258}Fm, ^{259}Fm and ^{260}Md. Their kinetic energies are higher by 30 to 40 MeV compared to those coming from the normal fissioning nuclei. Again, the drastic change between ^{257}Fm and ^{258}Fm is impressible. If we compare Figs.1. and 2., we can say that the typical cold fission is characterized by the symmetric and very narrow mass distribution, and exceptionally low intrinsic excitation energy of fragments.

This phenomena caused strong interests among theoreticians for the explanation. From theoretical point of view, the explanation is difficult because we have no reliable theory to calculate the mass distribution for the spontaneous fission in general. What we can have at most is some qualitative model to understand it. One of such model is proposed by Möller–Nix–Swiatecki [4]. What they pointed out is the existence of two discrete fission paths which have configurations quite different near their scission points. They calculated the potential energy surfaces in two–dimensional shape parameterization (energy is minimized with respect to other parameters). They found that for the cold fissioning nuclei, two fission paths exist which bifurcate at some deformation on the way to scission and end up at quite distinct deformations at the scission points. One of the scission configuration has rather compact shape compared to the other which has a typical scission shape of the normal actinide nuclei. Thus if the fission proceeds along the former path, it leads to the high relative kinetic energy as were shown in Fig.2., because the compact scission shape means the high relative Coulomb potential. Thus the model might be able to explain the kinetic energy characteristics but the feature of the mass distribution is not understood well. Another remaining problem is that the explanation uses only the collective potential energy property and neglects the effect of mass tensors. To obtain the reliable fission path in the multi–dimensional parameter space, we need to develop a model in which the effect of the kinetic term in addition to the potential term should be treated correctly. In this respect, the model we proposed in [5] seems to be a promising starting point.

2.Heavy–particle radioactivity

Most of the stable nuclei which have proton numbers larger than 40 are unstable

with respect to the two-body decay from the Q-value estimation. Alpha decay and fission are known as popular two-body decays. Sandulescu et al. pointed out the possibility of very asymmetric mass division in the fission process in 1980 [6]. Four years later, Rose and Jones [7] discovered the decay process $^{223}U \rightarrow {}^{209}Pb + {}^{14}C$, the partial half-life of which is about 10^{15} sec and the branching ratio to alpha decay, about 10^{-9}. After the discovery of ^{14}C radioactivity, many kinds of heavy-particle radioactivity have been confirmed [8]. They are the emissions of ^{23}F, ^{24}Ne, ^{26}Ne, ^{26}Mg, ^{30}Mg, ^{32}Si and ^{34}Si from variety of compound nuclei as is seen in Table 1. It is clear from this table that the phenomena are rather popular for the heavy nuclei. There are two alternative models to understand the phenomena, one is an extension of the theory of alpha decay and the other is an extension of the fission theory.

As a typical example of the alpha-decay school, I will introduce the method of Blendowske and Walliser [9]. In their treatment, the decay width for the heavy particle is expressed as

$$\Gamma = \hbar \frac{v}{2R_i} \cdot P \cdot S$$

where v is the velocity of the heavy particle inside the potential well which is obtained by the decay Q-value and R_i is the potential radius. P stands for the normal WKB penetration factor for the barrier of the heavy particle and S is the spectroscopic factor. This S represents the probability to observe the heavy particle in the ground state wave function of the parent nucleus. Spectroscopic factor S is expressed in the form

$$S(a) = [\, S(\alpha) \,]^{(a-1)/3}$$

where a is the mass number of the heavy particle and $S(\alpha)$ stands for the spectroscopic factor of alpha particle. This expression assumes that the spectroscopic factor should scale proportional to the power of the number of intrinsic freedom of heavy particle . The $S(\alpha)$ value, however, is thought to be an effective value and it depends on whether the heavy particle has even or odd mass number

$$S^{even}(\alpha) = 6.3 \times 10^{-3},$$
$$S^{odd}(\alpha) = 3.2 \times 10^{-3}.$$

Using this model and assuming the simple barrier shape, they obtained values shown in the column specified by BW in Table 1.

Another way to calculate the half lives is to use the similar method to fission and we call it as fission school. There are several groups in this school and I will introduce two typical ones. Shi and Swiatecki [10] assumed that the potential between the heavy particle and the residual nucleus is given by the Coulomb and the proximity potential. When the heavy particle is overlapping with the residual nucleus, they assumed intermediate shapes which smoothly connect the spherical parent nucleus and two spherical nuclei of heavy particle and the daughter nucleus. In this respect, their potential is essentially different from that of Blendowske and Walliser where the heavy particle is treated like a point object. The results of Shi and Swiatecki is shown in the column specified by SS in Table 1. As a second example, I will introduce the method of Poenaru et al. [11]. The essential difference of their method from that of Shi–Swiatecki is that the former used the Strutinsky prescription to calculate the potential energy for the decay process. Thus the barrier is calculated as a sum of the macroscopic liquid–drop part and the shell correction part. Their results is given in the column specified by Poe. in Table 1.

The agreement between the calculations and the data seen in Table 1 is unexpectedly good if we remember the fact that to reproduce the alpha–decay half–life is quite hard even now. We should keep in mind, however, that theories of heavy–particle decay include some fitting parameters.

3. Transient effect

The expression for the fission decay–width from the excited compound nucleus was given in the famous paper of Bohr and Wheeler [12] and is used even now. We should also pay attention, however, to the fact that Kramers proposed a generalization of it [13] one year after the paper of Bohr and Wheeler. The idea of Kramers is that there exists a frictional force acting to the motion of fission. This friction modifies the stationary current to the fission direction at the saddle point and as a result, the fission width turns out to be smaller than the value of Bohr and Wheeler. This was probably the first paper which pointed out the importance of dissipation in the collective nuclear motion. From the end of 1960's, the heavy–ion reaction became popular and heavy–ion fusion–fission process has been investigated quite extensively. The characteristic of the fusion–fission process is that it involves a high excitation energy and high angular momentum. The rotating–liquid–drop model tells us that as the

angular momentum increases, the fission barrier height decreases due to the centrifugal potential. This, in addition to the high excitation energy, increases the fission width considerable compared with the light–ion induced fission. Thus the fission life–time becomes quite short, to the order of 10^{-19} sec or even shorter. In such situation, a new phenomena is expected to occur, which is called as transient phenomena.

To explain this phenomena, I will start from the experimental data for the pre–scission neutron multiplicity. This quantity is defined as the number of neutrons emitted in coincidence with the fission fragments but omitting the neutrons emitted from the fragments. Thus it is the multiplicity of the neutrons emitted from the compound nucleus which proceed the fission process. Experimentally, the separation between the pre–scission and post–scission neutrons is carried out by observing the velocity spectra of neutrons in coincidence with those of the fission fragment. The pre–scission neutron multiplicity defined in this way is shown in Fig.3 [14] as a function of the excitation energy of the compound system for various heavy–ion fusion–fission process. Various curves are the calculated results by assuming the standard statistical model with different level density parameters. As is seen clearly from this figure, the data points deviate more and more from these lines as the excitation energy increases. A possible origin of this effect is the following.

The Bohr–Wheeler expression for the fission width involves the calculation of the flux at the saddle point deformation. Because the saddle deformation is displaced from the ground–state deformation which is near spherical, it might be possible to attach a time which the system needs to reach the saddle deformation starting from the ground–state deformation. We call this time as transient time. This is the time during which the system cannot fission. The rough estimate of the pre–scission neutron multiplicity is give by (Γ_n/Γ_f) where Γ_n is the neutron emission width and Γ_f is the fission width from the compound nucleus. During the transient time, the fission width is effectively hindered and therefore, the fission life–time $\hbar/\Gamma_f$ is elongated. In other word, the fission width is no longer a constant and we have to treat the time–dependent fission width. This causes the increase of the pre–scission neutron multiplicity. This situation is shown schematically in Fig.4.

In order to calculate the time–dependent fission width, we have to settle some models. Most popular one is the classical statistical model which makes use of solving a Fokker–Planck equation or Langevin equation. I will not give the detail of the method and explain only the final results. In this method, by solving one of above mentioned equations, the probability distribution d(p,q,t) is obtained. Here p is momentum and q is position of the fission coordinate and t is the time. The quantity

d stands for the probability that the fissioning motion has p and q at time t. Defining the quantity

$$\Pi(q_0,t) = \int_{-\infty}^{q_0} dq \int_{-\infty}^{+\infty} dp\ d(p,q,t)$$

where q_0 stands for the saddle–point configuration, we see that Π stands for the probability that the system has not fissioned at time t. Then the fission width is given by

$$\Gamma_f = -\hbar \frac{d}{dt} ln\ \Pi(q_0,t)$$

the meaning of which is easily understood from the definition of the decay width. An example of the fission width calculation according to this expression is given in Fig.5 [15]. In this case, the transient time of about 10^{-20} sec is obtained. To explain the recent experimental data, the transient time longer than this time seems to be required [16]. In this respect, a refinement of the theory will be necessary to reproduce the experimental data quantitatively.

References

[1] O. Hahn and F. Strassmann, Naturwiss., **27**, 11 (1939).
[2] D.C. Hoffman, Proc. IAEA Symp. on Phys. and Chem. of Fission, Jülich 1979 (IAEA,Vienna, 1980), vol II p275.
[3] D.C. Hoffman, Nucl.Phys. **A502**, 21c (1989).
[4] P. Möller, J.R. Nix and W.J. Swiatecki, Nucle.Phys., **A469**, 1 (1987).
[5] T. Kindo and A. Iwamoto, Phys.Lett. **B225**, 203 (1989).
[6] A. Sandulescu, D.N. Poenaru and W. Greiner, Sov.J.Part.Nucl., **11**, 528 (1980).
[7] H.J. Rose and G.A. Jones, Nature **307**, 245 (1984).
[8] P.B. Price, Nucl.Phys. **A502**, 41c (1989).
[9] R. Blendowski and H. Walliser, Phy.Rev.Lett. **61**, 1930 (1988).
[10] Y.J. Shi and W.J. Swiatecki, Nucl.Phys. **A438**, 450 (1985).
[11] D.N. Poenaru et al., publ.NP–54–86, Inst.Central de Fizica (Bucharest, Romania, 1986).
[12] N. Bohr and J.A. Wheeler, Phys.Rev. **56**, 426 (1939).

[13] H.A. Kramers, Physica **7**, 284 (1940).

[14] D.J. Hinde et al., Nucl.Phys. **A452**, 550 (1986)

[15] P. Grange et al., Phys.Rev. C**34**, 209 (1986).

[16] W.U. Hinde, D. Hilscher andd H. Rossner, Nucl.Phys. **A502**, 497c (1989).

Table 1 A summary of the partial half-lives of heavy-particle radioactivity taken from[8] together with the measured branching ratio.

Decay	E_k (MeV)	Theoretical Predictions of log T (refs.) Poe. (7)	P-P (35)	SqW (13)	S S (27)	BM (36)	BW (28)	SK (37)	IS (55)	Measured log T (sec)	-log B	ref.
^{221}Fr (^{14}C)	29.28	14.4	16.5	15.2	16.0	14.0	15.5	14.5	----	>15.77	>13.3	13;14
^{221}Ra (^{14}C)	30.34	14.3	14.7	14.1	14.8	>12.4	14.2	13.3	----	>14.35	>12.9	13;14
^{222}Ra (^{14}C)	30.97	11.2	13.3	11.2	11.6	11.2	11.8	11.8	10.5	11.02±0.06	9.43±0.06	13;16
^{223}Ra (^{14}C)	29.85	15.2	15.6	15.0	15.7	15.3	15.1	14.2	14.9	15.2±0.05	9.21±0.05	10;9;15;13;17
^{224}Ra (^{14}C)	28.63	15.9	18.0	16.0	16.8	16.1	16.2	17.0	15.3	15.9±0.12	10.37±0.12	13
^{225}Ac (^{14}C)	28.57	17.8	19.0	18.7	19.7	18.8	18.6	18.3	----	>18.34	>12.4	14
^{226}Ra (^{14}C)	26.46	21.0	22.9	21.0	22.2	21.2	21.1	22.5	21.7	21.33±0.2	10.6±0.2	16;14
^{231}Pa (^{23}F)	46.68	25.9	>23.4	26.0	25.5	----	----	----	----	>24.61	>12.74	30
^{230}Th (^{24}Ne)	51.75	25.3	26.1	24.8	24.9	24.4	24.8	25.2	----	24.64±0.07	12.25±0.07	29
^{232}Th (^{26}Ne)	49.70	28.8	29.6	29.1	28.4	28.7	27.9	29.4	----	>27.94	>10.3	12
^{231}Pa (^{24}Ne)	54.14	23.4	23.4	23.7	23.5	21.6	23.4	22.3	23.9	23.36±0.08	11.37±0.08	30
^{232}U (^{24}Ne)	55.86	20.8	21.8	20.7	20.0	20.2	20.8	20.6	19.8	21.06±0.1	11.7±0.1	31
^{233}U (^{24}Ne)	54.27	24.8	24.4	24.9	24.8	23.7	25.4	23.6	24.4	24.82±0.15	12.12±0.15	24;32
^{233}U (^{25}Ne)	54.32	25.0	>24.4	25.1	24.4	----	----	23.6	----			
^{234}U (^{24}Ne)	52.81	26.3	26.4	25.8	25.7	25.5	25.6	26.4	----	25.25±0.05	12.36±0.05	21;25
^{234}U (^{26}Ne)	52.87	26.5	>26.4	26.2	25.0	25.9	26.4	26.5	----			
^{234}U (^{28}Mg)	65.26	25.8	>26.4	25.4	25.7	25.7	25.4	25.8	25.7	25.75±0.06	12.86±0.06	21;25
^{237}Np (^{30}Mg)	65.52	27.5	27.7	28.3	27.7	>27.3	29.9	26.8	----	>27.27	>13.4	29
^{238}Pu (^{30}Mg)	67.00	25.7	>26.4	25.9	24.6	25.6	25.8	25.7	----	25.7±0.25	16.25±0.25	11
^{238}Pu (^{28}Mg)	67.32	26.0	>26.4	25.5	----	25.7	26.9	25.4	----			
^{238}Pu (^{32}Si)	78.95	25.1	26.4	25.7	----	26.0	25.7	25.5	----	25.3±0.16	15.86±0.16	11
^{241}Am (^{34}Si)	80.60	24.5	25.5	26.5	26.2	25.3	28.8	23.8	23.8	>25.3; >24.2	>15.1; >14.1	29;22;34
$\sigma_{\log T}$		0.45	1.33	0.28	0.67	0.71	0.35	0.82	0.6			

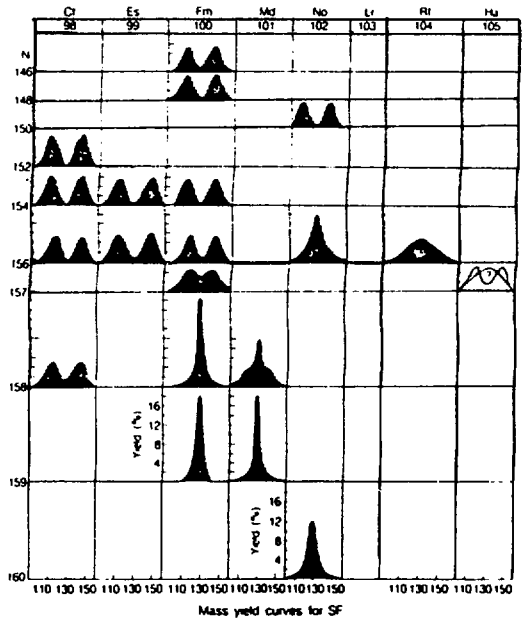

Fig. 1 Systematic of mass-yield distributions taken from [3]

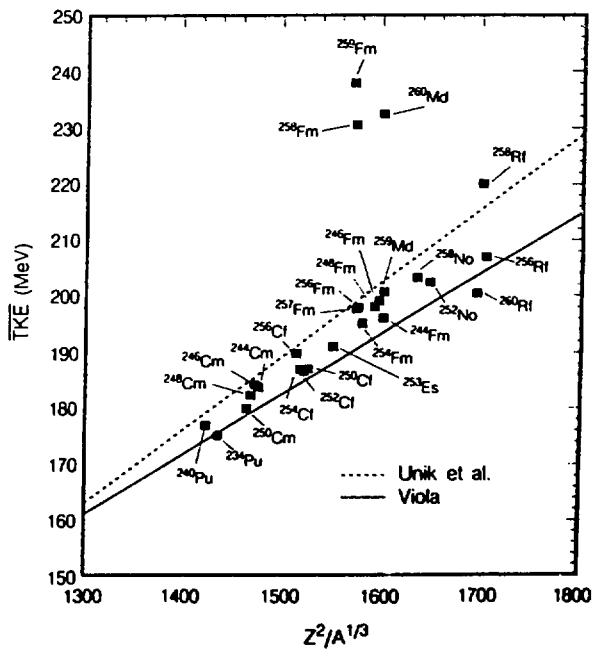

Fig. 2 Average relative kinetic energy of fragments taken from[3]. Solid and dashed curves are the systematic of Viola and Unik.

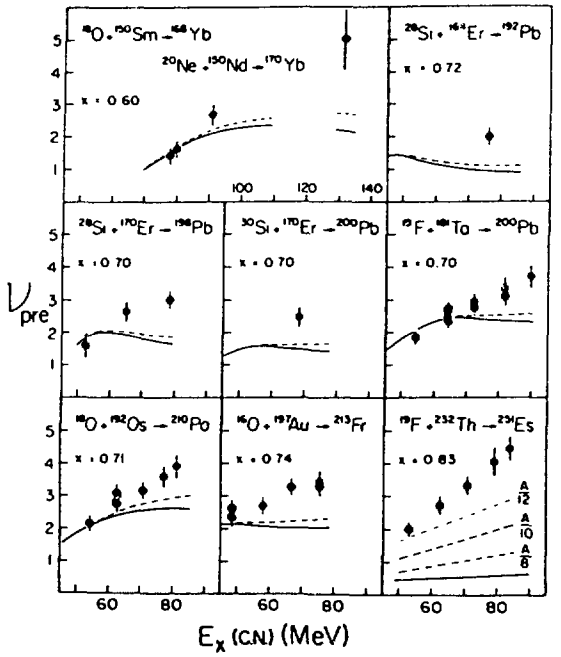

Fig. 3 Pre-scission neutron multiplicity n_ν as a function of the excitation energy of the compound nucleus taken from[14]. Curves are the statistical model calculation with changing level density parameters.

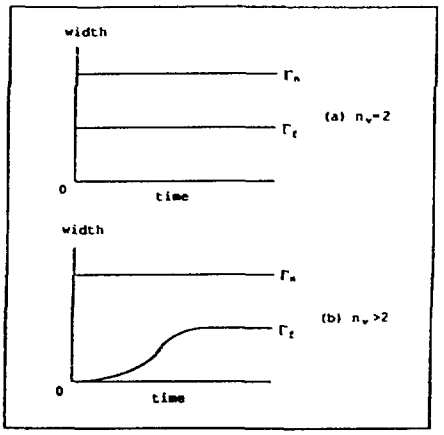

Fig. 4 Schematic picture of the effect of the transient time in fission width. Upper figure (a) corresponds to the standard case where the neutron multiplicity is about 2. Lower (b) corresponds to the time-dependent fission width and neutron multiplicity becomes larger than 2.

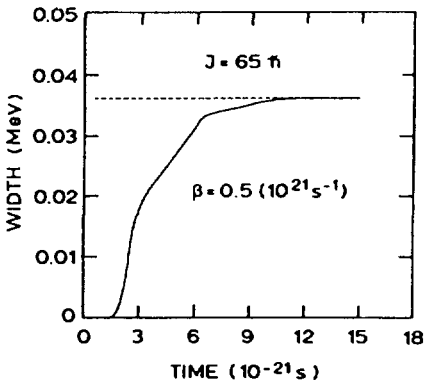

Fig. 5 Time dependence of the fission width calculated in[15]. The angular momentum is 65 unit and β is the reduced dissipation coefficient.

2.2.3 Topics at the NEANDC Specialists' Meeting on Neutron Activation Cross Sections for Fission and Fusion Energy Applications

Y. Ikeda

Japan Atomic Energy Research Institute
Tokai-mura, Ibaraki-ken 319-11 Japan

Following three international meetings concerning the neutron cross section data were held last September, 1989:

1) IAEA-CRP Consultants' Meeting on Measurements of Long-Lived Activation Cross Sections (Sep. 11-12) at ANL.
2) NEANDC Specialists' Meeting on Neutron Activation Cross Sections for Fission and Fusion Energy Applications (Sep. 13-15) at ANL.
3) Sixth Coordination Meeting for the Program to Meet Nuclear Data Needs for Fusion Energy (Sep. 19-21) at Ohio University.

Though the organizer of each meeting were different, the topics treated were closely related each other and many of participants attended at all of three meetings. Since the author participated on the second and third meetings, this report decribes mainly topics of the NEANDC meeting and the Sixth Coordination Meeting. A brief summary of the IAEA-CRP Meeting is also given.

1. NEANDC Specialists' Meeting

The purpose of this meeting were to review the current progress in the neutron activation cross section research, to examine data requirement and status of important applicatoion areas, to survey the method and resources available in the OECD/NEA family to address these needs, and to organize a working group to foment continued progress in this field.

Thirty five international specialists including seven Japanese participated in this meeting and discussed throughly current problems concerning experiment, evaluation and theory. A total number of 24 papers were presented. The titles and talkers are shown as follows ;

Technical Papers, Session I : Data Needs/Status

Session Leader : B. Patrick

1) S. Cierjacks and Y. Hino
   The Role of Sequential (x,n) Reactions on Element Activation of Fusion Reactor Materials and Related Nuclear Data Needs
2) E. Cheng
   Activation Cross Sections for Safety and Environmental Assessments of Fusion Reactors
3) J. Kopecky and H. Gruppelaar
   European Activation Library for Fusion Reactor Technology
4) J. C. Sublet, F. M. Mann and A. J. H. Goddard
   A One-Group Averaged Cross-Section Benchmark Comparison for Fusion Activation Studies

Technical Papers, Session II : Experimental Work

Session Leader : T. Katoh

5) Y. Ikeda and C. Konno
   A Program on Neutron Activation Cross Section Measurements at FNS for Fusion Applications
6) L. R. Greenwood and D. L. Bowers
   The Production of ^{49}V, ^{93}Mo, ^{93m}Nb and Other Long-Lived Isotopes in Fusion Materials with 14 MeV Neutrons
7) R. C. Haight
   Activation with an Intense Source of Monoenergetic Neutrons in the Range 8-14 MeV
8) T. Katoh, K. Kawade, H. Yamamoto, T. Iida and A. Takahashi
   Measurement of Formation Cross Sections of Short-Lived Nuclei by 13.4-14.9 MeV Neutrons
9) H. Liskien
   Improved Neutron Fluence Accuracies in Activation Experiments
10) W. Mannhart, D. L. Smith and J. W. Meadows
    Mesurement of the $^{47}Ti(n,p)^{47}Sc$ Reaction Cross Section Between 1.2 and 8 MeV
11) S. M. Qaim
    Neutron Activation Cross Section Measurements on Zr, Nb and Mo Using Radiochemical Techiques
12) T. B. Ryves, P. Kolkowski and A. C. Hooley
    Ho, Pb and Bi Cross sections for 14.3 MeV Neutrons

13) J. W. Meadows, D. L. Smith, G. Winkler, H. Vonach and M. Wagner
Intercomparison of ^{238}U Deposits Employed for Neutron Fluence Determination in Neutron Activation Cross Section Measurements

14) H. Vonach, M. Wagner and R. C. Haight
Neutron Activation Cross Sections of ^{58}Ni and ^{60}Ni for 8-12 MeV Neutrons

15) R. Zorro
Neutron Capture Cross Section Measurements in the Energy Region 2.0-7.7 MeV Using Activation Technigues

Technical Papers, Session III : Theoretical Work
Session Leader : D. Gardner

16) J. Kopecky and M. Uhl
Testing New Approaches to Calculate Radiative Capture Cross-Sections

17) D. G. Gardner and M. A. Gardner
Some Neutron and Photon Reactions on the Ground and Isomeric States of ^{236}Np, ^{237}Np.

18) N. Yamamuro
Calculation of Isomer States Production with a Simplified-Input Cross Section Calculation System

19) M. B. Chadwick and P.G. Young
Calculation of the Production Cross Sections of High-Spin Isomeric States in Hafnium

Technical Papers, Session IV : Evaluation Work
Session Leader : P. Young

20) Y. Kanda, Y. Uenohara, T. Kawano and Y. Tsuji
Estimation of Neutron Reaction Parameters in Reaction Model Formulae for Medium Nuclei Taking Accounts of Proton Induced Reaction Experiments

21) C. Y. Fu
A Review of Activation Cross Sections in the ENDF/B-VI General Purpose Files of Cr, Fe, Ni, Cu and Pb

22) Y. Nakajima et al.
Present Status of the JENDL Activation File

23) T. B. Ryves
A Simultaneous Evaluation of Some Important Cross Sections at

14.70 MeV

24) M. Wagner, A. Pavlik, B. Strohmaier, S. Tagesen and H. Vonach
Evaluation of Cross Sections for Important Neutron Dosimetry Reactions

Topical discussion sessions on 20 particular subjects were taken place in order to enhance the discussions. The items of topics and session leaders are listed below.

1) Standards and Dosimetry Cross Sections : H. Vonach
2) Material Damage : L. Greenwood
3) Waste Disposal : E. Cheng
4) 14-MeV Measurement : Y. Ikeda
5) Differential Studies : H. Liskien
6) Integral Studies : W. Mannhart
7) Activity Measurements : S. Qaim
8) Data Corrections : D. L. Smith
9) Data Uncertainties : W. Mannhart
10) Exotic Reactions : S. Qaim
11) New Mesurement Methods for 8-15 MeV : R. Haight
12) Developments in Basic Nuclear Theory : C. Y. Fu
13) Model Parameter Status and Prospects : M. Gardner
14) Nuclear Model Code Intercomparisons : P. Young
15) Merging of Theory and Experiment by Means of Statistical Methods : Y. Kanda
16) Uncertainties in Nuclear Model Results : H. Vonach
17) Evaluation Methodology : J. Kopecky
18) 14-MeV Evaluations : T. B. Ryves
19) Differential Evaluation : H. Vonach
20) Activation Cross Section Libraries : F. Mann

The first meeting of the NEANDC activation working Group (WG) took place. Twenty three individuals attended the meeting. The purpose was to organize WG and to define some technical projects to be investigated during the next couple of years. The summary were as follows :

1) A list of WG participants was established to facilitate good communication between the participants.
2) It was agreed that the WG meeting takes place periodically.

3) The WG participants are encouraged to contribute the NEA Fast Neutron Cross Section Newsletter.

4) Two initial WG projects have been launched ;

- Experimental project : leader, Prof. Vonach
  "Inter comparison of correction procedures for neutron spectrum using $^{58}Ni(n,p)$ as a test case."
- Theory project : leader, Dr. Cierjaks
  "Compntation of $^{60}Co(n,p)$ reaction cross section."

2. Sixth Coordination Meeting for the Program to Meet Nuclear Data Needs for Fusion Energy

After the NEANDC meeting, the coordination meeting was held at Ohio university during Sep. 19-21, 1989. This meeting has been organized by the Office of Nuclear Physics (ONP) of the US Department of Energy (DOE) in correspondance with a data need from the Office of Fusion Energy (OFE) of DOE. Representatives from ten principal facilities met together and discussed recent progresses and next actions to meet data request summarized by Dr. E. Cheng (GA), representative of OFE. The original members of this meeting are ANL, BNL, Colorado School of Mines, LLNL, LANL, Univ. of Michigan, NIST, ORNL, Ohio Univ. and TUNL of Duke Univ. In addition, nine international foreigners were attended. Considarable time was assigned to Task Forse Sessions to futher the discussion for the data request list (DRL).

General session

Dr. Whetstone (DOE) gave an overview talk concerning the recent US Fusion Energy Research environment. He stressed the importance in the activation nuclear data. Dr. Cheng talked the historical background of the meeting and mentioned severe situation on the badget of the US Fusion Program in 1990. Dr. D. Smith (ANL) sammarize the last NEANDC specialists' meeting. In successive sessions, papers. concerning progresses in the nuclear data for fusion energy research were presented by representatives from European countories, PRC and Japan as well as US principal perticipants. They reported the progress during three years since the last meeting in 1986 and the plans of research to be done in coming two years.

Task Force Session

The session was divided into two specific session ;

A "Experiment". : chairman Dr. D. Larson (ORNL),

B "Theory and Modeling" : chairman Dr. P. Young (LANL).

Items discussed in Task Force A are as follows :

1) Review of Task Force Efforts,
2) International Cooperation in Measurement,
3) Review of Experimental Capabilities,
4) Review of Current Request List,
5) Data Needs Observed During ENDF/B-VI Evaluation,
6) Review of Data Status from Last Meeting,
7) Charged Particle Data Needs.

The first item discussed was to review the activities of three working groups (WG) organized at the last meeting. Concerning the data base for ^{7}Li(n,n't) reactions a remarkable accomplishment was declared ; the uncertainty in the cross section at 14 MeV in ENDF/B-VI is less than 3%, which meets the data requirement from the view point of Fusion Energy. The second and third ones were to review 137 activation cross sections and to set priority among them.

The next business was No.6. Here following 6 important subjects were treated ;

1) Fuel Cycle Reaction (Charged Particle Reaction),
2) Neutron Multiplication, and Tritium Breeding in the Blanket, where ^{7}Li(n,n't), Pb(n,2n) and Be(n,2n) were included,
3) Neutron and Gamma-ray Emission Data,
4) High Priority Dosimetry Reactions,
5) High Priority Activation Cross Sections,
6) Radiation Damage Reactions.

The status of the Be(n,2n) was treated in a joint session of A and B. There, it was stated that the results of the new evaluation based on the current data base is almost acceptable and program are in the integral data testing.

One of topics of the session was to indentify the capability of the experimental facility to provide data to meet requirement in the DRL.

The meeting was expected large contribution by interlaboratory cooperation in the future.

The Task Forse Sesson B, discusse following items :

1) Status of the DWBA Calculation for the d+d Reactions and the Question of Suppression by Polarization,
2) Model Code Availability,
3) Code Comparison Activities,
4) Use of Dispersion Relations in Optical Model Calculations,
5) Status of the IAEA-CRP on level Densities.

3. IAEA Consultants' Meeting on Measurements of Long-Lived Activation Cross Sections

This meeting was held just befor the NEANDC meeting at ANL (Sep. 11-12, 1989). Almost all nembers of the meeting were overlapped with the NEANDC meeting members. Althoug I didn't attend the meeting, here the summary of the meeting is given by Table 1.

Table 1 Data status of activation cross sections related to the CRP of long-lived radionuclides for fusion technology

	Reaction	Status	Laboratory
1)	$^{27}Al(n,2n)^{26}Al$	data needs satisfied	
2)	$^{63}Cu(n,p)^{63}Ni$	2	Jüelich
		2	ANL/LANL/JAERI
		1	ANL
3)	$^{94}Mo(n,p)^{94}Nb$	1	ANL
4)	$^{104}Ag(n,2n)^{103}Ag$	1	IAEB
		1	Debrecen
		3	IRK
		2	ANL/LANL/JAERI
5)	$^{179}Hf(n,2n)^{178m2}Hf$	3	Harwell
		2	IAEB
		4	Oxford/LANL
		2	ANL/LANL/JAERI
6)	$^{182}W(n,n\alpha)^{178m2}Hf$	2	Harwell
7)	$^{151}Eu(n,2n)^{150m}Eu$	1	IAEB
		3	IRK
		1	Jüelich
		2	ANL/LANL/JAERI
8)	$^{153}Eu(n,2n)^{152g}Eu$	2	ANL/LANL/JAERI
		1	IAEB
		3	IRK
9)	$^{159}Tb(n.2n)^{158g}Tb$	2	Jüelich
		1	IAEB
		2	ANL/LANL/JAERI
		3	IRK
10)	$^{158}Dy(n,p)^{158g}Tb$		No work done
11)	$^{193}Ir(n,2n)^{192m2}Ir$	3	IRK
12)	$^{187}Re(n,2n)^{186m}Re$	3	IRK
13)	$^{62}Ni(n,\gamma)^{63}Ni$		No work done
14)	$^{98}Mo(n,\gamma)^{99}Mo$		(Chengdu, PRC)
15)	$^{165}Ho(n,\gamma)^{166m}Ho$		(Chengdu, PRC)
16)	$^{191}Ir(n,\gamma)^{192m}Ir$		No work done

1. Mesurement performed for CRP
2. Measurement in progress for CRP
3. Evaluation of existing data performed for CRP
4. Calculation in progress for CRP

2.2.4 Review of Nuclear Data Required for Nuclear Transmutation Systems of Long-Lived Radioactive Waste Utilizing Particle Accelerators

NORIO KISHIDA

Century Research Center Corporation
3-6-2, Nihonbashi-Honcho, Chuo-ku, Tokyo 103, Japan

In order to reduce the period for management of long-lived radioactive waste produced from nuclear fuel cycle facilities, waste disposal procedures based on nuclear transmutation have been proposed by several groups. Two of the proposed procedures are to utilize particle accelerators; one utilizes a high energy proton linac and the other a high energy electron linac. The former procedure intends to use the nuclear transmutation by proton-induced spallation reactions and the later one by photonuclear reactions with bremsstrahlung photon beams. If there are no evaluated nuclear data concerning the above two reactions, neutronic characteristics of transmutation facilities will not become clear. Cross-sections of both reactions are not included in currently existing neutron data files such as JENDL-3. Moreover these cross-sections reveal quite different behavior in comparison with those of low-energy neutron-induced reactions. In the present paper, reviewed are the current status and problems of experimental and evaluated nuclear data of the two reactions; because these data highly important to calculation on the neutronics of the transmutation facilities.

1. Introduction

It has well understood that the management of long-lived radioactive waste is a long-pending and the most important problem for further development of nuclear energy; the safe and economic method to manage the waste must be inevitably established if we hope to obtain stable public acceptance of nuclear energy. Recently detailed studies of the waste disposal management[(1)-(17)] based on nuclear transmutation are in progress in order to diminish general feelings of unrest about the management of radio-activity over several million years from now. The nuclear transmutation means a transmutation of long-lived radio-active nuclides to short-lived and/or stable nuclides by means of a certain

kind of nuclear reactions. If the waste management system can be realized technically and economically, a vast reduction will be expected for the period necessary for not only management and control not of transuranic nuclides(TRU) but also of decay heat from fission products(FP).

The following nuclear reactions are proposed and studied for the nuclear transmutation:

1. nuclear spallation reactions[1]-[6] induced by intense proton beams accelerated up to the energy of a few GeV,
2. photonuclear reactions[7]-[15] induced by bremsstrahlung gamma-rays having the end-point energy near 30 MeV, which is correspond to the upper limit of the giant E1(electric dipole) resonance(GDR),
3. fission reactions[17] induced by fast neutrons in a conventional FBR or an Actinide Burning Fast Reactor.

It seems to be evident that the nuclear data which will be necessary for the design of the facilities quite differ from the first two reactions to the third ones. This is because the first two reactions are very different from the third ones in reaction types and mechanisms. Whereas there are several nuclear data files of the third reactions, there are no files of the first and second reactions at all. Therefore, the author will survey both the present status of the nuclear data and some problems with evaluation of the spallation and photonuclear reactions.

2. Nuclear data for transmutation system with photonuclear reactions

In this section the author will review the present status of the nuclear data that will be required for designing a nuclear transmutation system[7]-[15] to utilize the photonuclear reactions. The author of Ref. 7 is planning to use the photonuclear reactions induced by bremsstrahlung gamma-rays which are generated by irradiating a certain converter target with an intense electron beam from a linear accelerator. The maximum energy of the gamma-rays is selected as such a manner that it covers the excitation energy of GDR. Therefore the author will review the photonuclear data of only GDR region.

Main nuclides considered as targets of the nuclear transmutation are ^{90}Sr, ^{137}Cs, ^{93}Zr, ^{99}Tc, ^{129}I and ^{135}Cs belonging to FP nuclides, and ^{237}Np, ^{241}Am, ^{243}Am, ^{242}Cm and ^{244}Cm belonging to TRU nuclides. No measurement of photoneutron cross-sections using monochromatic photon beams has been reported. The only available cross-sections is for ^{237}Np.[18] The photonuclear cross-sections were reported for a few isotopes of the above FP

nuclei.[18] Consequently it is still difficult to perform a precise estimate of time necessary for the nuclear transmutation. The photoneutron cross-sections[18),(19)] of ^{Nat}Sr are shown in Fig. 1. As shown in this figure, one can say generally that if a nucleus has an atomic number larger than about fifty, the excitation curves of photoneutron cross-sections have only one or two resonance peaks whose width is approximately a few MeV(see Ref. 20, for detailed description of photonuclear reactions). This resonance feature is quite different from that of low energy neutron capture cross-sections in resonance width and peak numbers. To see systematics of the photoneutron cross-sections, an example[19] of isotope dependence of the cross-sections is shown in Fig. 2. This figure shows that the position, width and strength of each GDR does not sharply depend on the mass number of each isotopes. In fact, it is well known[19] that systematics between photoneutron cross-sections and mass numbers exist. Therefore the photonuclear cross-sections of the FP nuclei may be predicted to an accuracy of $\pm 10\%$.

The secondary reactions caused by neutrons which are produced from the primary photonuclear reactions will occur in the targets of the nuclear transmutation facilities; this secondary reactions are very important for the realistic estimation of the transmutation time. Measurement of DDX for photoneutrons with monochromatic photon beams has not been reported at all as far as the nuclides concerned here. However, this DDX can be calculated using several nuclear theoretical models. As an example, an energy spectrum of neutrons emitted from ^{133}Cs(γ, xn) reaction at 20 MeV is shown in Fig. 3; this spectrum was calculated using the MCPNC code[21] that is being developed by the author and others. This figure shows that the spectrum can be considered as evaporated neutrons from a nucleus being in an equilibrium state and energy of the neutrons is less than 20 MeV. JENDL-3 is a general purpose file which was compiled so that it can cover reactions concerned with neutrons below 20 MeV. Hence build-up and decay calculation about the secondary reactions can be carried out using JENDL-3. However, the nuclear data of some yttrium isotopes, namely, ^{86,87,88}Y which will be produced by the secondary reactions, must be added to it.

Not only neutrons but also protons are emitted from photonuclear reactions of FP nuclei. But it is well known from many experiments and calculations that the ratio of the former to the later is larger than about 10 : 1. Consequently the nuclear data for proton reactions is unessential as far as one does not try to perform detailed burn-up calculation. If the data are inevitably essential, theoretical evaluation will be necessary owing to lack of experimental data.

The group to study on the nuclear transmutation[9)~(11)] to utilize the photonuclear reactions expects that the transmutation for TRU is realized through photofission reactions. The photofission and the neutron-induced fission cross-sections of ^{237}Np are shown in Figs. 4 and 5, respectively. These two figures show that the former is comparable

to the later. Hence the photonuclear transmutation for TRU is worth while examining the possibility. Photofission cross-sections of concerned TRU except ^{237}Np have not been measured using monochromatic photon beams. As far as the author examined the experimental cross-sections of some TRU nuclei, it is not clear whether those cross-sections have a certain sort of systematics or not. Consequently it is unclear to what precision the unmeasured cross-sections can be evaluated. Although each amount of FP yielded through the photofission is quite important to the burn-up calculation considering the secondary reactions, no one has reported on the measurement for (A, Z) distributions of FP with monochromatic photon beams. On the contrary a number of those measurement with bremsstrahlung beams have been reported, so there may be no other way to guess the (A, Z) distributions using monochromatic beams from those using bremsstrahlung ones. As an example the FP distributions for ^{238}U are shown in Fig. 6. They are not fairly different from those using fast neutrons; it appears that nuclides that are not produced through (n, f) reactions are not produced also through (γ, f) ones. The FP distributions can therefore be conjectured.

The author summarizes the current status of the nuclear data related to the nuclear transmutation utilizing the photonuclear reactions as follows. Direct measurement of the photonuclear cross-sections for the nuclei discussed in this section has not been reported except for ^{237}Np. Accordingly it is desirable to measure their cross-sections. However, the measurement is very difficult because it is rather dangerous to use a large amount of radioactive nucleus as experimental targets. Therefore those experimental data will not be obtained in the near future. Thus we must evaluate the photonuclear data by employing systematics among experimental data and certain theoretical models. Current neutron data files such as JENDL-3 include sufficiently species of nuclides and classes of nuclear reactions except for some yttrium isotopes noted above.

3. Nuclear data for transmutation system with proton-induced spallation reactions

Nakahara and Nishida[2] have completely specified the nuclear data that are necessary for the neutronic calculation of the nuclear transmutation to utilize proton-induced spallation reactions. Thus the author will merely repeat their conclusions.

The nuclear data newly required are as follows:

1. target nucleus : TRU and spallation products(SP),
2. incident particle energy : threshold energy to 1.5 GeV,
3. a type of incident particles : p, n, d, t, ^{3}He, α and π,

4. a class of cross-sections : total cross-sections,
elastic cross-sections,
particle yield cross-sections,
energy and angular distributions and
nuclear structure and decay data.

The spallation reactions produce neutron-poor nuclei which are not generated in nuclear fission reactors; the mass number of these nuclei range from one to a target mass number. In fact none of current nuclear data files dose satisfy the above requirements. It is however questionable whether such files are really necessary to carry out burn-up calculations or not. Further the author conjectures that evaluation for a greater part of SP nuclides will not be probably finished until the nuclear transmutation facility will start to run; for this evaluation task is extremely time consuming one. It is therefore desirable that the group concerning the nuclear transmutation makes clear what kind of nuclear data are really necessary.

4. Concluding remarks

As far as the nuclear transmutation of FP utilizing the photonuclear reactions is performed with incident γ-ray energy below 30 MeV, no intrinsically difficult problem exists in evaluation of both photon and neutron cross-sections. On the other, as for that with the spallation reactions, most of the required data has not been evaluated.

References

(1) NISHIDA, T. AND NAKAHARA, Y. : Analysis of transmutation of transuranic wastes by nuclear spallation reactions, Proc. of the 1988 Seminar on Nuclear Data, *JAERI-M* 88-065, p. 246(1988).

(2) NAKAHARA, Y. AND NISHIDA, T. : A study on TRU waste disposal and the current status of nuclear data, JNDC News **63**, *ISSN* 0385-4876, (in Japanese), p. 15(1987).

(3) KANNO, I., *et al.* : A study on TRU incineration system with proton accelerator, *Preprint* 1989 *Annual Mtg. of AESJ*, (in Japanese), L59.

(4) TAKADA, H., *et al.* : A study of incinerator by proton accelerator, *ibid.*, (in Japanese), L60.

(5) TAKADA, H., *et al.* : Conceptual study of TRU incineration system driven by proton accelerator, *Preprint* 1989 *Fall Mtg. of AESJ*, (in Japanese), H39.

(6) NISHIDA, T., *et al.* : TRU transmutation with high energy proton beam, presented in this seminar.

(7) KONASHI, K., *et al.* : Transmutation of radioactive wastes by γ-rays (I), *Preprint* 1987 *Fall Mtg. of AESJ*, (in Japanese), M58.

(8) SENDA, M., *et al.* : Transmutation of radioactive wastes by γ-rays (II), *ibid.*, (in Japanese), M59.

(9) MATSUMOTO, T., *et al.* : Feasibility of γ ray incineration of glass solidified wastes, *ibid.*, (in Japanese), M60.

(10) YAMADA, A., *et al.* : Incineration study of nuclear wastes by using the photodisintegration, *ibid.*, (in Japanese), M61.

(11) KASE, T., *et al.* : Incineration study of nuclear wastes by using the photodisintegration, *ibid.*, (in Japanese), M62.

(12) KONASHI, K., *et al.* : Transmutation of radioactive wastes by γ-rays (I) — Preliminary system design —, *Preprint* 1988 *Fall Mtg. of AESJ*, (in Japanese), J48.

(13) KONASHI, K., *et al.* : Transmutation of radioactive wastes by γ-rays (II) — Model analysis —, *ibid.*, (in Japanese), J49.

(14) KASE, T., *et al.* : Incineration study of nuclear wastes by using the photodisintegration, *ibid.*, (in Japanese), J50.

(15) TAKASHITA, H., *et al.* : Study of transmutation for F.P. — Transmutation by hybrid system —, *Preprint* 1989 *Annual Mtg. of AESJ*, (in Japanese), L57.

(16) HARADA, H., *et al.* : Study of transmutation for F.P. (II) — Nuclear transmutation by Coulomb excitation —, *ibid.*, (in Japanese), L58.

(17) TAKANO, H. : TRU disposal by nuclear transmutation and the current status of nuclear data — Case of fission reactors —, (in Japanese), JNDC News **67**, *ISSN* 0385-4876, (in Japanese), p. 30(1988)(see references there in, for nuclear transmutation by nuclear fission reactors).

(18) FULTZ, F. AND BERMAN, B. : *Atom. Data Nucl. Data Tables*, **38**, 199(1988).

(19) BERMAN, B. AND FULTZ, F. : *Rev. Mod. Phys.*, **47**, 713(1975).

(20) BERGERE, R. : Features of the giant E1 resonance, *Lecture notes in Physics* **61**, p. 1(1977), Springer-Verlag, New York.

(21) KISHIDA, N., *et al.* : Development of MCPNC code for evaluation of photonuclear reactions, *Preprint* 1989 *Fall Mtg. of AESJ*, (in Japanese), B15.

(22) GARBER, D. AND KINSEY, R. : Neutron Cross Sections, Vol. **II**, Curves, *BNL*-325, 3rd ed. (1976).

(23) JACOBS, E., *et al.* : *Phys. Rev.*, **C19**, 422(1979).

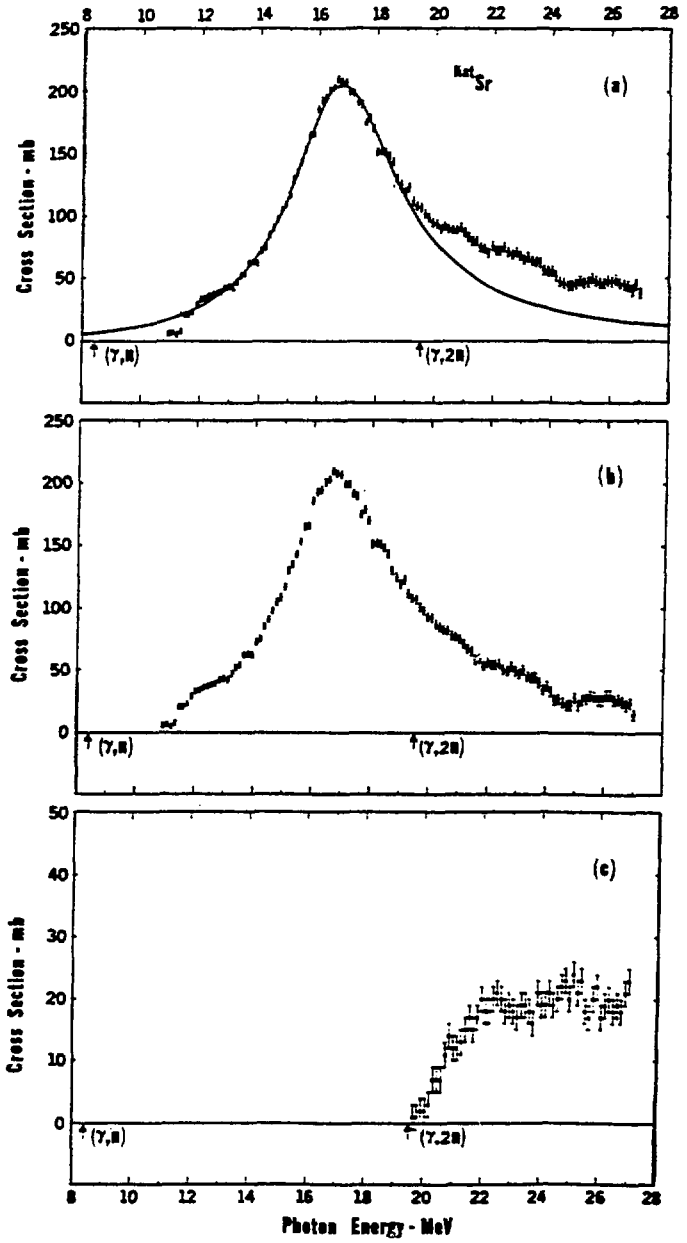

Fig. 1 Photoneutron cross-sections for ^{nat}Sr (reproduced from Ref. 19). (a) Total; (b) single; (c) double. The curve in (a) is a single-line Lorentz curve fitted to the cross-section data.

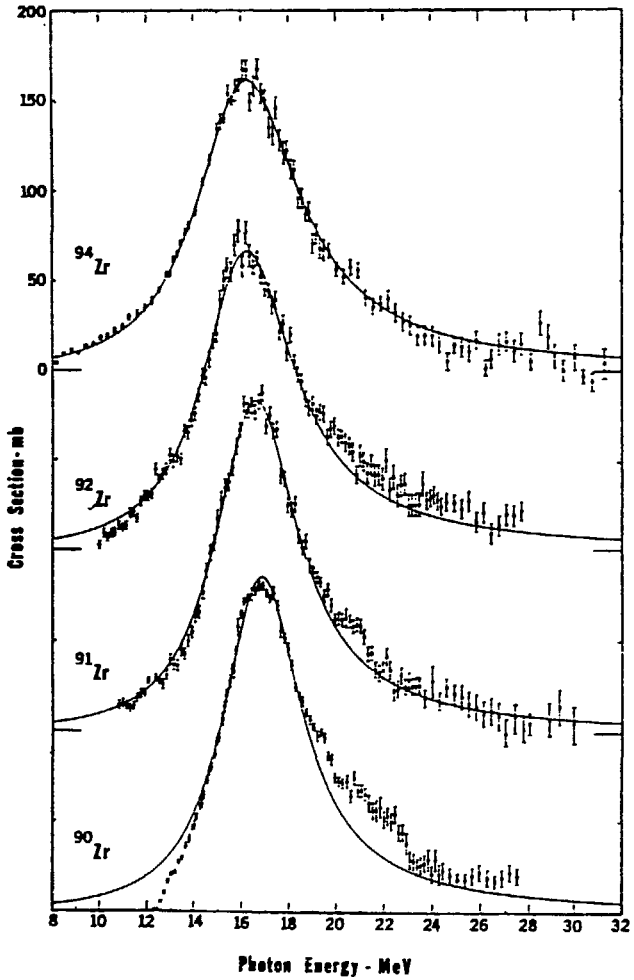

Fig. 2 Total photoneutron cross-sections for the zirconium isotopes (reproduced from Ref. 19)

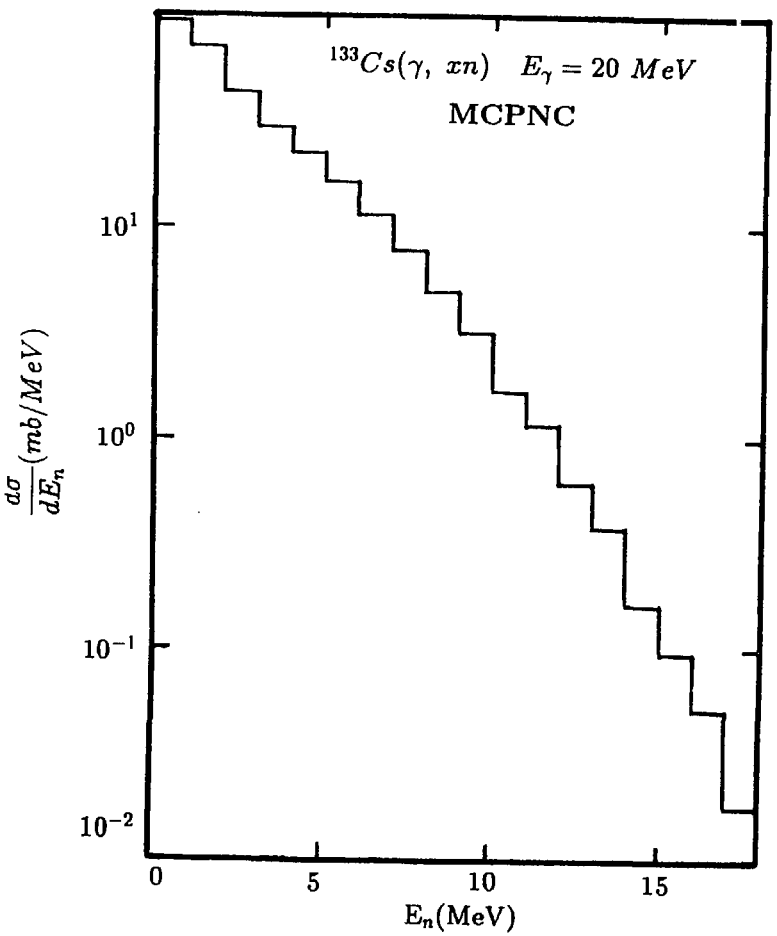

Fig. 3 Calculated neutron energy spectrum for photoneutrons from the ^{133}Cs(γ,xn) reaction at 20 MeV

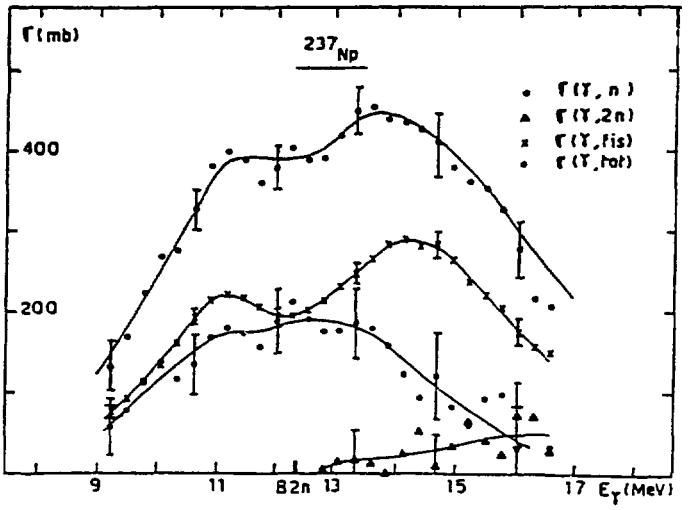

Fig. 4 Partial and total photonuclear cross-sections for ^{237}Np (reproduced from Ref. 20)

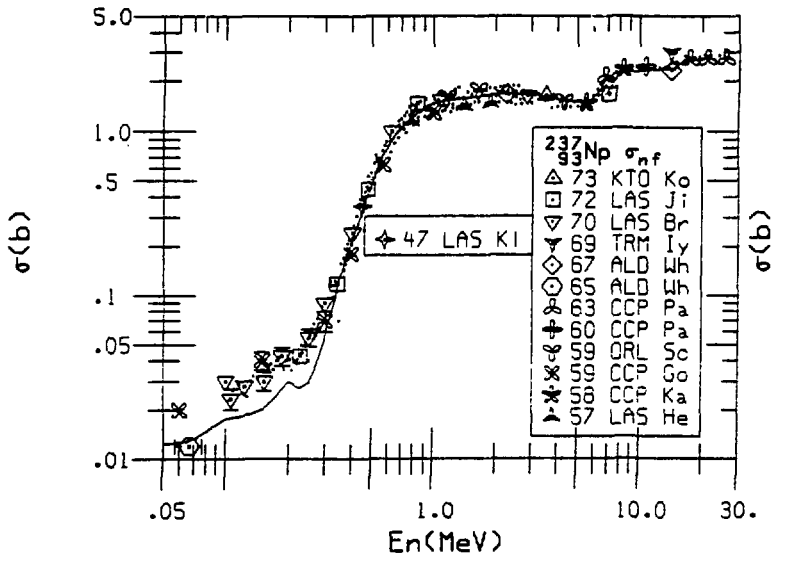

Fig. 5 Evaluated neutron-induced fission cross-section for ^{237}Np (reproduced from Ref. 22)

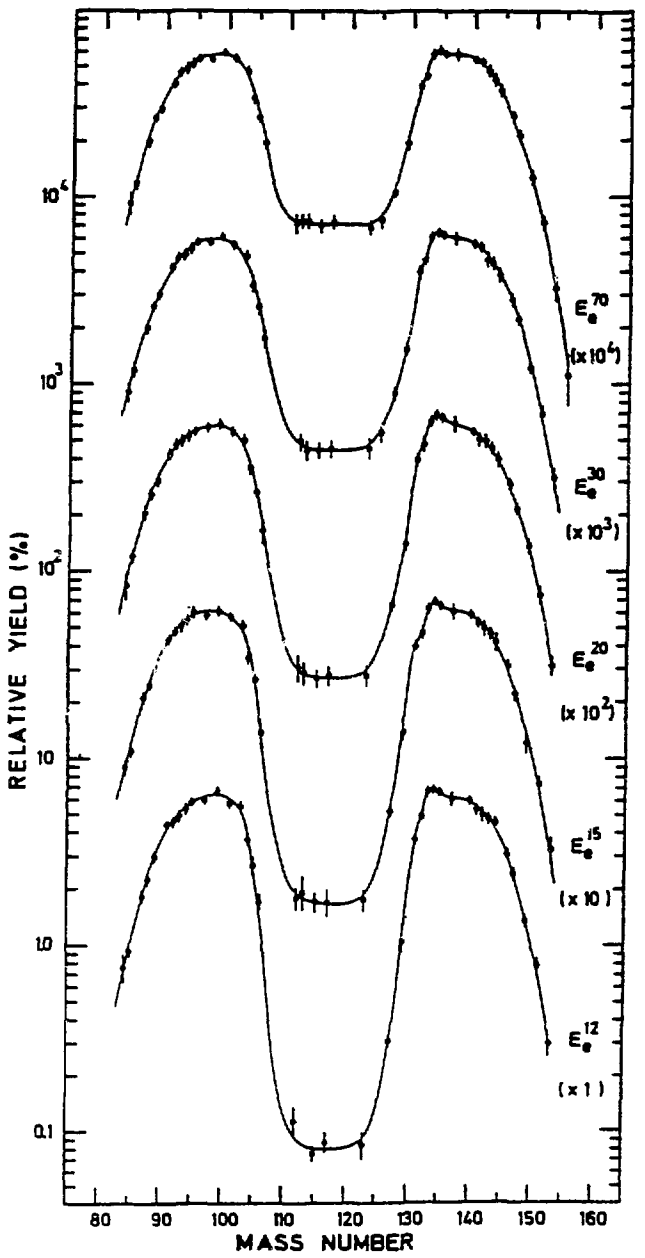

Fig. 6 Relative mass yield distributions for the photofission of ^{238}U (reproduced from Ref. 23)

2.3 Various Nuclear Data

2.3.1 Status of the Demand for Charged Particle Nuclear Data

Hiroyuki MATSUNOBU
Sumitomo Atomic Energy Industries, Ltd.

The Working Group on Charged Particle Nuclear Data was organized this year to prepare the data files on nuclear reactions induced by the charged particles. In advance of start of the activity, it is necessary to know the demand from the users of charged particle nuclear data in the various fields. This information was collected through the lectures in the special meeting of sigma and reactor physics committees and in working group meeting, and private communication. The outline of the status is as follows.

Ⅰ. Accelerator Shielding

The demand for charged particle nuclear data is most urgent in this field. Especially, the activation cross sections are most important, because the kind of nuclear reactions increases rapidly with increase of the incident particle energy. In addition, the importance of the decay data and total neutron yields in thick targets are also emphasized.

1. Incident particles : p, d, α, He, C, Ne, Ar, Kr, Xe
2. Targets: H, Li, C, N, O, Na, Mg, Al, Si, P, S, K, Ca, Ti, Fe, Cu, Ga, In, Au

   General target materials : Ta, W, Pt, Au, Hg, Pb
3. Important reactions : (p,n), (d,n), (α,n), (n,γ), (γ,n)
4. Nuclear data :

   activation cross sections, thick target neutron yields decay data (half-life time, branching ratio of decay mode, abundance)

Ⅱ. TRU Incineration with Spallation Reaction

Studies on TRU incineration by high energy accelerator have been carried out by using computation codes based on the Monte Carlo method (NMTC, HETC). Accordingly, the nuclear data of charged particles are not directly required. However, the experimental and evaluated data on double differential cross sections, production cross sections, neutron yields and so on are necessary in order to compare with the calculations.

Ⅲ. Fusion Plasma Applications

The charged particle nuclear data are important to four aspects of fusion studies : Plasma energetics, beam stopping in inertial confinement targets, first wall erosion, and radiation interactions in blanket materials.

Required Data

1. Fusion cross sections

   reactivities(Maxwellian) $\langle\sigma v\rangle_m$, beam-target(Maxwellian) $\langle\sigma v\rangle_b$, specialized reactivities $\langle\sigma v\rangle_j$

2. High-energy scattering

   Coulombic σ_{el}, nuclear elastic σ_{el}, nuclear inelastic σ_{in}

3. Charge-exchange σ_{cx}

4. Ionization σ_i

   Incident particles : p, d, t, ^{3}He

   Target nuclides : D, T, ^{3}He, ^{6}Li, ^{7}Li, ^{7}Be, ^{8}Be, ^{10}B, ^{11}B

   Energy range : < 20 MeV

Ⅳ. Medical Use

1. Radioactive isotopes for medical use and nuclear data required to their production

   54 nuclides (^{3}H, ^{7}Be, ～ ^{65}Zn), maximum : ～ 150 nuclides

   decay data, reaction data, range energy relationships

2. Charged particle data required to high energy accelerator for medical use

   i) Subjet materials

   air, soil, water, plastic, oil, paint, duralmine, steel, stainless steel, cable, heavy shielding materials, concrete, wood

   ii) Elements included in the above materials

   H, C, N, O, Na, Al, Si, P, Cl, Ar, K, Cr, Fe, Ni, Cu, Zn, Pb

   iii) Incident particles and energy

   p, α, C, N, O, Ne, Ar : ～ 800 MeV/amu

   iv) Necessary data

   activation cross section, neutron production cross section, neutron spectrum, fragmentation particle spectrum, total cross section

Ⅴ. Nuclear Fuel Cycle

The neutron yields and neutron energy spectra from the (α,n) reaction in thick targets are urgently required in the field of nuclear fuel cycle. The targets are TRU and their daughter nuclides produced via α- and β-decay. These data are essential in the design analyses of radiation shielding and criticality safety relating to the storage, transportation, and reprocessing of the spent fuel and high level waste.

α-emitter : 80 nuclides (^{210}Pb ～ ^{248}Cm)

n-emitter : ～40 elements and several compounds (UO_2, UC,...)

energy of α-particle : 3.7 ～ 11.2 MeV

2.3.2 Compilation of Charged Particle Nuclear Reaction Database and Database Conversion for International Coordination

Masaki CHIBA
Hokkaido University Computing Center
Kita-11 Nishi-5, Kita-ku, 060
Sapporo JAPAN

Abstract:

Practice for the past more than fifteen years of NRDF activity in compilation and international exchange of charged particle nuclear reaction data and their current status is reported. The way of the practice comprises major two parts: the one is to have its own data compiling format and data storage and retrieval system named NRDF for the need of regional users; the other is to have database translator from NRDF into EXFOR for the international data exchange. The attainment of NRDF is discussed against the conditions issued for a database used from outside.

1. Introduction

It is essential for constructing a database of charged particle nuclear reaction data (CPND) to get cooperation and support from researchers in the field of this country. We could see many cases that a database would become effective when a certain amount or more data had been accumulated. Data compilation of a database is also an elaborate and manpower consumming task. Especially in a scientific database, it requires some general and specific knowledge in the field. It is also necessary to fully utilize the advanced environment of computer facilities of this country. For these reasons, a new data compiling format and its data storage and retrieval system called NRDF(Nuclear Reaction Data File) is originally devised for CPND[1].

The other hand, if we wish a certain database to cover a given field in the world-wide extent, it is desirable for all the countries having activities in the field to share some efforts of compiling the data, at least produced from their own countries, and to exchange the data among these countries. In such a case, the participating countries must obey the agreed common data compiling scheme. Actually, there is an international data exchange format for nuclear reaction data called EXFOR[2]. NRDF data has a different scheme from EXFOR. Therefore NRDF as it is cannot have compatibility with EXFOR.

We must override these conflictions between the common format (i.e. EXFOR) and the way of having their own one (i.e. NRDF). The way we have adopted for the international coordination is to translate the data in NRDF into those of EXFOR[3].

We have been continuing the research and development of CPND database compiling with the original NRDF system for the past fifteen years[5, 6]. And also by having developed the database translator from NRDF to EXFOR, we have been participating internationally in the field. Followings will be reported of these practices. Finally the attainment of

NRDF will be summarized with respect to the conditions issued for a database used from outside[7].

2. Outline of NRDF

A research project of data compilation of charged particle nuclear reactions began in 1974 with approval of the experimental and the theoretical nuclear research communities in Japan. This research project was conducted by Professor H. Tanaka of Hokkaido University. The members of the project comprised several researchers in the fields of experimental and theoretical nuclear physics, and of information science. The project has bred a data storage and retrieval system called NRDF for charged particle nuclear reaction data. This system has several distinctive features such as free format description, set-structures of information blocks and data lunguage, and so on[1].

Data compilation with NRDF has been continued for the past 10 years. At the end of March 1989, total amount of compiled data is about 46 MB record, and 691 entries are stored on the NRDF system and they are available for retrieval.

This research project had been supported temporarily until 1986 with various research grants of the Ministry of Education, Research and Culture. The project was approved as a standing work in 1987. From this year, it has been given regular financial support. The project is now in more stable state in respect to data compiling activity.

3. Translation of NRDF into EXFOR

NRDF was originally designed mainly to satisfy regional needs and interests of nuclear physics research communities in this country. It has its own data compiling format and structure in order to include newly coming data types and to

have sufficient information to understand the data compiled. Therefore NRDF as it is could neither circulate itself nor contribute in compiling nuclear reaction data internationally. Nevertheless it may be clear that NRDF should share some responsibility in world-wide data compiling of CPND. The way we adopted to meet these demands is to translate the data of NRDF format into those of EXFOR format. We have developed a database translator called NTX, which is made up from "NRDF To EXFOR".

The first version of NTX was completed in 1982 and TRANS E001 was submitted. In 1983, TRANS E002 was submitted and the author visited IAEA and discussed about the result of the translation. It was found that the NTX should be revised to eliminate the defficiency.

The second version of NTX was completed in 1988. The main points of improvement are to utilize DBMS in storing and in retrieving NRDF data and dictionaries, and to incorporate some EXFOR programs delivered from NDS of IAEA to handle the translated EXFOR entries.

TRANS E003 and E004 were submitted in 1988. Entries in E004 are all revised ones of E003. E004 is the first TRANS accepted into EXFOR Master File. In 1989, TRANS E005 and TRANS E006 were submitted and the author attended the 10th IAEA Consultants' Meeting of the Nuclear Reaction Data Centers held at IAEA headquarters in Vienna.

NRDF is located at one of the centers and groupes which have been represented at meetings and have expressed interest in cooperation, and is now entered as SG(Study Group) in the EXFOR Systems Manual[6]. SG might be changed by a name more appropriate reflecting the current NRDF status in the EXFOR system.

4. Computer facility and NRDF distribution

The data storage and retrieval system of NRDF and the NTX database translation system are installed on the HITAC

M682 Computer system of Hokkaido University Computing Center. The M682 system is also connected to the National Science Information Network, so every researchers in the universities or colleges of the country can reach to NRDF through the Network.

The retrieval system of NRDF is also installed on the Center for Information Processing Education, Hokkaido University, the Institute for Nuclear Study, Tokyo University and the Research Center for Nuclear Physics, Osaka University.

5. Current NRDF organization and policy

5.1 Organization

With the change of the project status in 1987 as a turning point, the organization of NRDF project has been renewed. Current NRDF project comprises two committees and working staff.

(1) Advisory Committee

Various problems concerning the project such as policy of data compiling are inquired to the Advisory Committee for deliberation. This committee comprises 11 members of 10 different institutes. These members are assigned to the researchers of related fields of various institutes in order to get nation-wide cooperation and supports.

The committee members are as follows.

Yasuhisa ABE (Research Institute for Fundamental Physics, Kyoto Univ.)
Hidetugu IKEGAMI (Research Center for Nuclear Physics, Osaka Univ.)
Hajime OHNUMA (Tokyo Institute of Technology)
Hikonojo ORIHARA (Cyclotron and Radioisotope Center,

Tohoku Univ.)
Mitsuji KAWAI (Kyushu Univ.)
Teijiro SAITO (Tohoku Univ.)
Fumihiko SAKATA (Institute for Nuclear Study, Tokyo Univ.)
Naomoto SHIKAZONO (Japan Atomic Energy Research Institute)
Kozi NAKAI (National Institute for High Energy Physics)
Akira HASHIZUME (Institute of Physical and Chemical Research)
Hiroshi YOSHIDA(Tokyo Institute of Technology)

(2) NRDF Executive Committee

The Executive Committee is responsible for the project. This committee compr. 8 members of 3 different institutes.

Hajime TANAKA (Representative of NRDF, Sapporo-Gakuin Univ.)
Yoshinori AKAISHI(Executive Chairman, Hokkaido Univ.)
Shigeto OKABE (Hokkaido Univ.)
Toshiyuki KATAYAMA (Hokusei Univ.)
Kiyoshi KATO (Hokkaido Univ.)
Masaki CHIBA (Hokkaido Univ.)
Hiroyasu NAGATA (Hokkaido Univ.)
Hiroshi NOTO (Hokusei Univ.)

(3) Working staff

For data compilation, computer input and system maintenance, the project now has a staff of 4 part-timers.

Data compilation
Yoichi TEZUKA (Institute for Nuclear Study, Tokyo Univ.)
Tamaki NOJIRI (Research Center for Nuclear Physics, Osaka Univ.)

Computer input

Hitomi YOSHIDA

NRDF system maintenance
Toru HARADA (Hokkaido Univ.)

5.2 Policy for NRDF activity

The data compiled for the past years were proton incident nuclear reaction data in Nuclear Data Sheets from Vol. 29(1979) to Vol. 45(1985) and a part of charged particle nuclear data produced in Japan. In the new stage of our activity, we have reconfirmed the following policy.

(1) The amount of data to be compiled per year will be about 3.5 MB.
(2) The scope of data to be compiled is to be proton incident nuclear reaction data and charged particle nuclear reaction data produced in Japan.
(3) Distribution of NRDF data is supposed to be delivered through the National Center for Science Information System in the future. And also NRDF data with retrieval system is to be delivered and updated to the Institute for Nuclear Study, Tokyo University and the Research Center for Nuclear Physics, Osaka University.
(4) The charged particle data produced in Japan are to be translated into EXFOR.
(5) The NRDF activities are to be reported with "NRDF Annual Report".

The NRDF project is now running under this policy.

6. Summary

NRDF is a database being compiled by the NRDF groupe; that is produced in the country not imported. There are

four conditions raised in (7) for a database to be used from outside users, relating discussion of establishing the Database Center in JAERI.

We will conclude giving some summaries of our attainment against to these four items.

(1) Data completeness

If a certain research field is given, it may be seldom the research activities will be found at only one country of the world, especially in natural science. There would be many activities over many countries. Supposed to make a database covering over the given field completely, it seemes that international cooperation is essential. it is necessary for a certain country to share some responsibility in compiling the data, at least produced in the country. The data completeness might be achieved by exchanging the data compiled in such a way. This is the reason why we have been constructing NRDF of our own effort and translating the data in it into EXFOR.

(2) High-grade and user-friendly DBMS

The data storage and retrieval system of NRDF we are now using was wholly developed utilizing VSAM facility. At that time when the system was developed, there were not any ready-made commercial DBMS's available for numerical databases. The NRDF system was developed with its own original idea. It has newly devised storage structure for the numerical tables(1). However the data retrieval feature is such one that a document retrieval system has. Namely as a document retrieval system selects fewer documents for specified selection criteria step by step, The NRDF system can do also for the numerical tables.

Nowadays total amount of data accumulated in NRDF would have reached upto 50MB, some more facilities, for example, by which we can see the whole database with several aspects

are eagerly hoped to be installed. To realize these facilities that the current NRDF system does not have, it might be the best way to select a commercial DBMS of relational type and to develop revised NRDF system as an application of DBMS.

(3) User manual provision

User manual "GUIDE to NUCLEAR REACTION DATA FILE(NRDF)" has already been prepared in both Japanese and English(8). They are stored in the computer file, so they can also be seen from computer terminals or put into print.

(4) Announcement of development status to users

As stated in the policy of NRDF, "NRDF ANNUAL REPORT" has been published every year since 1987, and distributed to the persons or the institutes of related fields and the authorities concerned.

Acknowledgement

Author owes to Professor H. Tanaka and other NRDF members of their everlasting efforts in developing the NRDF system. He is especially thankful to Professor Y. Akaishi and Dr. K. Kato for their helps and disscussions in preparing this material.

References

(1) Togashi, M. and Tanaka, H. : An information management system for charged particle nuclear reaction data. journal of information science principles & practice, Vol. 4, No. 5, (1982), pp. 213-224.

(2) Calamand, A. and Lemmel, H. D. : Short guide to EXFOR, IAEA-NDS-1, (1974).

(3) Chiba, M., Katayama, T. and Tanaka, H. : A database translator of nuclear reaction data for international data exchange, journal of information science principles & practice, Vol. 12, No. 4, (1986), pp. 153-165.

(4) NRDF annual report 87(in Japanese), (1988-3).

(5) NRDF annual report 88(in Japanese), (1989-3).

(6) McLane, V. (ed): EXFOR Systems Manual, (1989-9).

(7) Kikuchi, Y. : Current Status of Database Development in JAERI, PROCEEDINGS OF THE 1989 SEMINAR ON NUCLEAR DATA, March 1989, JAERI-M 89-026.

(8) GUIDE to NUCLEAR REACTION DATA FILE(NRDF), Hokkaido University Computing Center, (1983-3).

2.4 Topics (II)

2.4.1 Development Plan in JAERI for High Intensity Proton Linear Accelerator

M. Mizumoto, M. Sugimoto, Y. Okumura, H. Shirakata
T. Nishida, H. Takada, I. Kanno, H. Yasuda, Y. Nakahara,
T. Takizuka and Y. Kaneko

Japan Atomic Energy Research Institute
Tokai-mura, Naka-gun, Ibaraki-ken

A high intensity proton linear accelerator has been recently holding an considerable attention for the future developments in nuclear technology. A proposal to incinerate radio active nuclear wastes (in particular, transuranium TRU nuclides) has been made by using spallation reaction with high energy proton beam. This spallation reaction will also produce intense secondary neutron, muon and pion beams. Various applied researches including nuclear data measurements will be carried out using these secondary beams. An accelerator, which the Japan Atomic Energy Research Institute (JAERI) has been proposing to construct as a long term research project, will be described in this report

1. Introduction

Studies of basic technologies for the transmutation of nuclear wastes and nuclide partitioning have been continued for last several years, although the geological disposal techniques are widely supported in the community. The Japanese Atomic Energy Commission has concluded in June 1987 that R&D efforts for these technologies should be substantially strengthened as the national research project, where the possible use of valuable resources in the wastes and improvements of safety assurance in management processes have to be evaluated. This national program called OMEGA (Option Making Extra Gains from Actinides and Fission Products) has started aiming at promoting research and development of the new technologies on nuclear waste partitioning and transmutation. As a part of the program, JAERI has set out several R&D plans for advanced partitioning technology, actinide burner fast reactor and spallation based

actinide transmutation.

In this proposal, nuclear spallation reaction with high energy (say above 1 GeV) proton beam is considered as one of the effective transmutation processes. The need for the development of high energy intensive proton linear accelerator (linac) is stressed for that purpose.

Such a high intensity proton linac is also expected to contribute to the developments in other various nuclear research fields. Nuclear spallation reaction with high energy proton beam will produce intense neutrons, which can be used for production of nuclear fuels in addition to the nuclear waste incineration. Applied researches such as nuclear data measurements, material sciences, radio isotope productions and muon catalyzed fusion will be carried out using these neutron, muon and pion beams.

2. A study of transmutation system

The basic concept of the incineration system with the proton spallation reaction has been studied in JAERI for last several years[1,2]. The main goal of the system is to process the TRU of which yearly production rate is about 30 kg typical for a 1000 MWe LWR. The detailed description about transmutation target, neutronics calculation and power dissipation calculation is given in the separate paper in this meeting[3]. Only essential part of the scheme will be briefly described in this paper.

Figure 1 shows a model of an accelerator driven target system in combination with a subcritical reactor. The proton energy is initially taken to be 1.5 GeV which was estimated most efficient from the preliminary calculations. The target and fuel assembly in the reactor are proposed similar to that used for common fast breeder reactor as shown in Fig. 2. Two kinds of coolant materials, Na and Pb-Bi are used for calculations. Harder neutron spectrum is preferable to make the transmutation effective, because the fission reaction rate become higher than the capture rate as the neutron energy increases.

Primary nuclear spallation reaction and following particle transport process were simulated by NMTC/JAERI code[4] in the neutron energy above the initially defined cutoff energy of 15 MeV. Below this energy, three dimensional Monte Carlo transport code was used. The keff value was taken

in the range of 0.9 to 0.95 for the calculation.

Two-dimensional power distribution calculations were made for Na and Pb-Bi cooled targets. The maximum achievable thermal powers were limited by the allowable temperature which was set 900°C in the fuel and cladding. The calculated maximum thermal output powers were 769 MW and 236 MW for the Na and the Pb-Bi cooling, respectively. Accordingly the averaged power densities were 472 W/cc and 145 W/cc with the required incident proton beam current of 20 mA and 7.8 mA for those targets. The power output for Na was found to be considerably higher than that of Pb-Bi due to the effective cooling capability.

From these calculations, the spallation neutron and the following induced fission neutrons can transmute TRU produced by nearly ten LWR in a subcritical assembly cooled by Na. As a by-product, this system can produce excess electric power of about 200-300 MW, a part of which can be used to operate the proton accelerator.

3. Framework of the accelerator development

The conceptual design of the engineering test accelerator with the beam energy of 1.5 GeV and the current of 10 mA proposed by JAERI is shown in Fig. 3. It is considered to require an marked technological developments. This engineering test accelerator will become a large scale accelerator compared to the presently operated proton accelerators which have been used mainly for basic nuclear physics experiments. In particular, the average proton beam current of 10 mA is nearly 10 - 50 times larger than that for existing accelerators. The comparison of the beam current of the operating and proposed proton accelerators is shown in Fig. 4. In order to obtain such high current beam, only linac can meet the requirement. Other circular accelerators such as cyclotron and synchrotron can accelerate a small amount of beam with a maximum current of about 1 mA. The beam spill can not be controlled efficiently in the case of circular accelerators, which will cause serious problems of high level activities in accelerator structures.

3.1 Conceptual design study of the accelerator system.

As the first step of the development, the low energy part of the accelerator structure in Fig. 3 will be studied, because the beam quality is mainly determined at the low energy part. They will consist of the following components; ion source, radio frequency quadruple (RFQ) and drift tube linac (DTL). High energy part of the accelerator (high β structure) will be partly considered in advanced of the 2nd step development. The various tests of the characteristics of the accelerator structures have to be carried out so that the experiences about the design and operation of the accelerator can be accumulated. The beam energy may be chosen below 10 MeV because in this energy region the proton induced reaction can be substantially avoided in the accelerator structural materials due to the Coulomb barrier.

3.2 Ion source

Duoplasmatrons and duoPIGatron[5] have been used in proton linac as an intense ion source. Multi-cusp type ion source has been recently developed for neutral beam injectors (NBI) as fusion reactor heating device. Development of new type of intense ion source will be still needed for high intensity operation. In the case of the accelerator, beam qualities such as emittance and beam size may be more severe than other ion sources in order to meet the requirement from the acceptance of following accelerator structures.

3.3 RFQ

Among the recent improvements of new accelerator structures for low velocity ion beams, the RFQ is the most significant development. It was first proposed by Kapchinskii and Teplyakov[6] and has been intensively developed at Los Alamos National Laboratory[7]. A continuous mode (CW) prototype version of the RFQ with 80 MHz was operated with 2 MeV and 50 mA as the initial accelerator structure for the FMIT[8]. As the low energy continuous operation, the RFQ1 has been recently tested at Chalk River with the 50 mA and 650 keV[5].

The RFQ is the only choice of the accelerator structure which can accelerate the average 10 mA proton beam up to 2 MeV with a good quality

of beam being accepted by next DTL structure. The selection of the RF frequency for the RFQ is very important because it will determine the various accelerator parameters such as the size of the structure, the beam quality and the required electric power. The frequency range between 100 and 300 MHz would be chosen with the injection voltage of 50 keV and the output energy of 2 MeV.

3.4 DTL

High electric field and high frequency for DTL tend to be chosen recently, because the higher effective shunt impedance and efficient longitudinal focusing result in short accelerator length. Our accelerator, however, needs the extremely small beam spill for the high energy part. The relatively lower frequency may be necessary in order to have large beam radius, probably say at least 200 - 400 MHz.

At the initial part of the DTL with the beam energy of 2 MeV, electromagnetic quadruples have to be used for the beam focusing. Permanent magnets now started to be used for the DTL structure to relax the heat removal problem. They are already in use for some of the DTL for low current operation, but their application to high current accelerators will have to be more carefully studied.

The heat deposition due to RF loss in the drift tube is expected to reach total heat release of several hundreds of kW. This heat loss will induce a large resonance frequency drift unless a suitable cooling is applied. The heat removal would be the main source of technical difficulty for the DTL development as well as for RFQ.

3.5 High β linac

The detailed development works of high β linac will be started after the first step accelerator development will be completed, because their R&D is still presently in progress. For example, there may be several possible candidates for the structures in either single cavity or coupled cavity structure. In particular, as to the coupled cavity structures, many candidates are now being investigated in various laboratories; side coupled structure (SCS), alternating periodic structure (APS), disk and

washer structure (DAW) and annular coupled structure (ACS). The choice will be dependent on many aspects such as the space of the accelerator building, the capacity of power supplies and availability of RF sources.

4. The time schedule of the developments

The research plan for developing the proton linac is now proposed by JAERI with the following time-schedule shown in Fig. 5.

In the 1st development step till 1995, the basic technologies will be investigated to develop the proton accelerator. The research building will be built at the Tokai Establishment of JAERI. The feasibility study of the accelerator plant will be carried out in this period. The various activities in the accelerator research field will be organized to provide technologies and staffs which are required to built such intensive accelerator. A low energy linac with a current of 10 mA and an energy of 10 MeV will be constructed and operated for those purposes.

In the 2nd step from 1996 to 2000, a proton accelerator for the research purposes (engineering test accelerator) with a 10 mA current and 1.5 GeV energy will be designed and constructed. The various engineering tests of incineration process including medium and large scale integral test, mock-up test and prototype experiments will be made with this accelerator. Some other accelerator applications such as nuclear data measurements, material researches, radio-isotope production, meson physics and radiation therapy will be carried out.

Finally as the 3rd step, a commercial incineration plant with an intensive proton linac will be constructed after the 2nd step research will be completed.

5. Summary

The survey activities and preparatory design studies will be continued through 1989 and 1990. The studies for optimization of accelerator system and conceptual design of accelerator structures will be started in 1990 followed by various R&D activities. The works for the design of a research building and utilities for the accelerator are planned in 1991.

References

(1) T. Nishida et al., "Research of TRU Transmutation System with Proton Accelerator" NEA/CRP 1989.

(2) T. Takizuka et al., "A Study of Incineration Target System", Proc. 5th Int. Conf. Emerging Nuclear Energy Systems, Karlsruhe, 1989

(3) T. Nishida et al., "TRU Transmutation with High Energy Proton Beam" presented in this 1989 Nuclear Data Seminar 1989.

(4) Y. Nakahara et al., "NMTC/JAERI A Simulation Code System for High Energy Nuclear Reactions and Nucleon -Meson Transport Processes", JAERI-M 82-198 (1982)

(5) R.M. Hutcheon and G.E. McMichael, "Low Power RF Tuning of The RFQ1 Accelerator", the 1984 Linear Accelerator Conference, Darmstadt, FRG, 1984

(6) I.M. Kapchinskii and V.A. Teplyakov, "Linear Ion Accelerator with Spatially Homogenous Strong Focusing", Prib. Tekh. Eksp. 119 No.2 (1970) 19

(7) J.E. Stovall, K.R. Crandall and R.W. Hamm, "Performance Characteristics of a 425 MHz RFQ Linac", 6th Conf. on Application of Accelerators in Research and Industry, Denton, Texas, November, IEEE NS-28 (1981) 1508

(8) D.D. Armstrong, "Status Report on FMIT", the 1984 Linear Accelerator Conference, Darmstadt, FRG, 1984

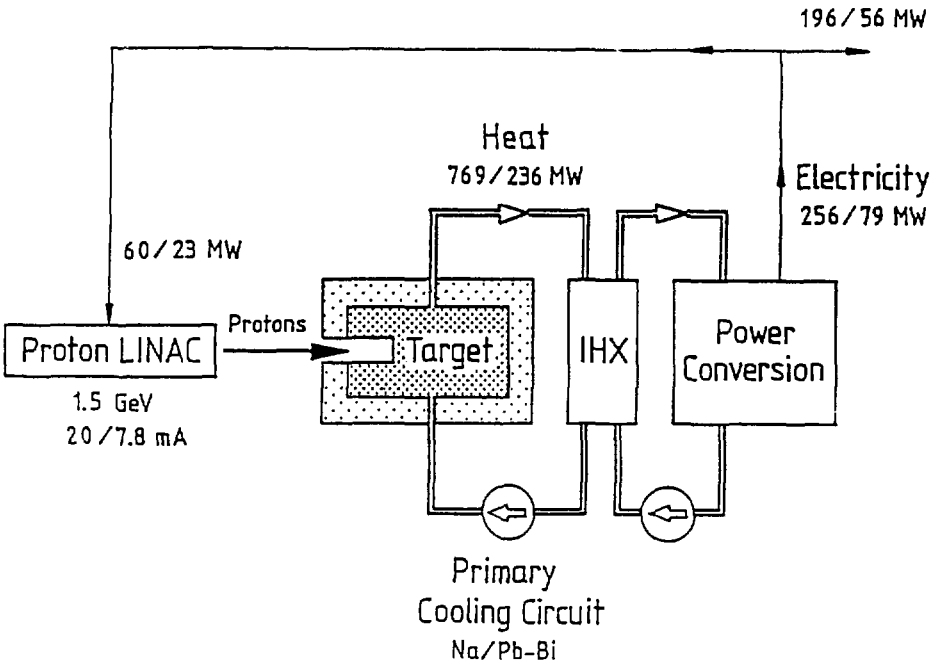

Fig. 1 Accelerator driven incineration target system

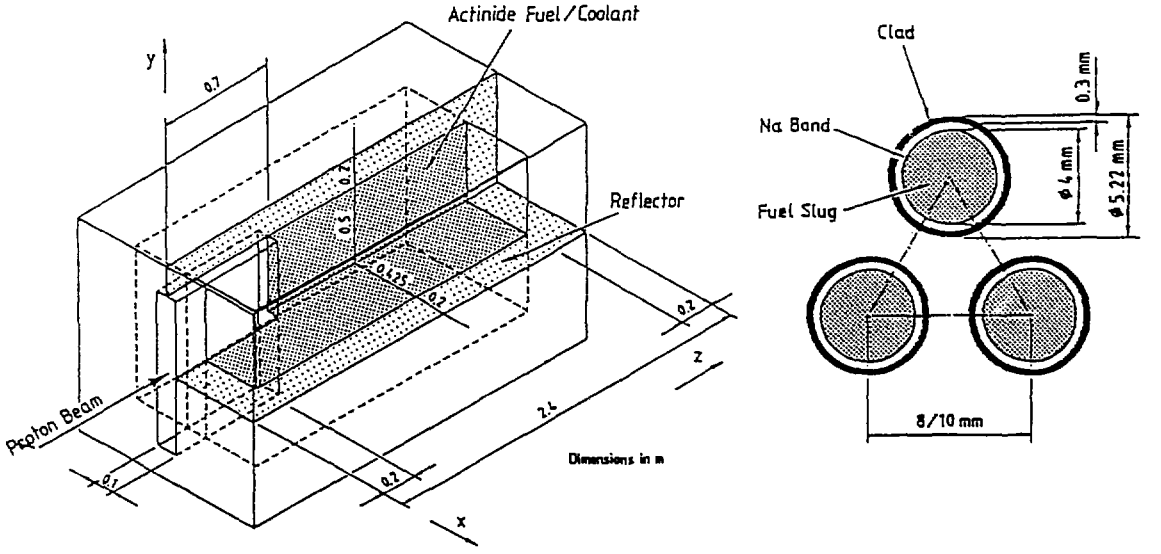

Fig. 2 Incineration target design and proposed fuel pins

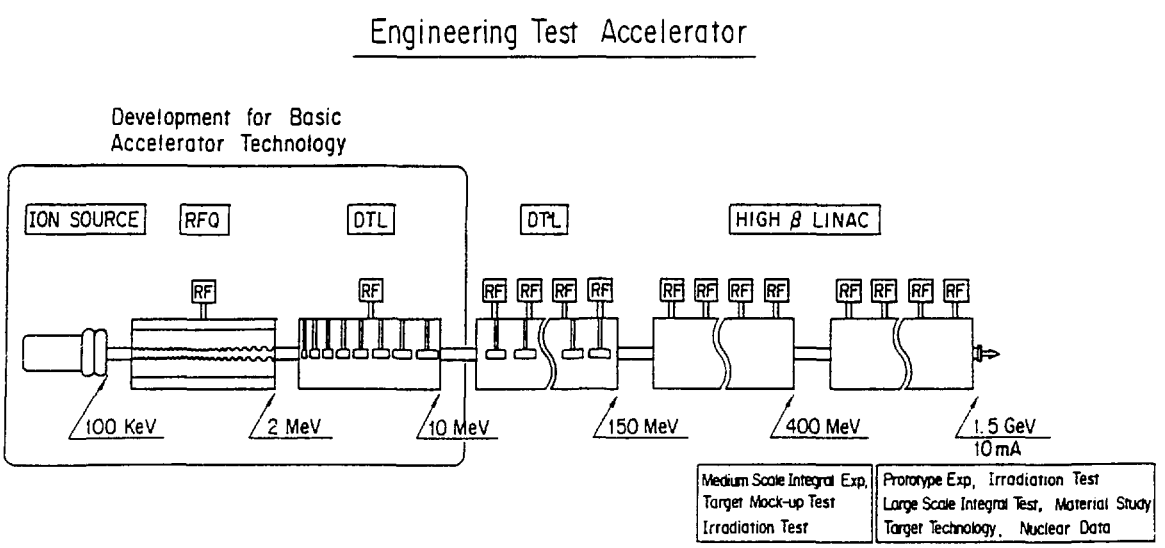

Fig. 3 Conceptual design of the JAERI Engineering Test Accelerator (ETA)

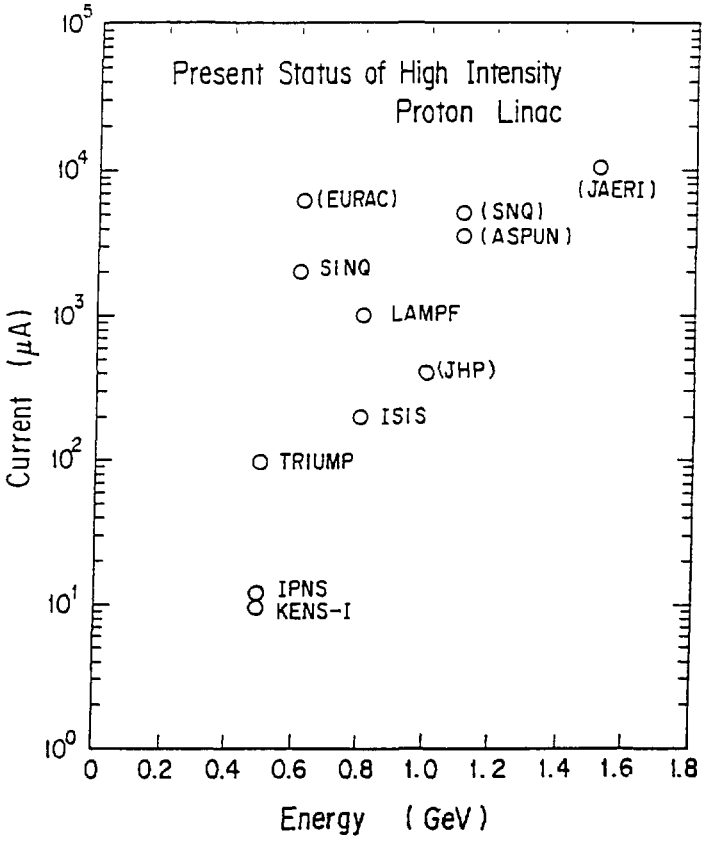

Fig. 4 Present status of high intensity proton accelerator

Schedule of Basic technology accelerator construction (10MeV、10mA)

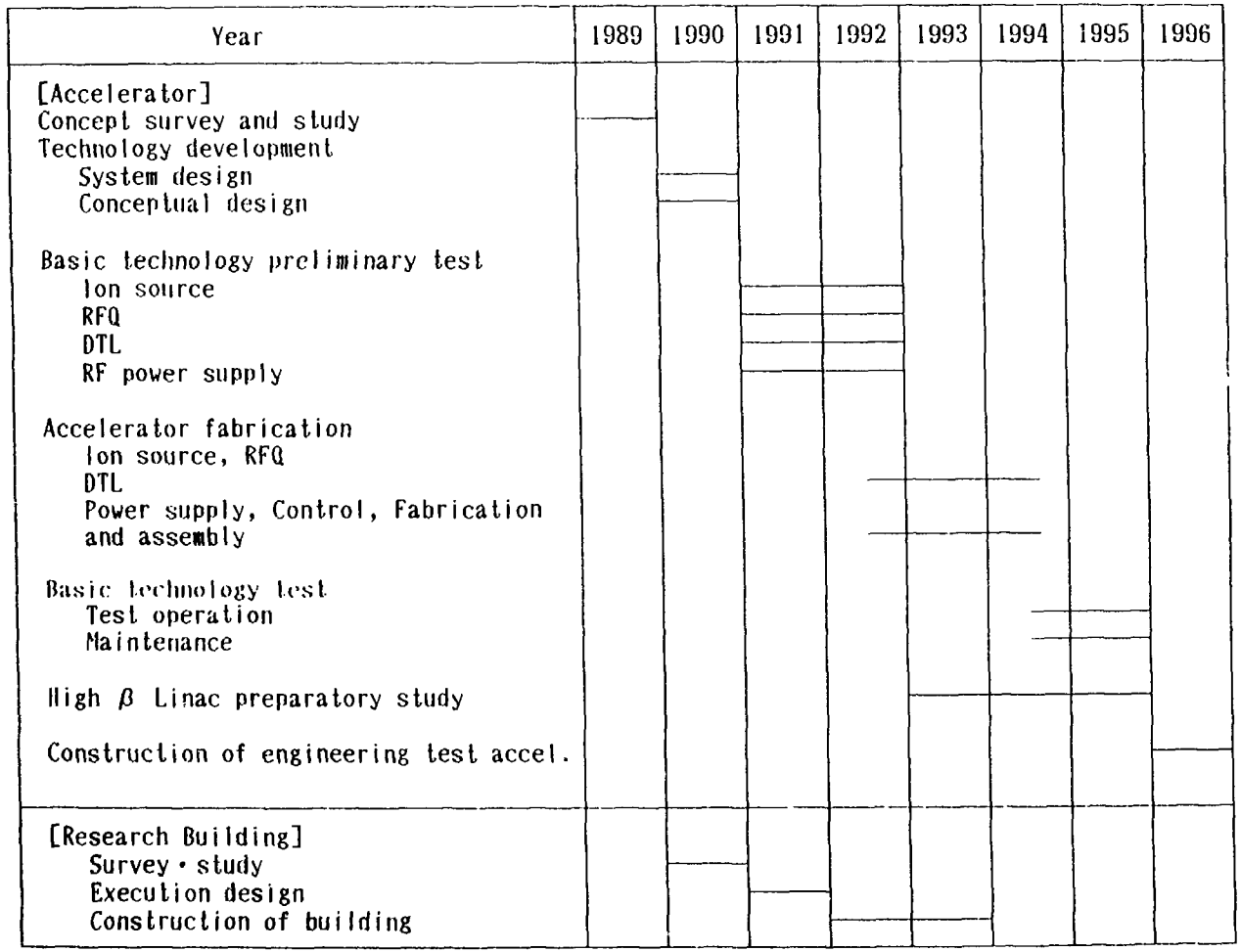

Fig. 5 Tentative schedule for high energy proton accelerator development

3. Papers Presented in Poster Session

3.1 Automation of Neutron Scattering Measurements at JAERI TANDEM

Masayoshi SUGIMOTO

Japan Atomic Eenergy Research Institute
Tokai-mura, Ibaraki-ken 319-11

The automation control system to set up the experimental apparatus and to manage acquisition and processing of the measured data is under development. The heart of this system consists of two personal computers dedicated to the equipment control and the data acquisition, respectively. The design concept is overviewed and the proposed user interface is described. The possibility for other applications is also discussed.

1. Introduction

We have carried out the neutron scattering measurements at JAERI TANDEM using the High Energy Neutron time-of-flight Spectrometer[1] with the data acquisition system used by many users commonly. This data acquisition system has been graded up (now, DEC VAX 11/780 and in near future, DEC VAXstation 3200), but the operator console software is basically same as that developed for the oldest hardware (DEC PDP 11/55) to maintain the compatibility of the user interface. The recent enormous evolution of microchip technology results in the personal systems (personal computers and workstations) with high cost performance, and we can construct the new system which performance is comparable to the super minicomputers in the past (such as DEC VAX 11/750). And moreover, such personal systems have a plenty of development tools, e.g. compilers for various kind of computer languages, database applications, Computer Aided Designing applications and some Artificial Intelligence tools, in a low cost. The essential point is that we can not only employ these applications but also develop them (or even the extension to the operating system) by ourselves. This is possible due to the simplicity of the personal systems hardware and the easiness of its use relative to the bigger sophisticated computer systems. The main drawback may come from the small capacity of the computing resources, such as memory, disk space and I/O

channels. So the up–to–date systems are generally configured as the multi processor or multi computer network systems to overcome this insufficiency.

A new system to control the experimental apparatus and the data taking of the neutron scattering measurements carried out at JAERI TANDEM, is now under development. The system can do the following tasks automatically:

(1) setting of the experimental conditions, such as the angle of the collimator shield, the position of the shadow bar, the sample position, etc.,

(2) setting of the data acquisition configuration, such as the preset counts, on–line data processing parameters, etc., and

(3) monitoring of current status of the experimental conditions, and responding to the malfunctions of the system.

In the following sections, we describe the hardware configuration of the proposed automation system, and the necessary operator console software. And the newly developed spreadsheet program to do many things including the physics calculations and the machine controls is introduced as the desirable user interface of the expected automation system.

2. Hardware configuration

2.1 General

The heart of this system consists of two personal computers, one is used for equipment controls and the other is used for data acquisition and processing, respectively. Fig. 1 illustrates the schematic diagram of the hardware configuration proposed currently. The control computer is NEC PC–9801RA with 16 MHz Intel 80386 cpu and the data acquisition computer is Hewlett–Packard HP Vectra RS/20 with 20 MHz Intel 80386 cpu. These two computers and a stand–alone CAMAC crate system are linked by the GPIB interface, which is used as the communication channel among these subsystems. The CAMAC crate system has, at least, a crate controller with GPIB interface and a 100 MHz scaler module to monitor the counting rates for the beam current, neutron monitor, and the loss events due to the dead time of the electronics system. In the future upgrade, the CAMAC system may become a gate to access the outer world by adding more CAMAC modules. This system has no magnetic tape device which is only the practical media to access the supercomputer at the computing center used for the theoretical calculations. Basically, we can almost do every work in the new system, even the laborious nuclear physics calculations. However, as the pathway to the supercomputers, we can use the existing data analysis computer

(DEC VAX 8550) installed at JAERI TANDEM. The obtained data are transferred through the serial communication line after each run in the experiments is completed. This process may be also used to store a large number of measured or processed data for saving the precious hard disk space and the pile of the floppy diskettes.

The equipment control computer has a bus extension box for controlling the experimental apparatus described in the next subsection. This bus extension box contains many digital I/O boards which communicate with the actual devices. The cables are connected through the junction box of the control panel, which is currently used for manual control. The data acquisition computer has an ADC interface bus box (CANBERRA MPA/PC) which accepts up to 8 ADCs and is configured either for single parameter, dual parameter or list mode. Each computer is equipped with a graphics display terminal, a mouse, and a Floppy Disk Drive. The printer and the plotter are occupied by both computers.

2.2 Equipment control

The items to be controlled during the experiments are (a) the rotating angle of the collimator shield of neutron detectors, (b) the relative position of the shadow bar to the target–sample–collimator geometry, and (c) the position of the scattering samples. Currently, these are controlled manually on the control panel, however, they are already modified to control by using the digital I/O signals. And a computer program to use them has been developed on the existing NEC PC-9801RA.

One possibility to enhance the equipment control is to tie up with the accelerator beam line control/monitor system. The most sensitive monitor for the accelerated ion beam is a neutron spectrum measured by neutron monitors. They have sub–nanosec timing resolutions, so their peak widths of the tof spectra are almost the unique monitor for the bunch width of the beam. And the counting rates of the generated neutron are the true monitor for the intensity of the beam current entered into the target and the effective thickness of the target materials. These quantities can be calculated by the on–line processing program on the data acquisition computer described in the section 2.3. And the results are monitored during the experiments and some warnings are issued when the beam condition is deteriorated. This system is so flexible that we can implement such a task in various ways, i.e. it can be done on either computer and sometimes done by both, cooperatively. The interface to the outer world, the accelerator control system here, can be easily done using another CAMAC module as the gateway.

2.3 Data acquisition control

2.3.1 Backgrounds

The data acquisition computer system is not yet obtained but we expect to start the development on December, 1989. At present we are considering the conversion of the various processing codes developed for the previous data acquisition system (VAX 11/780). Fig. 2 shows the block diagram for the previous data acquisition system, where the DEC PDP 11/55 is removed now and the signals from the MBD–11 is directly connected to DEC VAX 11/780. And within one or a couple of years, it will be replaced by the new DEC VAXstation 3200 system, which may support only the list mode data taking. There was an argument about which is better to employ such new system or develop our own system as the next data acquisition system, in our group. As a conclusion, we need the dedicated acquisitions system because of our special requirement for the multiple mode data acquisition (single parameter, dual parameter and list mode with at least 8 ADCs). Of course, there is another solution to use a hard–wired but somewhat intelligent Multi Channel Analyzer. This possibility is excluded since our demand is the flexible computer–controlled automation system.

2.3.2 Neutron detector system

We are using four large volume neutron detectors[1,2] as the main tof detectors shown in fig. 3. One detector has a dimension, 20cm ϕ x 35cm, and contains about 10 l liquid scintillator (NE213). The glass container is viewed by the two 5 in. ϕ photomultiplier(PM)s (RCA8854) at the front and rear sides with attaching the face plate adapters. The four detectors are stacked in a shield collimator as scattered neutrons enter from the front side of the glass container (from the left hand side to the right hand side in fig. 3). The electronics diagram for this detector is shown in fig. 4. The anode signals from the both PMs are fed into constant fraction discriminator(CFD)s, respectively, and the resulting timing pulses are ANDed with 20 nsec coincidence time. This excludes the PM noise signals and supplies a reference time signal used for the neutron gamma pulse shape discrimination. Each timing signal passes through the 50 nsec gate corresponds to the coincidence event, and is fed to OR logic(FAN IN), which gathers all events from the four detectors and supplies a start signal to the time–to–amplitude converter(TAC). The stop signals for TACs come from the beam pick off. After all, the time signals from the two PMs are converted to two tof linear signals(T_1 and T_2), respectively. These signals are

amplified/attenuated using biased amplifiers(and one output pulse is inverted when neutron energy is not too high: this process depends on α, the time compensation factor described below). The two outputs are summed and forms a time compensated tof linear signal(T_1－αT_2). From the nature of the sum of two linear signals, this method becomes to fail when the counting rate is high. So we need to pay much attention to the counting loss in this electronics. The other four linear signals(T_1, t_1－t_2, PH and PS) are used in the list mode data acquisition and for the software time compensation method, which are described in section 3.3.

2.3.3 Data acquisition and processing

In addition to those signals shown in fig. 4, there are duplicated neutron monitors, each of which consists of a small (5cm ϕ x 1.25cm) liquid scintillator (NE213) as the tof detector. All these output signals must be fed into the data acquisition system. So the capacity to accept up to 8 ADCs is the necessary condition for our acquisition computer system. At least, the resulting spectra are displayed on the graphics display in real time (the main body of such displaying program will be supplied by the maker of the acquisition system with its source code with some restrictions). And we need to add more features to do on－line data processing which will be highly specific to our measurements (e.g. processing the monitor spectra and obtaining the neutron source intensity or beam pulse width in real time, and in the case of list mode, processing the software time compensation as described in the section 3.3).

The usefulness of the computer based data acquisition system is that we can control the acquisition from the other computer system using a communication channel. In our case, the equipment control computer becomes a master and mainly controls the start and stop of the measurements according to the table describing the experimental conditions, and also controls the data acquisition computer, which should be synchronized to the equipment control computer.

3. Operator console software

3.1 Task of the master computer

Since the system has two computers linked with the GPIB interface, one of them must become a master of the GPIB interface. At present, we assign the equipment computer as a master, since its computing load is less than the other's

during the data taking period. The master computer memorizes a experimental table planned each for the scattering measurement. The experimental table defines (1) the setting values of the experimental apparatus, e.g. scattering angle and sample in/out, and (2) the condition of the data acquisition, e.g. preset time/counts and the options for the on-line data processing. The operator console software consists of three major parts:

(A) user interface to assign and change setting parameters in the experimental table, which is described separately in section 4,

(B) control of actual equipment through digital I/O boards and reading back their status values if possible, and

(C) communication with the data acquisition computer and the stand-alone CAMAC system, which monitors the beam current and counting loss informations.

The flow of the automatic acquisition is explained in fig. 5. Firstly, a series of the experimental conditions are prepared using the task A), and secondary, the setting values are sent to the actual devices using the task B) and also to the data acquisition computer and the CAMAC crate controller using the task C). After this initial set up is finished, and when no mistake is found, then console program issues the start command to all slave systems. The data taking will stop if the preset timer/count is satisfied or some alarm monitors interrupt to quit the acquisition. The former is issued by the data acquisition computer which has internal preset timer/counter for this purpose. The latter may come from both of computers depending on the kind of alarms. The stop signal is sent to the all subsystems through GPIB and the completion process starts to check the cause of the stop. If some intolerable malfunctions are found, the automatic control is quitted and the experimenter is called to remedy them. Finally, it checks the rest of the experimental table to be carried out, and if there are more experiments in the table, the next one is done from the beginning of the above steps.

If the cpu power is remaining enough for other works, it can perform some calculations, e.g. reaction kinematics to identify observed levels, Monte Carlo calculation for multiple scattering correction, or Legendre fitting to the obtained angular distribution, which are usually done by off-line processing.

3.2 Tasks of the data acquisition computer

The other computer is dedicated to the data acquisition, but its cpu time is consumed only by displaying the data when the data acquisition mode is in the single or dual parameter mode, because the data acquisition itself is carried out

on the single add-on board only for these modes. If the update rate of the spectrum display is allowed to be slow, lots of cpu time remain to do the on-line data processing at the data acquisition computer, too, such as the background subtraction, peak fitting, and conversion to the cross sections. However, in the case of list mode acquisition, the buffered data must be dumped into the hard disk so frequently to avoid buffer overflow, which becomes the additional load to the data acquisition computer. If that load is too heavy for the personal computer's cpu and the disk memory size, we must proceed to use the common data acquisition system based on the VAXstation 3200, which would have a better performance in that case.

3.3 On-line processing of the software time compensation

3.3.1 Monte Carlo simulation results

As the on-line processing of the list mode data, we can expect to perform the software time compensation [3,4]. Usually, the two timing signals from the same detector are processed as shown in the electronics block diagram in fig. 4, to give the best time resolution for the incident neutrons. This method works well for the narrow energy range of neutrons because the time compensation factor, α, in the formula $T_1-\alpha T_2$ depends on the incident neutron energy [5]. To distinct with the software time compensation, we call the usual time compensation method as the hardware time compensation. We performed the extensive Monte Carlo calculations to certifying the expected time resolution of our detector. The nominal processes taking into account are :

a) the production of the scintillations in the scintillator due to the specific energy loss at each small volume in the detector,

b) the propagation of the light through the scintillator medium including the attenuation, the reflection and the refraction at boundaries, and also the production of the photoelectrons at the photocathode,

c) the electrons multiplication in the PM and

d) the CR integrated anode pulse to be fed into the constant fraction discriminator(CFD).

All these processes are incorporated into one simulation program. Fig. 6 depicts the typical result of such a simulation. The scintillation photons are generated according to the theoretical model and decaying parameter obtained for NE213 liquid scintillator. The resulting time distribution is given in fig. 6 (a) with arbitrary vertical unit and horizontal unit in nsec. Due to the difference of the

distance to two PMs, PM1 and PM2, from the source point S, the time distributions of the photoelectrons at these PMs are so different as shown in fig. 6(b). That difference is preserved in the processes of the electron multiplication (fig. 6(c)) and CR integration (fig. 6(d)). Finally, the obtained output pulse is fed into the CFD and the timing signal is produced. The timing walk arises from the minor difference of the pulse shapes of the photoelectrons given in fig. 6(b) and their statistical fluctuations [4]. So it strongly depends on the efficiency of the light collection of produced scintillation by the PMs. The calculated light collection efficiency is given in fig. 7. The figure shows only the half plane of the detector cross section due to its symmetrical property. It can be seen that the large part of the detector has around 12–15 % efficiency but very high efficiency is expected to the events near the PM face. Fig. 8 shows the results about the timing resolution property. The figures in the upper half plane indicate the calculated standard deviations observed at the left side PM. It assumes that only 500 scintillation photons are produced at each source point. The time resolution deteriorates near the glass boundary of the detector volume. From these calculations, we can expect the sub–nanosec resolution to our detector at best. The lower half plane of the fig. 8 shows the relative delay time produced at the output of CFD. In the ideal case, the resulting lines corresponding to the same delay times should be parallel to the PM face and equally spaced. The calculated result shows fairly good property compared with such criterion. So our neutron detector would be used as the tof detectors for high energy neutrons.

3.3.2 Implementation of the software time compensation

From the above discussion, the detector has a good property enough to make a measurement for the monoenergetic neutrons by using the hardware time compensation method. However, there is a demand to measure the wide energy range of neutrons at once with the same detector set up. For this purpose, we must change the time compensation factor according to the incoming neutron energy. It is impossible to achieve by using the electronics modules, so we developed the new method to gain the best time resolution over all neutron energy [3,4]. In the on–line processing of such method, the four parameters are needed to get the resulting tof spectrum: (1) tof signal of the PM at the far side from the scattering sample, T_1, (2) time difference of two timing signals from two PMs, t_1–t_2, (3) pulse height to give the released energy, PH, and (4) pulse shape information to discriminate the gamma–ray events, PS. The schematic

process is described in fig. 9 and an example of such a process performed by the off-line processing is shown in fig. 10. Fig. 11 shows the results of the software time compensation lines(actually curves) for a detector. They are obtained from the measurements of the monoenergetic neutrons with the various energies from 4.9 to 13 MeV. These lines are the guidelines to do the software time compensation in the on-line processing. First, the list events are checked by the gates, which may be applied for each parameter independently or for the mapped data of two of four list parameters, as shown in fig. 9 (solid thick frames in the upper two maps). The gated events are supplied to the "software time compensator", which calculates the corrected T_1 values from the events T_1 and t_1-t_2 parameters according to the method described above and in the figure captions.

This process needs a lot of preparatory works before the actual measurements, i.e. the preparation of the software time compensation lines supplied to the software time compensator. It is desirable to produce such guide lines automatically, by taking the source neutron spectra at selected angles, and it may be done on the data acquisition computer, too.

4. Spreadsheet style user interface

As the user interface of the proposed automation system, we present the newly developed spreadsheet style program, called **LSSolver ver.2** [6]. The spreadsheet itself is a table and each cell defined by its column and row position may contain the value or text strings, so it can be used as the experimental table directly. As a possible implementation of the experimental table in the spreadsheet, one row defines the one measurement and each column in that row specifies a parameter value of the experimental conditions. Fig. 12 is a layout of such a example. The rows 1 through 3 are text strings to represent the titles of the items. Below the row 4, each row represent one measurement. The column A indicates the setting value to the rotating angle of the collimator shield in degrees. The actual setting value may have the different unit and be biased, so the reading values in the column B may be different from its setting value. The control of the shield collimator is done at column C, which has a macro strings to do a series of operations for the spreadsheet automatically. In this example, the cell C4 is a macro that means (1) go to the cell A4, G(A4), (2) save it as file "angle", US(angle), (3) execute a program "SET_IT.EXE" with an option

"/A", UE(SET_IT.EXE /A), (4) go to the cell B4, G(B4), and finally, (5) load the reading value returned in the file "angle", UL(angle). The program "SET_IT.EXE" is developed outside of the LSSolver. So it works without LSSolver program and can be modified independently. The option "/A" tells the program to set up the angle of the shield collimator, and the setting value is saved as the file "angle". The value to be sent to the device is converted from the setting value given in degrees, and the program controls the equipment and reads back its status value, which is returned to the file "angle". This method can be applied any other parameter settings of the equipment and the conditions of the data acquisitions. The row 5 has not been executed yet, so that the cell B5 is empty. If the cell C5 is executed, the new status value of the angle of the shield collimator is appeared at the cell B5.

The truly useful feature of LSSolver is the capability to calculate a vector or matrix using the various kinds of internal functions, and display the results on graphics screen instantly. By using this feature, we can fit the observed angular distributions with Legendre polynomials on the fly. Any other data analyses can be done with a minimal programming (i.e. defining some formula to manipulate the vector/matrix in the cells). And it can calculate some physics calculations also(e.g. reaction kinematics). Unfortunately, it has no nonlinear least squares fitting procedure, however, we can call such a program inside from the LSSolver using the similar method as described above, and compare the results graphically.

The LSSolver is originally developed for the nuclear data evaluation with the data and parameter covariance, especially for the small data set. So it includes the feature about least squares fitting with the covariances and most suitable to the data processing and analysis of the nuclear data measurements as we would like to use for the neutron scattering measurements. We are now seeking for its applications, and it is already used in the other field [6].

5. Summary

The automation system to control the expeirmental apparatus and the data acquisition for the neutron measurements at JAERI TANDEM is truly necessary one due to the insufficient manpower of the neutron group. We expect this system advances the efficient data taking and guarantees the good quality of the results. After the some further developments discussed above, this system will start to work in early 1990.

References

1) M.Sugimoto and Y.Yamanouti, "JAERI Tandem Neutron TOF Spectrometer" (in Japanese), Proc. of the 1983 Seminar on Nuclear Data, JAERI–M 84–010 (1984), p.312.

2) M.Sugimoto, Y.Yamanouti, S.Tanaka,Y.Furuta,M.Mizumoto and M.Hyakutake, "Fast Nuetron t–o–f Spectrometer for the scattering measurements", JAERI TANDEM Annual Report 1983, JAERI–M 84–129 (1984), p.89.

3) M.Sugimoto, Y.Yamanouti, Y.Furuta, M.Mizumoto, S.Nishihara and M.Hyakutake, "MEASUREMENTS OF FAST NEUTRON SACTTERING CROSS SECTIONS OF ALUMINUM", JAERI TANDEM, LINAC & V.D.G. Annual Report 1984, JAERI–M 85–104 (1985), p.185.

4) M.Sugimoto and Y.Yamanouti, "EFFECTS OF THE TIMING WALK ON THE TIME RESOLUTION OF THE LARGE VOLUME NEUTRON DETECTOR", JAERI TANDEM, LINAC & V.D.G. Annual Report 1985, JAERI–M 86–112 (1986), p.181.

5) J.D.Carlson, R.W. Finlay and D.E. Bainum, Nucl. Instr. and Methods 147 (1977) 353.

6) M.Sugimoto, "Data Oriented Programming using LSSolver", JAERI TANDEM, LINAC & V.D.G. Annual Report 1988, JAERI–M 89–119 (1989), p.60.

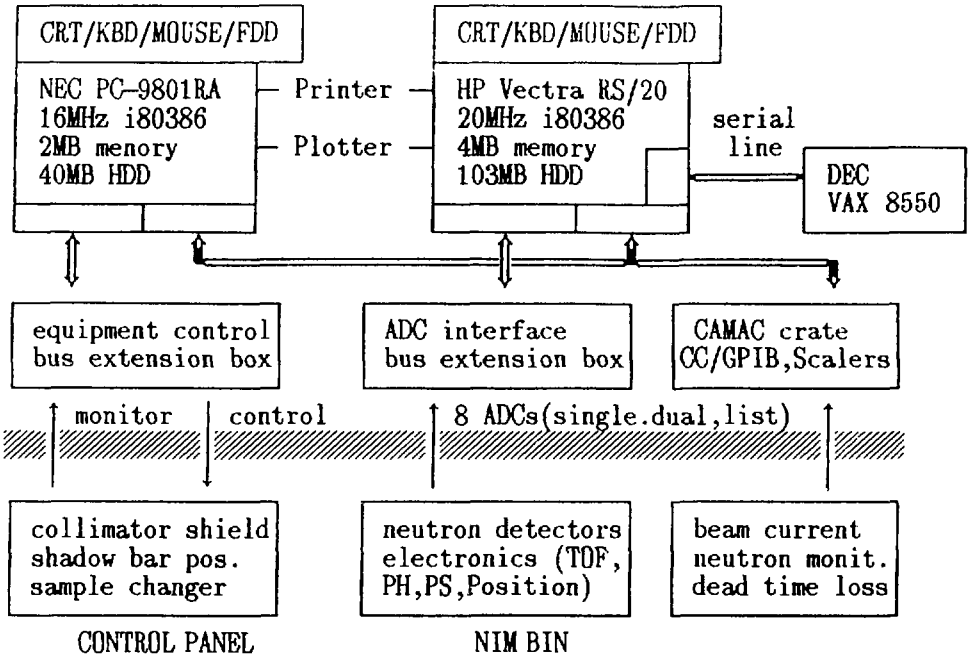

Fig. 1 Schematic diagram of hardware configuration of the automation system for the neutron scattering measurements

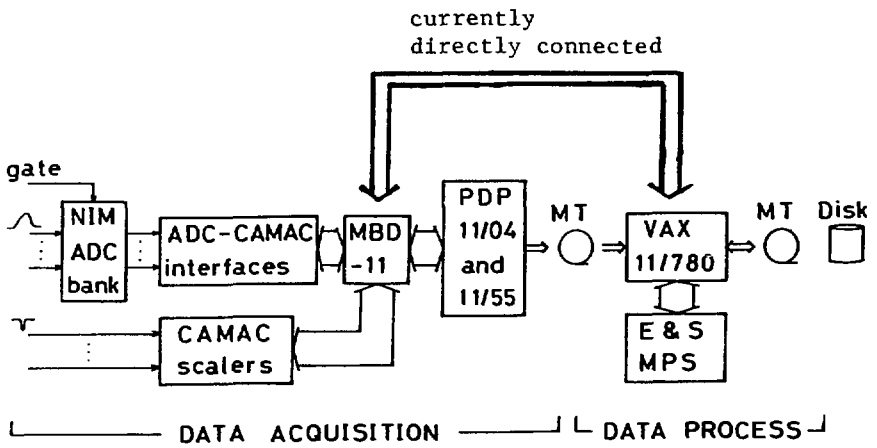

Fig. 2 Block diagram of the data acquisition system currently used at JAERI TANDEM

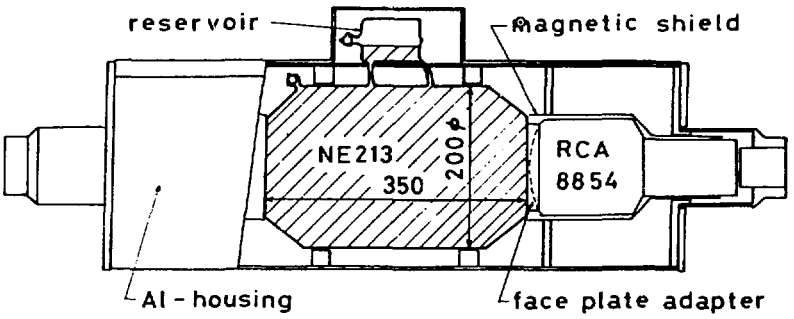

Fig. 3 Schematic view of the large volume neutron detector used as the time-of-flight spectrometer

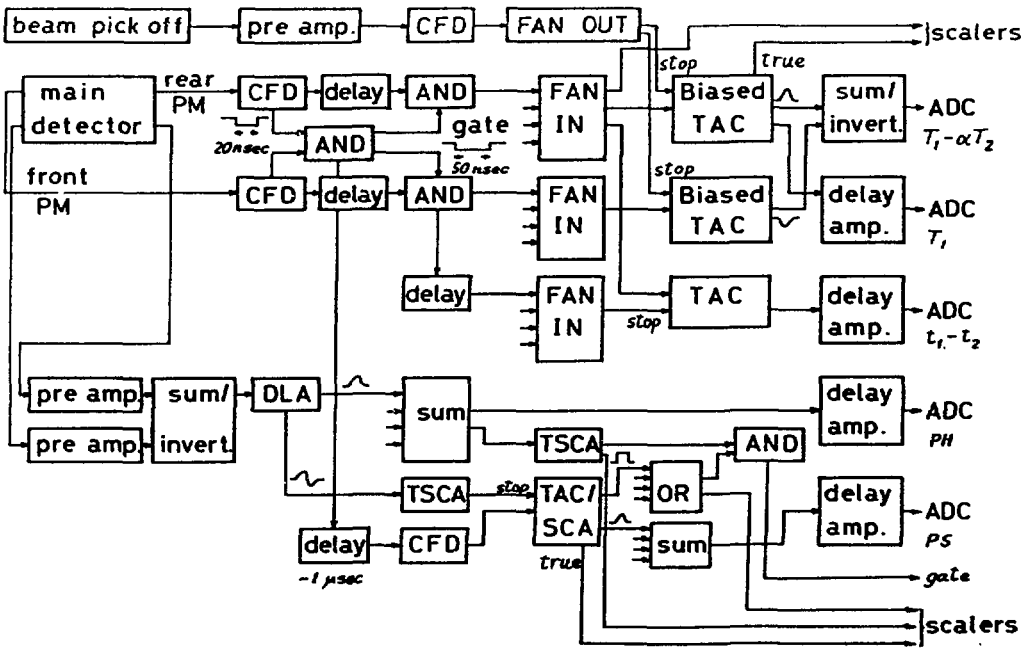

Fig. 4 Block diagram of the electronics for the neutron tof spectrometer at JAERI TANDEM

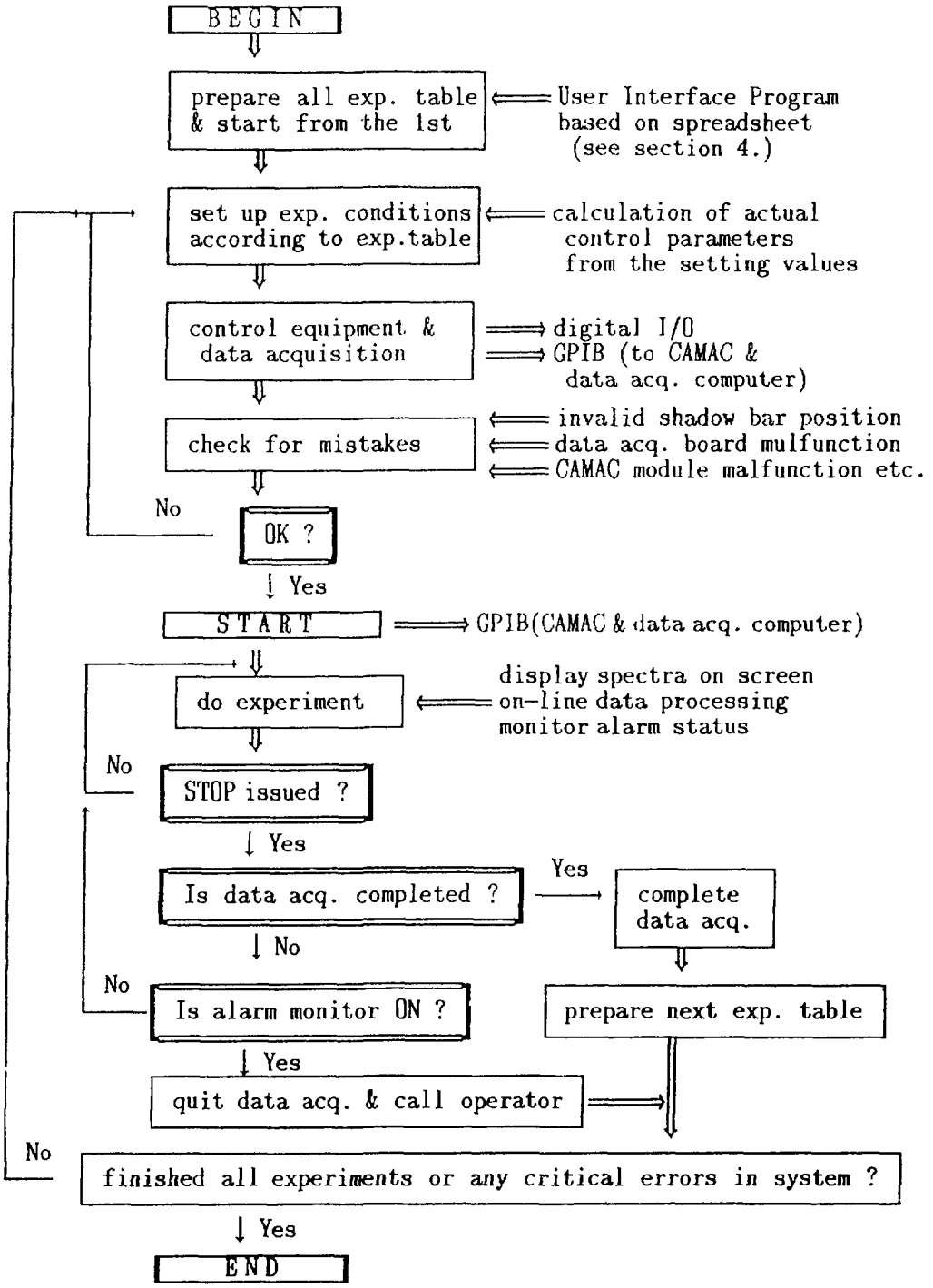

Fig. 5 Flow diagram of the automatic measurement of neutron scattering

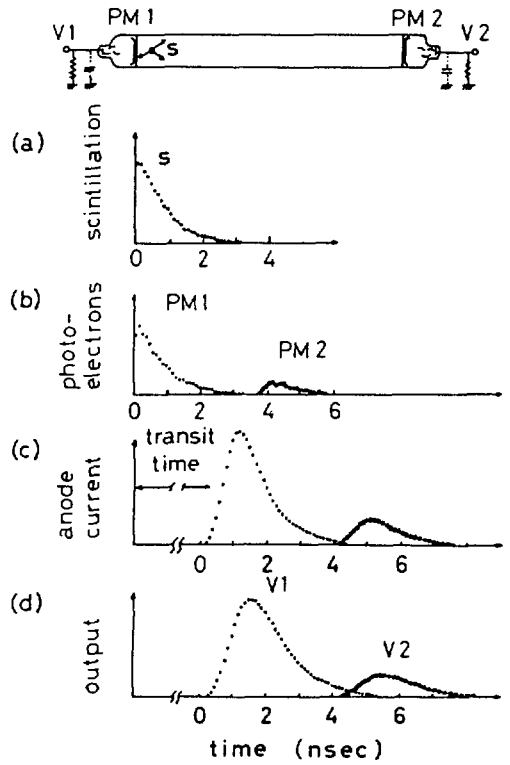

Fig. 6 Typical time distributions of photons or electron currents simulated by Monte Carlo method for the large volume neutron detector. The point "S" indicates the source point of the scintillations. PM1 and PM2 are two photomultipliers viewing the detector, and V1 and V2 are the voltage pulses output from PM1 and PM2, respectively. The (a) shows the time distribution produced at the source point "S", (b) is photoelectrons time distribution produced at each photomultiplier, (c) is the anode current pulse after electrons multiplication and (d) shows the final output, V1 and V2.

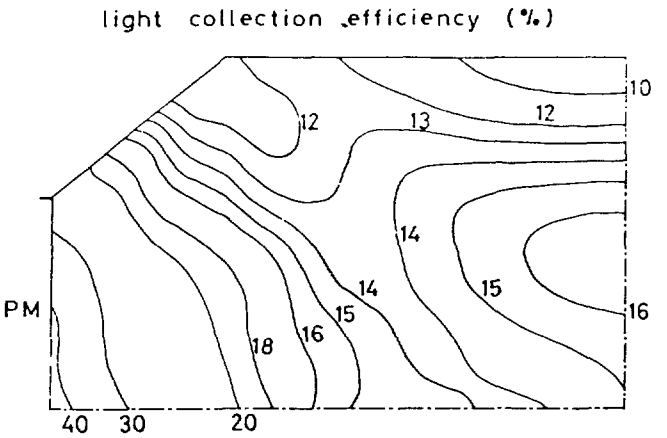

Fig. 7 The calculated light collection efficiency of a quadrant of the neutron detector. The indicated figures are sum of the contributions from the two photomultiplier (PM)s.

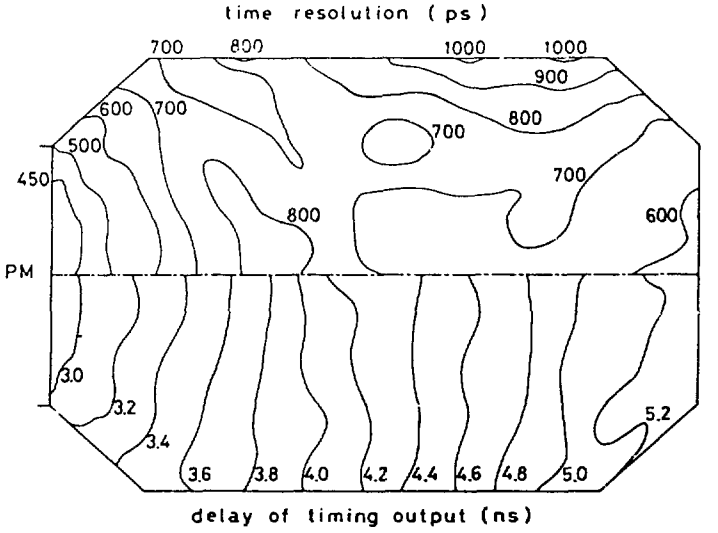

Fig. 8 The calculated timing resolution due to the statistical fluctuation of the photoelectrons time distributions given at the left hand side photomultiplier. The figures in the upper half give the standard deviations obtained from a bunch of calculations assumed that only 500 scintillation photons are generated at the source point. And the figures in the lower half show the resulting delay times produced at constant fraction discriminator, which give the information about the time compensation factor α in the time compensation formula $T_1 - \alpha T_2$. If these lines are parallel to each other and equally spaced, the time compensation using the time compensation formula becomes complete one.

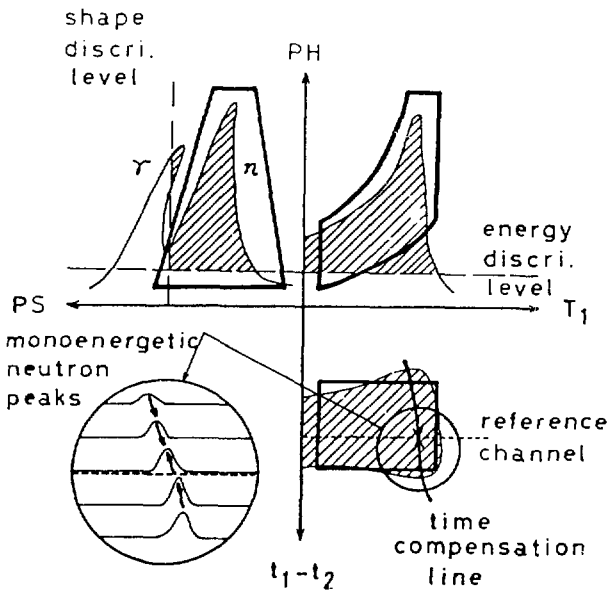

Fig. 9 Schematic view of the on-line processing of the software time compensation using four list mode parameters: (1) tof signal, T_1, from the photomultiplier at the far side from the scattering sample, (2) time difference, t_1-t_2, between the timing signals from two photomultipliers, respectively, for the same detector, (3) pulse height, PH, which represents the energy release in the detector, and (4) pulse shape information, PS, to discriminate the gamma events. The upper two figures define the desired neutron events to give the best result compromising of the resolution and efficiency. The bottom right figure shows the line (labelled by time compensation line), where all the neutrons events with the same energy are placed. The enlarged view of a part of the map is shown at the left side. The dashed line corresponds to the reference channel, where all other events with the same energy should be gathered using the compensation line (the up and down arrows inside the view area mean that the events in these peaks are given by the single energy neutrons and each T_1 (horizontal axis) spectrum is shifted to match its peak position to the reference's.

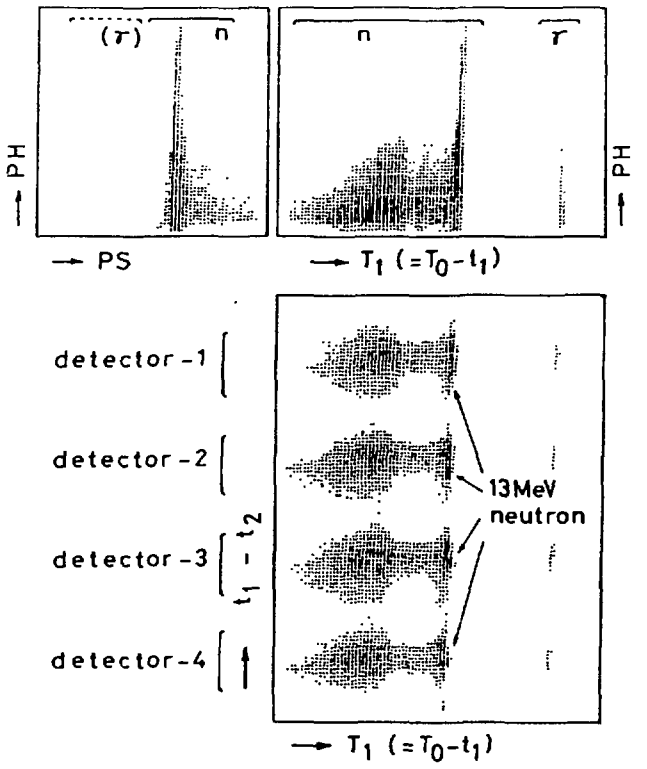

Fig. 10 An example of the event maps for the D(d,n) neutron source measured at En=13 MeV, obtained by using the off-line processing. The map for PS vs. PH (top left) shows the neutron-gamma discrimination works well in this case. The top right map, T_1 vs. PH, indicates the tof spectrum without any time compensation, which time resolution is out of use. The bottom right map, T_1 vs. t_1-t_2, shows the data which can produce a time compensation line at 13 MeV for each detector. The actually obtained line is shown in Fig. 11.

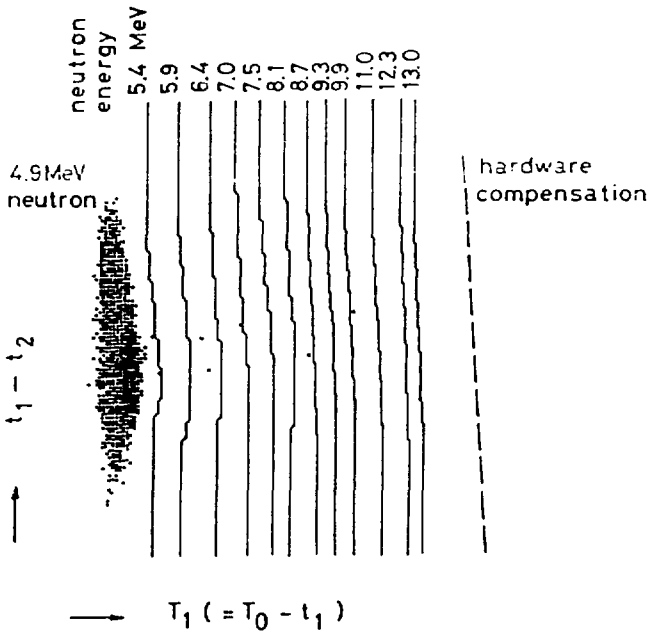

Fig. 11 The time compensation lines for a neutron detector obtained from the T_1 vs. t_1-t_2 maps for the monoenergetic neutrons with various energies from 5.4 to 13 MeV. The map shown at the right hand side is the data for 4.9 MeV neutrons. As the reference, the line corresponds to the "$T_1 - \alpha T_2$" compensation method is labelled by "hardware compensation".

row /column	A	B	C
1	scattering angle		
2	setting	reading	
3			
4	50	105.88	[:G(A4)US(angle)UE(SET_IT.EXE /A)G(B4)UL(angle)]
5	70		[:G(A5)US(angle)UE(SET_IT.EXE /A)G(B5)UL(angle)]
6			

Fig. 12 A layout of the spreadsheet for controlling the equipment and data acquisition. The A4 and A5 cells are the setting values of the scattering angles, and B4 and B5 are their read backed values, respectively. Now the experiment defined in row 4 has already done and experiment in row 5 is about to be carried out.

3.2 Nuclear Data of Charged-Particle Induced Reactions on Light Nuclei

N. Koori+ , Y. Watanabe, M. Eriguchi, M. Hyakutake* , Y. Wakuta, and I. Kumabe
Department of Nuclear Engineering, Kyushu University, Fukuoka, 812

Abstract: Theoretical interpretation of the ^{6,7}Li(p,p') scattering data, especially their analyzing powers, are described. Cross sections and analyzing powers of proton scattering are compared with those of neutron scattering. Furthermore, new data are given for the ^{6}Li(p,2p)nα and ^{12}C(p,p')3α reactions, which are mirror ones of ^{6}Li(n,2n)pα and ^{12}C(n,n')3α reactions, respectively.

Introduction

Our program of measurement and analyses of charged-particle induced reactions is based on accuracy of measured data on charged-particle reactions in comparison with neutron-induced reactions. In order to extract accurately interesting quantities from neutron data, we should assume reliable theoretical backgrounds for the extraction. Since nuclear reactions, however, are complex, further precise studies will be necessary to obtain solid theoretical backgrounds for interpretation of reaction mechanisms.

In this report, we describe advances in our measurement and theoretical interpretation of charged-particle induced reactions on light nuclei.

1. Analysis of ^{6,7}Li(p,p') scattering.

We have reported measurement of the polarized proton scattering on the ^{6,7}Li around 14 MeV[1]. In the analysis of the data on the basis of the spherical optical model (SOM) and coupled channel (CC) method, it has been clarified that the analysis cannot reproduce the inelastic scattering data, especially their analyzing powers, in spite of the fact that both differential cross sections and analyzing powers of the elastic scattering were fitted very well. Since the excited states of ^{6}Li (2.185 MeV, 3$^+$) and ^{7}Li (4.63 MeV, 7/2$^-$) can decay into the channels d+α and t+α, respectively, the optical potential for these exit channels should be different from those of the entrance channels. Changing mainly the parameters of the spin-orbit term, we tried to search the potential for the exit channel. Then, appreciable improvement in the fit was obtained for the analyzing powers, as shown for ^{6}Li and ^{7}Li in Fig.1 and 2. The derived exit channel optical potential parameters are summarized in Table 1 and 2.

+ Present address: College of General Education, The University of Tokushima, Tokushima.
* Present address: Sasebo Technical College, Sasebo.

2. Comparison of proton scattering with neutron scattering.

It is meaningful to compare the proton scattering with neutron scattering on the lithium isotopes. We calculated the differential cross sections and analyzing powers of the neutron scattering at 14 MeV, using the optical potentials obtained from the analysis of proton scattering. The calculated results for ^{6}Li+n and ^{7}Li+n scattering are compared with the experimental data in Fig. 3. The differential cross sections of the elastic scattering of ^{6}Li are reproduced well but those of the inelastic scattering are different in the angular distribution at forward and backward angles. On the other hand, the differential cross sections of the elastic scattering on ^{7}Li, which include those of the inelastic scattering leading to the 1st excited state, are also reproduced well, if the Coulomb barrier of about 2 MeV is taken into account. The neutron inelastic scattering indicates similar difference at forward and backward angles as the proton inelastic scattering. The analyzing powers for the ^{6}Li+n elastic scattering measured at TUNL[2] are reproduced very well by the calculation based on the present optical potential. As a result, the study on the proton scattering is valuable for modelling of nuclear reactions inclusive of neutron scattering, because much precise analyses are possible for proton scattering.

3. Measurement of ^{6}Li(p,2p)nα reaction at 14 MeV.

In the measured energy spectra of the ^{6}Li(p,p') scattering, it is seen the contribution from the ^{6}Li(p,2p)nα four-body breakup reaction is important in the low energy region. Since the reaction is the mirror reaction of the ^{6}Li(n,2n)pα reaction, detailed study of the ^{6}Li(p,2p)nα reaction may provide valuable information for understanding of its reaction mechanism. We have measured 2-proton correlation spectra of the reaction at 14 MeV, by means of the Tandem van de Graaff accelerator in Kyushu University. Some of the measured spectra are shown in Fig.4. Theoretical analysis is in progress.

4. Measurement of ^{12}C(p,p')3α reaction at 16 MeV.

The importance of ^{12}C(n,n')3α reaction is known for radiation damage effects in biology and material science[3]. In order to estimate accurate Kerma factor for the reaction, it is needed the modelling of the four-body breakup reaction. Instead of measuring the ^{12}C(n,n')3α reaction, we have precisely measured the ^{12}C(p,p')3α reaction at 16 MeV. Double differential proton emission cross sections measured at 20°, 60° and 120° are shown in Fig.5. Continuum region was observed in proton energies less than those corresponding to the 3^{-} peak. This region is affected by a contribution of proton emissions followed by 3α breakup process. As a preliminary analysis, the following two processes are considered using kinematical phase space distributions.

$^{12}C + p \rightarrow p' + \alpha_1 + {}^{8}Be(\rightarrow \alpha_2 + \alpha_3)$	3 body simultaneous breakup (3BSB) followed by a sequential decay

$^{12}C + p \rightarrow p' + \alpha_1 + \alpha_2 + \alpha_3$ 4 body simultaneous breakup (4BSB).

The calculated results are shown in the figure. The dashed-dotted curve represents proton spectra for the 4BSB process. The dashed curve shows the 3BSB component including both the sequential decays of ^{8}Be(g.s) and ^{8}Be(2.9MeV) states; the dotted curve is for the 3BSB process only with the decay of ^{8}Be(g.s.). As shown in the figure, the 4BSB is in better agreement with the measured continuum spectra, especially in proton energy below 2 MeV and above 4 MeV. This indicates that the 4BSB process may be more dominant than the 3BSB process in the 3α breakup reaction on ^{12}C.

To ensure the importance of the 4BSB process, we are planning to measure double differential α emission cross section at the same energy.

References

[1] N. Koori et al., JAERI-M 89-167 (1989);
N. Koori et al., Proc. Int. Conf. on Nuclear Data for Science and Technology, Mito (1988) p.1165.
[2] H.H. Hogue et al., Nucl. Sci. Eng. **68** (1979) 22.
[3] For example, D.J. Brenner et al., Nucl. Sci. Eng. **95** (1987) 311.

Table 1 Optical potential parameters for ^{6}Li

SOM

	V_0	r_0	a_0	W_S	r_i	a_i	V_{so}	r_{so}	a_{so}	χ_σ^2/N	χ_A^2/N
Present work	57.20	1.227	0.706	19.85	1.386	0.285	12.511	0.608	0.715	0.62	0.79
Bray et al.	41.3	1.050	0.745	2.38	1.923	0.654	2.85	1.020	0.2		
Dave et al.	41.3	1.507	0.663	18.08	1.616	0.196	5.5	1.15	0.5		
Chiba et al.	49.73	1.183	0.686	7.168	1.519	0.479	5.5	1.15	0.5	1.33	
* Exit channel potential for the 1st excited state (2.185 MeV, 3^+).											
Present work	25	5	3	12	1	2	22	4	3		

CC

	V_0	r_0	a_0	W_S	r_i	a_i	V_{so}	r_{so}	a_{so}	β_2	χ_σ^2/N	χ_A^2/N
Present work	67.25	0.947	0.526	2.865	1.089	0.925	12.81	0.442	1.492	1.26	16.3	24.8
Chiba et al.	47.06	1.243	0.594	9.811	1.286	0.240	5.5	1.15	0.5	1.099	3.52	

Table 2 Optical potential parameters for ^{7}Li

SOM

	V_0	r_0	a_0	W_S	r_i	a_i	V_{so}	r_{so}	a_{so}	χ_σ^2/N	χ_A^2/N
Present work	50.30	1.288	0.640	9.463	1.186	0.513	9.249	1.188	0.507	1.76	14.70
Dave et al.	37.73	1.504	0.565	13.80	1.512	0.185	5.5	1.15	0.5		
Chiba et al.	61.26	1.048	0.751	7.666	1.638	0.294	5.5	1.15	0.5	1.73	
* Exit channel potential for the 1st excited state (0.478 MeV, $1/2^-$).											
Present work	40	1.0	0.7	8	1.5	0.5	0	-	-		
* Exit channel potential for the 2nd excited state (4.63 MeV, $7/2^-$).											
Present work	35	3.5	2.0	8	2	1.5	10	4.0	2.0		

CC

	V_0	r_0	a_0	W_S	r_i	a_i	V_{so}	r_{so}	a_{so}	β_2	χ_σ^2/N	χ_A^2/N
Present work	52.23	1.127	0.583	2.529	1.571	0.732	6.565	1.141	0.432	0.961	26.96	2.81
Chiba et al.	52.01	1.187	0.636	11.14	1.434	0.133	5.5	1.15	0.5	0.956	3.9	

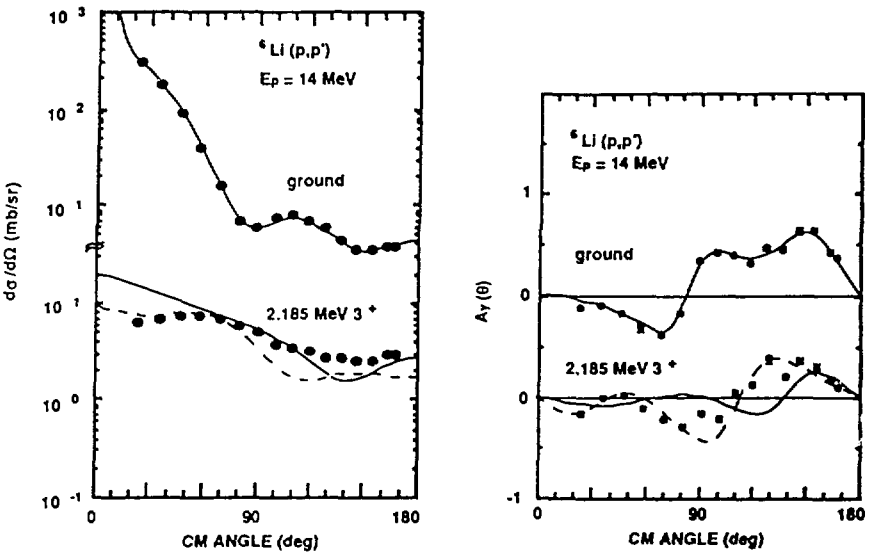

Fig. 1 Effect of changing the optical potential for the exit channel of the ^{6}Li(p,p') scattering at 14 MeV. Solid curves indicate the results for the SOM (for the elastic scattering) and DWBA (for the inelastic scattering) calculations. Dashed curve for the inelastic scattering indicates DWBA calculation with a different optical potential for the exit channel. The potential parameters for the 1st excited state of ^{6}Li are given in Table 1.

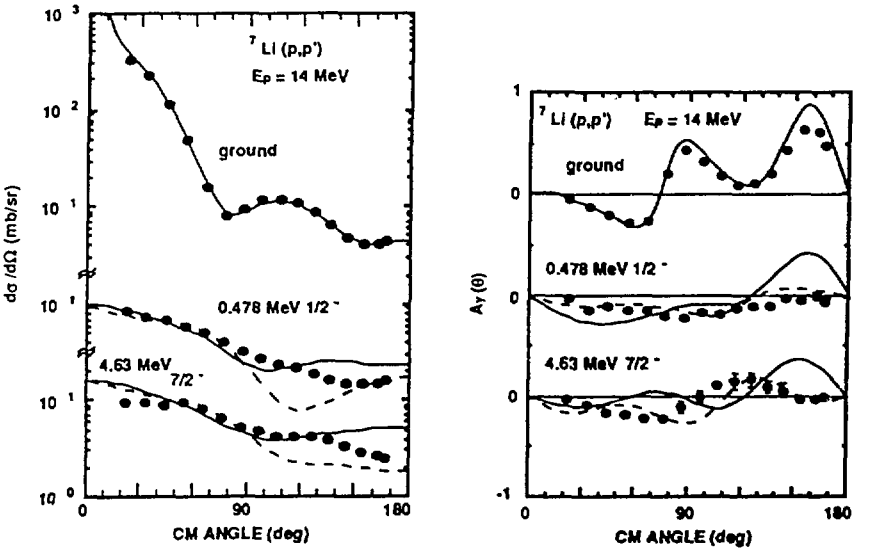

Fig. 2 Effect of changing the optical potential for the exit channel of the ^{7}Li(p,p') scattering at 14 MeV. Solid and dashed curves are similar as in Fig. 1. The potential parameters for the 1st and 2nd excited states of ^{7}Li are given in Table 2.

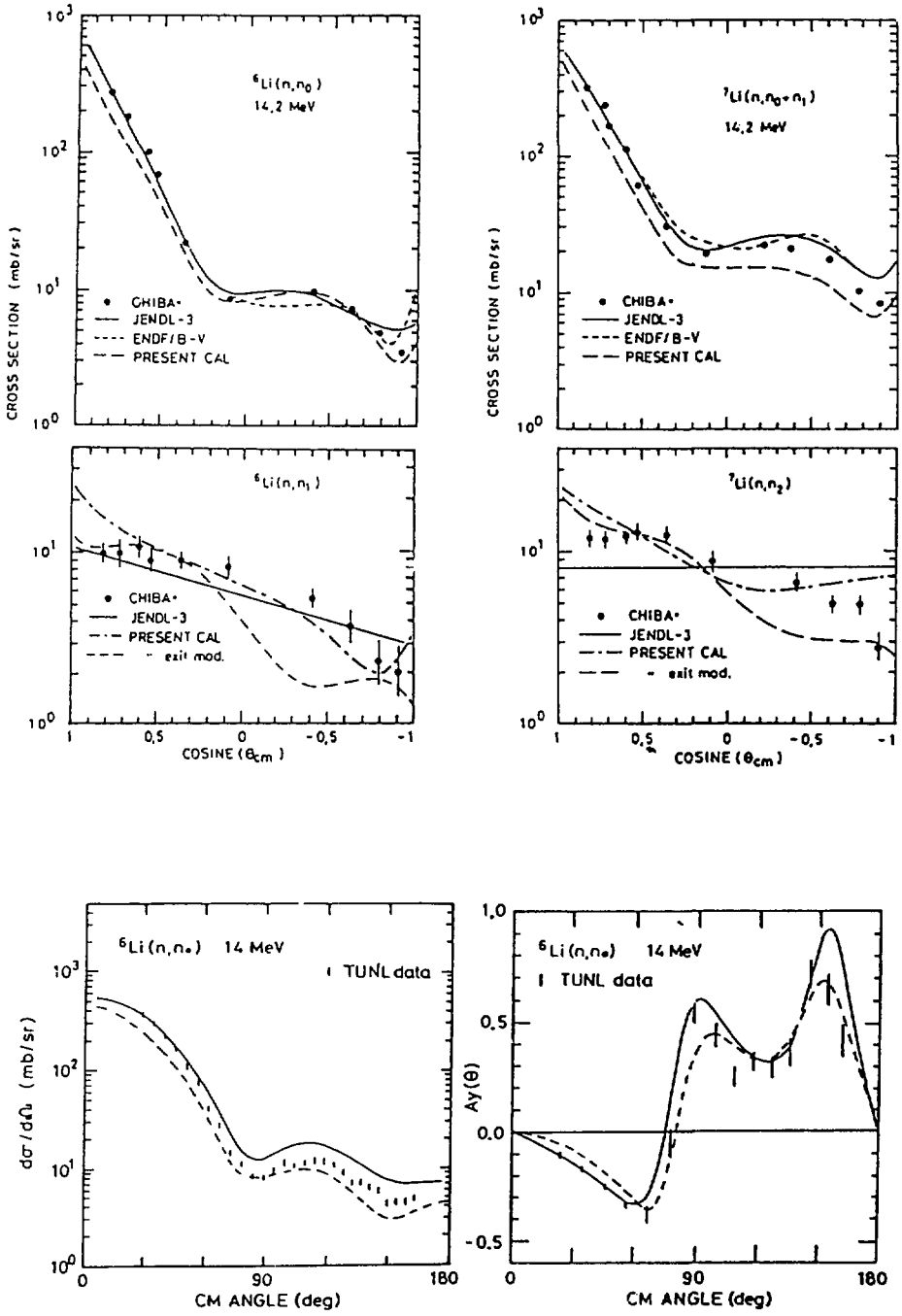

Fig. 3 Comparisons of the calculation, based on the potential parameters from the proton scattering, with the (n,n') scattering experimental data.

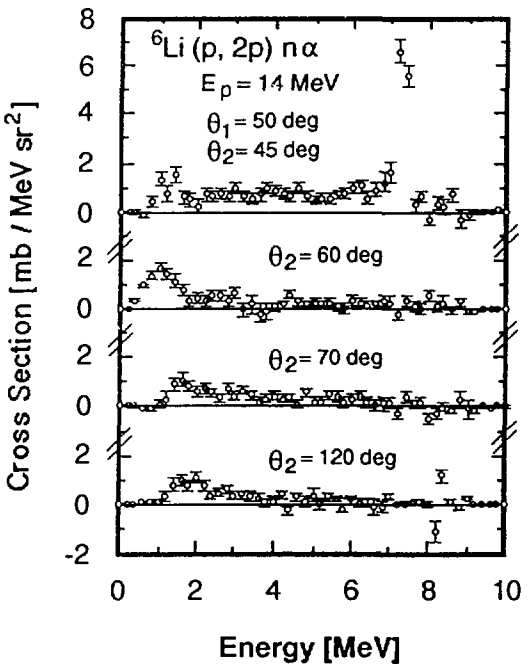

Fig. 4 Angular dependence of correlation spectra for the ^{6}Li(p,2p)nα reaction at 14 MeV. Four-body breakup process is evident in the low energy region.

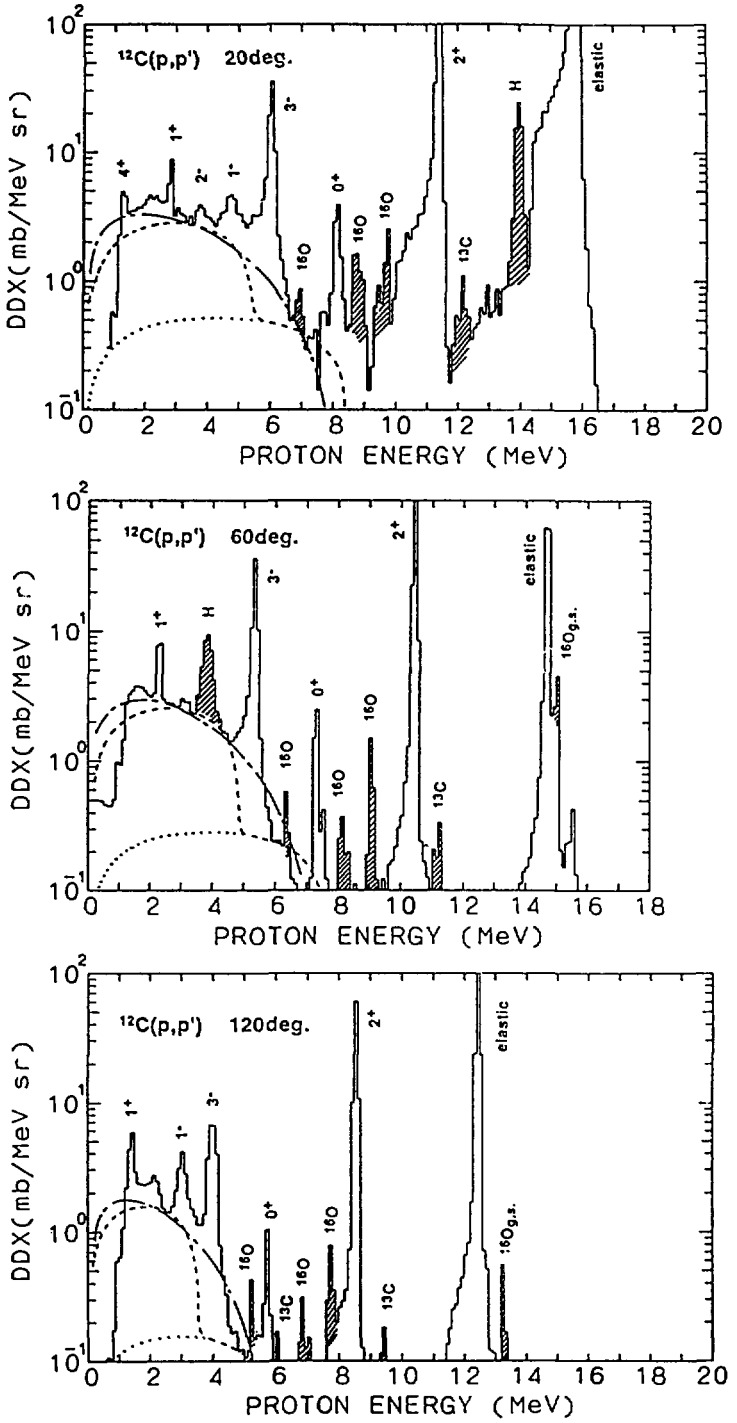

Fig. 5 Double differential proton emission cross sections measured at 20°, 60°, and 120° for 16 MeV proton induced reaction on carbon. Dashed-dotted curve is for the four-body simultaneous breakup (4BSB) process, dashed curve for the three-body simultaneous breakup (3BSB) process with the sequential decays of ^{8}Be(g.s.) and ^{8}Be(2.9MeV) states, and dotted curve for 3BSB process only with the decay of ^{8}Be(g.s.).

3.3 Nuclear Data of Charged-Particle Induced Reactions on Medium-Heavy Nuclei

Y. Watanabe, N. Koori+ , M. Hyakutake*, and I. Kumabe

Department of Nuclear Engineering, Kyushu University, Fukuoka 812, Japan

Measurements of double differential charged-particle emission cross sections are reported for proton-induced reactions on several medium-heavy nuclei in the bombarding proton energy range from 10 to 20 MeV. Some results of analyses based on preequilibrium models are summarized.

1. Introduction

Recently, the needs of charged-particle nuclear reaction data have been increasing in several applied fields: (1) Shielding for particle accelerators (2) Biomedical applications such as production of radio isotopes and cancer therapy (3) Material irradiation experiments concerning R & D for fusion technology (4) Space development, e.g. nuclear data for estimation of irradiation damage of LSI by cosmic ray.

We have performed experiments of proton induced reactions using the tandem Van de Graaff accelerator at Kyushu University for several years[1-4]. In these experiments, double differential charged-particle emission cross sections have been measured for proton-induced reactions on medium-heavy nuclei in the incident energy range from 10 to 20 MeV. The reactions measured are listed in Table 1.

The main purpose of these experiments was to understand the reaction mechanism of neutron-induced reactions through the study of proton-induced reactions and to apply the obtained information to evaluation of neutron nuclear data. In general, it is possible to obtain more precise and systematic data in proton experiments, by making use of some superiorities to neutron experiments, such as better counting statistics due to higher beam intensity and more easily variable incident energy. Therefore, the study of proton-induced reactions can become one of approaches for investigation of the common reaction mechanism related to both reactions. In present work, our interest was focused on continuum spectra with forward-peaked angular distribution of particles emitted via preequilibrium or precompound process.

The following studies have so far been done or are now in progress.

1. Shell and odd-even effects in the preequilibrium (p,p') and (p,α) reactions[1-4].
2. Incident energy dependence of preequilibrium (p,p') spectra[5].

+Present Address: College of General Education, The University of Tokushima, Tokushima.
*Present Address: Sasebo Technical College, Sasebo.

3. Systematics and parameterization of continuum angular distributions[6].
4. Simultaneous analysis of preequilibrium (p,p') and (p,n) spectra in terms of the two component exciton model.
5. Sub-coulomb barrier proton emission in (p,np) and (p,2p) reactions.
6. Isotope effect of (p,d) and (p,t) reactions on near-magic nuclei[7].

Some of the above-mentioned studies have already been published. In the present report, we describe the experimental procedure and the results for three subjects (1,2, and 4) selected from among those studies.

2. Experimental Procedure

2.1 Experimental Set-up

The experiment was performed using the tandem Van de Graaff accelerator at Kyushu University[8]. The proton beam after passing through an analyzing magnet was focused on a target placed at the center of a scattering chamber. The beam current on the target varied from about 20nA to 300nA depending on the beam energy and the detection angle. The smaller beam current was used at forward angles in order to reduce dead time for a detector system. The beam was collected in a Faraday-cup connected to a current integrator. The scattering chamber had a diameter of 1 m. A particle detector was mounted on a turnarm inside the chamber.

As the detecting system for emitted charged-particles, a ΔE-E counter telescope consisting of two or three silicon detectors(15μm, 75μm , and about 2000μm, respectively) was employed; a counter telescope consisting of two detectors for (p,p') and (p,α) reactions and that consisting of three detectors for (p,np), (p,2p), (p,d), and (p,t) reactions. Two ΔE detectors were surface barrier silicon detectors. A lithium-drifted silicon detector or a surface-barrier silicon detector was used as the E-detector. The schematic view is illustrated in Fig.1. A circular diaphragm of 6 mm diameter was used as a defining aperture for the (p,p') experiments and was located 178 mm from the target, while a defining aperture 2 mm wide and 5 mm high was placed just in front of the ΔE detector and situated 102 mm from the target for the (p,α) experiments. To reject electrons emitted from the target, a small permanent magnet was set in front of the defining aperture.

A block diagram of the electric circuit used for the (p,p') experiments is shown in Fig.2. The particle identification was made using an Osaka Denpa MPS-1230 particle identifier. Figure 3 shows a mass spectrum from the particle identifier obtained in the (p,p') experiment using ΔE(75μm)-E(2000μm) counter telescope. By selecting the corresponding part of the mass spectrum, the signals corresponding to each charged particle spectrum were fed to a multichannel analyzer Canberra Series 80 or EG&G MCA7800.

Measurements were performed between 20° and 160°, in steps of 20° for the (p,α) experiments and 10° for the (p,p') experiments, respectively. The beam intensity was determined with the current integrator connected to the Faraday cup, and was monitored by a detector located at a fixed backward angle to the incident beam direction in some cases where there is a possibility of sublimation of the target due to the heat generated by proton beam irradiation.

Targets used were self-supporting metallic foils, except for ^{128,130}Te which have 0.2 mg/cm^2 gold backings, and their characteristics is listed in Table 2.

2.2 Data processing

The measured pulse height spectra were converted to energy spectra and angular distributions in the c.m. system. There are two kinds of backgrounds to be considered in the data processing. One is the background that consists of discrete peaks due to light-element impurities on the targets, such as hydrogen, carbon, and oxygen. After these background peaks were identified using reaction kinematics calculations, they were subtracted by a peak fitting method or drawing a curve under the peak on the assumption that the spectrum must be smooth in the continuum region.

The other background is the continuous background due to the slit scattering of elastic protons by the detector aperture. This background becomes a serious problem in measurements of protons emitted from proton induced reactions. It was estimated under the assumption that the 30° spectrum measured using a thin gold target could be attributed to the degrated elastic protons, because emissions of charged particles with low energies are restricted essentially by a large coulomb barrier of the gold nucleus. The estimated background spectrum was subtracted from each measured proton spectrum after normalizing elastic peak counts. The background correction was rather large for data at forward angles (30° and 40°) and decreases rapidly with increasing angle and became negligible at backward angles. Note that the fraction of the correction was different among each experiment because the effect of slit-scattering depends on detector alignment and beam adjustment.

Absolute cross sections were determined by normalizing the experimental elastic cross sections to the optical model predictions at forward angles, because the errors arise from the nonuniformity of target thickness. The uncertainty associated with the normalization was estimated to be within 10% for each target. However, the relative uncertainty was better than the above value, and was estimated to be less than about 4%.

Finally, the experimental angular distributions for each 0.1 or 0.2 MeV energy bin were fitted with a series of Legendre polynomials up to l=4, and the polynomials were integrated to obtain an angle-integrated spectrum.

3. Experimental results and theoretical analyses

As two examples of the measured data, double differential cross sections are shown in Figs. 4 and 5 for ^{93}Nb(p,p')[3,4] and ^{118}Sn(p,α)[2], respectively. The angular distributions are peaked forward in the continuum between 6 and 14 MeV as shown in Fig.4, and similar forward peaked angular distributions are observed for the (p,α) reactions in Fig.5. These experimental results suggest that preequilibrium process or direct process is dominant in a high energy tail of the continuum spectra.

In a series of our studies on the continuum spectra, theoretical analyses for the measured energy spectra were performed in terms of the preequilibrium exciton model. Since several results have been described elsewhere in details[1-7], we will summarize only the essences here, selecting three subjects from among the studies mentioned in Introduction.

3.1 Shell and odd-even effects in the preequilibrium (p,p') and (p,α) reactions

From investigation of shell and odd-even effects in preequilibrium (p,p') and (p,α) spectra, it was found that there were no appreciable shell and odd-even effects of the target nuclei in the continuum spectra corresponding to excitations higher than 4 MeV of the residual nucleus[1-4]. A satisfactory interpretation for the result was given on the basis of microscopic state densities calculated from a modified uniform spacing model proposed by us. The measured energy spectra were in good agreement with those calculated in terms of the exciton model using a shell independent single-particle level density.

3.2 Incident energy dependence of preequilibrium (p,p') spectra

Incident energy dependence of preequilibrium (p,p') process was also investigated for 12-18 MeV (p,p') spectra for ^{98}Mo and ^{106}Pd[5]. In particular, the incident energy dependence of the K-value used in an empirical expression($M^2=KA^{-3}E^{-1}$) for average matrix element was inspected. As a result, the spectra calculated using a constant K-value(430MeV^3) showed good agreement with all measured spectra. An important role of isospin conservation in preequilibrium (p,p') process was also addressed in this analysis.

3.3 Simultaneous analysis of preequilibrium (p,p') and (p,n) spectra in terms of the two-component exciton model

To check the validity of some proposed preequilibrium models, it is of great interest to analyze simultaneously two dominant preequilibrium decay channels[(p,p') and (p,n) reactions] using the same model assumptions and model parameters. Since experimental data on 18 MeV (p,n) spectra for ^{90,91,92,94}Zr and ^{106,108,110}Pd as medium-heavy nuclei have been reported in Refs.[9,10], we measured (p,p') spectra for the same nuclei at the same bombarding proton

energy of 18 MeV. Both (p,p') and (p,n) spectra were analyzed in terms of the one- or two-component model[11] and a dependence of the K-value on the nature of emitted nucleon was examined.

From the analysis using the one-component exciton model, it was found that both (p,p') and (p,n) spectra were reproduced well by the calculation using the same K-value[463MeV^3] when Q-factor[12] was employed as the correction factor for the distinguishablity of proton and neutron degrees of freedom and effective Q values[13] was used. The result of the two-component exciton model calculation indicated that relative yield for proton and neutron emissions depends strongly on relative probability of exciting proton and neutron in a nucleus in the transition process from one-particle (1p) states to two-particle and one-hole (2p-1h) states. The calculated (p,p') and (p,n) spectra showed good agreement with the experimental ones when it was assumed that the relative probability was equal. Comparisons between the experimental and calculated spectra for ^{90}Zr and ^{94}Zr are shown in Fig.6. In the calculation using the two-component model, isospin conservation was not treated rigorously. That is, only $T_<$ component was treated by this model but $T_>$ component was calculated using the one-component model mentioned above. Therefore, more rigorous two-component model calculation including isospin conservation will be required for further studies on the preequilibrium (p,p') and (p,n) spectra.

4. Summary

Systematic measurements of double differential charged particle emission cross sections have been performed for proton-induced reactions on several medium-heavy nuclei, and those charged-particle nuclear reaction data were gathered in a data-form of double differential cross sections and angle-integrated spectra. From comparisons between the measured (p,p') and (p,α) spectra and those calculated using the preequilibrium exciton model, the preequilibrium process related to these reactions was intensively studied.

As a next step for the present works, we are now planning an extension of measurement of the continuum spectra for proton-induced reactions to the bombarding proton energy range from 20 to 40 MeV using a JAERI tandem Van de Graaff accelerator and theoretical analyses based on sophisticated models, such as the statistical multistep direct and compound theories[14].

Acknowledgments

We would like to thank members of the Nuclear Physics Laboratory of the Department of Physics, Kyushu University, for their assistance in operating the accelerator. We also wish to thank several students who worked together in our laboratory and graduated from the Department of Nuclear Engineering, Kyushu University, for their cooperation.

References

[1] I. Kumabe et al., Phys. Rev. C **35**, 467 (1987).
[2] I. Kumabe et al., Phys. Rev. C **38**, 2531 (1988).
[3] Y. Watanabe et al., Phys. Rev. C **36**, 1325 (1987).
[4] Y. Watanabe, Doctor thesis, Kyushu University (1988).
[5] Y. Watanabe et al., to be published in Z. Phys. A.
[6] I. Kumabe et al., to be published in Nucl. Scie. and Eng.
[7] I. Kumabe, Proceedings of the 1987 Seminar on Nuclear Data (JAERI M 88-065), p.212.
[8] Kyushu University Tandem Accelerator Laboratory Report (1980-1984).
[9] W. Scobel et al., Lawrence Livermore National laboratory Report No. UCID-20101, 1984 (unpublished).
[10] S.M. Grimes et al., Phys. Rev. C **13**, 2224 (1976).
[11] C. Kalbach, Phys. Rev. C **33**, 816 (1986): S.K. Gupta, Z. Phys. A **303**, 329 (1983): J. Dobes and E. Betak, Z. Phys. A **310**, 329 (1983).
[12] C. kalbach, Z. Phys. A **283**, 401 (1977).
[13] I. Kumabe and Y. Watanabe, Phys. Rev. C **36**, 543 (1987): *ibid.* **40**, 535 (1989).
[14] See, for example, P.E. Hodgson, *Proceedings of the International Conference on Nuclear Data for Science and Technology, Mito*, 1988, edited by S. Igarashi (Saikon Publishing 1988), p.655.

Table 1 A list of measured reactions

Reactions	Target Nuclei	Incident Energy
(p,α)	^{90}Zr, ^{92,94,96,98,100}Mo, ^{93}Nb, ^{106}Pd, Ag	15, 18 MeV
(p,α)	^{112}Cd, ^{118,120}Sn, Sb, ^{128,130}Te	18 MeV
(p,p')	^{90,91,92,94}Zr, ^{93}Nb, ^{92,94,96,98,100}Mo, ^{106,108,110}Pd, Ag, ^{60}Ni	18 MeV
(p,p')	^{98}Mo, ^{106}Pd	12,14,16 MeV
(p,np), (p,2p)	^{90}Zr, ^{92}Mo, ^{94}Mo, ^{54}Fe, ^{60}Ni	13.6-16.3 MeV
(p,d), (p,t)	^{92,94,96,98,100}Mo	19 MeV

Table 2 Target thickness and isotopic enrichment

Target Nucleus	Target thickness (μg/cm2)	Isotopic enrichment(%)
^{54}Fe	455	97.61
^{60}Ni	850	98.0
^{90}Zr	492	97.65
^{91}Zr	431	88.50
^{92}Zr	495	95.13
^{94}Zr	432	96.93
^{93}Nb	2576	100
^{92}Mo	506	98.27
^{94}Mo	588	93.90
^{96}Mo	473	96.80
^{98}Mo	450	97.10
^{100}Mo	744	97.27
^{106}Pd	1020	98.48
^{108}Pd	1480	98.11
^{110}Pd	977	97.73
Ag	1089	natural
^{112}Cd	1040	97.05
^{118}Sn	900	97.79
^{120}Sn	610	98.39
Sb	1110	natural
^{128}Te	1920	99.19
^{130}Te	2080	99.49

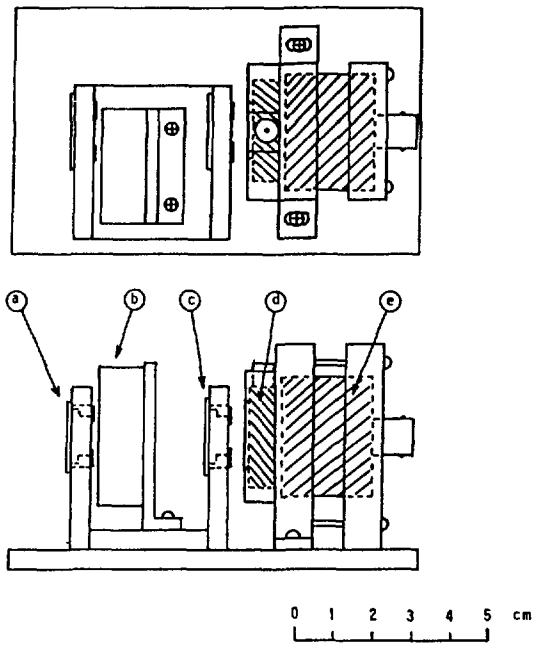

Fig. 1
A schematic view of a counter telescope used in (p,p') experiments. (a) circular diaphragm of 7 mm in diameter, (b) permanent magnet, (c) circular diaphragm of 6 mm in diameter for a defining aperture, (d) dE detector, (e) E detector

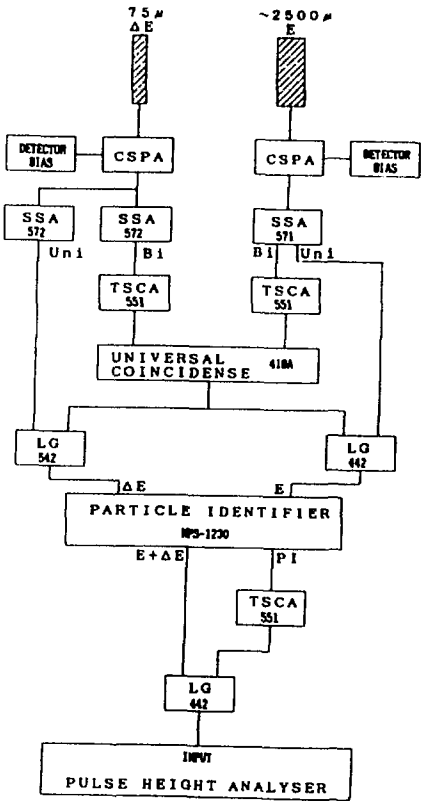

Fig. 2
A block diagram of the electric circuit used for (p,p') experiments

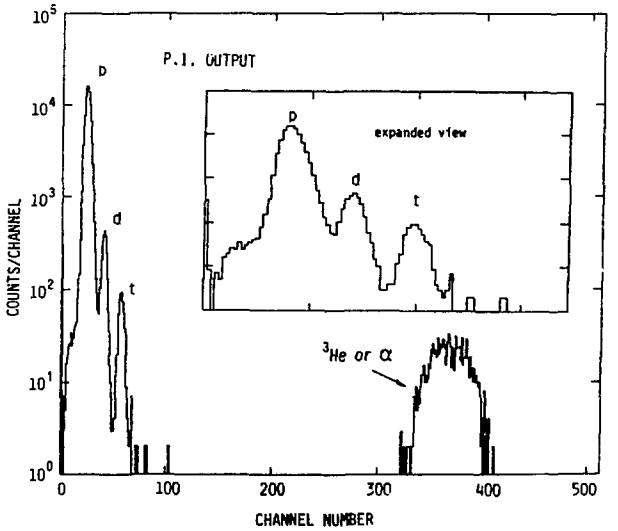

Fig. 3 A mass spectrum from the particle identifier

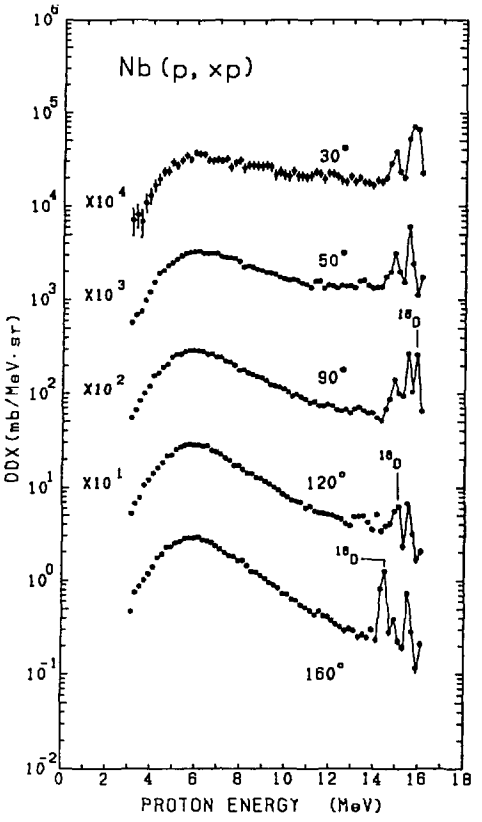

Fig. 4 Double differential cross sections for the ^{93}Nb(p,xp) reactions at 18 MeV

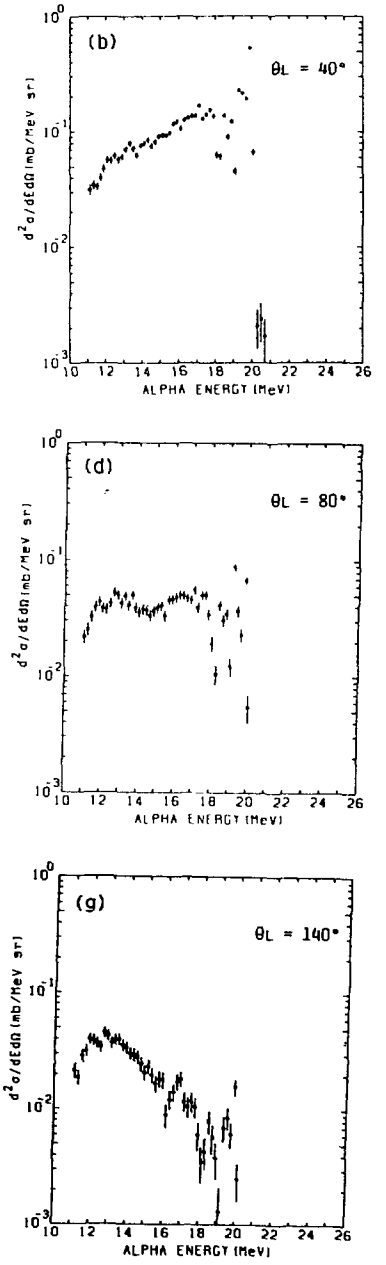

Fig. 5 Double differential cross sections of alpha particles from the ^{118}Sn(p,α) reaction for 18 MeV protons

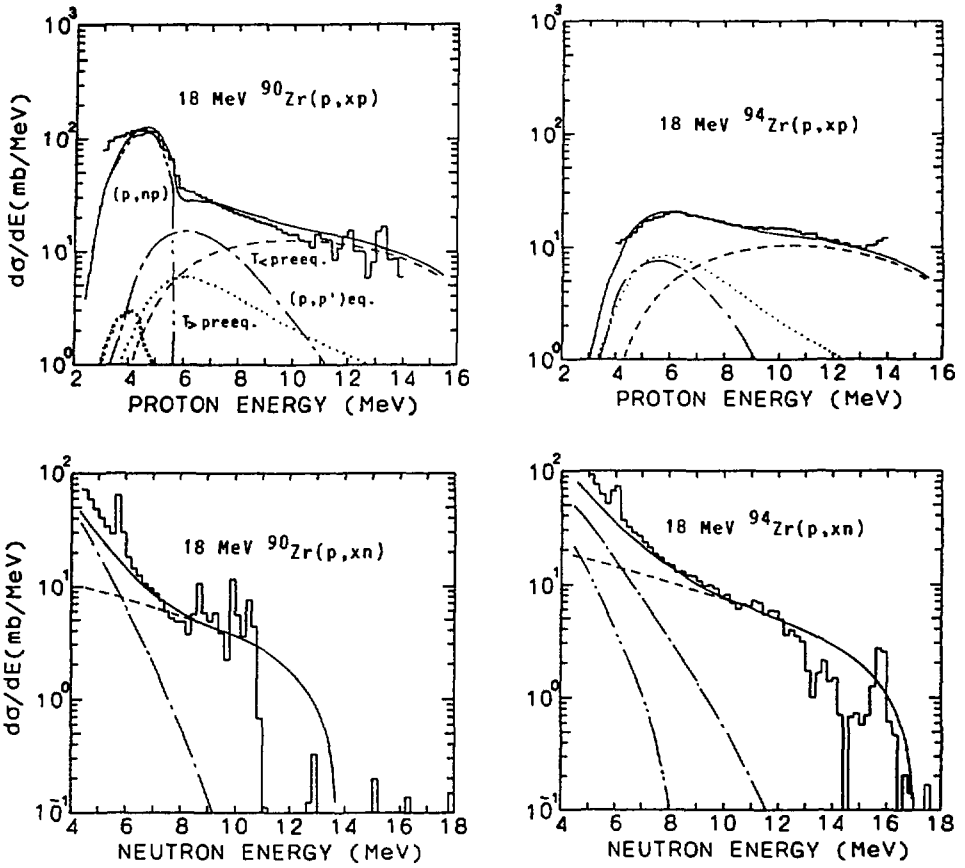

Fig. 6 Comparisons between experimental energy spectra and those calculated using the two-component exciton model for 18 MeV (p,p') and (p,n) reactions

3.4 Measurement of Helium Production Cross Section of Aluminum Irradiated by Proton

Yoshiyuki Takao, Yukinori Kanda, Sigeki Itadani,
Tuyoshi Takahashi, Hideki Eifuku, Muneaki Morinaga
and Akio Iwasaki

Department of Energy Conversion Engineering,
Kyushu University, Kasuga, Fukuoka 816, Japan

Abstract

The proton-induced helium production cross sections of aluminum have been measured using the Helium Atoms Measurement System. Eleven pieces of aluminum foil (chemical purity 99.999%, size $10 \times 10 \times 0.1 mm^3$) are prepared for samples. The samples are stacked and irradiated by 14MeV protons generated by a tandem accelerator. Helium production cross sections at several kinds of proton energy can be measured by using stacked samples at a time, because the proton energy is changed in the samples.

1. Introduction

In development of fusion reactor materials, helium production caused by irradiation of fast neutrons is one of the most important problems, which leads to swelling or brittle fracture. The experimental data of the helium production are useful for the selection of the first wall materials, but they are scarce. Because there are few facilities which can generate enough fluence of high energy neutrons (above 14MeV). Therefore, this subject, measuring helium production cross section for protons instead of neutrons, has been studied. This simulation will make it possible to measure helium production cross sections at several incident energy, because there are a number of accelerators which can generate enough fluence of high energy protons.

2. Experimental procedures

The experiments include three consecutive stages, which are sample preparation, irradiation of protons on the samples and measurements of the number of helium atoms using the Helium Atoms Measurement System.

2.1 Sample preparation

Eleven pieces of aluminum foil (chemical purity 99.999%, size $10 \times 10 \times 0.1 mm^3$) are prepared for samples. The samples are stacked and set on a sample holder and are installed in a Faraday cup. They are set in a vacuum chamber so as to coincide a perpendicular so the aluminum foil and one of proton beam(fig.1). The samples are held below a temperature of 50°C by liquid nitrogen during irradiation. It prevents the release of created helium atoms due to the diffusion above a certain temperature of 100°C.

2.2 Irradiation of protons

The samples are irradiated by 14MeV protons at Kyushu University Tandem Accelerator Laboratory. The number of protons is measured by using a current integrator and the samples were irradiated at a proton current of $0.5 \mu A$ to reach a positive charge of $5000 \mu C$. Helium production cross sections at several kinds of proton energy can be measured by using stacked samples at a time. They are calculated from the energy loss in the samples(1). Figure 2 shows the schematic diagram of a vacuum chamber. The vacuum chamber with a diameter of 100cm and a depth of 50cm has a moving arm which can move around the center of the vacuum chamber. By setting the sample holder which is an arc in figure on the moving arm, the changing of samples are easily achieved.

2.3 Measurement of the number of helium atoms

After irradiation, the number of helium atoms produced in the aluminum samples are measured by using the Helium Atoms Measurement System which was developed in our laboratory. This instrument consists of 5 main parts, which are a standard gas supply, a furnace, a trap, a mass spectrometer and a vacuum system. Three turbo molecular pumps (T.M.P.) are used for the vacuum system. The vacuum system keeps the instrument at an ultrahigh vacuum of 5×10^{-8}Torr. In the furnace, the samples are evaporated on a tungsten boat heated electrically and release the helium gas. Molecular sieves cooled by liquid nitrogen are used for the trap to remove the undesirable gas from the released gas of the samples. Helium contained in the released gas is analyzed by a quadrupole mass spectrometer. The number of helium atoms are determined by comparing the analyzed result of sample gas with that of standard helium gas. The number

of atoms of the standard helium gas is measured by using the standard gas supply. The standard gas supply consists of volume known vessels, an absolute pressure gauge and a thermometer.

3. Results

Though the helium production cross sections are determined by the number of protons and helium atoms, the number of helium atoms must be corrected for the loss and the gain of helium atoms from surfaces of individual samples. The loss is caused by the emission of helium atoms from the sample due to the kinetic energy of the (p, α) reaction. The gain is caused by the entrance of the emitted helium atoms from other samples into the sample.

The determination of helium production cross section including the correction is achieved through calculation and it is as in the following. Figure 3 shows the principle of the correction of helium atoms. A certain excitation function of the (p,xα) reaction is assumed and the number of helium atoms produced at a certain point in the samples is calculated from it. The proton energy at the point was determined by a helium stopping power(1). The energy distribution of the helium atoms are determined from the α particle spectrum at the given proton energy and the emitted angle. The ranges of the α particles are determined by this energy(2). Figure 4 shows the ranges of the ground state α particles against emitted angles and proton energy. The angular distribution of α particles is determined on the assumption that the emission of α particles are isotropic in center-of-mass system. The place where the produced α particles are trapped and the number of trapped α particles in the place are determined by these assumptions and calculations. When the results of this calculation agrees with the number of helium atoms measured experimentally, the assumed excitation function is the objective excitation function. When they are not agree, the calculation described above is repeated on another excitation function until both results agree.

Figure 5 shows the results of this study. The plots as the helium production cross sections of aluminum are the average cross sections for an energy interval at the sample position. The errors were estimated from statistical and systematic uncertainties.

References:

(1) Andersen, H.H., Ziegler, J.F.: "*Hydrogen Stopping Powers and Ranges in all Elements*", (1977), Pergamon Press, New York.

(2) Ziegler, J.F.: "*Helium Stopping Powers and Ranges in all Elemental Matter*", (1977), Pergamon Press, New York.

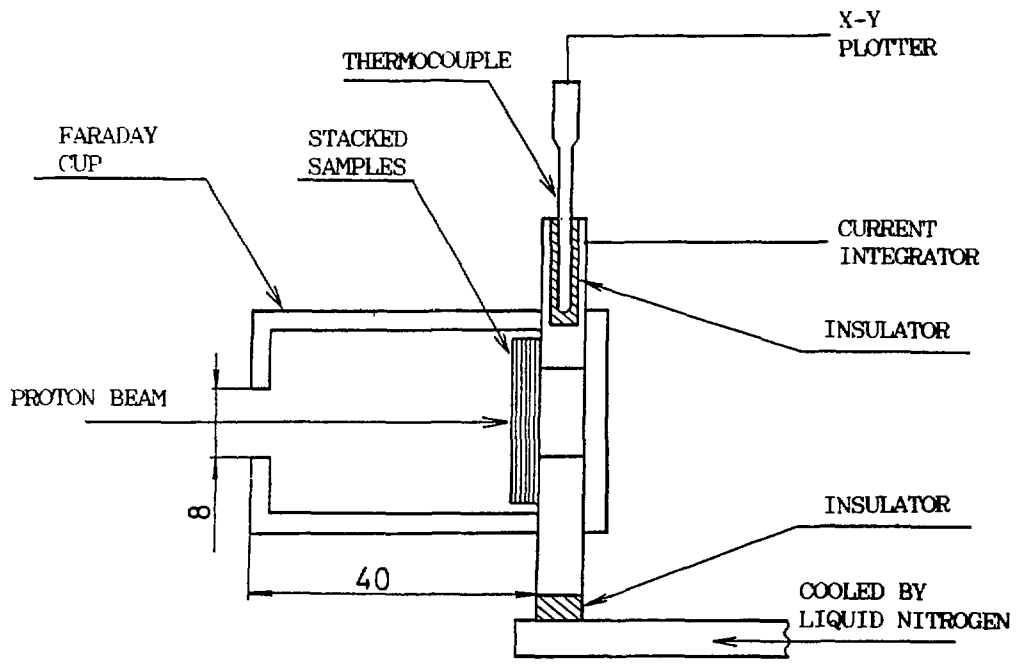

Fig. 1 Schematic diagram of the sample holder

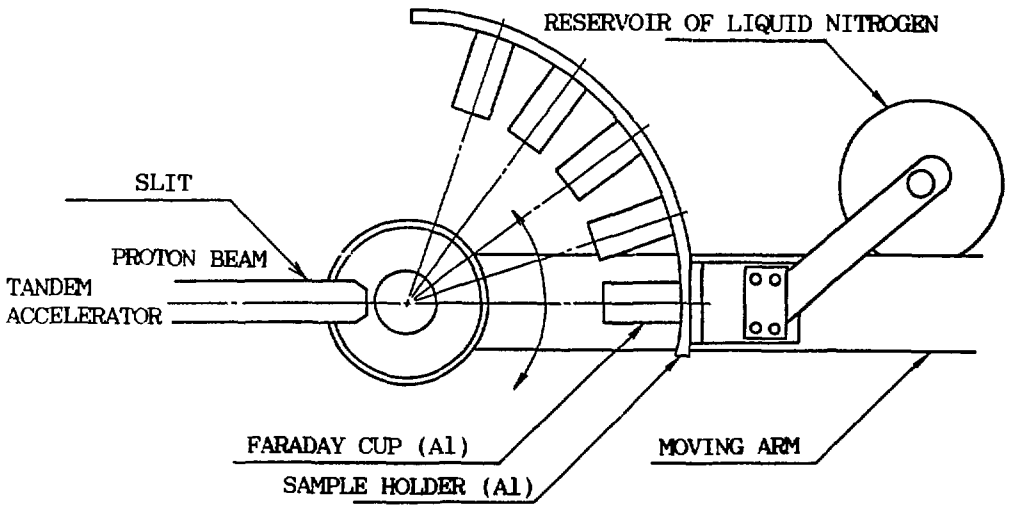

Fig. 2 Schematic diagram of the vacuum chamber

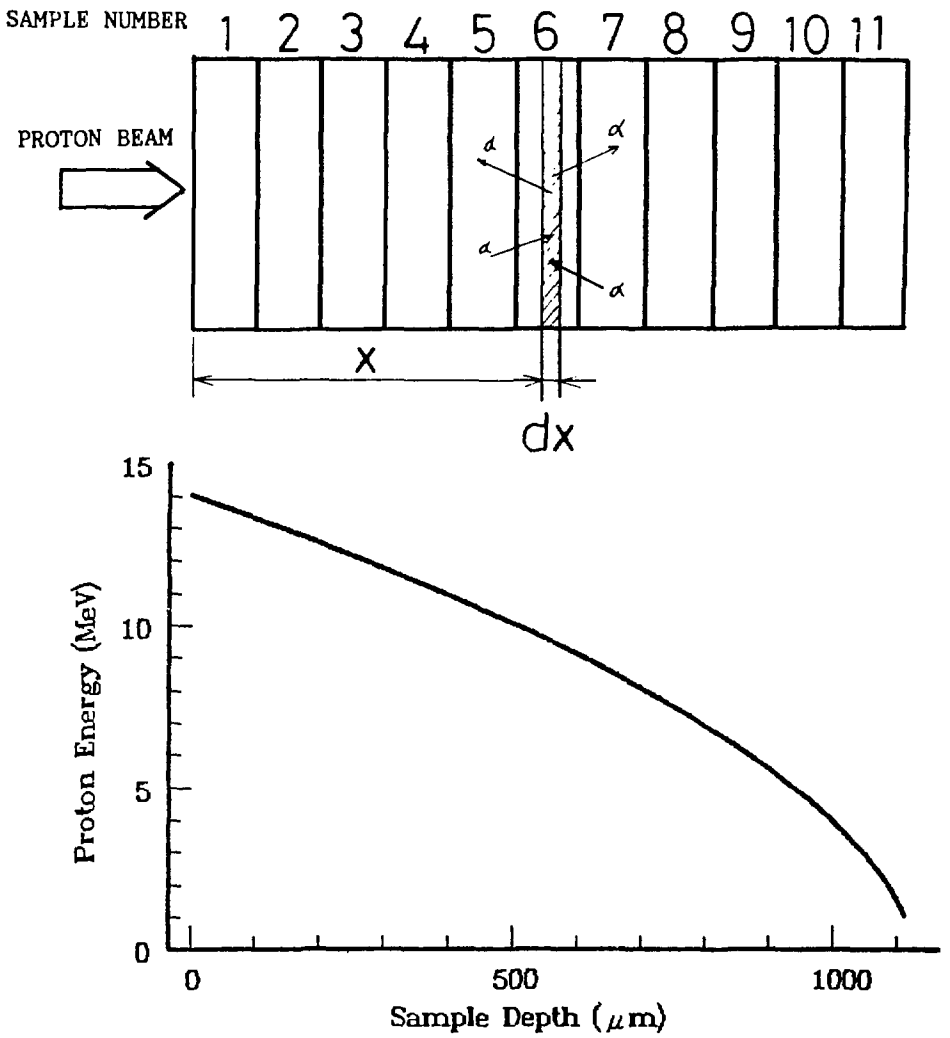

Fig. 3 The principle of the correction of helium atoms

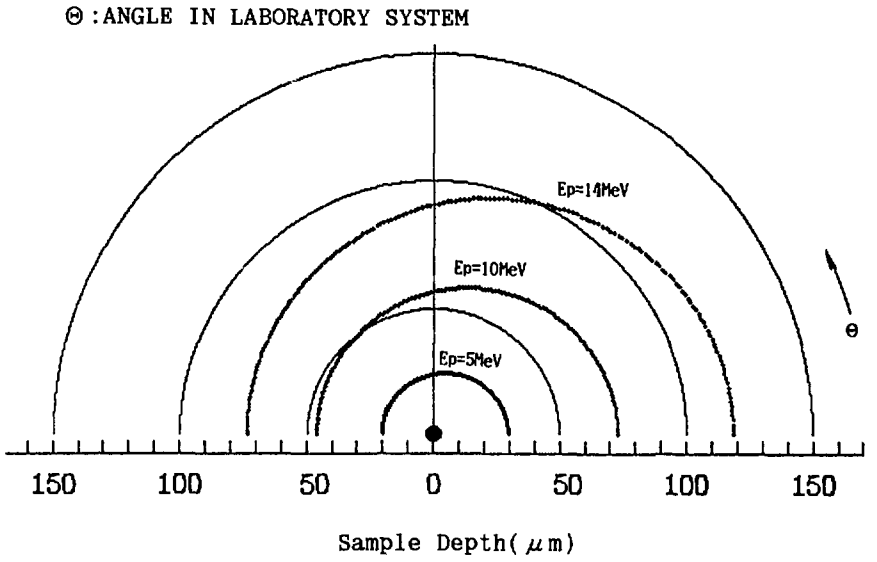

Fig. 4 The ranges of the ground state α particles in Al at several proton energy

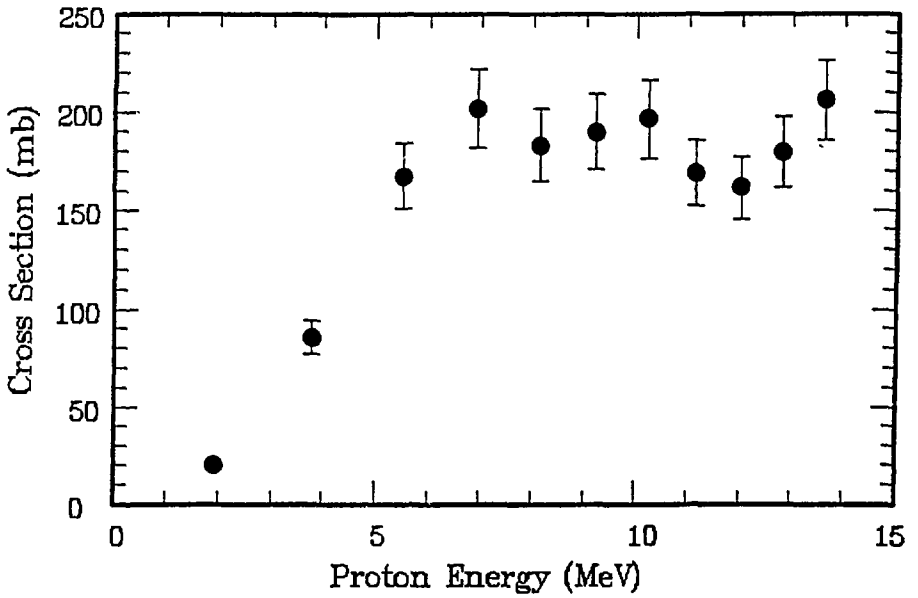

Fig. 5 Helium production cross sections of aluminum for proton

3.5 Technological Problem in Development of an Advanced Support System for Nuclear Data Evaluation

S. Iwasaki and K. Sugiyama
Department of Nuclear Engineering, Tohoku University
Aramaki-Aza-Aoba, Aobaku, Sendai 980, Japan

1. Introduction

We have been developing a support system for nuclear data evaluation on a 32-bit workstation for one and a half year using the knowledge engineering technology /1/. In this system, model codes for nuclear cross section calculation is systematized and handling process of each code using a set of parameters for a typical nuclear data evaluation is supported. This system have been considered to be a middle level among three kinds of the system; low level, middle level and high level system /1/. The low level is just a cross section calculation system using a set of default model parameters. The high level one means a practical support system for neutron nuclear data evaluation as done in the evaluation for JENDL-3. The middle level system is a prototype of the high level one and for establishment of fundamental technologies for the latter system.

There may be a wide gap between the low level and high level system, and there are many technical problems to be solved in order to approach the high level system. In this paper, we discuss the new technologies of the high level system from the point of view of the experience of development of the middle level one and their feasibility.

2. Outline of the Present Middle Level System

In this chapter, we briefly describe the feature of the present system in order to make the point of the later discussion clear. As stated above, the present system is a basic and experimental system to develop the support system for the nuclear data evaluation. The primary function of the system is considered to guide the user to perform the nuclear data calculation using several nuclear codes because this process was main part of the evaluation for JENDL-3 /2/. In the first version of the system the following tasks are supported;

for each code calculation,

- .preparation of an input parameter file to specific nuclear cross section code,
- .check of input parameters,
- .storage of input parameter sets to a data base for tracing of the previous evaluation later,
- .handling of output data files,

and for the whole model calculation process,

- .control of task flow related to the all code running in the evaluation.

Choice of initial parameter set and judgment of fitting should be done by user.

The knowledge of the task flow have been compiled in a collection of production rules and inferred by a backward chaining mechanism. Development environment was provided by an expert construction shell, Nexpert Object/3/ under UNIX operating system.

In the second version of the system, enhancement of the system was done by adding a function for the adjustment of the model parameters used in each nuclear code /4/ using the fuzzy logical inference; i.e.,

- .judgment of fitting which is a kind of pattern recognition,
- .estimation of parameters which are sensitive to improvement of the fitting to the experimental cross sections,
- .estimation of amount of variance of the selected parameters from the previous values employing the sensitivity coefficients of the parameters to the cross sections.

This method is considered to be a alternative method of the generalized least square fitting. Adaptation of the fuzzy logic inference enabled to save number of rules comparing with the case by set of the usual crisp logic rules, and give a sort of the mechanism of compromise of some contradicting rules as usually done by human to make decision.

3. Technological Problems for High Level Support System

Because a vast number of works, from primitive but time consumptive tasks to highly comprehensive ones, are repeatedly performed in the evaluation process, it is inevitable for evaluator to be supported to a high level in order to complete his work within a limited time. The process is consisted of many correlated tasks, and correspondingly, variety of knowledge and many levels of knowledge are connected with each other Thus, it is necessary to analyze tasks during the evaluation in order to design the knowledge base of the support system. The flow of tasks in the evaluation process is being analyzed in the subworking group of data base for nuclear data evaluation.

Through the authors study of the middle level system and discussion with other evaluators, we listed up the major tasks which would be more or less done by an average evaluator during the process of the nuclear data evaluation. They are totally as much as 33 items, as shown in Table 1, and are categorized into 5 groups which approximately correspond to modules discussed later.

From the point of view of the present state of the art of the knowledge engineering, it is reasonable to expect that the system support the tasks which are performed under relatively shallow knowledge*) and/or shallower part of deep knowledge*) of the evaluators can be developed.

Considering the effectiveness of the support to user and easiness to develop, the following seven terms which would be supposed to be supported by the advanced system can be picked up.

---

*) deep knowledge is on the understanding of the object/structure by model; in contrast, shallow knowledge is on the experience, a kind of know-how.

(1)collection of experimental data from data bases,
review of quality of each set of data,
grouping of the experimental data set in grade.
(2)review of theoretical models and codes,
selection of suitable combination of codes,
(3)parameter selection from parameter data base
review of parameter systematic.
(4)handling of codes system,
calculation of cross section by the code system.
(5)comparison of calculated results with experimental data,
and model parameter adjustment.
(6)estimation of the error and covariance of the result.
(7)overall assessment of evaluations results,
check and review of the results from the aspect of the integral experiment.

The item (6) is necessary as the future support system of Japan. In the previous middle level system, we focussed on the item no.3, 4, and 5.

comments on each item:
(1)-collection of experimental data from data bases,
-review of quality of each data set,
-grouping of the experimental data set in grade.

The practical resource of the experimental data for nuclear cross section is the EXFOR data file. Format of the EXFOR file /5/ was designed for the storage of descriptive and numerical data of the cross sections, and not suitable to access the data. Therefore it is unpractical to draw a set of necessary data directly from the file, and desirable to convert the EXFOR file into the other type of data which are fitted to modern data base management system. The relational type may be the most preferable. At least, the original EXFOR file should be broken down to some small sized and structured data file and an index file of the files to access should be formed.

In the EXFOR file, there exist many kinds of data from old to new ones, from ones with small errors to large errors, from reliable to unreliable ones. etc. If we plot all available data for a reaction, we may observe that there are some data points separated from the average value, or there are two or three cross section groups which deviate systematically from each other. It is unreasonable to treat the all data with equally weight. Therefore, the assessment of each cross section data and grade them by some criteria is inevitably important. In some cases, elimination of the lowest grade group from the object set of the data for the evaluation is necessary.

Designing of the knowledge base for the review and grouping of the experimental data set is most important but difficult issues. The first step to the system is to consider following factors; the year, experimental method(detector, neutron source, calibration, etc.), correction method, error analysis and amount of the systematic discrepancy of the data set from others. This is not the absolute standard, and final judgment should be done by evaluator.

(2)-review of theoretical models and codes,
-selection of suitable combination of codes,

Main part of this term is inherently related to the deep knowledge of the evaluator and difficult to develop. If we confine our aspect, however, to the use of the previous examples i.e., shallower part of the deep knowledge, it is not impossible to develop a system to suggest a method or a set of methods referring to the data base for methods adopted in the previous evaluation.

(3)-parameter selection from parameter data base
-review of parameter systematic.

This is closely connected to the item 3. Again, we confine to the nuclear model into the previously used ones. the data base of the parameter set can be developed and some set of initial parameters can be recommended. Actually, a data base for the parameter which had been used for the JENDL-3 evaluation is being compiled by JNDC nuclear evaluation data base sub-working group. There is no important technological problem in the term except for the design of the data base management.

(4)-handling of codes system,
-calculation of cross section by the code system.

This item is also related to the items 2 and 3. Basically the methods of the code handling have been done in the medium system. Refinement of the rules in the system, and structuring of the rule base should be done in order to make maintain the rule base and modification of the rule base easer. Extension of the code system is also desirable in order to calculate cross sections by different model codes for comparison.

(5)-comparison of calculated results with experimental data,
-model parameter adjustment.

Basic technology for judgment of fitting and parameter adjustment have already been developed in the medium level system using the fuzzy theory as described before. Improvement of the rule base system should be done. Further it is important to compile the rules based on the recent knowledge on determining or restriction of the parameters because the input parameters are not free, e.g., the dispersion relation of the optical potential which connect the real and imaginary part of it.

In parallel, the conventional generalized (Baysian) least squares method/6/ should be taken into account.

(6)-estimation of error and covariance.

The error and covariance of the cross section were completely neglected in the course of the evaluation of the JENDL-3 file except for the simultaneous evaluation for the actinide nuclei /6/. Fundamentally, the error estimation should be done in the evaluation similarly to the measurement. At present, the standard methodology for the estimation of the error of the cross sections evaluated using cooperatively the experimental data and theoretical model calculations have not been established. Study on this subject have been started in the sub-working group and it can expected to get a preliminary method in a few years.

(7)-overall assessment of evaluation results,
-check and review of the results from integral aspect.

Conventionally the overall syntactic check of the evaluated results have been done by the compilation group member and after that assessed from the integral test point of view by reactor physicist or end user group. However, except for the items which necessitate the very specific domain knowledge in the analysis, the syntactic check and cross section check by comparison with some simple integral experiments using a standard group cross sections should be done in the evaluator side and the results should be returned to the reevaluation process quickly.

The rules of the knowledge base for the assessment of the cross section can be derived by analyze the activities of the file compilation group and integral checks by several group for the JENDL-3 file in the period about 2years until release the file.

4. Integration of the Modules and User Interface

Previously discussed items correspond to knowledge base modules in the practical support system one by one. Each module may consist of several sub-modules, for example, a knowledge base for control of the module, a data base, a sub-module for data base access and a sub-module for display. In the whole system, there must be a key module (knowledge base) to integrate the modules and systematically control each module, scheduling the tasks, make a module to work or idle according to the user's intention. The presently proposed high level support system does not mean the automated evaluation system, but ideally a support system which assists the user to do whatever the user wants at any moment during the evaluation. Therefore, the role of the key module is very important. This module must have high flexibility in the case of lack or modification of some modules. Such kind of flexibility is essential to develop the high level system module by module in the term of several years.

High grade human interface is one of the most important feature of the proposed system. Extremely speaking, the conventional evaluation system did not consider or neglected the user interface , and forced the users to fit themselves to the computer system conversely. In order to develop a highly efficient computer system, it is necessary to provide an user friendly system which use the high level graphics technique.

Using multi-task and multi-window system, the following quantities and functions are presented in various types of graphics in a bitmap display concurrently; the important cross section curves, spectra, comparison with experiment and other evaluation, graphs showing variation from the previous calculation before parameter change; monitoring displays for key input parameter values, for performance of the evaluation, for the current tasks which are performed presently: e.g., accessing the experimental data base, code running, etc.; these help the user to acknowledge the progressing of the system.

In this system, the user can input the numerical values to the system by moving bar graphs through the mouse interface which minimizes the input error.

In the multitasking environment, the simultaneous evaluation for several nuclei become feasible. This is very convenient if the user want to evaluate the nuclei of which daughter nuclei are connected with each other through common parameters (for example, the evaluation for the stable isotopes in a single element). If the user wants, he can do some works not related to the evaluation work (e.g, mail by LAN or programing development, etc.) very easily.

Usually development of such high level graphic interface would take a considerable time, and it is recommended to use commercial tools if they want to implement the interface to the system in a short period. In figure 1, an image of display of the proposed advanced support system is shown.

5. Summary

We have been discussed the important issues of the technologies which are essential to develop the upgraded (high level) support system for the neutron nuclear data evaluation.

However, if we focus to systematized knowledge of the evaluators, which is shallow or deep, and intend to build a cooperative problem solving system between user and machine, the system would be in the extension of the presently developed technologies. An experimental system which can be practically used for the evaluation process would be developed within several years.

In order to make the system work efficiently, several data bases and management systems should be prepared; the cross section request data base, the data base for experimental cross sections from the EXFOR file, nuclear model/method/code data bases, and model parameter data base.

Development of knowledge acquisition mechanism and natural language interface are very interesting themes in the application of the knowledge engineering technology to the data evaluation, but may be future problems.

It is expected that present discussion would provide a useful guidance on the project for the practical system using artificial intelligence technology at JAERI nuclear data center.

The authors are indebted to valuable comments of the members of nuclear data evaluation sub-working group and appreciated to their thanks to Dr. Narita of Nuclear Data center for his helps.

References

/1/ S. Iwasaki et al., Proc. 1988 Seminar on Nucl. Data, JAERI-M89-026, p313 (JAERI 1989).
/2/ T. Asami et al., Journal of Atomic Energy Society of Japan, Vol.31, No.11, p1190 (1989).
/3/ Manual of Nexpert Object (Neuron Data Inc., 1988).
/4/ S. Iwasaki et al, Proc. of Fall meeting of Japan Atomic Energy Society, B16 (1989).
/5/ EXFOR MANUAL, BNL(1977).
/6/ F.H. Froener, Proc. Workshop on Applied Nuclear Theory and Nuclear Model Calculations for Nuclear Technology Applications, p170, Trieste, Italy, (World Scientific, 1989).

Table 1 List of major tasks during the process of nuclear data evaluation

		(1) <on the experimental data>
1	o	-survey of nuclear data requests related to the objective nucleus/nuclei.
2	o	-comprehension of importance reactions of the nuclei in the applications.
3	o	-collection and survey of experimental data in EXFOR file.
4		-collection and survey of recent experimental data in Japan and overseas.
5		-making numerical data set from the recent experiments
6	o	-inspection and assessment of each experimental data set.
7	o	-grading and grouping the experimental data sets after 6.
		(2) <on the theoretical model and calculation>
8	o	-survey of the previous evaluations or theoretical analysis.
9	*	-survey of the recent progress of theoretical models or method.
10		-check of availability of the codes of the modern theory/models.
11	*	-development of new codes if necessary.
12	*	-implementation of the new codes to the code system.
13	*	-understanding of each code and codes system.
14	o	-becoming familiar with each code and codes system.
		(3) <on the initial model parameters>
15	o	-collection and survey of parameter data for the model/codes in the system.
16	o	-collection and survey of basic data for determine the input parameter values for the codes.
17	o	-deduction of parameters using new basic data.
18	o	-survey of systematic of the parameters related to neighbor nuclei.
19	o	-selection of the candidate sets of the initial input parameters.
20	o	-estimation of the variational range of each parameter.
		(4) <calculation and parameter adjustment>
21	o	-test calculation by using above parameter sets.
22	o	-comparison of the calculation with the experimental data set.
23	o	-select the most reasonable and prospective combination of parameter set and experimental data set.
24	o	-detail calculation and comparison.
25	o	-estimation of high sensitive parameters for improving the fitting.
26	o	-estimation of amount of variation for above parameters.
27	o	-parameter adjustment by repeating the varying the parameters, calculation and comparison.
28	o	-trial calculation by changing the initial parameter set if necessary.
29	o	-trial calculation by changing the calculation model if necessary.
30	o	-trial comparison by changing the experimental data set if necessary.

(continue)

Table 1 (continued)

	(5) <compromise and final judgment>
31	* -compromise between the limit of performance of the model calculation due to the incompleteness of the adopted model/parameters.
32	* -replacement of some calculation data by other cross section curves based on the experimental data, if necessary.
33	* -final judgment of degree of satisfaction on the results compared with the data requests.

o:tasks which are totally or partially supported by the proposed high level system.
*:tasks which are considered to be difficult to support.

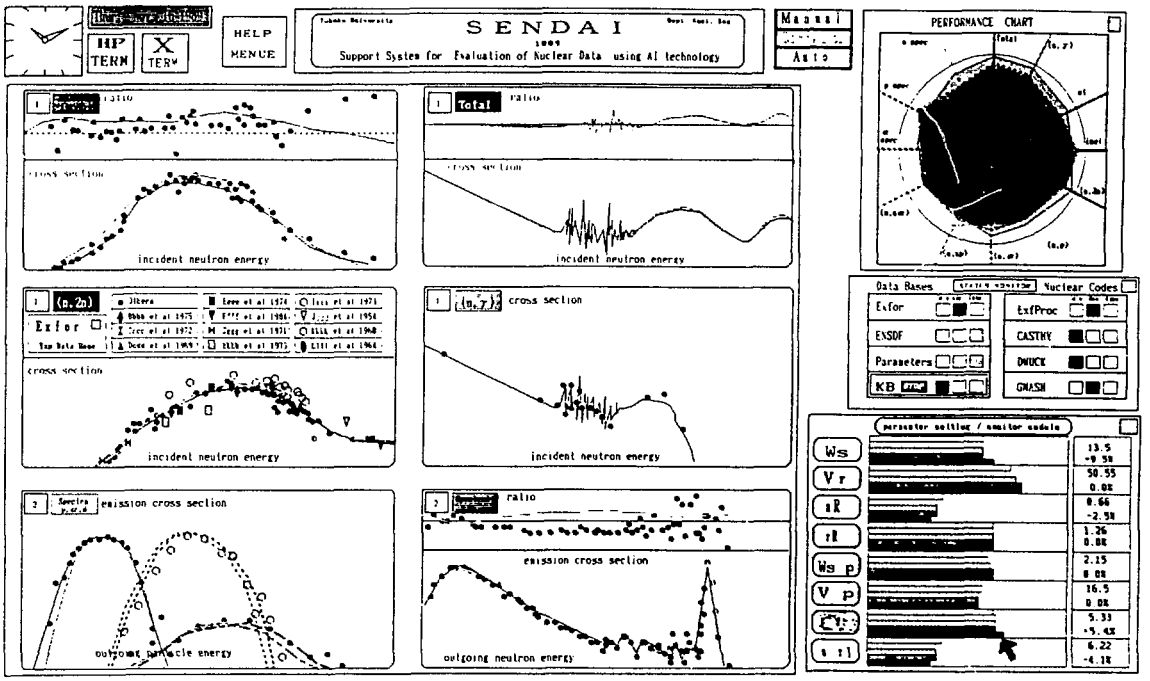

Fig. 1 An image of CRT display of the proposed advanced support system. Center and left hand side show various types of graphs for cross sections. Right lowermost corresponds to the variation of selected input parameters; the lowest bar graph of each parameter presents the most recent input parameters using sliding bar by the mouse. Right middle shows monitoring of the current processes, and the right uppermost is the radar chart for the achievement of the current evaluation compared with predetermined target.

3.6 Estimation of Reaction Model Parameters by Experimental Data and Statistical Technique

T.Kawano, Y.Kanda and Y.Uenohara*)
Department of Energy Conversion Engineering,
Kyushu Univ. Kasuga, Fukuoka 816, Japan

ABSTRACT : Optical model parameters and level density parameters for Hauser-Feshbach model calculations are estimated systematically for ^{58,60}Ni and ^{59}Co by using Bayesian method. The experimental data for estimation are neutron induced reactions (total, (n,p), (n,α), and (n,2n) cross sections, and proton, α-particle emission spectra by 14.8 MeV neutron) and proton induced reactions ((p,n) and (p, α)). The cross sections calculated with posterior parameters are improved compared with those calculated with prior ones.

1. INTRODUCTION

Evaluation of nuclear reaction cross sections needs model parameters when it is performed by means of model calculations. And evaluated values that are calculated by these parameters, should be consistent with experimental data. The calculations of optical model and Hauser-Feshbach model are utilized for evaluations, and they call for optical model parameters and level density parameters.

There are available parameter sets given by different experiments or methods as prior information. When it needs to improve these parameters in order to reproduce experimental data, it takes some trouble to determine these parameters individually, because some of these parameters correlate each other. Then Bayesian method is applied in this work.

---

*)Present address : Reactor Engineering Group,
Nuclear Engineering Laboratory, Toshiba Co.
4-1 Ukishima, Kawasaki 210, Japan

The experimental data that are usable in this estimation, are mainly the neutron induced reactions {total, (n,p), (n,α), and (n,2n)}, in addition, proton induced reactions are available as a reverse process of neutron reaction. As a result, the parameters relating to proton emission reactions can be estimated accurately.

2. CALCULATION

The methodological description and formulae for the parameter estimation are as follows.

$$P_1 = P_0 + X_0 A_0^t (A_0 X_0 A_0^t + V)^{-1} (Y - f(P_0)) \quad (1)$$

$$X_1 = X_0 - X_0 A_0^t (A_0 X_0 A_0^t + V)^{-1} A_0 X_0 \quad (2)$$

P,X : Parameter Vector and Covariance Matrix
Y,V : Experimental Data and Covariance Matrix
A : Sensitivity Matrix
0,1 : prior and posterior values

The computer code ELIESE-3[1] is used for an optical model calculation, and GNASH[2] is used for a Hauser-Feshbach model calculation. The prior parameters of the optical model for n, p and α are taken from Becchetti-Greenlees[3], Menet et al.[4] and Lemos[5], respectively. The prior level density parameters are taken from Gilbert-Cameron[6]. The target nuclides are ^{60}Ni, ^{58}Ni and ^{59}Co.

The diagonal elements of the prior covariance matrix X_0 is obtained by assuming fractional standard deviation of 30 % for level density parameters and that of 5 % for optical model parameters. The non-diagonal elements are assumed to be zero.

In this study, residual nuclei of (p,p) and (p,2p) reactions are also parameterized, because proton emission cross sections are larger than other competitive reactions for this mass range.

The used experimental data are shown in Table 1

3. RESULTS AND DISCUSSIONS

The prior and the posterior optical model parameters (OMP) are shown in Table 2. The level density parameters are shown in Fig. 1. Examples of the posterior cross sections calculated with the posterior parameters are compared with the prior cross sections in Fig. 2 to 5. In these figures, the solid lines indicate the prior cross sections, the dotted lines and dot-dashed lines are the posterior cross sections estimated by only neutron induced reactions, and by both neutron and proton induced reactions, respectively.

The OMP for neutron reaction is affected by an experimental total cross section. In this work, the measured cross sections are smaller than the calculated values using Becchetti-Greenlees's OMP. Hence, there are several ways of modification of OMP to reduce the total cross section, and, individual reaction cross sections must be consistent with experimental data. The Bayesian method reduces the total cross section by the most reasonable way of OMP modification.

As seen in Figs. 4, α emission reaction cross sections are smaller than the experimental data when Lemos's OMP is employed. A degree of modification of real part radius parameter (r_0), is large relative to that of the neutron and proton OMPs. The posterior cross sections of ^{58}Ni(n,α) agrees with the measured cross sections. The posterior α-spectra of ^{58,60}Ni(n,α), however, are somewhat different from measured data by Grimes et al.[7]. So, there is still room for discussion whether Lemos's OMP suits the prior one.

A little modification of the proton OMP is found when experimental data of neutron induced reactions are only used for estimation. When proton induced reaction data are taken into account, the radius parameters of both real and imaginary part tend to change largely. Hence, it may show that proton induced experimental data are usable for estimation of proton OMP. However, a number of available data is small, and it is difficult to make sure of these experimental data.

The level density parameters, a, almost become larger than the prior values, as seen in Fig. 1.

In Fig. 2, the prior cross section of ^{60}Ni(n,p) is larger than the measured cross sections. In order to reduce this calculated cross section, the *a* of ^{60}Co (a residual nucleus of ^{60}Ni(n,p) reaction) should be decreased and/or that of ^{60}Ni (a residual nucleus of ^{60}Ni(n,n'), which is competition reaction of (n,p)) should be increased. On the other hand, the *a* of ^{60}Co is affected by neutron induced reactions of ^{59}Co, because ^{60}Co is a compound nucleus of this reaction. Then the *a* of ^{60}Co is not decided by ^{60}Ni(n,p) data only.

In this estimation, valid experimental data are neutron and proton induced reaction of ^{58,60}Ni and ^{59}Co. If some *a* is influential in a number of different reactions, the *a* may be estimated reasonably, because these parameters are estimated by many grounds. On the contrary, if the *a* is used at a few stage, it is not decisive. For example, the *a* of ^{56}Fe is a residual nucleus of ^{60}Ni(n,nα), and it is influential in a cross section of ^{60}Ni(n,α). But this *a* is not modified, because this cross section is not used in this estimation.

Copper is a compound nucleus of proton induced reaction of Ni and its residual nuclei of neutron emission reactions. Then the level density parameters of Cu are estimated by proton reactions only, and they change flexibly relative to the other parameters.

4. CONCLUSION

The optical model parameters and the level density parameters for Mn to Cu are estimated systematically by applying Bayesian method. The optical model parameters are estimated within the several percent of prior ones when neutron experimental data are only used, and they are changed relatively large when proton experimental data are included. The overestimations are observed in the level density parameters for Ni and Co.

The estimated parameters improved the calculated cross sections. However, it is still difficult to state that the proton data are valid for the parameter estimation.

REFERENCES

[1] Igarashi,S. : JAERI-1224(1972).
[2] Young,P.G., Arthur,E.D. : LA-6947(1977)
[3] Becchetti,Jr.,F.F., Greenlees,G.W. :
Phys. Rev., 182,1190(1969).
[4] Menet,J.J.H. et al. : Phys. Rev., C4,1114(1971).
[5] Lemos,O.F. : Orsay Report, Series A, No.136(1972).
[6] Gilbert,A., Cameron, A.G.M. :
Canad. J. of Phys., 43,1446(1965).
[7] Grimes,S.M. et al. : Phys. Rev., C17,508(1978).

Table 1 Target nuclei, reactions (neutron or proton induced), and their residual nuclei.
Underlined reactions are used in the present work.

Target / Residual	^{60}Ni	^{58}Ni	^{59}Co
^{61}Cu	(p,γ)		
^{60}Cu	<u>(p,n)</u>		
^{59}Cu	(p,2n)	(p,γ)	
^{58}Cu		(p,n)	
^{57}Cu		(p,2n)	
^{61}Ni	(n,γ)		
^{60}Ni	(n,n')(p,p')		(p,γ)
^{59}Ni	(n,2n)(p,np)	(n,γ)	(p,n)
^{58}Ni		(n,n')(p,p')	(p,2n)
^{57}Ni		<u>(n,2n)(p,np)</u>	
^{60}Co	<u>(n,p)</u> <u>*Psp</u>		(n,γ)
^{59}Co	(n,np)		(n,n')(p,p')
^{58}Co		<u>(n,p)</u> <u>*Psp</u>	<u>(n,2n)</u>(p,np)
^{57}Co	(p,α)	(n,np)<u>(p,2p)</u>	
^{56}Co	(p,nα)		
^{55}Co		<u>(p,α)</u>	
^{54}Co		(p,nα)	
^{59}Fe			<u>(n,p)</u>
^{58}Fe			(n,np)
^{57}Fe	(n,α) <u>*αsp</u>		
^{56}Fe	(n,nα)		(p,α)
^{55}Fe		<u>(n,α)</u> <u>*αsp</u>	(p,nα)
^{54}Fe		(n,nα)	
^{56}Mn			<u>(n,α)</u>
^{55}Mn			(n,nα)
Total	<u>(n,total)</u>	(n,total)	<u>(n,total)</u>

*Psp, *αsp : Proton, α-Particle Emission Spectrum at 14.8MeV Neutron Energy

Table 2 Optical model parameters for neutron, proton, and α-particle. The upper row of posterior parameter: estimated by neutron-induced experimental data and the lower row: proton-induced experimental data are included.

	Neutron		Proton		α-Particle	
Parameter	Prior	Posterior	Prior	Posterior	Prior	Posterior
Real Potential V_0	56.3 [MeV]	51.65	49.9	47.03	193.0	189.07
		53.27		48.20		189.01
Imaginary Potential W_s *)	13.0 [MeV]	11.05	4.20	4.080	21.0	20.85
		10.54		4.172		20.88
Real Radius r_0	1.17 [fm]	1.206	1.16	1.161	1.37	1.489
		1.177		1.337		1.438
Imaginary Radius r_s *)	1.26 [fm]	1.118	1.37	1.437	1.37	1.274
		1.161		1.149		1.302

*) Volume absorption type for α-Potential.

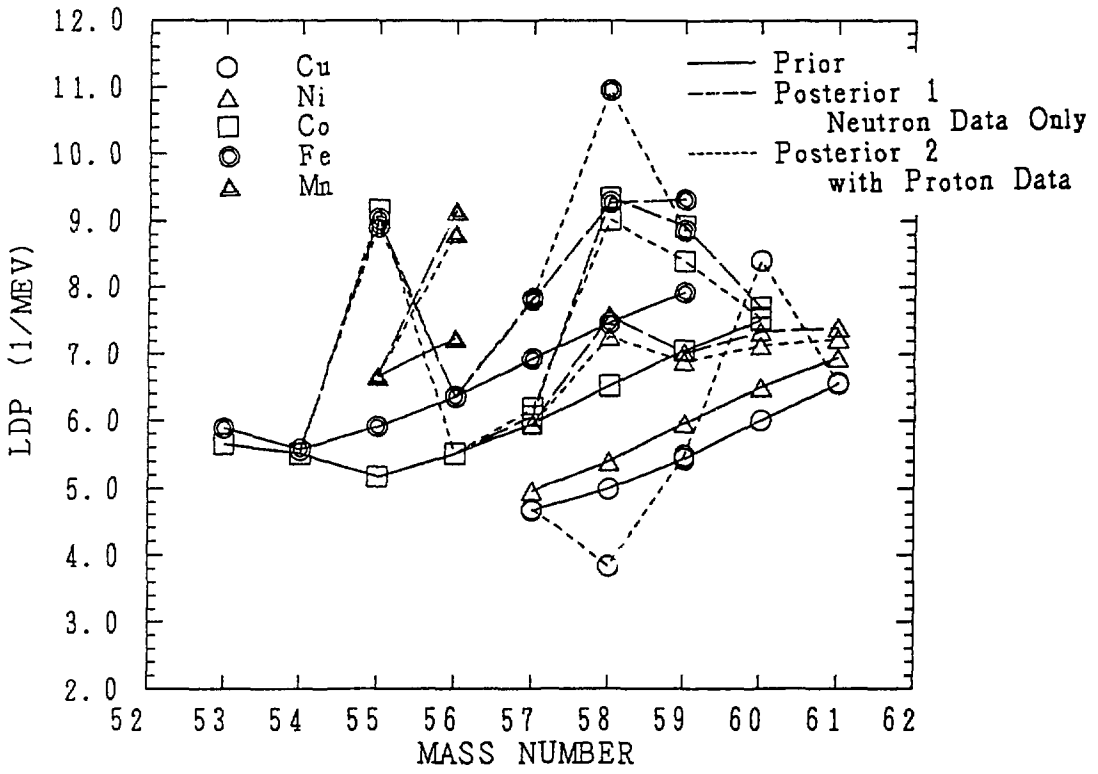

Fig. 1 Level density parameters for Mn, Fe, Co, and Ni.
Prior parameters
Posterior parameters
(used neutron induced reactions)
Posterior parameters
(used neutron and proton induced reactions)

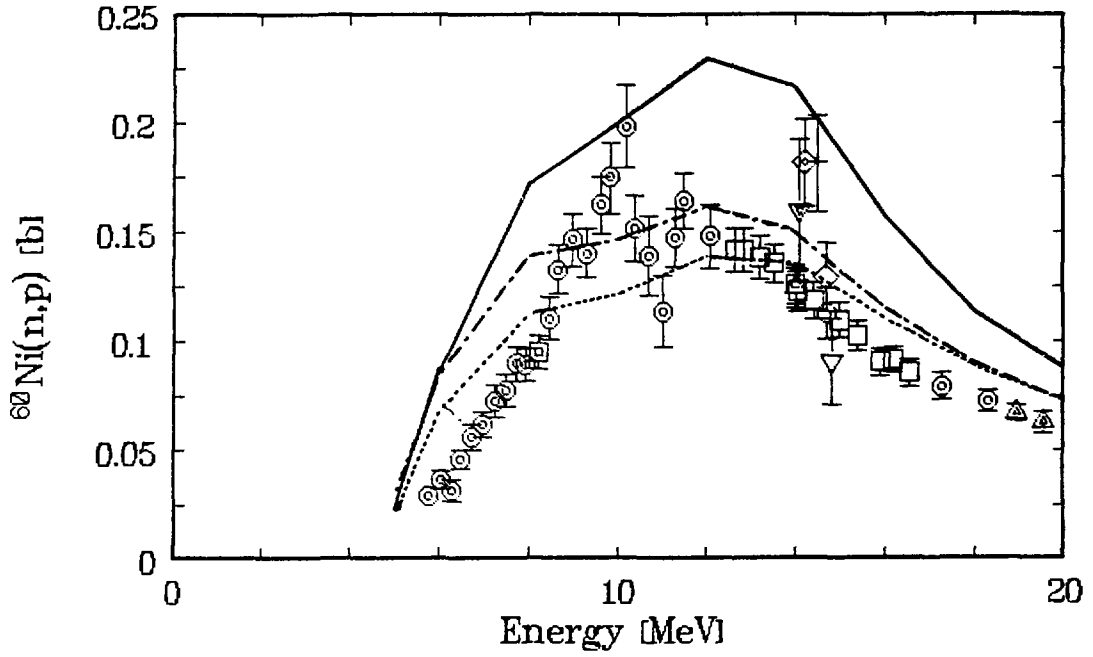

Fig. 2 Comparison of calculated ^{60}Ni(n,p) reaction cross sections with the experimenta data

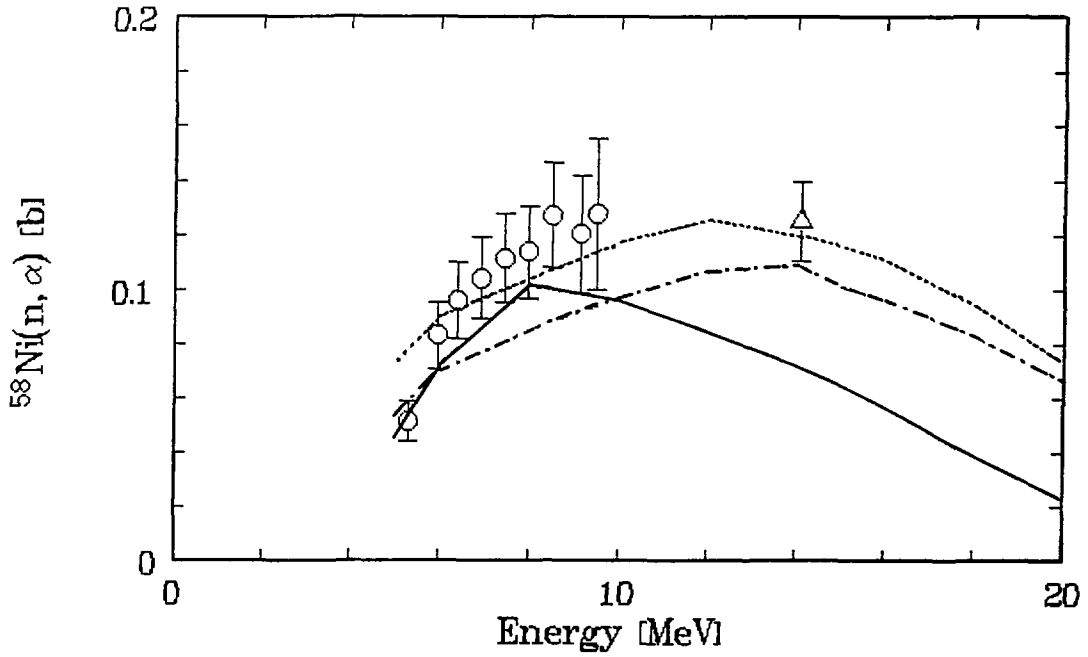

Fig. 3 Comparison of calculated ^{58}Ni(n,α) reaction cross sections with the experimental data

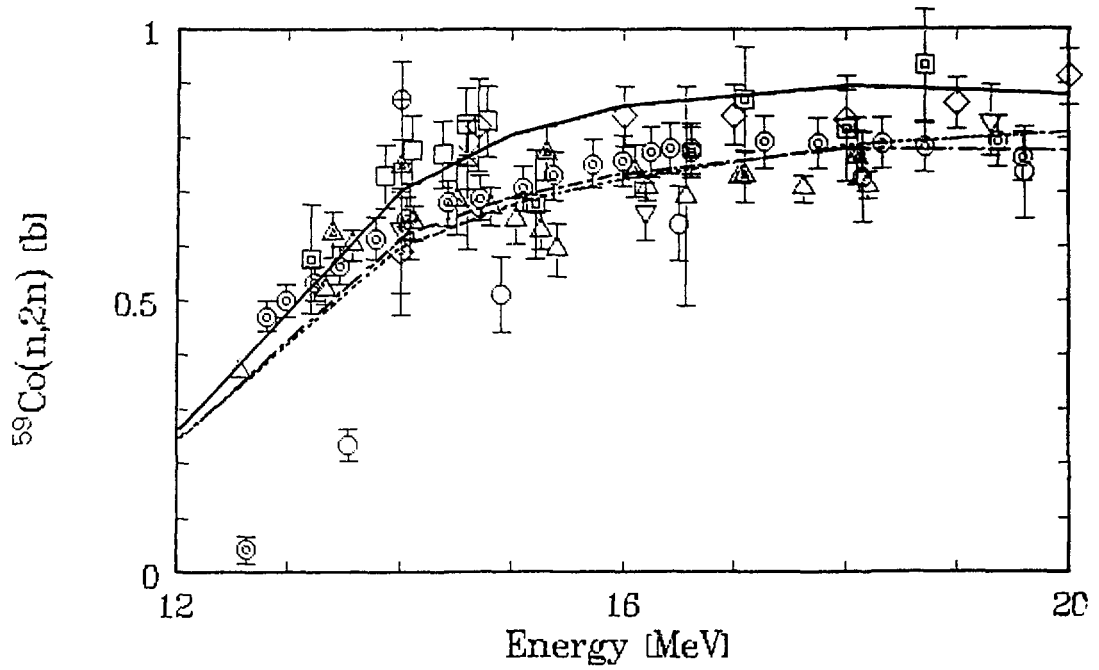

Fig. 4 Comparison of calculated $^{59}Co(n,2n)$ reaction cross sections with the experimental data

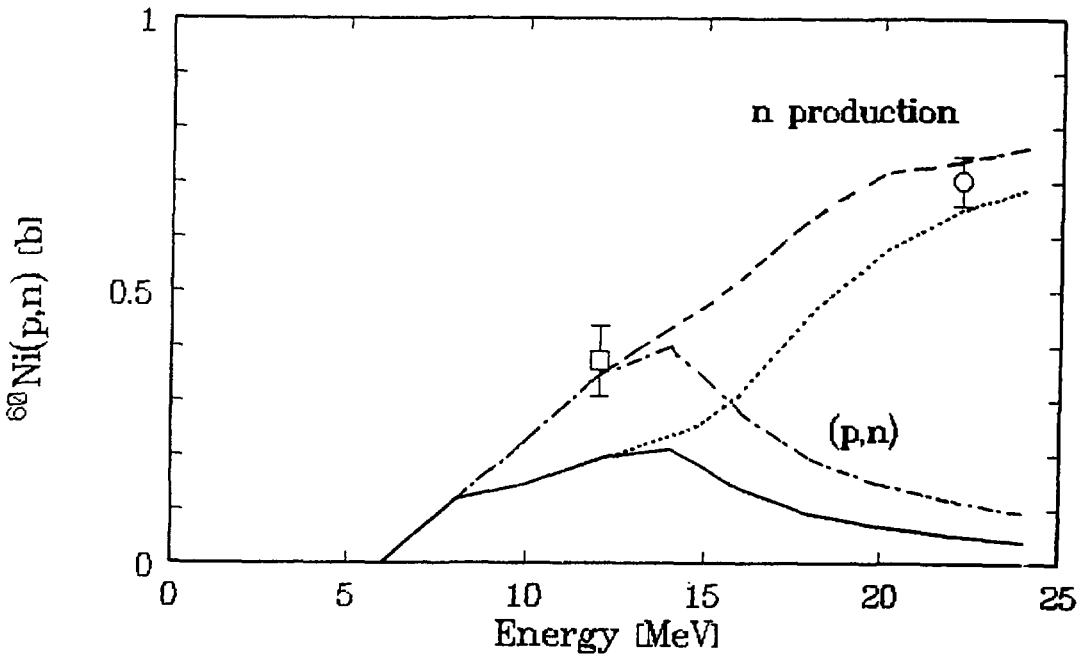

Fig. 5 Comparison of calculated $^{60}Ni(p,n)$ reaction cross sections with the experimental data

3.7 Measurement of Formation Cross Sections for Short-Lived Nuclei Produced by 14 MeV Neutrons (III)

T. Yamada, A. Osa, M. Shibata, K. Kawade, H. Yamamoto,

T. Katoh, T. Iida* and A. Takahashi*

Department of Nuclear Engineering, Nagoya University

*Department of Nuclear Engineering, Osaka University

Neutron activation cross sections of short-lived nuclei with half-lives between 0.5 and 20 m have been measured at neutron energy of 13.4 to 14.9 MeV by the activation method for 14 reactions; $^{26}Mg(n,\alpha),(n,n'p)$, $^{28}Si(n,p)$, $^{30}Si(n,\alpha),(n,n'p)$, $^{37}Cl(n,p)$, $^{52}Cr(n,p)$, $^{53}Cr(n,p),(n,n'p)$, $^{66}Zn(n,p)$, $^{67}Zn(n,n'p)$, $^{68}Zn(n,p)^{m}$, and $^{113}In(n,2n)^{m,g}$.

1. Introduction

Neutron activation cross section data around 14 MeV have become important from the viewpoint of fusion reactor technology, especially for calculation on radiation damage, nuclear transmutation, induced activity and so on.

Cross sections for the reactions leading to short-lived nuclei with half-lives between 0.5 and 20 m were measured by the activation method.

2. Experiment and results

Experiments were performed at the Intense 14-MeV-Neutron Source Facility (OKTAVIAN) of Osaka University. For the activation of samples, pneumatic tubes were set at 6 directions (between 0° and 155°) for the incident deuteron beam direction. The distances between the T-target and the irradiation points were 15 cm. The induced activities were measured with two Ge detectors (12 %, 16 %) at an equivalent distance of 5 cm. The amount of activities of some positron emitting nuclei which emitted nearly no gamma-rays was obtained from the intensities of the annihilation gamma-rays of 511 keV. The annihilation radiations were measured by

setting the irradiated samples between two 10 mm thick acrylic plates. An effect due to β^+ broadening in the absorber was examined by using the 514 keV gamma-ray from ^{85}Sr. The effect of broadening can be neglected for the positron energies less than 3 MeV, within the experimental errors of about 1 %. The effective reaction energy of incident neutrons were determined by the Zr/Nb method.[1] The errors are estimated to be less than 50 keV. The neutron flux at the sample points was monitored by using two aluminum foils (purity: 99.2 %, 1 cm x 1 cm x 0.2 mm). The reference reaction for the flux measurement was the $^{27}Al(n,p)^{27}Mg(9.46\ min)$ reaction, which was determined referring to the standard $^{27}Al(n,\alpha)^{24}Na$ reaction (ENDF/B-V). Separated isotopes or natural samples were used for irradiation. The samples were between 30 and 100 mg in weight (size: 1 cm x 1 cm).

In Table 1, measured reactions and associated data[2] of the half-life ($T_{1/2}$), the γ-ray energy (E_γ), the absolute intensity in photons per disintegration (I_γ) are listed together with the Q values and the fractional contribution of low energy neutrons (FC) discussed later.

Corrections were made for time fluctuation of the neutron flux, thickness of samples, self absorption of γ-ray, sum-peak effect of γ-ray, interfering reaction and contribution of low energy neutrons below 10 MeV (FC). The FC was calculated by

$$FC=\sum_{E_i=0}^{E_c}\phi(E_i)\cdot\sigma(E_i)\ /\{\sum_{E_i}^{E_c}\phi(E_i)\cdot\sigma(E_i)+\phi_x\cdot\sigma_x\}$$

where $\phi(E_i)$ and ϕ_x are neutron flux at E_i and E_x, respectively, and $\sigma(E_i)$ and σ_x are cross sections at E_i and E_x. A cut-off energy (E_c) was set on 10 MeV. Here we assumed that neutrons above E_c are nearly monoenergetic with an energy E_x. A correction factor (f_s) for the FC is given by $f_s=\{1-FC(n,x)\}/\{1-FC(n,\alpha)\}$, where $FC(n,x)$ and $FC(n,\alpha)$ are the FCs for the (n,x) reaction of interest and the standard $^{27}Al(n,\alpha)^{24}Na$ reaction, respectively. The details of the corrections are described elsewhere.[3]

The total errors (δ_t) were derived by combining the experimental error (δ_e) and the error of nuclear data (δ_r) in quadratic:

$$\delta_t^2 = \delta_e^2 + \delta_r^2 .$$

Estimated major sources of the errors are listed in Table 2. When good counting statistics were achieved, accuracies of the obtained cross sections were around 5 %. The results are listed in Table 3 and some of the results are shown in Fig. 1.

The authors wish to express their sincere thanks to Prof. K. Sumita for his support to this work and Messrs. H. Sugimoto, M. Datemichi and S. Yoshida for the operation of the OKTAVIAN accelerator. We wish to thank Prof. N. Yamamuro for his calculations of cross sections. We also thank Dr. S. Igarashi, Dr. T. Asami and Dr. T. Nakagawa of the JAERI Nuclear Data Center. This work was performed under the contract between Nagoya University and Japan Atomic Energy Research Institute (JAERI). Mrs. Mori is also thanked for her typing the manuscript.

References

(1) Lewis, V.E., Zieba, K.J.: Nucl. Instr. and Meth. 174(1980)141.

(2) Browne, E., Firestone, R.B., Shirley, V.S.: "Table of Radioactive Isotopes" John Wiley & Sons, New York (1986).

(3) Katoh, T., Kawade, K. and Yamamoto, H., JAERI-M 89-083 (1989)(in Japanese).

Table 1 Reactions and decay parameters

Reaction[a]	$T_{1/2}$	E_γ(keV)	I_γ(%)	Q(MeV)[b]	FC(%)[c]
$^{26}Mg(n,\alpha)^{23}Ne$	37.6s	439.9	32.9(10)	-5.41	2.1
$(n,np)^{25}Na$	59.6 s	389.7	12.65(22)	-14.144	0
$^{28}Si(n,p)^{28}Al$	2.241m	1779.0	100	-3.86	4.4
$^{30}Si(n,\alpha)^{27}Mg$	9.46m	843.8	73(1)	-4.20	1.9
$(n,np)^{29}Al$	6.56m	1273.4	91.3	-13.51	0
$^{37}Cl(n,p)^{37}S$	5.05m	3104.0	94.2(6)	-4.08	3.2
$^{52}Cr(n,p)^{52}V$	3.75m	1434.1	100	-3.19	3.2
$^{53}Cr(n,p)^{53}V$	1.61m	1006.2	90(2)	-2.65	0.8
$(n,np)^{52}V$	3.75m	1434.1	100(1)	-11.13	0
$^{66}Zn(n,p)^{66}Cu$	5.10m	1039.4	7.4(1.8)	-1.86	3.0
$^{67}Zn(n,np)^{66}Cu$	5.10m	1039.4	7.4(1.8)	-8.91	0
$^{68}Zn(n,p)^{68m}Cu$	3.75m	525.7	75(15)	-4.56	0.2
$^{113}In(n,2n)^{112m}In$	20.9m	155.5	12.8(4)	-9.59	0
$(n,2n)^{112g}In$	14.4m	511[d]	44	-9.44	0
$^{27}Al(n,\alpha)^{24}Na$[e]	14.959h	1368.6	99.994(3)	-3.13	2.1
$^{27}Al(n,p)^{27}Mg$	9.46m	843.8	73(1)	-1.83	6.2

a) (n,np) means [(n,d)+(n,n'p)+(n,pn)].

b) Q(n,n'p) is given here. Q(n,d)=Q(n,n'p)+2.225 MeV.

c) Fractional contribution of low energy neutrons, see the text.

d) Annihilation γ-ray from β^+.

e) Standard reaction (ENDF/B-V) used in this work.

Table 2 Principal sources of uncertainty in the measured cross sections

Experimental error (δ_e)	
Source of error	Uncertainty (%)
Counting statistics	0.5 ~ 40
Sample mass including purity	0.1
Neutron flux fluctuation	<0.1
Gamma-peak area evaluation	0.5
Detector efficiency	1.5($E_\gamma \geq 300$ keV), 3(300 ~ 80 keV), 5($E_\gamma < 80$ keV)
Efficiency calibration at 0.5 and 5 cm	1.0
Correction for true coincidence sum	<0.5
Correction for random coincidence sum	<0.5
Correction for sample thickness	0.5
Correction for self-absorption of γ-rays	0 ~ 1.0
Correction for low energy neutrons	30% of corrected amount
Secondary reference cross section for $^{27}Al(n,p)^{27}Mg$	0.5 (only statistics)

Error of nuclear data (δ_r)	
Source of error	Uncertainty (%)
Reference cross section for $^{27}Al(n,\alpha)^{24}Na$(ENDF/B-V)	3.0
Absolute γ-ray intensity	0 ~ 24
Half-life	0 ~ 5

Table 3 Activation cross-sections

Energy	$^{26}Mg(n,\alpha)^{23}Ne$	$^{26}Mg(n,n'p)^{25}Na$	$^{28}Si(n,p)^{28}Al$
14.87 MeV	29.7 ± 2.3 mb	3.9 ± 1.1 mb	219 ± 12 mb
14.64	32.6 ± 3.4	4.2 ± 1.7	229 ± 12
14.35	32.2 ± 3.2	3.0 ± 1.5	229 ± 12
14.02	29.2 ± 2.2	2.5 ± 1.8	254 ± 13
13.70	26.7 ± 3.4		265 ± 14
13.40	32.7 ± 2.7		254 ± 12

Energy	$^{30}Si(n,\alpha)^{27}Mg$	$^{30}Si(n,n'p)^{29}Al$	$^{37}Cl(n,p)^{37}S$
14.87 MeV	63.6 ± 2.6 mb	6.1 ± 0.4 mb	24.8 ± 2.3 mb
14.64	68.4 ± 3.3	5.8 ± 0.7	22.3 ± 2.0
14.35	64.3 ± 3.0	4.9 ± 0.5	22.4 ± 1.9
14.02	60.2 ± 3.1	3.8 ± 0.5	24.9 ± 3.0
13.70	60.0 ± 2.9	0.8 ± 0.3	25.9 ± 2.8
13.40	66.4 ± 2.7	0.4 ± 0.2	25.6 ± 2.2

Energy	$^{52}Cr(n,p)^{52}V$	$^{53}Cr(n,p)^{53}V$	$^{53}Cr(n,n'p)^{52}V$
14.87 MeV	74.4 ± 3.6 mb	42.8 ± 2.5 mb	13.2 ± 1.0 mb
14.64	73.6 ± 3.5	45.6 ± 3.2	9.5 ± 1.2
14.35	79.1 ± 3.6	44.4 ± 3.3	6.8 ± 1.0
14.02	80.4 ± 3.6	41.2 ± 3.2	4.9 ± 1.0
13.70	78.3 ± 3.7	44.9 ± 3.6	3.7 ± 0.9
13.40	85.6 ± 3.8	39.4 ± 2.1	2.7 ± 0.4

Energy	$^{66}Zn(n,p)^{66}Cu$	$^{67}Zn(n,n'p)^{66}Cu$	$^{68}Zn(n,p)^{68m}Cu$
14.87 MeV	74 ± 19 mb	35.9 ± 9.1 mb	5.5 ± 1.3 mb
14.64	70 ± 18	30.9 ± 8.5	4.6 ± 1.0
14.35	67 ± 17	24.9 ± 6.8	4.9 ± 1.1
14.02	72 ± 18	19.0 ± 5.0	4.2 ± 0.9
13.70	62 ± 19	12.9 ± 4.2	4.2 ± 0.9
13.40	74 ± 18	11.5 ± 3.3	3.0 ± 0.7

Energy	$^{113}In(n,2n)^{112m}In$	$^{113}In(n,2n)^{112g}In$
14.87 MeV	1.32 ± 0.12 b	279 ± 38 mb
14.64	1.31 ± 0.09	293 ± 34
14.35	1.25 ± 0.10	275 ± 26
14.02	1.19 ± 0.09	297 ± 34
13.70	1.24 ± 0.10	286 ± 29
13.40	1.00 ± 0.08	293 ± 31

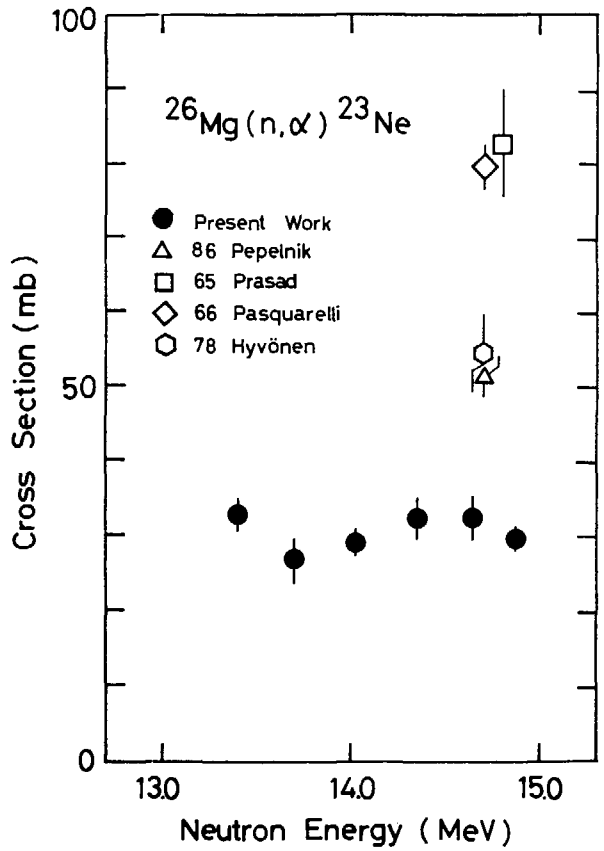

Fig. 1(1) Cross sections of $^{26}Mg(n,\alpha)^{23}Ne$

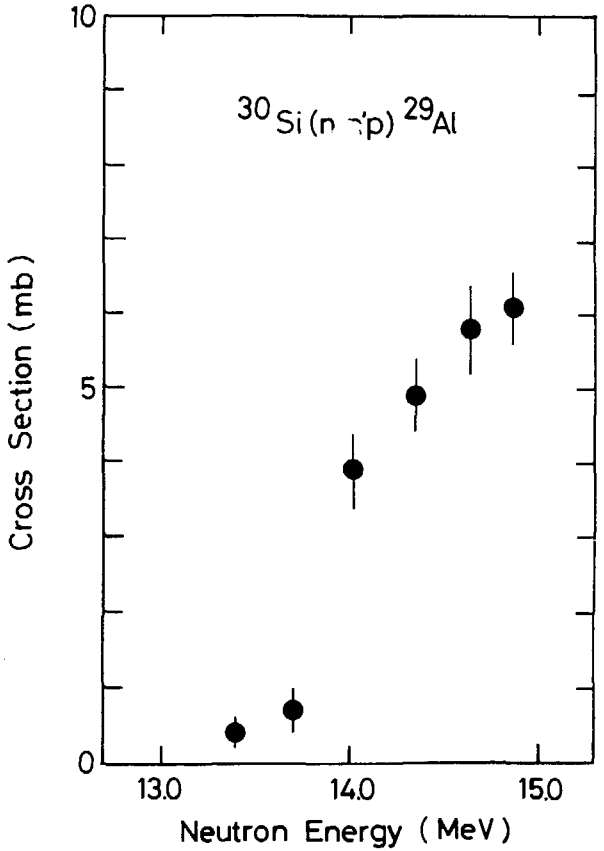

Fig. 1(2) Cross sections of $^{30}Si(n,n'p)^{29}Al$

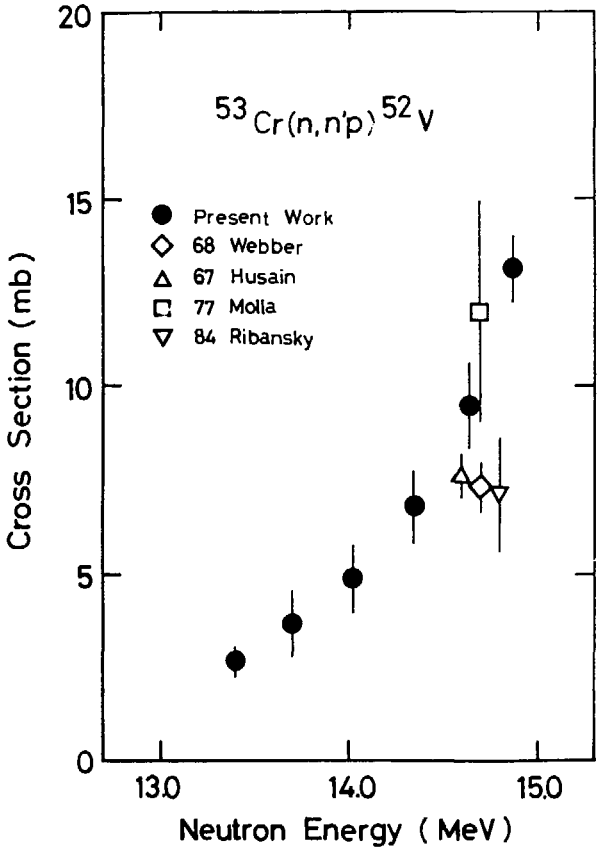

Fig. 1(3) Cross sections of $^{53}Cr(n,n'p)^{52}V$

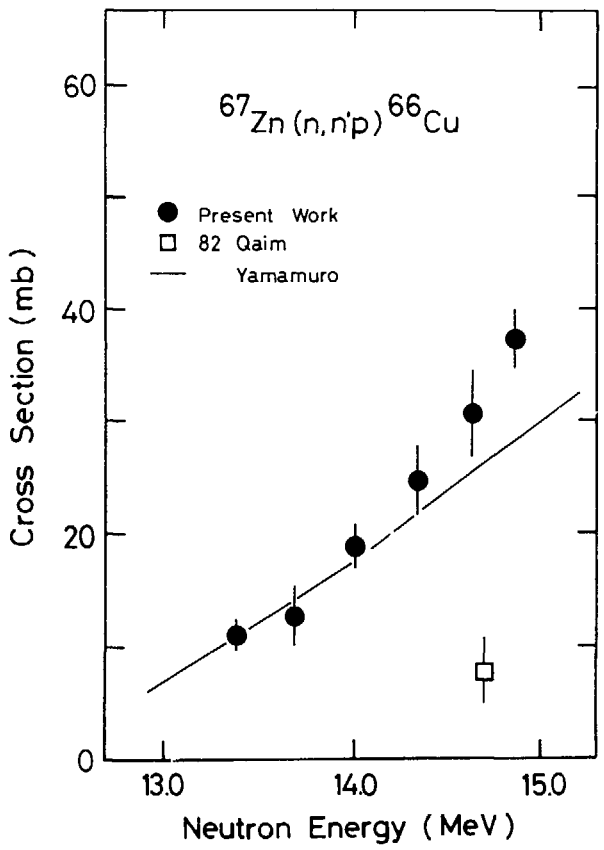

Fig. 1(4) Cross sections of $^{67}Zn(n,n'p)^{66}Cu$

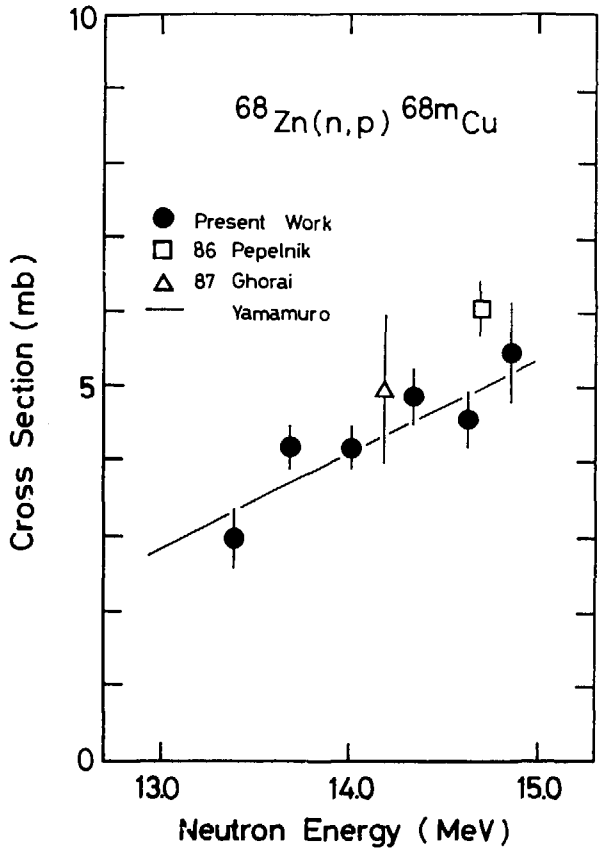

Fig. 1(5) Cross sections of $^{68}Zn(n,p)^{68m}Cu$

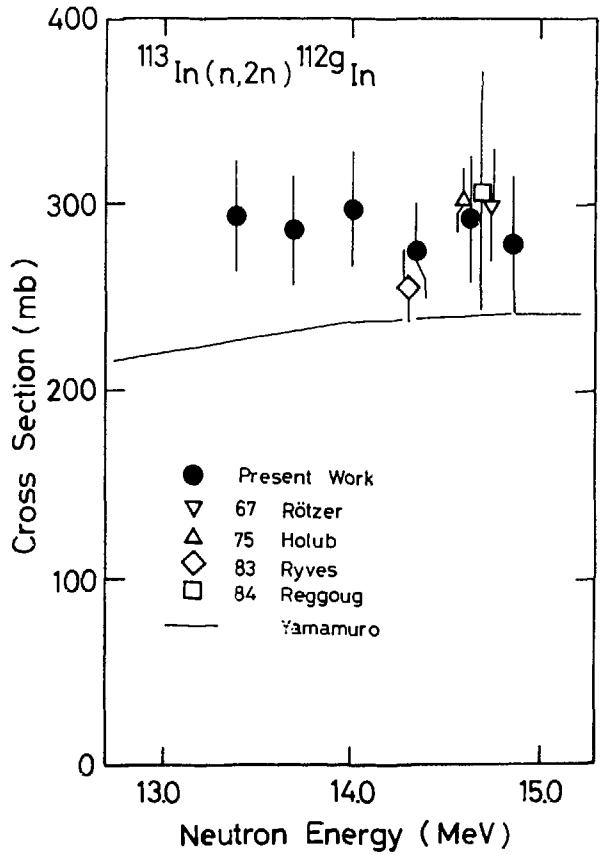

Fig. 1(6) Cross sections of $^{113}In(n,2n)^{112g}In$

3.8 Measurement of Production Cross Sections of Short-Lived Nuclei by Cyclic Activation Using a Pulsed Neutron Source

Junji Yamamoto, Jun Datemichi, Takeshi Kanaoka
Takuzo Takayama, Akito Takahashi and Kenji Sumita

Department of Nuclear Engineering, Osaka University
2-1 Yamada-oka, Suita 565

Cyclic activation using a pulsed neutron source is a very efficient technique to measure short-lived radioactivities. The technique has been utilized for the purpose of elemental analysis. In the present paper, the potentiality was discussed for application of this technique to the cross section measurements concerning the production of short-lived radioisotopes by neutron-induced reactions. An advanced system to measure energy spectra of emission γ-rays simultaneously with decays of the γ-rays was tested for the radioisotopes with half lives up to a few seconds. Some experimental results are presented with respect to the induced activities with half lives from 20.2 ms to 7.1 s.

1. Introduction

In the measurements of short-lived radioactivities by neutron-induced reactions, a currently used technique is to detect the activities after the transfer of samples using such a mechanical system as pneumatic tubes between a neutron source and a radiation detector. The induced activities by D-T fusion neutrons are one of the recent interests.[1),(2)] By means of the current technique, high accuracies have been attained for the measurements of activities with half lives more than a few seconds. As for the shorter half lives, fast pneumatic systems have been developed and cyclic activation has been carried out to compensate low counting statistics.[3),(4)] In the technique of mechanical sample transfer, however, the intense neutron sources for the irradiation with high

neutron fluxes are naturally required due to fast decays of radioisotopes during the sample transfer.

A technique of cyclic activation using a pulsed neutron source[5] was tested in order to apply to the measurements of production cross sections for the radioisotopes with half lives up to a few seconds. In the technique the radiation detector started counting immediately without the sample transfer after the neutron irradiation. Both of energy spectra and decays of the γ-rays emitted from the sample were measured. It was necessary to repeat the irradiation and the measurement with short period of times, since the radioactivity by one neutron burst was not sufficient in the counting statistics of the detector. At present the technique is available to only the isotopes that are emitting γ-rays. The outline of the experimental procedure and some of the results are mentioned in the following sections.

2. Experimental procedure and apparatus

The neutron source was an accelerator which generated 14 MeV neutrons at a TiT target bombarded with a D^+ beam. The duration of a neutron burst(Ti) and the period between the bursts(T) were controlled by making the D^+ beam pulsed. Taking account of the induced activities with the half lives from 1 ms to 10 s, we designed a beam controller so as to change continuously Ti and T from 0.3 ms to 54.3 m and 0.6 ms to 108.6 m, respectively. The controller was interlocked with the system of counting the induced activities, so that Ti and T as well as counting period(Tm) could be precisely determined and repeated. In Fig.2 that shows the electronics block diagram, a unit of "Timer for pulsed beam" corresponds to the controller.

Figure 1 illustrates the experimental arrangement. The induced activities were measured with a Ge detector, which was located at a distance of 75 cm from the sample. The detector was fairly well shielded against the direct neutrons from the source by making use of iron, concrete, polyethylene, lead and so on. A distance between the source and the sample was 15 cm. The samples were either disks or hollow cylinders; the size was 45 mm in diameter and 2 mm in thickness for the disk and 30 mm in outer diameter, 1 mm in thickness and 70 mm in length for the hollow cylinder. As shown in Fig.2 Tm was divided into

several sub-periods for the decay measurements and pulse height spectra(PHS's) were recorded in the respective segments. The counting duration for one segment could be chosen within the range from 1 ms to 900 s. Irradiating the sample and counting the activity were repeated in the same way and the PHS data were added in each segment to the previous ones until the statistical accuracies of the observed γ-rays became sufficient.

3. Results and discussion

Figure 3 shows the PHS's of γ-rays produced in ^{16}N by $^{16}O(n,p)$ reaction. The 6.13 and 7.12 MeV γ-rays, the emission probabilities of which are 68.8 and 5.0 %, respectively, decayed with the half life of 7.13 s. Due to the low counting statistics, only the 6.13 MeV γ-rays were sharply observable in the PHS's measured with the interval of 1 s. Ti and T were respectively 20 and 93 s, and the number of cyclic activation was 330. The decay curve of the 6.13 MeV γ-rays is shown in Fig.4, where the experimental data are fitted with a solid line by the least squares method. With the γ-ray energy and the half life we could confirm the radioisotope to be measured. The result for the shorter half life can be seen in Figs.5 and 6. The 472 keV γ-rays with the half life of 20.2 ms are the transition in the isomer of ^{24}Na by $^{27}Al(n,\alpha)$ reaction. Ti, T and the number of repetition were 80, 285 ms and 100,000, respectively.

Table 1 lists the production cross sections of ^{207m}Pb. The probable reactions are $^{208}Pb(n,2n)$ and $^{207}Pb(n,n')$ due to the use of natural lead as the sample. The half life is 0.81 s and the energies of emission γ-rays are 1.064 and 0.57 MeV which are the transitions from 1.633 MeV excitation to ground state via 0.57 MeV excitation. The two values, that were obtained from two measurements using the different samples and the different modes of pulsed neutrons, were compared with the previous results[6],[7]. Since natural lead was also used for the γ-ray shielding around the detector, a large source of error resulted from the background γ-rays with the same energies as those of γ-rays from the lead sample. In the case I the cyclic rate was extremely low, so that the large error was attributed to the poor counting statistics.

The advantages of the present method are:

(1)High accuracies can be attained with regard to the periods of the irradiation and the measurement because the cyclic activation is made electrically rather than mechanically.
(2)A low-output source of pulsed neutrons is available.
(3)Due to a long distance between the sample and the detector, the uncertainty of solid angle is small in estimating a detector efficiency and it is expected at the detector to reduce pileup signals of the γ-rays from the sample.
(4)Neutron energy spectrum of the irradiating source can be analyzed by means of a TOF technique using the pulsed neutrons.

The shortcomings are as follows.

(1)Background level is high due to the activation of the detector and the shield.
(2)Background run is necessary without the samples. The same condition of neutron source as that in the foreground run is required, so that the conditioning is important with respect to the stability and the reproductivity of the pulsed neutrons.
(3)The background γ-rays, that are induced by the neutrons scattered at the sample, cannot be eliminated.
(4)The massive samples are necessary.

4. Concluding remarks

The potentiality of cyclic activation using a pulsed neutron source was investigated for the application to the cross section measurements of short-lived radioisotopes. The present technique was confirmed to be applicable to the half lives from 20.2 ms to 7.1 s. In the calculations of detector responses for counting the activities, it was estimated that the responses of the cyclic activation for the half lives up to 5 s were greater than those of the conventional technique using the intense neutron sources.

References:

(1) Katoh,T., Kawade,K. and Yamamoto,H.:"Measurement of Activation Cross Sections", JAERI-M 89-083 (1989).

(2) Ikeda,Y., Konno,C., Nakamura,T., Oishi,K., Kawade,K., Yamamoto,H. and Katoh,T.:"Systematic Measurement of Neutron Activation Cross Section at Energy Range from 13.3 to 15.0 MeV Using FNS Facility". Proc. the Int'l Conf. on Nuclear Data for Science and Technology, JAERI, 257(1989).

(3) Pepelnik,R., Anders,B. and Bahal,B.M.:"Measurements of 14 MeV Neutron Activation Cross Sections", Proc. the Int'l Conf. on Nuclear Data for Basic and Applied Science, vol.1, 221(Santa Fe, New Mexico, 1985).

(4) Amemiya,S., Itoh,M., Kawade,K., Yamamoto,H. and Katoh,T.: J. Nucl. Sci. Technol., 11(9), 395(1974).

(5) Givens,W.W., Mills,Jr.W.R. and Caldwell,R.L.:"Activation Analysis Using a Pulsed Neutron Source and Cyclic counting", Pacific Conf. Chemistry and Spectroscopy(ACS, Anaheim, California, 1967).

(6) Amemiya,S., Bhoraskar,V.N., Katoh,K. and Katoh,T.: J. Nucl. Sci. Technol., 18(5), 323(1981).

(7) Janczyszyn,L. and Gorski,L.: J. Radioanal. Chem., 14, 201(1973).

Table 1 Production cross sections of ^{207m}Pb

	I	II
T	13.2 s	500ns
Ti	3.0	3
Tw	0.2	400
Tm	0.8	68
sample	45-mm ϕ	O.D. 30-mm, L. 70-mm
	2-mm thick	I.D. 28-mm
cross section	1010± 520 mb	860± 55 mb
previous results	930± 80 mb[6]	
	480± 70 mb[7]	

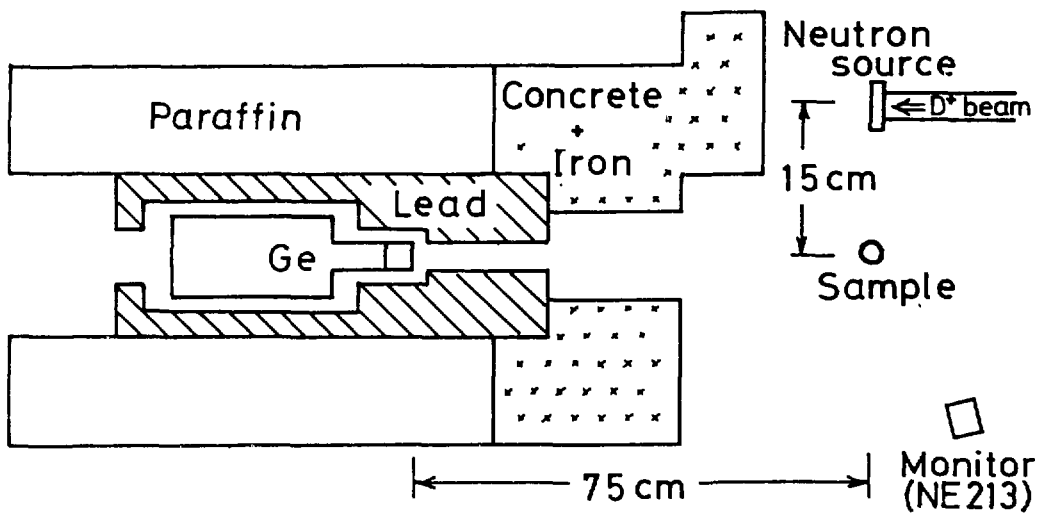

Fig. 1 Experimental arrangement

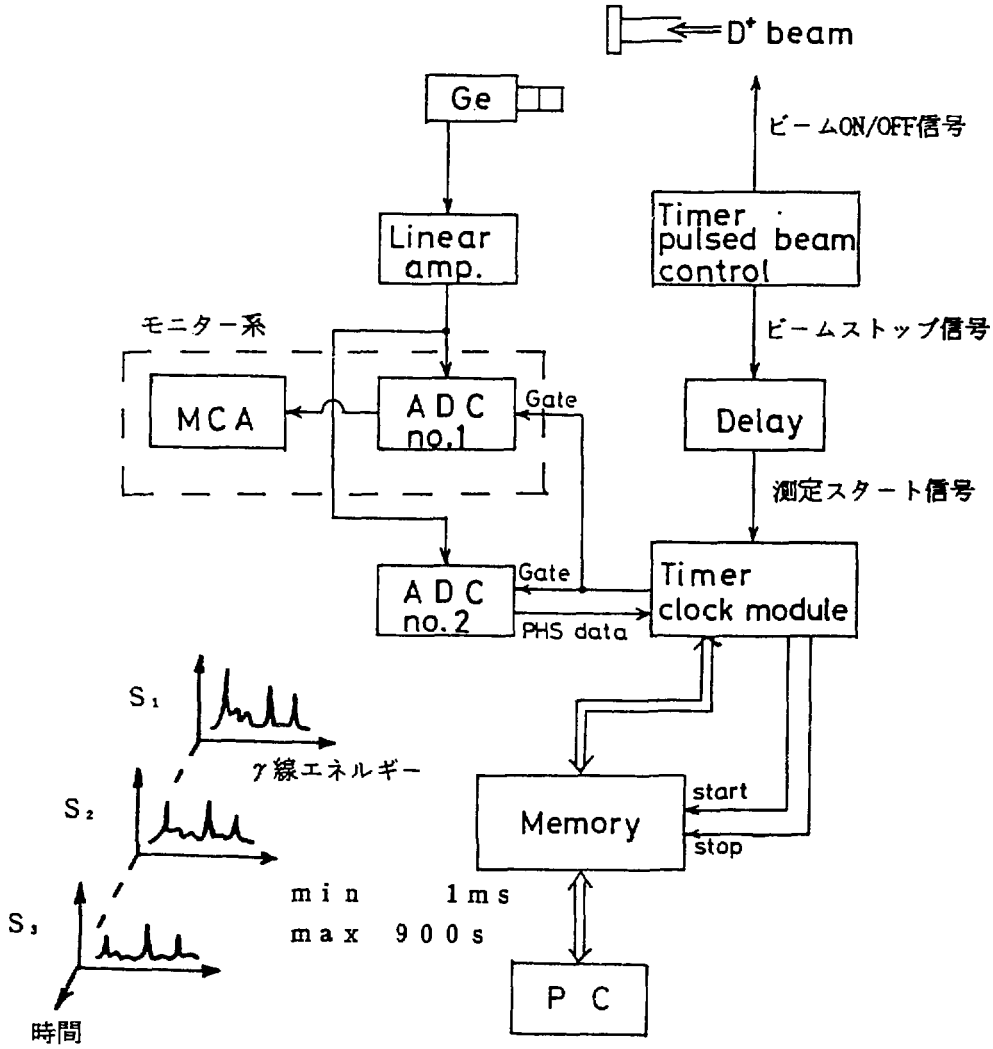

Fig. 2 Electronics block diagram

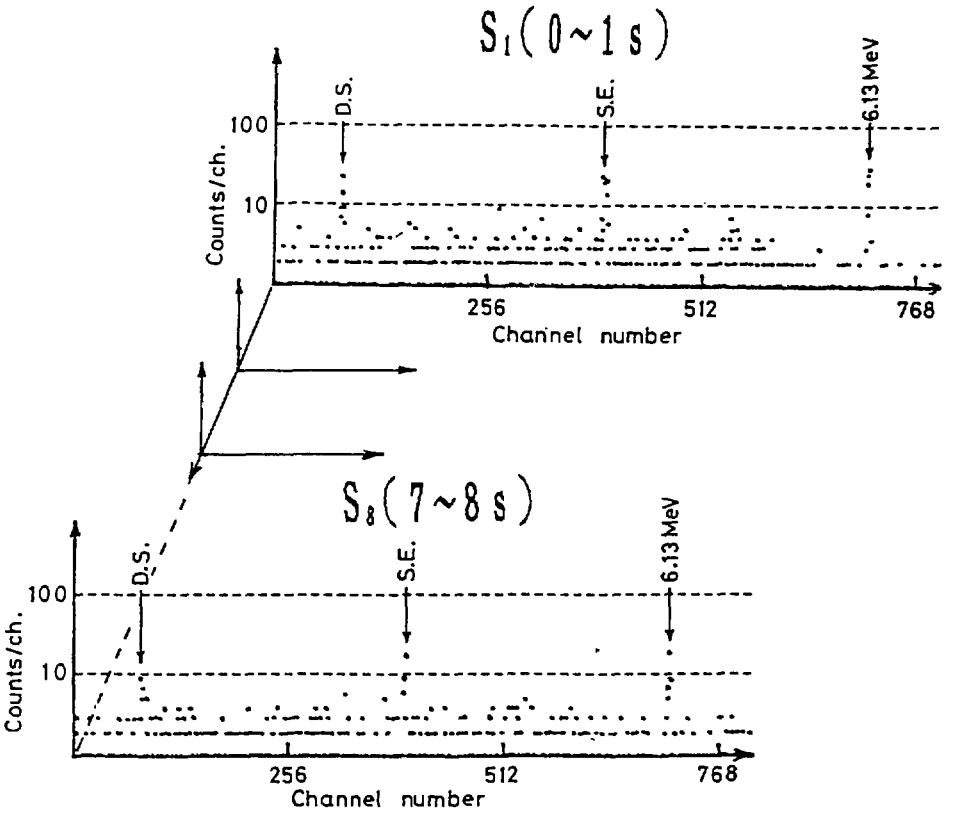

Fig. 3 Pulse height spectra of γ-rays from sample of water

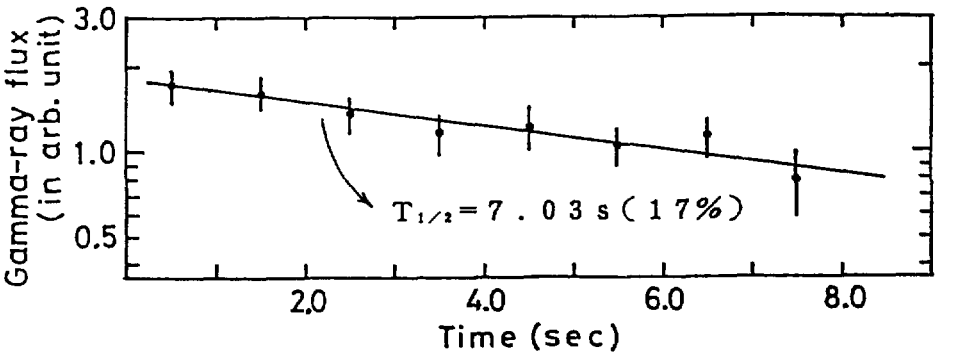

Fig. 4 Decay of 6.13 MeV γ-rays emitted from ^{16}N

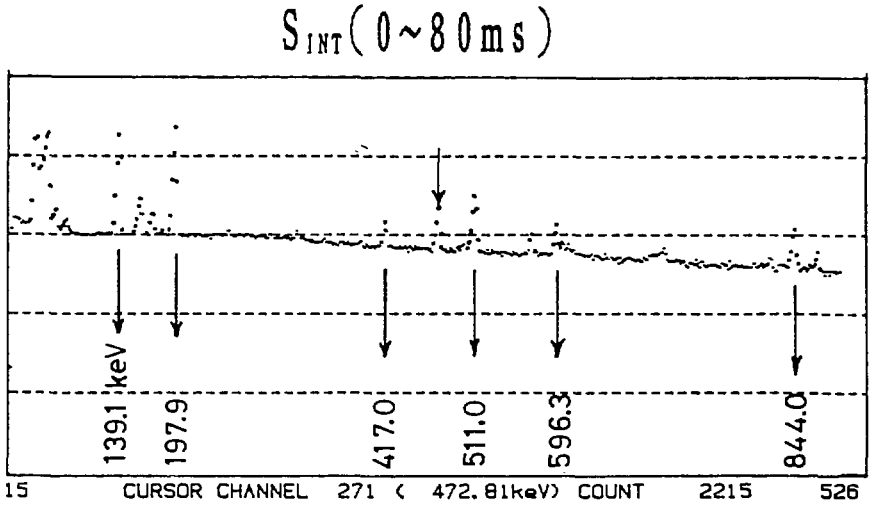

Fig. 5 Pulse height spectrum of γ-rays from aluminum sample

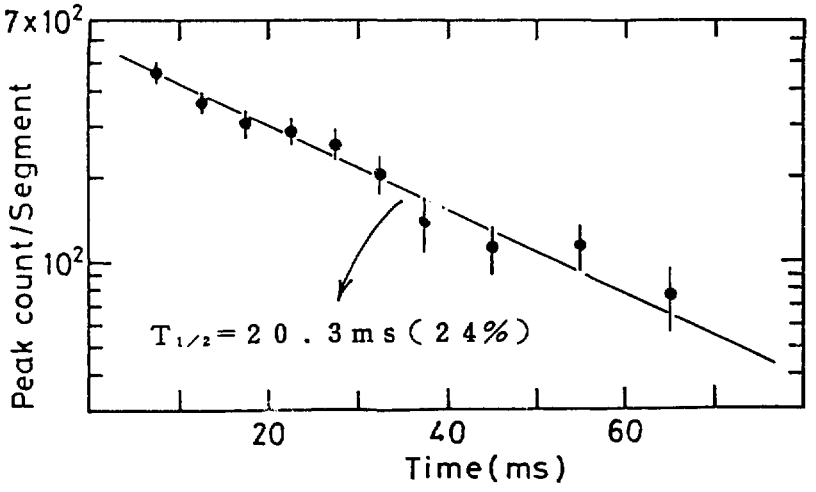

Fig. 6 Decay of 472 keV γ-rays in $^{27}Al(n,\alpha)^{24m}Na$ activity

3.9 Secondary Charged Particle Spectrometer Based on Two-Dimensional E-TOF Analysis

Seiji Ogino and Akito Takahashi

Department of Nuclear Engineering, Osaka University

This paper shows a spectrometer technique to measure energy spectral data for neutron-induced secondary charged particles -i.e. proton and alpha-particle, etc.- by analyzing energy (E) and time-of-flight(TOF) of charged particles in the two-dimensional E-TOF domain. Major problem in the measurement is how to decrease the backgrounds caused by neutron-induced charged particles and gamma-rays produced in the detector itself and from surrounding structural materials of the spectrometer. By reducing these backgrounds, energy spectra of neutron-induced secondary charged particles could be measured.

INTRODUCTION

Energy spectral data for neutron-induced secondary charged particles are basic nuclear data for the estimation of the damage and nuclear heating in materials under high fluence fast neutron fields. In general, the measurement of secondary charged particle spectrum is difficult, and experimental data are therefore scarce. Most of the available data have been measured with a quadrupole spectrometer based on the E-$\triangle$E analysis[1]. With this spectrometer intense neutron-source and complicated technique are required to attain sufficient energy resolution and particle separation . New spectrometer techniques based on other principles are therefore expected. The spectrometer based on two-dimensional E-TOF analysis is one of the

expected techniques to measure neutron-induced secondary charged particles.

EXPERIMENT

Between the secondary charged particle energy(E) and the time-of-flight(TOF), we have the following relation

$$T = L\sqrt{M/2E}$$

where M and E are the mass and the energy of secondary charged particle, and T and L are the time-of-flight and the length between a sample and a detector. Two-dimensional E-TOF distribution of charged particles are shown in Fig. 1. If the spectrometer has sufficient energy resolution, good time resolution, enough counting rate and no backgrounds, we can detect the charged particles on the curved lines in Fig. 1. Actually, the separation of charged particles becomes difficult due to insufficiencies of energy resolution, time resolution, and counting rate.

Some of backgrounds may pile up on the curved lines. In other words, one of merits of the two-dimensional analysis is due to the fact that the background counts out of the curved lines can be automatically rejected.

After the separation of charged particles , we can obtain the energy spectrum data by integrating proper counts along the TOF-axis or the E(pulse height)-axis.

The block diagram of the measuring system is shown in Fig. 2. The system measures energy(E) and time-of-flight(TOF) gated with two parallel pulse shape discrimination circuits.

Schematic view of the E-TOF experiment is shown in Fig. 3. Shielding materials and a charged particle detector are arranged in a 1mϕ × 1m long vacuum vessel. An aluminum sample with 15μm thick × 7cm diam. was used. A CsI(Tl) scintillator with 2mm thick × 5cm diam. was used for the charged particle detector. An NE102 plastic scintillator was used for test runs; in this case the pulse shape discrimination was impossible, so that the NE102 plastic scintillator was unsuitablefor charged particle detector in the field of relatively high level gamma-rays field.

The flight path between the sample and the detector was 53cm.

Major problem in the measurement is how to decrease the backgrounds caused by neutron-induced charged particles and gamma-rays produced in the detector itself and from surrounding structural materials of the spectrometer.

Reduction of the gamma-ray background was successfully achieved by the pulse shape discrimination technique by analyzing rise-time(RT) distributions of signals induced by charged particles and gamma-rays. The results for two-dimensional energy(E)-rise time(RT) distributions before and after separating gamma-rays are shown in Fig. 4 and Fig. 5. These results show drastic reduction of gamma-rays-origined backgrounds.

Reduction of the charged particle background can be achieved by setting the detector as far from the neutron-source as possible and by using the shadow bar shield between the neutron source and the detector; however, such arrangement also reduces the solid angle for detecting charged particles from the sample. In order to seek an optimum set of mixed materials and their arrengement, many background runs have been tried. The two-dimensional RT-TOF analyses have been also used for the optimization.

These results show that the reduction of backgrounds with the iron + lead shielding set was optimum.

RESULT AND DISCUSSION

An example of measured results of two-dimensional E-TOF distribution is shown in Fig. 6, where ①, a straight line, shows signals induced by direct 14MeV neutrons, ② shows a curve of signals induced by protons and ③ shows a curve of signals induced by alpha particles. Further reduction of back grounds is required to measure clearly the alpha particle trajectory curve.

Rejecting proton-signals by the pulse shape discrimination, the measurement for α-particles was made, and the measured result (foreground) is shown in Fig. 7.

Signals induced by direct 14MeV neutrons ①, a curve of signals by the $^{27}Al(n, \alpha)$ alpha-particles ② and a curve of signals by neutron-induced alpha-particles at the vacuum wall ③ are shown in Fig. 7. These results show that the rejection of proton signals is

necessary to measure clearly the alpha-particle trajectory curve.

Proton energy spectrum from the Al(n,xp) reaction deduced from the TOF channel (integrated along the pulse height axis) is shown in Fig. 8 compared with the Grimes' experiment[2]; the present result gives a harder spectrum.

Proton energy spectrum from the Al(n,xp) reaction obtained from the pulse height channel (integrated along the TOF axis) is shown in Fig. 9 compared with the Grimes' experiment ; the present result gives a relatively good agreement, though slight difference exist. Maybe, short flight path and insufficient energy resolution caused the difference between the two spectra. We can say that the energy spectrum data obtained from the pulse height channel was better than that deduced from the TOF channel.

Alpha-particle energy spectrum(fore-grounds) from the Al(n,xα) reaction deduced from the TOF channel is shown in Fig. 10 compared with the Grimes' experiment. The present α-spectrum is harder than that of Grimes.

CONCLUSION

In order to measure energy spectrum data for neutron-induced secondary charged particles , a new type spectrometer based on the two-dimensional E-TOF analysis has been tested. Major problem of reducing backgrounds was almost solved by the pulse shape discrimination technique after many background test runs. The present system can be applied to measure cross sections and spectra of secondary charged particles, calibrating with the recoil proton peaks in the E-TOF domain by the elastic scatterings of hydrogen in a thin polyethylene sample at various angles between the incident and the particle-out-going directions.

Reference

1) Grimes, S. M., et al.; Phys. Rev., C17 508 (1978)

2) Grimes, S. M., et al.; NSE:62, 187-194(1977)

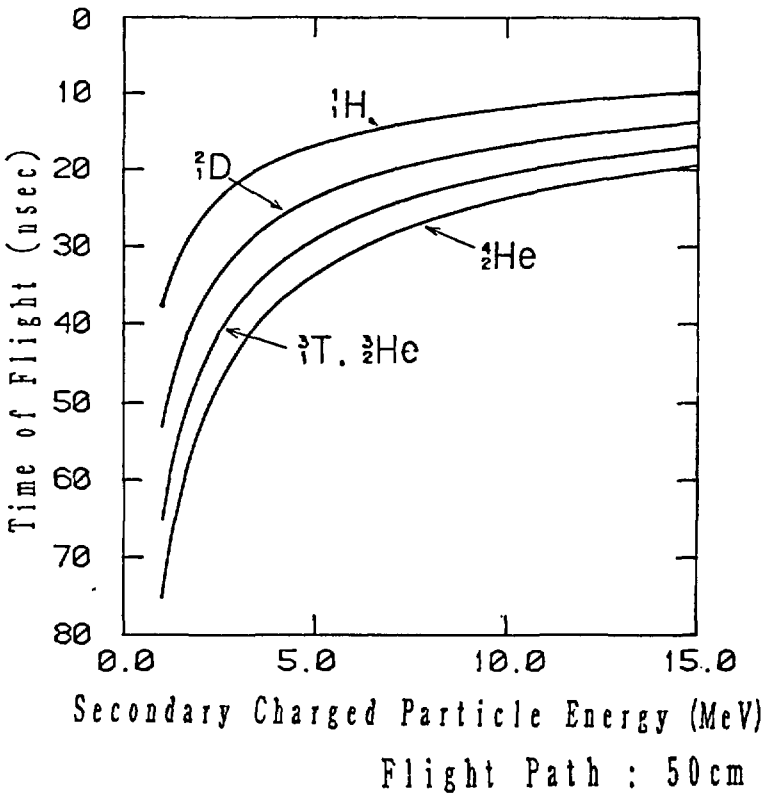

Fig. 1 Two-dimensional distribution of secondary charged particles

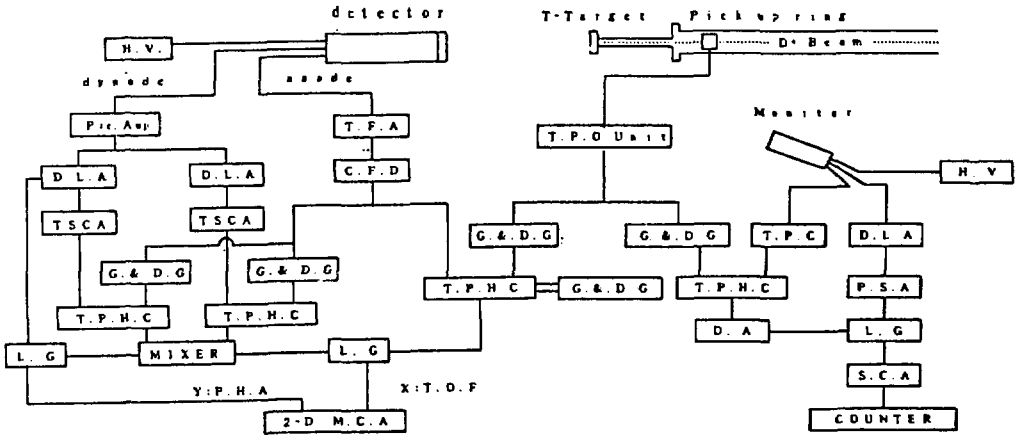

Fig. 2 The block diagram of the measuring system

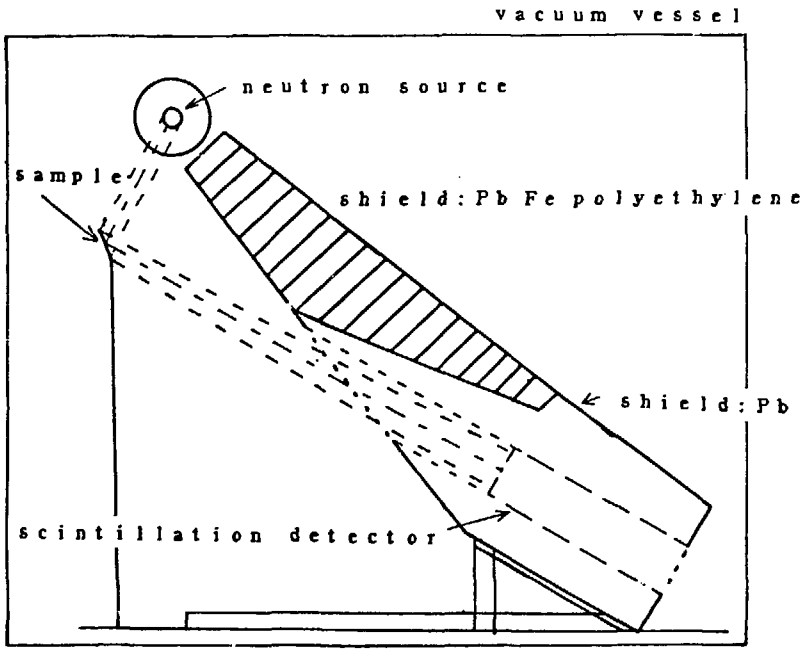

Fig. 3 Schematic view of E-TOF experiment

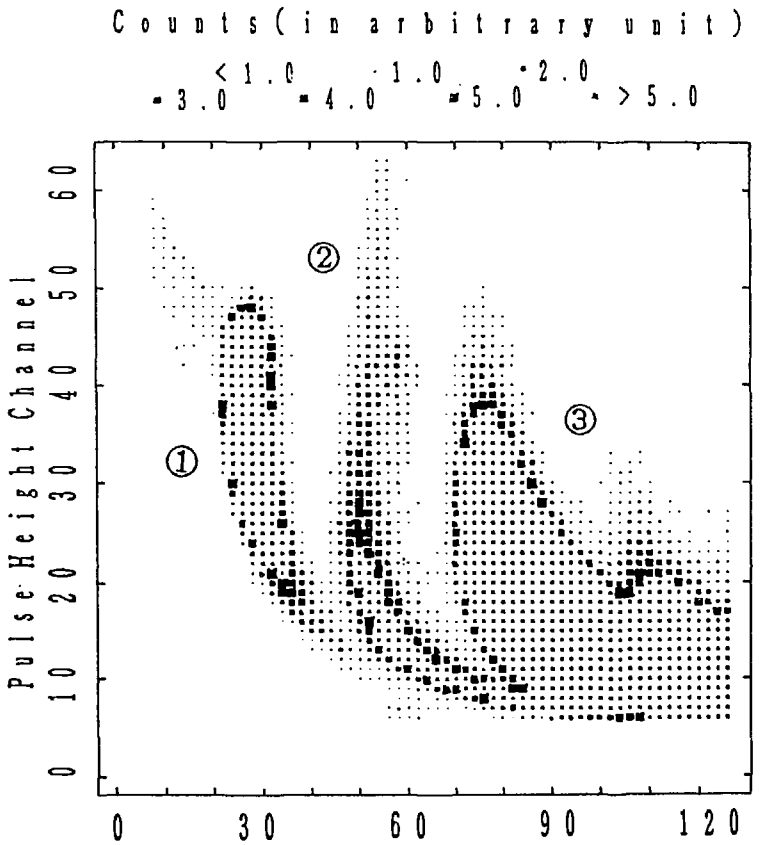

Fig. 4 Two-dimensional energy (E) - rise time (RT) distribution for charged particles and gamma rays: ① shows alpha-particles, ② protons, and ③ gamma rays

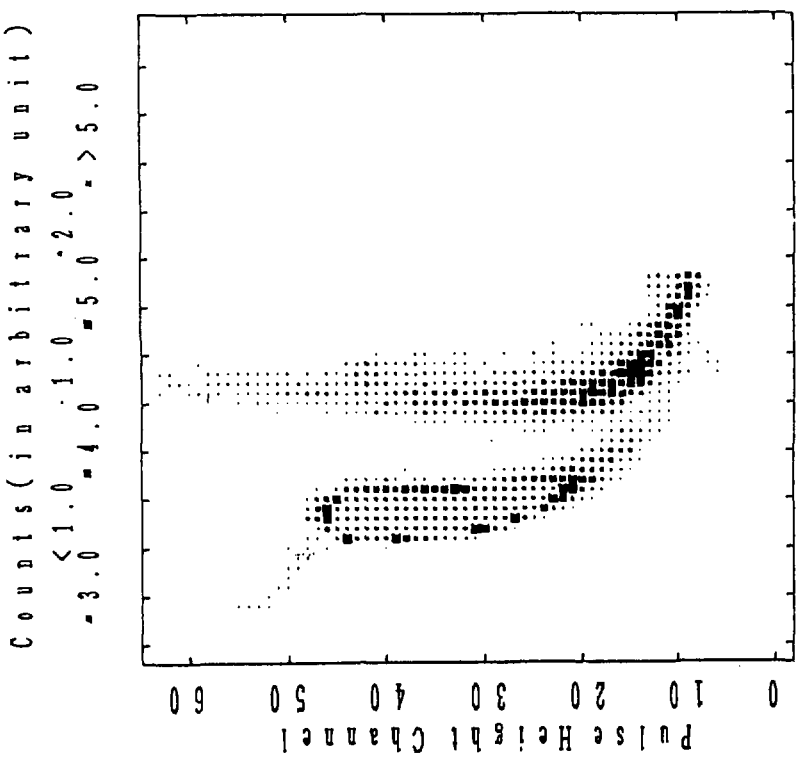

Fig. 5 Two-dimensiona energy (E) - rise time (RT) distribution after the pulse shape discrimination: this shows that reduction of gamma rays could be achieved.

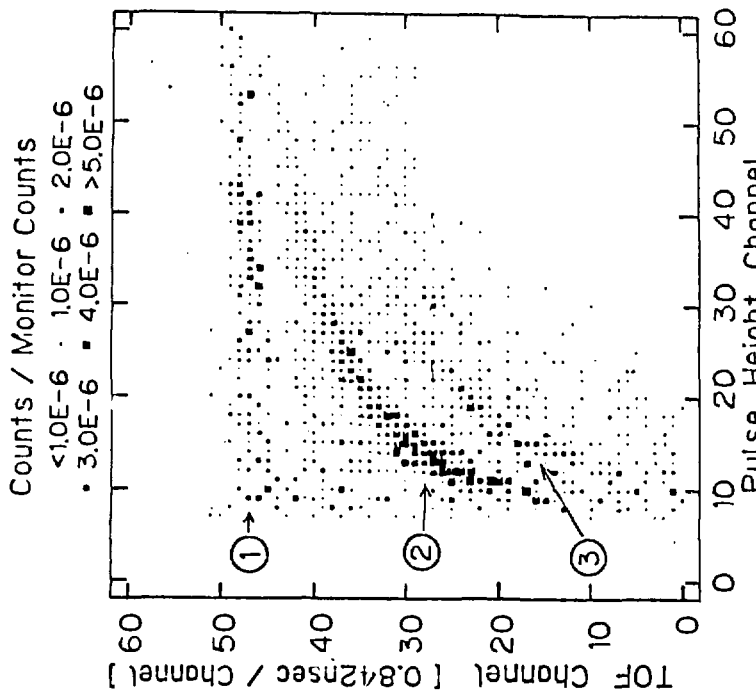

Fig. 6 Two-dimensional E-TOF distribution for secondary charged particles, for Al sample with E =14 MeV: ① shows the direct 14 MeV neutron-induced protons and alpha-particles, ② the $^{27}Al(n,p)$ protons and ③ the $^{27}Al(n,\alpha)$ alpha-particles.

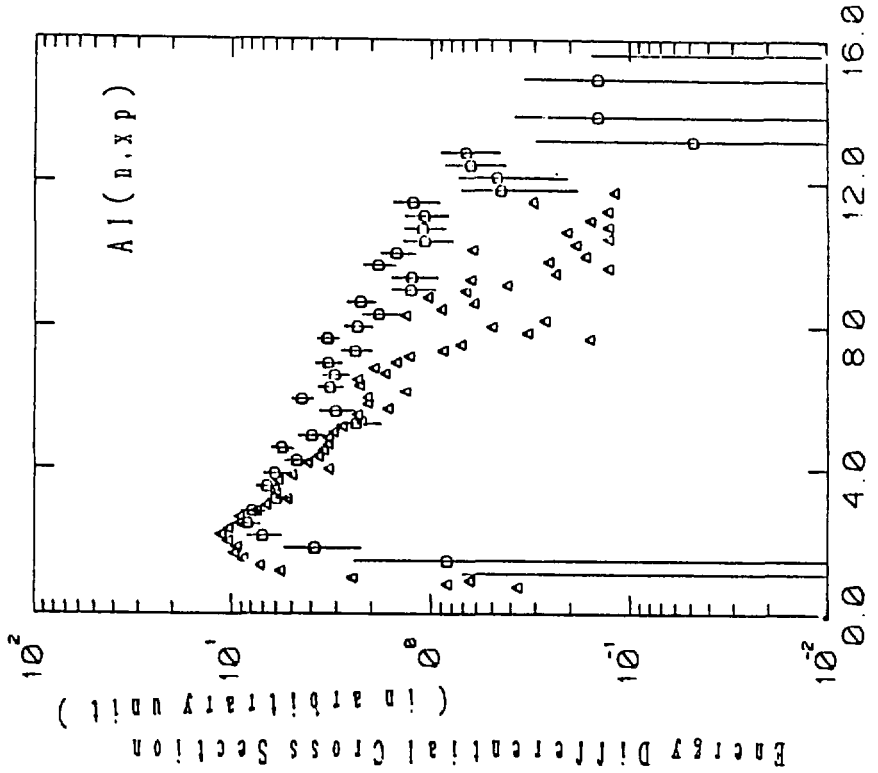

Fig. 8 Proton energy spectra from $^{27}Al(n,xp)$ with E_n=14 MeV at 90°: the present experiment based on T.O.F. channel (open circles) and Grimes' experiment for E_n=15 MeV at 75° (triangles)

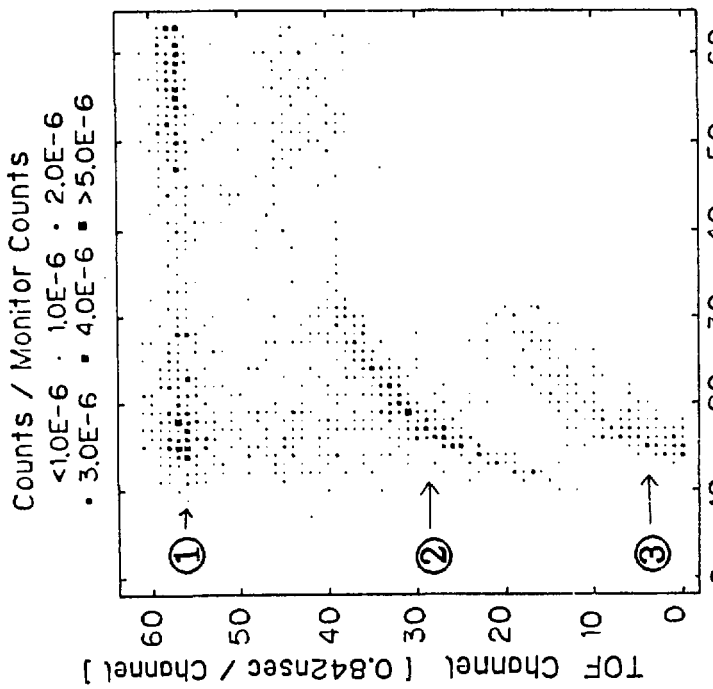

Fig. 7 Two-dimensional E-TOF distribution (fore grounds) for secondary alpha-particles for Al sample with E_n=14 MeV after the reduction of protons and gamma rays by the pulse shape discrimination

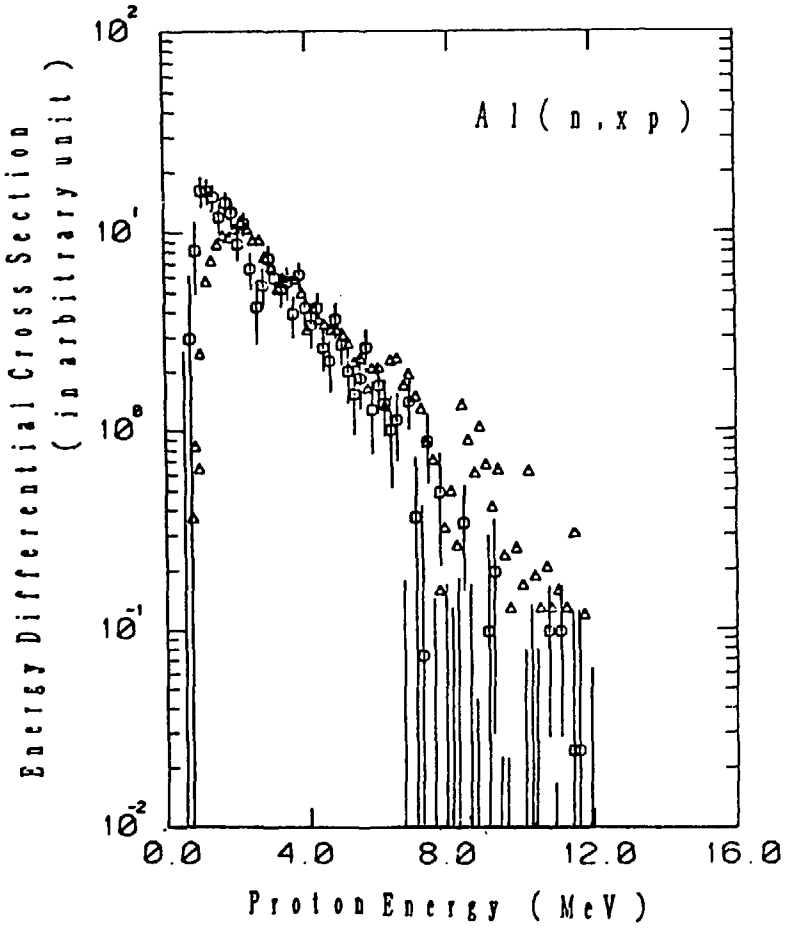

Fig. 9 Proton energy spectra from $^{27}Al(n,xp)$ with E_n=14 MeV at 90°: the present experiment based on pulse height channel (open circles) and Grimes' experiment for E_n=15 MeV at 75° (triangles)

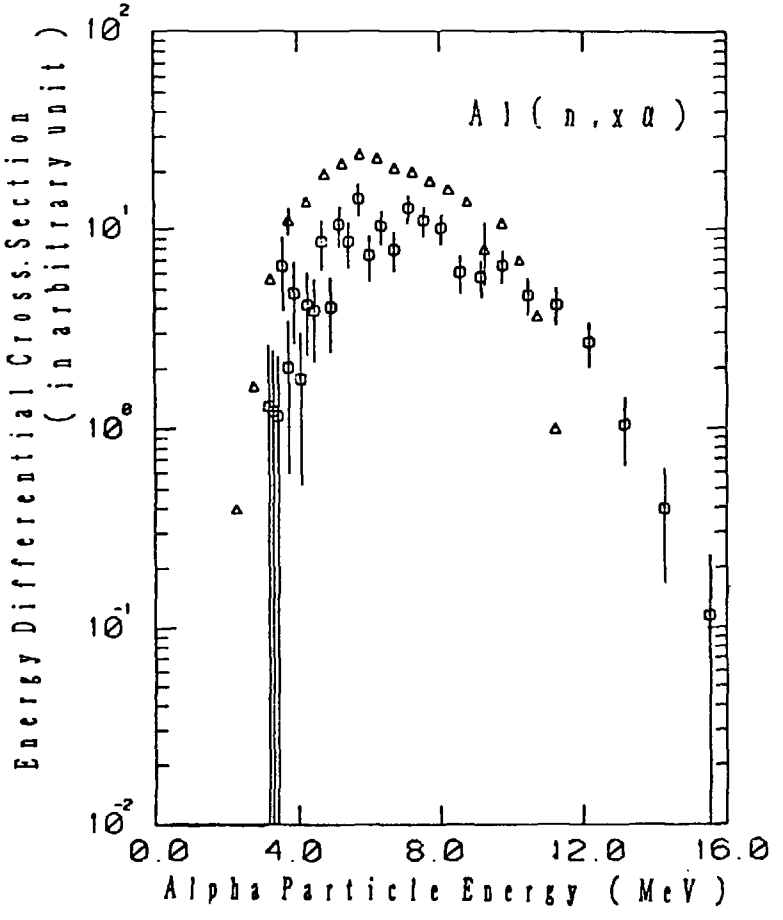

Fig. 10 Alpha-particle energy spectra from $^{27}Al(n,x\alpha)$ with E_n=14 MeV at 90°: the present experiment (fore grounds) based on T.O.F. channel (open circles) and Grimes' experiment for E_n=15 MeV (triangles)

3.10 Average Cross Section Measurement for Several Dosimetry Reactions in Thick Target Li(d,n) Neutron Field

J.R. Dumais, S. Tanaka, N. Odano, S. Iwasaki and K. Sugiyama

Department of Nuclear Engineering
Tohoku University
Aramaki-Aoba, Aoba-Ku, Sendai 980
Japan

Abstract: Average cross sections have been measured for several dosimetry reactions by means of activation method in thick target Li(d,n) neutron field which had continuous energy spectrum ranging from a few hundred KeV to 18 MeV. The aim of this study is to verify cross section data of the recently evaluated JENDL-3 and the IRDF-82 dosimetry files by comparison of the calculated average cross sections with the experimental ones. Standard deviations in both values were estimated on the basis of the variance-covariance analysis. Absolute value of the neutron flux was normalized at 14 MeV by measurement of the reaction rate of the $^{27}Al(n,\alpha)^{24}Na$ standard reaction in the T+d neutron field with the same arrangement. The results show that the calculated average cross sections using the above evaluated values are consistent with the experimental values, except for $^{58}Ni(n,2n)^{57}Ni$ reaction.

(Average Cross Section, Thick Lithium Target, Integral Measurement, $^{27}Al(n,\alpha)^{24}Na$, Activation)

Introduction

Verification for cross section data of neutron nuclear reactions can be done by two types of method of experiment, those are the differential and integral measurements. The differential measurement using neutrons of a monochromatic energy in order to check the cross section at the specific energy point. By this method, many times of experiments are required for comparing with an evaluated cross section data over the wide range of neutron energy. An alternative of this method is the integral measurement, where average cross section is obtained for a certain range of the neutron energy.

As well known, the fission neutrons from reactor and Cf-252 are often used for the integral measurement, but for these neutron energy spectra, the neutron fluence in high energy is rather weak. Such integral experiments are not suitable for reliable verification of cross section data on reactions with high threshold energies. Requirement for the reliable nuclear

reaction cross section is increasing in the fields of application of activation detector dosimetry on fast reactors and proposed fusion reactor[1]. Some integral measurements were done by utilizing accelerator neutrons, which produced rather high energy neutrons[2],[3].

In the present experiment, a 4.5 MV Dynamitron accelerator of Tohoku University had been used for cross section measurements with the activation technique.

Experimental Procedures

Intense neutrons with energy from few hundred KeV to 18 MeV were produced by bombarding thick lithium target with deuterons of 2 MeV. The deuteron beam current was 10 μA. The thickness of the lithium target was 1 mm, which was called thick target. The target was fabricated from lithium metal melted and flattened on a copper disk in the vacuum environment. Experimental arrangement for the present experiment is shown in Fig.1.

The procedure of present irradiation experiment consists of the following two items:

1. Irradiation with the Li+d neutron source.
   Five kinds of samples, Al, Ti, Fe, Ni and Co, were placed at 50 mm from neutron source. Irradiation of two runs, 10 and 24 hours were performed according to the half lives of residual nuclei of the reactions.
2. Irradiation with the T+d neutron source.
   This irradiation was used for normalization of the Li+d neutron fluence, and was done with the same experimental arrangement to the above. The samples of Al, Zr and Nb were irradiated for 15 hours.

Each of the irradiated samples has 19 mm in diameter and 0.1 - 0.3 mm in thickness. Energy spectra of the neutron sources were determined with a technique using time of flight. Two kinds of NE-213 scintillation counters (2"x2" and 1"x1") were used as the main detector and the monitor, respectively.

Activities of the irradiated samples were measured using gamma ray counting method with a 80 cc HP- Germanium detector.

Neutron Spectrum Determination

To obtain the neutron spectrum, it is important to know the efficiency of NE-213 scintillation counter. The spontaneous fission neutrons from a Cf-252 source[4] and a Monte Carlo calculational code, 05S[5] were utilized to determine the relative neutron detection efficiency. By using Cf-252, the neutron spectrum with energy range from few hundred KeV to 6 MeV was measured using TOF technique for detected neutrons and fission gamma rays. The neutron energy from 6 MeV to 18 MeV, the 05S code was utilized with the Compton edge of 1.275 MeV gamma ray from Na-22 used as basic standard of pulse height output. The relative efficiency curve from the calculation code was normalized in the energy range from 4 to 6 MeV with the efficiency curve from the

Cf-252 neutron measurement. The absolute efficiency was obtained from measured value of the cross section of the $^{27}Al(n,\alpha)^{24}Na$ reaction, which is the standard cross section with high reliability in energy range 14 - 15 MeV[6]. The cross section data of $^{27}Al(n,\alpha)^{24}Na$ reaction was taken from INDC-NSF'80 (Vonach et. al.)[7]. The neutron energy spectrum is shown in Fig.2.

Error Analysis

Average cross section values can be determined using the following equations:

Calculated value (C-value):

$$\langle \sigma \rangle_c = \frac{\Sigma \phi_i \sigma_i \Delta E_i}{\Sigma \phi_i \Delta E_i} \quad \ldots \quad (1)$$

Experimental value (E-value):

$$\langle \sigma \rangle_E = \frac{R}{\Sigma \phi_i \Delta E_i} \quad \ldots \quad (2)$$

where, $\langle \sigma \rangle$ = average cross section
ϕ = neutron fluence
σ = cross section (taken from JENDL-3/IRDF-82)
ΔE = energy interval
R = measured reaction rate
i = number of group.

Propagation of error on the average cross section were done using variance-covariance analysis which is based on reference (8). Error on the calculated average cross section is derived from Eq.1, and can be written as

$$Var\langle \sigma \rangle = (\overline{S_\phi} \cdot \vec{E_\phi})^T \cdot \overline{C_\phi} \cdot (\overline{S_\phi} \cdot \vec{E_\phi}) + (\overline{S_\sigma} \cdot \vec{E_\sigma})^T \cdot \overline{C_\sigma} \cdot (\overline{S_\sigma} \cdot \vec{E_\sigma}) \quad \ldots \quad (3)$$

where,
S_ϕ and S_σ = sensitivity of average cross section on neutron fluence and cross section, respectively
E_ϕ and E_σ = error of neutron fluence and cross section
C_ϕ and C_σ = correlation matrix of neutron fluence and cross section, respectively
T = transposed matrix.

Error on the experimental value can be derived from Eq.2, which depends on error of reaction rate and neutron fluence. Covariance data for cross sections were taken from dosimetry files, e.g. JENDL-3[9] and IRDF-82. Error of reaction rate was derived from the activity measurement of the sample. Error on the neutron fluence was derived from:

- Statistical error
- neutron energy on the TOF measurement

- efficiency of neutron detector
- error on normalizing by $^{27}Al(n,\alpha)^{24}Na$ reaction rate

In this experiment, the neutron fluence was calculated as

$$\phi(E) = N(E) / \varepsilon(E) \quad \ldots \quad (4)$$

where N(E) is neutron counting and $\varepsilon(E)$ is the efficiency of the neutron detector. In this case, each of the neutron fluence $\phi(E)$, the variables N(E), $\varepsilon(E)$ and E was divided into 70 groups. Correlations on those variables are considered as follows:

ϕ_i, ε_i, E_i ------ correlated between each groups
N_i ------ no correlation
N_i, ε_i, E_i ------ no correlation on each parameter.

Covariance of the i^{th} and j^{th} group of the neutron fluence was determined as [10]

$$M\phi_{ij} = \delta_{ij}\phi_i\phi_j (\delta N/N)_i \cdot (\delta N/N)_j + \phi_i\phi_j \cdot M\varepsilon_{ij} / (\varepsilon_i \cdot \varepsilon_j) + (\partial\phi/\partial E)_i \cdot (\partial\phi/\partial E)_j \cdot ME_{ij} \quad \ldots\ldots \quad (5)$$

where,

$M\phi$ = covariance matrix of the neutron fluence
ϕ = the neutron fluence
δN = error of neutron counting on TOF spectrum
N = neutron counting on TOF spectrum
$M\varepsilon$ = covariance matrix of efficiency
ε = efficiency of neutron detector
ME = covariance matrix of neutron energy
i, j = i^{th} group and j^{th} group
$\delta_{ij} = 1$, if $i = j$
$= 0$, if $i \neq j$

Experimental Results

The ratios of calculation to experiment result for average cross section and its uncertainties are given in table 1 and table 2, according to the result on JENDL-3 and IRDF-82 dosimetry files, respectively. Fig.3 shows the C/E values based on table 1 and table 2.

The result of this study can be summarized as follows:

- With respect to the low threshold energy reaction, i.e., $^{58}Ni(n,p)^{58}Co$, the experimental average cross section consistent with the calculated ones. The discrepancies are 4% and 1% for JENDL-3 and IRDF-82, respectively.
- Middle threshold energy (around 5 MeV) reaction group, $^{27}Al(n,\alpha)^{24}Na$, $^{48}Ti(n,p)^{48}Sc$ and $^{56}Fe(n,p)^{56}Mn$ show consistent results with small discrepancies from 3 to 9%.
- As for two (n,2n) reactions with high threshold energies, the result for $^{59}Co(n,2n)^{58}Co$ reaction is satisfactory with the discrepancies of 2% for IRDF-82 and 3% for JENDL-3, while for the $^{58}Ni(n,2n)^{57}Ni$ reaction the calculated shows lower value relative to the experimental value by 12% for JENDL-3 and by 22% for

IRDF-82. These large discrepancies comparing to those of other reactions ranging from 1 to 9%, are suggested that the cross section data of this reaction from the new JENDL-3 file is still lower than the expected value.

References

1) G. Winkler et.al.: Proc. International Conf. on Nuclear Data for Sci. and Tech., Antwerp, p.400, ECSC, EEC, EAEC (Brussel and Luxemburg 1983).
2) L.R. Greenwood et.al.: Nuclear Technology, 41 p.109 (1978).
3) Y. Uwamino et.al.: Fall Meeting of The Atomic Energy Society of Japan, p.199-201 (1986).
4) W. Mannhart, IAEA-TECDOC-410, p.158 (1987).
5) R.E. Textor and V.V. Verbinski:"05S Monte Carlo Code", ORNL-4160, OakRidge National Laboratory (1968).
6) Y. Ikeda et.al.: Fall Meeting of The Atomic Energy Society of Japan, p.258 (1987).
7) H. Vonach et.al., INDC-36/LN, Nuclear Standards File, Version'80 (1981).
8) D.L. Smith : Report ANL-NDM/62 (1981).
9) JAERI Nuclear Data Center : "JENDL-3", Private Communication (1989).
10) A. Crametz et.al.: Proc. International Conf. on Nuclear Data for Sci. and Tech., Antwerp, p.902, ECSC, EEC, EAEC (Brussel and Luxemburg 1983).

Table 1 Results for average cross sections from the measured and the calculated values using JENDL-3

REACTION	CALC. (JENDL-3)		EXPERIMENT		C / E and (% ERROR)
	$<\sigma>_C$ (barn)	ERROR (%)	$<\sigma>_E$ (barn)	ERROR (%)	
$^{27}Al(n,\alpha)^{24}Na$	2.24×10^{-2}	6.3	2.11×10^{-2}	7.2	1.06 (9.6)
$^{48}Ti(n,p)^{48}Sc$	1.07×10^{-2}	13.1	1.04×10^{-2}	6.5	1.03 (14.6)
$^{56}Fe(n,p)^{56}Mn$	2.05×10^{-2}	5.0	2.14×10^{-2}	7.4	0.96 (8.9)
$^{58}Ni(n,p)^{58}Co$	1.55×10^{-1}	6.5	1.62×10^{-1}	7.1	0.96 (9.6)
$^{58}Ni(n,2n)^{57}Ni$	2.95×10^{-3}	19.0	3.37×10^{-3}	7.9	0.88 (20.6)
$^{59}Co(n,2n)^{58}Co$	8.99×10^{-2}	11.0	9.30×10^{-2}	7.8	0.97 (13.5)

Table 2 Results for average cross sections from the measured and the calculated values using IRDF-82

REACTION	CALC. (IRDF-82)		EXPERIMENT		C / E and (% ERROR)
	$<\sigma>_C$ (barn)	ERROR (%)	$<\sigma>_E$ (barn)	ERROR (%)	
$^{27}Al(n,\alpha)^{24}Na$	2.29×10^{-2}	5.2	2.11×10^{-2}	7.2	1.09 (8.9)
$^{48}Ti(n,p)^{48}Sc$	1.07×10^{-2}	13.1	1.04×10^{-2}	6.5	1.03 (14.6)
$^{56}Fe(n,p)^{56}Mn$	2.00×10^{-2}	5.0	2.14×10^{-2}	7.4	0.93 (8.9)
$^{58}Ni(n,p)^{58}Co$	1.60×10^{-1}	6.9	1.62×10^{-1}	7.1	0.99 (9.9)
$^{58}Ni(n,2n)^{57}Ni$	2.62×10^{-3}	18.3	3.37×10^{-3}	7.9	0.78 (19.9)
$^{59}Co(n,2n)^{58}Co$	9.11×10^{-2}	11.0	9.30×10^{-2}	7.8	0.98 (13.5)

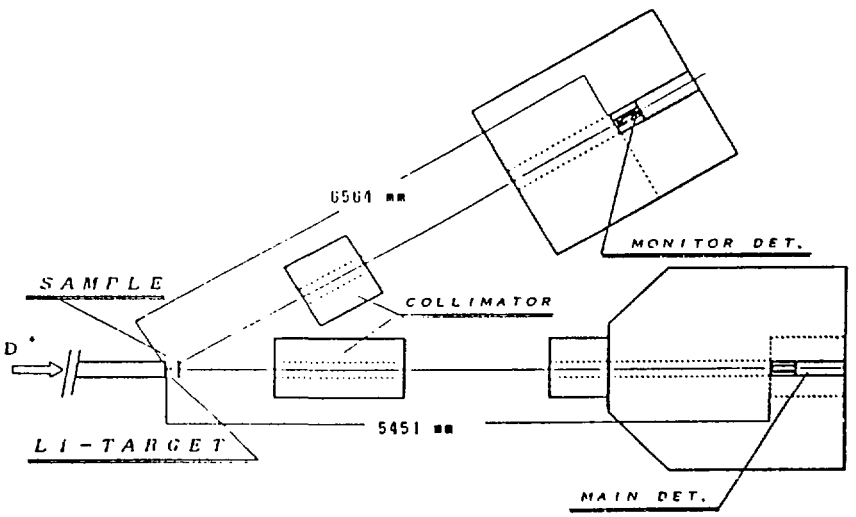

Fig. 1 Arrangement for the present experiment

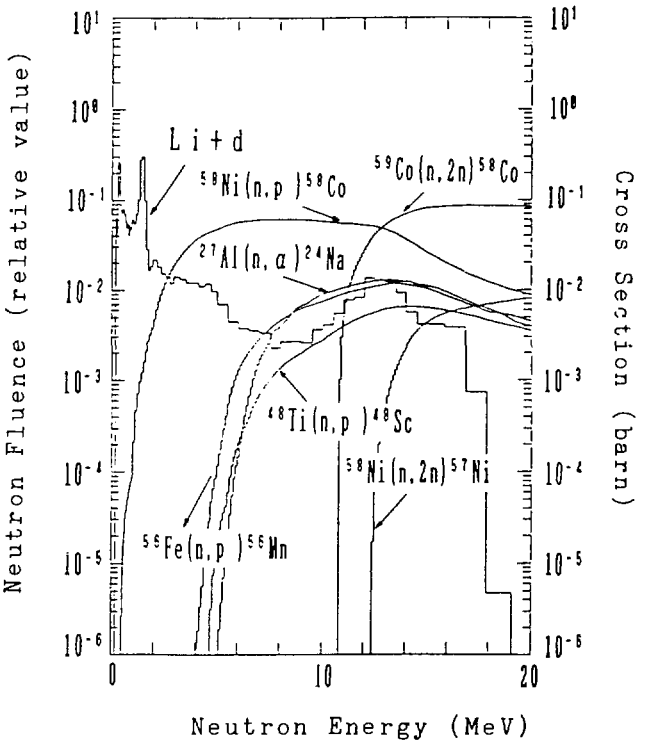

Fig. 2 Neutron energy spectrum of the Li(d,n) neutron source with six reaction cross section curves (taken from the JENDL-3) that used in the present experiment

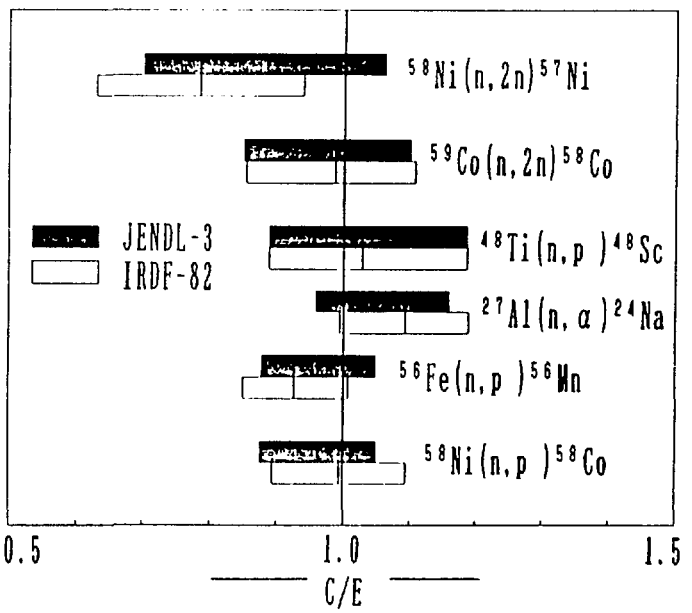

Fig. 3 Schematic comparisons for the average cross sections of JENDL-3 and IRDF-82

3.11 The Measurement of Leakage Neutron Spectra from Various Sphere Piles with 14 MeV Neutrons – Al, Mo and W –

Chihiro ICHIHARA, Shu A. HAYASHI, Katsuhei KOBAYASHI,
Research Reactor Institute, Kyotc University, Osaka, Japan

Itsuro Kimura
Faculty of Engineering, Kyoto University, Kyoto, Japan

Junji YAMAMOTO, Akito TAKAHASHI
Faculty of Engineering, Osaka University, Suita, Japan

In order to perform the bench mark test of the newly compiled JENDL-3 nuclear data file, neutron leakage spectra from three kinds of materials were measured. The results were compared with the calculations using MCNP Monte Carlo code and pointwise cross section library processed from JENDL-3T and other data files, ENDF/B-IV, ENDL-85. Measured samples were aluminum, molybdenum and tungsten. The experiments were performed by using an intense 14 MeV pulsed neutrons and a time-of-flight (TOF) technique in the energy range between 100 keV and 15 MeV.

1. Introduction

An integral experiment plays an important role for the verification of the nuclear data files and the calculation methods. The compilation of JENDL-3 has been conducted and was published[1]. Prior to the publication, the test version of the JENDL-3, named JENDL-3T(Revision-0 and -1), was supplied for a bench mark test. We have measured leakage neutron spectra from sphere piles of various kinds of the fusion reactor candidate material by using a time-of-flight(TOF) technique with 14 MeV neutrons at the intense neutron source OKTAVIAN[2]. The results were compared with theoretical calculations using

JENDL-3T and other data files[3),4)].

In the present paper, the leakage neutron spectra from sphere piles of aluminum, molybdenum and tungsten which are the possible candidate materials for the fusion reactor are studied.

2. Experiment

2.1 Sample piles

a) Aluminum pile

Aluminum sample pile consists of 32.8 kg of atomized aluminum powder whose grain size was between 0.2 and 1.0 mm and the purity of >99.7%. The sample was packed with stainless steel spherical shell 39.9 cm in outer diameter and 2 mm thick. This shell has a void 20 cm in outer diameter at its center and the beam hole of 11.1 cm in diameter. The thickness of the aluminum is therefore about 9.5 cm along the radial axis. Fig.1 shows the geometry of aluminum sample pile.

b) Molybdenum pile

Molybdenum sample pile consists of about 236 kg of molybdenum powder with natural abundance. The purity of molybdenum was greater than 99.9%. The spherical shell with 60.9 cm outer diameter and 4.5 mm thickness is made of mild steel . This shell is equipped with a beam hole 5 cm in diameter and no center void. Fig.2 gives the dimension of this shell.

c) Tungsten pile

About 118.6 kg of tungsten powder with natural abundance was packed in the same shell as the aluminum one. The purity of tungsten was >99.9%. Table 1 shows the list of the measured sample piles; pile diameter, packing density and sample thickness (in unit of cm and mean free paths for 14 MeV neutrons, respectively).

2.2 Experimental arrangement

The experiment was performed using an intense pulse beam line of OKTAVIAN. with a time-of -flight (TOF) technique at OKTAVIAN at Osaka University. The experimental arrangement is shown in Fig.3. The energy of the incident deuterons was about

250 keV. A tritium neutron production target was set at the center of the pile.

A pre-collimator system made of polyethylene-iron multi-layers was set between the pile and the detector to reduce the neutron background. The aperture size of this collimator was determined so that the whole surface of the piles facing to the detector could be viewed.

An NE-218 cylindrical liquid scintillation counter (12.7 cm in diameter and 5.08 cm long) was used as a neutron detector. This detector was located 10.5 m from the center of the pile and at the angle of 55° with respect to the incident deuteron beam. The detector efficiency was determined by combining the theoretical calculation by using a Monte Carlo code and the relative efficiency derived from the TOF measurements of ^{252}Cf spontaneous fission spectrum and the neutron leakage spectrum from a graphite sphere.

Niobium foils were attached to the target and were irradiated during each run. By counting the radioactivity of ^{92m}Nb induced through $^{93}Nb(n,2n)$ reaction, neutron fluence during the experiment was determined. The absolute neutron flux was derived from the measured TOF data in the manner stated elsewhere.[5)]

3. Calculations

The calculation of the leakage neutron spectra was performed by using a 3-dimensional Monte Carlo neutron transport code, MCNP[6)]. The continuous energy cross section libraries for this code were prepared from JENDL-3T (Revision-0 for molybdenum, and -1 for aluminum and tungsten) with NJOY[7)] processing code. For the reference, the calculation using the libraries from ENDF/B-IV and ENDL-85 was also performed.

4. Results and concluding remarks

The measured leakage spectra from three sample piles are shown in Figs.4 to 6 in comparison with the calculated spectra.

a) Aluminum sample

Fig.3 shows the experimental and calculated leakage spec-

trum from the aluminum pile. Both data file predict the measured spectrum pretty well. However, both of them underestimate the measured one in the energy range between 3 MeV and 13 MeV. Taking into account that inelastically scattered neutrons are dominant in this energy region of the leakage spectrum, inelastic level scattering cross sections have to be improved. As the broad peak below 8 MeV is mainly consists of secondary neutrons produced with (n,2n) reactions, the discrepancy in the energy range between 3 MeV and 8 MeV is possibly caused by the ambiguities of this reaction cross sections.

b) Molybdenum sample

In the Fig.5, the leakage spectra from molybdenum 60 cm pile are shown. Though the calculation using JENDL-3T and ENDL-85 are very similar, both calculation can not predict the measured spectrum. This shows that the inelastic scattering cross section and/or (n,2n) cross sections of both JENDL-3T and ENDL-85 data file have common problems.

c) Tungsten sample

The leakage spectra from tungsten pile are shown in Fig.6. The calculation with JENDL-3T differs considerably from the measured one below the elastic scattering peak. Since tungsten is expected for shielding material, this discrepancy is serious. Furthermore, disagreement in the energy range between 2 MeV and 5 MeV is observed. This is possibly caused by the insufficient evaluation of (n,2n) reaction cross section near threshold energy. The threshold energy itself might be inaccurate.

Of the three elements stated above, aluminum with only one isotope is pretty well evaluated by both JENDL-3T and ENDF/b-IV data file except for slight problem possibly in the non-elastic scattering cross sections. However, for the other two materials with numbers of isotopes, not only ENDL-85 data file but new JENDL-3T are still not free from severe problem.

Acknowledgement

Part of this study has been supported by the Scientific Promotion for Fusion Research from the Ministry of Education,

Science and Culture, Japan. This work was undertaken with the framework of the co-operative research program of OKTAVIAN facility.

References

1) ASAMI,T. et al.:"Japanese Evaluated Nuclear Data Library Version 3, JENDL-3", J.Atomic Enrgy Soc. Japan, 31[11]
2) SUMITA, K. et al.:"Osaka University Intense 14 MeV Neutron Sourece and its Utilization for Fusion Studies", Proc. 12th Symp. Fusion Technology, B-24, KFA Juelich, Sept. 1982
3) ICHIHARA,C et al.:"Measurement of Leakage Neutron Spectra from Various Sphere Piles with 14 MeV Neutrons", Proc. the 1987 Seminar on Nuclea Data, JAERI-M 88-065, 263(1987)
4) ICHIHARA,C et al.:"The Measurement of Leakage Neutron Spectra from Various Sphere Piles with 14 MeV Neutrons", Proc. 1988 Seminar on Nuclea Data, JAERI-M 89-026, 222(1989)
5) TAKAHASHI,A. et al.:"Measurement of Neutron Multiplication by Lead Shells and Leakage Spectra from Lithium, Graphite and Stainless Steel Slabs", OKTAVIAN Report, C-83-02(1983)
6) BRIESMEISTER,J.F. ed.:"MCNP - A General Monte Carlo Code for Neutron and Photon Transport", LA-7396-M, Rev.2, 1986
7) MACFARLANE,R.E. et al.:"The NJOY Nuclear Data Processing System, vol.1: User's Manual", LA-9303-M, vol.1(ENDF324) (1982)

Table 1 List of the sample piles; pile diameter, packing density, sample thickness

Pile	Dia. (cm)	Density (g/cm^3)	Sample-Thick. (cm)	(MFPs)
Al	40	1.22	9.8	0.5
Mo	61	2.15	27.5	1.5
W	40	4.18	9.8	0.8

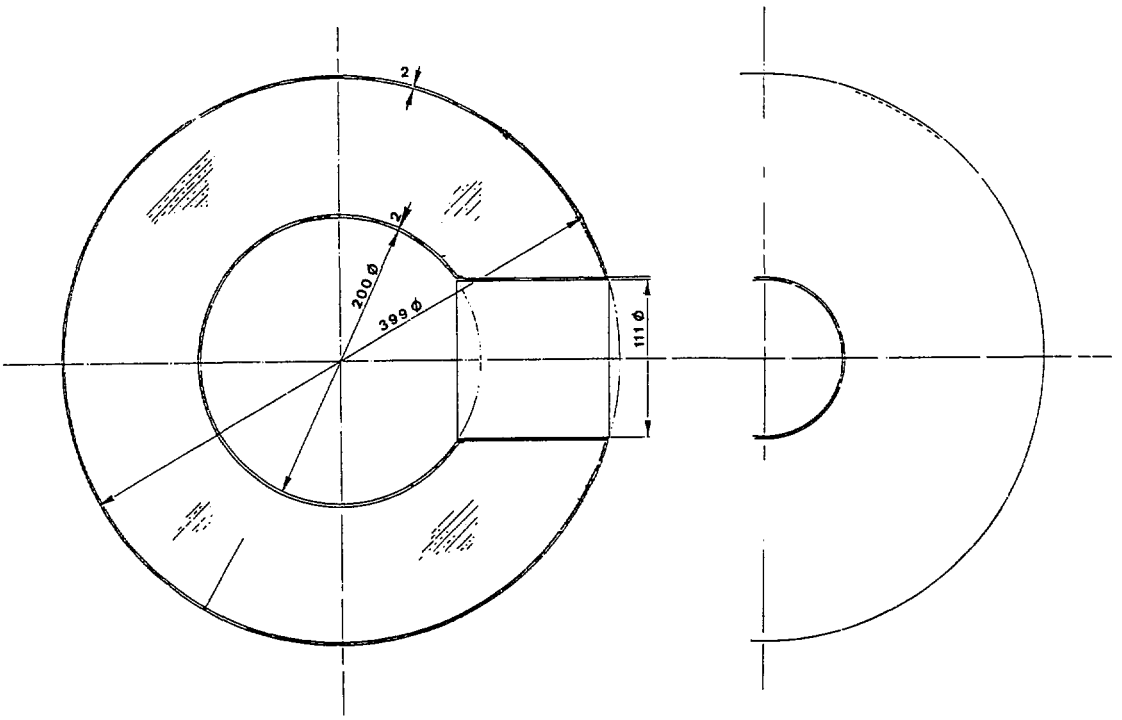

Fig. 1 The geometries of the 40 cm diameter spherical shell for use with aluminum and tungsten sample piles

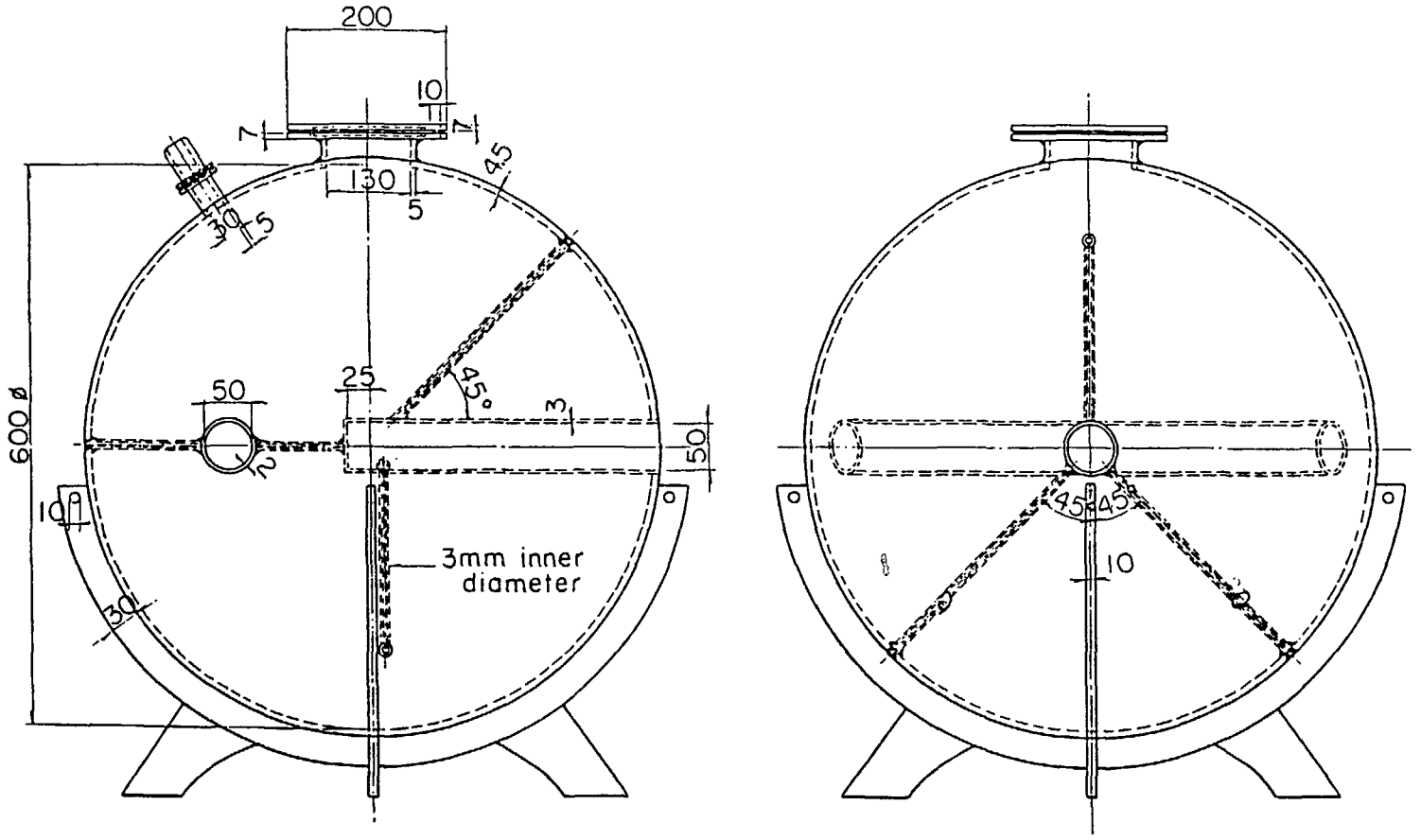

Fig. 2 The geometries of the 60 cm diameter spherical shell for use with molybdenum pile

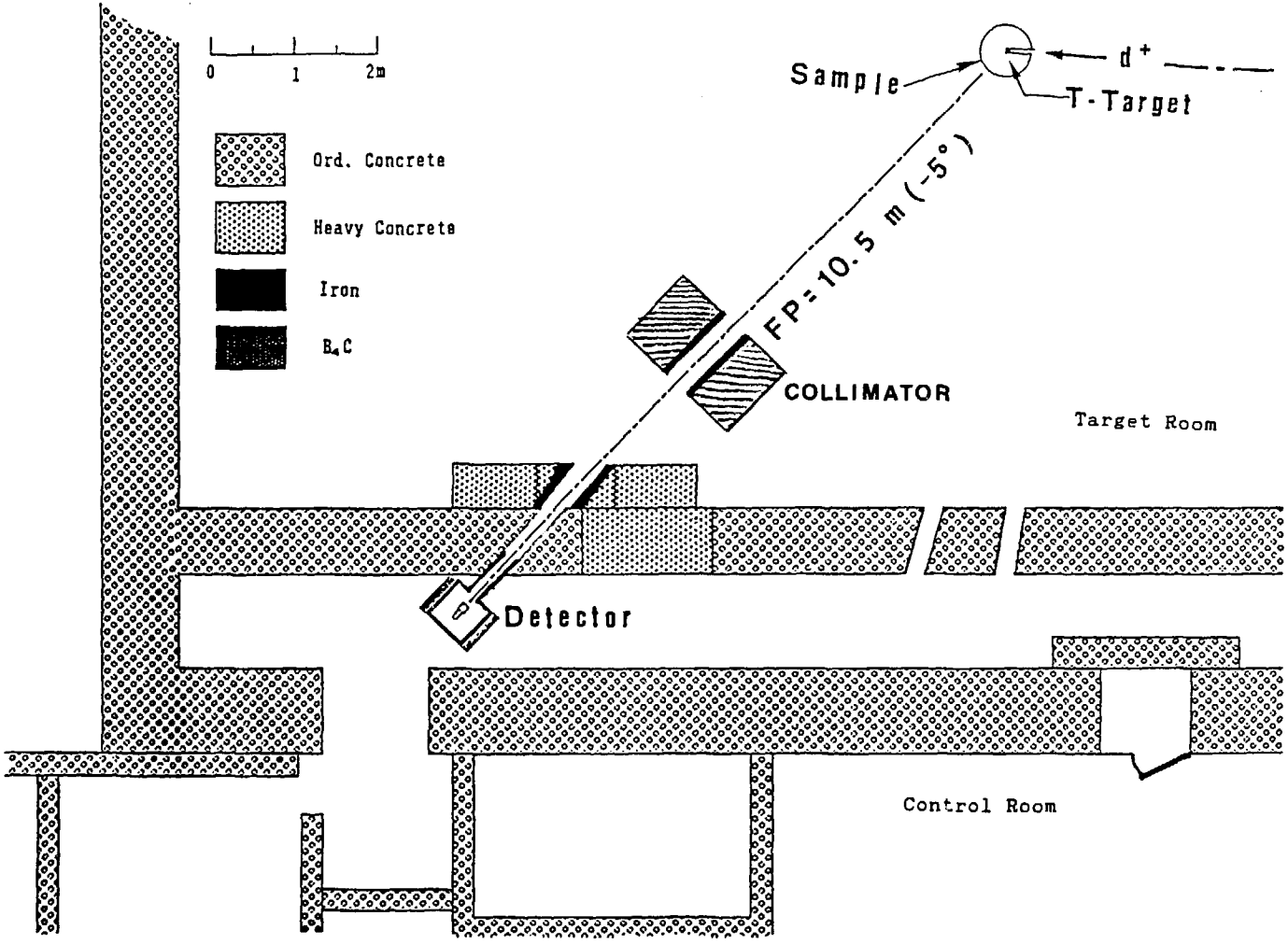

Fig. 3 Experimental arrangement in OKTAVIAN facility

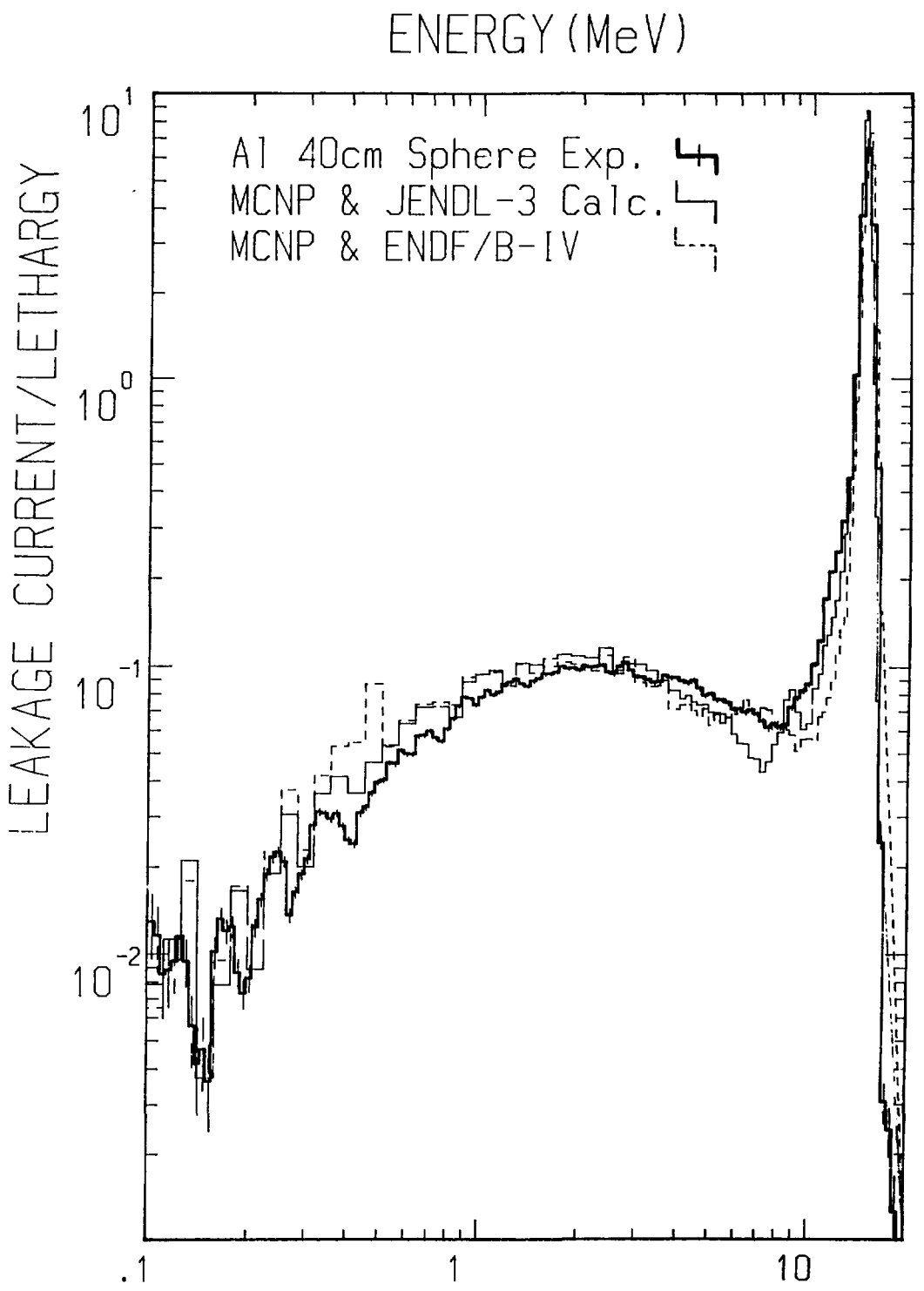

Fig. 4 Experimental and calculated leakage spectra from aluminum pile

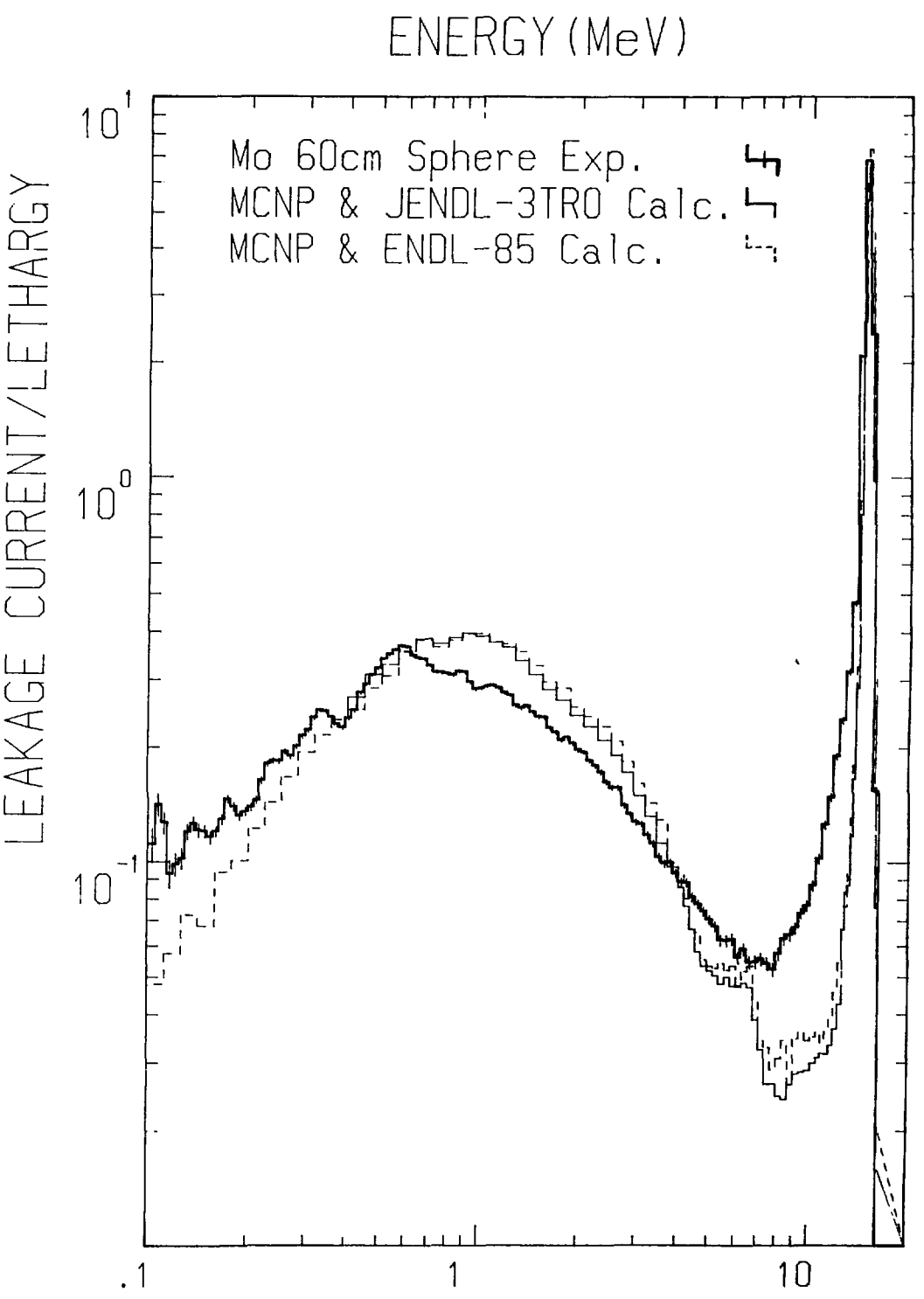

Fig. 5 Experimental and calculated leakage spectra from molybdenum pile

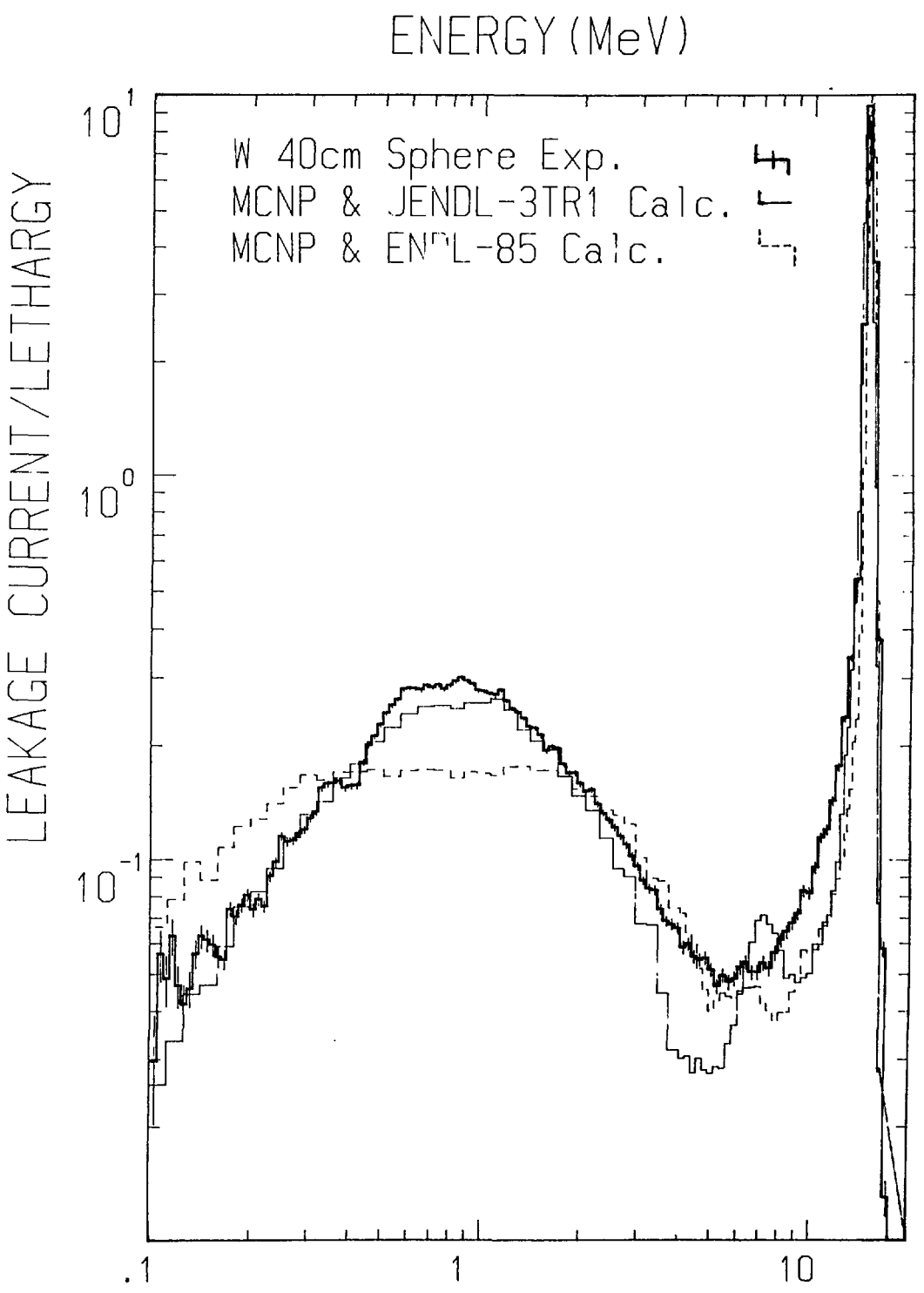

Fig. 6 Experimental and calculated spectra from tungsten pile

3.12 Comparison of Calculated Shielding Properties by JENDL-3 with Those by ENDF/B-IV

KOICHI MAKI, KAZUAKI KOSAKO,
HIROSHI MAEKAWA, YASUSHI SEKI
Fusion Experimental Reactor Team
Naka Fusion Research Establishment,
Department of Reactor Engineering
Tokai Research Establishment
Japan Atomic Energy Research Institute
Tokai-mura, Ibaraki-ken, Japan

ABSTRACT

Fusion nuclear group constant set "FUSION-J3" has been constructed from JENDL-3, Japanese evaluated nuclear data file, published in September 1989. Using FUSION-J3, shielding properties were calculated in fusion reactor inboard shield to guard for superconductive toroidal magnets against neutron and gamma ray. The results were compared with those by the nuclear group constant set VITAMIN-C based on ENDF/B-IV. From the comparison, both neutron spectra in the first wall with FUSION-J3 and VITAMIN-C are in approximately agreement with each other. The former in winding pack is less than the latter by 30% in the energy region below 1 keV. Gamma ray spectra with FUSION-J3 are larger than 1.5-3 times of those by VITAMIN-C in the first wall and this discrepancy becomes larger in the winding pack region far from the first wall.

I. INTRODUCTION

Guard for superconductive toroidal magnets against radiation, neutron and gamma ray, is one of the most important subjects for shielding design in fusion reactors. Up to now, the nuclear group constant set GICX40[1] has been used in fusion reactor neutronic calculations. The set was constructed more than ten years ago. Therefore, a new nuclear group constant set for fusion reactor neutronic calculation has been required to be constructed on the basis of a new Japanese evaluated nuclear data file, JENDL-3[2]. Since JENDL-3 was published in September

1989, the fusion nuclear group constant set "FUSION-J3" has been constructed from the file.

Using FUSION-J3, shielding properties were calculated in fusion reactor inboard shield. The thickness of inboard shield makes a large effect on the reactor major radius. Therefore, the thickness should be designed as thin as possible. The differences between shielding properties by used nuclear group constant sets must be understood.

Purposes of the present report are to compare the shielding properties calculated by FUSION-J3 with those by the nuclear group constant set VITAMIN-C[3] based on ENDF/B-IV, and to understand and find out problems in FUSION-J3 and further JENDL-3.

One dimensional calculation model and inboard shield configurations of problems 1a to 1d in ITER concept are explained in Chapter II. In inboard shield calculation, differences between shielding properties by FUSION-J3 and those by VITAMIN-C are discussed in Chapter III.

II. CALCULATIONAL MODEL

One dimensional transport code 'ANISN' is adapted to shielding calculations with P5-S8. A torus model, one dimensional cylinder model, is applied to ITER (International Thermonuclear Fusion Reactor as represented in Fig.1) mid-plane. ITER has major radius of 5.8m, minor radius of 2.2m and neutron first wall loading of 1MW/m^2, etc. as shown in Table 1. Shielding properties in inboard shield are surveyed for various shielding configurations, problems 1a to 1d. Representing Fig.2, the problem 1a is composed of SS (stainless steel) and water, the problem 1b of SS and borated water, the problem 1c of SS-water and lead, and the problem 1d of SS-water and B4C. Purpose of shielding calculation on the problem 1a is to understand differences between shielding characteristics calculated by FUSION-3 and by VITAMIN-C as basic shield configurations. Purpose of problems 1b, 1c and 1d are to understand differences between calculated shielding property improvement with borated water, lead and B4C zones, respectively, by applying FUSION-J3 and those by VITAMIN-C

The nuclear group constant set FUSION-J3 is the coupled constant set composed of neutron 125 groups and gamma ray 40 groups. The energy group structures of neutron and gamma ray are represented in Table 2, and 40 nuclides including in FUSION-J3 are listed in Table 3. On the other hand, VITAMIN-C consists of neutron 46 groups and gamma ray 21 groups.

III. RESULTS AND DISCUSSION

Neutron and gamma ray fluxes, and nuclear heating rates in the first wall and winding pack in TFC were estimated. From these results, we discussed as follows;

[1] Fast and total neutron, and gamma ray fluxes

Fast and total neutron, and gamma ray fluxes are calculated by FUSION-J3 and VITAMIN-C as shown in Tables 4 to 7. Fast and total neutron fluxes by FUSION-J3 in the first wall are approximately in agreement with those by VITAMIN-C. In the winding pack, the fluxes with FUSION-J3 are larger than those with VITAMIN-C by about 20% except problem 1c. In problem 1c the shield has 3cm thickness lead zone near the toroidal magnets and the fluxes with FUSION-J3 are less than the those with VITAMIN-C by about 20% in the winding pack. Total neutron fluxes with FUSION-J3 become further larger in the winding pack.

On the other hand, gamma ray flux in the first wall with FUSION-J3 is less than that with VITAMIN-C by 20%. The former in the winding pack is further less than the latter by 30-40%.

From these results, it can be seen that the gamma ray production cross sections in JENDL-3 are probably less than those in ENDF/B-IV.

[2] Nuclear heating rates

Neutron heating rates with FUSION-J3 are larger than those with VITAMIN-C by 15% and 50% in the first wall and winding pack, respectively, as shown in Tables 4 to 7. While neutron heating rates in carbon tile with FUSION-J3 are estimated approximately 60% of those

with VITAMIN-C in spite of agreement in neutron fluxes with both. This fact implies that carbon heating constant, KERMA factor, is probably underestimated by more than 40%.

On the other hand, gamma ray heating rates with FUSION-J3 in the first wall and in the winding pack are less than those with VITAMIN-C by 25% and 40-50%, respectively.

These results also suggest that the gamma ray production cross sections in JENDL-3 are possible to be smaller than those in ENDF/B-IV.

[3] Neutron and gamma ray spectra

Both neutron spectra in the first wall with FUSION-J3 and VITAMIN-C are approximately in agreement with each other. The spectra with FUSION-J3 in winding pack is larger than the latter by 30% in the energy range below 1 keV to 1 eV as in Figs.3-6. The neutron spectra with JENDL-3 have a tendency to be softened more than those of ENDF/B-IV in the region far from the first wall such as the superconductive magnet region.

Gamma ray spectra with FUSION-J3 are larger than 1.5 times partially 3 times of those by VITAMIN-C in the first wall and these discrepancies become larger up to 3 times in the winding pack in the energy range from 3 MeV to 200 keV as shown in Figs.7-10. The discrepancy in the gamma ray spectra in the energy range suggests that capture gamma cross sections are probably underestimated in JENDL-3.

[4] Comparison with experiments in gamma ray heating rates

Gamma ray heating rates calculated with 2-dimensional slab model with both group constant sets, GICX40 and GICXFNS are represented in Fig.11 together with the experimental values by FNS. From this figure, the values with VITAMIN-C are in approximately agreement with the experimental ones in the region 50 to 70cm from the surface. The values by FUSION-J3 are underestimated in comparison with the experimental values. This fact implies also that capture gamma cross sections are probably underestimated.

IV. CONCLUSION

Shielding properties for superconductive magnets calculated by FUSION-J3 based on JENDL-3 were compared with those by VITAMIN-C based on ENDF/B-IV. Discrepancies between them were discussed. From these results, following concluding remarks are obtained.

1) Fast and total neutron fluxes by FUSION-J3 are approximately in agreement with those by VITAMIN-C in the first wall region, but in the winding pack region those by FUSION-J3 are larger than by VITAMIN-C.
2) Neutron spectra by FUSION-J3 approximately agree with those by VITAMIN-C and differences between them appear in the energy range below several keV in the winding pack.
3) Neutron spectra with JENDL-3 have a tendency to be softened more than those of ENFD/B-IV in the region far from the first wall such as superconductive magnet region.
4) Total gamma ray fluxes by FUSION-J3 are smaller than those by VITAMIN-C in all regions and this discrepancy becomes larger in accordance with far from the first wall.
5) Differences between gamma ray spectra by FUSION-J3 and those by VITAMIN-C appear in the energy range from 3MeV to 200 keV in the first wall and in the winding pack.
6) Neutron heating constant of carbon in FUSION-J3 is probably underestimated, since neutron heating rate in carbon tile is less than that with VITAMIN-C by 40%.
7) Gamma production cross sections of JENDL-3 are probably underestimated, since gamma ray fluxes with FUSION-J3 are smaller than those with VITAMIN-C by 20% and 40% in the first wall and in the winding pack, respectively.

REFERENCE

1) Y. SEKI and H. IIDA, JAERI-M8818, (1980).
2) T. ASAMI, et al. "Japanese Evaluated Nuclear Data Library Version 3, JENDL-3" J. Atomic Energy Society of Japan Vol.31, 1190(Nov. 1989).
3) R. W. ROUSSIN et al., ORNL-RSIC-37.

Table 1 ITER basic design parameters

Major radius	(m)	6.0
Minor radius	(m)	2.15
Aspect ratio		2.78
Plasma current (nominal), (MA)		22.
Elongation κ	(95%)	~ 2.0
Triangularity δ	(95%)	~ 0.38
Toroidal field on axis	(T)	4.85
Plasma voluem	(m^3)	1079.
Wall loading	(MW/m^2)	~ 1.0
Fusion power	(GW)	~ 1.0
Neutron fluence (MW a/m^2)		1.0

Table 2 Neutron 125 energy group structure and gamma-ray 40 energy group structure in FUSION-J3

	Neutron 125 groups ENERGY (EV)			Neutron 125 groups ENERGY (EV)	
1	1.65E+07	1.62E+07	41	6.07E+06	5.70E+06
2	1.62E+07	1.60E+07	42	5.70E+06	5.35E+06
3	1.60E+07	1.57E+07	43	5.35E+06	5.03E+06
4	1.57E+07	1.55E+07	44	5.03E+06	4.72E+06
5	1.55E+07	1.53E+07	45	4.72E+06	4.44E+06
6	1.53E+07	1.50E+07	46	4.44E+06	4.17E+06
7	1.50E+07	1.49E+07	47	4.17E+06	3.92E+06
8	1.48E+07	1.46E+07	48	3.92E+06	3.68E+06
9	1.46E+07	1.43E+07	49	3.68E+06	3.46E+06
10	1.43E+07	1.41E+07	50	3.46E+06	3.25E+06
11	1.41E+07	1.39E+07	51	3.25E+06	3.05E+06
12	1.39E+07	1.37E+07	52	3.05E+06	2.87E+06
13	1.37E+07	1.35E+07	53	2.87E+06	2.69E+06
14	1.35E+07	1.33E+07	54	2.69E+06	2.53E+06
15	1.33E+07	1.30E+07	55	2.53E+06	2.38E+06
16	1.30E+07	1.28E+07	56	2.38E+06	2.23E+06
17	1.28E+07	1.26E+07	57	2.23E+06	2.10E+06
18	1.26E+07	1.25E+07	58	2.10E+06	1.97E+06
19	1.25E+07	1.23E+07	59	1.97E+06	1.85E+06
20	1.23E+07	1.21E+07	60	1.85E+06	1.74E+06
21	1.21E+07	1.19E+07	61	1.74E+06	1.53E+06
22	1.89E+07	1.17E+07	62	1.53E+06	1.35E+06
23	1.17E+07	1.15E+07	63	1.35E+06	1.19E+06
24	1.15E+07	1.13E+07	64	1.19E+06	1.05E+06
25	1.13E+07	1.12E+07	65	1.05E+06	9.30E+05
26	1.12E+07	1.10E+07	66	9.30E+05	8.21E+05
27	1.10E+07	1.08E+07	67	8.21E+05	7.24E+05
28	1.08E+07	1.07E+07	68	7.24E+05	6.39E+05
29	1.07E+07	1.05E+07	69	6.39E+05	5.64E+05
30	1.05E+07	1.03E+07	70	5.64E+05	4.98E+05
31	1.03E+07	1.02E+07	71	4.98E+05	4.39E+05
32	1.02E+07	1.00E+07	72	4.39E+05	3.88E+05
33	1.00E+07	9.39E+06	73	3.88E+05	3.42E+05
34	9.34E+06	8.83E+06	74	3.42E+05	3.02E+05
35	8.83E+06	8.29E+06	75	3.02E+05	2.67E+05
36	8.29E+06	7.79E+06	76	2.67E+05	2.35E+05
37	7.79E+06	7.32E+06	77	2.35E+05	2.08E+05
38	7.32E+06	6.87E+06	78	2.08E+05	1.83E+05
39	6.87E+06	6.46E+06	79	1.83E+05	1.62E+05
40	6.46E+06	6.07E+06	80	1.62E+05	1.43E+05

(continue)

Table 2 Neutron 125 energy group structure and gamma-ray 40 energy group structure in FUSION-J3 (continued)

Neutron 125 groups

	ENERGY (EV)	
81	1.43E+05	1.26E+05
82	1.26E+05	1.11E+05
83	1.11E+05	9.80E+04
84	9.80E+04	8.65E+04
85	8.65E+04	7.64E+04
86	7.64E+04	6.74E+04
87	6.74E+04	5.95E+04
88	5.95E+04	5.25E+04
89	5.25E+04	4.63E+ 4
90	4.63E+04	4.09E+04
91	4.09E+04	3.61E+04
92	3.61E+04	3.18E+04
93	3.18E+04	2.81E+04
94	2.81E+04	2.48E+04
95	2.48E+04	2.19E+04
96	2.19E+04	1.93E+04
97	1.93E+04	1.50E+04
98	1.50E+04	1.17E+04
99	1.17E+04	9.12E+03
100	9.12E+03	7.10E+03
101	7.10E+03	5.53E+03
102	5.53E+03	4.31E+03
103	4.31E+03	3.36E+03
104	3.36E+03	2.61E+03
105	2.61E+03	2.04E+03
106	2.04E+03	1.59E+03
107	1.59E+03	1.23E+03
108	1.23E+03	9.61E+02
109	9.61E+02	5.83E+02
110	5.83E+02	3.54E+02
111	3.54E+02	2.15E+02
112	2.15E+02	1.30E+02
113	1.30E+02	7.89E+01
114	7.89E+01	4.79E+01
115	4.79E+01	2.90E+01
116	2.90E+01	1.76E+01
117	1.76E+01	1.07E+01
118	1.07E+01	6.48E+00
119	6.48E+00	3.93E+00
120	3.93E+00	2.38E+00
121	2.38E+00	1.45E+00
122	1.45E+00	8.76E-01
123	8.76E-01	5.32E-01
124	5.32E-01	3.22E-01
125	3.22E-01	1.00E-01

Gamma ray 40 groups

	ENERGY (EV)	
1	1.40E+07	1.20E+07
2	1.20E+07	1.00E+07
3	1.00E+07	9.00E+06
4	9.00E+06	8.00E+06
5	8.00E+06	7.50E+06
6	7.50E+06	7.00E+06
7	7.00E+06	6.50E+06
8	6.50E+06	6.00E+06
9	6.00E+06	5.50E+06
10	5.50E+06	5.00E+06
11	5.00E+06	4.50E+06
12	4.50E+06	4.00E+06
13	4.00E+06	3.50E+06
14	3.50E+06	3.00E+06
15	3.00E+06	2.50E+06
16	2.50E+06	2.25E+06
17	2.25E+06	2.00E+06
18	2.00E+06	1.75E+06
19	1.75E+06	1.50E+06
20	1.50E+06	1.38E+06
21	1.38E+06	1.25E+06
22	1.25E+06	1.13E+06
23	1.13E+06	1.00E+06
24	1.00E+06	9.00E+05
25	9.00E+05	8.00E+05
26	8.00E+05	7.00E+05
27	7.00E+05	6.00E+05
28	6.00E+05	5.20E+05
29	5.20E+05	5.00E+05
30	5.00E+05	4.00E+05
31	4.00E+05	3.00E+05
32	3.00E+05	2.00E+05
33	2.00E+05	1.50E+05
34	1.50E+05	1.00E+05
35	1.00E+05	8.00E+04
36	8.00E+04	6.00E+04
37	6.00E+04	4.50E+04
38	4.50E+04	3.00E+04
39	3.00E+04	2.00E+04
40	2.00E+04	1.00E+04

Table 3 Forty nuclides in FUSION-J3 set for ANISN input P_0-P_5

No.	Nucl.	MT No.	No.	Nucl.	MT No.
1	^{1}H	1 — 6	21	Ca	121 — 126
2	^{2}D	7 — 12	22	Ti	127 — 132
3	^{3}He	13 — 18	23	V	133 — 138
4	^{4}He	19 — 24	24	^{51}Cr	139 — 144
5	^{6}Li	25 — 30	25	^{55}Mn	145 — 150
6	^{7}Li	31 — 36	26	Fe	151 — 156
7	^{9}Be	37 — 42	27	Co	157 — 162
8	^{10}B	43 — 48	28	Ni	163 — 168
9	^{11}B	49 — 54	29	Cu	169 — 174
10	^{12}C	55 — 60	30	Zr	175 — 180
11	^{14}N	61 — 66	31	^{93}Nb	181 — 186
12	^{16}O	67 — 72	32	Mo	187 — 192
13	^{19}F	73 — 78	33	Cd	193 — 198
14	^{23}Na	79 — 84	34	W	199 — 204
15	Mg	85 — 90	35	Pb	205 — 210
16	^{27}Al	91 — 96	36	^{209}Bi	211 — 216
17	Si	97 — 102	37	^{232}Th	217 — 222
18	^{31}P	103 — 108	38	^{235}U	223 — 228
19	S	109 — 114	39	^{238}U	229 — 234
20	K	115 — 120	40	^{239}Pu	235 — 240

Table 4 Neutron and gamma ray fluxes, and nuclear heating rates estimated by GICX40, FUSION-J3 and VITAMIN-C in ITER benchmark Problem 1a

Items & Positions	Transport x'sec Data base Reaction x'sec GICX40	FUSION-J3 JENDL-3 JENDL-3	VITAMIN-C ENDF/B-IV MACKLIB-IV
Neutron & γ flux (/cm^2 · s)			
First wall (R:815-816cm)			
fast neutron (E_n>0.1MeV)	2.377E+14	2.477E+14	2.485E+14
total neutron (E_n<14.1MeV)	3.822E+14	3.923E+14	3.851E+14
gamma ray flux(total)	1.572E+14	2.029E+14	2.615E+14
Carbon tile (R:344-345cm)			
fast neutron (E_n>0.1MeV)	1.959E+14	2.062E+14	2.063E+14
total neutron (E_n<14.1MeV)	3.364E+14	3.451E+14	3.377E+14
gamma ray flux(total)	1.364E+14	1.737E+14	2.264E+14
Winding pack (R:257-259cm)			
fast neutron (E_n>0.1MeV)	8.320E+09	1.237E+10	1.083E+10
total neutron (E_n<14.1MeV)	2.014E+10	3.208E+10	2.545E+10
gamma ray flux(total)	4.0162+09	6.217E+09	1.099E+10
Nuclear heating rates (w/cm^3)			
First wall (R:815-816cm) n	5.976E+0	7.447E+0	6.482E+0
γ	7.246E+0	7.573E+0	9.918E+0
total	1.322E+1	1.502E+1	1.640E+1
Carbon tile (R:344-345cm) n	3.688E+0	3.133E+0	4.975E+0
γ	1.253E+0	1.232E+0	1.687E+0
total	4.941E+0	4.365E+0	6.662E+0
Winding pack(R:257-259cm) n	2.800E-5	7.226E-5	4.373E-5
γ	2.868E-4	3.652E-4	5.924E-4
total	3.148E-4	4.374E-4	6.361E-4

Table 5 Neutron and gamma ray fluxes, and nuclear heating rates estimated by GICX40, FUSION-J3 and VITAMIN-C in ITER benchmark Problem 1b

Items & Positions	Transport x'sec Data base Reaction x'sec GICX40	FUSION-J3 JENDL-3 JENDL-3	VITAMIN-C ENDF/B-IV MACKLIB-IV
Neutron & γ flux (/cm^2 · s)			
First wall (R:815-816cm)			
fast neutron (E_n>0.1MeV)	2.380E+14	2.477E+14	2.485E+14
total neutron (E_n<14.1MeV)	3.823E+14	3.921E+14	3.848E+14
gamma ray flux(total)	1.573E+14	1.998E+14	2.607E+14
Carbon tile (R:344-345cm)			
fast neutron (E_n>0.1MeV)	1.966E+14	2.062E+14	2.063E+14
total neutron (E_n<14.1MeV)	3.347E+14	3.445E+14	3.371E+14
gamma ray flux(total)	1.365E+14	1.724E+14	2.246E+14
Winding pack (R:257-259cm)			
fast neutron (E_n>0.1MeV)	8.313E+09	1.232E+10	1.078E+10
total neutron (E_n<14.1MeV)	2.013E+10	3.190E+10	2.531E+10
gamma ray flux(total)	4.067E+09	5.981E+09	1.041E+10
Nuclear heating rates (w/cm^3)			
First wall (R:815-816cm) n	5.986E+0	7.439E+0	6.482E+0
γ	7.236E+0	7.537E+0	9.869E+0
total	1.322E+1	1.498E+1	1.635E+1
Carbon tile (R:344-345cm) n	3.709E+0	3.133E+0	4.975E+0
γ	1.248E+0	1.213E+0	1.664E+0
total	4.957E+0	4.346E+0	6.639E+0
Winding pack(R:257-259cm) n	2.760E-5	7.156E-5	4.345E-5
γ	2.789E-4	3.470E-4	5.585E-4
total	3.065E-4	4.185E-4	6.020E-4

Table 6 Neutron and gamma ray fluxes, and nuclear heating rates estimated by GICX40, FUSION-J3 and VITAMIN-C in ITER benchmark Problem 1c

Items & Positions / Transport x'sec Data base / Reaction x'sec	GICX40 ENDF/B-III, IV GICX40	FUSION-J3 JENDL-3 JENDL-3	VITAMIN-C ENDF/B-IV MACKLIB-IV
Neutron & γ flux (/cm^2 · s)			
First wall (R:815-816cm)			
fast neutron (E_n>0.1MeV)	2.380E+14	2.477E+14	2.485E+14
total neutron (E_n<14.1MeV)	3.826E+14	3.923E+14	3.851E+14
gamma ray flux(total)	1.574E+14	2.004E+14	2.615E+14
Carbon tile (R:344-345cm)			
fast neutron (E_n>0.1MeV)	1.966E+14	2.062E+14	2.063E+14
total neutron (E_n<14.1MeV)	3.354E+14	3.451E+14	3.377E+14
gamma ray flux(total)	1.367E+14	1.738E+14	2.264E+14
Winding pack (R:257-259cm)			
fast neutron (E_n>0.1MeV)	1.150E+10	1.232E+10	1.470E+10
total neutron (E_n<14.1MeV)	2.853E+10	4.457E+10	3.541E+10
gamma ray flux(total)	4.587E+09	7.177E+09	1.042E+10
Nuclear heating rates (w/cm^3)			
First wall (R:815-816cm) n	5.986E+0	7.447E+0	6.482E+0
γ	7.254E+0	7.573E+0	9.918E+0
total	1.324E+1	1.502E+1	1.640E+1
Carbon tile (R:344-345cm) n	3.709E+0	3.133E+0	4.975E+0
γ	1.256E+0	1.232E+0	1.687E+0
total	4.964E+0	4.365E+0	6.662E+0
Winding pack(R:257-259cm) n	3.445E-5	9.354E-5	5.502E-5
γ	3.186E-4	3.995E-4	5.777E-4
total	3.530E-4	4.930E-4	6.327E-4

Table 7 Neutron and gamma ray fluxes, and nuclear heating rates estimated by GICX40, FUSION-J3 and VITAMIN-C in ITER benchmark Problem 1d

Items & Positions / Transport x'sec Data base / Reaction x'sec	GICX40 ENDF/B-III, IV GICX40	FUSION-J3 JENDL-3 JENDL-3	VITAMIN-C ENDF/B-IV MACKLIB-IV
Neutron & γ flux (/cm^2 · s)			
First wall (R:815-816cm)			
fast neutron (E_n>0.1MeV)	2.380E+14	2.477E+14	2.485E+14
total neutron (E_n<14.1MeV)	3.826E+14	3.923E+14	3.851E+14
gamma ray flux(total)	1.574E+14	2.004E+14	2.615E+14
Carbon tile (R:344-345cm)			
fast neutron (E_n>0.1MeV)	1.966E+14	2.062E+14	2.083E+14
total neutron (E_n<14.1MeV)	3.354E+14	3.451E+14	3.377E+14
gamma ray flux(total)	1.367E+14	1.738E+14	2.264E+14
Winding pack (R:257-259cm)			
fast neutron (E_n>0.1MeV)	7.523E+09	1.112E+10	9.434E+9
total neutron (E_n<14.1MeV)	1.542E+10	2.456E+10	1.977E+10
gamma ray flux(total)	3.392E+09	4.071E+09	9.168E+09
Nuclear heating rates (w/cm^3)			
First wall (R:815-816cm) n	5.986E+0	7.447E+0	6.482E+0
γ	7.254E+0	7.573E+0	9.918E+0
total	1.324E+1	1.502E+1	1.640E+1
Carbon tile (R:344-345cm) n	3.709E+0	3.133E+0	4.975E+0
γ	1.256E+0	1.232E+0	1.687E+0
total	4.965E+0	4.365E+0	6.662E+0
Winding pack(R:257-259cm) n	2.542E-5	5.048E-5	3.662E-5
γ	2.130E-4	2.022E-4	4.604E-4
total	2.384E-4	2.807E-4	4.970E-4

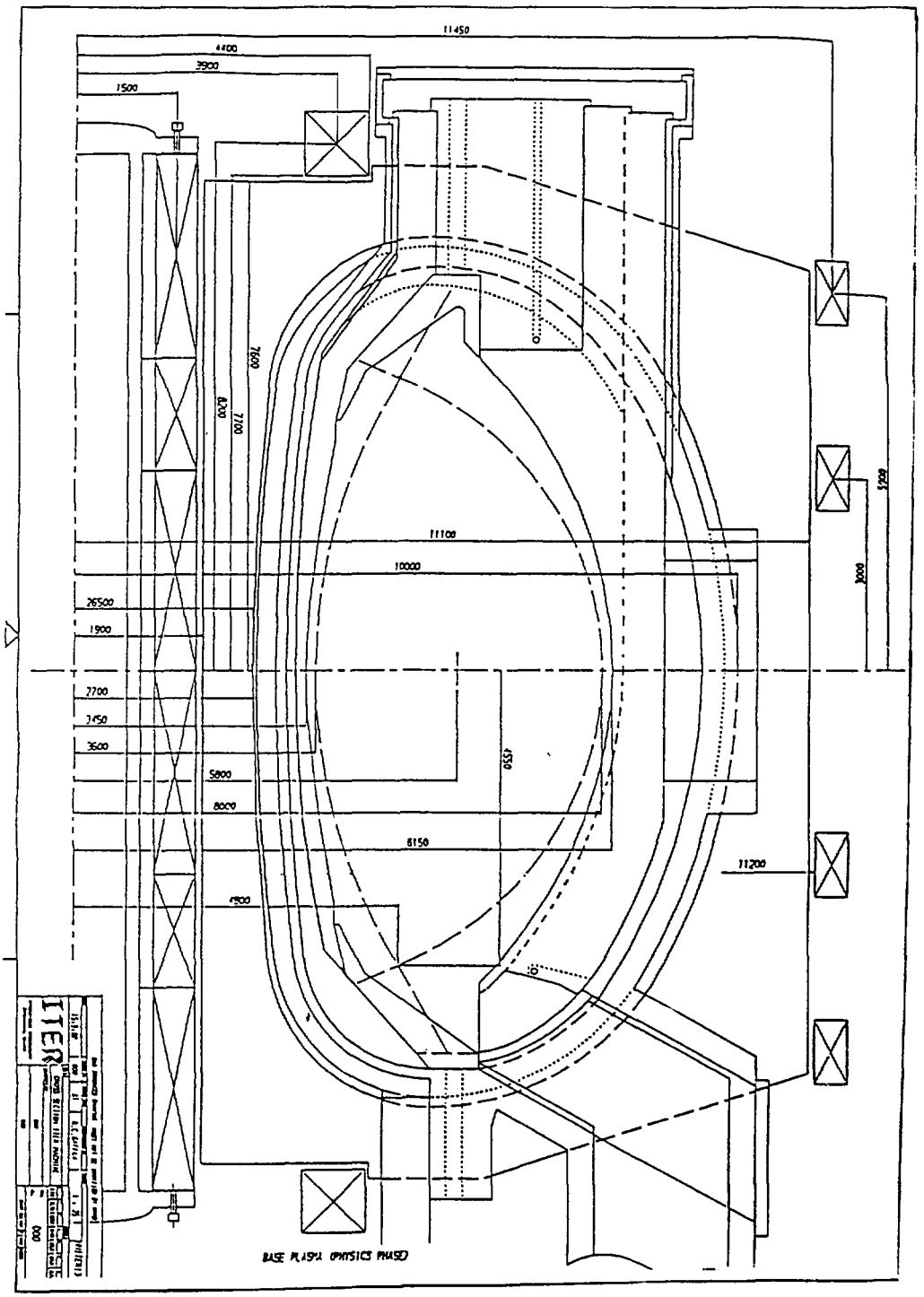

Fig. 1 Poloidal cross section of ITER physics phase

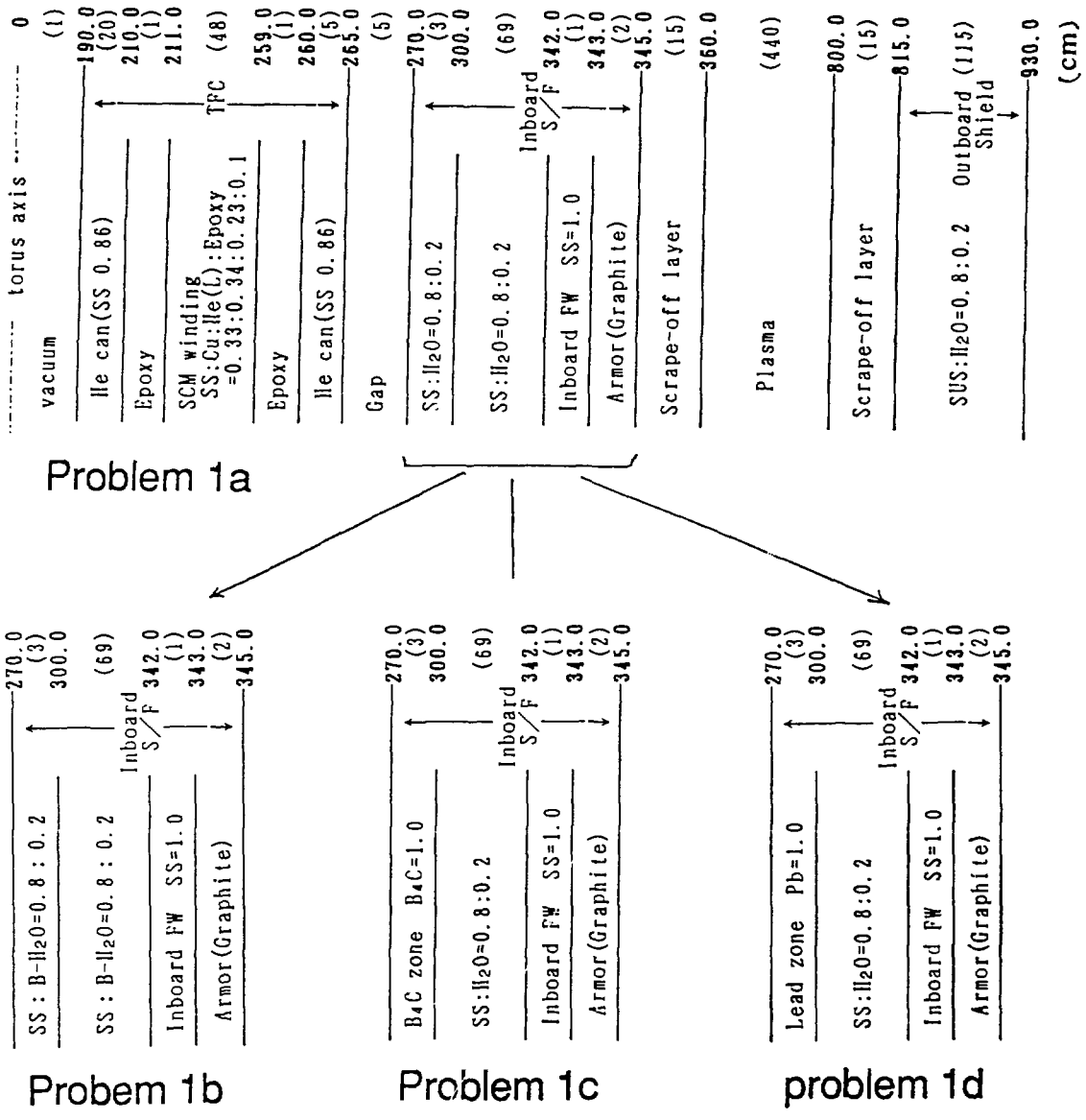

Fig. 2 One dimensional torus model for ITER mid plane

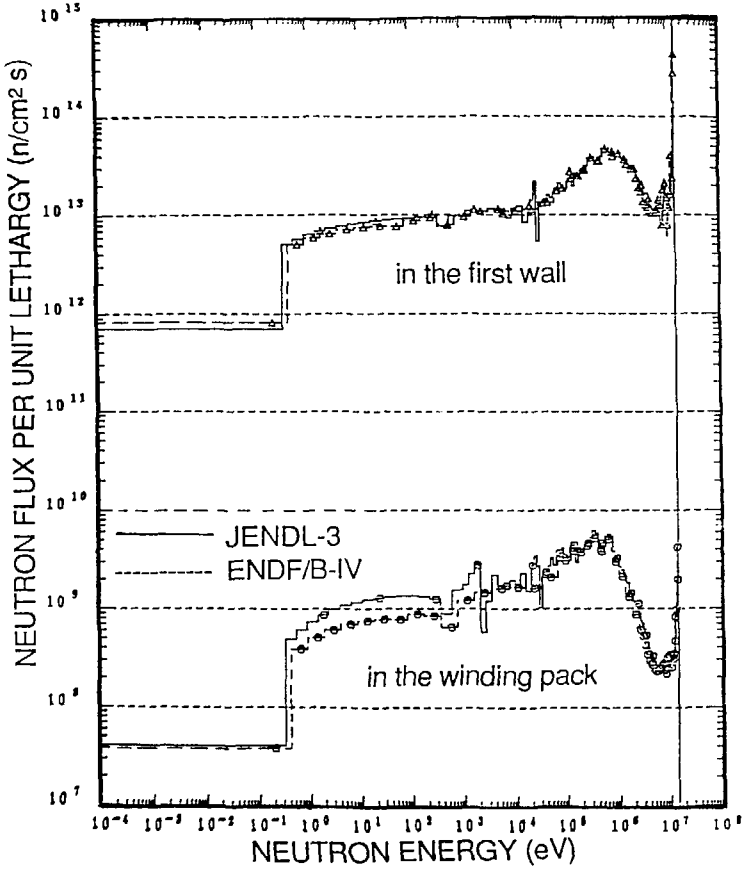

Fig. 3 Comparison of neutron spectra in the first wall and in the winding pack by JENDL-3 with those by ENDF/B-IV (problem. 1a)

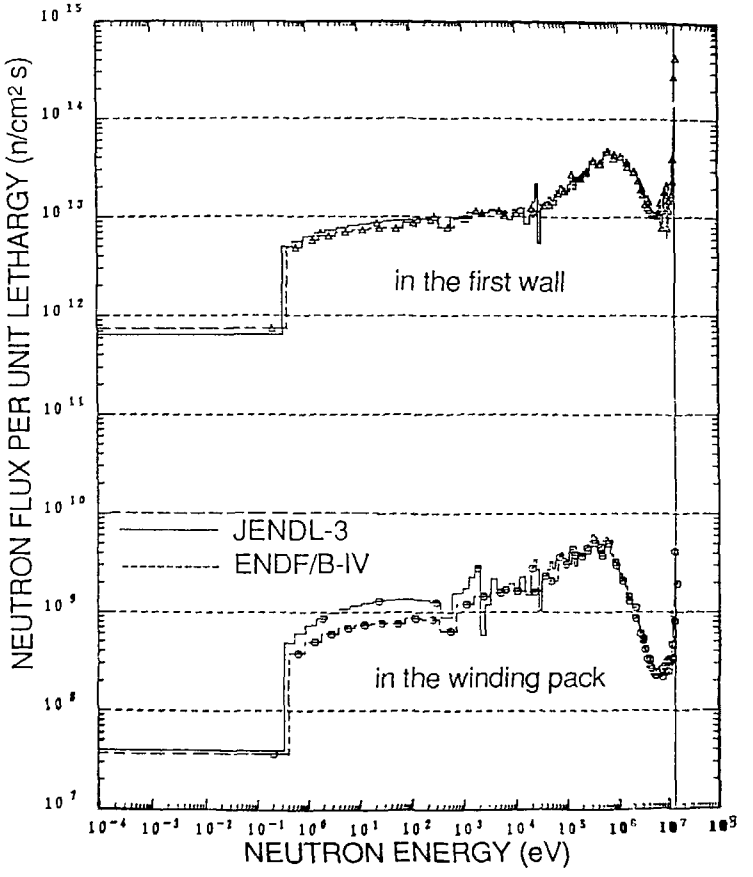

Fig. 4 Comparison of neutron spectra in the first wall and in the winding pack by JENDL-3 with those by ENDF/B-IV (problem. 1b)

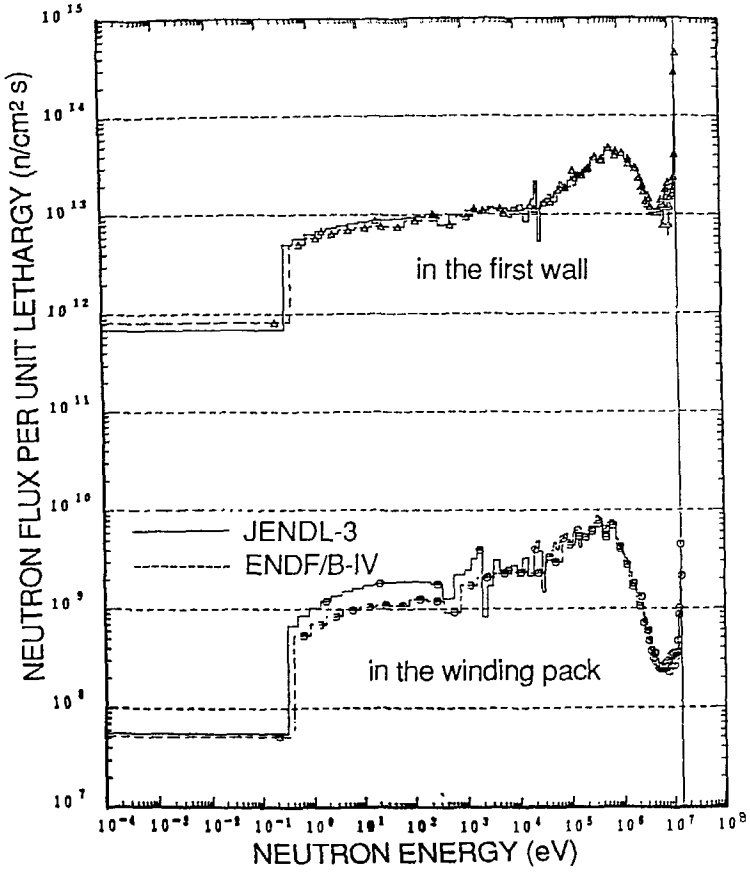

Fig. 5 Comparison of neutron spectra in the first wall and in the winding pack by JENDL-3 with those by ENDF/B-IV (problem. 1c)

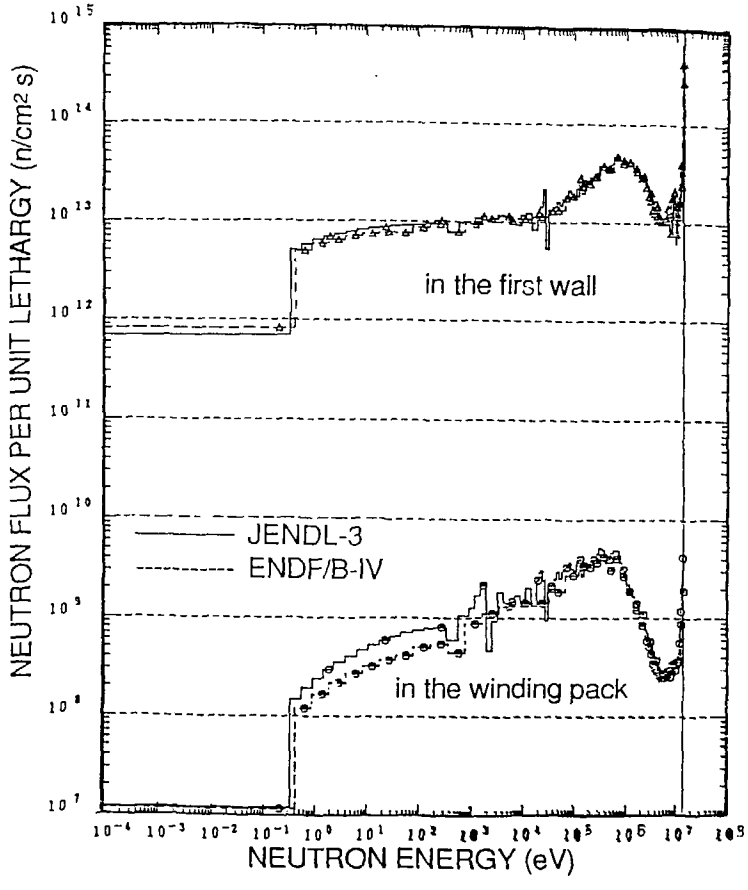

Fig. 6 Comparison of neutron spectra in the first wall and in the winding pack by JENDL-3 with those by ENDF/B-IV (problem. 1d)

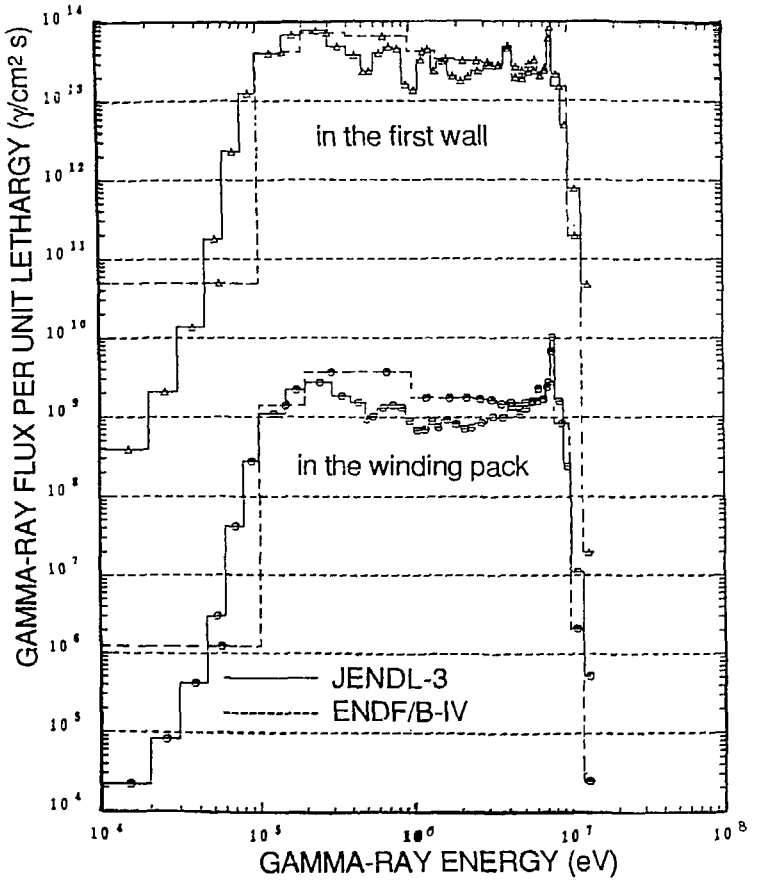

Fig. 7 Comparison of gamma-ray spectra in the first wall and in the winding pack by JENDL-3 with those by ENDF/B-IV (problem. 1a)

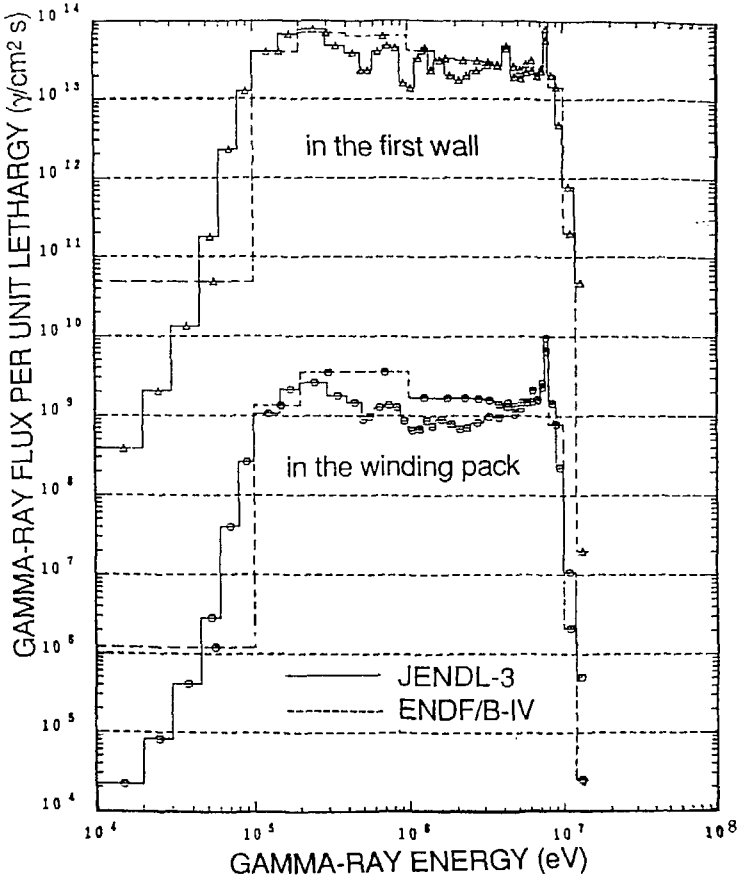

Fig. 8 Comparison of gamma-ray spectra in the first wall and in the winding pack by JENDL-3 with those by ENDF/B-IV (problem. 1b)

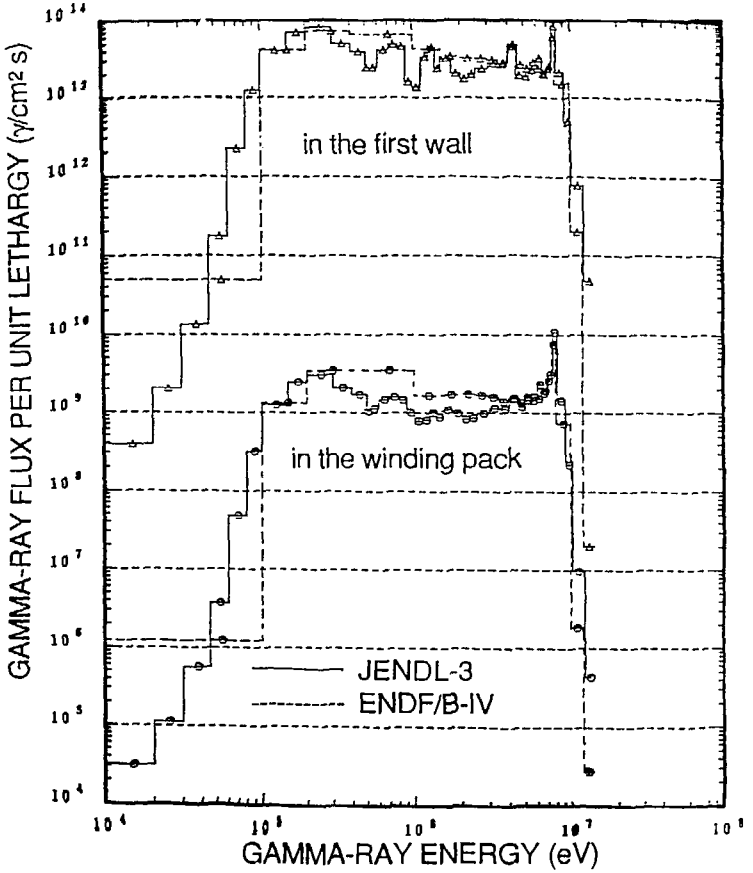

Fig. 9 Comparison of gamma-ray spectra in the first wall and in the winding pack by JENDL-3 with those by ENDF/B-IV (problem. 1c)

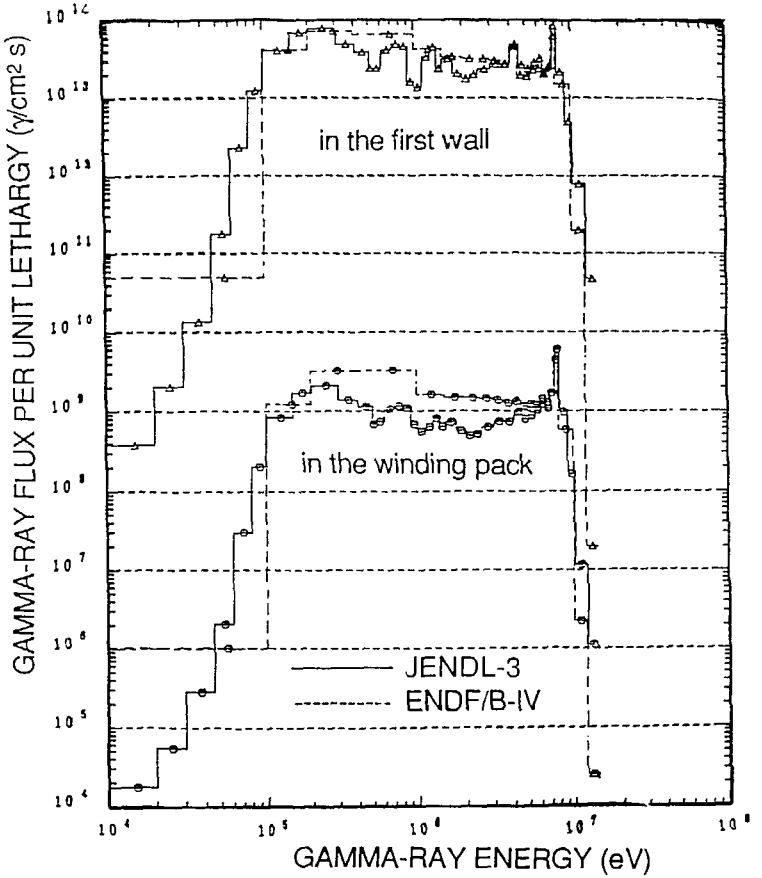

Fig. 10 Comparison of gamma-ray spectra in the first wall and in the winding pack by JENDL-3 with those by ENDF/B-IV (problem 1d)

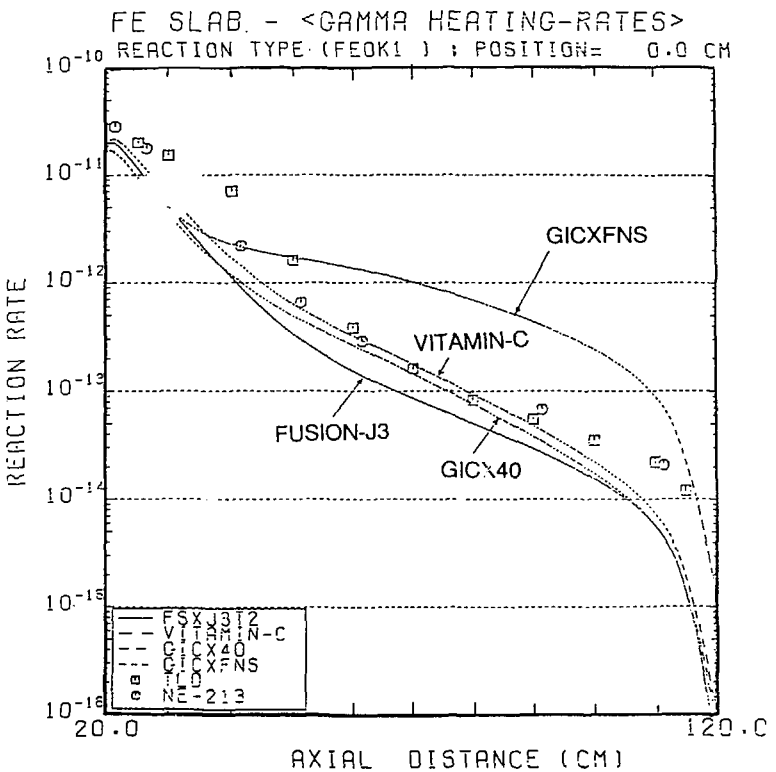

Fig. 11 Comparison of calculated gamma-ray heating rate by various nuclear group constant sets with experimental values

3.13 Analysis of Neutron Benchmark Experiments to Evaluate the JENDL-3 by the Continuous Energy Monte Carlo Code

K. Ueki[1], K. Sakurai[2], and M.Kawai[3]

1) Ship Research Institute
2) Japan Atomic Energy Institute
3) Nuclear Engineering Laboratory, Toshiba Corporation.

Abstract

The pointwise cross sections on which the JENDL-3 nuclear data library was based were prepared by using the NJOY-83 and the MACROS code system to analyze neutron shielding experiment by the continuous energy Monte Carlo Code MCNP. To evaluate the iron cross sections in the JENDL-3, the ORNL and the WINFRITH iron neutron shielding benchmark experiments were selected to the present purpose. Those two benchmark experiments have not only the reaction rates or the detector responses but also the neutron energy spectra covering a wide energy region. The Monte Carlo MCNP calculations were carried out with the pointwise cross sections from the ENDF/B-IV as well as the JENDL-3. The reliability of the iron cross sections in the JENDL-3 were evaluated through the comparisons and the discussions of the calculated results with experiments.

1. Introduction

Recently, the evaluated nuclear data library JENDL-3 was completed and the library was released from the Nuclear Data Center of the JAERI. Taking this situation, the evaluation work of the cross sections in the LENDL-3 library was started at some organizations. In this study, the pointwise cross sections on which the JENDL-3 library was based were prepared by using a nuclear data processing code system to analyze the neutron shielding experiments by the continuous energy Monte Carlo code MCNP[1].

At first, the pointwise neutron cross sections were compiled from the JENDL-3 for the twenty four nuclides by using the

nuclear date processing code system NJOY-83[2], which is a modified version of the NJOY, and with the library compilation code MACROS. However, those processed nuclides were limited up to zirconium, and the more heavy nuclides like lead and uranium are under planning to compile, yet.

In the next place, the ORNL and the WINFRITH iron neutron shielding experiments[3,4] were selected as suitable objects for the evaluation of iron cross sections. Those two benchmark experiments have not only the reaction rates or the detector responses but also the neutron energy spectra covering a wide energy area. The Monte Carlo calculations were carried out by the MCNP code with the pointwise cross sections from the ENDF-B/Ⅳ[5] as well as the JENDL-3 to compare the calculations with the two libraries.

At the last, the iron cross sections in the JENDL-3 were evaluated by the comparison of the energy spectrum between the Monte Carlo calculations with the JENDL-3 and the ENDF-B/Ⅳ and the experiments.

Even though the Monte Carlo calculations can not get rid of the statistical error completely in the results, the calculations by the continuous energy Monte Carlo code with the pointwize cross sections, like the MCNP code, is to be free from the computational error due to the group collapsing process, the taking process of the self-shielding factor, and the energy group structures in the groupwized cross sections. This is the reason why the MCNP code was employed to evaluate the nuclear data of the JENDL-3 in the present study.

To reduce the statistical error in the Monte Carlo calculations, the next event surface crossing(NESX) estimator was newly prepared for the MCNP code and used intensively. Also, the weight window importance parameter were given differently for four energy groups in each divided cell. The computer was the HITAC 680 of the Tokyo University.

2. Analysis of ORNL Iron Neutron Transmission Experiment

A series of deep-penetration neutron transmission measurements through thick iron slabs have been performed at the ORNL Tower Shielding Facility(TSF) using a collimated beam of reactor

neutrons as a source[3]. The measurements were carried out behind various combinations of 5-ft-square slabs and the source neutron beam was tightly collimated. Therefore, the effect of side leakage, even for the thick sample of iron, did not need to take into account in the calculations. Figure 1 shows a schematic arrangement of the experimental configurations for the iron slabs. The neutron source intensity at outlet of the iron collar was 6.8207×10^6 n/min/watt in Fig. 1. Also, experimental configurations for the iron slab measurements are summarized in Table 1.

The MCNP calculations for the ORNL iron neutron shielding problem were carried out with the JENDL-3 and the ENDF/B-Ⅳ libraries to the three cases ; the first was on the count rates of the Bonner ball as shown in Fig's 2,3, and 4, the second was on the neutron energy spectrum between ~40 KeV and 1.5 MeV, as shown in Fig.5, and the third was on the spectrum above 0.8 MeV, as shown in Fig.6. The objected iron thicknesses were 12- and 36-in.

Except a little underestimation to the 12-in. iron calculated results for the 3-in. Bonner Ball response, fairly good values of the C/E (Calculation/ Experiment) were obtained from the MCNP calculations for the 12- and 36-in. iron thickness with both the JENDL-3 and the ENDF/B-Ⅳ libraries to the other Bonner ball responses. However, the results with the JENDL-3 were a little less than those of the ENDF/B-Ⅳ, in all the calculations.

Figure 5 shows the comparison of neutron energy spectra between the MCNP calculated with the JENDL-3 and the ENDF/B-Ⅳ and the measurements. The FSD's (fractional standard deviation) are excellent of 0.033 ~0.089 in each energy bin. The MCNP calculated neutron energy fluxes overestimate the measured fluxes significantly between ~40 KeV and ~100 KeV. However, fairly good agreement with the experiment was obtained between ~100 KeV and ~1 MeV.

Comparison of the continuous energy Monte Carlo code MCNP calculated with the JENDL-3 and the ENDF-B/Ⅳ libraries and the measured spectra above 0.8 MeV on the center-line behind 12 in. of iron in Fig.1 is indicated in Fig.6. The FSD's are good

within 0.022~0.135 at each energy bin. On the while, the Monte Carlo calculated energy spectra indicates fairly good agreement with the measured values. However, the calculated spectrum with the JENDL-3 is underestimated the measurement significantly between ~1 MeV and ~3 MeV. Meanwhile, the spectrum with the ENDF-B/Ⅳ shows good agreement with the experiment in the same energy region. Above 3 MeV, the agreement between the monte Carlo calculated spectra and the measured spectrum is excellent.

3. Analysis of WINFRITH Iron Neutron Penetration Experiment

The iron neutron penetration experiment was carried out in the ASPIS shielding facility at AEE WINFRITH[4]. A low-power natural uranium converter plate, driven by the source reactor NESTOR, provided a large thin disc source of fission neutrons at the interface of the graphite moderator and the extensive iron shield. The neutron energy spectra were measured at four selected positions using the proportional counters and the NE213 spectrometers. The reaction rates were also obtained using three threshold detectors and one activation detector.

The MCNP calculated reaction rates of the Rh(n,n') threshold detector which has effective reaction cross sections above 0.1 MeV neutrons are summarized in Table 2. The calculated results indicate fairly good values of the C/E at all the detector locations. The magnitudes of the C/E are between 1.09 and 0.77 for the JENDL-3 and between 1.29 and 0.99 for the ENDF/B-Ⅳ.

Comparison of the calculated iron neutron spectra with the JENDL-3 and the ENDF/B-Ⅳ and the measurements at 56.83- and 85.41-cm-depth in Fig.7 are shown in Fig's 8 and 9, respectively. The MCNP calculated energy spectra with both the libraries indicate fairly good agreement with the measured spectra at both the 56.83- and 85.41-cm-depth detector locations in the range from ~10 KeV to ~1 MeV, on the whole. However, making detailed comparison between Fig.8 and Fig.9, the calculated spectra with the JENDL-3 under estimate s above 0.5 MeV neutrons with thicknes, and unfortunately the FSD's above 1 MeV are not enough to evaluate the iron cross sections in the libraries.

4. Summary and Discussions

The MCNP calculations with the JENDL-3 and the ENDF/B-Ⅳ iron cross sections obtained the following remarks

1) The calculated leakage energy fluxes of the ORNL iron neutron shielding problem shows almost same tendency to the WINFRITH problem in the same neutron energy area of it. The overestimation of the calculated energy fluxes is significant between ~20 Kev and ~100 Kev for both the ORNL and the WINFRITH iron experiment, so that the iron cross sections in the JENDL-3 are to be small in such a energy region.

2) The calculated energy fluxes between ~100 KeV and ~1 MeV agreed fairly well with the measurements, furthermore, there was no significant difference of the calculated spectra between the JENDL-3 and the ENDF/B-Ⅳ, so that the iron cross sections are to be reliable in such a energy region.

3) The calculated fast neutron energy fluxes between 0.8 MeV and 3 MeV indicate underestimation, but the calculated energy fluxes show fairly good agreement between 3MeV and 9MeV with the ORNL iron benchmark experiment. The magnitude of the underestimation of the calculated energy fluxes is fairly significant between ~0.8 MeV and 3 MeV, so that the iron cross sections in the JENDL-3 are to be large in such a energy region. However, the iron cross sections in the both libraries are to be reliable between ~3 MeV and ~9 MeV.

References

1) MCNP-A General Purpose Monte Carlo Code for Neutron and Photon Transport, LA-7396-M (Rev.) Version 2B, Los Alamos Monte Carlo Group, Los Alamos National Laboratory (1981).
2) R.E. MacFarlane, et al, "The NJOY Nuclear Date Processing System", LA-9303-M (1982).
3) R.E. Maeker and F.J. Muckenthaler, Nucl. Sci. Eng., 52 227 (1973).
4) M.D. Carter, M.M. Chestnutt, and A.K.McCracken., "The ASPIS Iron Benchmark Experiment-Results and Calculational Model", Proc. of Specialists' Meeting on Nuclear Date and Bench Marks for Reactor Shielding, Paris, 297 (Oct. 1980).

5) "ENDF/B Summary Documentation", BNLNCS-17541 (ENDF-201), 2nd ed. (ENDF/B-IV), D. Garber, Ed., available from the National Nuclear Date Center, Brookhaven National Laboratory, Upton, New York (Oct. 1975).

Table 1 Experimental configurations for the iron transmission measurements

Iron Slab Thickness (in.)	Detector Locations			Detector Type
	Centerline Distance behind Slab (in.)	Radial Distance from Centerline (in.)	Observation Angle[a] with Respect to Centerline (deg)	
0.52	127 123 90	0 33 90	0 15 45	^{10}B Spectrometer
1.55	152 146 107	0 39 107	0 15 45	Bonner Balls
	126 122 89	0 32.5 89	0 15 45	^{10}B Spectrometer
4.05	158 116	42.5 116	15 45	NE-213 Spectrometer
6.06	162	0	0	NE-213 Spectrometer
12.13	141 136 100	0 36.5 100	0 15 45	Bonner Balls
	156 150 110	0 40.5 110	0 15 45	NE-213 Spectrometer
12.25	10 10	0 12	0 50	Benjamin Spectrometer
24.41	128 124 90.5	0 33 90.5	0 15 45	Bonner Balls
36.56	115 111 81.5	0 30 81.5	0 15 45	Bonner Balls

[a]The observation angle is defined as the angle between the centerline and a line connecting the detector and the midpoint of the emergent face of the slab. The vertex of this angle is the pivot point for the angular traverses.

Table 2 Comparison of Rh(n,n') reaction rates between measured and calculated values along the axis of the ASPIS iron

(dps atom^{-1}/5.63×10^{7} n/s)

Exp. & Calculation \ Location (cm)		5.4	22.54	56.83	85.41	113.98
Experiment		3.86×10^{-21}	8.46×10^{-22}	7.90×10^{-23}	1.66×10^{-23}	4.25×10^{-24}
ENDF/B-IV 100,000 Histories	(FSD)	3.83×10^{-21} (0.027)	9.06×10^{-22} (0.024)	1.02×10^{-22} (0.027)	1.94×10^{-23} (0.029)	4.34×10^{-24} (0.030)
	C/E	0.99	1.07	1.29	1.17	1.02
JENDL-3 109,000 Histories	(FSD)	3.97×10^{-21} (0.027)	9.23×10^{-22} (0.023)	8.33×10^{-23} (0.028)	1.59×10^{-23} (0.032)	3.29×10^{-24} (0.033)
	C/E	1.03	1.09	1.05	0.96	0.77

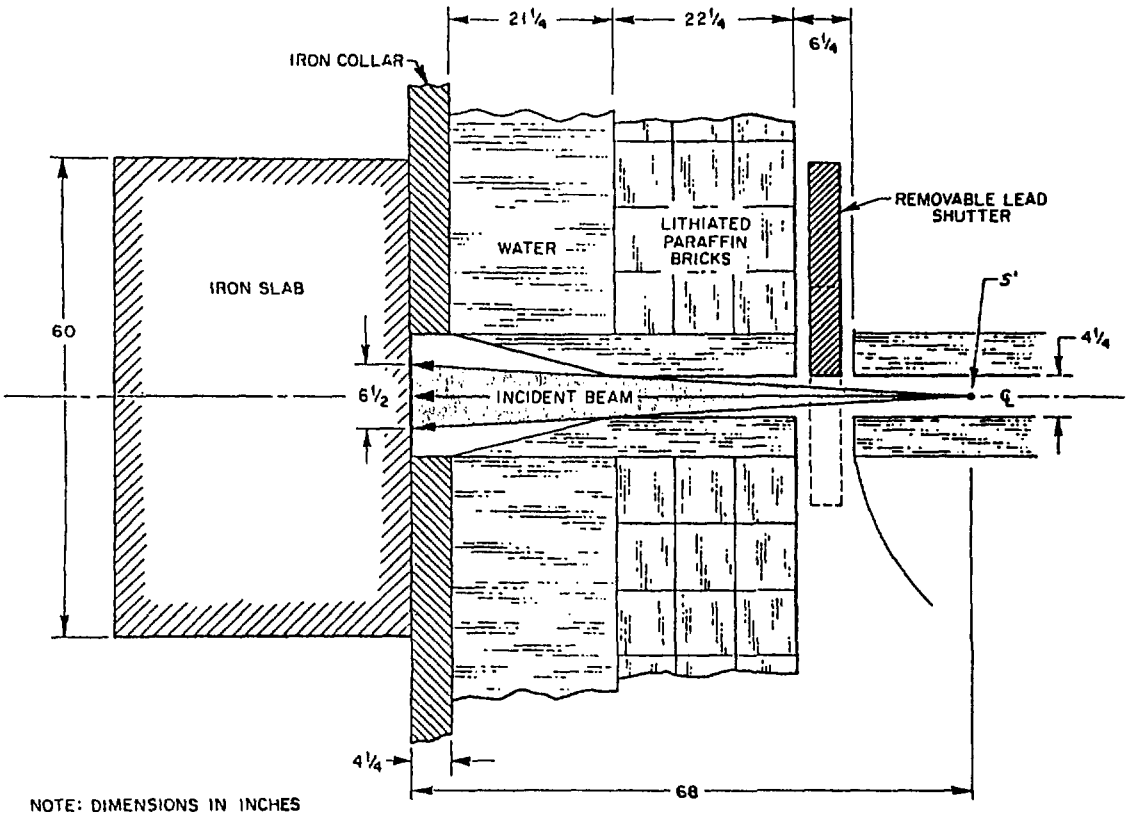

Fig. 1 Experimental configuration for the 4 1/4 - in. -diam collimator with the 3-ft-thick iron slab in place. This collimator was used for all of the measurements except those made behind 18 in. of stainless steel.
Source intensity: $3.186\times10^{4}\times\pi(3.25\times2.54)^{2}=6.8207\times10^{6}$ n/min/Watt

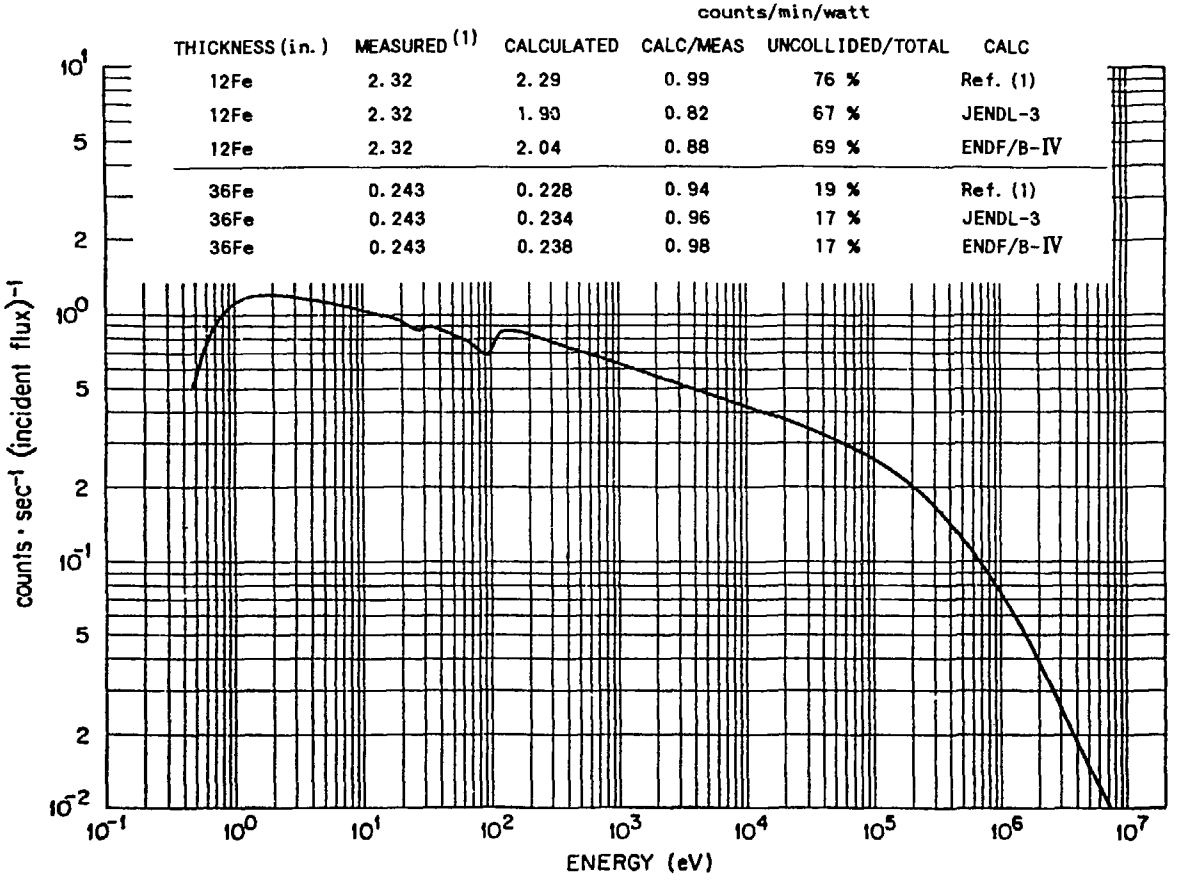

Fig. 2 Results for 3-in. Bonner ball on the centerline. Comparison of calculated and measured counting rates and its response function

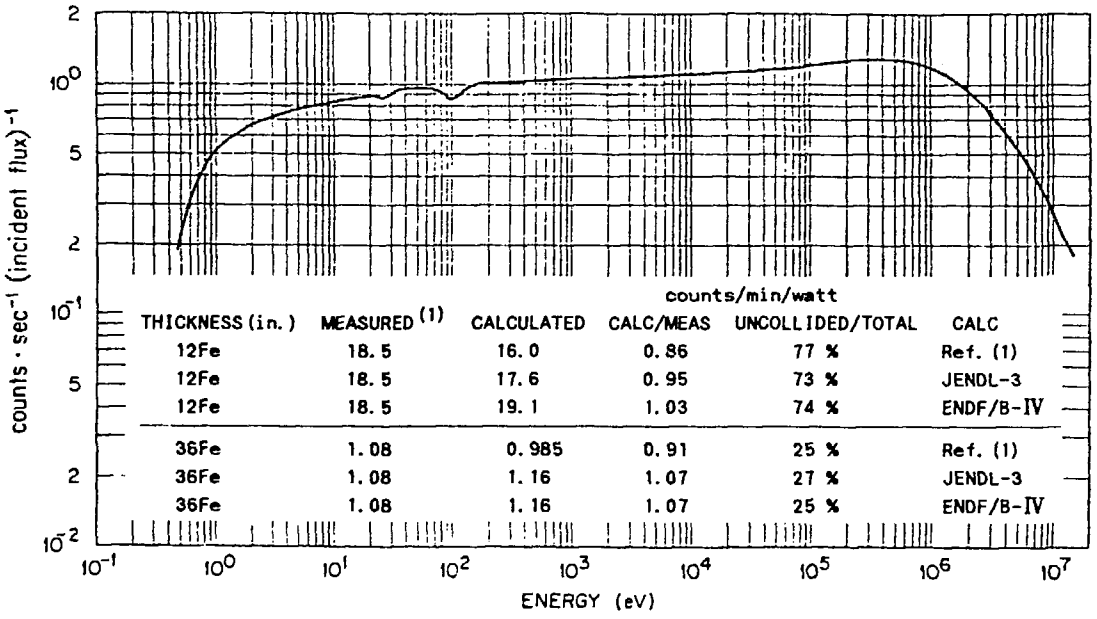

Fig. 3 Results for 6-in. Bonner ball on the centerline. Comparison of calculated and measured counting rates and its response function

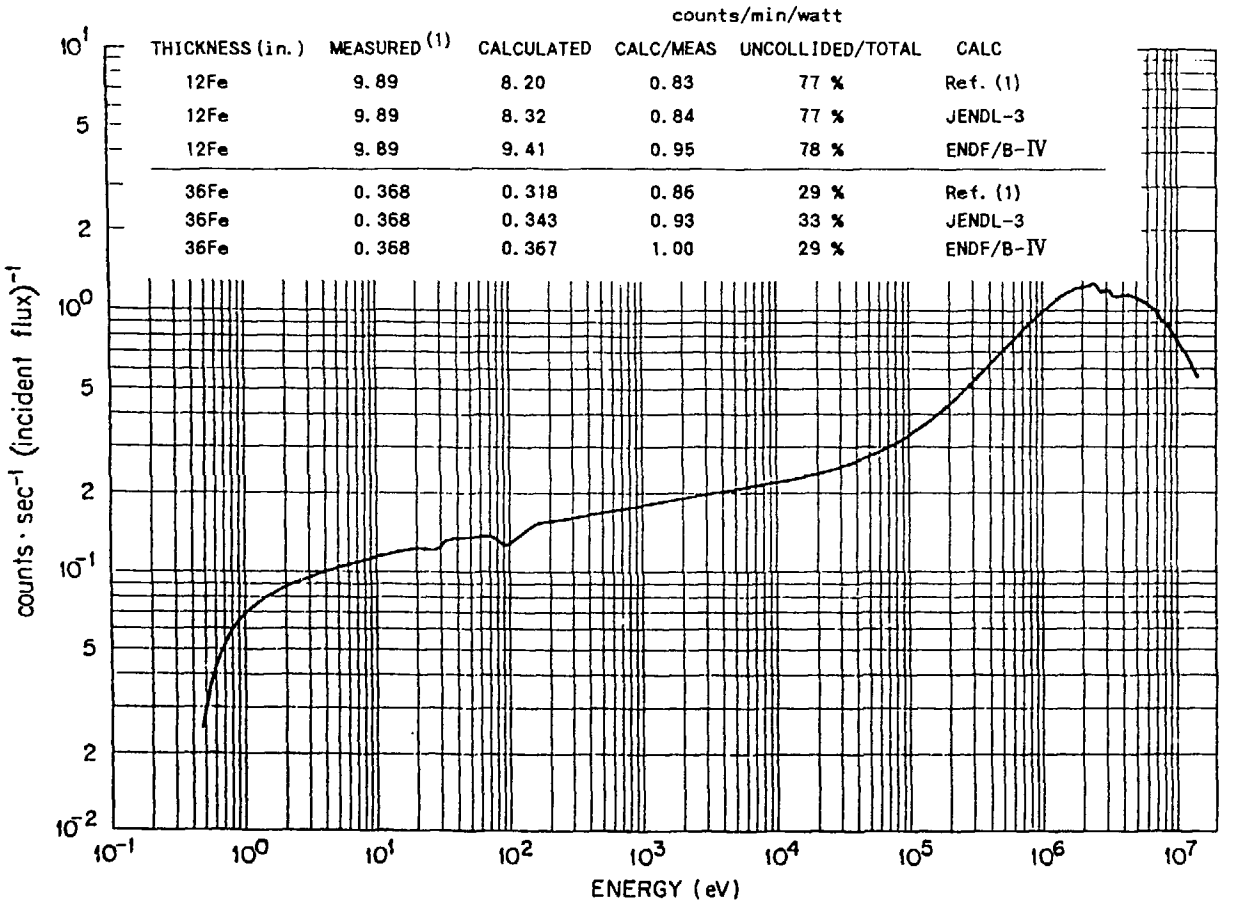

Fig. 4 Results for 10-in. Bonner ball on the centerline. Comparison of calculated and measured counting rates and its response function

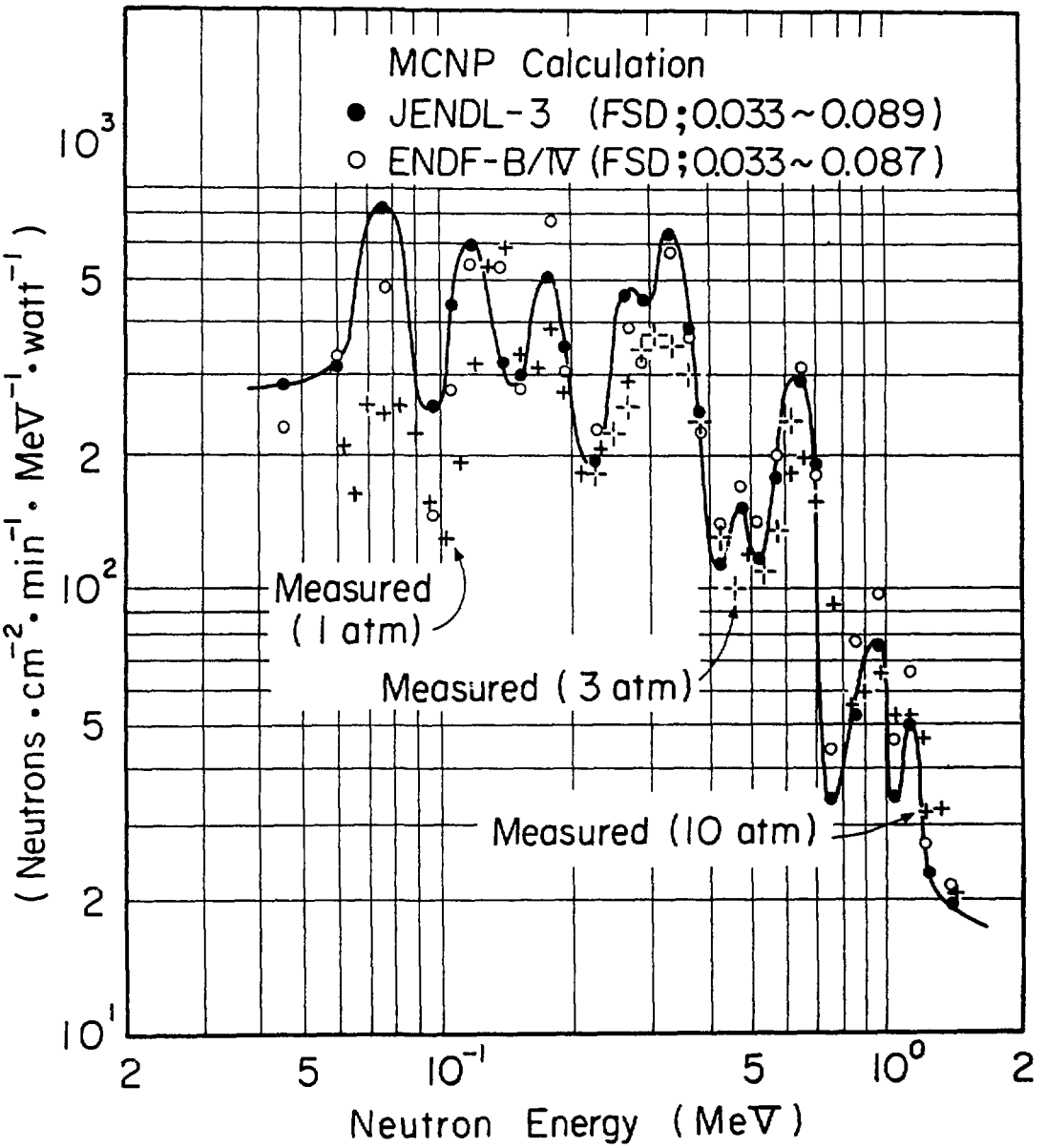

Fig. 5 Comparison of MCNP calculated and measured spectra[3] between 60 keV and 1.5 MeV on the centerline behind 12 in. of iron

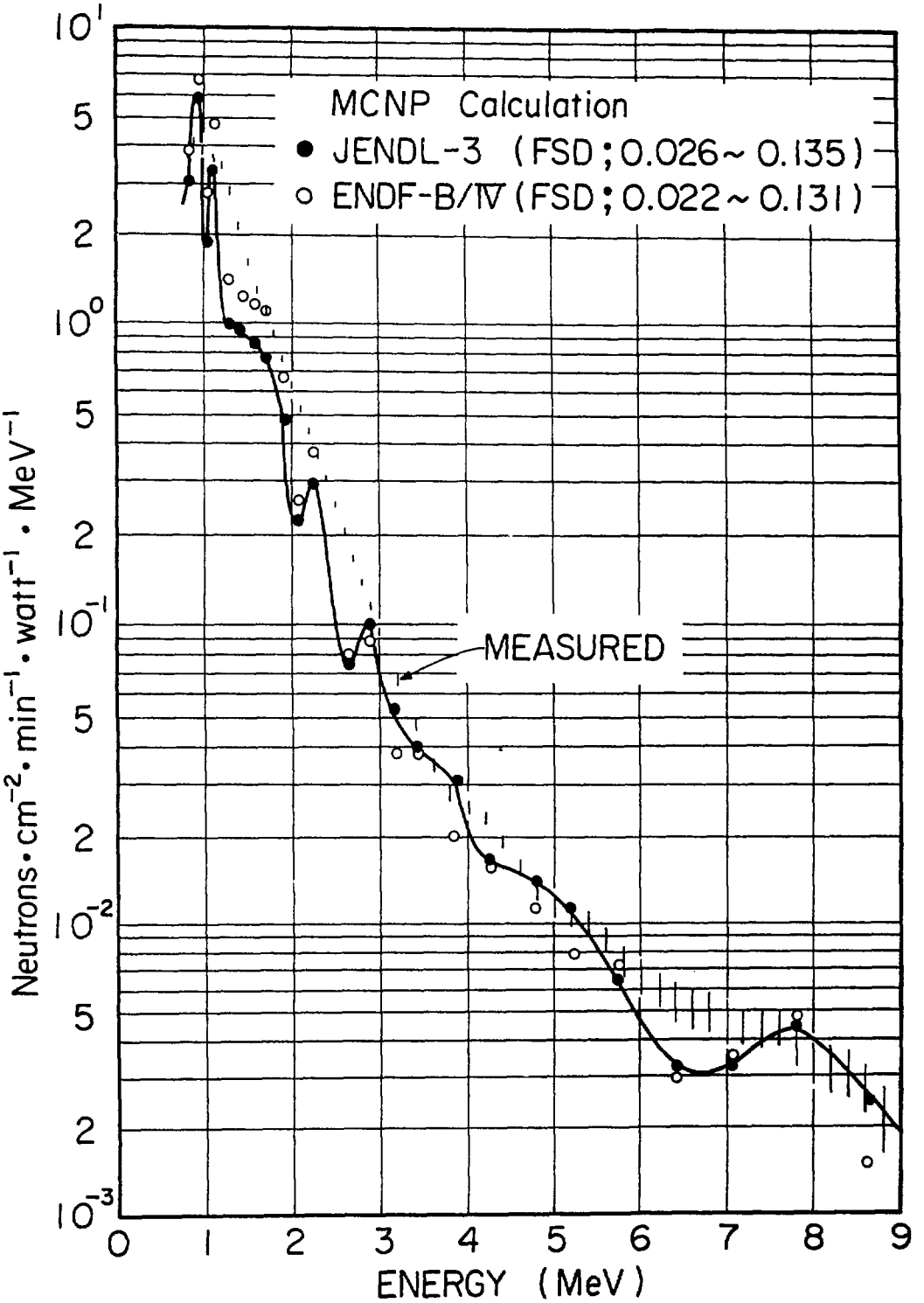

Fig. 6 Comparison of MCNP calculated and measured spectra above 0.8 MeV on the centerline behind 12 in. of iron

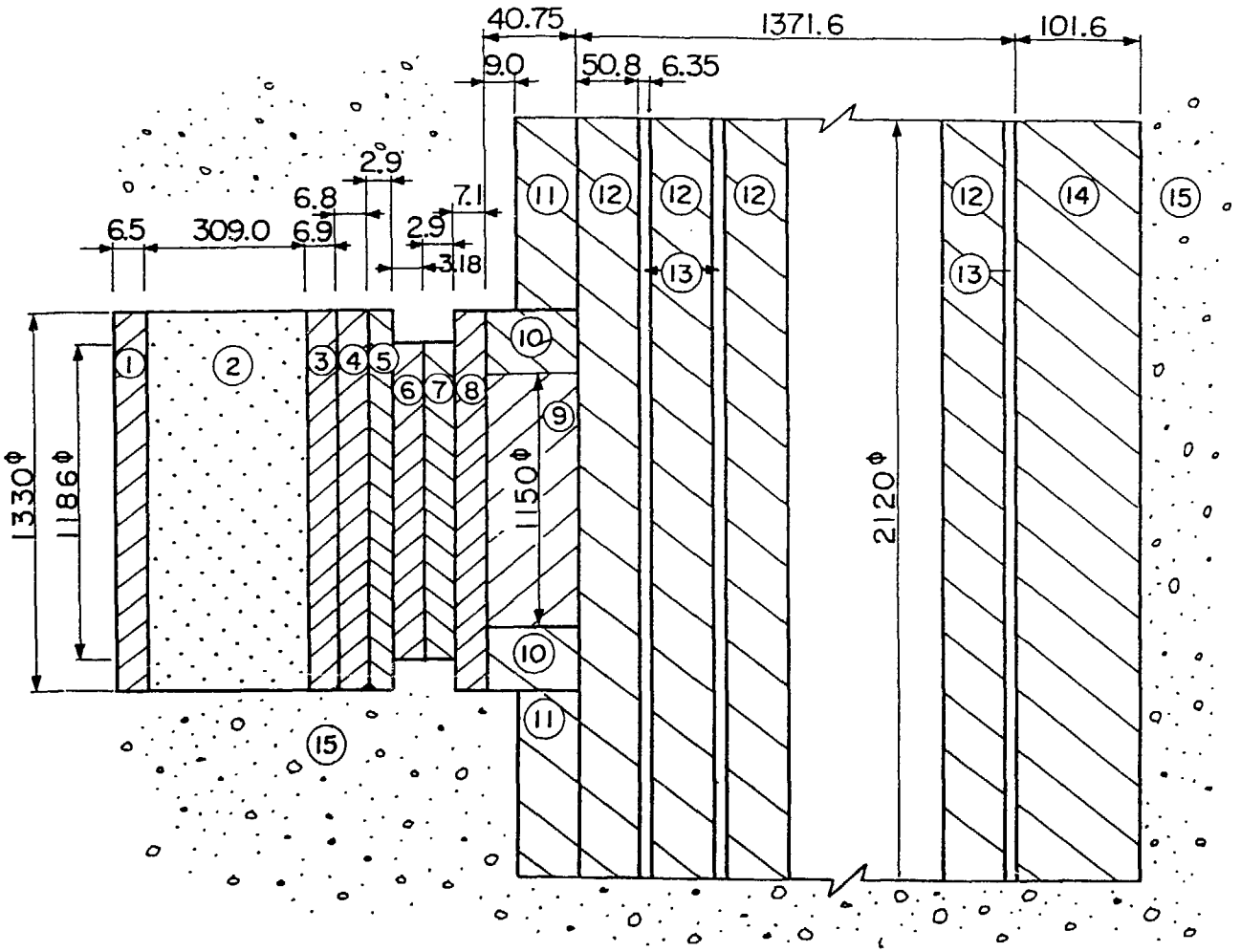

Fig. 7 Schematic arrangement of the iron neutron shielding experiment at the WINFRITH

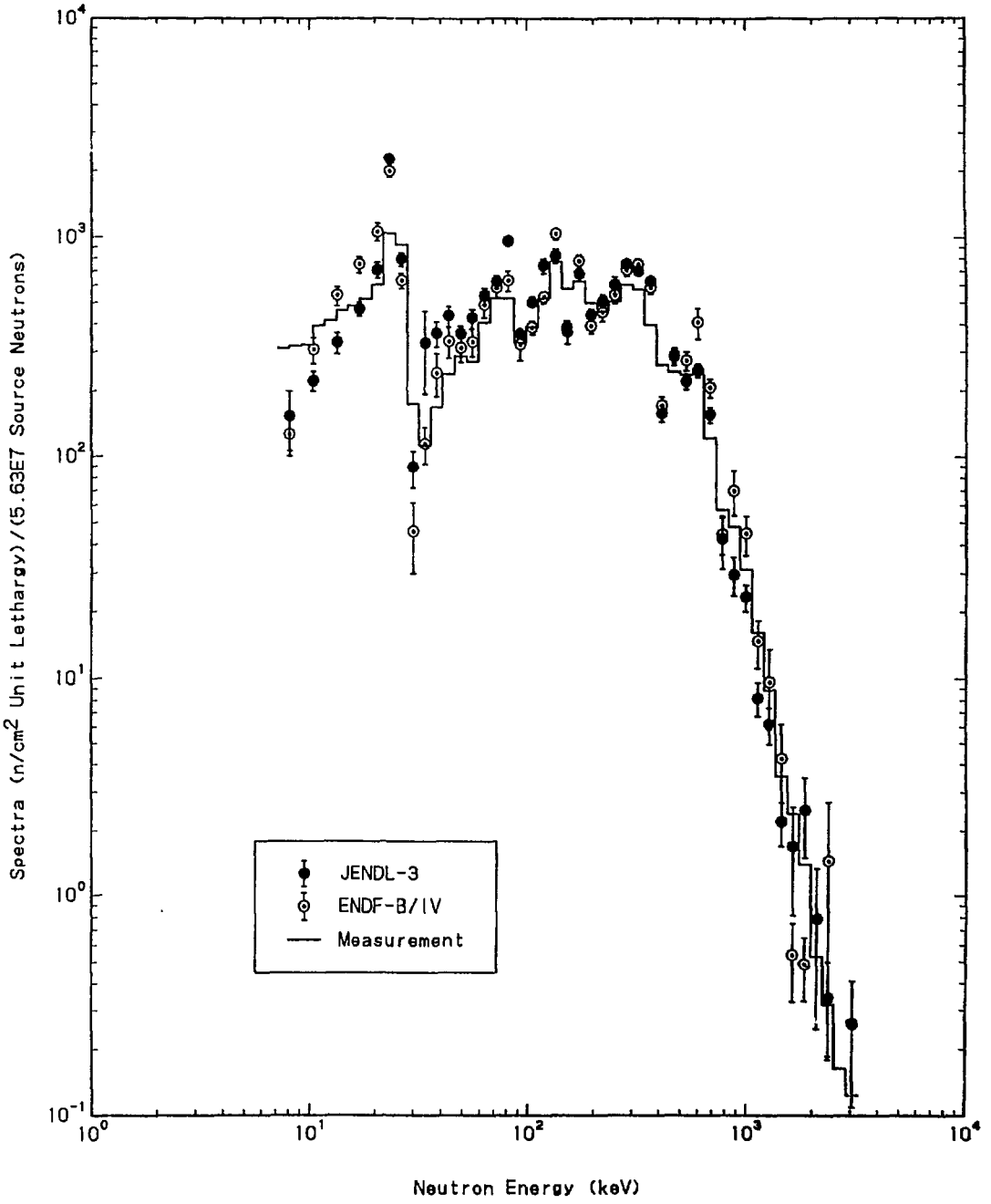

Fig. 8 Comparison of measured and MCNP calculated neutron spectra at 56.83 cm-depth

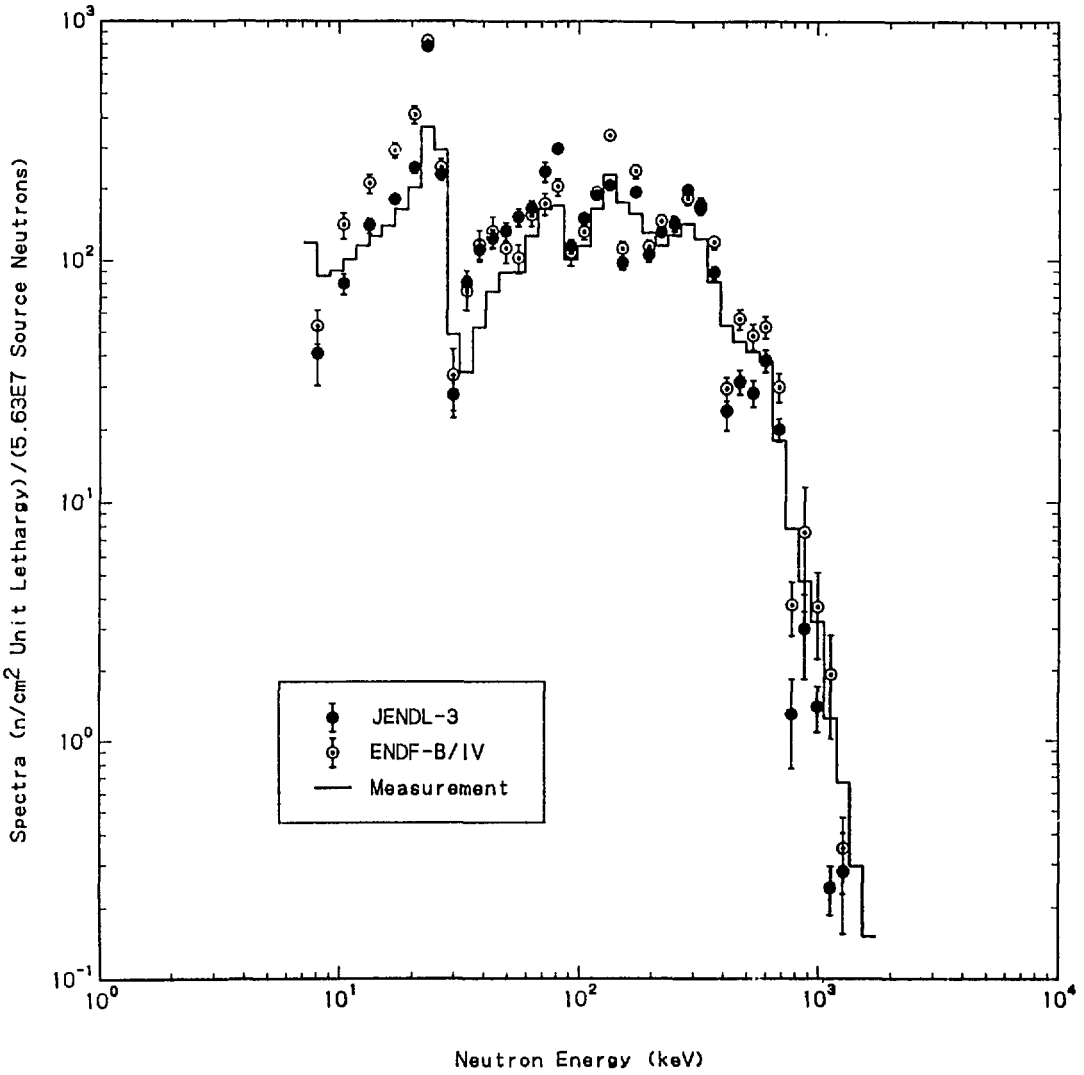

Fig. 9 Comparison of measured and MCNP calculated neutron spectra at 85.41 cm-depth

3.14 Development of the JENDL Special Purpose Data File for PKA Spectra, DPA Cross Sections and Kerma Factors

Shungo IIJIMA, Masayoshi KAWAI

Nuclear Engineering Laboratory, Toshiba Corporation

Method of calculation of the neutron-induced primary knock-on atom spectra, atom displacement cross sections and kerma factors is presented based on the nuclear data from the evaluated data file of ENDF/B-5 format, supplementing the emitted charged particle spectra from nuclear cross section calculation code. Approximate and compact formulas of DPA cross section and kerma factor were derived for the reaction sum involving multi-particle emissions. The formulas are valid for medium and heavy mass nuclei. Examples of calculation on iron are given for neutron energies up to 40 MeV. Comparison was made with the kerma factor caluclated by Howerton and Caswell et al. below 20 MeV and the DPA cross section with RADHEAT-V4 and TENJIN-2 code below 15 MeV. It is shown that the high energy kerma factor is governed by the charged particle emission, while the high energy DPA cross section is mainly determined from neutron optical potential.

1. Introduction

There is an increasing demand for the data of PKA (primary knock-on atom) spectra, DPA (displacement per atom) cross sections and kerma (kinetic energy release in matter) factors induced by neutron reactions with materials. These data, abbreviated as PKA/Kerma data hereafter, are applied to the calculation of heat generation in fusion reactor, study of radiation damage, neutron therapy, radiological biology, and the calculation of detector responses.

At the subworking group of PKA/Kerma data, JNDC, the compilation of PKA/Kerma data file in in progress as a part of JENDL special purpose data file[1] for neutron energy range from 10^{-5} eV to 20 MeV. It should be also borne in mind that the kerma factors of light elements are required up to 100 MeV for neutron therapy and DPA cross sections up to 50 MeV for damage study.

It has been rather customary in calculation of PKA/Kerma data to use rather crude approximations for particle emission spectra. However, PKA/Kerma data are derivable mostly from the recent evalulated neutron data file of ENDF/B-5 format, if the data above 20MeV and the data for the emitted charged particle spectra are supplemented by cross section calculation codes.

In the present paper, the method of calculation of the PKA /Kerma data is described to be consistent with JENDL-3. Especially an approximate and compact expression is given of the kerma factor and DPA cross section for reaction sum involving multi-particle emission processes. Examples of calculation are given for iron for neutron energies below 40 MeV. The results are compared with the calculation of kerma factor by Howerton[2] and Caswell et al.[3] and that of DPA cross section by RADHEAT-V4 code[4].

2. Reaction Kinematics and PKA Spectrum

Kerma factor (per atom) and DPA cross section in the standard NRT model[5] are written by

$$KF(E_N) = \sum_x \int (E_p+E_k)\sigma_{n,x}(E_R,\varepsilon_e,\theta_c)\,d\varepsilon_c d\Omega_c \tag{1}$$

$$\sigma_{DPA}(E_N) = \frac{0.8}{2\varepsilon_d} \sum_x \int \frac{E_p}{1+kg(E_p)}\,\sigma_{n,x}(E_N,E_p)\,dE_p \tag{2}$$

Here,

E_N : incident neutron energy

E_R : relative incident energy

E_p : recoil atom energy in laboratory system

E_k : emitted charged particle energy in laboratory system

ε_d : displacement energy of atom from crystal lattice

$kg(E_p)$: correction factor for elctronic energy loss by Lindhard and Robinson[6]

$\sigma(E_R,\varepsilon_c,\theta_c)$: double differential cross section in C.M. system

$\sigma(E_N,E_p)$: angle-integrated PKA spectrum

In Eq.(1), suffix K is for charged particle emission reaction.

PKA spectrum is obtained by converting the cross section given in C.M system to the laboratory frame. The double differential and the angle-integrated PKA spectra for the first stage reaction are

$$\sigma(E_N,E_p,\theta_p) = \left(\frac{M}{m_1}\right)^{3/2} \sqrt{\frac{E_p}{\varepsilon_c}}\,\sigma(E_R,\varepsilon_c,\theta_c) \tag{3}$$

$$\sigma(E_N,E_p) = \frac{\pi M}{\sqrt{m_1 m_2}} \int_{\varepsilon_c^{(1)}}^{\varepsilon_c^{(2)}} d\varepsilon_c\, \frac{1}{\sqrt{\varepsilon_c E_G}}\,\sigma(E_R,\varepsilon_c,\theta_c) \tag{4}$$

Here, E_R and E_G are respectively the relative incident energy and the energy of the center-of-gravity.

$$E_R = (m_{02}/M)E_N,$$

$$E_G = \frac{1}{2} MV^2 = (m_{01}/M)E_N ,$$

where, $M = m_{01} + m_{02} = m_1 + m_2$.
Reaction kinematics and the symbols are illustrated in Fig. 1 right.
Suffix c is for the quantities in C.M. system.

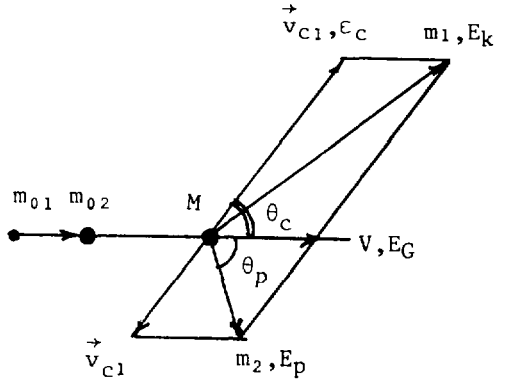

Fig. 1 Kinematics of nuclear reaction

(E_p, θ_p) and (δ_c, θ_c) are the energies and the angles of recoil atom in laboratory system and of emitted particle in C.M. system, respectively.
Kinematics relation gives

$$E_p = \frac{m_2}{M} E_G + \frac{m_1}{M} \varepsilon_c - 2\sqrt{\frac{m_1 m_2}{M^2} E_G \varepsilon_c \mu_c} , \tag{5}$$

$$\mu_p \equiv \cos\theta_p = (1-\eta_c\mu_c)/\sqrt{1 + \eta^2 - 2\eta_c\mu_c} , \tag{6}$$

$$\eta_c \equiv v_{c2}/V = \sqrt{\frac{m_1\varepsilon_c}{m_2 E_G}} .$$

The energy and angle of the emitted particle in laboratory system are obtained by interchanging m_1 and m_2, and replacing μ_c by $-\mu_c$ in Eqs. (5) and (6).

$$E_K = \frac{m_1}{M} E_G + \frac{m_2}{M} \varepsilon_c + 2\sqrt{\frac{m_1 m_2}{M^2} E_G \varepsilon_c \mu_c} \tag{7}$$

Naturally, $E_p + E_k = E_G + \varepsilon_c$.

It is noted that the Eqs.(3) through (7) are independent of

the incident particle and the target nucleus, and hence these equations can be applied as they are for the case of natural decay and the successive emission of particles if E_G is replaced by the kinetic energy of moving compound nucleus.

In case of the second stage reaction, the PKA spctrum is expressed by applying twice the Jacobians in Eqs.(3) and (4). To this calculation, the spectra of both the 1st and 2nd particles in C.M. system are necessary. For emissions of more than 3 particles, not only the analytical calculation becomes very tedious but also we must keep all the informations of particle spectra at every stage of emission. A Monte Carlo type approach may then be prefered.

3. Calculation of Kerma Factor

Kerma factor defined by Eq.(1) is written as

$$KF(E_N) = \sum_x (\overline{E}_p + \overline{E}_k)\sigma_{n,x}(E_N) \qquad (8)$$

Here, $\overline{E}_p$ and $\overline{E}_k$ are the average values of E_p and E_k over the double differential spectrum in the C.M. system. For the 1st stage reaction these are obtained from Eqs.(5) and (7).
For the second stage reaction, new $\overline{E}_p'$ and $\overline{E}_k'$ are

$$\overline{E}_p' = (m_2'/M')\overline{E}_p + (m_1'/M')\overline{\varepsilon}_c' \quad , \qquad (9)$$

$$\overline{E}_k' = (m_1'/M')\overline{E}_p + (m_2'/M')\overline{\varepsilon}_c' \quad , \qquad (10)$$

where m_1' and m_2' are the masses of the 2nd particle and the 2nd recoil atom, and $M' = m_1' + M_2'$. Similar procedure can be used for emission of 3 or more particles.

Thus all we have to know are the average energies and the cosine of the angles of emitted particles in the C.M. system. These are either extracted from the evaluated data file or calculated by GNASH[7], TNG[8], PEGASUS[9] etc.

The average recoil energy from neutron capture gamma-rays may be written as

$$\bar{E}_p \simeq E_G + (\overline{\varepsilon_\gamma^2}/2MC^2)Y_\gamma \qquad (11)$$

where Y_γ is the multiplicity of gamma-rays.
It is easily seen that the recoil from gamma-ray emission is important only for low energy neutron capture. For other reaction gamma-rays the recoil is negligibly small compared with the first recoil due to particle emission. This is an essential point in simplifying the calculation of kerma factor and DPA cross section.

Kerma factors due to the elastic and the discrete inelastic scatterings are calculated from an evaluated data file without ambiguities. For other reactions the calculation of reaction-wise kerma factor is rather complicated. However, by taking the sum over reactions using the above expressions of average energies of recoil atom and particles, we obtain an approximate but a compact formula :

$$KF(E_N) \simeq (m_2/M)E_G\sigma_R + (m^{(n)}/M)\bar{\varepsilon}_n\sigma_{n\text{-prod}} + \sum_x^{p,d,\alpha} \bar{\varepsilon}_x\sigma_{x\text{-prod}} - 2\sqrt{\frac{m_1^{(n)}m_2}{M^2} E_G\, \bar{\varepsilon}_n^{(1)}\bar{\mu}_n^{(1)}\sigma_{n,nx}^{(1)}} \qquad (12)$$

Here, superfix (1) denotes the 1st stage quantities, and

σ_R = reaction cross section

$\sigma_{x\text{-prod}}$ = particle production cross section,

$\bar{\varepsilon}_x$ = average energy of emitted particle in C.M. system.

In deriving Eq.(12) it was assumed that the mass of compound nucleus is much greater than that of the emitted particle, and that the emissions of second (and more) particles are isotropic.

The angular distributions of particles emitted from the first stage are of the preequilibrium nature. These are calculated from the systematics of Kalbach-Mann or Kumabe et al.[10], or from the theory of Mantzouranis et al.[11] with refraction effect at incident nuclear surface.[9]

On the Energy Balance Method

Kerma factor is often calculated by using the energy balance

$$KF(E_N) = \sum_x (E_N + Q_{n,x})\sigma_{n,x} - (\overline{E}_n\sigma_{n\text{-prod}} + \overline{E}_\gamma\sigma_{\gamma\text{-prod}}) \cdot \qquad (13)$$

However, the result is very senitive to the slight violation of energy balance in the data file. Kerma factor for neutron energy below a few MeV is of the order of magnitude of (E_N/A) while each term on the r.h.s of Eq.(13) is of the magnitude of E_N . Thus, for medium-weight nucleus the energy balance must be assured better than 2 % to calculate kerma factor within 100 % error. When charged particle emissions become prominent then the energy balance method can be reliable.

4. Calcualtion of DPA Cross Section

DPA cross sections for elastic and the discrete inelastic scatterings are better calculated directly from PKA spectra. For other reactions involving multi-particle emissions the calculation of PKA spectra is not easy. However, summing over the reactions and making use that the Lindhard correction factor is a relatively slowly varying function of E_p (as shown in Fig. 2), DPA cross section may be expressed approximately

$$\sigma_{DPA}(E_N) \equiv \frac{1}{1+kg(\overline{E}_p)} \sum_x E_p\sigma_{n,x}(E_N) \ , \qquad (14)$$

$$\overline{E}_p\sigma_R \equiv \sum_x \overline{E}_p\sigma_{n,x} \simeq (m_2/M)E_G\sigma_R + \sum_x^{n,p,d,\alpha} (m_1^{(x)}/M)\overline{\epsilon}_x\sigma_{x\text{-prod}} \cdot \qquad (15)$$

Numerical estimation for iron shows that Eq. (14) holds

within a few percent accuracy for summed reaction other than elastic and the discrete inelastic scattterings at E_N = 15 MeV. This may be because the PKA spectra for (n,n'x) and (n,px) are spread rather narrowly around $E_P = E_G$. This is not true for (n, α) reaction, but the cross section is small compared with that of other reactions. On the other hand, Eq. (14) is in overestimation by about 30 % for elastic and the discrete inelastic scatterings, reflecting broad PKA spectra for these reactions spanning E_p values from 0 to $4E_G$. The validity of the approximation depends on the target elements (worse for lighter element).

5. Examples of Calculation

Calculation was performed for iron for neutron energies below 50 MeV. JENDL-3 data was used below 20 MeV. GNASH code was used to calculate cross sections above 20 MeV as well as the average energies of emitted protons, alphas and deuterons in all energy range. The values of parameters used in GNASH calculation above 20 MeV are somewhat different from the ones used in iron cross section evaluation for JENDL-3 below 20 MeV.

Figure 3 shows the normalized PKA spectrum for elastic scattering at 15 MeV. The normalized angular distribution in C.M. system is also depicted to show the correspondence with PKA spectrum structure. Fig. 4 shows the normalized PKA spectra for the inelastic scatterings to Q=-825 keV and -2.11 MeV discrete levels (mixed levels for natural iron) at 15 MeV. The coupled channel calculation was used to these levels in JENDL-3 giving strongly anisotropic angular distributions, which are reflected on PKA spectra. Figure 5 gives the average energy of emitted particles in C.M. system versus incident neutron energy.

In Fig. 6, the present calculation is compared with the

calculations by Howerton[2] and Caswell et al.[3]. All results agree within 10 %, though above 16 MeV Howerton's value is about 20 % lower than the present and Caswell's values.

Calculated kerma factor and its components of Fe-56 below 50 MeV are shown in Fig. 7. At high energy, the terms due to charged particle emissions are dominant. Therefore, the accuracy of calculation of high energy kerma factor depends on the nuclear model for charged particle emission.

Figure 8 shows the DPA cross section of natural iron. The displacement energy was taken as 40 eV. Present calculation was compared with that by RADHEAT V-4[4] code using ENDF/B-IV cross section and by TENJIN-2 code [12] using JENDL-2 data. Present result is in good agreement with RADHEAT V-4(ENDF/B-IV) calculation. Discrepancy between TENJIN-2 result for neutron energy above 6 MeV seems to be due to the difference in the neutron spectra from inelastic scattering to continuum levels in JENDL-2, since TENJIN-2(JENDL-3) calculation agrees well with the present calculation (Aruga,T.: priv.comm).

Natural iron DPA cross section and its components for neutron energy below 50 MeV are shown in Fig. 9. High energy DPA cross section is governed mostly by the $E_G\sigma_R$ and the elastic scattering terms. These are determined mostly by neutron optical potential, not depending on the reaction mechanism.

Acknowledgement :

Author is thankful to the members of PKA Sectrum/ Kerma Factor Data subworking group of Japanese Nuclear Data Committee for discussions. He is indebted to Dr. K. Shibata at Nuclear Data Center, JAERI for preparing multi-group JENDL-3 data of structural materials.

References :

(1) IIjima, S. : JENDL Special Purpose Data files and Related Nuclear Data, Proc. 1988 Nuclear Data Seminar, March, 1989, JAERI-M 89-026,. p.148

(2) Howerton,R.J. : Calculated Neutron Kerma Fctors based on the LLNL ENDL Data File, UCRL-50400, Vol 27, Jan. 1986

(3) Caswell, R.S., Coyne,J.J., Rndolph, M.L. : Kerma Factors of Elements and Compounds for Neutron Energies bewlow 30 MeV, Int. J. Appl. Radiat . Isot., 23, 1227 (1982),

(4) Yamano, N.,Koyama, K.,Minami, K.: Proc. 6-th Int. Conf. on Radiation shielding, May, 1983, Tokyo, Vol. 1, p.331, (1983)

(5) Robinson, M.T.,Torrens, I.M.: Recommendation for Displacement Calculation for Reactor/Accelerator Studies in Austenitic Steels, Nucl. Eng. & Design, 33, 91 (1975)

(6) Lindhard, J. et al. : Kgl. Danske Vidensk Selsk. mat-fys. Medd., 33 (1963) Np.10
Robinson, M.T. : Proc. B.N.E.S. Conf. on Nuclear Fission Reactors, Culham 1969 (BNES, London), p.364

(7) Young,P.G., Arthur,A.D. : GNASH code, LA-6947(1977)

(8) Shıbata,K. Fu,C.Y. : TNG code, ORNL/TM-10381(1987)

(9) Iijima,S. et al. : PEGASUS code, JAERI-M 87-025 p.337 (1987)

(10) Kumabe,I. et al. : Systematics and Parametrization of Continuum Angular distributions, Proc. 1988 Nuclear Data Seminar, JAERI-M 89-026, p.243

(11) Mantzouranis, G.,et al.: Phys.Lett. 578, 220 (1978)

(13) Aruga, T., Shiraishi, K. : Comparison of Neutron Radiation Damage Parameters obtined by using JENDL-3T and ENDF-B-IV Libraries, Poc. 1988 Nuclear Data Seminar, JAERI-M 89-026, p.342

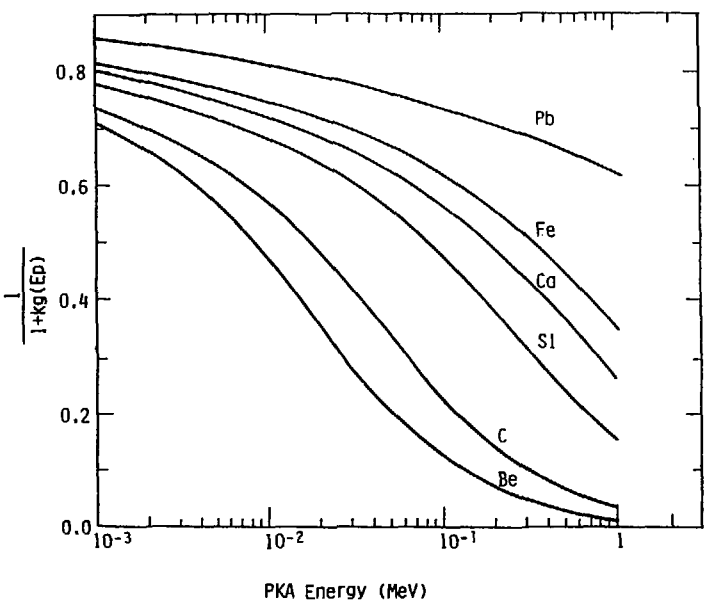

Fig. 2 Correction factor by Lindhard and Robinson

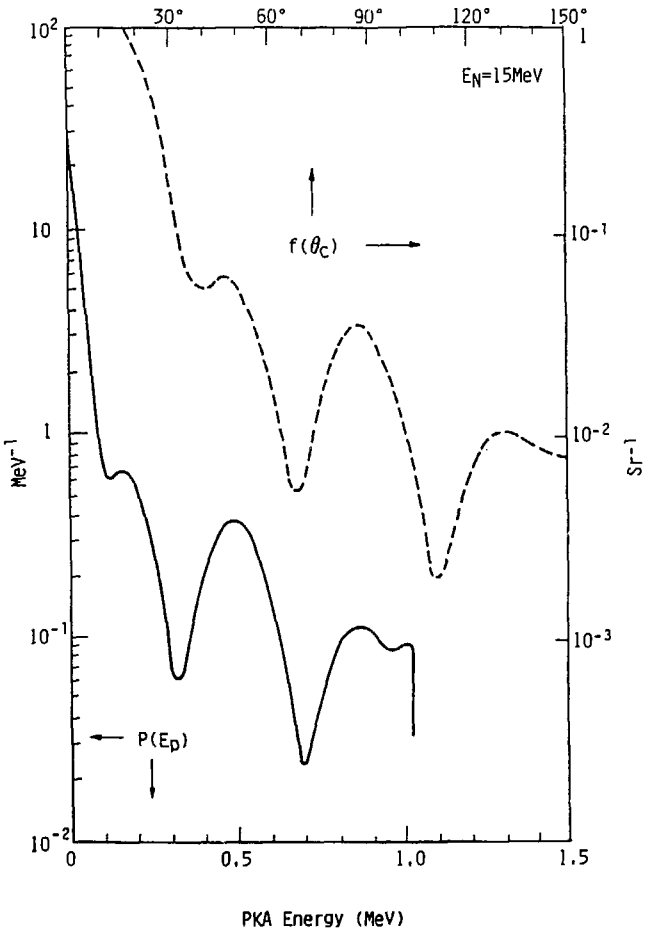

Fig. 3 Normalized PKA spectrum and angular distributions for natural iron from elastic scattering at E_n = 15 MeV

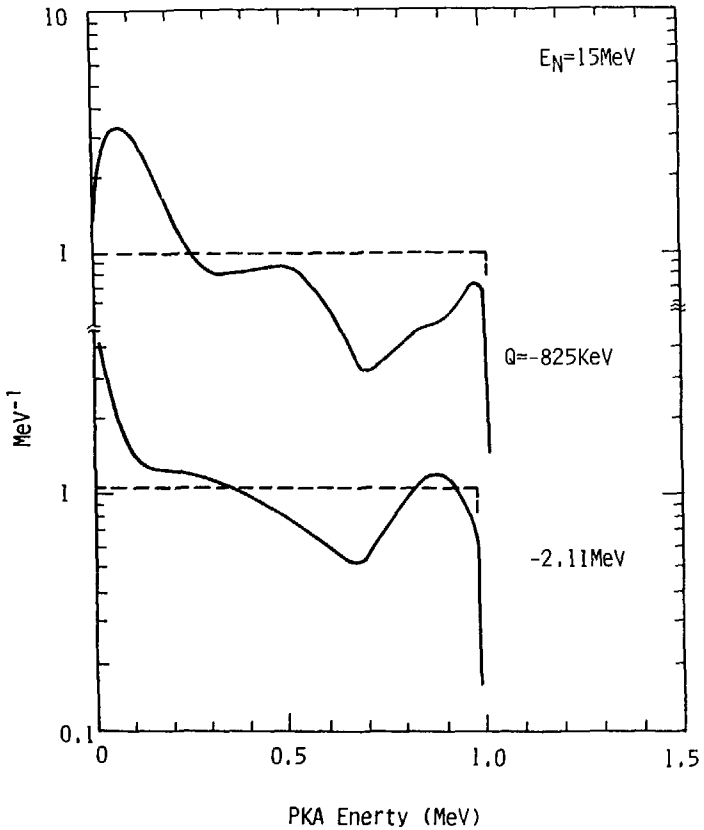

Fig. 4 Normalized PKA spectra for natural iron. Inelastic scattering to 825 keV and 2.11 MeV levels at E_n = 15 MeV. Dashed lines are those calculated by assuming isotropic angular distributions.

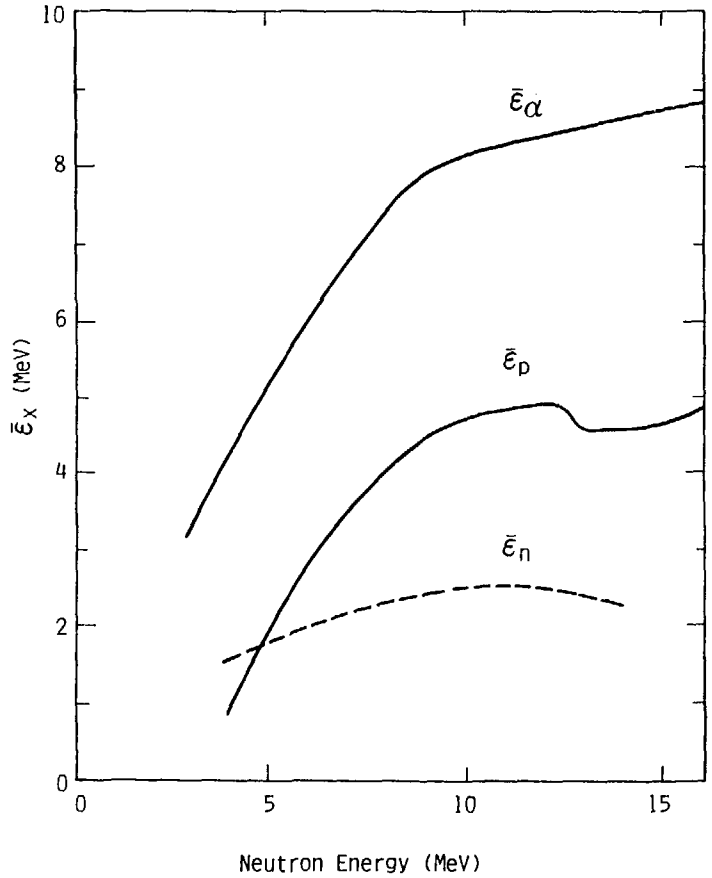

Fig. 5 Average energies of emitted particles as a function of incident neutron energy

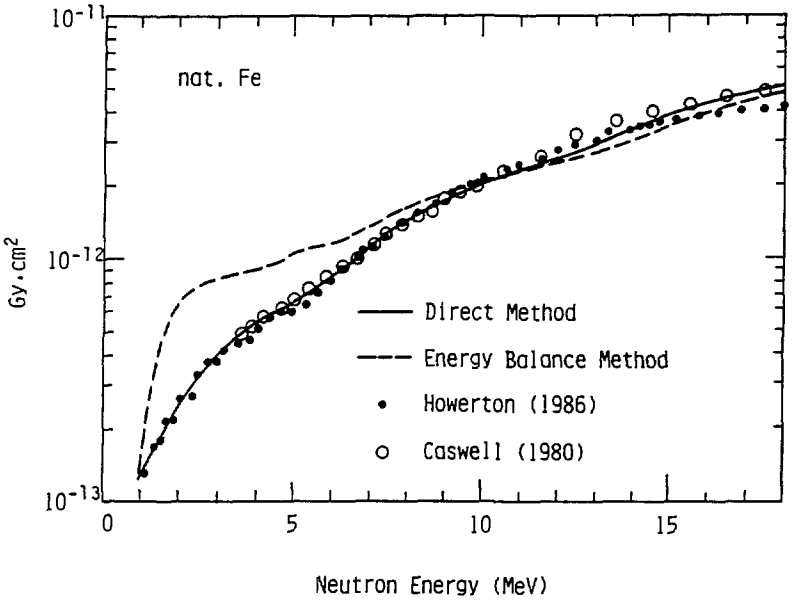

Fig. 6 Kerma factor of natural iron below 20 MeV. Comparison of the present calculation with those by Howerton and Caswell et al.

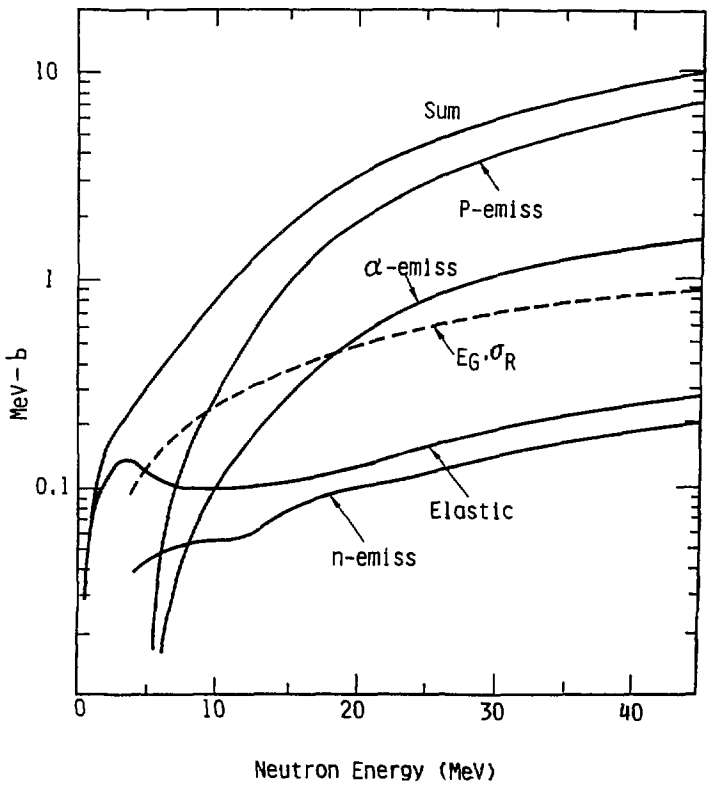

Fig. 7 Kerma factor and its components of natural iron for neutron energy up to 50 MeV

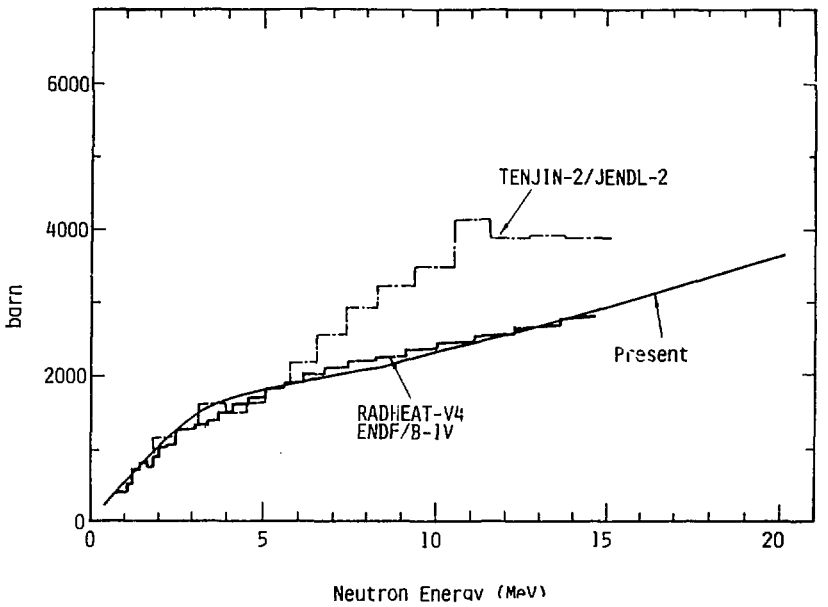

Fig. 8 DPA cross section of natural iron. Comparison of the present calculation with that by RADHEAT V-4 code using ENDF/B-IV and by TENJIN-2 code using JENDL-2

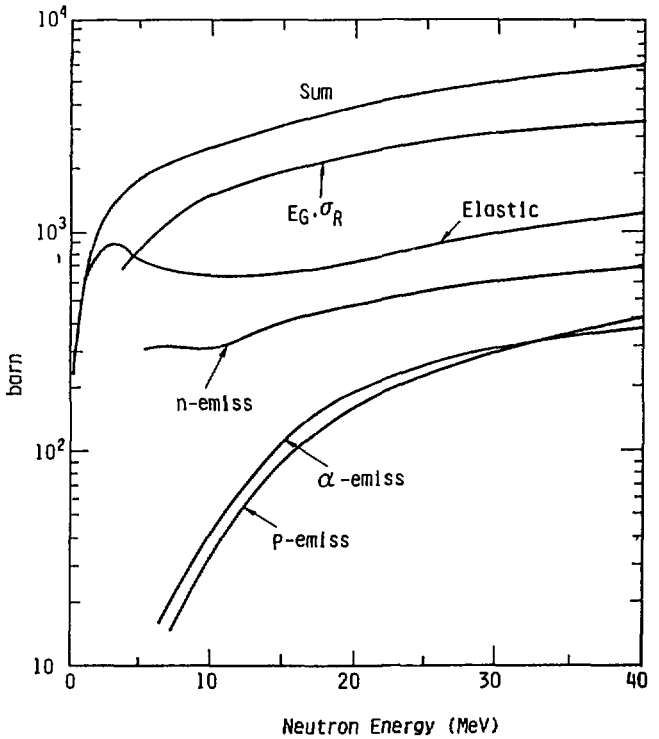

Fig. 9 DPA cross section and its components of natural iron for neutron energies below 50 MeV

3.15 TRU Transmutation with High Energy Proton Beam

Takahiko Nishida, Hiroshi Takada, Ikuo Kanno, Takakazu Takizuka,
Motoharu Mizumoto, Yasuaki Nakahara, Yoshihiko Kaneko

Departments of Reactor Engineering, Physics and
High Temperature Engineering
Japan Atomic Energy Research Institute
Tokai-mura, Naka-gun, Ibaraki-ken
319-11, Japan

Nuclear spallation reaction with high energy proton beam has been studied to be efficiently used for nuclear transmutation of the long-lived nuclides generated in the spent fuel in the power reactor. In particular effective incineration of the transurainum nuclides (TRU) is able to be performed by this reaction. A national program called, OMEGA, has started aiming at promoting research and development of new technologies on nuclear waste partitioning and transmutation. JAERI has proposed the R&D plan for TRU transmutation by proton accelerators with the following items ; 1) basic analysis of nuclear spallation and development of simulation code system, 2) design study of TRU transmutation plant, 3) spallation integral experiment and 4) development of an intensive high energy proton accelerator. In this paper we report the proceeding status of these research items, mainly about 1) and 2).

1. Introduction

The higher actinides and fission products in the high-level waste are hazardous due to their nuclear activities. Of particular concern are the nuclides with very long half-life whose hazard potentiality remains high for millions of years. Although the vitrification and geological disposal techniques have been widely accepted in many countries, it is worthwhile that partitioning long-lived nuclides from high-level wastes and their transmutation are re-examined at present. The possible use of valuable resources in the wastes and the upgrade of safety assurance in waste managnent can be performed by establishing the se technologies.

Nuclear spallation reactions with high energy proton beam (above 1 GeV) and the subsequent high energy neutron reaction (below 15 MeV) can be efficiently applied for the transmutation process. In particular, the transmutation of transuranium nuclides (TRU) is feasible.

In Japan, a national program, called OMEGA, has started aiming at promoting research and development of the new technologies on nuclear waste partitioning and transmutation as the long term program. As a part of the program, Japan Atomic Energy Research Institute set out the R&D plan for TRU transmutation with proton accelerators. Owing to the remarkable progress in recent accelerator technology, high energy proton -induced spallation and subsequent fast neutron reactions become more attractive as a means of nuclear transmutation. Desirable features of proton accelerator-driven transmutation plants are pointed out as follows,

(1) High efficeincy of neutron production

40 ~ 60 neutrons are emitted per one incident proton of 1.5 GeV in the spallation reaction of a TRU nuclide.

(2) Less hazardous radioactive products than transmutation through fission

Most of radioactive products from spallation reaction have half-lives shorter than those of long-lived fission products.

(3) Simple and Safe operation of plant

The plant can be immediately shut down by terminating proton beam because the reactor core (target) is always kept subcritical.

(4) Flexibility of design of reactor core

The rector core does not require the criticality. Then, the core design can be done under the relaxed neutronic conditions. The positive reactivity coefficients are acceptable.

(5) Energy balance

The reactor core containing the spallation target can supply sufficient electricity to operate the accelerator.

(6) Application to other various fields

* An intensive high energy proton source.
* An intensive neutron source.
* Useful nuclide productions including tritium and ^{3}He and short-life RI .
* Breeding of fissile nuclides
* Material researches
* Radiation therapy using proton, neutron and meson.

However there are many technological items requiring researches and developments as given below,

(a) High-energy and high-current proton accelerator of 1.5 GeV and several tens of mA),

(b) Subcritical reactor containing the neutron producing target bombarded with intensive proton beams,

(c) Transuranium reprocessing and fuel fabrication technology.

In the present paper the present status of research at JAERI is described for the following items :

1) basic research of nuclear spallation and development of its code system,
2) basic design study of TRU transmutation system,
3) spallation integral experiment,
4) development of an intensive high energy proton accelerator.

2. Accelerator transmutation research at JAERI

Since TRU nuclides, generally, have larger cross sections for high energy particle than fission products, the feasibility of TRU transmutation seems more promising. Our basic idea is to transmute them in a target directly by the high energy proton-induced spallation and subsequently by the fission due to neutrons transported into the energy

range lower than 15 MeV. A hybrid system, subcritical reactor with TRU fuels drived by an intensive proton linear accelerator, is investigated.

2.1 Improvement of simulation codes and calculational models

A computing study has been carried out at JAERI to develop our idea to a realistic engineering concept since 1980. We have been upgrading the nuclear spallation codes NUCLEUS[1] and NMTC/JAERI[2].

There are some discrepancies between calculated and experimental results for both the spallation neutron spectrum and the mass yield distribution of residual nuclei.[3], [4] We have made some modifications in the intranuclear cascade model to eliminate the discrepancies by taking intoacount the nucleon-cluster collision and correcting the angular distribution of Δ- particle. Nuclear reactions in the intranuclear cascade process are treated as a sequence of nucleon-nucleon two body collision.[5] However in the energy range of nucleons below 200 MeV, the two body collision is not a good approximation. In addition the mean free path evaluated from the imaginary part of the potential in the optical model is several times longer[6] than that given by the intranuclear cascade model. The nucleon-cluster collision term is considered to be effective to modify the intranuclear cascade model. The cluster is assumed to be composed of two or four nucleons. The probabilities of the nucleon-cluster collision are parametrically given as a function of the energy. When a collision occurs, the Pauli's exclusion effect is checked with respect to each nucleon. Since the forbidden events occur more frequently in the nucleon-cluster collision than in the nucleon-nucleon one, the inclusion of the nucleon-cluster collision results in prolonging effectively the mean free path of the particle injected on a nucleus. The inelastic collision plays an important role in the high energy region above 600 MeV because of its large cross section and is treated via the formation of Δ particle[7] which is heavier by about 300 MeV than the nucleons. If the incident energy is as high as 800 MeV, a nucleon which produced Δ- particle can be recoiled with suffieciently high energy. As the behavier of the particle, however, is not studied in detail, we calculated its effect by assuming that the Δ- particle is recoiled only in the backward direction of 135～180 ° in the center of mass system. Figure 1 shows

the results of mass yields for 1 GeV proton incidence on gold and Figure 2 shows those of spallation neutron spectra for 800 MeV proton incidence on uranium. As seen from these figures our modification has improved the current calculation method well and better agreements with the experimental data have been obtained.

It is also important to obtain the basic and exact knowledge concerning the transmutation of radioactive waste with long lifetime to the ones with short lifetime or stable ones, using high energy protons generated by a linear accelerator. The time evolution calculation of buildup and decay of all the nuclides produced in the target irradiated continuously by proton beams is necessary. However there are no code which make the exact calculation possible because of the enormous consumption of computing time and computer memory, and the insufficient compilation of nuclear data in the energy range higher than 20 MeV for nuclides. Therefore we adopt a calculative model based on the one point approximation for these processes. The one point depletion code DCHAIN[8] andits supplemental nuclear data library had been developed at JAERI on thebasis of the Bateman method for the calculations of decay and build-up of fission products in a nuclear reactor. This code is being improved to be able to calculate the build-up and decay schemes of all products including spallation products (SP) and nuclide production due to proton and neutron fluxes. The nuclear data in the energy range higher than 20 MeV, as shown in Fig.3, are being compiled also. After proton-induced nuclear spallation reactions, a variety of nuclei, especially many neutron-deficient nuclide with mass numbers greater than 180, are produced.[1] Figure 4 shows the (N, Z) ditribution of the nuclides which are generated in the spallation reaction and whose decay constants are unknown yet. The β decay constants of some products of those have been computed by using the gross theory code of β decay.[9] The yields of SP were calculated for target nuclei such as ^{237}NP, ^{238}Pu, ^{239}Pu, ^{240}Pu, ^{241}Am, ^{242}Am, ^{242}Cm and ^{244}Cm in the incident proton energy range, 0.1 GeV to 1.5 GeV,using NUCLEUS.

2.2 Basic Design study of TRU transmutation plant

For the incineration of transuranium waste(TRUW),[10),11),12] we have been making studies on the concept of spalllation target system

driven by an accelerated proton beam. The following conditions are assumed for the design of the target system :

(1) It can transmute the TRUW produced by several commercial 1000 MWe LWR with 33 GWd/t burnup. The spent fuel is reprocessed after 90 days cooling, where 99.5 % of U and Pu are recovered. Fission products and residual U are removed from waste actinides by partitioning process.

(2) It can incinerate about 10 % of TRU fuels a year, (i.e., almost 3 tons of TRU fuel).

(3) It must have the passive safety feature.

(4) It employs the proton accelerator with 1.5 GeV and ~10 mA.

(5) It can generate enough electricity to operate the accelerator with a generation factor and an accelerator efficiency factor to be 0.3 and 0.5, respectively,

Figure 5 (a) shows a model of accelerator-driven TRU target system with high power proton beams. Thermal energy from the target is removed and converted to electricity by a conventional steam cycle. A part of the electric power is supplied to the proton accelerator. This target system is included in a TRU-fueled reactor operated at subcritical (k_{eff} : 0.9~ 0.95). The target is 2 m long in the beam direction, 1 m high and 0.85 m wide (Fig. 5(b)). It is surrounded by stainless steel reflector of 0.2 m thickness. Beam window is located at a depth of 0.7 m from the front face and has a rectangular cross section with dimensions of 1 m high and 0.1 m wide.

The heat produced in the TRU fuel is removed by forced circulation of liquid metal coolant. Heat removal performance is a crucial factor to determine the rate of TRU transformation in the target. Here two liquid metal coolants, Na and Pb-Bi, are compared. Na is an excellent heat transfer medium and commonly used for LMFBRs, and Pb-Bi is a coolant favorable for spallation neutron source.

The target employs metallic alloy fuel of TRUs. A metallic fueled core provides considerably harder neutron spectrum than one with oxide fuel. Harder neutron spectrum will make the transmutation more effective because of the higher ratio of fission cross section to capture one for TRU nuclides with increasing neutron energy. The fuel consists of two types of alloys, Np-22Pu-20Zr and AmCm-35Pu-5Y. These alloys are expected to have a sufficiently high phase stability and are

proposed for an actinide burner fast reactor[13]. Here Pu is initially added to the fuel in order to lower the reactivity swing. Because of low melting point of actinides, e.g. 640 ℃ for Np, actinides should be alloyed to achieve a high linear power rating. With addition of 20 wt% of Zr, melting point of Np is supposed to increase up to about 900 ℃. One of the disadvantages of actinide alloy fuel is low thermal conductivity at high temperature. The fuel assembly in the target is similar to that commonly employed in LMFBR design. The fuel pin has a diameter of 4mm and cladded with HT-9 steel. To keep the effective multiplication factor around 0.95, the pin pitches are chosen 8 mm and 10 mm for Na and Pb-Bi cooled targets, respectively.

For neutronic calculations the target-core system is simplified as an axial symmetric cylinder with a length of 2 m and a diameter of 1.04 m surrounded by an annular reflector of 0.2 m thickness. A circular beam window located at the centerline has a diameter of 0.36 m, and the maximum beam diameter is 0.2 m. The nuclear spallation reaction and particle transport process above the cutoff energy of 15 MeV are calculated by NMTC/JAERI code [2]. Below 15 MeV the three-dimensional Monte Carlo neutron transport code MORSE-DD[14] is used with 52 neutron group cross section library derived from JENDL-2 and ENDF-B4, where neutrons slowing down through spallation process are treated as the source. The results of the neutronic calculations for the target-core model are summarized in Table 1. In the present system, the number of TRU nuclei transmuted by fast fission is much larger than that by spallation reaction. Two-dimensional power distributions fo the Na and Pb-Bi cooled target-cores are shown in Figs. 6 (a) and (b), respectively. The Pb-Bi cooled target has larger power peaking, and the maximum power density occurs in the region close to the beam window. Thermal hydraulic calculations for the target are done to determinethe maximum achievable thermal power within the maximum allowable temperature limits of fuel and cladding. Maximum temperature in the TRU fuel must remain below its melting point (900 ℃). Maximum temperature of the cladding tube would be limited to 650 ℃. and coolant temperature at the target-core inlet is set to 300 ℃. Upper limits of coolant velocity are taken as 8 m/s and 2.35 m/s for Na and Pb-Bi coolants, respectvely. The temperature distributions along the hottest fuel pins, cooled by Na and

Pb-Bi, are shown in Figs. 7 (a) and (b). In both cases, the maximum thermal power is limited by the maximum allowable fuel temperature of 900 ℃. In the case of Na cooling, the maximum thermal power is 769 MW with the target-averaged power density of 472 W/cc and then the beam current of 20 mA required. For Pb-Bi cooling, the maximum thermal power is 236 MW with the target- averaged power density of 145 W/cc, requiring 7.8 mA beam current. The maximum power of Pb-Bi cooled target is considerably lower than that of Na cooled one. This is mainly attributed to lower thermal conductivity of the coolant , wider fuel pin pitch and higher powe peaking factor than in the case of Na cooling.

2.3 Spallation intergal experiment

For examining the actual efficiency of TRU transmutation, spallation experiments on a target irradiated by high energy protons have to be carried out.[15),16),17),18)] Our research group is preparing a seris of integral experiments for some heavy targets, which consist of a)lead , b)depleted uranium imbedded in lead and c)depleted uranium respectively, using high energy proton beams with energy of more than 0.5 GeV.

The neutron transport code MORSE-DD was combined with the spallation code NMTC/JAERI for making the analysis of a target system used in the experiment as shown in Fig. 8. Preliminary analyses have been made mainly for the experimental target of depleted uranium which is a cylider(60 cm ϕ x 100 cm) with a beam injecting hole(7 cm ϕ x 20 cm) at the front face. Figure 9 (a) shows the axial distribution of proton and neutron fluxes above 15 MeV and total neutron flux in the ene rgy range less than 500 MeV. As seen in the figure, most of neutrons in the target except near the proton-injected region are likely produced in the fast fission reaction below 15 MeV. Total neutron flux decreases by two orders from its maximum value at the bottom face but only by a factor of 1.5 at the side surface in Fig. 9 (b). The energy spectrum of neutrons escaped from a depleted uranium target has a peak around 100 keV, while that in the case of lead target is flat in the energy range less than 1 MeV because of no fast fissions as shown in Figs. 9 (c) and (d).

At first the spallation products and emitted particles in a lead

target are measured in the experiment to ascertain the spallation transmutation of TRU and to verify the overall feasibility of predicting spallation performance by the simulation codes. Figure 10 shows the illustration of a lead cylider target contained in SUS container with 100 cm length and 60 cm diameter. The target has several experimental holes parallel to the central axis of cylinder, which are pluged by specimen wires (Ni, Al, Au, Nb, Cu, Fe) to measure high energy reaction products and the neutron energy at each position with γ activation method by a Ge(Li) detector. Proton beams with energy of 500 MeV, the intensity of which can be controlled by the switching magnet newly equipped on the beam line, goes to the target from the left direction. For many cases specimen in the target are irradiated with the beam current of 100~10 nA in an hour andcooled in about five hours to obtain their activities suitable to measurement.

For the next step, a uranium target is used to simulate the TRU target spallation experiment before the direct irradiation of TRU nuclides. We are planning a series of proton-induced spallation integral experiments on depleted uranium targets to examine the characteristics of a spallation target.

2.4 Development of intensive proton accelerator

The development of proton accelerator proposed for spallation transmutation is considered to be an extraordinary technoiogical challenge. The proton beam current 10 mA is nearly 10~100 times larger than that for exisiting machines for basic nuclear physics experiment. The intensive proton accelerator is positioned far beyond the experiment area. Only linear accelerator can passively satisfy the requirements of high beam current with higher efficiency of beam extraction than other circular machines such as cyclotrons and synchrotron. High beam quality is required to reduce beam spills as small as possible because of the severe problem for the high energy radiation protection.

The research plan for developing the high-energy proton linac (1.5 GeV, 10 mA) is now proposed at JAERI. Figure 11 shows a schematic illustration of the proposal arragement of engineering test proton linac in total length ~ 700 m, which consists of (a)ion source, (b) Radio Frequency Quadrupole linac, (c) Drift Tube Linacs and (d) DTL &

high β linac with the output beam energies of 100 keV, 2 MeV, 10 MeV and 1.5 GeV respectively.

As the first step of the development, the low energy part of the accelerator structure included in the solid line square as shown in Fig. 11 will be carefully studied through the construction of the smaller linac with current of 10 mA and energy of 10 MeV, because the beam quality is mainly determined at the low energy part. The accelerator structure will consist of these components as follows ; the ion source, RFQ and DTL. High β structure will be considered seriously as the 2nd step of the development.

3. Summary

Improvements of spallation reaction simulation codes have been made aiming at predicting the transmutation ability with high precisions. The upgrade of the simulation codes and development of code system for design sutdies of transmutation plant would be begun in the near future . Preliminary design studies were made for the accelerator-driven TRU transmutation target system. When the Na cooled target-core is operated at the thermal power of 769 MW and the beam current of 20 mA, this system can transmute about 250 kg TRU annually. Improvement and optimization of target-core system design will also be required for more efficient transmutation.

A series of spallation integral experiments for a lead target is prepared and a uranium target will be used for the second step of experiment. The investigations of basic technologies have started in order to develop the high-energy and high-current proton accelerator for spallation transmutation. At first the smaller size linac with current of 10 mA and energy of 10 MeV will be constructed.

This Research & Development should be actively performed as the part of national program.

Acknowledgement

The authors would like to express thanks to Dr. K. Ishibashi for his valuable advice and discussions.

References

1) T. Nishida, Y. Nakahara, T. Tsutsui: JAERI-M 86-116 (1986) (in Japanese)

2) Y. Nakahara, T. Tsutsui: JAERI-M 82-198 (1982) (in Japanese)

3) S.D. Howe et al.: " Neutron Spectra from 800 MeV (p, xn) reactions on target of Al, Cu, In, Pb and U," LA-UR-85-3360 (1985)

4) S.B. Kaufman, E.P. Steinberg : Phys. Rev. C, 22, 167 (1980)

5) R. Serber: Phys. Rev., 72, 1114(1947)

6) H.O. Meyer, P. Schwandt : Phys. Lett., 107B, 353 (1981)

7) R.M. Sternheimer, S.J. Lindenbaum: Phys. Rev. 105, 1874 (1957) ; 109, 1723 (1958) ; 123, 333 (1961).

8) K. Tasaka : JAERI-M 8727 (1980)

9) T. Yoshida : JAERI-M 6313 (1975)(in Japanese)

10) P. Bounnaure, et al., " Actinide Transmutation by Spallation in the Light of Recent Cyclotron Development," NEACRP-A-910 (1988).

11) T. Mukaiyama, et al.,:" Conceptual Study of Actinide Burner Reactors," Proc. 1988 Int. Reactor Physics Conf. (Jackson Hole, 1988)

12) T. Takizuka, et al.,:" A Study of Incineration Target System," Proc. 5th Int. Conf. Emerg. Nucl. Energ. Sys. (Karlsruhe, 1989) (to be published)

13) H. Takano, T. Mukaiyama :" Nuclear Characteristic Analysis of TRU Burner Rreactors", JAERI-M 89-072 (1989)(in Japanese)

14) M. Nakagawa, et al., " MORSE-DD A Monte Carlo Code Using Multi-Group Double Differential Form Cross Sections," JAERI-M 84-126 (1984)

15) S.S. Cierjacks, et al.:"High Energy Particle Spectra from Spallation Target," ICANS-V, (1981)

16) H. Takahashi :"Analysis of Neutron Yield from High-energy Proton Bombardment of Uranium Targets", Nucl. Sci. Eng. 87 432-443 (1984)

17) W. Amian, N.F. Peek, D.J. Shaddan, G. Sterzenbach : " Production Rates of Spallation and Fission Products in Depleted Uranium and Natural Lead Targets Bombarded by 600 MeV and 1100 MeV Protons", Proc. of ICANS-VII, (1983)

18) J.S. Gilmore, G.J. Russell, H. Robinson, R.E. Prael : " Fertile-to-Fissile and Fission Measurements for Depleted Uranium and Thorium Bombarded by 800 MeV Protons", Nucl. Sci. Eng. 99, 44 (1988)

Table 1 Nuclear characteristics of the reactor core of incineration plant

Coolant		Na	Pb-Bi
Effective Multiplication Factor		0.95	0.96
Spallations/Proton	total	6.82	7.21
	actinide	1.66	0.53
Emitted Neutrons/Proton		37.9	53.9
Fissions/Proton	(> 15 MeV)	0.963	0.395
	(< 15 MeV)	194	151
Average Neutron Energy [keV]		269	306

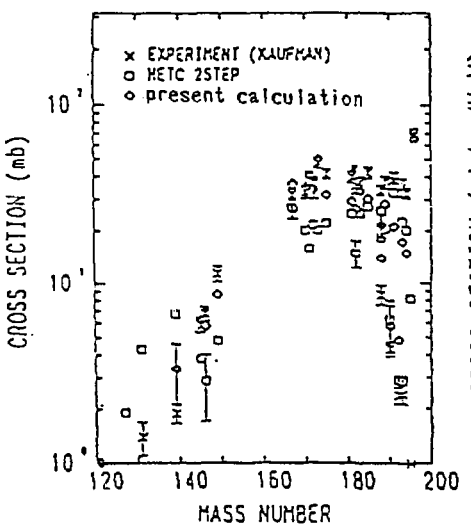

Fig. 1
Mass yield distribution for 1 GeV proton incidence on a gold nucleus

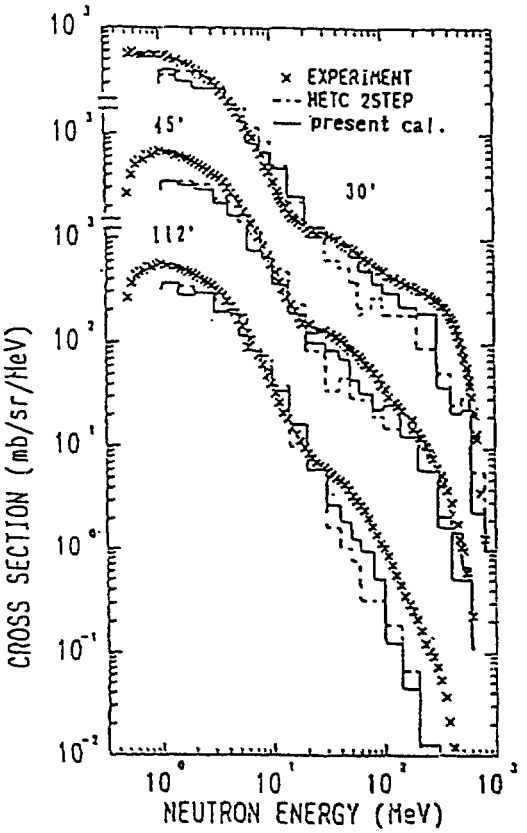

Fig. 2
Spallation neutron spectra for 800 MeV proton incidence on a uranium nucleus

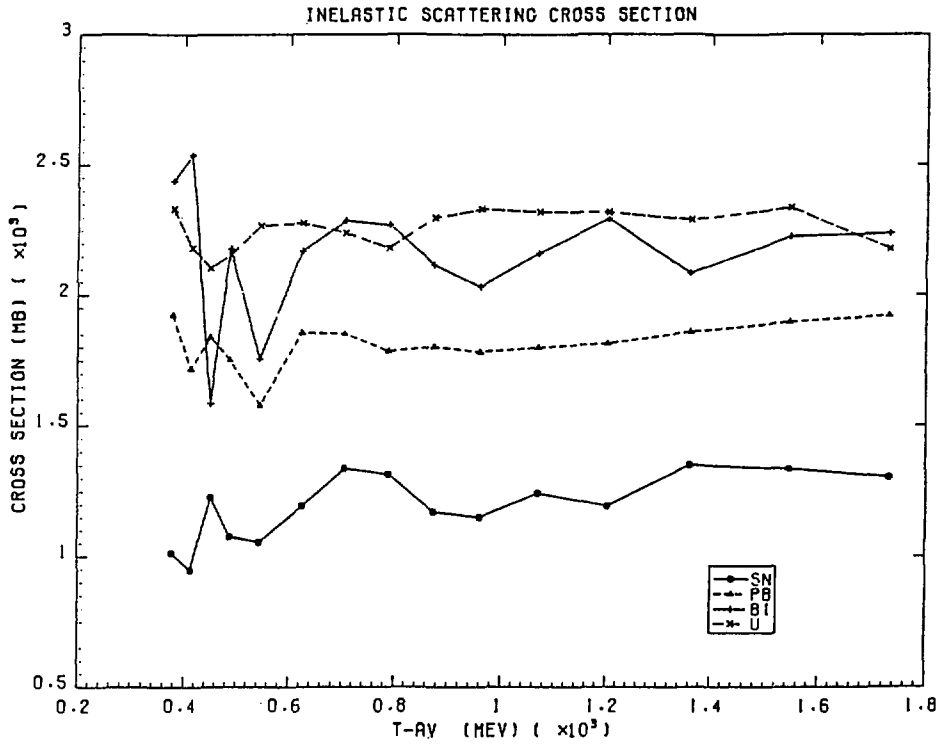

Fig. 3 Inelastic scattering cross section of heavy metals such as U, Bi, Pb and Sn in the energy range of 0.2 to 1.8 GeV

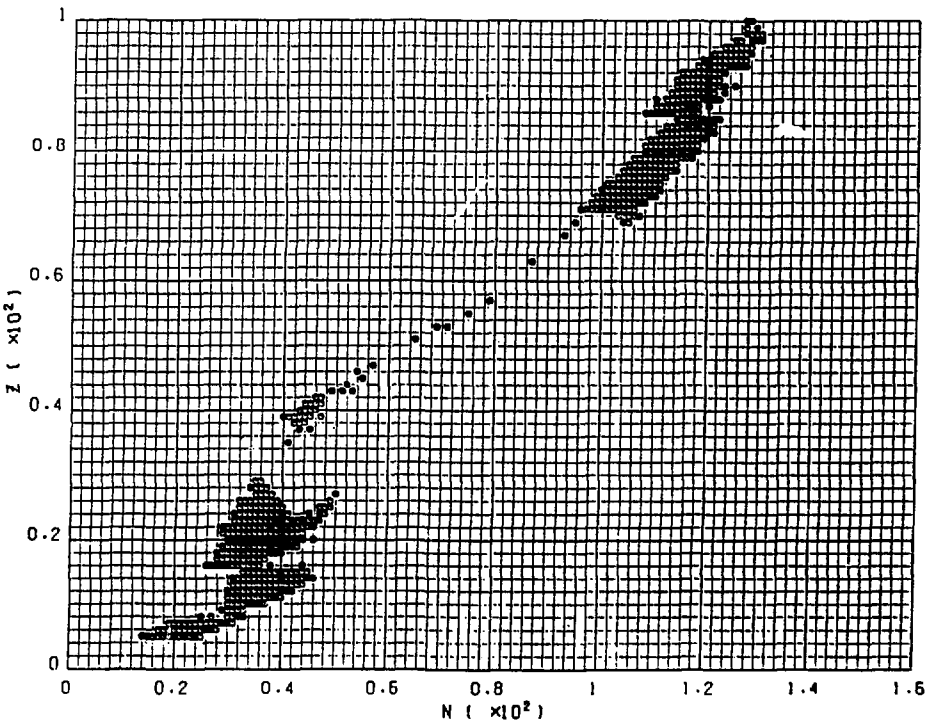

Fig. 4 Distribution of nuclides which are generated in the nuclear spallation reaction with unknown half life times on the plane of neutron number and atomic number

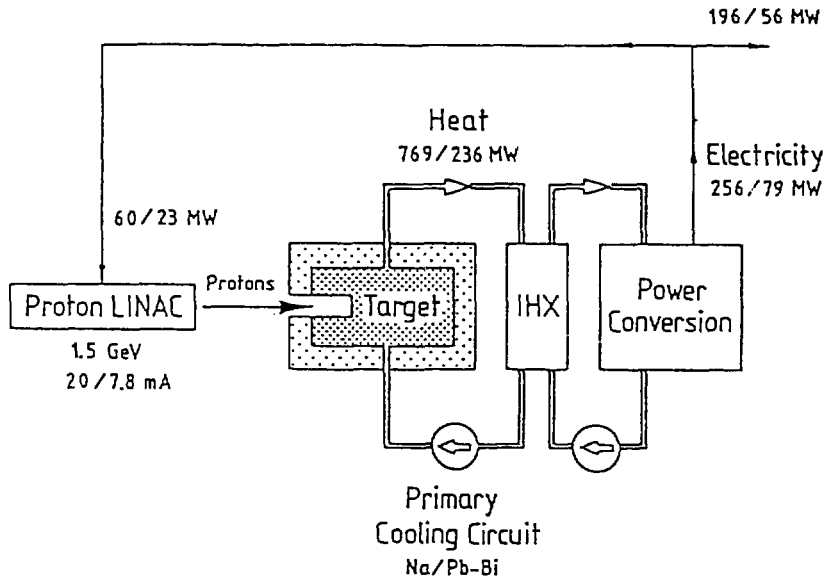

(a) System diagram

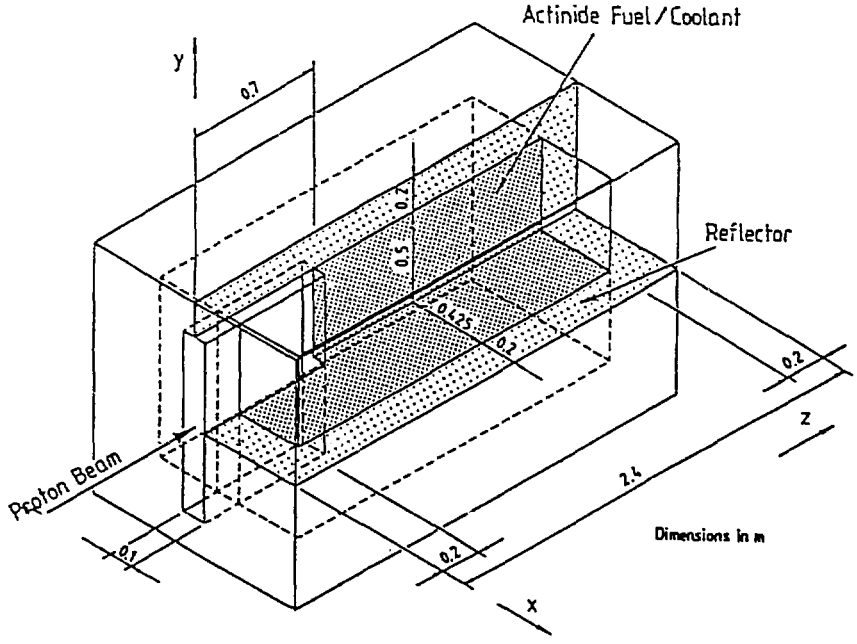

(b) Reactor core

Fig. 5 Concept of accelerator-driven incineration reactor

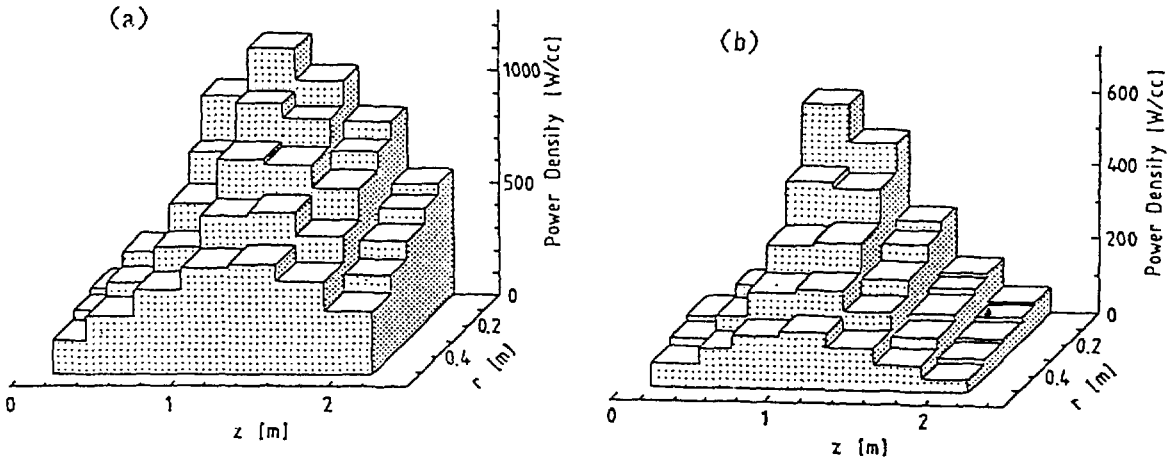

Fig. 6 Power distributions in (a) Na cooled and (b) Pb-Bi cooled cores

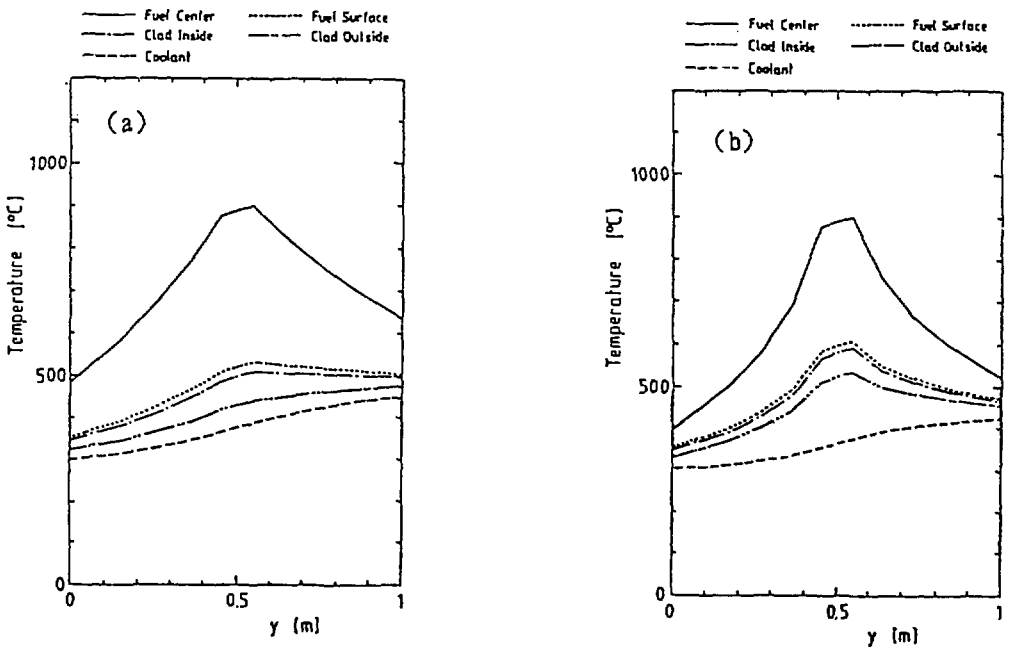

Fig. 7 Temperature distributions in (a) Na cooled and (b) Pb-Bi cooled cores

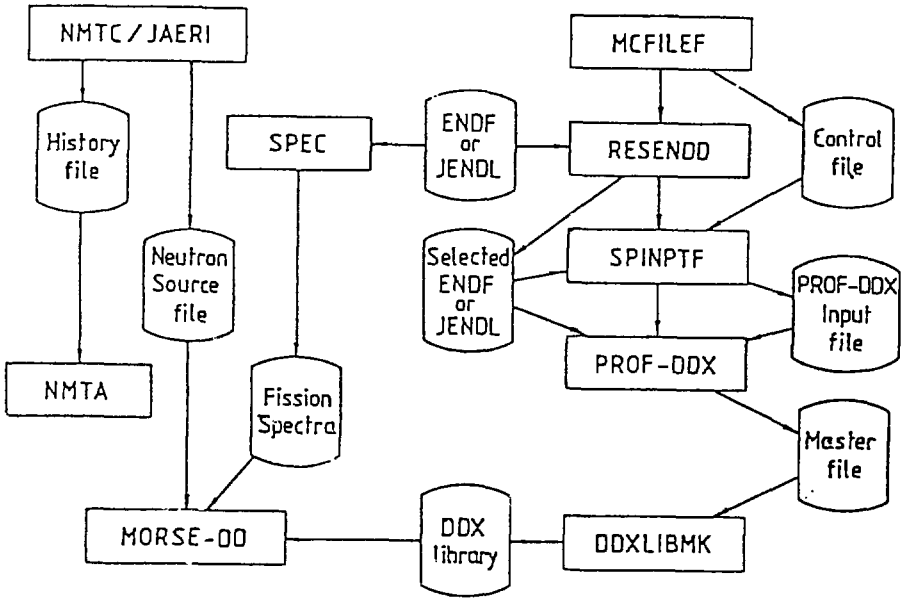

Fig. 8 Code system developed for spallation & transport calculation

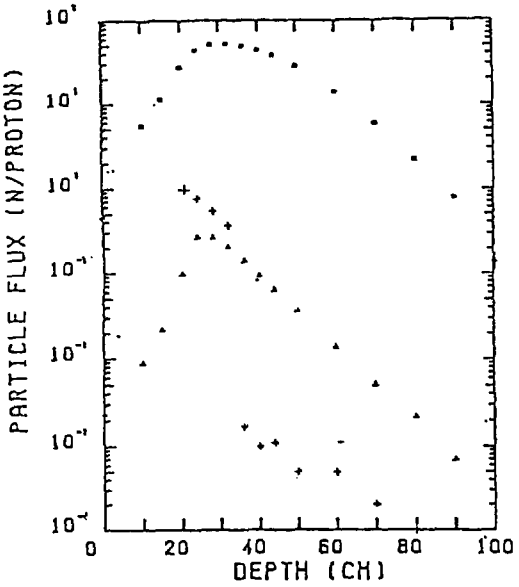

(a) axial distribution of proton and neutron fluxes
○ : total neutron flux
△ : neutron flux above 15 MeV
+ : proton flux above 15 MeV

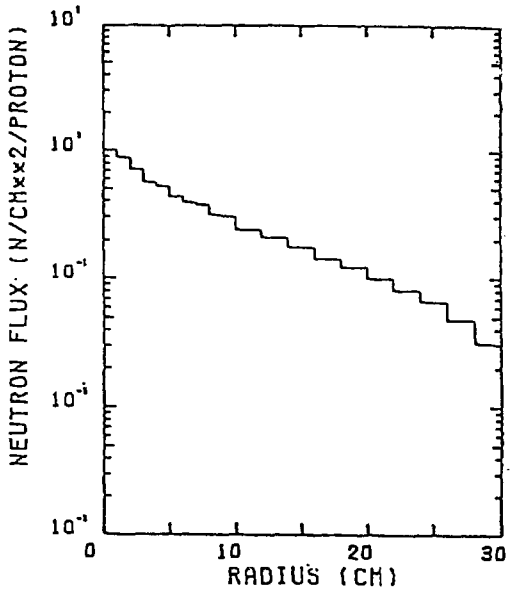

(b) total neutron flux distribution in the radial direction

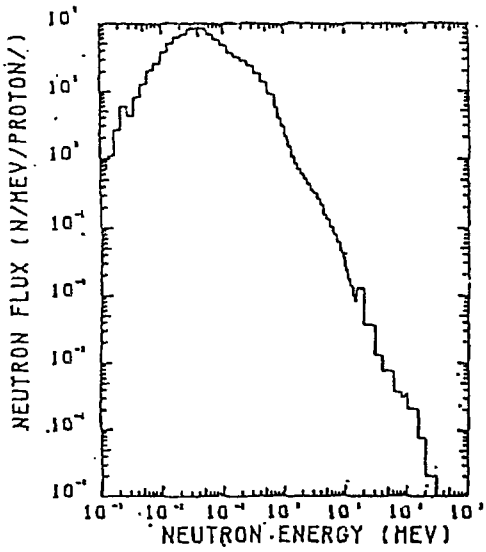

(c) energy spectrum of neutrons from a depleted uranium target

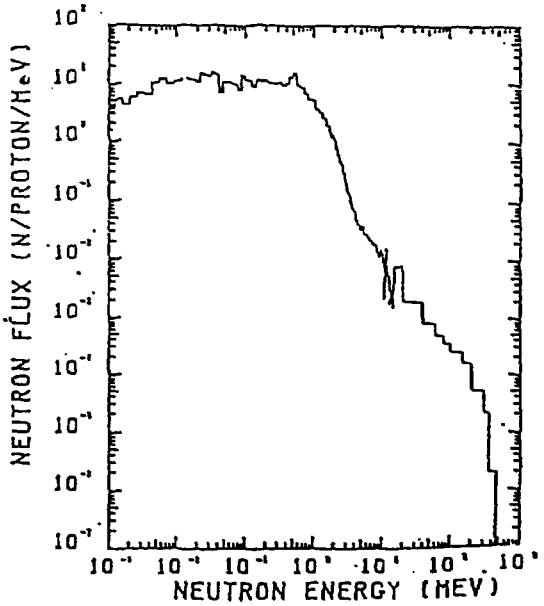

(d) energy spectrum of neutrons from a lead target

Fig. 9 Preliminary neutronic calculations for experimental bulk system to validate prediction accuracy of NMTC/JAERI

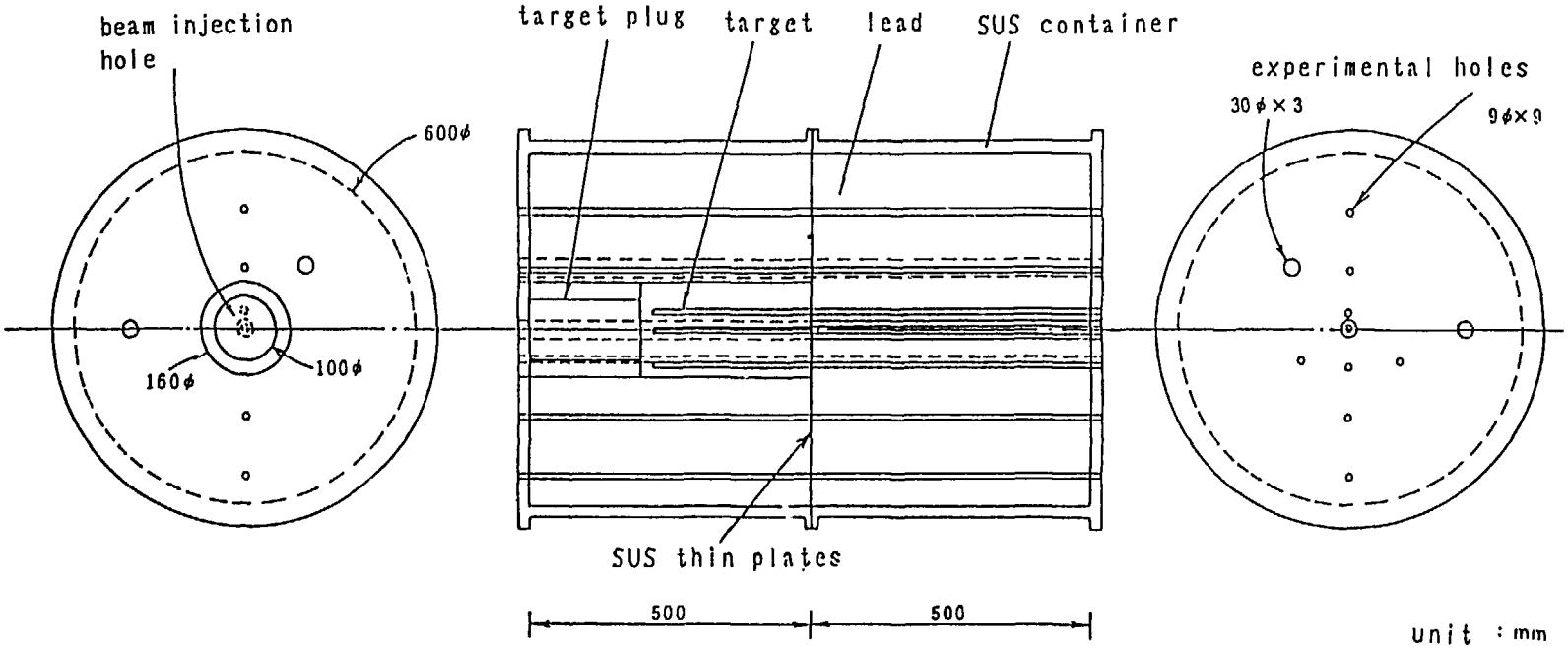

Fig. 10 Design of a lead cylindrical bulk system used for the spallation integral experiment

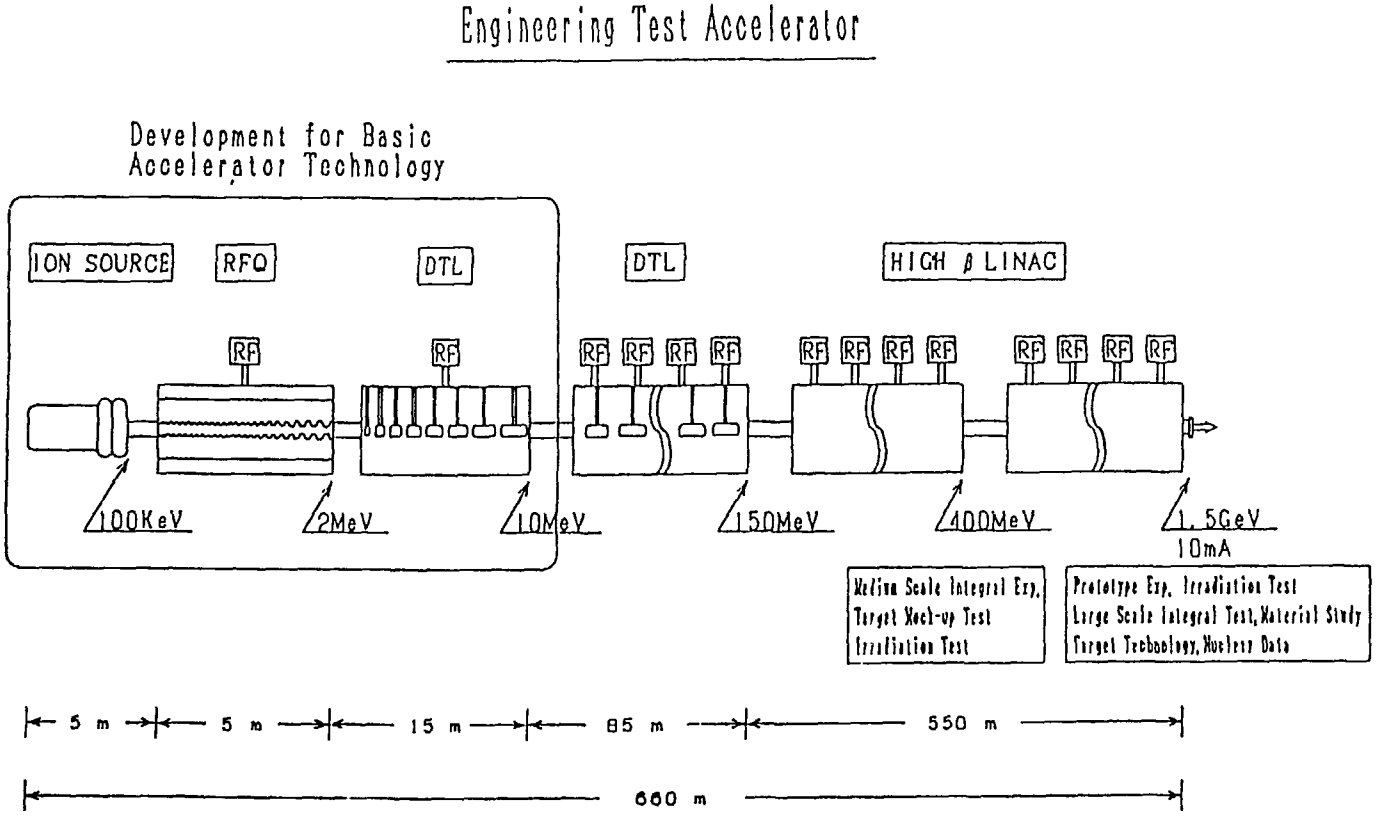

Fig. 11 Layout of intensive proton accelerator for engineering test

3.16 Proton Induced Spallation Reaction Calculation Considering the Intranuclear High-Momentum Nucleons and the Preequilibrium Effect

K. Ishibashi, Y. Miura, T. Sakae, Y. Matsumoto, Y. Watanabe,
A. Katase,* H. Takada,** T. Nishida,** Y. Nakahara** and Y. Kaneko**

Department of Nuclear Engineering, Kyushu University
Hakozaki, Higashi-ku, Fukuoka-shi

Abstract

The double differential cross section of neutron production is calculated for the spallation reaction that is induced by incident protons of several hundred MeV. The intranuclear nucleons with high-momentum component are introduced into the High Energy Transport Code (HETC). The consideration of such nucleons is useful in the reproduction of the yield of the high-energy neutrons in the backward direction. The intranuclear cascade process calculation is terminated taking the pre-equilibrium effect into account in a local manner. The use of this method successfully represents the shape of the neutron spectra of an intermediate energy.

1. Introduction

The spallation reaction is caused by bombarding targets with particles having an energy above a few hundred MeV. The reaction produces a number of neutrons and the plan is apply it to such facilities as the intense spallation neutron source and the transmutation of long-lived radioactive wastes. Some computer codes have been developed for designing these spallation facilities. Nucleon Meson Transport Code (NMTC)[1,2] and High Energy Transport Code (HETC)[3,4] are famous as Monte-Carlo particle-transport codes in the energy region of the spallation reaction. These codes basically consist of two types of calculations, which are on the intra-nuclear spallation reaction and the inter-nuclear particle transport. This paper deals with only the former calculation, and concerns itself with the experimental data taken by the use of thin targets.

These codes employ the intranuclear-cascade evaporation (INCE)[1,2]

* Faculty of Engineering, Tohwa University
** Japan Atomic Energy Research Institute

model for calculation of the spallation reaction. This model consists of two processes of intranuclear-cascade and evaporation, and is coded with the Monte Carlo algorithm. The programs reproduce the overall characteristics of the spallation reaction fairly well. Nevertheless, the calculation results have some systematic discrepancy from experimental data. For example, the yield of the high-energy neutrons emitted in the backward direction are underestimated by an order of magnitude. Although the experimental energy spectra of neutrons have a shoulder in the region of 20 to 50 MeV, the computation results do not possess this shoulder at all. We will attempt to clarify the reason for the disagreement, and to modify the HETC to improve its characteristics. In the present paper, the intranuclear nucleons with high momentum are introduced into the intranuclear cascade calculation, and the preequilibrium effects are considered at the end of this cascade process.

2. Improvement of the HETC

The experimental neutron spectra are shown in Fig. 1 by the use of cross marks. The experiment[5] was made at SIN, where protons of 585 MeV were incident on a thin lead target. The dashed lines represent the results of the HETC that is based on the INCE model. The program used was the version that was modified by F. Atchison[4] to incorporate the high-energy fission. The level density parameter was chosen as A/8 MeV^{-1}, and was slightly corrected[2] depending on the atomic mass A and number Z of the nucleus according to LeCouteur. The differences between results of the calculation and the experiment are as follows:

1) In the backward direction, the dashed lines underpredict the yield of the experimental high-energy neutrons above 100 MeV.
2) The shoulders in the experimental spectra in the region of 20 to 50 MeV do not appear in the calculation results.

2.1 Intranuclear nucleons with higher momentum

In the HETC, the Fermi gas model was assumed for the momentum distribution of the intranuclear nucleons. This code presumed the degenerated Fermi distribution of the zero temperature. It is suggested, however,that there may exist some nucleons that have a higher momentum[6] than that of the degenerated Fermi distribution. For momentum distribution, reference 6 gave the following probability W(p) per unit volume in the momentum space:

$$W(p)= W_0 \{\exp(-(p/p_0)^2) + \varepsilon_0\exp(-(p/q_0)^2) + \varepsilon_1\exp(-(p/q_1)^2) \} , \quad (1)$$

where p is the momentum, $p_0 = \sqrt{(2/5)}k_f$, ε_0=0.03, $q_0 = \sqrt{(6/5)}k_f$, ε_1 = 0.003, q_1 = 0.5 GeV/c, k_f is the Fermi momentum, and W_0 is a normalization factor. The third term in Eq.(1) was derived from a correlated two-nucleon-cluster model. This term represents the effective momentum component which is useful for representing the collision phenomena. Equation (1) is composed of three terms that have a function type of $\exp(-x^2)$. Since the surface area of the sphere of the momentum space is proportional to p^2, the probability density function is given by the sum of functions with the type of $x^2 \exp(-x^2)$. We sample the nucleon momentum by the Monte Carlo algorithm in accordance with the calculation method of the HETC.

The solid lines in Fig. 1 show the calculated results using the momentum distribution given by Eq. (1). At an angle of 150 degrees, the dashed lines produced by the standard HETC appreciably underpredicted the neutron spectra for an energy above 100 MeV. This discrepancy is removed by the calculation that assumes the distribution of Eq. (1). However, the neutrons of 15 to 50 MeV are overestimated in the solid lines. Adoption of nucleons with the higher momentum thus leads to the emission of neutrons of higher energy.

2.2 Termination of the intranuclear cascade process

The cascade process assumes that incident nucleons collide with the intranuclear nucleons in a manner of the quasifree collision and Pauli's exclusion law is applied to this collision. In the standard HETC, a cutoff energy E_c is used[2] for terminating the calculation of the cascade process: When no particles in the nucleus go over the potential barrier E_c for particle emission, the cascade process is terminated. From the results in section 2.1, it is important to reduce the number of emitted neutrons in the energy region of 15 to 50 MeV.

From the view point of the cascade model, the mean free path of particles moving in a nucleus increases rapidly as the kinetic energy is reduced below 80 MeV. This is because Pauli's exclusion law inhibits the particle collision to a great extent at the low energy.[7] The probability of the particle emission increases with the mean free path. Hence, the above behavior of the mean free path is considered to be the reasons for the overestimation in the range of 15 to 50 MeV in section 2.1. In the low energy region, thus, the cascade model represents the neutron spectra that are different from the actual phenomena.

To improve the spectra in this region, we utilize a probability

density function $f(E_c)$ for terminating the cascade process in a reasonable way. By using a parameter E_0, the function is written by

$$f(E_c) = 2\,E_0^{-1}\,(1-E_c/E_0)\ . \qquad (2)$$

The value of E_c is thus chosen from 0 to E_0 with an energy dependent probability. The usual evaporation calculation of the HETC is made after the termination with this method. The calculation results are shown in Figs. 2 to 7 where E_0 = 40 MeV. Whereas the experiments for uranium and lead were made at LANL at an incident proton energy of 800 MeV,[8,9] that for uranium, lead, indium and iron were done at SIN at 585 MeV.[5] In Figs. 2 and 3, the data of 30° were taken from reference 9 and that of 45 and 110° from reference 8. The solid and dashed lines indicate the results of the present calculation and the standard HETC, respectively. The target nucleus and the incident proton energy for Fig. 5 are both the same as Fig. 1. The overestimation of neutron yield appeared for the solid lines in the region of 15 to 50 MeV in Fig. 1. This tendency is greatly improved in the solid lines in Fig. 5, and the shape of the shoulder in this energy range is reproduced to a considerable extent. Such an improvement is seen for all solid lines in Figs. 2 to 7.

3. Discussion on the cutoff energy

The use of the probability density function $f(E_c)$ led to the successful reproduction of the shoulder in the neutron spectra. To clarify the reasons for this improvement, we first calculate the particle emission probability on the basis of the cascade model. The emission probability of a particle moving in a nucleus is averaged for all location and orientation as follows:

$$\Gamma_{cas} = \frac{\iint \exp(-d(r,\Omega)/\lambda)\,dr\,d\Omega}{\iint dr\,d\Omega}\ , \qquad (3)$$

where r and Ω are the location and orientation vectors of the particle considered in a nucleus, respectively. The function $d(r,\Omega)$ shows the distance between the particle location and the nuclear boundary along the vector Ω. The mean free path λ is determined[7] by both the binary collision cross section and the nucleon density in the nucleus, taking Pauli's exclusion law into account. The value of λ then is dependent on the kinetic energy of the moving particle. The average emission probability of neutron Γ_{cas} is shown in Fig. 8 for nuclei of aluminum to lead. The excitation energy scaled in the abscissa indicates the kinetic energy that is subtracted by the Fermi energy.

The emission probability of particle Γ_{pre} is also obtained by

the exciton model with a few exciton state. The probability Γ_{pre} is calculated for a nucleus having an excitation energy E and containing p particles and h holes (n=p+h excitons):

$$\Gamma_{pre} = \frac{1}{p} \frac{\int_{v}^{E-B} \lambda_c(p,h,E,T)dT}{\lambda_- + \lambda_0 + \lambda_+ + \int_{v}^{E-B} \lambda_c(p,h,E,T)dT} , \quad (4)$$

Where λ_c is the probability of particle emission per unit time and energy. For the interaction of particles and holes, λ_+ is the probability for creation of a particle-hole pair per unit time, while λ_- is that for recombination of the pair. The symbol λ_0 shows the probability of the interaction that leads to no change of number of particles and holes. In the integral of λ_c , T is the kinetic energy of the particle after emission, B the binding energy, and v the potential barrier. The value of v is taken to be zero for neutron emission for simplicity. A two-particle (p=2) and one-hole (h=1) state is chosen for computation. The Kalbach constant [10,11] used for the transition matrix element is k = 100 to 600 MeV ^{3} . The ratio of $\Gamma_{pre}/\Gamma_{cas}$ is plotted for neutron emission in Fig. 9 for lead nucleus. While the abscissa shows the excitation energy per exciton E/(p+h) for Γ_{pre} , it does the kinetic energy subtracted by the Fermi energy for Γ_{cas} . The ratio increases linearly up to about 60 MeV, and then becomes constant. As seen in the figure, Γ_{pre} is nearly equal to Γ_{cas} at about 50 MeV for K=400 to 600 MeV^3 for lead. The energy for $\Gamma_{pre} \sim \Gamma_{cas}$ increases slowly with decreasing the mass number, and for instance becomes 10 % larger for indium than for lead.

Let us suppose that a nucleus is near the end of the cascade process and contains a particle which would have a kinetic energy T outside the nucleus. The value of T is expressed by the excitation energy of the particle subtracted by the binding energy B. In such a case, this paper treated the particle as follows: The cascade calculation was terminated with the probability proportional to f(T) given by Eq.(2), whereas it was continued with that proportional to $E_0/2\ (2/E_0-f(T)) = T/E_0$. In other words, the probability of the particle to stay in this process decreases linearly with kinetic energy T. When the shape of the results at about K=500 MeV^{-1} is taken into account, therefore, the probability proportional to T/E_0 is a good correction of the cascade model with regard to the preequilibrium effect. The three-exciton state was chosen in Fig. 9, and it seems to be reasonably consistent to the cutoff parameter of E_0=40 MeV below which the pre-

equilibrium effect becomes appreciable.

On the other hand, when particles are emitted from the pre-equilibrium state, their average kinetic energy after emission is close to the excitation energy per exciton. The average number of excitons produced in the cascade process is actually about 15 in the case of 585 MeV proton incidence on lead. The use of the whole number of excitons into Eq. (4), however, leads to a lower excitation energy per exciton, and fails to explain the empirical magnitude of E_0. Hence, the pre-equilibrium state of a few excitons is plausible near the end of each history of cascade. We considers that the kinetic energy of particles in such state may be much higher than in the usual preequilibrium state widely accepted in the intermediate energy region. In fact, if the intranuclear particle has a kinetic energy of 80 MeV, for instance, its de Broglie wave length is 3.1 fm and is fairly short in comparison with a size of nucleus. The usefulness of considering a few excitons suggests to us that the preequilibrium effect does not extend over the entire nucleus, but works in a local manner.

4. Monte Carlo calculation based on the exciton model

Between the intranuclear-cascade and the evaporation processes, the exciton model[10] is adopted for the calculation of the preequilibrium process in the whole region of the nucleus. The Monte Carlo algorithm[12] is again used for the computation. The exciton model calculation is started by the use of exact numbers of both particles and holes that have been produced in the intranuclear cascade calculation. The angular distribution of neutrons that are emitted from this process is determined by the systematics given by Kalbach-Mann.[13] Even I's are utilized in this study, since it is considered to correspond to the multistep compound process.[13] This preequilibrium calculation is followed by the usual evaporation process of HETC.

The computation results are shown in Fig. 10, where 585 MeV protons were incident on lead. While the dashed lines indicate the results of the standard HETC, the solid ones show that of the present calculation. The shoulders at the energy of 15 to 50 MeV are reproduced well in almost the same manner as in Fig. 5. In the backward direction, the solid lines at 10 to 15 MeV are closer to the experimental data in Fig. 10 than that do in Fig. 5. The present calculation of the exciton model produces neutrons having an almost isotropic angular distribution. In contrast, the cascade process gives the neutrons emitted with a

forward-peaked angular distribution. In the forward direction, thus, the cascade process yields the intermediate-energy neutrons of which number is a few times as large as that of the exciton model. The effect of the exciton model on the intermediate-energy neutron spectra is not appreciable in this direction. Therefore, the introduction of the exciton model into the HETC was useful only to represent the backward neutrons of the intermediate energy.

5. Conclusion

We considered the intranuclear nucleons with higher momentum, and successfully reproduce the experimental high-energy neutrons in the backward direction. The preequilibrium effect was considered in a local manner, and this was introduced as a simple probability density function for terminating the intranuclear cascade process. The resultant neutron spectra reproduced the shoulders of the experimental data in the region of 20 to 50 MeV. The exciton model was coded with a Monte Carlo algorithm. The effect of the exciton model calculation was not so appreciable except for the intermediate energy neutron in the backward direction.

Acknowledgment

The authors gratefully acknowledge F. Atchison of PSI for his supplying his version of the HETC.

References

(1) COLEMAN, W.A., ARMSTRONG, T.W.: Nucl. Sci. Eng. 43, 353 (1971).
(2) NAKAHARA, Y., TSUTSUI, T.: JAERI-M 82-198 (1982).
(3) ARMSTRONG, T.W., et al.: Nucl. Sci. Eng., 49, 82 (1972).
(4) ATCHISON, F.: RL-81-006 (1981).
(5) CIERJACKS, S., et al.: Phys. Rev. C36, 1976 (1987).
(6) HANEISHI, Y., FUJITA, T.: Phys. Rev. C33, 260 (1986).
(7) KIKUCHI, K., KAWAI, M.: "Nuclear Matter and Nuclear Reactions" p.33 (1968), North-Holland, Amsterdam.
(8) Howe, S.D., et al.: LANL-85-3660 (1985).
(9) MEIER, M.M., et al.: Radiation Effects, 96, 1415 (1986).
(10) Gidima, K.K.: Nucl. Phys. A401, 329 (1983).
(11) KALBACH, C.C.: Nucl. Phys. A210, 590 (1973).
(12) NAKAHARA, Y., NISHIDA, T.: JAERI-M 86-074 (1986).
(13) KALBACH, C., MANN, F.M.: Phys. Rev. C23, 112 (1981).

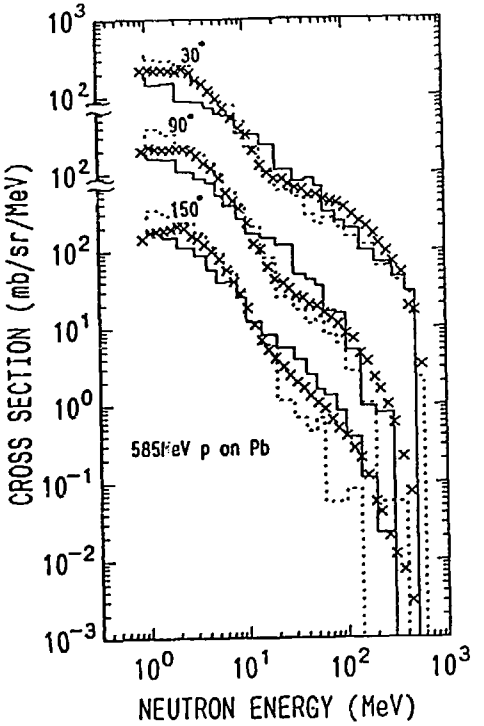

Fig. 1
Double differential cross section for lead at laboratory angles of 30, 90 and 150°. The incident proton energy is 585 MeV. Cross marks indicate the experimental data.[5] Dashed lines show the calculation results of the standard HETC, and solid ones that of the present method with the high momentum component and the cutoff energy of E_c=0.

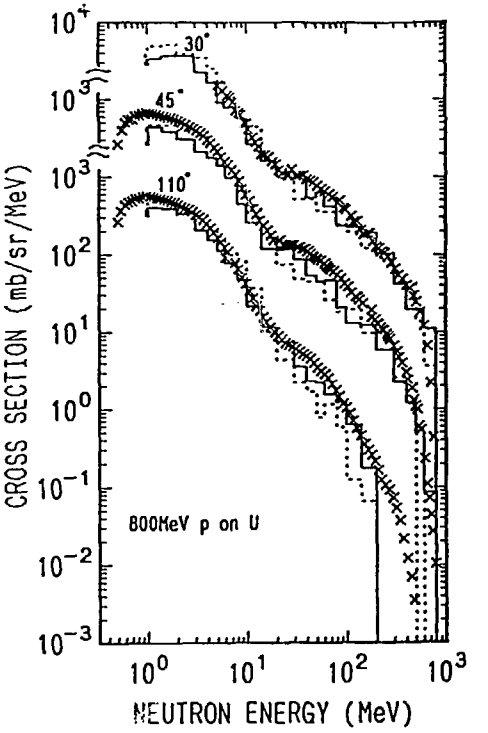

Fig. 2
Double differential cross section for uranium at laboratory angles of 30, 45 and 110°. The incident proton energy is 800 MeV. Cross marks indicate experimental data.[8,9] Dashed lines show the calculation results of the standard HETC, and solid ones that of the present method which considers the high momentum component and the cutoff probability $f(E_c)$ with E_o=40 MeV.

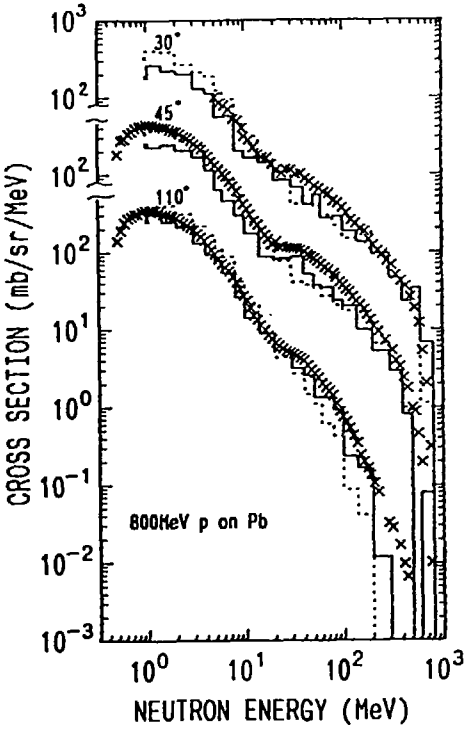

Fig. 3
Double differential cross section for lead at laboratory angles of 30, 45 and 110°. The incident proton energy is 800 MeV. The other explanation is the same as in Fig. 2.

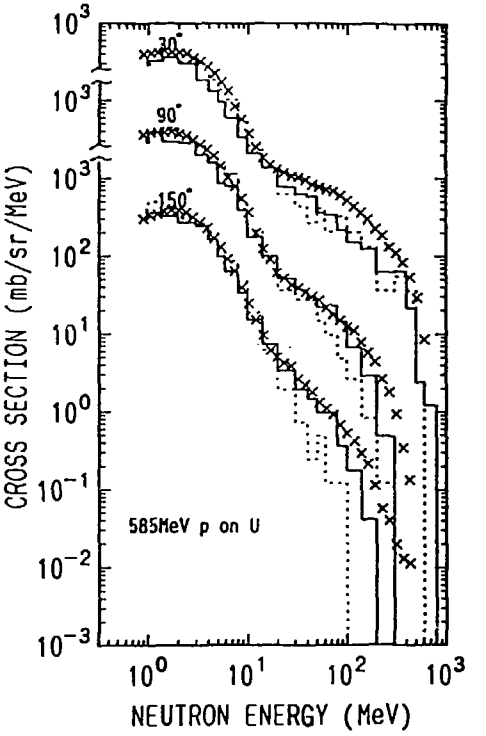

Fig. 4
Double differential cross section for uranium at laboratory angles of 30, 90 and 150°. The incident proton energy is 585 MeV. Cross marks indicate experimental data.[5] Dashed lines show the calculation results of the standard HETC, and solid ones that of the present method which considers the high momentum component and the cutoff probability $f(E_C)$ with E_O=40 MeV.

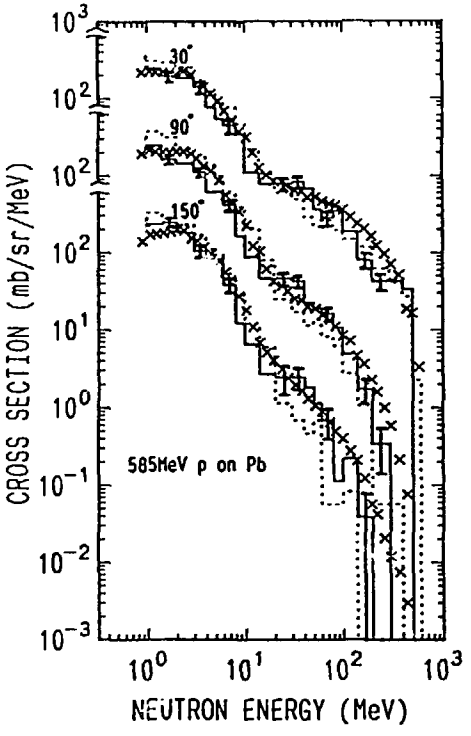

Fig. 5
Double differential cross section for lead at laboratory angles of 30, 90 and 150°. The incident proton energy is 585 MeV. The other explanation is the same as in Fig. 4.

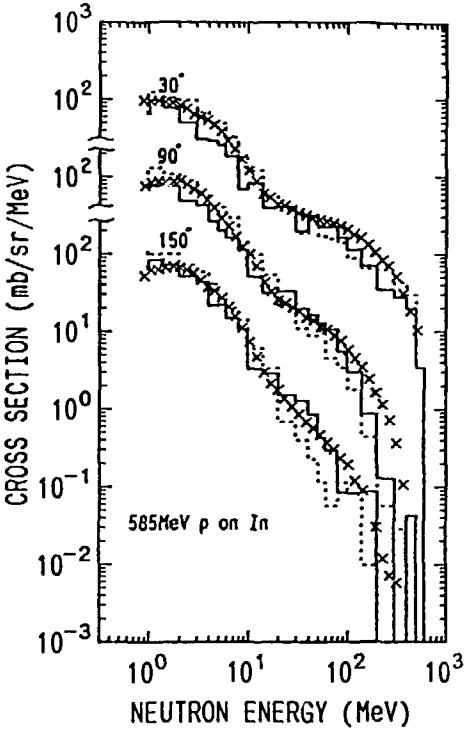

Fig. 6
Double differential cross section for indium at laboratory angles of 30, 90 and 150°. The incident proton energy is 585 MeV. The other explanation is the same as in Fig. 4.

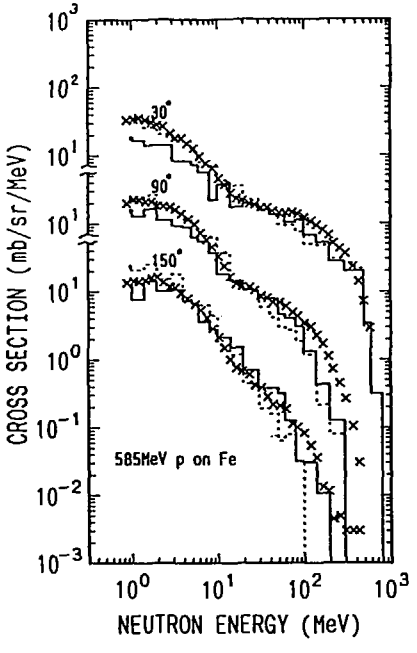

Fig. 7
Double differential cross section for iron at laboratory angles of 30, 90 and 150°. The incident proton energy is 585 MeV. The other explanation is the same as in Fig. 4.

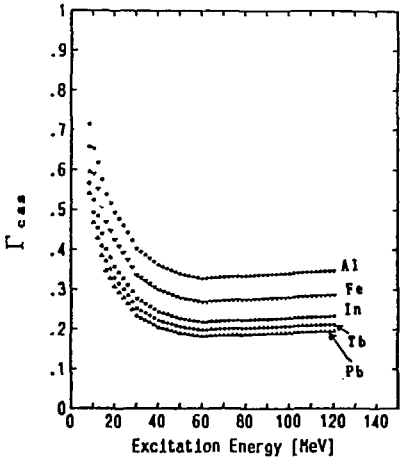

Fig. 8
The particle emission probability calculated from the intranuclear cascade model. The abscissa indicates the kinetic energy of neutron subtracted by the Fermi energy.

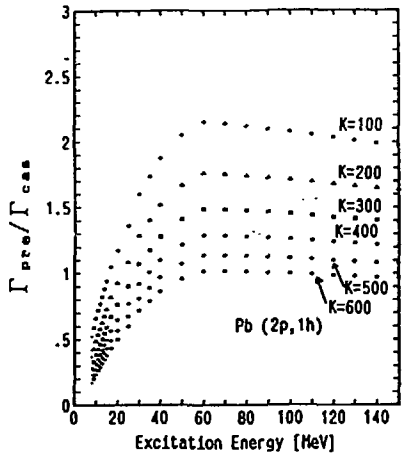

Fig. 9
The ratio of the particle emission probability based on the exciton model to that on the intranuclear-cascade model. A two-particle and one-hole state was assumed for the exciton model calculation.

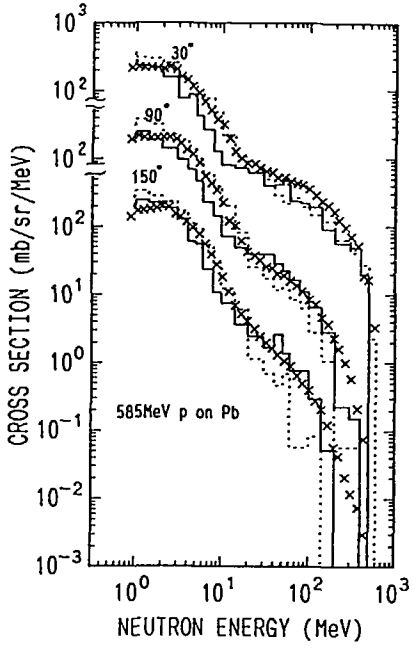

Fig. 10
Double differential cross section for lead taking the exciton model into account. The incident proton energy is 585 MeV. Cross marks indicate experimental data.[5] Dashed lines show the calculation results of the standard HETC, and solid ones that of the present method which utilizes the Monte Carlo exciton model in addition to the high momentum component and the cutoff probability $f(E_c)$ with E_o=50 MeV.

3.17 Measurement of the U-238 Capture Cross Section with Neutron Filtered Beams

Katsuhei Kobayashi, Shuji Yamamoto and Yoshiaki Fujita
Research Reactor Institute, Kyoto University
Kumatori-cho, Sennan-gun, Osaka 590-04 Japan

By using the linac time-of-flight method and Fe and/or Si filtered neutrons of 24, 55 and 146 keV, the ^{238}U neutron capture cross sections were measured relative to the standard cross section for the $^{10}B(n,\alpha\gamma)$ reaction with a pair of C_6D_6 scintillator placed at the 12.4 m station. The measured value at 24 keV was normalized to 0.47 b appeared in the ENDF/B-VI file. The present data agree with the recent evaluations in ENDF/B-VI and JENDL-3 released very recently, and moreover with the recent measurement by Kazakov et al. The experimental uncertainties are 6 to 8 %, which are mainly derived from the counting statistics in the filtered neutrons. More careful works may be required in the data correction and uncertainty analysis for the present preliminary measurement.

1. Introduction

The new evaluated data for the $^{238}U(n,\gamma)$ reaction cross section appeared in the recent papers[1-3] have been revised to be smaller by more than 5 to 10 % than old evaluated data and/or most of the experimental data in the energy region from 10 to 300 keV. The revised data, however, show a good agreement with the experimental data which have recently measured by Kazakov et

al.[4]. The evaluated data also gave better agreement with the integral measurements in effective multiplication constants and spectral indices of ^{238}U capture related data such as $\sigma_c(238)/\sigma_f(235)$ or $\sigma_c(238)/\sigma_f(239)$[2]. Moreover, the evaluated data file JENDL-3 has been released very recently[5]. In such a situation for the ^{238}U data, much interest has been paid to the capture cross section, especially in the ten to hundreds keV energy region.

Neutron total cross section minima are observed at 24 keV for iron and 55 and 146 keV for silicon, respectively[6-9]. Then, the thick layer of Fe and/or Si materials can produce semi-monoenergetic neutrons from the white neutron beam as filtered beams of 24 keV, 55 and 146 keV, respectively. The thick filter materials can reduce backgrounds from the intense source to give a good signal-to-background ratio, and are useful for the determination of background level and for the precise measurement of neutron capture cross sections[9,10]. Especially, the filtered beam techniques are adequate to the capture cross section measurement with high gamma-ray background like an uranium sample.

In the present measurement, capture cross section for ^{238}U has been obtained by the iron and silicon filtered beams and the time-of-flight method using a linear accelerator (linac). The obtained results were normalized to the reference value of 0.47 b at 24 keV and compared with the recent measurement and evaluation at energies of 55 and 146 keV.

2. Experimental Method

The capture cross section measurement was made by the time-of-flight (TOF) method using the 46 MeV electron linear accelera-

tor at the Research Reactor Institute, Kyoto University (KURRI). The experimental arrangement is shown in Fig. 1.

Bursts of fast neutrons were produced from the water-cooled photoneutron target, which was made of 12 sheets of Ta plates 4.8 cm in diameter with an effective thickness of 3 cm[11]. This target was set at the center of an octagonal water tank, 30 cm diameter and 8 cm thick, to moderate the neutron energies.

Experimental parameters and conditions for the Fe- and Si-filtered beams are summarized in Table 1. The ^{238}U capture sample used was in the form of natural uranium metallic plate, 3 x 3 cm square and 1.5 mm thick. The energy dependent cross section for the $^{10}B(n,\alpha\gamma)$ reaction was taken as a standard[12] for the ^{238}U capture measurement at 24, 55 and 146 keV. Background measurement for the filtered beam experiment was made to experimentally investigate the effect of scattered neutrons with a Pb plate, 5 x 5 cm square and 3 mm thick. A 0.5 mm thick Cd filter was applied to suppress overlap of thermal neutrons from previous pulses. Energies of the TOF neutrons from source to detector were checked by the resonance structures from the Fe filters. Total thickness of each Fe and Si material is 20 cm and 92 cm, respectively, and the typical filtered beams obtained are shown in Figs. 2 and 3.

A pair of C_6D_6 scintillators (NE-230) 11 cm in diameter and 5 cm thick was mounted on an RCA-4525 photomultiplier and used as a capture gamma-ray detector located at 12.4 m distant from the photoneutron Ta target. Capture signals from the scintillators were fed into a fast amplifier and discriminator. A coincidence circuit was employed between the scintillators to improve the signal-to-noise ratio for the ^{238}U capture measurement. A time digitizer was initiated by the KURRI linac burst and the TOF data were stored in a data acquisition system, Canberra's Series 88 multi-parameter analyzer which was linked to a PDP-11/34 comput-

er.

In order to normalize the neutron intensity between the experimental runs, a BF_3 counter was inserted in the neutron beam to measure the TOF spectrum.

3. Data-Taking and Reduction

Capture events were observed by integrating the data in the TOF channel region of the full width at half maximum (FWHM) of the filtered neutrons, as seen in Figs. 2 and 3. The background levels were determined from the time spectrum data in the front and rear channel regions of the relevant filtered neutrons. Moreover, background counts for the filtered neutrons were deduced with a lead sample equivalent to the thickness of the scattering cross section for the uranium capture sample. It was found that the background contribution to the ^{238}U capture counts was almost 40 % at 55 and 146 keV.

Capture events for ^{10}B and ^{238}U samples are counted with the following procedures:

For 24 keV,

$$C_{24}(B) = \eta_{24}(B)\, Y_{24}(B)\, F_{24}\,, \qquad Y_{24}(B) = N_B\, t_B\, \sigma_{24}(B)$$

$$C_{24}(U) = \eta_{24}(U)\, Y_{24}(U)\, F_{24}\,, \qquad Y_{24}(U) = N_U\, t_U\, \sigma_{24}(U).$$

For x keV(146 and/or 55 keV),

$$C_x(B) = \eta_x(B)\, Y_x(B)\, F_x\,, \qquad Y_x(B) = N_B\, t_B\, \sigma_x(B)$$

$$C_x(U) = \eta_x(U)\, Y_x(U)\, F_x\,, \qquad Y_x(U) = N_U\, t_U\, \sigma_x(U)\,.$$

C, η, Y, F, N, and t show count, efficiency, yield, flux, atomic density and sample thickness, and the subscripts 24 and x mean the relevant filter energy, and B and U indicate ^{10}B and ^{238}U samples, respectively. Since the cross section values for the $^{10}B(n,\alpha\gamma)$ reaction are well known, we referred it as a standard[12], for the present measurement. By assuming the relation

$\eta_{24}(U) = \eta_X(U)$, the capture cross section can be easily obtained as

$$\sigma_X(U) = \frac{C_{24}(B)}{C_{24}(U)} \cdot \frac{C_X(U)}{C_X(B)} \cdot \frac{\sigma_X(B)}{\sigma_{24}(B)} \times \sigma_{24}(U) \quad ,$$

where $\sigma_{24}(E)$ is a reference value of the ^{238}U capture cross section at 24 keV.

4. Results and Discussion

Preliminary results for the $^{238}U(n,\gamma)$ reaction are given in Figs. 4 and 5, whose original drawings were taken from the Fröhner's paper[3], comparing with other measurements and the evaluated data JENDL-3. When we normalize our data to 0.47 b at 24 keV in ENDF/B-VI appeared in the cited figure, the cross sections at 55 and 146 keV are 0.291 b and 0.147 b, respectively, with the experimental uncertainties of 6 to 8 %. We have assumed the detection efficiencies of C_6D_6 scintillators at 24 keV are equivalent to those at 55 and 146 keV. Contribution by the $^{235}U(n,f)$ reaction for the natural uranium sample was also corrected as the cross section ratio to the $^{238}U(n,\gamma)$ reaction.

Not only recent evaluation data appeared in the Fröhner's paper but also JENDL-3 data are in reasonably agreement with the present measurements in general. Previous measurements are rather higher, especially in the energy region above 100 keV, than the present data and the above new evaluations. However, the experimental data by Kazakov et al.[4] are in tendency to be lower than old measurements and show a good agreement with the recent evaluations and the presently measured values.

More careful works may be required to complete the data correction and uncertainty analysis for the present preliminary

measurements, including absolute measurement of the cross section with filtered neutrons.

References:

1) Fröhner, F. H., Proc. Int. Reactor Physics Conf., Jackson Hole, p.III-171 (1988).
2) Hasegawa, A., JAERI-M 89-026, p.90 (1989).
3) Fröhner, F. H., Nucl. Sci. Eng., 103, 119 (1989).
4) Kazakov, L. E., et al., Yad. Const., 3, 37 (1986).
5) JAERI Nuclear Data Center, JENDL-3 (1989).
6) Block, R. C., et al., J. Nucl. Sci. Technol., 12, 1 (1975).
7) Kobayashi, K., et al., Ann. Nucl. Energy, 4, 449 (1977).
8) Fujita, Y., et al., J. Nucl. Sci. Technol., 21, 879 (1984).
9) Cierjacks, S.(Ed.), "Neutron Sources for Basic Physics and Application", An OECD/NEA Report, Pergamon Press, pp.177-196 (1983).
10) Kobayashi, K., J. Nucl. Sci. Technol., 18, 823 (1981).
11) Kobayashi, K., Ann. Rep. Res. Reactor Inst. Kyoto Univ., Vol.22, 142 (1989).
12) IAEA Technical Reports Series No.277, "Nuclear Data Standards for Nuclear Measurements", IAEA, Vienna (1983).

Table 1 Experimental parameters and conditions

Parameters	Fe filtered beam	Si filterd beam
Samples	^{10}B: 0.369 g/cm^2 ^{238}U: natural U 1.5 mm thick plate	^{10}B: 0.369 g/cm^2 ^{238}U: natural U 1.5 mm thick plate
Filters	15* + 5 cm	30* + 46 + 16 cm
Filtered neutron	24 keV	146 keV 55 keV
Linac operation:		
pulse repetition	250 pps	250 pps
pulse width	0.22 μsec	0.22 μsec
average current	140 μA	140 μA
Detectors	C_6D_6 scinti.	C_6D_6 scinti.
Monitor	BF_3 counter#	BF_3 counter#
Time analyzer:		
channel width	20 nsec(Capture) 125 nsec(Monitor)	20 nsec(Capture) 125 nsec(Monitor)
No. of channel	1024	1024

* Placed in front of the TOF tube in the target room.

\# Placed in the TOF beam (at about 10 m).

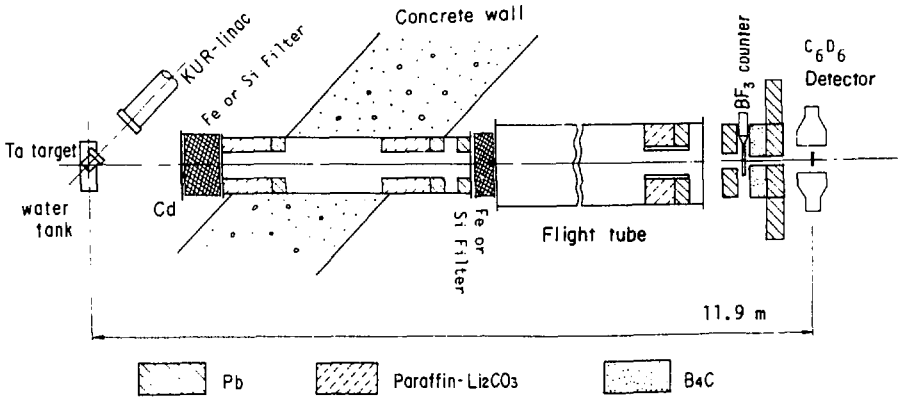

Fig. 1 Experimental arrangement for the capture measurement

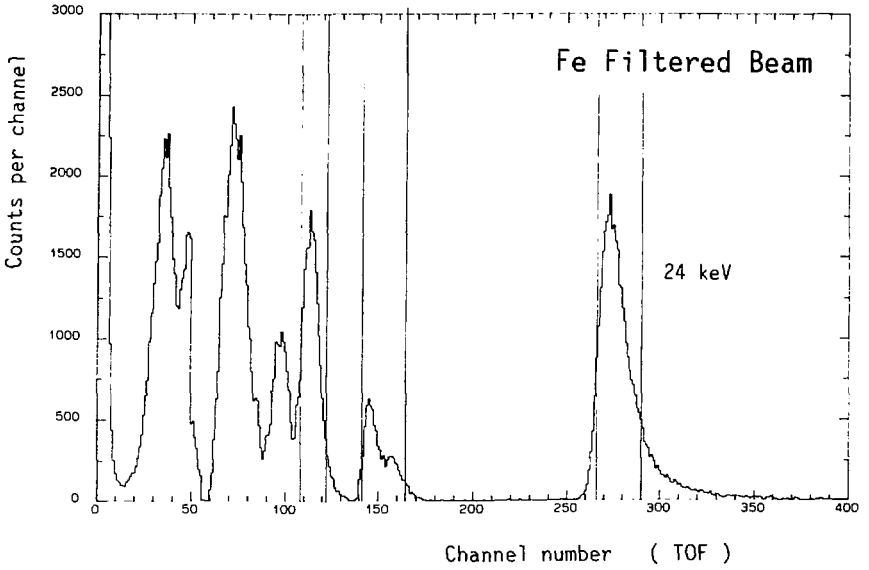

Fig. 2 Fe filtered beam measured by the TOF method

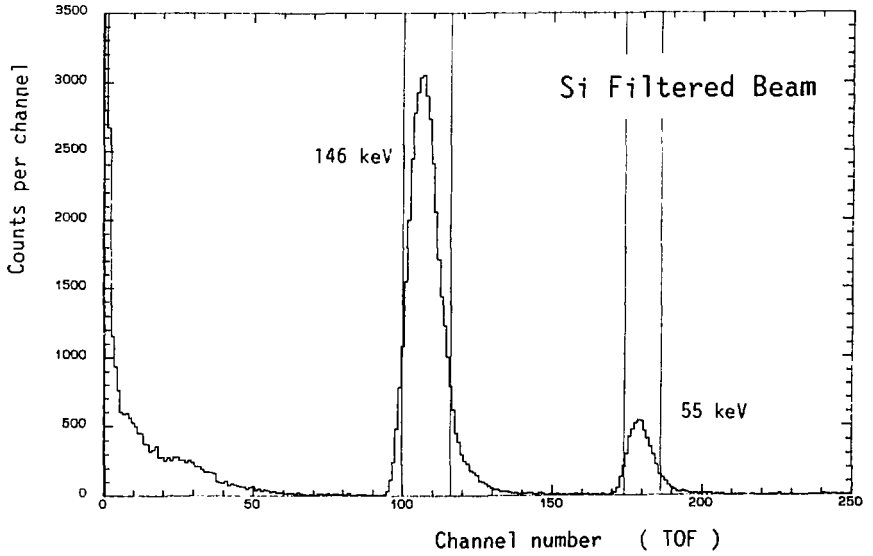

Fig. 3 Si filtered beam measured by the TOF method

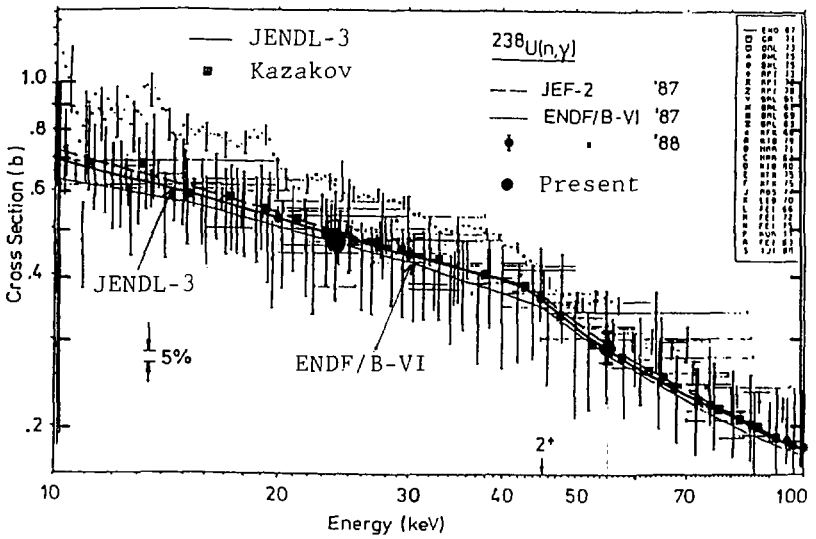

Fig. 4 Comparison ofthe present capture cross sections and the previous measurements and recent evaluations (10 to 100 keV)

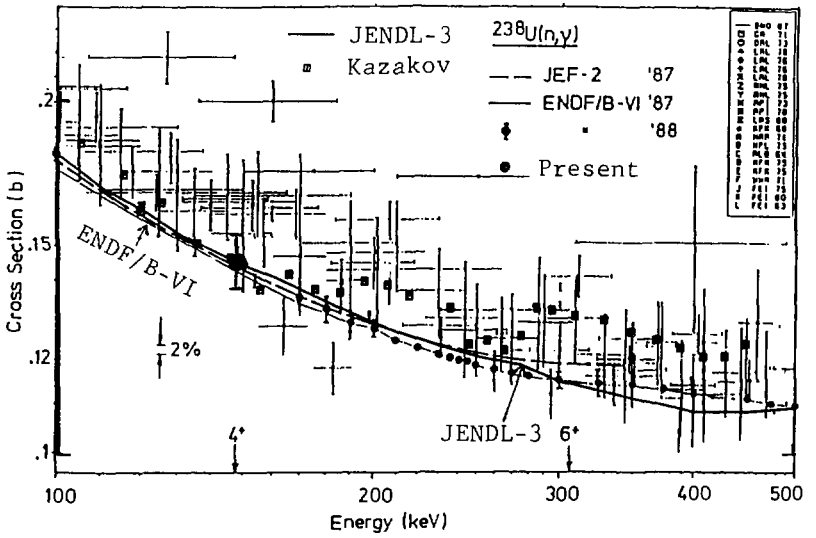

Fig. 5 Comparison of the present capture cross sections and the previous measurements and recent evaluations (100 to 500 keV)

3.18 Application of Post Acceleration Beam Chopper for Neutron Emission Cross Section Measurements

M.Baba, S.Matsuyama, M.Fujisawa, T.Iwasaki, S.Iwasaki and R.Sakamoto

Department of Nuclear Engineering, Tohoku University, 980 Sendai

A post acceleration beam chopping system was newly installed for Tohoku University 4.5MV Dynamitron accelerator to reduce the pulsed beam duration and has been applied successfully for improvement of energy resolution in fast neutron time-of-flight experiments. Using the chopper, new measurements were carried out for double-differential neutron emission cross sections of ^{12}C and ^{6}Li for 14 MeV incident energy.

1. Introduction

We have been carrying out the measurements of neutron scattering and neutron emission cross sections with the time-of-flight (TOF) technique using the pulsed neutron beam provided by Tohoku University 4.5 MV Dynamitron accelerator [1-3]. In these experiments, the "wing" which is the tail component in the pulsed beam disturbed clear separation of inelastically-scattered neutrons from nearby large peaks due to elastic scattering or discrete inelastic scattering, while 1.5 to 2 ns resolution was obtained in FWHM.

The "wing" was traced to be due to strongly asymmetric geometry of the lens-pulser system in the high-voltage terminal, but was expected to be eliminated by chopping again the accelerated beam [4,5]. Therefore, we have designed and installed a post-acceleration-chopping system (PACS) to remove the "wing" and even to shorten the pulsed-beam duration [4,5].

PACS proved to be very effective for improvement of energy resolution of the TOF spectrometer and has been applied for various experiments. By using PACS, new measurements of DDXs were carried out with improved resolution for ^{12}C and ^{6}Li.

2. Post Acceleration Chopping System

PACS sweeps the accelerated pulsed beam across a chopping slit with a pair of deflector plates and eliminates the "wing" in primary beam [4,5]. It is also effective for reduction of spurious components and dark current, and useful as a stand-alone beam pulser or sweeper.

The design parameters of PACS were found out using Monte-Carlo calculations considering the optics and space-time correlation of ion beam and interference with existing accelerator devices [4,5]. The beam optics was traced using the code "TRANSPORT" [6] and taken into Monte-Carlo calculations.

The layout of PACS is shown in Fig.1. The deflector plates, 50 cm long with 2.5 cm spacing, are placed upstream of the switching magnet to enable common use of PACS in all the beam lines following the switching magnet. (In Fig.1, only one beam port is shown.) Figure 2 illustrates the electronics block diagram of PACS. The deflector plates are fed with 8 MHz RF synchronized with the accelerated beam. High voltage RF, variable from 0 to 10 kVp-p, is furnished by a tank circuit driven by a commercial wide-band linear-amplifier; this scheme is advantageous because of fewer high-voltage items necessary and of simpler fabrication, tuning and maintenance. Synchronization of RF with the beam is realized by triggering the amplifier with the frequency-multiplied and phase-adjusted beam pick-off signal obtained with the capacitive pick-up tube just before the deflector. The chopping slit is located about 2.5 m downstream of the deflector plates with opening around 5 mm; the slit is placed vertically to avoid interference with the beam-energy stabilizing system based on the slit-feedback method. The tank elements and the deflector electrodes are electrically shielded with aluminum plates for reduction of RF noise disturbing the experimental apparatuses.

The performance of PACS was tested by observing time spectra of gamma-rays and neutrons emitted from neutron targets and scattering samples. PACS operated fairly reliably while it required occasional phase adjustment to compensate the drifting of phase delay and/or beam path.

Figures 3(a) and 3(b) illustrate the examples of test measurements; they are the emission spectra for 14 MeV incident energy from samples of polyethylene, 1 cm in dia. and 5 cm long, and elemental nickel, 2.5 cm in dia. and 4 cm long, measured at flight path length of 6.5 m using a NE213 scintillator, 5" in dia. and 2" thick. As shown in Fig.3(a), PACS makes much clear the separation between the peaks of scattered neutrons by removing the "wing" of pulsed beam. In Fig.3(b), the first levels of ^{58}Ni & ^{60}Ni are separated satisfactorily from the ground state even at the path length of 6.5 m. Thus, PACS proved to be very effective for neutron TOF experiments, especially for scattering experiments which require clear separation between the neutrons originating from different reaction processes.

3. DDX Measurements of ^{12}C and ^{6}Li

DDXs of ^{12}C and ^{6}Li were measured with improved energy resolution applying PACS. The experimental and data reduction procedures are identical with those described previously [1-3]. The neutron detector was a NE213 scintillator, 14 cm in dia. and 10 cm thick, and the flight path was 6 m long.

^{12}C: In Figs.4 and 5(a)-(c), shown are the results of DDX and partial cross sections derived from the DDXs, together with previous data by Kikuchi et al. in our laboratory [3] and the evaluations. The present data show very good agreement with previous ones for the ground state, the 1-st (Q=-4.44 MeV) and 3-rd (Q=-9.63 MeV) levels, and for low energy continuum region. For the 2-nd (Q=-7.76MeV) level, however, new data are much lower than previous ones and close to the experimental values at OKTAVIAN measured with 9 m long flight path [7], and ENDF/B-V evaluation probably based on the experiment using double-scintillator technique [8]. The present lower values for the 2-nd level are due to greatly reduced pulse "wing" by PACS.

The summary of the present partial cross section results is presented in Table 1 together with the evaluated data. The total cross section obtained by summing up the presently derived partial cross sections agree with those by ENDF/B-V and JENDL-3 which were based on high-precision direct measurements. Therefore, the present experiments eliminated the inconsistency between the partial cross sections and the total cross section [2] owing to the improved peak separation by PACS.

^{6}Li: Typical results of ^{6}Li DDX are shown in Fig.6, together with our previous data by Chiba et al., [1] and JENDL-3. The present results reproduce very well the previous ones; this result implies previous data were not distorted seriously by pulse "wing" existing in previous experiment.

The experimental data show higher values than JENDL-3 in the region between 6 MeV and 12 MeV of emission energy. This trend seems consistent with the fact that the analyses using the JENDL-3 data underpredict the several MeV region of LLNL pulsed sphere experiments for ^{6}Li [9].

Therefore, we attempted to derive a partial cross sections from the DDX data. Figure 7 shows the least-squares analysis of emission spectrum for derivation of partial contributions where the spectrum is assumed to consist of discrete components due to five discrete states indicated in the Fig.7, and of continuum parts due to the (n,n'd) and the (n,2n) reactions [1]. The experimental spectrum is described very well by the superposition of these com-

ponents provided that the neutrons from the (n,n'd) and the (n,2n) reactions are described, respectively, by the three-body phase space and the evaporation spectra [1].

The results of partial cross sections obtained through the fits are shown in Fig.8. The partial cross sections are generally higher than JENDL-3 for the first (Q=-2.18MeV), second (Q=-3.56 MeV) and the third (Q=-4.31 MeV) levels as suggested from the comparison of DDXs.

4. Summary

A post acceleration beam chopping system has been developed and applied for double-differential neutron cross section measurements. The chopper improved effectively the pulsed beam quality and energy resolution in time-of-flight experiments. New experimental data are presented for double-differential neutron emission spectra and partial scattering cross sections of ^{12}C and ^{6}Li obtained by use of the chopper.

Acknowledgment

The authors wish to thank Dr.H.Shibata of University of Tokyo for valuable suggestions. They also indebted to Messrs. T.Takahashi, K.Komatsu and T.Nagaya for their support in fabrication of PACS.

References:

1.S.Chiba et al.; J.Nucl.Sci.Technol.,22 771(1985)

2.M.Baba et al.; Radiation Effects 92-96 223(1986)

3.M.Baba et al.; Proc.Int.Conf., "Nuclear Data for Science & Technology." (1988 Mito) p.209, 294

4.S.Matsuyama et al.; NETU 50 p.6, NETU 51 p.6 (Department Nuclear Engineering, Tohoku University)

5.M.Fujisawa et al.; Proc. 2-nd Symp. "Tandem Accelerator Technology" (1989 Tokyo Institute of Technology) p.108 (in Japanese)

6.K.L.Brawn; SLAC Report No.91(1974)

7.A.Takahashi et al.; J.Nucl.Sci.Technol.,25 215(1988)

8.G.A.Grin et al.; Helv.Phys.Acta.,42 990(1969)

9.H.Maekawa et al.;JAERI-M 88-065 p.198

Table 1 Summary of the ^{12}C partial scattering cross sections

En=14.1MeV

	Present	ENDF/B-V	JENDL3
G.S.	784.2±45.0	797.0	793.8
Q=-4.44MeV	203.8±11.5	186.8	183.0
Q=-7.65MeV	10.5± 1.0	13.0	9.8
Q=-9.64MeV	62.5± 4.3	63.6	77.9
Continuum	130.1± 8.6	161.7	161.2
Absorption	81.4*	81.4	73.3
Total	1272.5±47.4	1303.4	1299.7
(n,n')3α	202.0±13.0	238.3	248.9

*ENDF/B-V

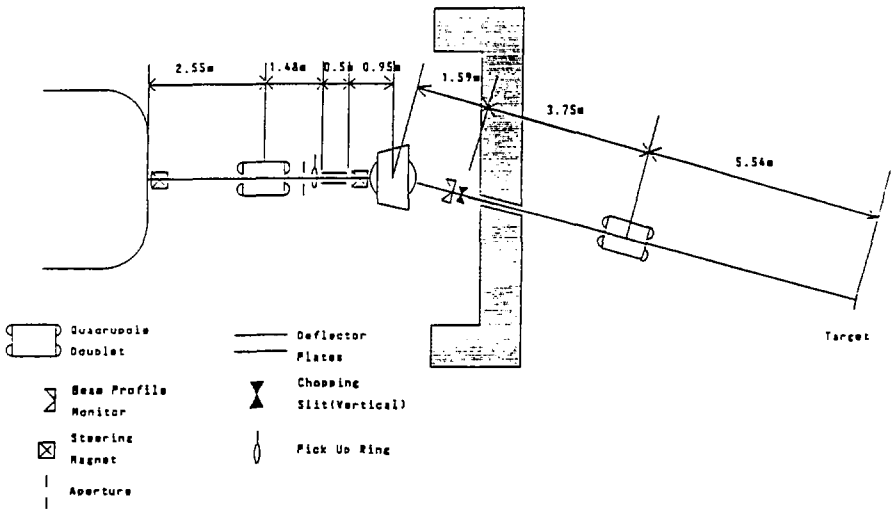

Fig. 1 Layout of post-acceleration chopping system for Dynamitron Accelerator

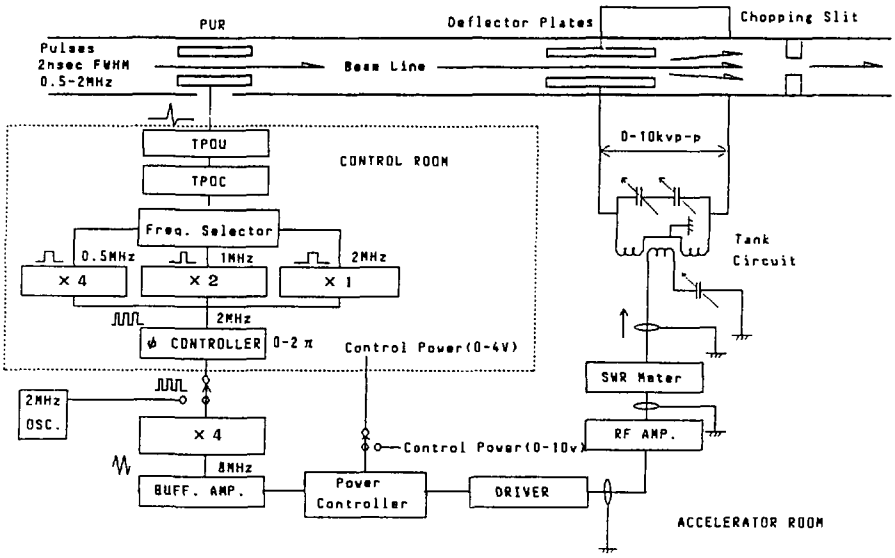

Fig. 2 Electronics schematic diagram of post acceleration chopping system

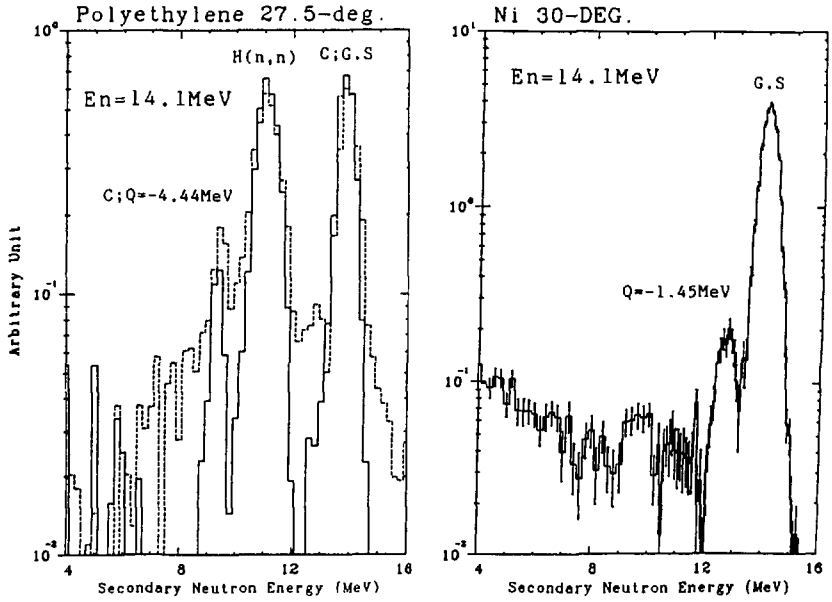

(a) polyethylene (b) nickel

Fig. 3 Neutron emission spectra for 14.1 MeV incident neutrons, measured using chopper; dash-line shows the results without operating chopper.

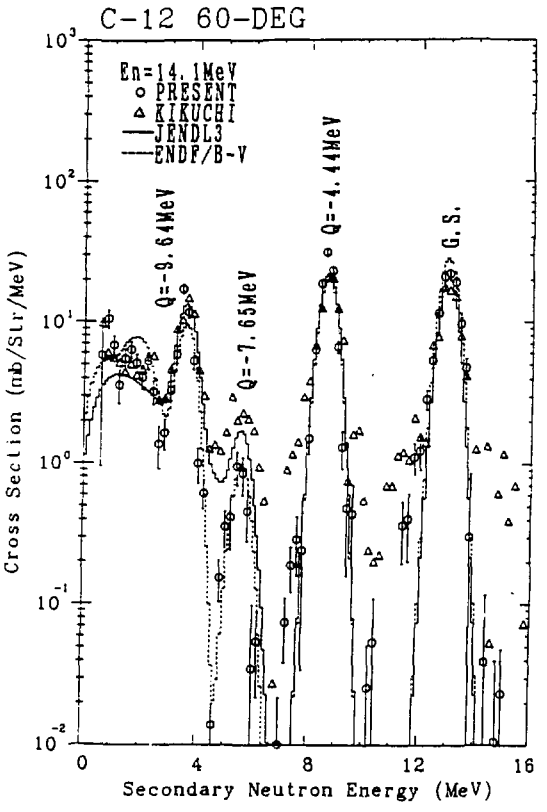

Fig. 4 Neutron emission spectra of ^{12}C, compared with our previous data (Kikuchi) and evaluated data

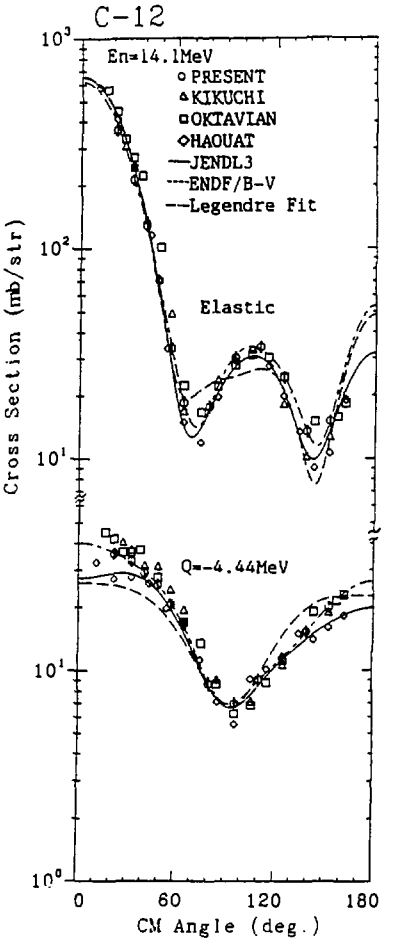

Fig. 5(a)
Differential scattering cross sections of ^{12}C for 14.1 MeV neutrons

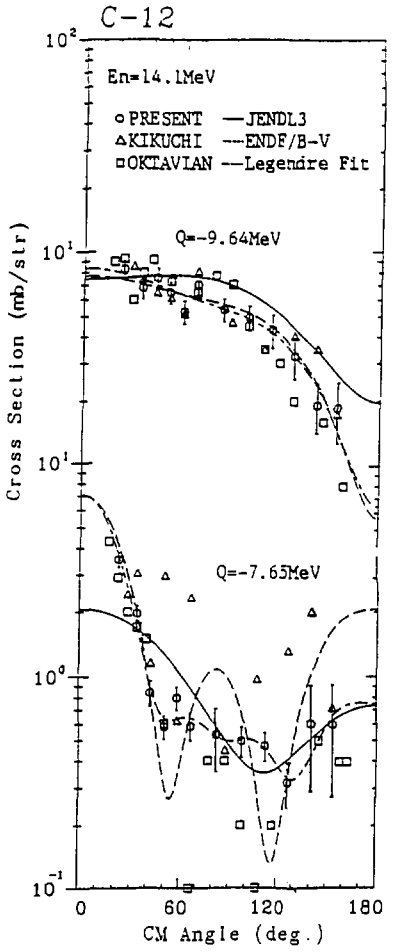

Fig. 5(b)
Differential scattering cross sections of ^{12}C for 14.1 MeV neutrons

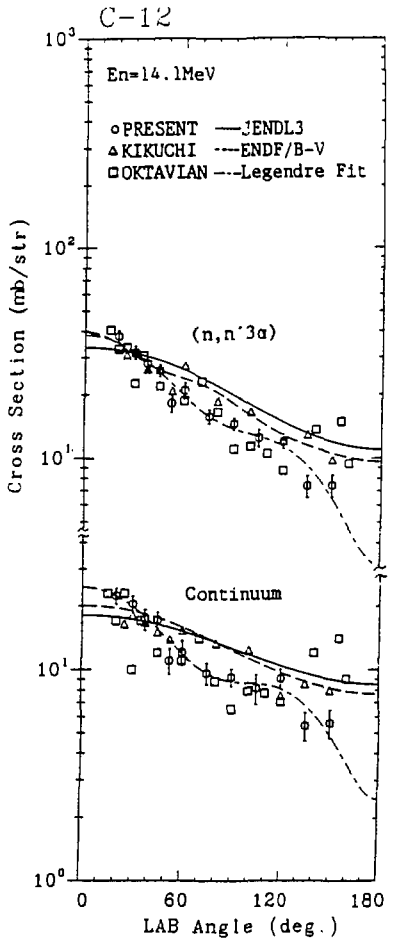

Fig. 5(c)
Differential scattering cross sections of ^{12}C for 14.1 MeV neutrons

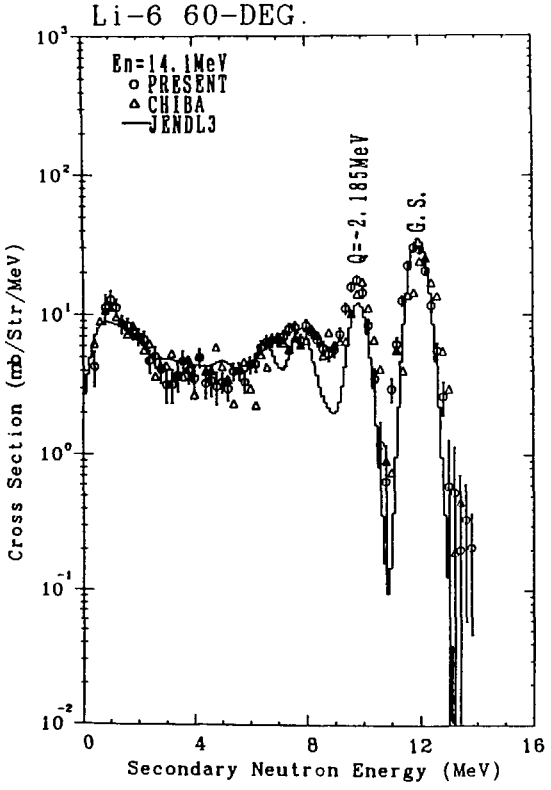

Fig. 6 Neutron emission spectrum of ^{6}Li

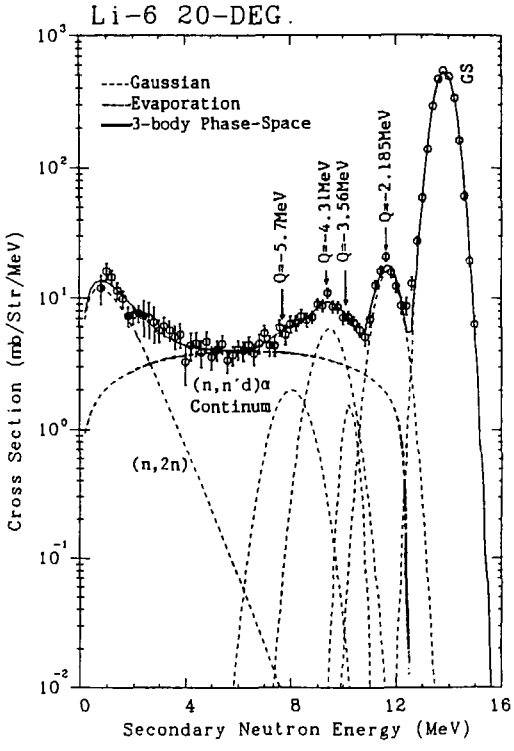

Fig. 7 Least-squares analysis of ^{6}Li neutron emission spectrum

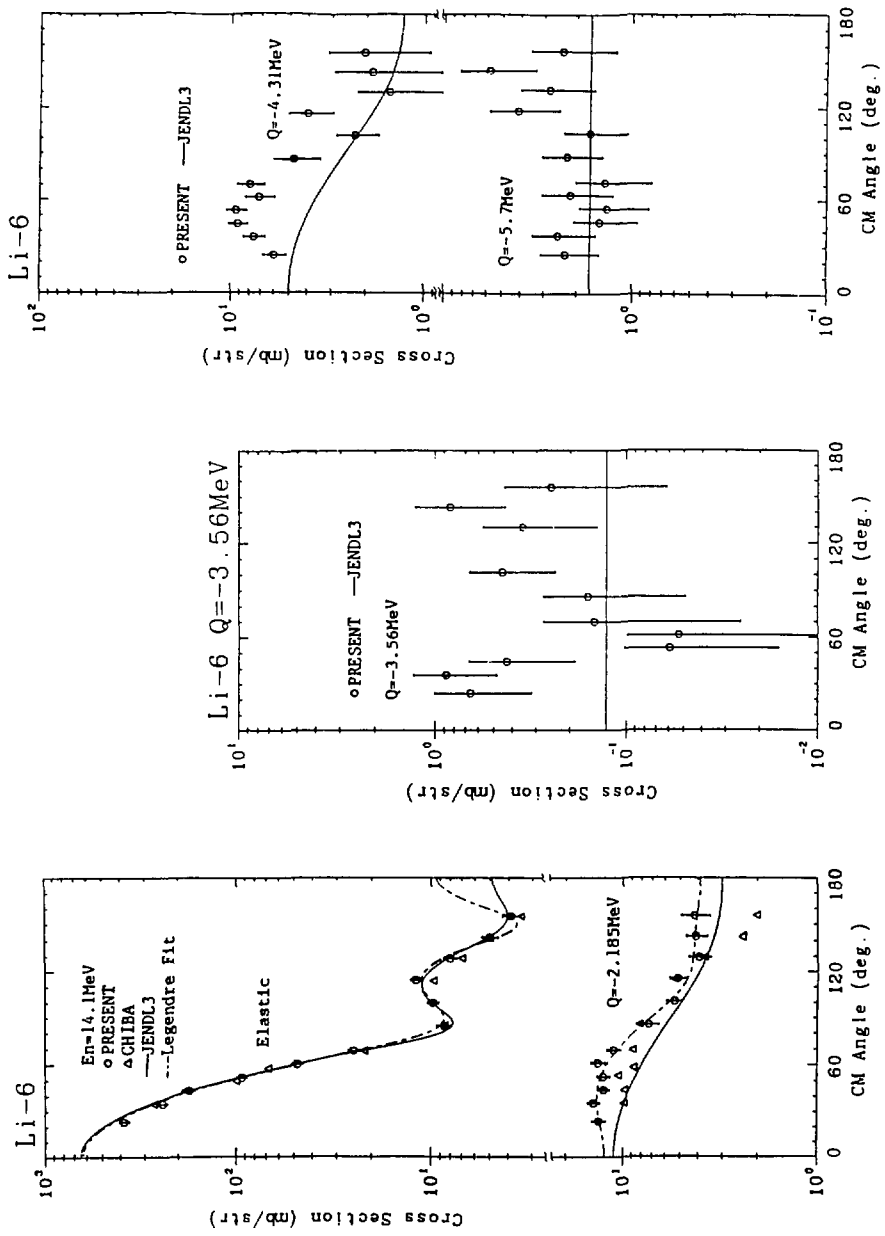

Fig. 8 Differential neutron scattering cross sections of ^{6}Li at 14.1 MeV

3.19 Neutron Cross Section Calculation for ^{56}Fe and ^{235}U in the up to 50 MeV Energy Range

K. Hida and S. Iijima
Nuclear Engineering Laboratory,
Toshiba Corporation
4-1, Ukishima-cho, Kawasaki-ku, Kawasaki-shi, 210

Neutron cross sections are calculated for ^{56}Fe and ^{235}U in the up to 50 MeV energy range. For ^{56}Fe, a comparison is made between ALICE and GNASH using the same calculational parameters. It was found that the difference becomes appreciable when many particle emissions dominate in the high energy region. Calculations are made for ^{235}U only with ALICE, because of its fission cross section calculation capability. Comparisons with experimental data are also given.

1. Introduction

Current evaluated nuclear data libraries include the data induced by neutrons up to 20 MeV incident energy. However, the needs for higher energy data become increased in many fields: astronomy, space technologies, radiation therapy, isotope productions, application of the spallation reactions (accelerator breeding, transmutation of TRU and FP, intense neutron sources, and other nuclear fields), and accelerator shielding. To fulfill their requirements completely, nuclear data should be prepared for protons as well as neutrons in MeV to GeV region.

In this paper, neutron induced data are calculated up to 50 MeV incident energy as the first step for the forthcoming evaluation. We employ two computer codes for calculating these data, namely, ALICE[1,2] and GNASH.[3] While both codes are based on the statistical and preequilibrium processes, GNASH is more sophisticated whereas ALICE is more versatile. One of our aims is a comparison between the two computer codes. The other aim is to examine the ALICE applicability to calculating the actinide cross sections with fission competition.

2. Brief Computer Codes Description

Table 1 summarizes the principal differences between GNASH and ALICE. GNASH is based on the multistep Hauser-Feshbach theory[4] and the

Gilbert-Cameron composite level density formula[5] with low lying discrete levels. The transmission coefficients must be calculated with an external optical model code and provided as input data. In his nuclear cross section calculation system SINCROS,[6] Yamamuro has directly joined the optical model code ELIESE-3[7] to GNASH in which the dimensions for the relevant arrays are extended for the up to 50 MeV incident energy.

ALICE calculates the equilibrium processes with the Weisskopf-Ewing evaporation model[8] or an s-wave approximation.[9] The level density is represented by the Fermi gas model with no discrete level. The transmission coefficients for the entrance channel are provided as input data, or are calculated with parabolic model or in an internal optical model subroutine. The inverse reaction cross sections are provided as input data or calculated with a classical sharp cutoff algorithm or the optical model subroutine. Once the particle widths are calculated for the compound nucleus using the relevant level densities, the same widths are used for the daughter nuclei in subsequent reactions. ALICE accounts for the fission competition, based on the Bohr-Wheeler transition state approach[10] with the single barrier but no tunneling effect.

The preequilibrium modeling is different between the two codes. GNASH is based on the exciton model,[11] while ALICE is based on the geometry-dependent hybrid model.[1] The difference in the underlying physical concept lies in the approximation on the mixing among configurations of the same exciton number; strong mixing in the exciton model versus no mixing in the hybrid model.[12] In the geometry-dependent hybrid model option for ALICE, the nuclear surface diffuseness was introduced to take into account the enhanced particle emissions from the nuclear surface. The Kalbach constant is important to calculate the intranuclear collision probabilities in the exciton model in GNASH, while calculation of those probabilities in ALICE is parameter free. The angular distribution cannot be calculated in the original GNASH. Thus, the Kalbach-Mann systematics[13] are implemented in the SINCROS system. It can be calculated in ALICE, based on nucleon-nucleon scattering kinematics for an incident nucleon on a Fermi gas.[14]

3. Cross Section Calculations

Fe-56

A code comparison is the principal object for ^{56}Fe calculations. To

carry out a reasonable comparison, ALICE was modified so that the Fermi gas level density parameters common to GNASH can be provided as input data. The default parameters in the SINCROS system are used. The transmission coefficients and the inverse reaction cross sections are calculated with ELIESE-3, using the default optical potentials in the SINCROS system given in Table 2. The Kalbach constant used in GNASH is 130 MeV^3, and the equilibrium process is calculated with the evaporation model in ALICE.

The results are given for particle production cross sections in Fig. 1 and isotope production cross sections in Figs. 2 through 4. The agreement between the two codes is fairly good in the low energy region below 15 MeV, but becomes poorer in the higher energy region where many particle emissions occur. The particle emission spectra, bombarded by 15 MeV neutrons, are shown in Figs. 5 and 6 along with the experimental spectra. The calculated angle-integrated spectra agree with each other, but do not agree with the measurements; the agreement could be improved by adjusting, e.g., the level density parameters. The angle-dependent particle spectra are calculated only with ALICE. The agreement is poor, not only with the experiments but also with the Kalbach-Mann systematics.

U-235

For ^{235}U, only ALICE is used because GNASH cannot calculate the fission cross sections. The fission barrier heights defaulted in ALICE are Sierk's rotating finite range model and Cohen's rotating liquid drop model. The transition state level density is represented by the Fermi gas model with a different parameter from the ground state deformation. The ratio a_f/a_n is provided as input data, which is used for all nuclei appearing in the calculation. In the following calculations, photon, neutron, and fission channels are taken into account; a_n=A/9 is used for the ground state deformation with the mass number A; and the entrance channel transmission coefficients and the inverse reaction cross sections are internally calculated using the default optical potential.

The fission cross sections, calculated by using the default barrier heights, are compared with the experimental data in Fig. 7. Since the agreement is poor, the barrier heights and the transition state level density parameter are adjusted so as to reproduce the measured data. The resulting level density parameter, a_f/a_n=0.98, however, is physically unacceptable, because the degree of freedom is higher at the saddle point

than at the ground state deformation and hence a_f/a_n should be greater than 1.0. In contrast to the acceptable agreement of the fission cross sections with experiments as shown in Fig. 8, the agreement between the neutron emitting cross sections shown in Fig. 9 is very poor. This is mainly because the spherical optical potential is not appropriate for calculating the reaction cross sections for the deformed actinide nuclei.

4. Conclusions

The neutron cross sections are calculated up to 50 MeV for ^{56}Fe and ^{235}U. For ^{56}Fe, a code comparison was made between GNASH and ALICE by using the same calculational parameters. Although the cross sections agree fairly well with each other in the lower energies, the difference becomes significant when many particle emissions dominate in the higher energies. Accumulated experience in the use of GNASH has confirmed its applicability below 20 MeV. Hence, GNASH is recommended to use in evaluating non-fissionable nuclei in the higher energy region. The fission and neutron emitting cross sections for ^{235}U, calculated with ALICE, do not agree satisfactorily with the experimental data. The main cause may be attributed to the reaction cross sections calculated with the spherical optical potential. Since, however, ALICE is capable of calculating the fission cross sections, its refinement would be useful for future work.

References

(1) Blann, M. and Vonach, H.K., *Phys. Rev.*, C28, 1475 (1983).
(2) Blann, M. and Komoto, T.T., *Phys. Rev.*, C29, 1678 (1983).
(3) Young, P.G. and Arthur, E.D., LA-6947 (1977).
(4) Hauser, W. and Feshbach, H., *Phys. Rev.*, 87, 336 (1952).
(5) Gilbert, A. and Cameron, A.G.W., *Can. J. Phys.*, 43, 1446 (1965).
(6) Yamamuro, N., *JAERI-M* 88-140 (1988).
(7) Igarasi, S., *JAERI* 1224 (1972).
(8) Weisskopf, V.F. and Ewing, D.H., *Phys. Rev.*, 57, 472 (1940).
(9) Blann, M. and Beckerman, M., *Nucleonika*, 23, 1 (1978).
(10) Bohr, N., and Wheeler, J.A.W., *Phys. Rev.*, 56, 426 (1939).
(11) Griffin, J.J., *Phys. Rev. Lett.*, 17, 478 (1966).
(12) Bisplinghoff, J., *Phys. Rev.*, C33, 1569 (1986).
(13) Kalbach, C. and Mann, F.M., *Phys. Rev.*, C23, 112 (1981).
(14) Blann, M., Scobel, W., and Plechaty, E., *Phys. Rev.*, C30, 1493 (1984).

Table 1 Brief computer codes description

Code	GNASH	ALICE
Version	EGNASH (SINCROS-I)	ALICE/LIVERMORE 85 300
No. of parents	10	9(Z) X 22(A)
Particles	photon, n, p, alpha, d, t, ^{3}He	photon, n, p, alpha, d, fission
Max. En (MeV)	50	300
Eq. process	multistep Hauser-Feshbach	evaporation or s-wave approximation
Level density	Gilbert-Cameron discrete levels	Fermi gas no discrete level
Preeq. model	exciton model	geometry-dependent hybrid model
Ang. dist.	Kalbach-Mann systematics	nucleon-nucleon scattering

Table 2 Default optical potentials

Particle	GNASH[6]	ALICE[1]
n	Walter-Guss	modified Wilmore-Hodgson
p	Perey	modified Perey
alpha	Lemos	unknown
d	Lohr-Haebaeli	unknown
t, ^{3}He	Bechetti-Greenlees	not included

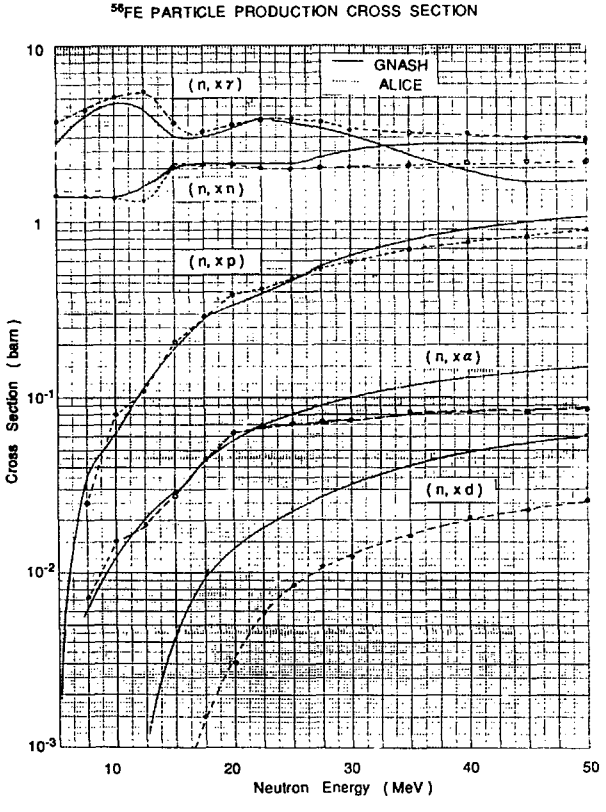

Fig. 1 ^{56}Fe (n,x) particle production cross section

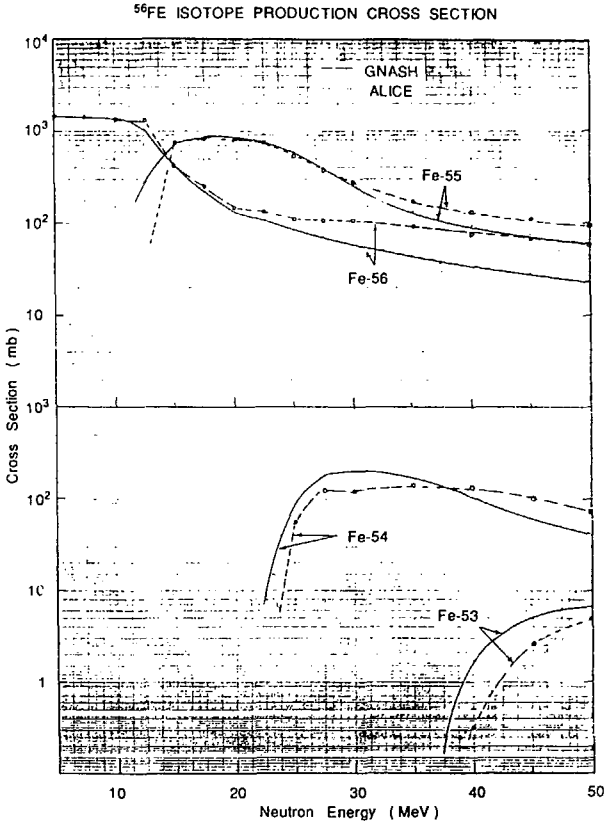

Fig. 2 Fe isotope production cross section from ^{56}Fe (n,x) reaction

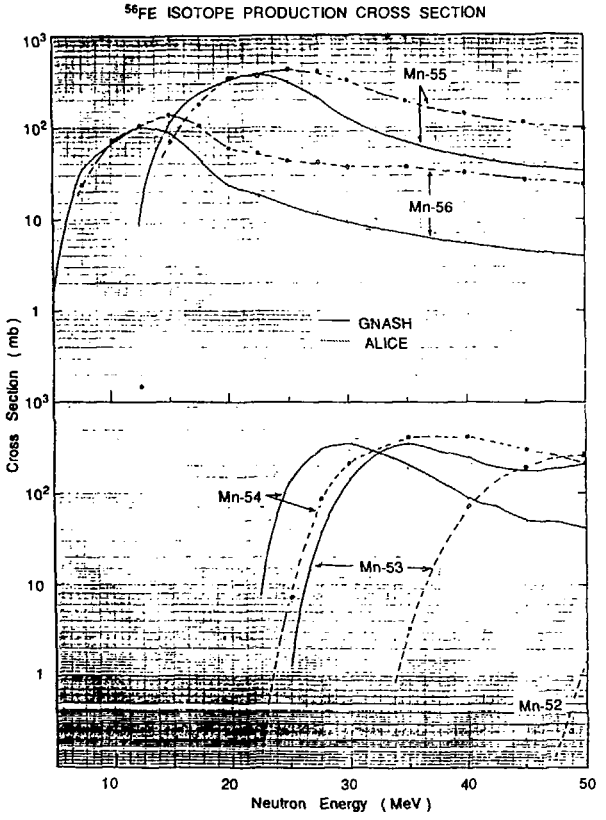

Fig. 3 Mn isotope production cross section from ^{56}Fe (n,x) reaction

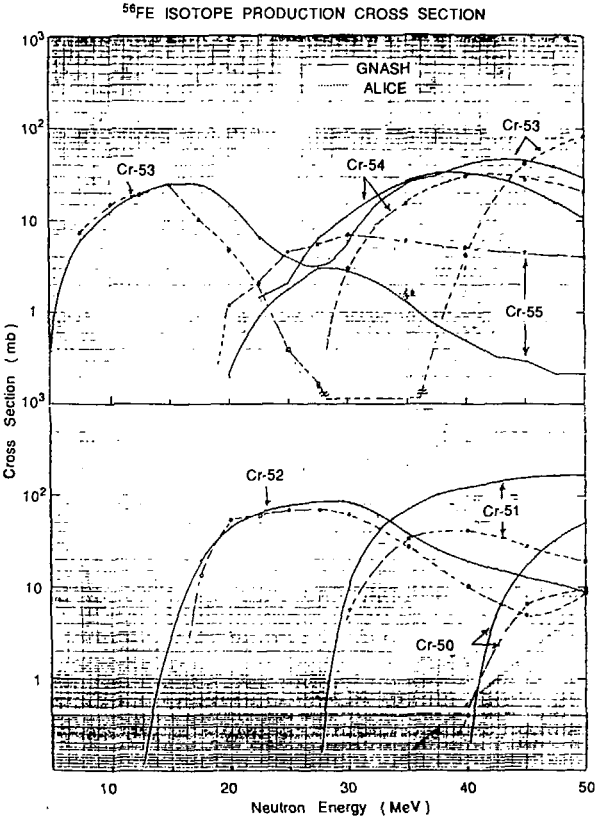

Fig. 4 Cr isotope production cross section from ^{56}Fe (n,x) reaction

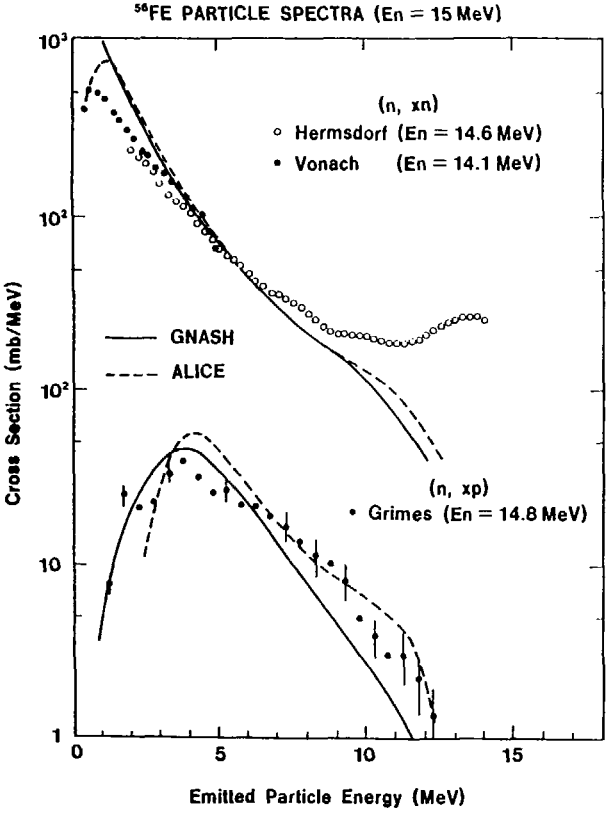

Fig. 5 ^{56}Fe neutron and proton emission spectra

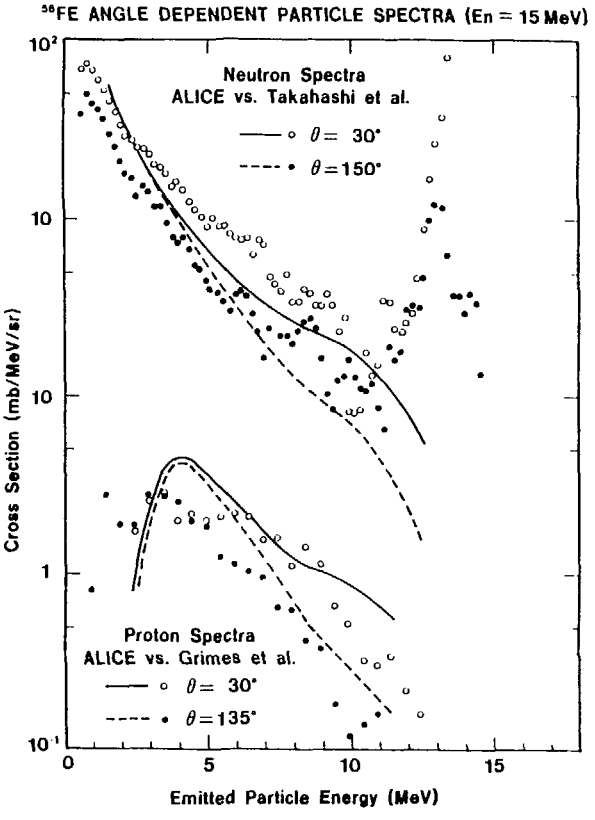

Fig. 6 ^{56}Fe angle-dependent neutron and proton emission spectra

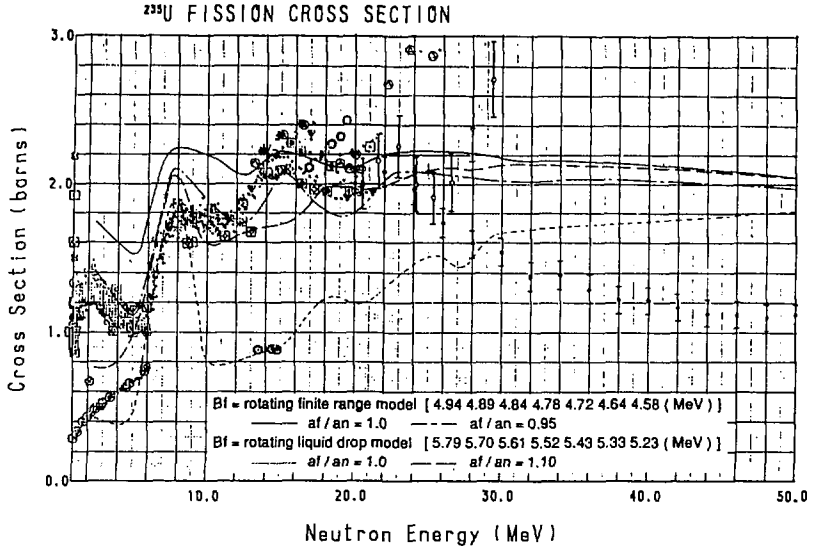

Fig. 7 ^{235}U fission cross sections calculated with default barrier heights

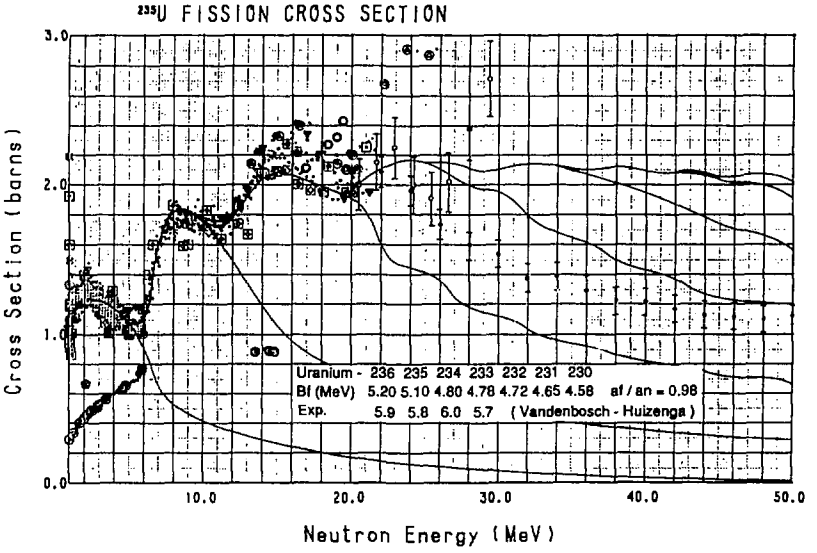

Fig. 8 ^{235}U fission cross sections calculated with adjusted barrier heights and the transition state level densities

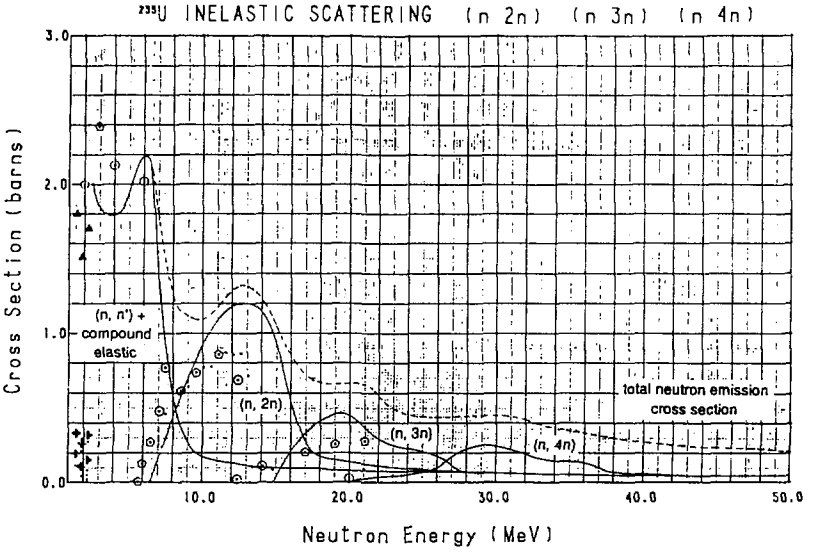

Fig. 9 ^{235}U (n,n'), (n,2n), (n,3n), and (n,4n) cross sections

3.20 One Group Actinide Cross Section Set Based on JENDL-3 and Calculation of ^{232}U Production in Light Water Reactors

Fumihiro Masukawa and Tsuneo Nakagawa
Japan Atomic Energy Research Institute
Tokai-mura, Naka-gun, Ibaraki-ken, Japan
and
Shungo Iijima
Toshiba Corporation
4-1, Ukishima-cho, Kawasaki-ku, Kawasaki, Japan

An extensive one-group cross section set was generated based on JENDL-3 with typical ORIGEN2 spectra of LWRs and FBR, and was compared with ORIGEN2/82 and ENDF/B-V data. Using this cross section set, ^{232}U inventory in LWR was calculated under a clean burnup condition. The effect of lead time before reactor operation is shown as important for a quantitative calculation of ^{232}U inventory. Sensitivity study was made to identify the dominant nuclide transmutation paths and the effect of cross section differences relative to ORIGEN2/82 library.

1. Introduction

^{232}U is formed in ^{235}U/Pu fueled reactor by about 1 ppb at discharge and decays with half-life of 69 y giving rise to a descendant ^{208}Tl which emits strong 2.6 MeV gamma-rays. Hence, accurate prediction of ^{232}U in spent fuel within 10 - 20 % accuracy is required from the aspects of the utilization of reprocessed uranium and assessment of the environmental effect of radioactive waste.

There have been number of calculations concerning ^{232}U production in LWRs and FBRs. Yet it seems not clear that the required accuracy of prediction was attained or not. The reason is probably that (1) the adopted cross section data base is not always well documented, (2) the complexity of nuclide transmutation paths of ^{232}U production prevents the perspectiveness of the calculated results, and (3) the data of nuclide analysis of spent fuel are not well benchmarked.

ORIGEN2 code[1] is frequently used for calculation of actinide inventories using ORIGEN2/82 library[2),3)]. However, in a past decade, there has been significant progress in the knowledge of nuclear data for minor actinides.

Hence, ORIGEN2/82 library should be revised in the light of recent data. Also, questions are often raised from users about the accuracy of ORIGEN2 results.

As an application of actinide cross section data in JENDL-3 to fuel cycle evaluation, the ^{232}U inventory in LWRs was calculated in the present work. Comparison was made with the calculation using ORIGEN2/82 library through direct calculation and the sensitivity analysis.

In Sec. 2, one-group actinide cross sections of JENDL-3 are given in tabular form for typical PWR, BWR, and FBR in comparison with ORIGEN2/82 and ENDF/B-V data. Significant discrepancies among the evaluated data are pointed out and discussed. In Sec. 3, the nuclide transmutation paths are studied carefully including the effect of the lead time before fuel loading as a parameter. The ^{232}U inventories in typical PWR and BWR were calculated under an ideal clean burnup condition using the one-group cross sections. In Sec. 4, the sensitivities of cross sections to ^{232}U inventory are calculated. The sensitivity study was made to identify the dominant transmutation paths and the effect of cross section differences to ^{232}U production.

2. One Group Cross Section Sets

The actinide cross sections of JENDL-3 ranging from ^{230}Th to ^{248}Cm were averaged by typical reactor spectra. The self-shielding effect was not included in the calculation. Besides JENDL-3, ENDF/B-V was also processed and used for comparison with ORIGEN2/82 library.

The typical reactor spectra used for this weighting are the ORIGEN2 spectra of PWRU (for PWR-UO_2), BWRU (for BWR-UO_2), and EMOPU/U/U/C (for the early FBR-MOX core). These spectra are shown in Fig. 1. The ORIGEN2 spectra for LWRs are given only below 10 MeV. In the calculation of spectrum-weighted (n,2n) and (n,3n) cross sections, the neutron spectrum above 10 MeV was supplemented with the Madland-Nix type[4] ^{235}U fission spectrum adopted in JENDL-3. This gives a lower spectrum than the Maxwellian spectrum in the high energy region.

Table 1 lists the spectrum-weighted fission and capture cross sections. Since the self-shielding effect was not included, the fission and capture cross sections for ^{235}U and ^{239}Pu, and the capture cross sections for ^{238}U and ^{240}Pu are not given. Among the average values, discrepancies exceeding 20 % are observed for reactions as follows;

for LWRs, $^{230}Th(n,\gamma)$, $^{231}Pa(n,f)$, $^{236}Pu(n,f)$, $^{242m}Am(n,f)$, $^{242m}Am(n,\gamma)$, $^{242}Cm(n,f)$, $^{242}Cm(n,\gamma)$, $^{243}Cm(n,f)$, $^{243}Cm(n,\gamma)$,

and for FBR, $^{230}Th(n,\gamma)$, $^{231}Pa(n,f)$, $^{231}Pa(n,\gamma)$, $^{232}U(n,\gamma)$, $^{236}U(n,\gamma)$, $^{236}Pu(n,f)$, $^{236}Pu(n,\gamma)$, $^{242m}Am(n,\gamma)$, $^{243}Am(n,\gamma)$, $^{242}Cm(n,f)$, $^{242}Cm(n,\gamma)$, $^{243}Cm(n,\gamma)$, $^{244}Cm(n,\gamma)$, $^{246}Cm(n,\gamma)$, $^{247}Cm(n,\gamma)$.

The cross section profiles of $^{236}U(n,\gamma)$, $^{237}Np(n,\gamma)$, and absorption cross section of ^{236}Pu are shown in Figs. 2 through 4.

Table 2 shows the same comparison for (n,2n) and (n,3n) cross sections. For these reaction cross sections, the discrepancies are considerable, often exceeding a factor of 2. This is partly because of the ambiguity of cross section data near reaction thresholds. Another problem is that the spectrum-weighted (n,2n) and (n,3n) cross sections are very sensitive to the fraction of neutron spectrum above their threshould energy to the whole spectrum. The fraction contributing to this reaction is about only 2 %. The (n,2n) cross sections of ^{237}Np and ^{238}U, and (n,3n) cross section of ^{234}U are shown in Figs. 5 through 7. These reactions are important to estimate ^{232}U formation.

3. Calculation of ^{232}U Inventory

To estimate ^{232}U production analytically, the method of Bateman[5] is used. The following paths are considered for its formation ;

a. $^{235}U \rightarrow ^{236}U \rightarrow ^{237}Np \rightarrow ^{236m}Np \rightarrow ^{236}Pu \rightarrow ^{232}U$,
b. $^{238}U \rightarrow ^{237}Np \rightarrow ^{236m}Np \rightarrow ^{236}Pu \rightarrow ^{232}U$,
c. $^{234}U \rightarrow ^{230}Th \rightarrow ^{231}Pa \rightarrow ^{232}U$,
d. $^{235}U \rightarrow ^{231}Pa \rightarrow ^{232}U$,
e. $^{234}U \rightarrow ^{232}U$,
f. $^{234}U \rightarrow ^{233}U \rightarrow ^{232}U$,
g. $^{235}U \rightarrow ^{236}U \rightarrow ^{232}Th \rightarrow ^{233}U \rightarrow ^{232}U$,
h. $^{238}U \rightarrow ^{239}Pu \rightarrow ^{240}Pu \rightarrow ^{241}Pu \rightarrow ^{241}Am \rightarrow ^{237}Np \rightarrow$
$\rightarrow ^{236m}Np \rightarrow ^{236}Pu \rightarrow ^{232}U$.

The paths c and d are due to the natural decay of the initial ^{234}U and ^{235}U followed by strong neutron captures. The importance of these paths depends on the irradiation time and the lead time. The latter is the time elapsed from the production of yellow cake to the reactor operation. The lead time for commercial LWRs is considered about one year. In the present

study, the lead time and the irradiation condition were taken as parameters.

The ^{232}U production in LWRs was calculated by assuming an irradiation with the total neutron flux of 3.4×10^{14} n/cm^2/s for PWR and 2.2×10^{14} n/cm^2/s for BWR, and by using the JENDL-3 based one group cross sections and ORIGEN2/82 library. However, the cross sections of (n,γ) and (n,f) of ^{235}U, and (n,γ) of ^{238}U were taken from the ORIGEN2/82 because of the reason mentioned above. The paths f,g,h were found to give very small contributions to the ^{232}U production. Hence we considered only the paths a through e .

Figure 8 shows ^{232}U production for each formation path, using JENDL-3 and/or ORIGEN2/82 library with no lead time. Note that ^{236}Pu , whose half life is relatively short (2.85 years) , is added to ^{232}U production so as to obtain maximum estimation. The path of a is found to be most important. Its contribution exceeds 50 % at 1-year irradiation and runs up to 60 - 70 % after 2 year irradiation. The difference between results with JENDL-3 and ORIGEN2/82 is not so large as expected from differences between the two cross section sets and less than 20 % after 1 year irradiation. As described in Sec. 4, this is because of the cancellation of cross section differences.

From only this result, it seems that the paths of c and d are not so important. But taking account of the effect of the lead time, these paths become more important. Table 3 shows the lead time effect on ^{232}U formation as compared with the case of zero lead time. From this table, it is observed that only 1-year lead time makes 12 % increment after 2-year irradiation. And the longer the lead time, and/or the shorter the irradiation time, the effect becomes more significant.

4. Sensitivity Study

To identify the key reactions and the effect of the uncertainties of the cross sections to the ^{232}U formation, the sensitivity study was performed. The sensitivity coefficients of the cross sections to the ^{232}U production were calculated analytically using Bateman's expression for nuclide densities.

Figure 9 shows the relative sensitivities of the various cross sections to the ^{232}U + ^{236}Pu density. The lead time was assumed to be 1 year. The asterisk of ^{237}Np (n,2n*) means the reaction leading to the short time isomer. From this figure, it is seen that ^{237}Np (n,2n*) is the most important reaction. The (n,γ) cross sections of ^{235}U and ^{236}U are the second important, and have almost the same sensitivities, for they are adjacent in the same major path. At short irradiation, ^{238}U(n,2n) in path b, ^{231}Pa(n,γ)

and $^{230}Th(n,\gamma)$ in path c, and $^{234}U(n,3n)$ in path e have comparable sensitivities to those of the (n,γ) cross sections of ^{235}U and ^{236}U in path a. As irradiation time increases, the effects of the reactions become less important to the ^{232}U formation, and $^{235}U(n,f)$, absorptions by ^{236}Pu and ^{237}Np become significant.

Figure 10 shows the changes of the ^{232}U + ^{236}Pu production caused by change of each reaction cross section from ORIGEN2/82 to JENDL-3. It is observed that the effects of the cross section changes in the same path are negated each other, for example , $^{236}U(n,\gamma)$ and $^{237}Np(n,2n^*)$, absorptions of ^{236}Pu and ^{237}Np.

5. Summary

An infinite dilution one-group cross-section sets for actinides ranging from ^{230}Th to ^{248}Cm was generated from JENDL-3 and ENDF/B-V for typical LWRs and FBR spectra in ORIGEN2. Modification to include the self-shielding effect and extension to other neutron spectral fields are planned to provide a reliable cross section data base for fuel cycle evaluation.

By using the one-group cross section sets as well as ORIGEN2/82, the ^{232}U inventory in LWR was calculated and the dominant path of the ^{232}U production was studied. It was found that the path of a mentioned in Sec. 3 was the most important, and the $^{237}Np(n,2n^*)$ cross section was the most sensitive to the results. It was also shown that for a quantitative calculation of ^{232}U inventory the lead time before fuel loading should be taken into account. The calculations of ^{232}U production for LWR using JENDL-3 and ORIGEN2/82 are in reasonable agreement in spite of the considerable discrepancies in the cross sections. The sensitivity analysis, however, showed that the agreement of both results was largely due to the cancellation of effects of individual cross section differences.

Although there has been significant progress in the actinide nuclear data, cross sections of many minor actinides are still not known experimentally or not evaluated with sufficient accuracies. The integral data on nuclide inventories of spent fuel will be helpful to improve the present status of the minor actinide cross sections, as shown in this work.

References

1. Croff, A. G., " ORIGEN2 - A Revised and Updated Version of the Oak Ridge Isotope Generation and Depletion Code, " ORNL-5621 (1980)
2. Croff, A. G., et al., " Revised Uranium-Plutonium Cycle PWR and BWR Models for the ORIGEN Computer Code, " ORNL/TM-6051 (1978)
3. Croff, A. G., et al., " LMFBR Models for the ORIGEN2 Computer Code, " ORNL/TM-7176 (1981)
4. Madland, D. G., and J. R. Nix, " New Calculation of Prompt Fission Neutron Spectra and Average Prompt Neutron Multiplicities, " Nucl. Sci. Eng., **81**, 213 (1982)
5. Vondy, D. R., " Development of a General Method of Explicit Solution to the Nuclide Chain Equations for Digital Machine Calculations, " ORNL/TM-361 (1962)

Table 1 The spectrum-weighted fission and capture cross sections

(BARN)

NUCLIDE		PWR (N,F)	PWR (N,G)	BWR (N,F)	BWR (N,G)	FBR (N,F)	FBR (N,G)	NUCLIDE		PWR (N,F)	PWR (N,G)	BWR (N,F)	BWR (N,G)	FBR (N,F)	FBR (N,G)
TH-230	JENDL-3	0.0520	28.0	0.0448	29.1	0.0304	0.360	PU-240	JENDL-3	0.547	***	0.497	***	0.391	***
	ENDF/B5	0.0576	23.3	0.0486	24.2	0.0322	0.168		ENDF/B5	***	***	***	***	***	***
	ORIGEN2	0.0578	23.5	0.0489	24.4	0.0344	0.197		ORIGEN2	0.584	104.	0.527	111.	0.411	0.513
TH-232	JENDL-3	0.0239	3.07	0.0192	3.21	0.0119	0.349	PU-241	JENDL-3	139.	46.3	142.	47.5	2.48	0.465
	ENDF/B5	***	***	***	***	***	***		ENDF/B5	***	***	***	***	***	***
	ORIGEN2	0.0222	3.05	0.0179	3.20	0.0119	0.383		ORIGEN2	118.	38.7	126.	41.5	2.51	0.462
PA-231	JENDL-3	0.292	59.9	0.257	61.9	0.197	1.74	PU-242	JENDL-3	0.398	30.2	0.353	31.2	0.275	0.467
	ENDFB/5	0.355	56.5	0.317	58.4	0.257	2.96		ENDF/B5	0.398	33.8	0.354	34.8	0.276	0.425
	ORIGEN2	0.368	67.4	0.330	69.8	0.275	2.94		ORIGEN2	0.415	31.7	0.404	33.1	0.296	0.427
PA-233	JENDL-3	0.107	25.2	0.0916	26.1	0.0643	1.37	AM-241	JENDL-3	1.14	120.	1.10	124.	0.290	1.68
	ENDF/B5	***	***	***	***	***	***		ENDF/B5	1.12	121.	1.08	124.	0.311	1.69
	ORIGEN2	0.146	24.7	0.119	25.6	0.0768	1.06		ORIGEN2	1.12	119.	1.13	122.	0.333	1.73
U -232	JENDL-3	16.2	9.69	16.7	10.0	1.99	0.281	AM-242M	JENDL-3	780.	153.	796.	156.	3.03	0.528
	ENDF/B5	18.2	12.9	18.8	13.4	2.19	0.650		ENDF/B5	814.	165.	831.	168.	3.89	0.380
	ORIGEN2	16.8	11.3	17.3	11.7	2.30	0.653		ORIGEN2	466.	98.0	476.	100.	4.04	0.393
U -233	JENDL-3	65.8	7.91	67.6	8.14	2.67	0.242	AM-243	JENDL-3	0.417	51.4	0.371	53.3	0.213	1.51
	ENDF/B5	***	***	***	***	***	***		ENDF/B5	0.393	50.8	0.339	52.7	0.245	1.02
	ORIGEN2	62.3	7.58	64.5	7.84	2.73	0.268		ORIGEN2	0.396	49.8	0.385	51.6	0.261	1.08
U -234	JENDL-3	0.461	22.6	0.415	23.6	0.338	0.496	CM-242	JENDL-3	1.46	4.51	1.42	4.68	0.739	0.490
	ENDF/B5	0.497	23.6	0.452	24.6	0.347	0.579		ENDF/B5	0.576	5.91	0.530	6.14	0.179	0.300
	ORIGEN2	0.450	19.2	0.397	20.9	0.371	0.611		ORIGEN2	0.559	5.80	0.555	6.03	0.191	0.337
U -235	JENDL-3	***	***	***	***	***	***	CM-243	JENDL-3	94.9	15.4	97.6	15.8	2.94	0.361
	ENDF/B5	***	***	***	***	***	***		ENDF/B5	111.	11.5	114.	11.8	2.57	0.234
	ORIGEN2	46.7	10.5	50.0	11.2	1.92	0.558		ORIGEN2	71.7	8.39	74.1	8.70	2.68	0.244
U -236	JENDL-3	0.297	8.53	0.273	8.98	0.110	0.428	CM-244	JENDL-3	0.800	15.9	0.750	16.9	0.442	0.665
	ENDF/B5	0.295	8.59	0.272	9.05	0.112	0.535		ENDF/B5	0.876	14.1	0.831	15.0	0.442	0.816
	ORIGEN2	0.198	7.54	0.165	8.25	0.119	0.551		ORIGEN2	0.875	13.8	0.871	14.4	0.472	0.834
U -238	JENDL-3	0.0939	***	0.0763	***	0.0477	***	CM-245	JENDL-3	150.	24.1	154.	24.7	2.60	0.336
	ENDF/B5	***	***	***	***	***	***		ENDF/B5	184.	31.4	189.	32.2	2.61	0.313
	ORIGEN2	0.100	0.902	0.0808	0.919	0.0499	0.288		ORIGEN2	171.	29.1	175.	29.7	2.65	0.311
NP-237	JENDL-3	0.478	37.9	0.426	39.1	0.343	1.58	CM-246	JENDL-3	0.527	3.18	0.479	3.30	0.289	0.327
	ENDF/B5	0.488	35.2	0.436	36.3	0.352	1.62		ENDF/B5	0.572	2.92	0.516	3.02	0.286	0.222
	ORIGEN2	0.524	32.1	0.462	34.1	0.377	1.52		ORIGEN2	0.576	2.91	0.568	3.03	0.307	0.235
PU-236	JENDL-3	14.6	21.1	14.8	21.9	0.675	0.914	CM-247	JENDL-3	22.2	17.5	22.9	18.1	2.26	0.462
	ENDF/B5	22.3	21.4	22.8	22.0	1.47	0.368		ENDF/B5	25.3	16.4	26.2	17.1	1.93	0.305
	ORIGEN2	20.6	20.4	21.4	21.1	1.53	0.392		ORIGEN2	25.5	16.5	26.2	17.0	1.93	0.305
PU-238	JENDL-3	2.73	40.8	2.73	41.9	1.13	0.649	CM-248	JENDL-3	0.728	6.70	0.698	7.10	0.307	0.250
	ENDF/B5	2.63	42.3	2.63	43.4	1.13	0.708		ENDF/B5	0.694	6.45	0.649	6.82	0.321	0.232
	ORIGEN2	2.47	34.7	2.49	37.3	1.19	0.731		ORIGEN2	0.756	6.32	0.756	6.60	0.343	0.248
PU-239	JENDL-3	***	***	***	***	***	***								
	ENDF/B5	***	***	***	***	***	***								
	ORIGEN2	106.	58.6	114.	63.1	1.85	0.502								

Table 2 The spectrum-weighted (n,2n) and (n,3n) cross sections

(MILLI-BARN)

NUCLIDE		P W R	B W R	F B R
TH-232	JENDL-3	4.44	3.22	2.05
	ENDF/B5	***	***	***
	ORIGEN2	5.09	3.74	1.79
U -233	JENDL-3	0.562	0.408	0.250
	ENDF/B5	***	***	***
	ORIGEN2	2.86	2.10	0.641
U -234 (N,2N)	JENDL-3	1.46	1.06	0.694
	ENDF/B5	0.461	0.336	0.234
	ORIGEN2	2.86	2.10	0.641
U -234 (N,3N)	JENDL-3	4.03-3	2.94-3	3.75-3
	ENDF/B5	4.47-3	3.26-3	4.10-3
	ORIGEN2	1.35-2	1.03-2	2.01-3
U -238	JENDL-3	3.74	2.71	1.69
	ENDF/B5	***	***	***
	ORIGEN2	5.53	4.04	1.78
NP-237	JENDL-3	0.947	0.688	0.457
	ENDF/B5	0.432	0.314	0.209
	ORIGEN2	1.06	0.813	0.501
PU-239	JENDL-3	1.09	0.793	0.468
	ENDF/B5	***	***	***
	ORIGEN2	1.12	0.818	0.382

Table 3 The lead time effect on ^{232}U production [%] (Relative to the case of the zero lead time)

Irradiation Time (Years)	0.5	1	2	3	4
Lead Time (Years) 0.5	+23	+12	+5.9	+3.8	+2.8
" 1	+45	+25	+12	+7.5	+5.3
" 2	+91	+49	+24	+15	+11

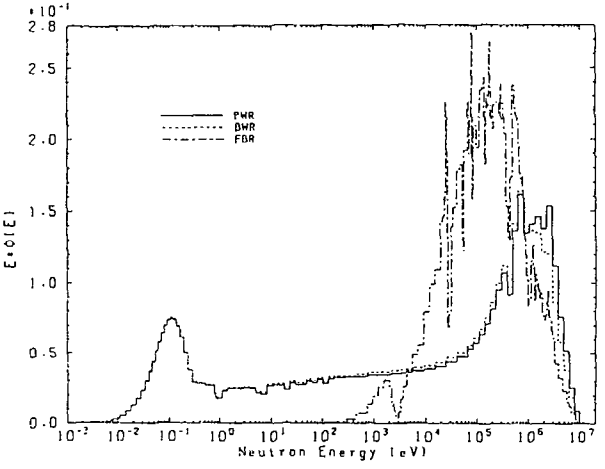

Fig. 1 Typical neutron energy spectra

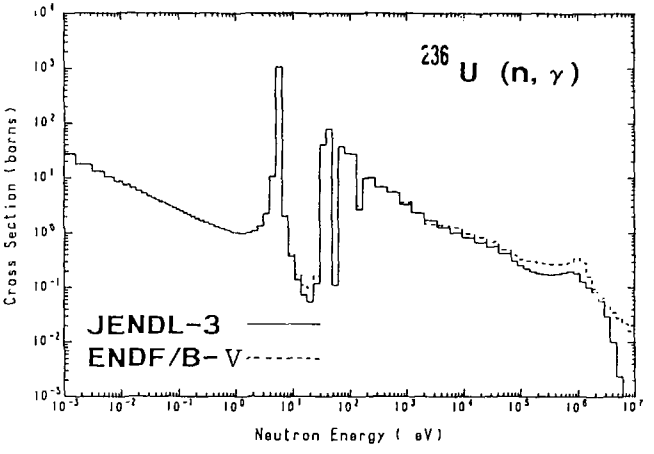

Fig. 2 ^{236}U (n,γ) cross section

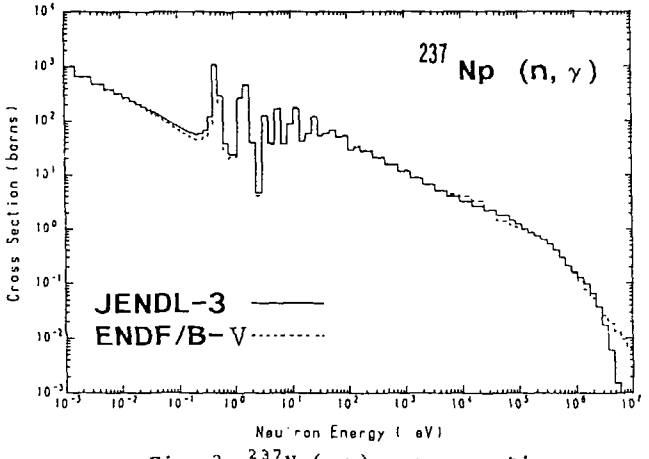

Fig. 3 ^{237}Np(n,γ) cross section

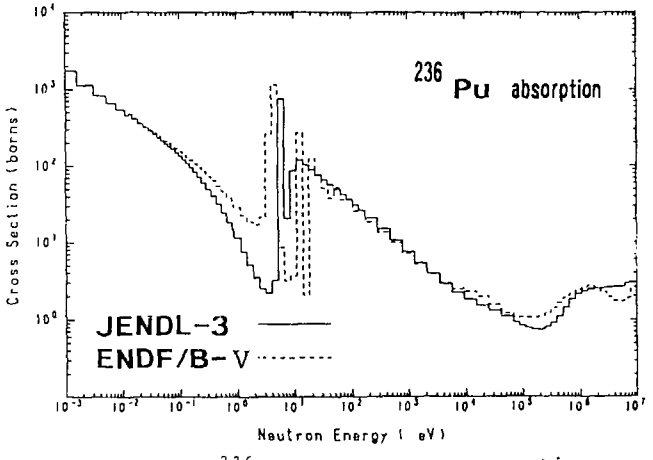

Fig. 4 ^{236}Pu absorption cross section

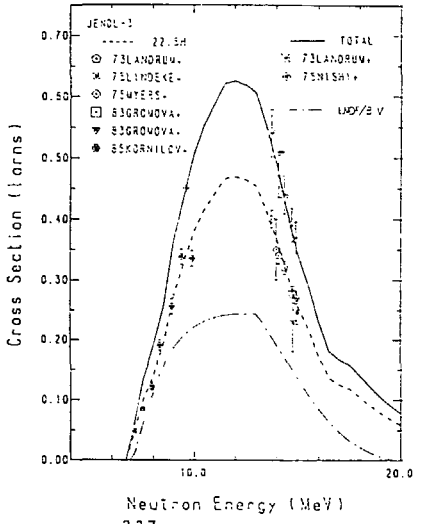

Fig. 5 ^{237}Np(n,2n) cross section

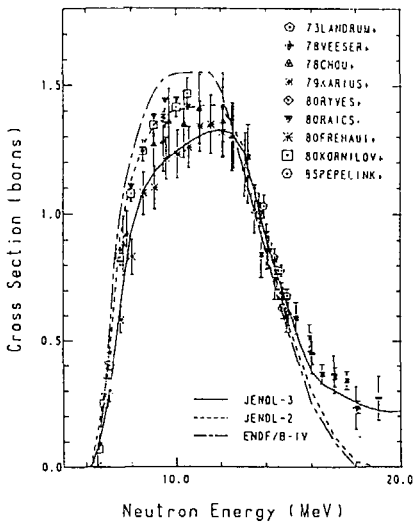

Fig. 6 ^{238}U(n,2n) cross section

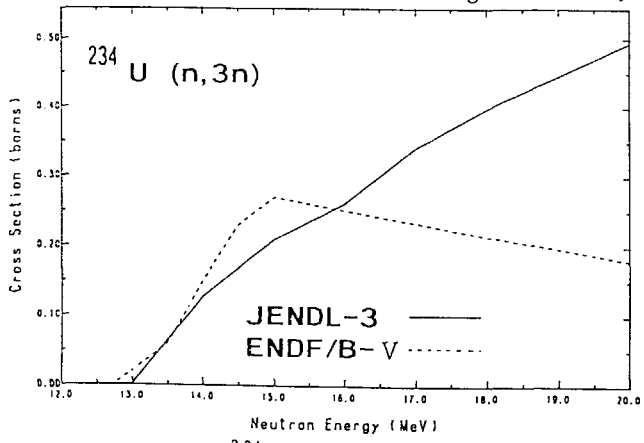

Fig. 7 ^{234}U(n,3n) cross section

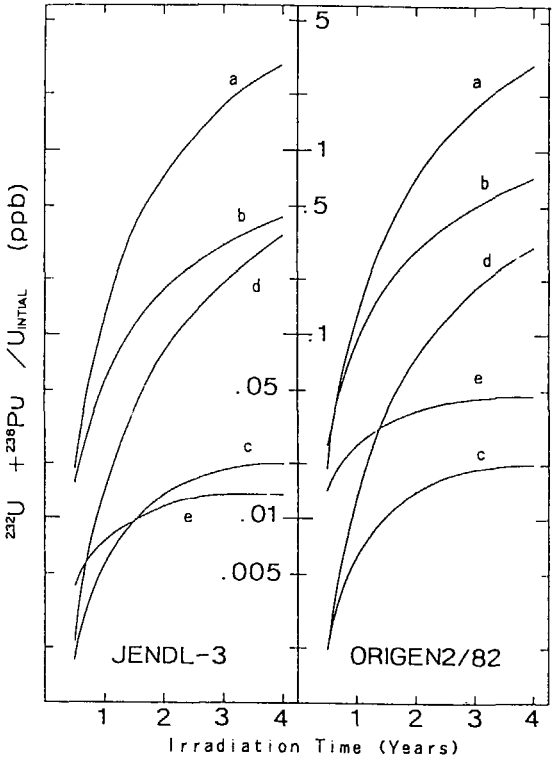

Fig. 8 ^{232}U+^{236}Pu production for each formation path

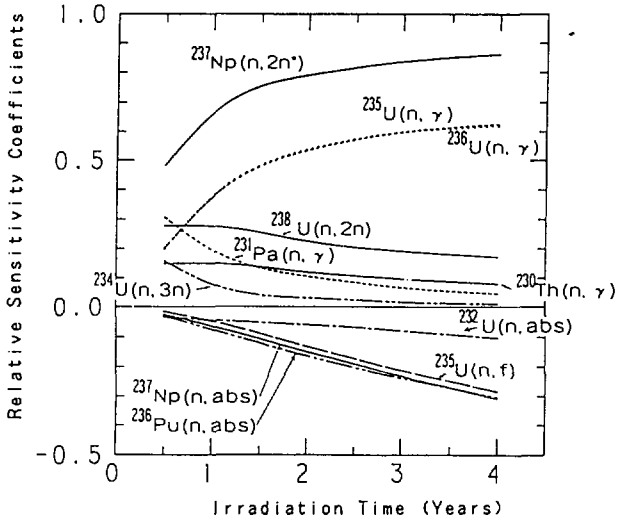

Fig. 9 Sensitivities of important cross sections to the ^{232}U production

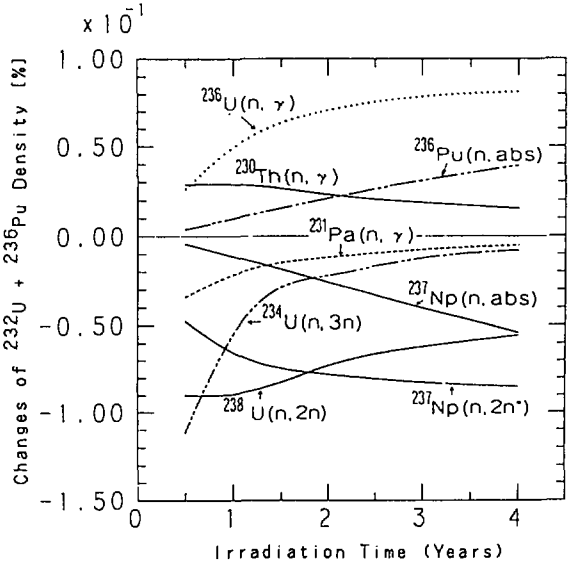

Fig. 10 Effect of disrepancies of important cross sections